ISSN 1018-5593

ANNUAL·REPORT·93

European Commission

Institute FOR Transuranium Elements

JOINT
RESEARCH
CENTRE
EUROPEAN COMMISSION

Report

EUR 15741 EN

COMMISSION OF THE EUROPEAN COMMUNITIES

Joint Research Centre

INSTITUTE
FOR TRANSURANIUM ELEMENTS
KARLSRUHE

Annual Report 1993

TUAR-93

1994

EUR 15741 EN

Published by the
EUROPEAN COMMISSION
Directorate-General XIII
Telecommunications, Information Market and Exploitation of Research
L-2920 Luxembourg

This report was compiled and edited by H. E. Schmidt, J. Richter, and L. Ruczka

Inquiries for more details should be addressed to the Programme Office,
Institute for Transuranium Elements, P. O. Box 2340, D-76125 Karlsruhe,
Phone 07247-951-386, FAX 07247-951-591

For further information concerning JRC programmes please contact the
Directorate General Science, Research and Development of the
European Commission, 200 rue de la Loi, B-1049 Brussels, Belgium

Luxembourg: Office for Official Publications of the European Communities, 1994

ISBN 92-826-4367-0

Printed in *Germany*

Abstract

Basic Safety Research with Nuclear Fuels concentrated in 1993 on studies of high burn-up UO_2 in order to elucidate mechanisms leading to changes in structure and composition at the outer surface of the fuel pellets (RIM effect). The structural changes (polygonisation) observed after extended irradiation could be reproduced in simulation experiments by high dose ion implantation with fission products. For the first time, the oxygen potential in the rim region of high burn-up fuel could be determined. - In a theoretical study, heat exchange mechanisms operative in uranium dioxide at elevated temperatures were identified and possible contributions (lattice vibrational and electronic) to the specific heat of UO_2 were further analysed. - After conclusion of Knudsen cell effusion measurements with simulated fuel (SIMfuel), a specimen of irradiated UO_2 was introduced into the installation and a first series of vapour pressure measurements with genuine high burn-up fuel was successfully performed. The equipment is now ready to be used for high burn-up fuel analyses and source term studies. - New program options became available for the TRANSURANUS fuel pin code which is more and more being used by external partners from science, industry, and licensing authorities.

Safety Aspects of Fuel Operation and Handling were dominant in the design and execution of the POMPEI high burn-up irradiation experiment under execution in the Petten High Flux Reactor. Besides equipment for studying the long-term irradiation behaviour of mixed nitrides, the POMPEI device contains technetium samples for transmutation studies. - Slightly radioactive aerosols (UO_2) were introduced into the installation to study the mechanisms governing the transport of big particles in ducts under turbulent flow conditions.

Actinide Determination and Recycling concentrated on partitioning and transmutation studies: The results of the first series of fast flux minor actinide oxide irradiations (SUPERFACT I) were analysed, possible P&T schemes were reviewed and two methods for actinide partitioning from highly active waste, based on TRPO and on CMPO,were tested with real HAW and in there performance compared.

Electrochemical techniques were extensively used to investigate UO_2 corrosion in aqueous solution in the context of studies on the **Characterisation of Waste Forms and of High Burn-Up Fuel.** Leaching studies under highly oxidizing conditions were performed with LWR fuel, and the comparison of leach rates of UO_2 and glass in the presence of granite was continued. In order to clarify the chemistry at the fuel periphery, the properties of cesium uranate compounds were studied and material from the cladding/fuel interface was analysed by ICP-mass spectrometry.

Preparative work for **Basic Actinide Research** concentrated on magnetic compounds of the $ThMn_{12}$ structure type and on actinide containing compounds with compositions 1:1:3, 1:1:1, and 2:2:1. A theory of the optical properties of thorium. protactinium, and uranium was developed. Magnetic moments, exchange interactions and ordering temperatures of gadolinium and curium under pressure were calculated. Single crystals of NpAs were subject to resonant magnetic X-ray scattering experiments. Mössbauer investigations with neptunium compounds were continued, muon spin rotation studies were performed with uranium compounds with the $AuCu_3$ structure. The electrical resistance of PuSb and the optical response of NpSb and PuSb were investigated under pressure, and a new high-pressure X-ray diffraction study of americium was undertaken.

Under **Exploratory Research**, the frequency dependence of acoustic aerosol agglomeration was investigated in detail.

The majority of the Institute's **Scientific-Technical Support to Community Policies** concerned work for the safeguarding of fissile materials: Preparations for the installation and operation of on-site analytical laboratories in Sellafield and La Hague were continued, and new analytical techniques - ICP-MS in combination with laser ablation and glow discharge mass spectrometry, and the determination of $^{238}Pu/^{239}Pu$ ratios via total evaporation mass spectrometry - were perfected.

Contract Work was pursued along several lines: The radiotherapeutical study involving ^{213}Bi and ^{225}Ac was extended to the interaction of these nuclides with human cells.The preparation and characterisation of MA-containing alloys for transmutation studies was continued. Fission product release studies and pre-test fuel characterisation were performed for the PHEBUS PF project. Fuel discs with various characteristics were fabricated and sent to Halden for an irradiation experiment aimed to clarify mechanisms and consequences of the RIM effect.

Commission of the European Communities
Joint Research Centre

TUAR 93

European Institute
for Transuranium Elements
Annual Report

January - December 1993

Table of Contents

MAIN ACHIEVEMENTS AND MILESTONES

Foreword

to the Annual Progress Report 1993
of the European Institute for Transuranium Elements
by J. van Geel, Director

Research on the safety of nuclear power is pursued with high priority according to well defined internationally coordinated programmes. Nevertheless, it seems worthwhile to take, from time to time, a fresh look at the problems involved and to reconsider medium and long-term safety strategies in fuel and waste management so as to pave the way for their wider public acceptance.

When reflecting on future nuclear systems one should be aware of the fact that, with the third generation of nuclear reactors on the drawing boards, we still pursue a first generation fuel cycle strategy. This is not due to a lack of imagination, but a consequence of major economic and political constraints. More than thirty years have elapsed since these strategies were defined. In response to todays much wider public awareness of environmental problems, large efforts are necessary to readjust the balance of safety and economy.

Apart from reactor safety, the issues to reconsider are waste management and fissile materials control. And it is under this aspect, that during the coming years research efforts will have to be stepped up to study the technical possibilities, the limitations and the safety aspects of nuclear incineration, the implications of direct storage of spent fuel, the possibilities to further improve safeguarding measures, and the potential of new types of fuel. Thereby keeping in mind that nuclear power should remain economically competitive with conventional sources of energy. Which means that any improvement must be compatible with present day reactor designs or their derivatives, and that efforts have to be made to exploit the existing concepts to their very limits.

Long-range planning of nuclear safety research should, in addition, take into account also the expected availability of huge stockpiles of HEU and Pu from disarmament activities, as well as the necessity to implement a world-wide accepted nuclear safety culture.

The Institute for Transuranium Elements is prepared to contribute to the solution of the above problems.

Karlsruhe, in May 1994

Executive Summary

In **Basic Safety Research on Nuclear Fuels**, work to provide basic fuel data and the improvement of existing fuel pin behaviour codes was the main objective in 1993. The emphasis was on the behaviour of LWR fuel at high burn-up. Studies on simulated high burn-up fuel (SIMFUEL) were continued and advanced diagnostic techniques were used to investigate fuel structures resulting from heavy ion bombardment. A wealth of data from previous post-irradiation examinations of high burn-up fuel was analysed and evaluated, and an in-pile experiment to produce and to study specific structural changes at the fuel surface (rim effect) was prepared and initiated. - Work related to reactor safety dealt with experimental source term studies by Knudsen cell effusion measurements. A laser flash apparatus for measuring the thermal diffusivity of irradiated samples underwent extensive "cold" testing.

Safety Aspects of Fuel Operation and Handling were studied by investigating the operational limits of future fuels in the Petten High Flux Reactor (experiments NILOC 3 and NILOC 4). Extremely high burn-ups (up to 27.8 at/o) will be achieved in the course of 1994 with the POMPEI device, which contains also a number of technetium- and Tc/Ru-pellets in order to obtain information on their long-term irradiation behaviour in transmutation experiments. - Detailed information on the transport of large radioactive aerosol particles with diameters >10 µm was obtained from an evaluation of the latest TRABI experiments.

Partitioning and transmutation of long-lived nuclear waste constituents dominated the activities in the field of **Actinide Determination and Recycling** also in 1993. After the successful conclusion of a first series of pilot experiments to transmute minor actinides in oxide form into short-lived fission products in a fast reactor, a thorough analysis of the pre- and post-irradiation data has been performed in order to compare calculated and measured transmutation rates. - The present status of research in the field of P&T has been reviewed and advantages and drawbacks of various transmutation schemes have been compared. - Partitioning studies have been performed with different extractants. - Preparations for a second large-scale irradiation in a fast flux (SUPERFACT II) to test the technical feasibility of the concept has been started.

Studies on the **Characterisation of Waste Forms and of High Burn-Up Fuel** in 1993 were concerned a) with spent fuel properties and their variation under long-term storage conditions and b) with fuel and fission product behaviour at extended burn-up. Electrochemical fuel properties determine, to a large extent, the stability of UO_2 in a final repository and the rates of UO_2 and fission product leaching at groundwater contact. It thus appeared desirable to study these properties in detail with fresh and irradiated material. First "cold" tests are reported with a set-up which is to be used for the investigation of irradiated UO_2 in a hot cell. These studies are complemented by investigations of the leaching behaviour of irradiated UO_2 under highly oxidizing conditions, and by a comparison of the leach rates from spent UO_2, $ThPuO_2$, from MOX fuel and unirradiated UO_2. In addition, the study of the influence of granite on spent fuel leaching has been continued. A thorough investigation of UO_2 oxidation during dry storage, at temperatures below 500 °C, is under preparation. - An instrument for the non-destructive spent fuel characterisation, based on passive neutron and gamma interrogation, has been refined and underwent testing with irradiated UO_2 and MOX fuel rods. - Preliminary results of hot cell annealing tests with subsequent determination of the spatial fission product distribution in the fuel and the analysis of the released fission products became available. They have to be substantiated.

In **Actinide Research,** work on the preparation, the crystal chemistry and the study of physical properties of families of isostructural actinide compounds was continued. Samples prepared at the Institute were used for collaborative investigations of the Hall effect (with CEN Grenoble), for Mössbauer spectroscopy (with CEN Grenoble and TU München), for neutron scattering experiments (in Grenoble and in Los Alamos), for X-ray scattering studies (at the Brookhaven National Laboratory), for measurements of specific heat and of magnetic properties (at the University of Amsterdam) and for muon spin rotation studies (in collaboration with TU München). Of particular interest were compounds with compositions 1:13, 1:1:1, and 2:2:1. Binary technetium alloys were synthesized. - Theoretical studies concerned the optical properties of thorium, protactinium, and uranium metals. The magnetic moments, exchange mechanisms and ordering temperatures of gadolinium and curium under pressure were calculated. - NpAs single crystals were subject to resonant X-ray magnetic scattering experiments. - X-ray and high-resolution UV photoelectron emission studies clarified the 5f electron localisation in a- and d-plutonium. - Mössbauer investigations were extended to $Np_{0.5}U_{0.5}Pd_2Al_3$, $Np_{0.3}U_{0.7}Pd_2Al_3$ and $NpNi_2Al_3$, the latter being the isostructural Np analogue to the heavy fermion superconductor UNi_2Al_3. The Np compound, in contrast to UNi_2Al_3 , showed magnetic order. - In high pressure studies, the resistivity and the superconductive properties of americium were studied up to 25 GPa and the variations of structural and physical properties of certain actinide compounds with pressure were compared. The optical reflectivity of NpSb and PuSb was measured and its pressure dependence studied at room temperature between ambient pressure and 60 GPa .

Exploratory Research dealt with an investigation of the temporal change in size distribution of glycol fog droplets subject to soundwaves with frequencies of 10 kHz and 21 kHz. The results could be well understood and extrapolated to other frequencies with the help of a dimensionless particle size scaling parameter.

In 1993, **S/T-Support to the Services of the European Commission** concerned the transfer of technologies developed in ITU laboratories to external industrial users (DG XIII) and supporting work for the analysis of fissile materials (DG XVII).

In order to adapt the acoustic aerosol scavenging technique to industrial air cleaning, experiments with glycol fog were carried out in which larger "inertial" particles were added in several bursts. As one would expect for orthokinetic agglomeration, the agglomeration coefficient increased linearly with the number of inertial particles added. It could be shown, however, that also hydrodynamic interactions contribute significantly to the agglomeration process.

Work has started to adapt a six-wavelength pyrometer, which was originally designed for measurements of high temperatures ($>$ 1400 K), to a lower temperature range, which should make the instrument more attractive for a wide range of industrial applications.

Field testing of equipment for on-site sample conditioning by robots in the Gatchina pilot reprocessing facility was continued. Comparative analyses of samples, which had been prepared with improved techniques, were carried out at the Khlopin Radium Institute in St.Petersburg (Russia), in the IAEA Safeguards laboratories in Seibersdorf (Austria) and at ITU. A final evaluation of the results is foreseen for 1994.

Components for the safeguards analysis at the on-site laboratory in Sellafield (OSL) were tested under realistic conditions, and various non-destructive analytical methods were adapted for use in the British reprocessing plant.

A number of improvements were necessary to optimize the expert system used at ITU for the evaluation of safeguards analyses, and the main VAX installation had to be upgraded.

Training of staff for the on-site lab at the La Hague plant in France was continued with three teams of four operators each, working under simulated realistic conditions.

Analytical techniques for safeguards applications were developed and further refined. Isobaric interferences could be eliminated by the use of isotope-dilution ion-chromatography in combination with mass spectrometry for the determination of Pu and Nd in spent fuel. Laser ablation combined with ICP-MS has successfully been employed for measuring the spatial distribution of fission products across a spent fuel rod section. The glow discharge mass spectrometer underwent hot testing with isotope abundance studies and trace metal analysis in uranium metal. - ^{238}Pu/^{239}Pu ratios could be determined with high precision from total evaporation mass spectrometry data.

Following a request from the International Atomic Energy Agency, methods of monitoring undeclared Pu and HEU production were suggested. Further testing of the suggested methods will be carried out in a specially designed "clean room".

In 1993, new **contracts with Third Parties** worth 1.670 kECU have been signed. This brings the total volume of contracts under execution at ITU on December 31, 1993 to 23 million ECU. By the end of 1993, additional contracts totalling 412 kECU were under negotiation.

Among the main achievements of the reporting period was the in-vitro demonstration of cell killing with specific ^{213}Bi-labelled antibodies. The results justified the continuation of preclinical studies with ^{225}Ac- and ^{213}Bi-immunoconjugates for application in the treatment of cancer.

Preparations to produce minor actinide-containing metallic test fuel for irradiation in the PHENIX reactor were terminated. Fabrication of the fuel is to start early in 1994.

Irradiated fuel rods from the BR3 reactor in Mol were characterised by several methods for the PHEBUS-PF in-pile fission product release experiments to be performed in Cadarache, France. - The thermal conductivity of the ceramic shroud material of the PHEBUS-PF in-pile set-up was measured and its structural and chemical stability during typical thermal treatments tested.

Post-irradiation examination of power reactor fuel rods by destructive and non-destructive techniques was continued according to schedule.

182 UO_2-based fuel specimens were fabricated and shipped to Halden, Norway, for an irradiation experiment designed to investigate and evaluate the effect of microstructural changes in the outer regions of LWR fuel pellets (RIM-effect) on fuel rod performance.

Work performed at the Institute for Transuranium Elements in 1993 resulted in 96 publications in books or periodicals or in the form of reports (published or submitted) and in 107 contributions to conferences, workshops or seminars held during the reporting period. Six patents were granted, five patent proposals have been submitted.

Close collaborative contacts were maintained in 1993 with some 80 scientific and industrial institutions in 20 countries in Europe and overseas.

MAIN ACHIEVEMENTS AND MILESTONES

1. Specific Programmes

1.1 Basic Safety Research on Nuclear Fuels

Introduction

The work to improve the safety of nuclear fuels by providing missing basic data and by improving the different computer codes available in the institute to model fuel behavior was continued. Emphasis was given to understand the high burnup behavior of LWR fuel. This was achieved by performing parallel work on i) simulated high burnup fuel, SIMFUEL, ii) by using nuclear techniques and heavy ion accelerators to produce and study damage structures similar to those occurring in high burnup fuel (the "RIM effect"), iii) by evaluating and modelling the large data base on post-irradiation examination of high burnup fuel, and iv) by planning and producing the fuel for a tailor-made high burnup reactor irradiation.

In addition, the investigations on high temperature physics of nuclear materials, the cooperation with the international reactor safety project PHEBUS PF and the development of the fuel performance code TRANSURANUS as well as its release to an increasing number of research and licensing organisations were continued.

Structural investigations and basic studies on fuels

Work on the RIM effect

Polygonization of UO_2 due to high dose ion implantation with fission products

The studies on the RIM structure of high burnup UO_2 fuel were continued with oxygen potential measurements on pieces recovered from the RIM zone of a UO_2 fuel with an average burnup of 7.6 % FIMA, actually the same fuel as used before for a detailed TEM investigation (see TUAR 92, p. 17), and with an extensive ion implantation study to simulate the RIM structure with inactive UO_2.

As is well known [e.g. 1], resonance capture by U-238 of neutrons in the eV-energy range leads to the formation of fissile Pu-239 and thus to a higher burnup near the fuel surface. The rim region is usually restricted to this high burnup zone which is up to 200 µm wide. It exhibits the appearance of a "cauliflower structure". A grain subdivision process, the mechanism of which is still subject of investigations, causes each original grain of the sintered UO_2 with typical diameters of 5 to 15 µm to divide into up to 10^5 very small grains. The question how far this zone will extend into the UO_2 pellets if their average burnup is increased to the critical value for grain subdivision is still open.

This process is of large scientific interest, and it has a considerable technological importance [1]: i) the high fission rate and thus the high heat production in the rim zone flattens the temperature profile in the UO_2 fuel rod, while the increased burnup and the high porosity in the rim region reduce its thermal conductivity. This creates a heat barrier increasing the central fuel temperatures. ii) Increased gas release can be expected as a consequence. iii) The high concentration of fission products and of Pu together with the small grain size near the surface are of concern for spent fuel storage and disposal since in the case of water access, leaching starts in this zone with the highest radiotoxicity. iv) Finally, the response of a fuel with the rim structure in the case of a reactivity-initiated accident is not known and for its understanding, more detailed information on the rim structure must be available.

Ion implantation work to simulate the RIM structure

UO_2 single crystals of good quality and of <100>, <111> and <110> orientations were selected, polished with diamond paste down to 0.25 µm and then annealed at 1450 °C in Ar/H_2

for 30 min to recover the polishing damage. Rutherford backscattering, RBS, analysis with 2 MeV He-ions in the channeling mode showed minimum (aligned) yields, χ_{min}, near to the theoretically expected values, e.g. χ_{min} = 0.03 for room temperature and 0.02 for 77 K and for <100> orientation.

Xe-ion beams were obtained from the ion implantor at Kernforschungszentrum Karlsruhe, Institut für Nukleare Festkörperphysik. Most implantations were done at room temperature, but some crystals were implanted at 77 K or 773 K using the cryostat coupled to both the implantor and a Van de Graaff accelerator [2] or a heating stage in the implantation chamber. Most implantations were performed in the fluence range of $1\text{x}10^{16}$ to $1\text{x}10^{17}$ ions/cm^2 at 300 keV energy. The RBS spectra were evaluated with the aid of the RUMP code [3]. Some experiments were also performed with iodine and cesium beams. Range profiles were calculated with the TRIM code [4]. RBS/channeling measurements were performed with $^4He^+$-ion beams at 2 MeV energy.

For additional detailed analyses of the structural changes occurring in the implanted layers, x-ray techniques were employed [5]. In particular, rocking curves or omega-scans were measured to obtain the width of the (mosaic) spread of the small crystals formed by ion implantation to doses above the critical level. In such X-ray work, the detector is placed on a reflex and the sample rotated in small steps through the reflection position such that slightly misoriented blocks contribute to the reflection one after the other.

The surfaces of the implanted specimens were also analysed by scanning electron microscopy and some specimens, including sintered UO_2, were investigated by transmission electron microscopy using the 200 kV Hitachi H700 HST microscope which is equipped with secondary imaging facilities and a Tracor Northern TN 550 energy dispersive x-ray analysis system.

Results

In a first series of experiments, UO_2 single crystals of <100> orientation were implanted with fluences of or in excess of $4\text{x}10^{16}$ Xe-ions/cm^2 at 300 keV energy at liquid nitrogen temperature (77 K), at ambient temperature and at 500 °C (773 K). In experiments with volatile or gaseous elements (Kr, Xe, Cs, I) at high fluences, one has to consider the possible loss of the implanted impurity during implantation. A recent SIMS depth profile study [6] has shown that, e.g., Cs gets redistributed in ion-implanted UO_2, leading to a peak in the near-surface concentration superimposed on a depleted residual depth profile, most probably due to radiation-enhanced diffusion and radiation-induced segregation. The quantity of the impurity remaining in the solid is thus not necessarily identical with the implantation fluence. Therefore, the implanted quantities were measured by RBS analysis of an Al-foil which partly covered the UO_2 and which was simultaneously implanted. Al, due to the thin, but very stable oxide film on its surface, is known to have a "sticking factor" of 1, and the measured doses were usually in good agreement with those deduced from direct measurements of the beam current. The concentrations and the range profiles of the implanted fission products, were deduced from the RBS spectra. Fig. 1.1 shows an example.

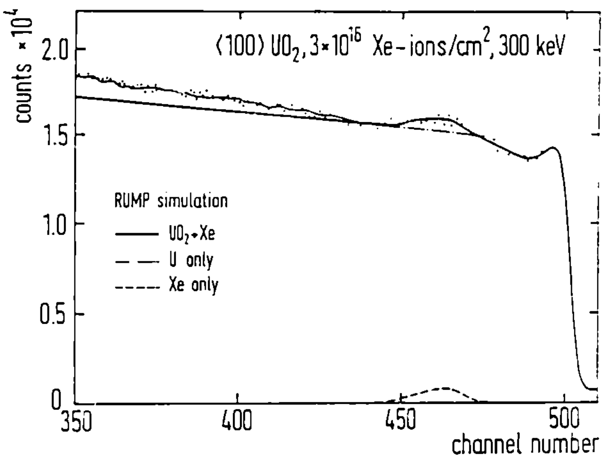

Fig. 1.1 High energy part of the RBS spectrum of a <100> UO_2 single crystal implanted at room temperature with $3\text{x}10^{16}$ Xe-ions/cm^2 of 300 keV energy, compared with RUMP calculations of the whole spectrum (UO_2 + Xe) and of the component spectra for U and Xe

These spectra are rather complicated and their analysis is by no means straight forward. Also, the determination of an impurity which is less heavy than the matrix is difficult with RBS. For these evaluations, the RUMP computer simulation code with the automatic parameter search subroutine PERT was used. The retained quantity of the impurity (called dose in the following) was often smaller than the implanted quantity (called fluence), even at 300 keV energy where contributions due to sputtering are small, in contrast to implantation at low energies. In the following, both values of fluence and dose are therefore given, whenever necessary.

Fig. 1.1 shows a measured random RBS spectrum for a <100> UO_2 crystal implanted with $3x10^{16}$ Xe-ions/cm^2 at 300 keV. Both the simulated spectrum and the U- and the Xe-portions of the total spectrum are shown. The divergence of the experimental and the simulated spectra below channel 420 can be attributed to multiple scattering effects occurring with the heavy U-atoms. These are not taken into account by the RUMP code used here.

Fig. 1.2a compares a random spectrum with an aligned one for a <100> UO_2 single crystal implanted at liquid nitrogen temperature (77 K) with $5.2x10^{16}$ Xe-ions/cm^2 (300 keV) and then warmed up to room temperature. The step in the random spectrum which extends from the surface to channel 460 can be attributed to the high concentration of Xe. The most important feature is that the scattering yield of the aligned crystal in the vicinity of the surface reaches the random level. This means that the implanted region of the crystal behaves as *if it would be* amorphous. In the following, it will be shown that this is not the case. To distinguish this peak from the well known surface peaks due to disordered surface atoms, and from the damage peak around the range of the implanted ions due to displaced lattice atoms, we will call this peak PP in the following. PP stands for peak due to polygonization, since the following sections will show that a polycrystalline structure with small grains is formed giving rise to PP formation.

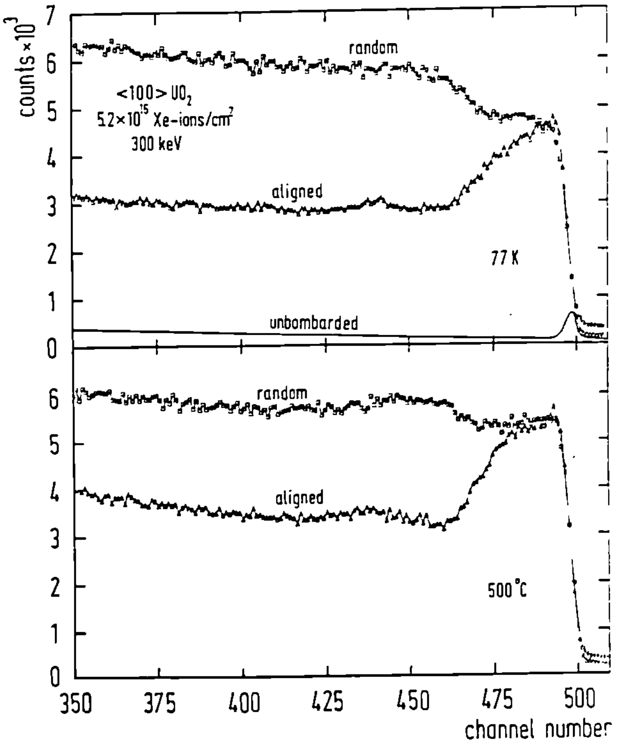

Fig. 1.2 a)Random and aligned RBS spectra of a <100> UO_2 single crystal implanted at 77 K with 5.2 x 10^{16} Xe-ions/cm^2 of 300 keV energy and warmed to 293 K. The spectrum of the unbombarded aligned crystal is shown for comparison b)Parallel experiment with implantation at 500 °C

The same phenomenon was observed in a hot implant at 500 °C with (nominally) $5x10^{16}$ Xe-ions/cm^2 (Fig. 1.2b). Here also, the broad peak due to the implanted layer reached the random level. A further crystal was implanted at ambient temperature and showed similar RBS spectra as the ones in Fig. 1.2. These three crystals were subsequently annealed up to 1500 °C (see below).

The dose dependence for Xe-implants was measured in detail at room temperature and at 500 °C:

Room temperature implantations: UO_2 single crystals of <110> orientation were implanted stepwise with 300 keV Xe-ions. Following each step, they were in situ analysed using a 2 MeV He-beam. Fig. 1.3 shows a random and aligned

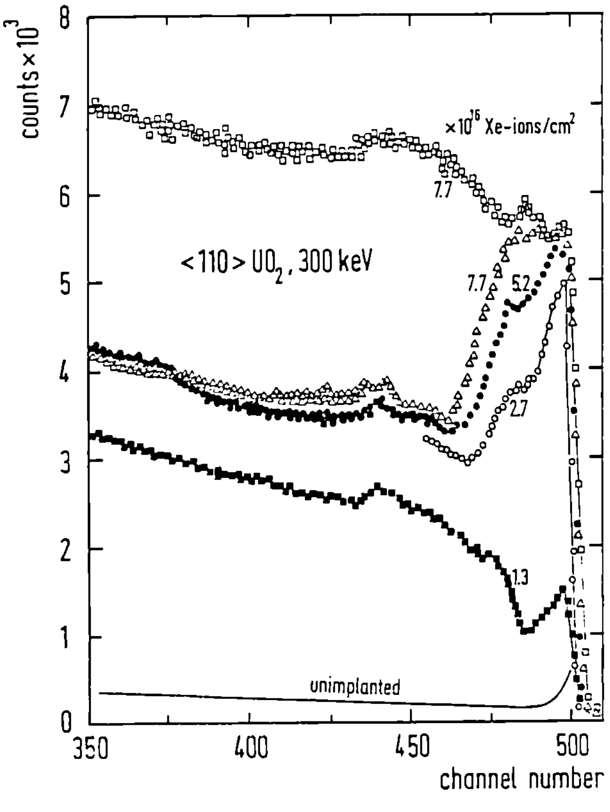

Fig. 1.3 Random and aligned RBS spectra of a <110> UO_2 single crystal implanted at RT with increasing doses of 300 keV Xe-ions

spectra for an unimplanted crystal and for Xe-doses of 1.3, 2.7, 5.2 and 7.7 x 10^{16} ions/cm^2. The random spectrum is that for 7.7x10^{16} ions/cm^2. The fluences were 1, 3, 7 and 10x10^{16} ions/cm^2. Similar experiments were performed with other crystals. For the smaller implantation doses (below the critical value for formation of a PP), there is a slow increase of the damage peak (channels 430 to 480) as well as of the surface peak (channels 480 to 510). A dramatic change occurs if the dose reaches or exceeds about 3x10^{16} ions/cm^2. The dechanneling yield in the near-surface region increases rapidly towards the random level. This was also observed with other crystals bombarded with other fluences up to 1x10^{17} Xe-ions/cm^2. At doses exceeding the critical value, i.e. the dose needed for the sudden formation of a PP, there was an increase in the thickness of the PP between channels 460 to 500 towards the shape shown in Fig. 1.2b, as is obvious from Fig. 1.3. This critical dose may depend on crystal orientation. Typical values are 3 to 5x10^{16} Xe-ions/cm^2.

Some crystals of <110> orientations implanted with doses slightly exceeding the critical one, i.e. ~ 5x10^{16} Xe-ions/cm^2, were further analyzed for their channeling properties by tilting them through different planes. Fig. 1.4 shows a Θ scan in a {110} plane, and an α-scan, i.e. a scan in a {100} plane. The open circles are for the near surface region (channels 470 - 500) whereas the full dots represent the undamaged bulk region (channels 350 - 400). While the Θ scan is typical for a high dose implantation (not leading to complete randomization), the α-scan shows an anomalous behavior. The minimum in the scan for the transformed near-surface region is shifted by about 1° with respect to the scan for the bulk crystal. The material in this region shows thus a small misalignment in its orientation.

The implanted crystals were all analysed in scanning electron microscopy. The unbombarded crystals showed featureless mirror-like surfaces whereas at the high doses leading to a PP very bumpy surfaces with small holes were observed. Parallel TEM work using high dose Xe-implanted sintered UO_2 showed the formation of very small grains with diameters of a fraction of a μm similar to the observation in the rim area of high burnup UO_2 fuel. The original grain size of this particular material was 3 to 5 μm.

Implantations at 500 °C: In order to study the effect of irradiation temperature, a <100> UO_2 single crystal was implanted with different doses at 500 °C. As shown in Fig. 1.2, a PP was formed also at 500 °C. It was absent up to doses of 2x10^{16} ions/cm^2 and it was completely developed in the range of 5 - 7x10^{16} Xe-ions/cm^2. For the implanted dose of 7x10^{16} ions/cm^2, the retained amount was 6x10^{16} ions/cm^2. The polygonization process at 500 °C can thus be assumed to be similar to that occurring at room temperature.

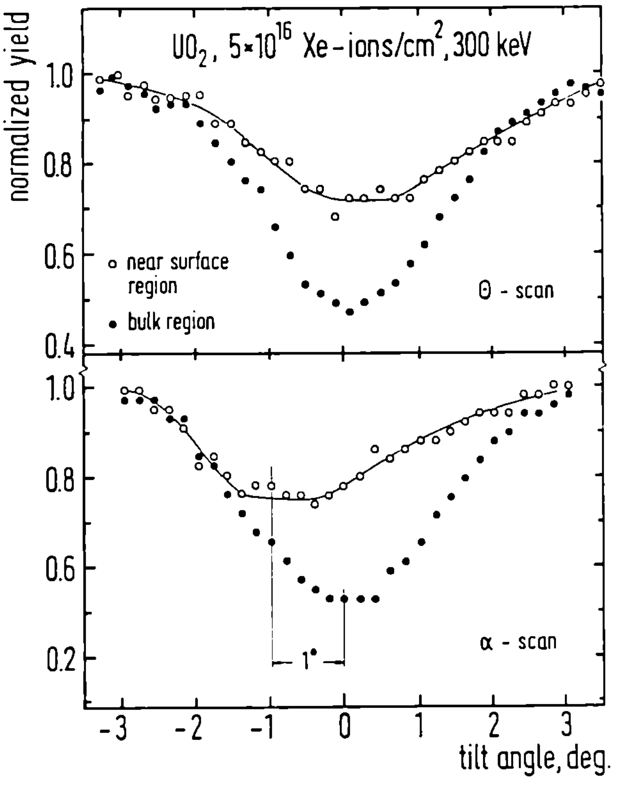

Fig. 1.4 Angular scans of 2 MeV He-ions backscattered from a <110> UO_2 single crystal implanted with 5x10^{16} Xe-ions/cm^2 of 300 keV. A Θ-scan in a {110} plane and an α-scan in a {100} plane are shown. The open circles represent the implanted region, the full dots the bulk crystal

Annealing Behavior

Some of the high dose implanted crystals were annealed in a furnace (Ar/8% H_2, 30 min). A crystal implanted at room temperature to develop a PP was annealed up to 1500 °C (sequence 400, 550, 850, 1000, 1200, 1400, 1500 °C). This crystal showed a PP that did not completely reach the random level in RBS/channeling following implantation. The PP was fully developed reaching the random level following an anneal at 850 °C. Further annealing did not change the shape of the spectra until 1400 °C was reached, when the PP changed shape (extending further into the crystal). Annealing at 1500 °C produced nearly complete recovery, with a minimum aligned yield, χ_{min} = 0.035. These temperatures are by far higher than those needed to recover the defects causing the conventional damage peaks [7].

The crystal implanted at 500 °C (Fig. 1.2b) was annealed at 700, 850, 1000, 1200, 1400 and 1500 °C. There were no changes in the RBS spectra before 1400 °C were reached. At 1400 °C χ_{min} was 0.3. At 1500 °C, a χ_{min} of 0.05 was measured indicating nearly complete recovery. The crystal implanted at 77 K and showing a PP (Fig. 1.2a) was annealed at 400 °C. The PP did not change significantly (actually it shrank by about 10 %), but there was an indication of Xe-release since the Xe peak (see Fig. 1.1) was reduced.

X-ray analysis

Further information on the structure of the implanted layer at doses leading to the formation of a PP was obtained with X-ray analyses of the implanted surfaces. Both (Θ, 2 Θ) and Ω-scans of unimplanted crystals (see Fig. 1.5, upper part) showed that the crystals used in the present study were of very good quality. The measured lattice parameters corresponded well to those of perfect UO_2.

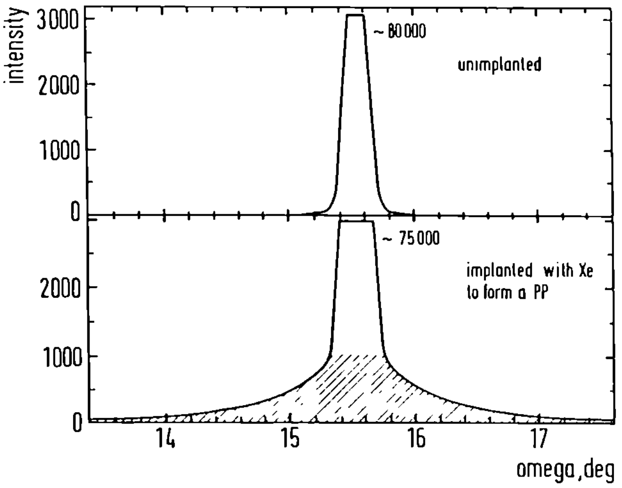

Fig. 1.5 X-ray diffraction analysis (Ω scans) of an unbombarded UO_2 crystal (upper part) and a crystal bombarded with $5x10^{16}$ Xe-ions/cm^2 (lower part), showing a mosaic structure with a misalignment of about 1 to 2 degrees

High dose xenon implantation ($\geq$ $5x10^{16}$ ions/cm^2) produced important changes in both scans. In the (Θ, 2 Θ) scans, the single peaks (as observed for virgin crystals) were split into two well separated peaks, e.g. the peak at 46.96 °, corresponding to the undistorted lattice and thus probably to the undamaged underlying crystal, developed a second peak at 46.59° corresponding to a larger lattice parameter, indicating accumulated radiation damage. Two further minor peaks were indicated at 46.30 and 47.30°. The Ω-scans such as shown in the lower part of Fig. 1.5 indicate clearly that the region giving rise to a PP in RBS/channeling is **not amorphous** but has rather a mosaic structure of small crystallites with a slight misalignement of 1 to 2 degrees. A large number of similar scans was made with different crystals. The main result was always the same though some scans showed larger misalignments of up to ± 4 degrees.

Conclusions and summary

In the reporting period, new information on polygonization of UO_2 due to ion implantation of importance for the formation of the rim effect in high burnup UO_2 nuclear fuels was obtained. Ion beam techniques (Rutherford backscattering/channeling), X-ray and electron microscope analyses were used to deduce this information.

Channeling experiments proved the existence of a critical dose for implantation with 300 keV Xe-ions for the formation of a "polygonization peak" in the aligned spectra reaching the random level. Further channeling experiments, scans in X-ray analysis and electron microscopy showed that the modified implanted layers did not turn amorphous but rather developed a structure of small crystallites which were misaligned by a few degrees. We thus deal with a phase change of the type single crystal - polycrystal, as e.g. previously reported to occur in MgO [8]. This process is very similar to the "grain subdivision" occurring in high burnup fuel, i.e. the rim effect.

The transformation could be produced at 77 K, room temperature and 500 °C in the same dose range. The critical dose may vary with crystal orientation. Whereas radiation defects anneal in UO_2 at rather low temperatures (500 to 800 °C for U-defects at low damage levels; at high damage levels, annealing starts at ~ 700 °C and reaches 50 % at 1200 °C), the transformed structure did not change during 1200 °C anneals, and 1500 °C were necessary to restore the original structure. This is a further proof that the observed effects are really a new type of a structural change rather than just accumulation of radiation damage.

The transformation was also achieved with iodine whereas Cs which showed a pronounced radiation-enhanced outdiffusion did not lead to the formation of a polygonization peak in the channeling spectra (see below). These results show that the presence of a high enough concentration of the impurity (Xe or I) is necessary, whereas damage accumulation alone is not sufficient for the phase change. The critical dose for polygonization observed here corresponds to an impurity concentration reached in a reactor in the burnup range of about 5 to 7 at.%.

The probable mechanism of the polygonization is still the one suggested previously [1], i.e. a cleavage process and microfracture probably caused by the high pressure of athermally formed small fission gas bubbles. This process would also lead to a partial loss of Xe, possibly intensified by additional microcracks as they were recently observed in Xe-implanted ZrO_2 [9]. Such bubbles have been seen in TEM in as-implanted UO_2, and RBS-channeling work with Xe-implantation at lower energies strongly indicates the athermal formation of **solid** epitaxially oriented rare gas precipitates in UO_2 [10]. To maintain Xe in UO_2 solid at room temperature, pressures of the order of 10^4 bar are needed.

Condensed rare gases are also known to exist in the outer part of cold regions of reactor irradiated UO_2. The mechanisms of rim formation and of the polygonization observed here may therefore well be identical. If this is so, the present study indicates that the process is rather independent of temperature in the range 77 K to 773 K and that the presence of a critical concentration of insoluble fission products is decisive.

References

[1] Hj. Matzke, J. Nucl. Mater. **189** (1992) 141

[2] R. Kaufmann, J. Geerk and F. Ratzel, Nucl. Instrum. Methods **205** (1983) 293

[3] L.R. Doolittle, Nucl. Instrum. Methods in Physics Research **B 9** (1985) 344

[4] J. Biersack, Chapter 1 in Ion Beam Modification of Insulators, Eds. P. Mazzoldi and G.W. Arnold, Elsevier, Amsterdam (1987)

[5] G. Linker, Report Kernforschungszentrum Karlsruhe KfK-3146 (1981)

[6] W.H. Hocking, R.A. Verrall, P.G. Lucuta and Hj. Matzke, Radiation Effects and Defects in Solids **125** (1993) 299

[7] Hj. Matzke and A. Turos, J. Nucl. Mater. **188** (1992) 285

[8] Hj. Matzke and J.L. Whitton, Can. J. Phys. **44** (1966) 995

[9] M.G. Norton, W. Jiang, J.T. Dickinson, L.C. Jensen and S.C. Langford, J. Am. Ceram. Soc. **76** (1993) 2076

[10] A. Turos, Hj. Matzke and O. Meyer, Nucl. Instrum. Methods in Physics Research **B65** (1992) 315

Oxygen potential in the RIM region of high burnup UO_2 fuel

1. Introduction

The oxygen potential $\Delta G(O_2)$ of unirradiated UO_2 and $UO_{2\pm x}$ has been frequently studied and modelled as a function of the O/U-ratio. It shows the well known S-shaped curve with a large increase in $\Delta G(O_2)$ at the stoichiometric composition (from about -500 to about -300 kJ/mol at 1000 K) when going from UO_{2-x} to UO_{2+x}. A number of studies shows that $\Delta G(O_2)$ is increased when rare earths RE fission products are introduced into UO_2, more so for $(U,RE)O_{2-x}$ than for $(U,RE)O_{2+x}$. This phenomenon is well known and understood, since it occurs also in mixed oxide fast breeder fuel $(U,Pu)O_{2-x}$. The evolution of $\Delta G(O_2)$ during irradiation is still a pending question. Yet, knowledge of the oxygen potential and of the oxygen-to-metal ratio at increasing burnup are the basis for understanding and predicting important phenomena such as inside clad corrosion, reaction between fuel and fission products (e.g. formation of cesium uranates, oxidation of Mo), diffusion and gas release rates, fuel plasticity, creep properties, etc.

Commonly, the fuel is assumed to oxidize with increasing burnup, in particular for Pu-fission, which is predominant in the rim region. Actually, needle-shaped precipitates were sometimes observed in optical micrographs of the outer zones of high burnup UO_2 fuel and these were sometimes suggested to represent U_4O_9 precipitates which would indicate significant increases in the O/U-ratio. On the other hand, the rim region is adjacent to the clad which should act as oxygen sink, and thermodynamics predicts that excess oxygen in UO_{2+x} should migrate towards the centre of the fuel (see below). It is therefore of great interest to measure the oxygen potential in the rim region of a high burnup fuel. The highest burnup in the rim region of the fuel studied here was in excess of 200 GWd/tM. Additional measurements were performed with fuel pieces from the inner, unrestructured part of the fuel. It will be shown in the following that the fuel in the rim zone did not oxidize; it actually was slightly substoichiometric at the end of irradiation.

The fuel investigated in the present study originated from a fuel rod irradiated in the Danish heavy water reactor at Risø. The fuel pellets had a diameter of 12.7 mm. The initial enrichment in U-235 was low (1.46 %). However, the average burnup was high and amounted to 75 GWd/tM for the cross section from which the fuel pieces for oxygen potential measurements were taken. The highest burnup in the rim region, as calculated by Kinoshita et al. using the codes ANRB and VIMBURN [1] and as determined from the local concentration of Nd was about 2.8 times higher, i.e. in excess of 200 GWd/tM. Because of this high burnup, and since a very detailed electron microscopy study of both the rim area and the central area of the same fuel is available [see TUAR 92, p. 17], pieces from this fuel rod were used for oxygen potential measurements.

The miniaturized galvanic cell, used previously successfully to measure oxygen profiles in fast breeder $(U,Pu)O_{2-x}$ fuel [2, 3] and to determine the dependence of $\Delta G(O_2)$ on burnup up to very high values of 13.6 % FIMA in such substoichiometric mixed oxide fuel [3] was modified to enable reliable measurements for the originally expected hyperstoichiometric compositions UO_{2+x} of the high burnup UO_2. In the previous version of the miniature cell, oxygen potentials above about -250 kJ/mole could not be measured accurately. The modified system is shown in Fig. 1.6. The main difference to the previous system is a closed emf-cell with a pressure-loaded Pt-sealing. Both systems are based on the electrochemical cell:

Pt / sample (irradiated oxide) / ThO_2-Y_2O_3 electrolyte / reference / Pt.

The reference system is usually Fe/FeO, but Ni/NiO can also be used. The electrolyte is a crucible of Y_2O_3-doped ThO_2, with the new version using a Pt-lid under pressure providing contact with the sample and preventing the developing oxygen pressure to be pumped away. Electrical contacts to the lid and the reference electrode are made with the Pt wires of Pt/Pt-10 % Rh thermocouples. The cell is suspended in an alumina tube connected to a vacuum system. The lid is closed following a first evacuation. The set-up is placed in an inert atmosphere glove box with adequate lead shielding at the irradiated UO_2 sample. The cell was shown to work reliably with UO_{2+x} even at high x-values (see e.g. TUAR 91, p. 33).

These control measurements proved that the cell works correctly at and even clearly above -200 kJ/mol. The range in $\Delta G(O_2)$ which can be covered with the miniaturized cells is thus extended from below about -650 to above about -150 kJ/mol.

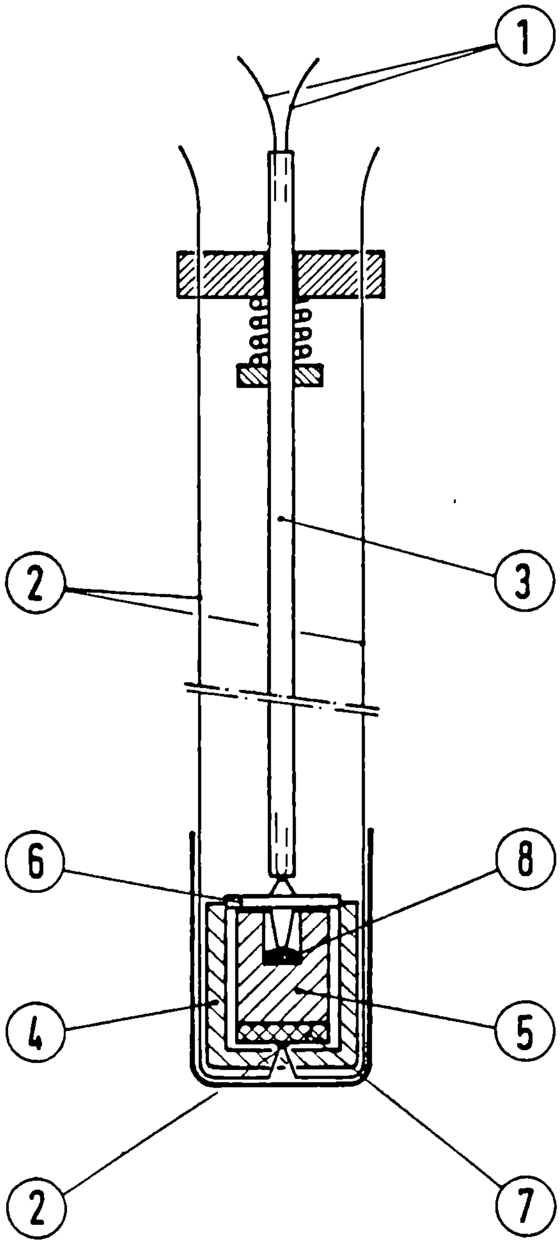

Fig. 1.6 Schematic drawing of the modified miniaturized galvanic cell: (1, 2) thermocouples and electric contacts; (3) Al_2O_3 capillary (4) Al_2O_3 crucible; (5) Y_2O_3-doped ThO_2 electrolyte crucible; (6) spring-loaded Pt-lid; (7) Fe/FeO reference electrode; (8) irradiated UO_2 sample or UO_2 and UO_{2+x} control specimen

Measurements on irradiated fuel

Fig. 1.7 shows the results on specimens of a few mg weight which definitely originated from the **restructured rim zone**. An exact radial location within this narrow zone of < 0.5 mm width was not possible. The burnups of the different pieces were thus probably different, and they fell into

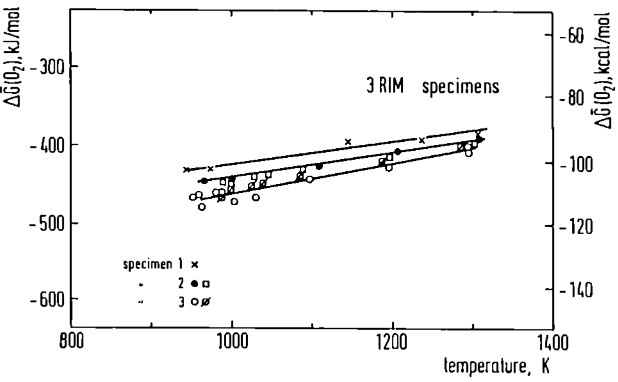

Fig. 1.7 Oxygen potential measurements on 3 small fuel pieces recovered from the rim region of a fuel rod with a very high cross-section averaged burnup of 75 GWd/tM

the range of > 75 to ≤ 200 GWd/tM. It is rather likely that within these pieces, a gradient in burnup existed. This may explain the small scatter in the data. The important result is that all oxygen potentials were very low, actually they all fell into the range of nominally stoichiometric, unirradiated UO_2, despite of the very high burnup in the rim zone.

Fig. 1.8 compares these results with those obtained on material taken from near the **centre of the fuel**. The $\Delta G(O_2)$ values in the centre are

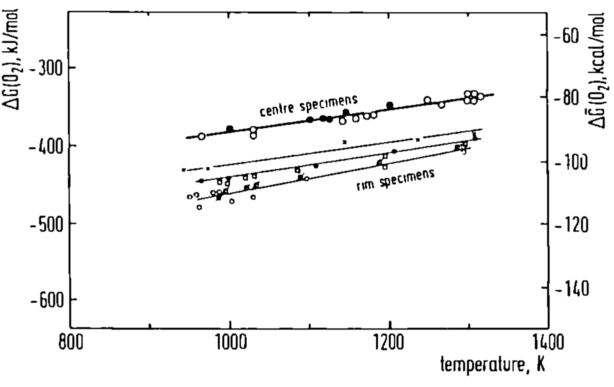

Fig. 1.8 Comparison of the results of Fig. 1.7 with results obtained on small fuel pieces recovered from the inner part of the fuel rod

higher than those of the rim material but only by about 50 kJ/mole. They are thus also very low and do not indicate any significant increase in O/M-ratio. This is seen in Fig. 1.9 which shows a plot of literature results for $\Delta G(O_2)$ measurements on unirradiated UO_2 and UO_{2+x} for T = 750 °C, as chosen by Une et al. [4] in their paper on measurements with irradiated BWR fuel. Included are some results on unirradiated UO_2 and UO_{2+x} obtained in the present work while testing the modified emf-cell and the dependence obtained from the model of Lindemer and Besmann [5]. Arrows indicate the measured $\Delta G(O_2)$ values of the present high burnup UO_2 fuel.

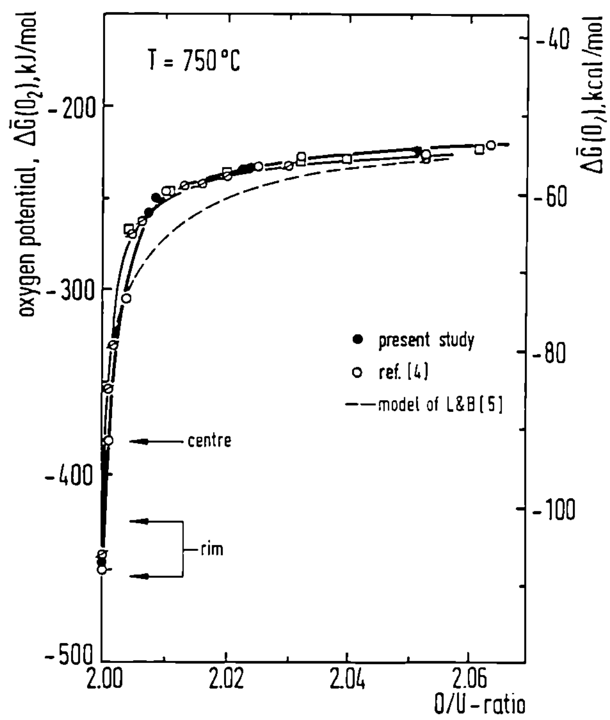

Fig. 1.9 Oxygen potential data for unirradiated UO_{2+x} at 750 °C, including the data for unirradiated UO_{2+x} obtained with the modified cell as well as the results for the high burnup rim specimens

Discussion

It is often reported that fission is oxidizing the fuel since the fission products consume less oxygen than is liberated by fission of (tetravalent) U and Pu. Though two fission products are formed from each U (or Pu) atom, many of the fission products are present as metals (Tc, Ru, Rh, Pd and partially Mo) or gases (Kr, Xe), and many of them are trivalent (lanthanides) (see, however, remarks below). Fission of Pu is expected to be more oxidizing than fission of U, owing to the shift in the fission yield spectrum: Pu fission produces much more noble metal fission products (Ru, Rh, Pd) and much less oxide formers (mainly Y, Sr, Zr) than U-fission.

Early experiments and estimates by Davies and Ewart [6] yielded the following picture:

- U thermal fission is hardly oxidizing (UO_2 is predicted to oxidize to $UO_{2.004}$ at 10 % burnup)
- Pu thermal fission is significantly oxidizing (MO_2 is predicted to oxidize to $MO_{2.060}$ at 10 % burnup)
- Pu fast fission acts similarly ($MO_{2.053}$ at 10 % burnup)

The values for Pu fission were confirmed by emf measurements on irradiated MO_{2-x} fuel in previous work [7]: an increase Δ(O/M) of 0.0065 per at.% burnup was measured.

Kleykamp provided later [8, 9] a more sophisticated picture, allowing for the consequences of the formation of $(U, Pu, RE)O_2$ phases, the formation of $(U,Pu)Pd_3$ precipitates, the oxidation of Mo, the formation of phases such as Cs_2MoO_4, compound formation of alkali metals with chalcogen fission products and with U and Pu, and oxygen gettering at the clad. For fast breeder $(U,Pu)O_2$ fuel, this yielded a delayed O/M-increase of the originally substoichiometric MO_{2-x} in the near-stoichiometric range of the fuel. This increase is thus not linear with burnup, the main reason being that metallic phase formation is preferred at low oxygen potentials and that Mo (becoming oxidized to Mo^{6+}) and Cs (e.g. forming uranates) act as oxygen sinks at high burnup and high oxygen potentials. Kleykamp predicted [9] that $(U,Pu)O_{1.97}$ should oxidize fast in the beginning, e.g. to $(U,Pu)O_{1.994}$ at 5 % burnup and then more slowly to e.g. $MO_{1.998}$ at 7 % burnup. The average Δ(O/M) per at.% burnup would thus be just half of the above value of Davies and Ewart. For high power UO_2 LWR fuel [8], Kleykamp predicted a shift Δ(O/M) of 0.0013 per at.% burnup, hence e.g. a composition of $UO_{2.0065}$ at 5 % burnup of originally stoichiometric UO_2. However, based on a careful X-ray micro analysis of both the fuel and of the Zircaloy clad, he predicted UO_2 fuel operated at high power, hence at high temperatures, to remain essentially stoichiometric since any excess oxygen due to a possible hyperstoichiometry of the starting fuel or due to the above formation of excess oxygen by fission would diffuse to the clad and be gettered in a reaction layer. This reaction zone was analysed in a high-power fuel rod of 4.3 at.% burnup to consist of a Cs-Zr-O phase and ZrO_2 or α-Zr(O) layers, causing a constant O/M-ratio of 2.000 + (0.001 - 0.005) over the fuel radius. This effective gettering would be expected to be reduced at low power (colder fuel).

To complicate the situation even further, there is the suggestion of MacInnes and Winter [10] that, in addition, the fission rare gases, normally considered to be inert (occupying neutral trivacancy sites) and not forming part of the O/M-balance, may be located in charged vacancy clusters (e.g. one cation plus one oxygen vacancy, binding one oxygen atom per Kr or Xe atom) thus potentially reducing the fuel; or the observation made in previous work at TU that Te can be substitutioned in UO_2 thus also affecting the O/M-development. The situation is thus rather complex. Note also that conventional O/M ratio measurements have not been performed yet on irradiated fuel. However, the oxygen potentials were measured in a few studies: by Adamson et al. [11] on UO_2 at rather low burnup (11.4 and 18.9 GWd/tM), by Une and coworkers [4] on BWR fuel (UO_2 and $(U,Gd)O_2$) up to 35 GWd/t and on $(U,Pu)O_{2-x}$ up to very high burnups in the institute [e.g. 2, 3, 7]. These results, together with the present ones, are shown in Fig. 1.10. Unfortunately, the relations between O/M-ratio and $\Delta G(O_2)$ of high burnup fuel are not as well known as those for the (unirradiated) U-O system. However, similarly reliable data as for $UO_{2\pm x}$ have been obtained on UO_2 containing one additive, usually based on emf measurements and thermogravimetry. Examples are the systems $(U,Gd)O_{2\pm x}$, $(U,Nd)O_{2\pm x}$, $(U,Pr)O_{2+x}$, $(U,La)O_{2+x}$, $(U,Ce)O_{2\pm x}$, $(U,Y)O_{2+x}$ etc. In addition, there is the very extensive work on $(U,Pu)O_{2\pm x}$ extended by data on $(U,Pu,Nd)O_{2\pm x}$.

Rather generally, dissolution of trivalent rare earth ions in UO_2, hence replacement of U^{4+} by RE^{3+} ions requires either introduction of oxygen vacancies or an increase in the oxidation state of the remaining U-ions (some U^{4+} is oxidised to U^{5+} if RE^{3+} are in solid solution), thus causing the $\Delta G(O_2)$ to increase (become less negative). A similar trend is observed for mixed oxides with a cation which is more easily reduced to the trivalent state than U, e.g. Pu and Ce in $(U,Pu)O_2$ and $(U,Ce)O_2$. The consequence can be illustrated by the behavior of $(U,Gd)O_{2\pm x}$ [12, 13]: for a fixed temperature, e.g. 1000 °C, the $\Delta G(O_2)$ for stoichiometric UO_2 is more negative by about 85 kJ/mol than that for stoichiometric $(U_{0.96}Gd_{0.04})O_2$, or: at the oxygen potential for stoichiometric UO_2, the $(U_{0.96}Gd_{0.04})$-oxide is (very slightly) substoichiometric. The difference in $\Delta G(O_2)$ is smaller for hyperstoichiometric compositions, i.e. ~ 10 kJ/mol for O/M = 2.03, but the trend is the same.

High burnup fuel contains, of course, many different fission products including different REs. Attempts have been made to evaluate the relation of O/M versus $\Delta G(O_2)$ by "simulating" the burnup by adding different fission products to UO_2 (or

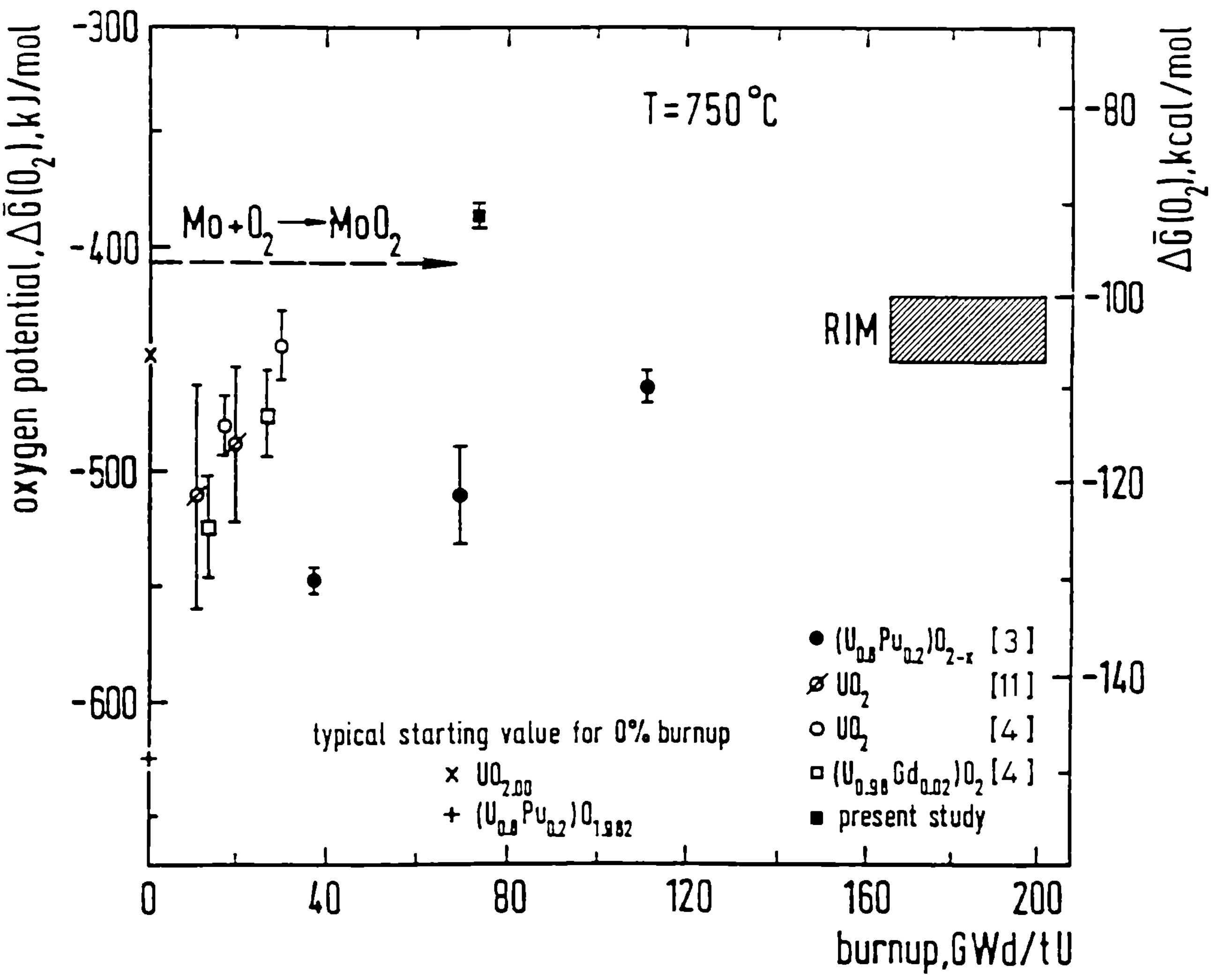

Fig. 1.10 Burnup dependence of the oxygen potential at 750 °C for different irradiated oxide fuels

$(U,Pu)O_2$) in the fabrication step. This was done by Woodley [14] and in the institute for $(U,Pu)O_2$, and by Une and Oguma [15] for UO_2 with added Zr, Ce, Pr, Nd and Y, simulating 2, 5 and 10 at.% burnup. More recently, a well characterized SIMFUEL with 11 or even 17 additives has been produced [16] for 1.5, 3, 6 and 8 at.% burnup and is being used to measure the relation of $\Delta G(O_2)$ versus O/M-ratio [17]. The trend is similar to that described above. For a given O/M, the $\Delta G(O_2)$ is slightly higher in SIMFUEL than in UO_2, roughly corresponding to the content in rare earths. For instance, Une and Oguma [15] report an increase in $\Delta G(O_2)$ at 1000 °C for near-stoichiometric $UO_{2.002}$ of 21 kJ/mol for 5 at.% burnup. As another example, the above SIMFUEL work [17] yielded, this time for a constant $\Delta G(O_2)$ = -246 kJ/mol at 1000 °C, O/M-ratios of 2.0025, 2.001 and 2.0005 for UO_2, and for 3 at.% and 6 at.% SIMFUEL, respectively.

For the present specimens, we deal with a well defined burnup of 75 GWd/tM in the centre, and values between this number and up to and in excess of 200 GWd/tM in the rim region. Since the fuel was only slightly enriched (1.46 %), most fissions were due to Pu which formed during the irradiation. At end of life, hence during the present emf measurements, the fuel is expected to contain about 1 % Pu in the centre and up to 3 % in the rim region. We expect thus that the O/M-ratio in the centre is that of virgin $UO_{2(+x)}$ lowered by the presence of 1 % Pu and some 3.5 at.% REs. The above results for $(U_{0.96}Gd_{0.04})O_2$ will therefore be representative (or else the SIMFUEL results for 8 % burnup). The measured $\Delta G(O_2)$ values correspond about to those of $UO_{2.001}$ for virgin fuel, or to very slightly substoichiometric $(U_{0.96}Gd_{0.04})O_2$ or 8 % SIMFUEL, with an O/M-ratio of ~ 1.9995. Certainly, there is no oxidation towards significantly hyperstoichiometric fuel.

In the rim area, the uncertainty of the exact radial location causes an uncertainty in the burnup of the measured specimens, because of the burnup-gradient in the rim region. If we accept average values of 14 % burnup and 2 % Pu, we expect that the measured $\Delta G(O_2)$, corresponding practically to stoichiometric virgin UO_2, represents a slightly substoichiometric composition with an O/M-ratio of about 1.999. Note that a composition with much more REs, i.e. $(U_{0.86}Gd_{0.14})O_{1.996}$ has, at 750 °C, a significantly lower $\Delta G(O_2)$ of ~ -500 kJ/mol [12] whereas $(U_{0.9}La_{0.1})O_{1.999}$ has practically the same $\Delta G(O_2)$ as the present rim-specimens. It is thus certainly safe to conclude that the rim area of the present fuel has a composition above O/M = 1.996 and below O/M = 2.000. Despite the fact that near to all fission is due to Pu the fuel did not oxidise in the rim area either.

Conclusions and summary

The present results answer the open question on the oxygen potential (or the O/M-ratio) in the porous, small grain size "cauliflower structure" of the rim-zone of a UO_2 rod with a high cross-section averaged burnup of 7.6 % FIMA; the large majority of the fission was due to Pu. Therefore, a pronounced oxidation could have been thought to have occurred. Basically, four methods exist to determine O/M-ratios of (irradiated) oxide fuels. These are thermogravimetry, measurements of lattice parameters, determination of Mo/MoO_2 ratios and measurements of the electromotive force, emf of galvanic cells. Thermogravimetry of the tiny available specimens of the rim-zone would yield large errors. Lattice parameters are not only influenced by changes in O/U-ratio, but also by the ingrowth of Pu and of fission products which are soluble in the UO_2 lattice, and, very importantly, by radiation damage due to fission and α-decay making any deduction on the O/M-ratio very questionable. The Mo/MoO_2 method necessitates careful X-ray microanalysis examinations, is only applicable in the range of coexistence of Mo and MoO_2 and is also difficult to perform in the thin rim zone. Therefore, direct measurements of the oxygen potential were performed using electromotive force measurements which allow to deduce the O/M-ratio. A preexisting miniature emf-cell was modified to enable measurements of oxygen potentials up to values of -150 kJ/mol, corresponding to O/U-ratios of about 2.1 at the experimental temperatures used.

Different small fuel pieces originating from the rim zone were analysed with this cell. The oxygen potential of pieces from the centre of a fuel pellet was also measured. The values in the centre were higher by about 50 to 80 kJ/mol than those in the rim, but in both cases, these values were very similar to those of unirradiated nominally stoichiometric or "near-stoichiometric UO_2", with x in UO_{2+x} being ≤ 0.001. A significant oxidation of the fuel due to the high burnup did thus not take place.

Note, in this respect, that models like those of Lindemer and Besmann [9] have to be used to predict the value for exactly stoichiometric UO_2. Such models yield very low values of about -600 kJ/mol at 750 °C, the temperature used in Fig. 1.10. The results plotted on the ordinate in Fig. 1.9, hence -450 kJ/mol would, according to the model of Lindemer and Besmann, correspond to about $UO_{2.00005}$.

With increasing burnup, the content of rare earths fission products increases and, therefore, the $\Delta G(O_2)$ is higher for a constant O/M-ratio than the value of unirradiated UO_2 with the same O/U-ratio. If we use the data [12] for $(U_{0.96}Gd_{0.04})O_{2\pm x}$ as representing the composition in the centre (7.6 at.% burnup) and the data [5] for $(U_{0.9}La_{0.1})O_{2\pm x}$ as representing the composition of the rim zone (up to 20 at.% burnup), we obtain very slightly hypostoichiometric compositions $(U, f.p)O_{2-x}$ with x ~ 0.0005 in the centre and 0.001 at the rim.

It is thus obvious that the high burnup, predominantly due to fission of Pu, did not cause an oxidation of the fuel, neither in the centre nor at the rim. The formation of the rim structure does therefore not seem to be related to the oxidative nature of Pu fission.

Whereas this conclusion is unambiguous, there are ambiguities concerning the conclusions about the oxidative nature of fission. As shown in Fig. 1.10, the measured oxygen potentials reached those of Mo-oxidation (see dashed line $Mo+O_2 \rightarrow MoO_2$ in Fig. 1.10). EDX analysis of metal particles in the rim zone showed in all cases that there was Mo in these particles, even in the rim zone. Yet, Mo oxidation may have used up some oxygen. A second sink for oxygen is the Zircaloy clad. Oxygen diffusion towards the clad is known to occur in highly rated fuel rods (hence at high temperatures) causing the formation of a corrosion layer of approximate composition ZrO_2 [18], though actually thermodiffusion should cause excess oxygen to migrate up the temperature gradient towards the centre of the fuel [19]. Kleykamp pointed out [18] that this reaction with the Zircaloy would limit the cross-section averaged O/M-ratio of the fuel studied by himself (LWR UO_2 fuel with 5.9 at.% burnup) to $UO_{2.0025} \pm 0.0025$. Since the fuel is not a closed system, these reactions influence the development of $\Delta G(O_2)$ and of the O/M-ratio with burnup. For the specific case of the fuel of the present study, a corrosion layer of 15 to 20 µm thickness was found on the inner clad surface. Assuming that this layer is essentially ZrO_2 and that a part of the order of one third of the Mo in the fuel was oxidized would yield a Δ(O/M) of about 0.002 per at.% burnup (if the fuel would be a closed system, hence in an inert clad and in the absence of Mo oxidation).

In conclusion, the available evidence shows that the oxygen potential of the present high burnup fuel does not surpass the values of the Mo/MoO_2 equilibrium. Even in the "cauliflower" structure of the rim zone, and at burnups far in excess of 10 at.%, the fuel is not oxidised above $UO_{2.000}$.

References

[1] T. Matsumura and T. Kameyama, IAEA Technical Meeting on Water Reactor Fuel Element Computer Modelling in Steady-State, Transient and Accident Conditions, Preston, UK (1988) paper 1.6

[2] T. Ewart, K. Lassmann, Hj. Matzke, L. Manes and A. Saunders, J. Nucl. Mater. **124** (1984) 44

[3] Hj. Matzke, J. Ottaviani, D. Pellottiero and J. Rouault, J. Nucl. Mater. **160** (1988) 142

[4] K. Une, Y. Tominaga and S. Kashibe, J. Nucl. Sci. Techn. (Japan) **28** (1991) 409

[5] T.B. Lindemer and T.M. Besmann, J. Nucl. Mater. **130** (1985) 473

[6] J.H. Davies and F.T. Ewart, J. Nucl. Mater. **41** (1971) 143

[7] F.T. Ewart, C. M. Mari, S. Fourcaudot, Hj. Matzke, L. Manes and F. Toci, in Thermodynamics of Nuclear Materials 1979, IAEA, Vienna I (1980) 369

[8] H. Kleykamp, J. Nucl. Mater. **84** (1979) 109

[9] H. Kleykamp, J. Nucl. Mater. **131** (1985) 221

[10] D.A. MacInnes and P.W. Winter, J. Phys. Chem. Sol. **49** (1988) 143

[11] M.G. Adamson, E.A. Aitken, S.K. Evans and J.H. Davies, in "Thermo-dynamics of Nuclear Materials 1974", IAEA Vienna, Vol. 1 (1975) **59**

[12] K. Une and M. Oguma, J. Nucl. Mater. **110** (1982) 215; **115** (1983) 84; **131** (1985) 144

[13] T. Lindemer and A.L. Sutton, Jr., J. Amer. Ceram. Soc. **71** (1988) 553

[14] R.E. Woodley, J. Nucl. Mater. **74** (1978) 290

[15] K. Une and M. Oguma, J. Nucl. Sci. Techn. (Japan) **20** (1983) 844

[16] P.G. Lucuta, R.A. Verrall, Hj. Matzke and B.J. Palmer, J. Nucl. Mater. **178** (1991) 48

[17] Hj. Matzke and P.G. Lucuta, unpublished results

[18] H. Kleykamp, J. Nucl. Mater. **171** (1990) 181

[19] C. Sari and G. Schumacher, J. Nucl. Mater. **61** (1976) 192

Thermal conductivity of simulated high burnup UO_2 fuel

The thermal conductivity of UO_2 is an important parameter since it determines fuel operating temperatures and therefore influences almost all processes related to fuel performance and behavior. Degradation in fuel thermal conductivity λ occur during irradiation because of fission product build-up (dissolved and precipitated), formation of cracks, pores and gas bubbles, and possible changes in the oxygen to uranium O/U, ratio.

Previous experimental result (TUAR 91, p. 26; TUAR 92, p. 24) on SIMFUEL (SIMulated high burnup UO_2 FUEL) had shown an important decrease in λ with increasing burnup. SIMFUEL replicates the chemical state and microstructure of irradiated fuel by adding inactive elements to UO_2 powder in amounts appropriate for the chosen burnups. Burnups of 1.5, 3 and 8 % were used. The preparation route features high energy grinding and spray drying to achieve homogeneous dispersion, and sintering provides the atomic-scale mixing. The phase structure is therefore representative of high burnup fuel which operated at high temperatures - without fission gas bubbles. Extensive characterization has shown solute fission-product atoms dissolved in the UO_2 oxide fluorite matrix and two types of precipitated fission products: spherical metallic Mo-Ru-Rh-Pd compounds and ceramic perovskite-type phases such as Ba(Sr)-zirconate [1].

Based on the earlier experimental results (TUAR 91, p. 26; 92, p. 24 and [2]), the effects of increased concentrations of fission products on λ of UO_2 were analyzed in the reporting period by evaluating their effect on the phonon heat current, considering the two key aspects [3]:

i) the contribution of the precipitated solid fission products, and
ii) the effect of the dissolved solid fission products.

Correction for precipitated phases:
The solid precipitated fission products can be treated in a manner exactly analogous so that used for pores, as both are dispersed phases

through the fluorite matrix of SIMFUEL and their conductivities differ from that of the matrix. Maxwell introduced a porosity factor, κ_p for corrections on thermal conductivity [4]:

$$\kappa_p = \frac{\lambda}{\lambda_m} = \frac{1-p}{1+\frac{1}{2}p} \tag{1}$$

where λ and λ_m are the measured and corrected conductivities and p is the pores fractional volume. Maxwell's factor (1) gives good results for uniformly dispersed spherical sintering pores, and could therefore be applied to the measured values of UO_2 thermal conductivity. These results are in good agreement (within ± 0.75 %) with Loeb's correction for porosity, which was used earlier by us [2]. For a dispersed second phase, Schulz [5] calculated a generalized relation that is the same as Maxwell's formula to the first order, but it accounts for the thermal conductivity of a dispersed phase.

This treatment is easily modified to account for the highly conducting precipitated phases formed in irradiated fuel. (The thermal conductivity of the precipitated metallic fission products is of the order of 100 W/mK, compared to 8 W/mK for the matrix at room temperature). For a volume fraction q of precipitated fission products, and thermal conductivity λ_2, since λ_2 (for metals) $> \lambda_m$, λ, the above relation, approximates to a Maxwell-type correction factor:

$$\kappa_q = \frac{\lambda}{\lambda_m} = \frac{1+2q}{1-q} \tag{2}$$

For an isotropic 3-phase random mixture of pores of conductivity λ_1 (volume fraction p), precipitated fission products of conductivity λ_2 (volume fraction q) and the continuous fluorite matrix phase of conductivity λ_m, Schulz's formula can be written as:

$$1-p-q = \left(\frac{\lambda_m}{\lambda}\right)^{1/3} \times \left(\frac{\lambda_1+\lambda_2-\lambda}{\lambda_1+\lambda_2-\lambda_m}\right) \tag{3}$$

which gives a generalized Maxwell-type correction factor for precipitates and porosity:

$$\kappa = \frac{\lambda}{\lambda_m} = \frac{2(1-p+2q)}{p+2(1-q)} \tag{4}$$

We used this relation to correct the measured thermal conductivities of SIMFUEL (Tab. 1.1).

The volume fractions of the precipitated phases were calculated from SIMFUEL chemical compositions and phase structure. They range from 0.4 to 0.5 vol% for the 1.5 at% burnup composition and from 2.0 to 3.0 vol% in the case of 8 at% burnup SIMFUEL. The average values listed in Tab. 1.1 were used in the present analysis. The corrected thermal conductivities of fully dense UO_2 and SIMFUEL matrix are listed in Tab. 1.1. These values for thermal conductivity of SIMFUEL **matrix** are by 1.3 %, 2.7 % and 7.2 % lower for the 1.5, 3 and 8 at% burnups than the directly measured values when no corrections for the precipitated fission products were considered.

Consequently, the precipitated fission products increase the thermal conductivity of the fuel by 1.3 %, 2.7 % and 7.2 % for the 1.5 at%, 3 at% and 8 at% burnup SIMFUEL, respectively. This contribution to the fuel thermal conductivity is shown in Fig. 1.11, where the conductivity of fully dense 8 at% burnup SIMFUEL with and without the precipitated fission product effect is compared with that of the fully dense UO_2. The contribution of the precipitated solid fission products gives an average of about 1 % increase in the fuel thermal conductivity for each 1 at% burnup.

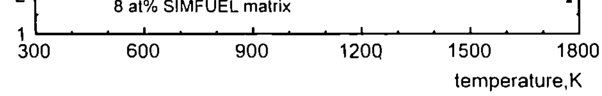

Fig. 1.11 Thermal conductivity of fully dense UO_2, 8 at% burnup SIMFUEL and 8 at% burnup matrix displaying the contribution of the precipitated fission products

Thermal conductivity of the fluorite matrix

The dissolved fission products in the SIMFUEL fluorite matrix cause the reduction in fuel thermal conductivity, and this degradation was analyzed in the reporting period using the phonon

Tab. 1.1 Measured and corrected thermal conductivity of 0, 1.5, 3 and 8 at% burnup SIMFUEL for various temperatures.

p	0.022	0.0221	0.0244	0.0132	**Maxwell Correction Factor (Eq. (2))**			
q	nil	0.0045	0.009	0.025	0.967	0.981	0.990	1.056
	UO_2	**1.5 at**	**3 at%**	**8 at%**	UO_2	**1.5 at**	**3 at%**	**8 at%**

Temp. (K)	Measured Conductivity (W/m K)				Corrected Conductivity (W/m K)			
300	8.281	7.183	5.773	4.413	8.561	7.325	5.829	4.178
473	6.994	6.161	5.182	4.081	7.230	6.282	5.232	3.863
673	5.511	4.984	4.356	3.656	5.697	5.083	4.398	3.462
873	4.670	4.290	3.832	3.209	4.828	4.375	3.869	3.038
1073	3.750	3.473	3.232	2.866	3.877	3.542	3.263	2.714
1273	3.211	3.027	2.877	2.564	3.319	3.087	2.905	2.427
1473	2.889	2.749	2.560	2.318	2.987	2.804	2.585	2.194
1673	2.520	2.406	2.275	2.076	2.605	2.453	2.297	1.965
1773	2.353	2.279	2.190	1.984	2.432	2.324	2.211	1.878

heat current theory [6]. The scattering parameter of the phonons, which describes the strength of the scattering by dissolved fission products in the fuel matrix, was defined as a function of the phonon frequency and determined using two different approaches:

- by comparing the measured thermal conductivities of SIMFUEL to that of UO_2 at various temperatures, and
- by using a relation based on the measured SIMFUEL thermal conductivity and the average mass of the dissolved fission products.

Strength of scattering by dissolved fission products

The thermal conductivity of a dielectric solid can be expressed by an integral over the phonon spectrum [6-8] as:

$$\lambda = \int_0^{\omega_D} k(\omega)d\omega = \frac{1}{3}\int_0^{\omega_D} C(\omega)\, v\, l(\omega)\, d\omega \qquad (5)$$

The integration is over all phonon frequencies, ω, from 0 to the Debye frequency (upper cut-off), ω_D, v is the speed of the lattice waves (considered identical to the speed of sound), $C(\omega)$ is the heat capacity per unit volume at the frequency ω, and $l(\omega)$ the phonon mean free path. In the investigated temperature range, from 300 to 1800 K, the specific heat was calculated with the Debye approximation.The phonon mean free path is limited by various interaction processes, such as anharmonic phonon interactions and phonon scattering by substitutional atoms. Each process limits the mean free path independently to a first approximation, and so adds in the customary "parallel" manner [3]. In the final evaluation it is convenient to define a frequency ω' such that for a given temperature and substitutional atoms the phonon scattering by dissolved additives in the matrix equals the intrinsic scattering:

$$l_0(\omega', T) = l_p(\omega') \qquad (6)$$

In the final evaluation (see [3] for more details), the conductivity, λ_m, of the SIMFUEL matrix, which contains dissolved atoms, can be related to the "reference" conductivity of pure UO_2 at the

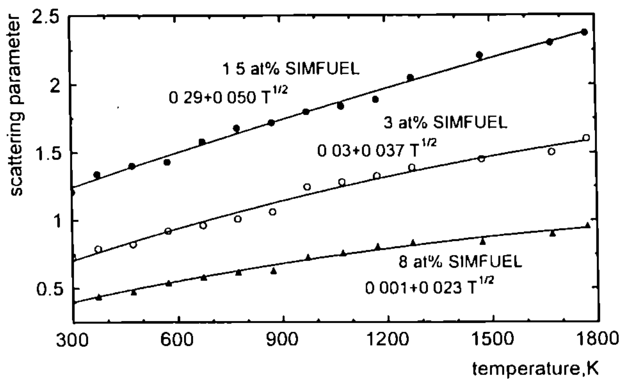

Fig. 1.12 Scattering by the dissolved fission products in 1.5, 3 and 8 at% SIMFUEL as function of the temperature. The lines represent the best fit as a square root temperature dependence

same temperature. The ratio between the SIMFUEL matrix and UO_2 conductivity (at the same temperature) is obtained:

$$\lambda_m / \lambda_0 = (\omega' / \omega_D) \arctan (\omega_D / \omega') \qquad (7)$$

The ratio between the phonon frequency (ω') at which scattering by dissolved additives in the matrix equals intrinsic scattering, and the Debye frequency (ω_D), is a measure of the point defect scattering strength by the dissolved fission products. This ratio is called scattering parameter and is used in the present analysis. The ratio λ_m/λ_0 values, deduced from Tab 1.1, were used in equation (6) to find graphically the scattering parameter (ω'/ω_D) for each temperature and burnup; the values obtained are given in Tab. 1.2.

The variation of this parameter versus the temperature for the burnups of 1.5, 3 and 8 at% is displayed in Fig. 1.12. The line of best fit was drawn as a function of the absolute temperature according to the theoretical variation $(\omega'/\omega_D) \propto T^{1/2}$ and is shown as well in Fig. 1.12. The coefficients of the $T^{1/2}$ relation in the fitted curves of 1.5, 3 and 8 at% burnups are in the ratios of 1.38, 1.61 and 2.21, respectively. Since ω'/ω_D should vary with concentration c as $c^{1/2}$, the curves are expected to be in the ratio 1.41, 1.63 and 2.3. We thus obtain good agreement between the experimental data and the theoretical variation with the concentration of the dissolved atoms.

This expression (7) holds for:

- the strong scattering when $\omega' < \omega_D$ and there is a $T^{-1/2}$ dependence of matrix thermal conductivity λ_m, and
- the weak phonon scattering when ω' is in ex-

Tab. 1.2 Calculated scattering parameter by the dissolved fission products using heat current theory and mass difference scattering for the high burnup UO_2 fluorite matrix.

	Scattering Parameter by Dissolved Fission Products					
	From Eq. (7)			From Eq. (14)		
				a = .5469 nm	a = .5467 nm	a = .5464 nm
Temp. (K)	1.5 at%	3 at%	8 at%	1.5 at%	3 at%	8 at%
300	1.208	0.717	0.414	1.21	0.73	0.40
473	1.403	0.819	0.472	1.39	0.81	0.48
673	1.581	0.955	0.581	1.57	0.97	0.58
873	1.721	1.056	0.633	1.72	1.06	0.65
1073	1.842	1.283	0.761	1.86	1.30	0.75
1273	2.050	1.387	0.835	2.04	1.40	0.85
1473	2.211	1.449	0.846	2.23	1.46	0.86
1673	2.298	1.500	0.900	2.32	1.51	0.92
1773	2.367	1.598	0.953	2.38	1.59	0.97

cess of ω_D and the matrix thermal conductivity reduces to the standard hyperbolic form.

In the limit when $\omega' < \omega_D$ (weak phonon scattering), one can expand the arctan to a third power in the argument and one arrives at the standard additive resistance form $1/\lambda_m = A(\beta) + B(\beta)T$ used earlier to fit SIMFUEL thermal resistivity data (without correction for precipitated fission products) [2]. A linear parametric variation with the burnup, β, for the parameters $A(\beta)$ and $B(\beta)$, including the effects from both, precipitated and dissolved fission products was found:

$$A = A_0 + A_1\beta = 0.053 + (0.016 \pm 0.0015)\beta \quad (\mathrm{mKW^{-1}}) \tag{8}$$

$$B = B_0 + B_1\beta = [2.2 - (0.005 \pm 0.002)\beta]10^{-4} \quad (\mathrm{mW^{-1}}) \tag{9}$$

This dependence shows a significant effect of the burnup on the phonon scattering by the lattice imperfections (coefficient A), and a small effect on the temperature-dependent coefficient B (the term $B \cdot T$ describes the contribution from the anharmonic phonon-phonon interactions). Both coefficients, A and B have a linear dependence on burnup. However, the negative slope (coefficient B_1) found for B in SIMFUEL data implies weaker phonon-phonon interaction with burnup increase which is unlikely. This inconsistency disappears if the degradation of SIMFUEL matrix thermal conductivity is considered (after corrections for the precipitated fission products were applied):

$$R_m = 1/\lambda_m = (0.0432 + 0.0155\beta) + (0.202 + 0.0025\beta)10^{-3}T \quad (\mathrm{mK/W}) \tag{10}$$

Our A_0 and B_0 coefficients corresponding to "pure" UO_2 are in good agreement with some of those previously reported (see e.g. [2]). However, the additive form of thermal resistivity is limited to the investigated temperature range where the weak phonon scattering by dissolved fission products are dominant. The use of equation (7) allows to obtain an optimum value of the phonon scattering parameter by the dissolved fission products in the fluorite matrix for both weak and strong phonon scattering effects.

Strength of the scattering by dissolved fission products from the mass difference

The above scattering parameter can also be obtained by utilizing the average mass difference between the host uranium atoms and the dissolved atoms. This is a more common method to calculate the strength of phonon scattering by dissolved additives. For a mass difference ΔM, Klemens [6] defined the parameter A, which is directly related to ω'/ω_D:

$$A = C(\Delta M/M)^2 a^3 (4\pi v^3)^{-1} \tag{11}$$

where a^3, v are the atomic volume and the phonon velocity and C is the additives concentration. The present analysis is on a "per molecule" basis, so that c is the number of metal solute atoms per U-atom and a^3 is replaced by $3a^3$ to retain consistency. Klemens also provided the relationsship between the parameter A and our scattering parameter ω'/ω_D [8]

$$(\omega'/\omega_D)^2 = \frac{2kv^2}{3\pi}(a^3\omega_D)^{-1}[\lambda_m C(\Delta M/M)^2]^{-1} \tag{12}$$

where λ_m (T) is the matrix thermal conductivity at the same temperature as the value of ω'/ω_D. Using the definition of the Debye frequency [7]

$$\omega_D^3 = 6\pi^2 v^3/a^3 \tag{13}$$

ω_D can be eliminated in the right term of equ. (12), and after some rearrangement, the following relation is obtained:

$$(\omega'/\omega_D)^2 = 0.0544\,kv\,(\lambda_m a^2)^{-1}[C(\Delta M/M)^2]^{-1} \tag{14}$$

Thermal conductivities (Tab. 1.1), the lattice parameters of the 1.5, 3 and 8 at% burnup SIMFUEL, and $v = 4 \cdot 10^3$ m/s were used to calculate the scattering parameters due to the dissolved fission products. Considering the chemical state of SIMFUEL, roughly 70 wt% of the additives are dissolved in the matrix (La, Nd, Ce, Ba, Y, Sr, Zr) and 30 wt% are precipitated in the metallic and ceramic phases. Using the atomic mass of the dissolved fission products, the mass-difference factor can be calculated as $\Sigma_i C_i (\Delta M/M)$ for each burnup composition. With these values, the scattering parameters ω'/ω_D were obtained; they are listed in Tab. 1.2. The scattering parameters calculated from the mass defect are in good agreement with those deduced from the phonon heat current analysis. For example, the calculated values from mass-defect scattering: $\omega'/\omega_D = 0.40$ for 8 at% SIMFUEL at room temperature; $\omega'/\omega_D = 1.40$ for 3 at% burnup at 1273 K; and $\omega'/\omega_D = 2.38$ for 1.5 at% burnup at 1773 K agree well with the values of 0.41, 1.39 and 2.37, respectively, obtained from the phonon heat current analysis.

Conclusions

The thermal conductivity of irradiated UO_2 fuel is dependent on porosity, O/M-ratio, and burnup, as well as on temperature.
In the reporting period, the thermal conductivity of SIMFUEL was modelled as a function of burnup taking into consideration two key microstructural features of irradiated high-burnup fuel:

- the precipitated fission-product phases, and
- the dissolved fission products in the SIMFUEL matrix.

The precipitated phases in SIMFUEL have a higher thermal conductivity than the matrix and their contribution could be modelled by a method similar to that used for porosity, i.e., by a correction factor dependent on their volume fraction. The corrections for e.g. the 3 at% burnup SIMFUEL with a volume fraction of 0.9 % for the precipitated fission products yielded an increase of about 2.7 % in the thermal conductivity.

The degradation of the matrix conductivity due to the dissolved fission products could be analyzed by considering their effect on the phonon heat current. The scattering parameter of the phonons by dissolved additives in the matrix, defined as a function of the phonon frequency, was determined by two different approaches:

- by comparing the measured thermal conductivities of SIMFUEL to that of UO_2 at various temperatures, and
- by a more commonly used relation based on the measured thermal conductivity and the average mass of the dissolved fission products.

The derived values for the scattering parameter follow the theoretically predicted square root dependence on the temperature and the concentration of the dissolved additives. The results indicate that the degradation of the matrix thermal conductivity, in the absence of fission-gas bubbles, can be explained by the phonon scattering from the dissolved fission products.

This work, as the other studies with SIMFUEL, has been performed in cooperation with AECL Research, Canada (see refs. [1-3]).

References

[1] P.G. Lucuta, R.A. Verrall, Hj. Matzke and B. Palmer, J. Nucl. Mater. **178** (1991) 48

[2] P.G. Lucuta, Hj. Matzke, R.A. Verrall and H.A. Tasman, J. Nucl. Mater. **188** (1992) 198

[3] P.G. Lucuta, Hj. Matzke, R.A. Verrall and P.G. Klemens, Proc. 22nd Int. Thermal Conductivity Conference, Tempe, Arizona, Nov. 1993, p. 894

[4] J.C. Maxwell, "A Treatise on Electricity and Magnetism", Oxford Univ. Press, London 3rd ed, vol. 1 (1892)

[5] B. Schulz, Kernforschungszentrum Karlsruhe, Report KfK-1988 (1974)

[6] P.G. Klemens, Phys. Rev. **119** (1960) 507

[7] P.G. Klemens, Nucl. Instr. & Methods Phys. Res. **229** [B] (1984) 204

[8] P.G. Klemens, High Temp. - High Pressures **17** (1985) 41

Studies on the behaviour of cesium in UO_2

Mobility of Cs in Oxide Fuel under irradiation

Thermally activated diffusion and release of Cs in operating oxide fuel elements is a well known phenomenon evidenced by radial and axial redistribution of Cs. More recently, another aspect of Cs-mobility gained importance, i.e. the "jog" formation (for joint oxyde-gaine): At burnups between 7 and 9 % (heavy metal) in FBR mixed oxide pins, the fuel-to-clad joint opens and gets filled with a fission product oxide phase, Cs and Mo being the main components [1]. This burnup corresponds to that of the formation of the RIM structure in LWR fuels (see above). It was therefore of interest, to include Cs-ion beams into the separate effect studies to investigate the parameters of the RIM formation (see above).

Previous investigations of depth profiles of UO_2 and SIMFUEL implanted with the alkalis Rb and Cs using secondary ion mass spectrometry (SIMS) had revealed a pronounced spike in the near surface concentration of Rb and Cs [2]. This spike was superimposed on the depleted residual projected-range profile and was explained to be due to redistribution of Cs during the implantation, caused by radiation-enhanced diffusion. Fig. 1.13 shows schematically the key factors for these 40 keV implantations.

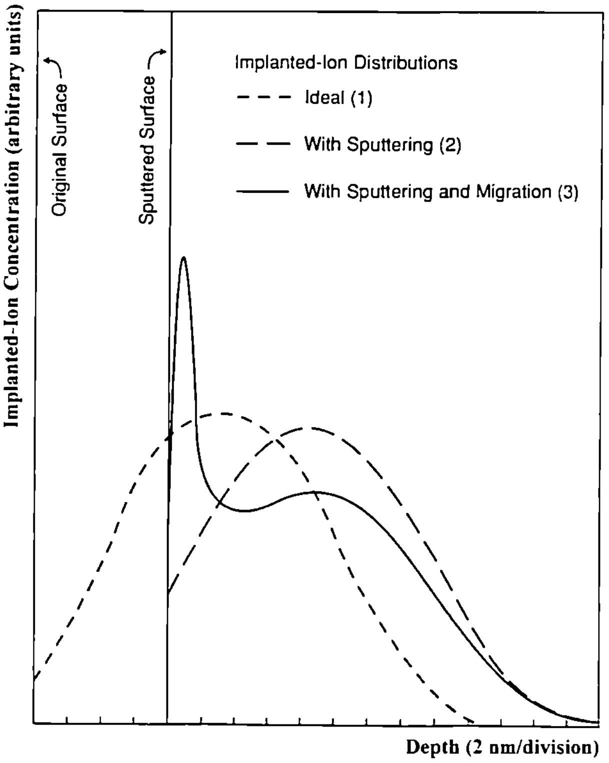

Fig. 1.13 Schematic illustration of the key factors affecting the evolution of the ^{133}Cs distribution in UO_2 during ion implantation at 40 keV. The ideal implanted-ion curve is based on a calculated projected-range profile. Direct sputtering effects were estimated by summing a suite of staggered ideal profiles and then rescaling. The impact of surface segregation as well as sputtering is qualitatively depicted by the third curve.

A detailed investigation of the phenomena occurring during the implantation with 300 keV Cs-ions was performed in the reporting period. The conditions were the same as those used for Xe. For Xe-implantation, polygonization of the surface occurred as reported above (see also ref. [3]). For exactly the same implantation conditions (energy, range, concentration, damage level), no polygonization was seen for Cs-implantations. Even when increasing the implanted dose of Cs to much higher values (up to $12x10^{16}$ ions/cm^2), no polygonization peak was seen in Rutherford backscattering / channeling measurements.

The above results for xenon prove polygonization and indicate the formation of a block structure. The driving force for such an effect can be a strain field built up during implantation. It is not a priori clear whether this strain build-up is due to accumulation of Xe-atoms, to defect-impurity interactions, and/or to radiation defects. If the third factor is playing the crucial role in polygonization, implantations with different ions of similar mass as Xe (other fission products) should produce the same effect. With this aim in mind, the implantations with 300 keV cesium ions were performed.

These implantations showed (instead of a polygonization peak) damage saturation for fluences $\geq 6x10^{16}$ Cs-ions/cm^2 with the damage peak in RBS/channeling spectra reaching about half of the random level. The analysis of the random spectra, and parallel SEM examinations of the implanted surfaces gave an explanation why in this case the polygonization peak was absent. Fig. 1.14 shows Cs depth distributions deduced with the aid of the RUMP code. The total amount of Cs retained reached a saturation level (or possibly even a maximum) of $4.4x10^{16}$ Cs-ions/cm^2 at an implanted fluence of $6x10^{16}$ Cs-ions/cm^2. Loss, or release, of Cs is clearly indicated by the formation of a second peak corresponding to surface segregation of Cs. This second peak is first indicated by a shoulder at the fluence of $4x10^{16}$ ions/cm and is

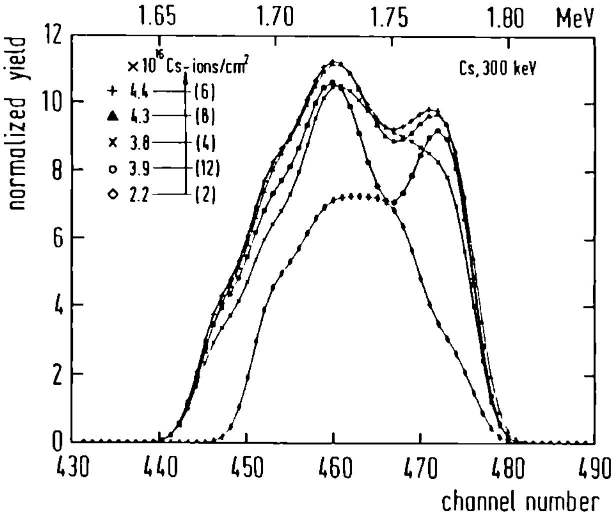

Fig. 1.14 Cesium depth distributions deduced from fittings of the random RBS spectra with the RUMP code. The retained doses and the implanted fluences (values in brackets) of the 300 keV Cs-ions are given in the figure.

most pronounced at the highest fluence of 12×10^{16} ions/cm^2. At this fluence, the retained dose was only 33 %, i.e. 3.9×10^{16} ions/cm^2. SEM analysis showed that large amounts of Cs were expelled from the solid and were accumulated at the edge of the implanted area (see Fig. 1.15). EDX analysis confirmed that the annulus visible on the SEM micrograph has Cs as main component. This loss of Cs apparently prevents the formation of a polygonization peak. This implies that a high concentration of insoluble foreign atoms is needed for grain subdivision to occur, a high damage concentration alone is not sufficient. The results show also clearly that radiation-enhanced mobility of Cs, even at low temperatures, can cause Cs-release. In addition to bulk diffusion, surface diffusion is also largely enhanced by radiation, as shown by the formation of the Cs-annulus at the edge of the bombarded area.

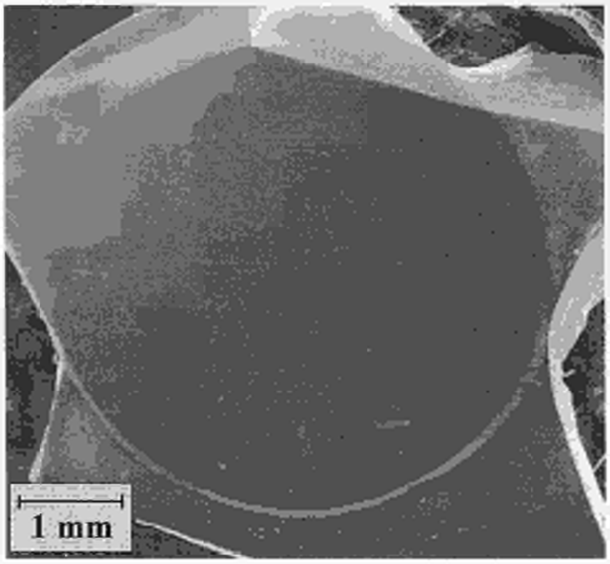

Fig. 1.15 SEM picture of the implanted crystal showing a Cs-annulus at the edge of the implanted area just underneath the mask used to define the beam area.

References

[1] M. Tourasse, M. Boidron and B. Pasquet, in Nuclear Materials for Fission Reactors, Eds. Hj. Matzke and G. Schumacher, Special volume J. Nucl. Mater. 188 (1992) 49

[2] W.H. Hocking, R.A. Verrall, P. G. Lucuta and Hj. Matzke, Rad. Effects & Defects in Solids 125 (1993) 299

[3] Hj. Matzke, A. Turos and G. Linker, Nucl. Instrum. Meth. in Phys. Research B, in print

Effects of exposure to water on the fine-grained RIM region of high burn-up LWR fuel.

A small fuel sample taken from the rim of the pin AF 21-2 irradiated to 7.6 % FIMA (see TUAR 92, p. 17) which had been thoroughly characterised by TEM and SEM and showed the small grain structure characteristic of high burn up fuel, was further examined by SEM after exposure to water at room temperature for various times. The purpose of this examination was to determine whether there was any change to the microstructure of the fuel which might be relevant to the leaching behaviour of high burn-up spent fuel during long term storage.

Fig.1.16 shows the typical fine-grain structure of the fuel, revealed particularly clearly in an open pore on a fracture surface. The mean grain size is approximately 0.15 µm. This piece was then immersed in distilled water for accumulative total times of 15 mins., 120 mins. and 362 hrs. and allowed to dry in air before being re-examined in the SEM. In each case it was possible to find and photograph the same area after treatment.

Fig. 1.17 shows the same area as Fig. 1.16 following 15 mins. exposure to water. Very little, if any, significant change can be detected after this short exposure time, as is also the case after 120 mins. However after 362 hrs. the sample shows detectable surface microstructural changes, as can be seen in Fig. 1.18. These are also demonstrated at higher magnification in Fig. 1.19, which shows a comparison of part of Fig. 1.18 with the as-received state of Fig. 1.16.

The apparent changes can be characterised as follows:

1) An opening up of the boundaries, at an apparent rate of ~ 0.05 nm/hr. or ~ 1nm/d, i.e. the grain boundaries open up at twice this rate. However, this does not necessarily correspond to a value for the uniform surface dissolution rate since the measurements are made on a grain edge (for example at point A) and not on a flat grain surface. Note, in this respect that the above rate corresponds to that of uniform surface dissolution of highly radiation-damaged UO_2, whereas UO_2 with little damage shows a much lower rate of < 0.1 nm/d [1].

2) A change in the surface roughness of the exposed grain faces (for example at point B),

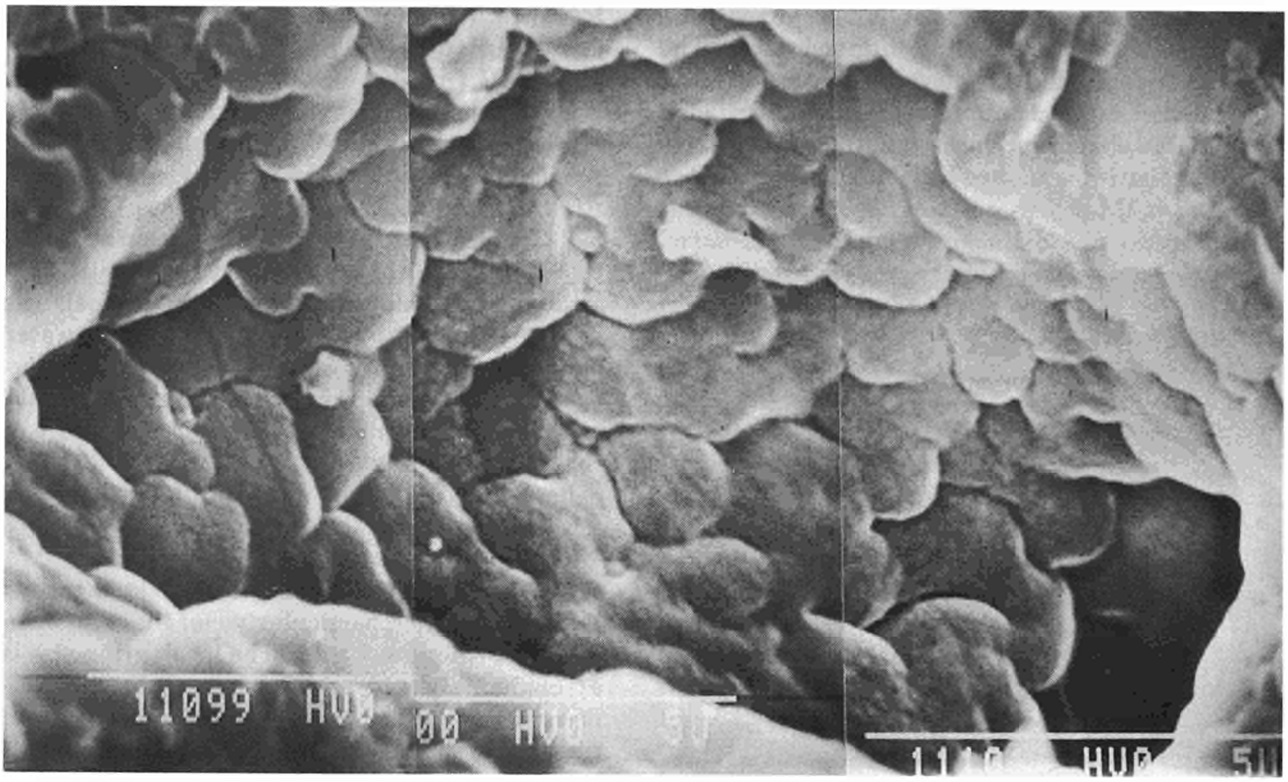

Fig. 1.16 Scanning Electron Microscope (SEM) image of a small piece of LWR fuel taken from the periphery of the fuel, showing the small grain structure of the UO_2.

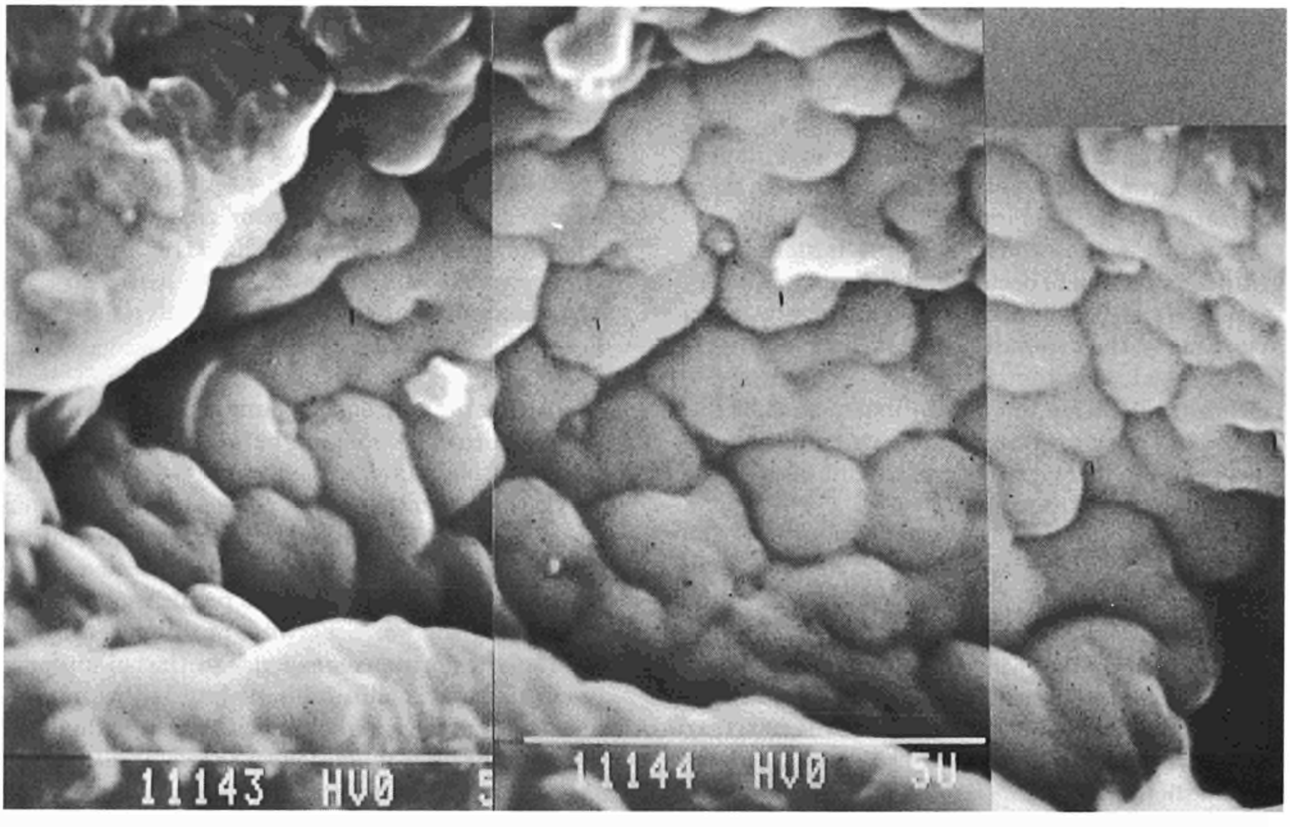

Fig. 1.17 A SEM micrograph of the same area after exposure to distilled water at room temperature for 15 mins. There is no significant change visible in the microstructure at this resolution.

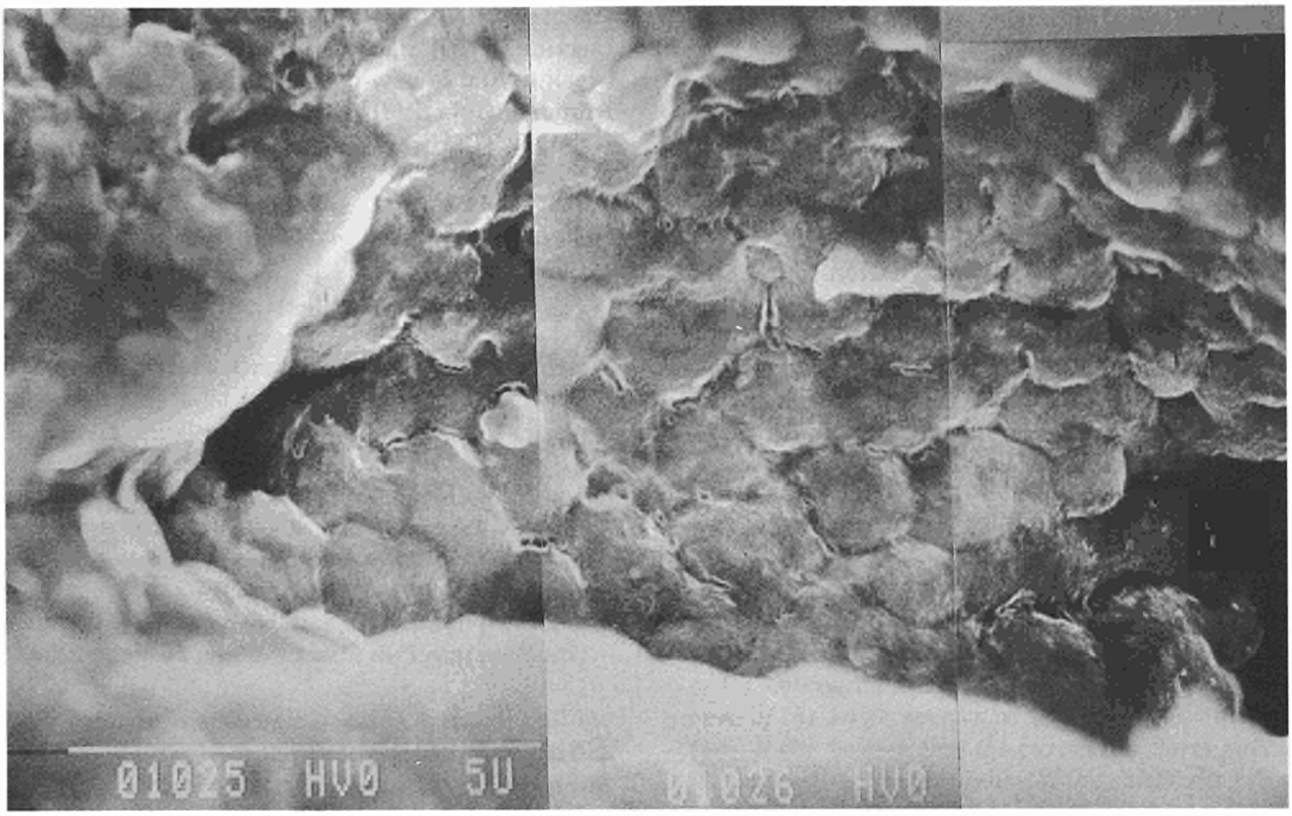

Fig. 1.18 A SEM micrograph of the same area after exposure to distilled water at room temperature for a total period of 362 hrs. The micrograph shows significant loss of material from the exposed grain boundaries, and a change in the character of the exposed grain faces.

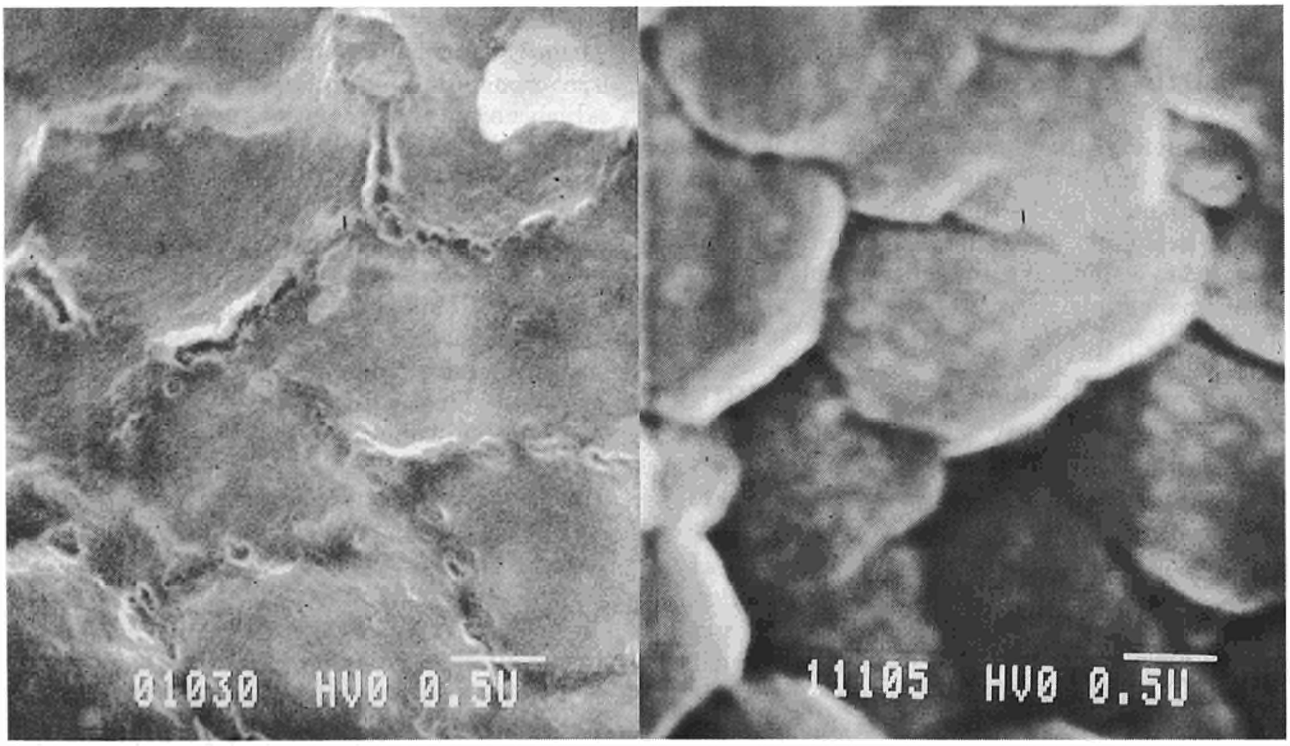

Fig. 1.19 A comparison of the same area before and after treatment at a higher magnification.

indicating enhanced leaching as compared with unirradiated UO_2.

3) The formation of ledge structures, such as that shown at point C, which appear to be associated with faint surface features on the original grains.

Thus this preliminary examination shows that there is a quite appreciable affect of water on the rim structure of the fuel. Since this is of relevance to the behaviour of the fuel under the conditions of long-term storage, a thorough investigation under controlled conditions and different temperatures is planned.

Reference

[1] Hj. Matzke, J. Nucl. Mater. 190 (1992) 101

Studies of problems related to reactor safety

Ultrasonic thermometers for PHEBUS project

The novel concept of control and evaluation electronics Black Box Mark 3 and the accompanying software have been implemented and are operational [1].

Unfortunately, the signals from both thermometers installed in FPT0 were lost progressively, and completely by the time of the test, and could not be exploited. The failures are tentatively attributed to water leaks, the cause of which is presently under study.

Ultrasonic thermometry for PHEBUS FPT1-5: Technology transfer

A comprehensive report of fabrication details [2] has been prepared and was discussed with the succeeding team involved [3].

Ultrasonic thermometry for PHEBUS FPT1-5: Sensor preparation

The problem of interference from multiple reflections in multiple-section sensors has been studied in great detail [4]. A consequently suggested 7-section sensor has been accepted as a universal design, and is now being fabricated in sufficient numbers (about 15) for all forthcoming experiments FPT1 through FPT5.

References

[1] H.A. Tasman and Th. Hock: Black Box Mark 3: Control and Evaluation Electronics and Software for Ultrasonic Thermometry. Technical Note K0293174 (July 1993)

[2] H.A. Tasman, D. Pellottiero, B. Introvigne: Thermomètre à Ultrason - Conception, Fabrication, Etalonnage. Note Technique K0293165 (Février 1993)

[3] CEA-CEN-Saclay/SETIC/LIFT

[4] H.A. Tasman: Design of Multiple-Section Sensors for Ultrasonic Thermometry. Technical Note K0293173 (September 1993)

Source term studies

Knudsen cell effusion measurements on SIMFUEL

As reported in TUAR92, two shielded Knudsen cells for measurements of the fission product vaporisation from irradiated fuels were constructed.

Experiments with SIMFUEL have been performed in order to test the sensitivity of the mass spectrometers, and explore the conditions under which a highly heterogeneous system is to be analyzed.

The experiments have been performed between 1000 and 2600 K, under ultra-high vacuum. Two types of spectra were recorded. First a general scanning up to mass 300 was performed; the relevant peaks were then selected and, in a second measurement, the corresponding mass windows were individually measured with higher accuracy.

Particular attention was devoted to the detection of volatile elements like Ba and Sr, which were, however, present in the original SIMFUEL in the form of very stable zirconates.

Fig. 1.20 shows the effusion rate of strontium measured in three different experiments where the sample was respectively in the form of a single piece, of coarsely crushed fragments and of finely crushed grains. The measured vapor effu-

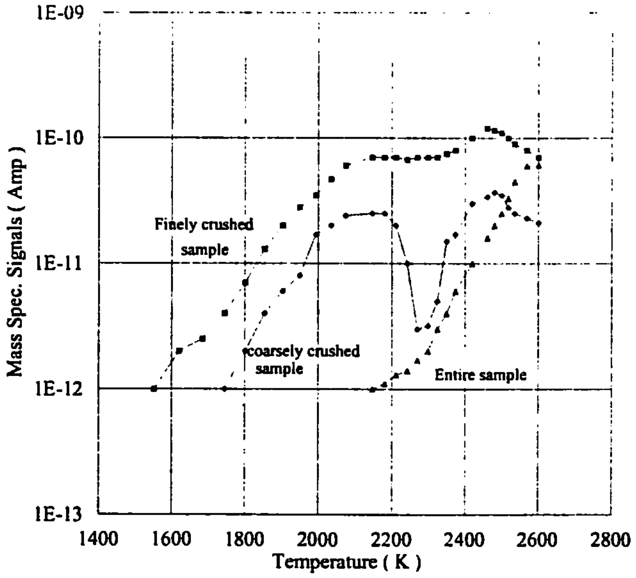

Fig. 1.20 Effusion rate of strontium from SIMFUEL samples prepared with different methods.

sion rates in the three cases are markedly different. In the finely crushed sample vapors are detected at temperatures as low as 1000 K, and the effusion rates increase continuously with temperature. In the bulk sample nothing was effectively detected up to approximately 1800 K, a temperature at which also the UO_2 matrix exhibits a significant evaporation. In the fragmented sample the results are in between: a low temperature evaporation stage is observed, but this comes to exhaustion at circa 2300 K, and only at higher temperatures is a signal upswing observed, attaining a maximum at 2500 K. The behaviour of barium is analogous. Cerium, lanthanum and neodymium (whose observed major vapor species over SIMFUEL was the monoxide) show a regular increase in the evaporation rate with temperature, with curves almost parallel to that of the UO_2 vapor (Fig.1.21a, b); this suggests that these elements are in solid solution in the matrix.

Palladium appears already at relatively low temperatures (1800-2000 K) in the crushed sample, whilst in the bulk one the onset of significant evaporation is shifted up to 2200-2300 K. In all the examined samples, zirconium and the other three elements of the initial metallic phase, molybdenum, ruthenium and rhodium, were under the detection limits up to the highest attained temperature (2550 K), (both in the elementary form and in other expectable compounds). The absence of zirconium vapors indicates that, after decomposing of the initial perovskite phase, Zr remains in the matrix as a dioxide, a compound with an extremely low equilibrium vapor pressure.

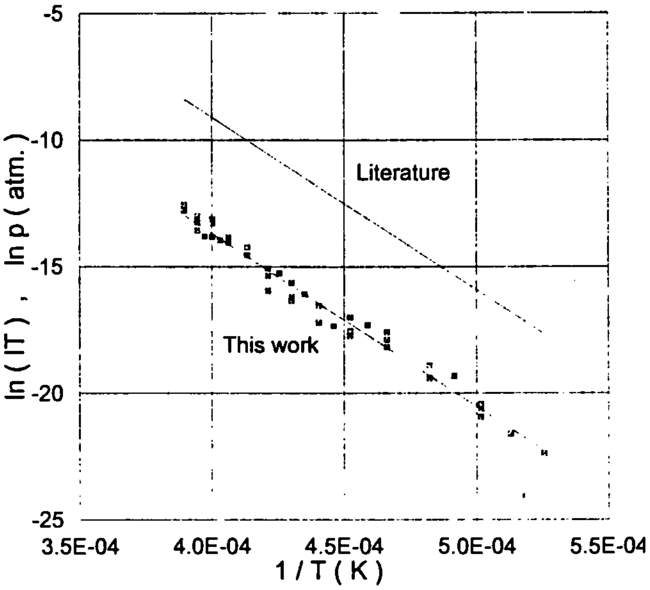

Fig. 1.21a Vaporisation rate of UO2 (product temperature times ion beam current) as a function of 1/T compared with the equilibrium partial pressure of the same species as taken from the literature. It can be seen that the curves are fairly parallel, indicating the constancy of the calibration factor of the mass spectrometer.

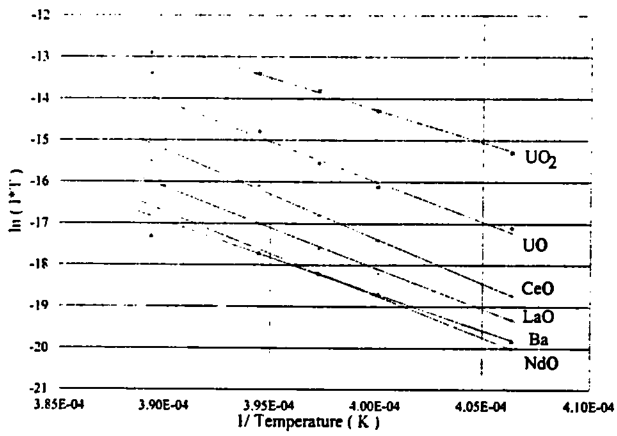

Fig. 1.21b Vaporization rate of the main vapor species, compared to that of UO_2.

These prelimimary results enable us to delineate the analytical problem faced in these experiments.

The system investigated was likely not in chemical equilibrium during the experiment, therefore measurements of thermodynamic quantities can hardly be obtained with the usual models for Knudsen effusion. Furthermore, the experiments show that embedded phases are present whose vapors can only be detected if the sample is crushed, and, even so, the results may finally depend on the sample preparation methods.

Yet, this state of things, which is based on a simple analytical approach, may present insurmountable difficulties, but still provides useful information if the data are interpreted on the basis of a detailed description of the initial structure of the sample and of the restructuring kinetics during the measurements.

Actually, the objective of the Knudsen cell effusion experiments on SIMFUEL and on irradiated fuels is not to obtain primary thermodynamic data, but rather to check the consistency of the predictions of our fuel restructuring models and of a distinct set of hypotheses concerning the chemical state of the fission products.

Finally, these results confirm that the release of fission products from nuclear fuels under overheating conditions is dependent on their initial distribution in the various phases, structural sinks and pockets of the sintered pellet, and, furthermore, on the restructuring kinetics during the temperature transient.

The experimental data will be therefore interpreted and evaluated within a well defined analytical scheme, where the following different aspects are examined:

The presence of open ("vented ") phases on the grain boundaries.
The behavior of the intragranular finely dispersed phases.
The evaporation conditions of the solid solutions.
The effusion kinetics and the limits of the equilibrium conditions during the thermal treatments.
The wash-out conditions for the minor impurities.

Finally, in the scenario of the analysis of large-scale tests like PHEBUS.PF, which at present draw the attention of most of the "source term" modeling specialists, Knudsen cell effusion experiments can be optimally used to validate and corroborate the basic thermochemical models. Furthermore, these experiments should indicate to which extent the various fission products release phenomena are reproducible, and which are the non-controlled effective parameters. This is not a secondary aspect of the problem, since, due to the very large amount of data involved, the management of the mechanistic code calculations for predicting the primary source term events has to be better defined than in the simpler case of fission gas release.

Benchmark modelling exercise for the PHEBUS

The Institute has participated in the PHEBUS benchmark exercise for the prediction of release of a number of fission products, including short-lived radionuclides. The codes FUTURE, MITRA and CHEMIF have been sequentially used for the calculation of the fuel structural changes, the diffusion and release of the whole set of fission product inventory, and of the chemical reactions within the fuel and during the primary release stage.

The transient test, labeled FPTO, was applied to fresh fuel after a 9 day conditioning irradiation in the PHEBUS reactor, and was carried out at the end of 1993, shortly before the compilation of this report. The experimental data are presently being compared with the model predictions.

If, on one side, the transient test FPTO is supposed to represent a simple reference case where the fuel burnup effects are absent, on the other one the calculation of the fuel behavior is facing particular difficulties. First, because during the transient fuel restructuring is not predominantly driven by the precipitation and expansion of the volatile fission products, but rather by the more uncertain thermal restructuring of the as fabricated fuel. Secondly, because the fission products amounts involved, and hence the dynamic parameters (pressures, stresses and deformations) are two orders of magnitude lower than in the case of fuel irradiated at typical burnups; in this case in the computer codes a number of problems (e.g. phase nucleation, limits of solubility, capillarity effects) lead to a degradation of the calculation precision.

The two proposed cases, respectively corresponding to two different temperature ramps (1A and 1B) have been calculated. The ramp difference entails changes in the fuel response, mostly regarding the time at which the onset of massive release is expected. As for the rest, the transient development is similar in the two cases, so that only transient 1B is reported here.

Fig. 1.22 shows the assumed temperature evolution in the test in three annular zones of the pellet. It can be seen that the central one is heated up to close the melting point. The characteristic precipitation behavior of rare gases (Xe,Kr) is shown in Fig. 1.23: the gas, initially frozen in lattice positions (by irradiation-induced dynamical solution) precipitates first into intragranular bubbles. When temperature reaches approxi-

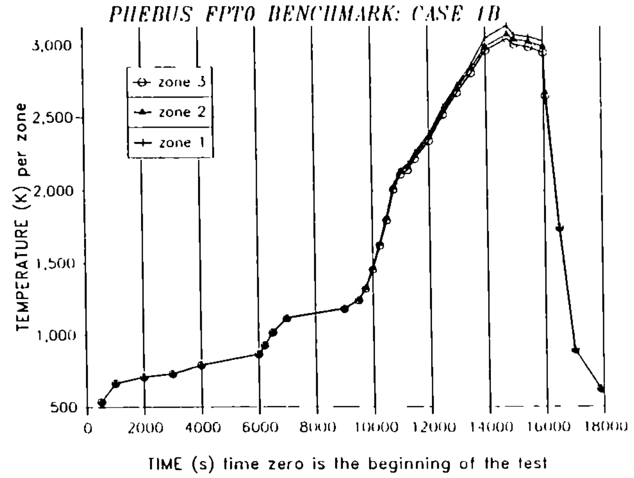

Fig. 1.22 Temperature evolution of the benchmark case 1B for the PHEBUS FPT0 experiment.

mately 2000 K these migrate or are swept out by moving grain boundaries and more than 90% of the gas is eventually collected in intergranular pores wherefrom it escapes when percolation conditions are attained. This is controlled by the interlinking factor of the grain boundary porosity, which is plotted in Fig. 1.24.

The diffusion and release of short lived isotopes is described by a complex equation whose solution is provided by MITRA. Fig. 1.25 shows the total amount of the main xenon isotopes leaving the fuel as a function of transient time. Radioactive decay and neutron capture effects are included in the calculation of various amounts. Fig. 1.26 shows the release of ^{137}Cs and three iodine isotopes. Due to the short irradiation period the code predicts that these two elements are mostly present in the same precipitates, so that their release curves are almost parallel.

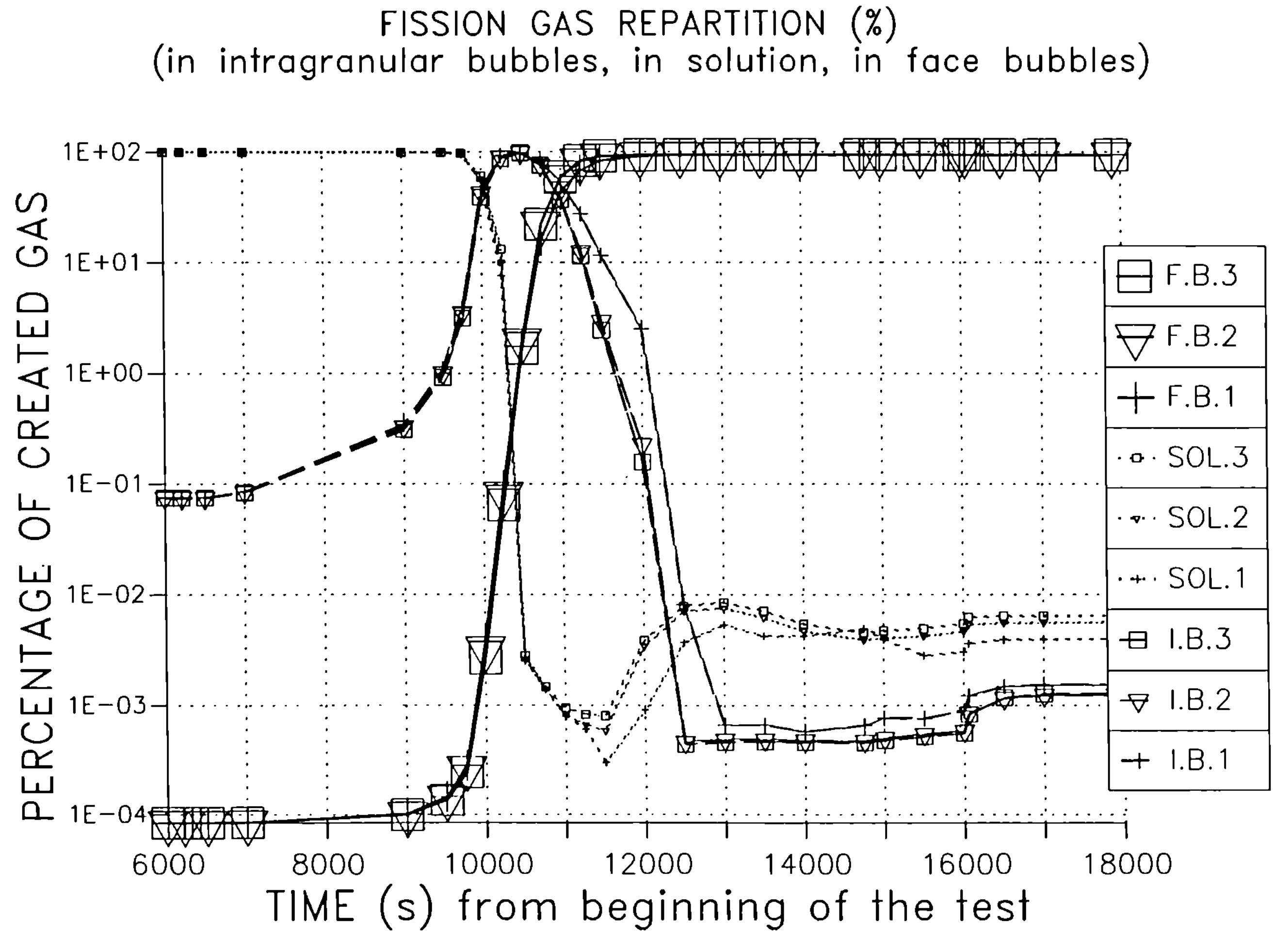

Fig. 1.23 Behavior of the gross concentration of fission gas as predicted by FUTURE.

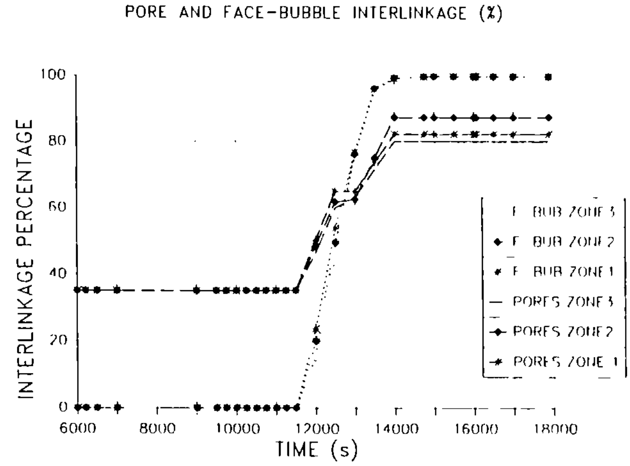

Fig. 1.24 Evolution of the interlinking factor of the grain-boundary porosity as a function of transient time.

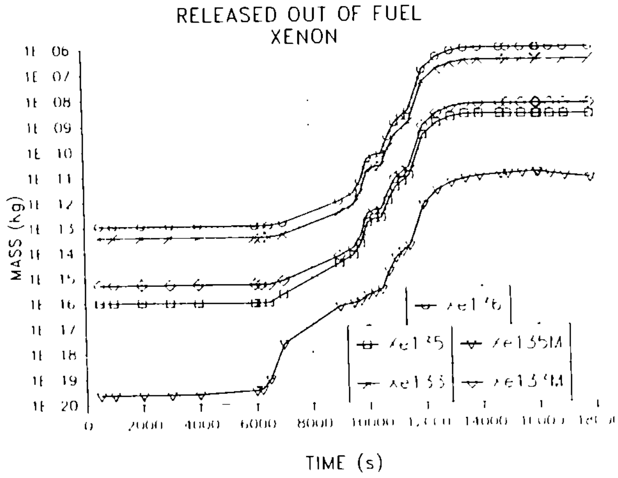

Fig. 1.25 Predicted release of the main xenon isotopes.

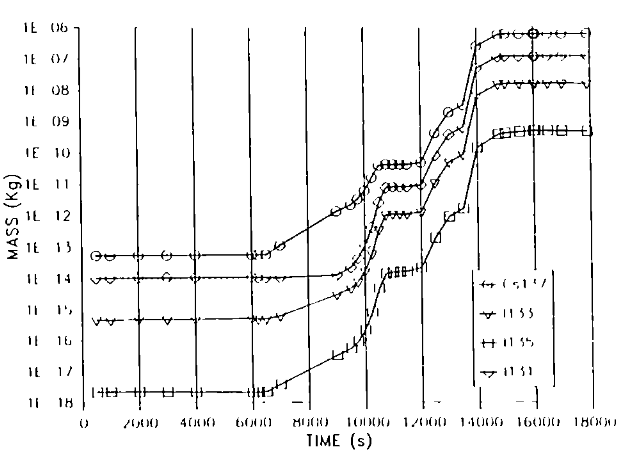

Fig. 1.26 Predicted release of iodine and cesium isotopes.

Fig. 1.27 presents the amount of some of volatile and non volatile fission products which are accumulated in the open porosity on the grain boundaries. The amount released is then associated to vaporization.

A sample of the major fission products chemical species calculated in different fuel annular zones and selected transient timesteps, are reported in Tab. 1.3. The various compounds are listed here, in the order of importance, from the top to the bottom and from the left to the right. The cladding is expected to be progressively oxydized starting from 9000 seconds after transient beginning until 14000 seconds, time at which cladding oxydation is completed. From inspection of the data of Tab. 1.3 one can see that essential changes in the chemical equilibrium take place when zirconium in the cladding is totally oxydized. A cladding breeching is conservatively calculated to occur after 9000 seconds. At this moment, steam starts reacting with the fuel/cladding system. The presence of zirconium buffering is determinant for chemical equilibrium of the fission products. The iodine chemistry is first affected, with the appearance of HI and the disappearance of the diodides. After 15000s the cladding is completely oxydized and the fuel temperature increases up to approximately 3000 K. Under these conditions, molybdenum is fully oxydized. According to the resulting chemical equilibrium, caesium should be mostly in metallic form, though molybdates and tellurides are also present. A complete oxydation of caesium is predicted in the final cooling-down stage, where both molybdates and uranates are formed.

The complete output of the FUTURE/MITRA/CHEMIF code system calculations is available in the form of a set of computer files of approximately 2-3 MB size; a detailed description of the fuel restructuring parameters and of the radiochemical and diffusional behavior of the individual nuclides are given as a function of the irradiation and transient time. A program for display of selected data is also available, however, due to the very large number of parameters involved, these results are obviously only meaningful in the context of very specific questions which may arise in the treatment of the generalized source term problem.

Tab. 1.3 Fate of the major fission products during the various steps of case 1B.

TIME	ZONE and T(K)	CHEMICAL SPECIES (decreasing abundance)
1000-2000s	all ' 710K	Mo --> Mo Ru --> Ru La --> La2UO6 Sr --> SrUO3 Te --> Cs2Te I --> BaI2. CsI. Cs2I2 Cs --> Cs2Te. Cs. CsI
7000-9000s	Hyp.1: all ' 1180K	Mo --> Mo Ru --> Ru La --> La2UO6 Sr --> SrUO3. Sr. SrI. SrI2 Te --> Te. Cs2Te. Te2 I --> CsI. BaI2. BaI. I. SrI. SrI2 Cs --> Cs. CsI. Cs2Te
7000-9000s	Hyp.2: external zone steam + cladding # 1180K	Mo --> Mo Ru --> Ru La --> La2UO6 Sr --> Sr. SrUO3. SrZrO3. SrI Te --> ZrTe2. H2Te. Te. Cs2Te. Te2 I --> HI. CsI. BaI. I Cs --> Cs. Cs2Te. CsI 5% Zr from clad oxydised
10000-10250s	internal zones no steam # 1630K	Mo --> Mo Ru --> Ru La --> La2UO6 Sr --> Sr, SrI, SrI2 Te --> Te, Te2, Cs2Te I --> I, CsI, BaI2, BaI, SrI, SrI2 Cs --> Cs. CsI, Cs2Te
10000-10250s	external zone steam + cladding # 1630K	Mo --> Mo Ru --> Ru La --> La2UO6 Sr --> Sr Te --> Te, H2Te, Te2 I --> HI, I Cs --> Cs 27.4% Zr from clad oxydised
11500-12000s	internal zones no steam # 2360K	Mo --> Mo Ru --> Ru La --> La2UO6 Sr --> Sr. SrI, SrI2 Te --> Te. Te2. Cs2Te I --> I, CsI, BaI. BaI2. SrI, SrI2 Cs --> Cs. CsI, Cs2Te
11500-12000s	external zone steam + cladding # 2360K	Mo --> Mo Ru --> Ru La --> La2UO6 Sr --> Sr Te --> Te, H2Te, Te2 I --> HI, I Cs --> Cs 58.8% Zr from clad oxydised
13000-13500s	internal zones no steam # 2840K	Mo --> Mo Ru --> Ru La --> La2UO6 Sr --> Sr. SrI, SrI2. SrO Te --> Te, Cs2Te. Te2. TeO I --> I. CsI. SrI, BaI2. SrI2 Cs --> Cs. CsI, Cs2Te, Cs2
13000-13500s	external zone steam + cladding # 2804K	Mo --> Mo Ru --> Ru La --> La2UO6 Sr --> Sr. SrO Te --> Te. H2Te. Te2. TeO. Cs2Te I --> HI. I Cs --> Cs 85.6% Zr from clad oxydised
14000-14750s	central zone no steam # 3000K	Mo --> Mo. MoO2 Ru --> Ru La --> La2UO6 Sr --> Sr. SrI. SrI2. SrO Te --> Te. Cs2Te. Te2. TeO I --> I. CsI, SrI. BaI2. SrI2. I2 Cs --> Cs. CsI. Cs2Te. Cs2
14000-14750s	middle zone # 3000K (0.02 mole steam)	Mo --> MoO3. MoO2. Mo. Cs2MoO4 Ru --> Ru La --> La2UO6 Sr --> SrZrO3. SrO. Sr Te --> Te. TeO. H2Te.Te2. Cs2Te I --> HI, I, CsI Cs --> Cs. Cs2Te. Cs2MoO4. CsO. CsI
14000-14750s	external zone steam + cladding 3000K	Mo --> Mo. MoO2 Ru --> Ru La --> La2UO6 Sr --> Sr. SrO Te --> Te. H2Te. Te2. TeO I --> HI. I Cs --> Cs. Cs2Te 100% Zr from clad oxydised
14000-14750s	external zone # 3000K 100% clad. oxydised + (0.02 mole steam)	Mo --> MoO3. MoO2. Mo Ru --> Ru La --> La2UO6 Sr --> SrZrO3. SrO. Sr Te --> Te. TeO. H2Te. Cs2Te I --> HI. I Cs --> Cs
15500-16000s	central zone (0.05 mole steam) 3000K	Mo --> MoO3. MoO2. Mo. Cs2MoO4 Ru --> Ru La --> La2UO6 Sr --> SrZrO3. SrO. Sr Te --> Te. TeO. H2Te. Cs2Te. Te2 I --> HI. I Cs --> Cs. Cs2Te. Cs2MoO4. Cs2O. Cs2. CsI
15500-16000s	middle zone (0.10 mole steam) 2990K	Mo --> MoO3. MoO2. Mo. Cs2MoO4 Ru --> Ru La --> La2UO6 Sr --> SrZrO3. SrO. Sr Te --> Te. TeO. H2Te. Te2. Cs2Te I --> HI. I Cs --> Cs. Cs2Te
15500-16000s	external zone 100% Zr from clad oxydised + (0.50 mole steam) 2947K	Mo --> MoO3. MoO2 Ru --> Ru La --> La2UO6 Sr --> SrO. Sr Te --> Te, TeO. H2Te I --> HI. I Cs --> Cs
> 17890s	all ' 623K no Zr from clad (0.002 mole steam)	Mo --> CS2Mo2O7. MoO2. SrMoO4 Ru --> Ru La --> La2UO6 Sr --> SrUO3. SrUO4. SrMoO4 Te --> TeI2. Te. Te2. H2Te I --> TeI2. HI Cs --> Cs2Mo2O7
> 17890s	all ' 623K no Zr from clad (0.08 mole steam or more)	Mo --> MoO3 Ru --> Ru La --> La2UO6 Sr --> SrUO4 Te --> TeO2 I --> HIO. HI Cs --> Cs2U4O12

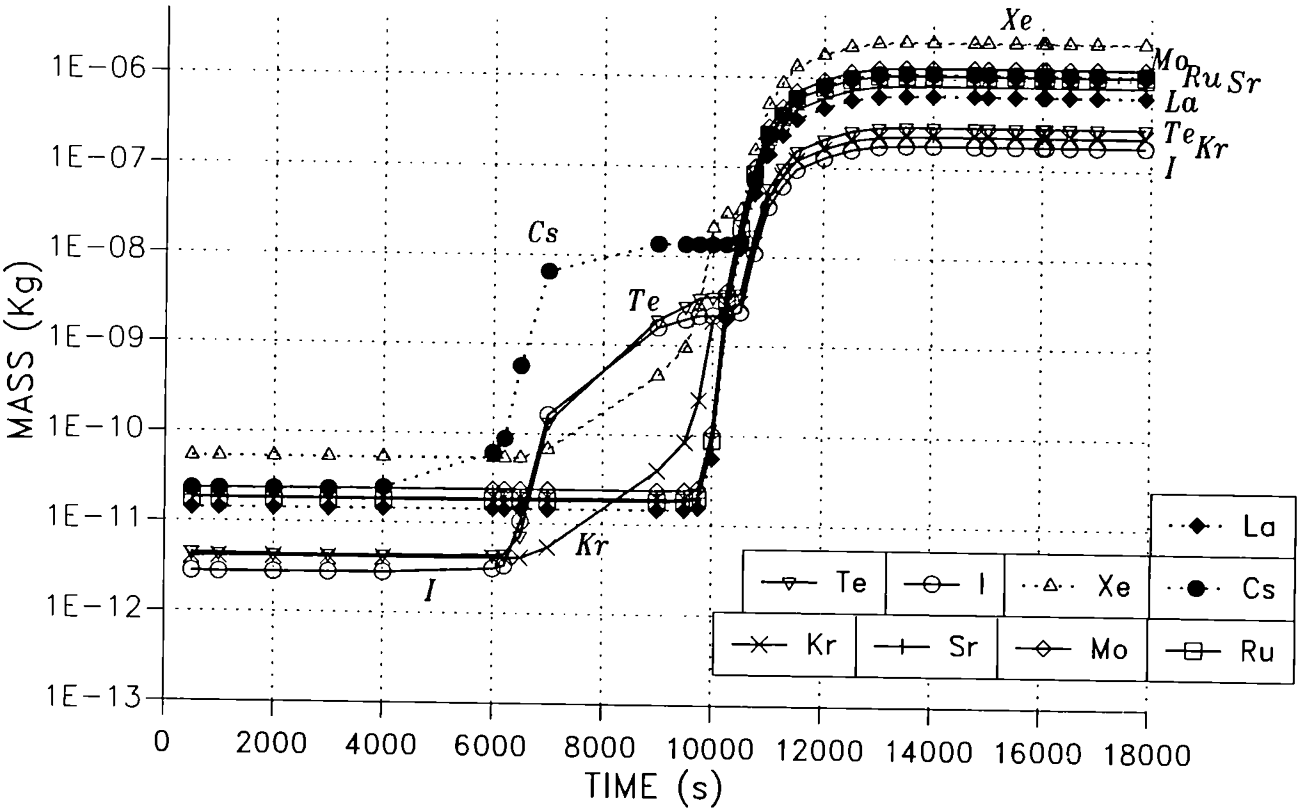

Fig. 1.27 Synoptic view of release of the main fission products.

Studies of high-temperature properties

Introduction

Two topics account for much of the research carried out in '93: thermodynamics of UO_2 at high temperature and behavior of the radioactive fission products in irradiated fuel.

There has been a surge in studies of the high temperature defect properties of urania, that began in 1992 when the heat capacity anomalies around the lambda transition temperature were measured in our group. Several aspects concerning the heat exchange mechanisms above 2000 K were then investigated, leading to interesting conclusions which are reported in detail here below.

The research on fission product chemistry and release was still running on two parallel rails: the preparation of laboratory Knudsen cell effusion experiments on irradiated fuel samples, and the calculation of the release kinetics of volatile fission products and related chemical equilibrium reactions. The latter study, carried out on the FPT-0 benchmark exercise proposed by the PHEBUS Project for the prediction of the source term in the first test with very low burnup fuel, enabled us to individuate the relevant kinetics aspects during a typical reactor accident. The results, reported here, are also to be seen as a propedeutic analysis for our next Knudsen cell experiments, where the same phenomena shall be investigated under defined effusion conditions.

This year's schedule shows a marked increase in activities concerning advanced methods for thermal diffusivity measurements. A laser-flash apparatus (LAF.I) was constructed and tested for implementation in the hot cells. In spite of the difficulties connected with remote manipulation, which required several mechanical expedients, this machine proved finally to be very versatile and its optical adjustment extremely accurate.

Furthermore, novel methods for the measurements of thermal diffusivity in heterogeneous samples are being investigated, based on ultrafast transient thermography; experimental devices are planned which should enable measurements to be easily carried out on complex systems like irradiated fuel rod under conditions near to reactor operation.

Finally, in spinoff research small programs are continuing on the development of multichannel pyrometry. Devoted to particular industrial application, this program is getting funds for equipment and staff from the DGXII. Instruments have been contructed which are abie to perform pyrometric measurements under non-conventional conditions. In particular, new methods for automatic calibration, and systematic and random error compensation have been developed, which render this type of instrument much more practicable and reliable.

Thermodynamics of UO_2

Heat exchange mechanisms in UO_2

The heat capacity of nuclear oxide-fuel is an important quantity in the analysis of severe reactor accidents in which rapid adiabatic core temperature excursions are considered. Although the thermodynamic properties of UO_2 have been carefully measured in the last decades, solid and liquid measurements above 2500K are still scanty and difficult to interpret. For this reason, within the framework of the Research Safety Program of the European Communities, the high temperature heat capacity of solid and liquid uranium dioxide has been recently thoroughly investigated in the temperature range 2500K-8000K [1, 2]. The consolidated experimental data now enable a more accurate quantitative analysis to be carried out on the elementary heat exchange mechanisms operating in the different temperature regimes. Aim of the work in the reported year was to provide an unified simple picture of the high temperature behavior of C_p.

Fig. 1.28 shows the complete set of experimental measurements of C_p above RT in nominally stoichiometric UO_2. The solid data are obtained by differentiation of enthalpy measurements [3, 4, 5, 6] and, in the vicinity of the λ-peak, by direct dynamic measurements [2]. The liquid data are taken from ref. [1]. The error bars are indicated in different temperature regimes. The measurement accuracy decreases with increasing temperature as a consequence both of the deterioration of the calorimetric and thermal measurements and of the uncontrolled variation of the chemical composition of the sample. Finally, in the liquid, where non-smoothed data are plotted, the error is mainly due to the particularly difficult experimental method adopted [7]. The full line, which represents the least-square fitting of the experimental points, is sufficiently well defined to be used in the analysis of the data.

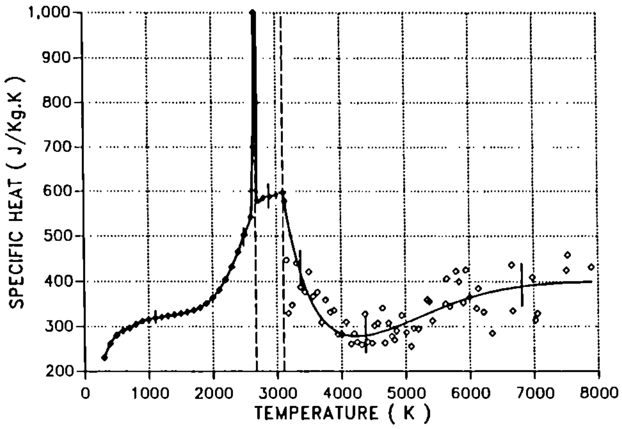

Fig. 1.28 Heat capacity of nominally stoichiometric UO_2: Experimental points and LSQ-fitting curve.

The curve $C_p = C_p(T)$ can be qualitatively subdivided into six segments, according to the dominant heat exchange mechanisms operating in the respective temperature intervals.

1. From RT to 1000K: The increase in heat capacity with temperature in this stage is governed by progressive excitation of the harmonic lattice vibrations which can be approximately described by a single effective Debye model. Since the Debye temperature of UO_2 in this temperature range is less than 600K, the Debye function is almost unity by $T > 1000$ K, where $C_p^{harm.}$ attains the Neumann-Kopp asymptotic limit of 9R, characteristic of a crystal based on a triatomic molecule.
   A minor contribution is provided by thermal excitation of localized electrons of $U^{4+}(5f)^2$ in the crystal field (CF) levels. At low temperatures this contribution is approximately proportional to T, whilst at high temperatures, where the concentration of U^{4+} decreases by disproportioning into U^{3+} and U^{5+}, becomes essentially temperature-independent.

2. From 1000K to 1500K: C_p continues to increase weakly with T due to the progressive increase in the anharmonicity of the lattice vibrations as reflected in the thermal expansion of the material. The slope of $C_p(T)$ due to these effects, measured in different compounds having similar mechanical properties, reveals an almost constant trend which can be used to extrapolate $C_p^{anharm.}$ to higher temperatures.
3. From 1500K to 2670K ($=T_t$): The additional increase in C_p in this temperature interval is caused by formation of lattice and electronic defects. The C_p peak measured at approximately $T = 0.8T_m$ (which indicates a sharp thermodynamic transition) is very similar to that observed in other ionic fluorides which exhibit a superionic λ-transition. Following ref. [8], this transition is interpreted as a cooperative process involving the creation of defects in the sublattice of the more mobile atomic species, leading to a sudden increase in the oxygen Frenkel pair concentration at a defined critical temperature, T_t [5]. This assumption was later corroborated by neutron scattering measurements of oxygen defect concentration n_F as a function of temperature [9], which show a steep inflection point at $T = T_t$. Moreover, the d.c. electrical conductivity of UO_2 is known to sharply increase in this temperature interval [10], entailing a further contribution to the heat capacity.
4. From T_t to T_m: C_p is characterized by a steep descending flank of the transition peak, due to the rapid saturation of the defect concentration (anion-disordered phase), followed by a weakly increasing stage due to the onset of the creation of more energetic atomic defects (UO_2 -Schottky trios).
5. From T_m to 4500K : the heat capacity decreases to the level attained at 1000K, indicating that all the thermally activated processes have completely saturated, leaving only atomic vibrations to support further heat exchanges.
6. From 4500K to 8000K: a C_p upswing is observed with activation energy comparable to that needed in the solid to excite the electrons of the deeper 2p-based valence band.

From this overview of the elementary mechanisms contributing to the heat capacity of UO_2 one realizes that the central problem for a comprehensive microscopic model of the system is the description of the atomic and electronic defect behavior described in points 3) and 4). Actually, in this temperature range, other relevant thermodynamic and thermophysical properties (defect concentrations, electrical and thermal conductivity [11], creep rate [12], and, probably, self-diffusion coefficient [13]) present "anomalies" which should be encompassed and explained by realistic models.

The λ-transition in UO_2

For a long time, the results concerning the λ-transition in UO_2 obtained by differentiating enthalpy, H, have been very controversial and even the existence of the transition was initially questioned by some authors, who interpreted the C_p peak obtained by finite-difference calculation of dH/dt (even that using a more sophisticated numerical analysis [14]) as an experimental artifact. Only more recent experiments specifically aimed at detecting this effect [2] could provide unambiguous and more detailed evidence. By using a thermo-analytical method based on the cooling curve analysis of a laser pulse heated sample, a pre-melting transition was observed in the form of a marked minimum in the cooling rate dT/dt. Since under fixed heat loss conditions dT/dt is inversely proportional to C_p, the C_p transition peak could be reproduced with good accuracy by using an appropriate numerical analysis. Fig. 1.29a shows the results obtained in a nominally stoichiometric sample. The transition appears at 2670K and the resulting heat capacity peak (Fig. 1.29b) - over the assumed "unperturbed" C_p background is high and very narrow; this explains the difficulty of detecting the transition by perform-

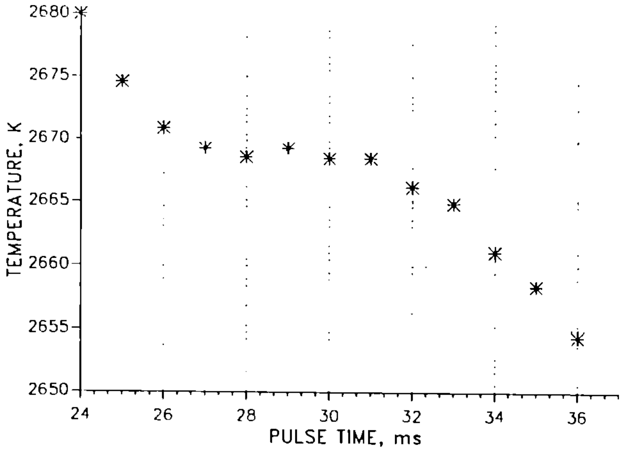

Fig. 1.29a Cooling curve of a UO_2 sphere of 1 mm diameter, showing a λ-transition at 2670K, in the form of a strong decrease in the cooling rate. The sample was laser-heated up to the pulse time indicated by 'OFF'.

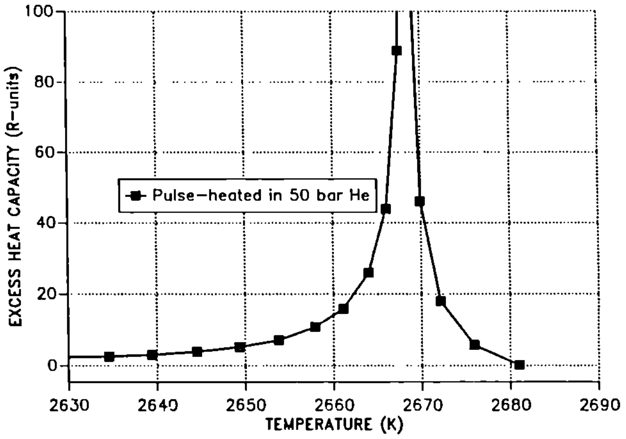

Fig. 1.29b Heat capacity peak due to the λ-transition, from the data of Fig. 1.29a .

ing numerical differentiation of H. The experiments have been repeated under both reducing and oxydizing atmospheres, and the following interesting results obtained:

1. For O/U < 2 the transition temperature increases with increasing reduction. Moreover, in reduced samples, supercooling effects are observed, involving an inversion in sign of dT/dt. This provides a clear indication that the transition producing the cooling rate perturbation was of first-order.
2. Under oxydizing conditions (O/U > 2) no inflection points are detected during cooling, and it appears that there is no transition of the kind found in stoichiometric and sub-stoichiometric UO_2.

Cooperative point defects formation in UO_2

Microscopic models for lattice and electronic defect formation have been examined with the intention of explaining the high temperature behavior of C_p in UO_2, in the context of the experimental evidence already mentioned (i.e. magnitude of $C_p(T)$, position and nature of the premelting transition and its dependence on stoichiometry, together with equilibrium defect concentration as a function of temperature). Three types of defects are considered here: a) oxygen Frenkel pairs, b) neutral trios of Schottky vacancies, and c) a valence alteration of the lattice cations. Their respective formation reactions are written as:

$$O_L^{2-} + V_I^O \rightarrow V_L^O + O_I^{2-} \quad (1)$$

$$U_L^{4-} + 2O_L^{2-} \rightarrow V_L^U + 2V_L^O \quad (2)$$

$$2U^{4+} \rightarrow U^{3+} + U^{5+} \quad (3)$$

where the symbols are self-explanatory. Once the free energies of formation of the three reactions are given, the corresponding Law of Mass Action equations together with three additional constraint equations dictated by charge neutrality, chemical composition and structural configuration of the fluorite crystal unit cell, are sufficient to define the equilibrium concentrations of the defects involved. A few remarks concerning the relation between the formation of these defects in UO_2 and the observed λ-transition are here in order.

1. The λ-transitions occurs in the vicinity of 2650K in both stoichiometric and nearly stoichiometric UO_2, and are primarily due to cooperative (anti)Frenkel anion disorder, whose associated free energy of formation is much lower than that of the Schottky trio disorder (see e.g. [15, 16]) to which the Frenkel disorder is coupled (in the Law of Mass Action) via the equilibrium oxygen vacancy concentration. In turn, the Schottky defect concentration is dependent on the disproportionation fraction of U^{4+} (see below). Near the stoichiometric O/U ratio this fraction is close to unity even at high temperatures, and hence the ionic disorder can be decoupied from the electronic. Furthermore, since the Schottky trio formation energy is nearly twice that of an oxygen Frenkel pair, the two types of defects are effectively formed and reach saturation in different temperature intervals. Therefore, in a first approximation, Frenkel disorder can be solved for independently of the Schottky disorder.
2. Assuming that the bonding in UO_2 is principally ionic, the cations in the stoichiometric material are nominally $U^{4+}(5f)^2$; the possibility of relatively low energy fluctuations about this configuration (to U^{5+} and U^{3+}) permits then:
   a. the accommodation within the fluorite phase of a large degree of non-stoichiometry; in the hyperstoichiometric case the excess oxygen is assumed to occupy interstitial sites with formation of neu-

   tralizing U^{5+} ions, whilst the hypostoichiometric case is characterized by oxygen vacancies and U^{3+} ions.

   b. Intrinsic electronic semiconductivity [10] in stoichiometric UO_2 originating from the thermally induced cation disproportionation $2U^{4+} \rightarrow U^{3+} + U^{5+}$ [17, 18, 19]; in this context it is worth remarking that near the C_p peak temperature, T_t, the d.c. electrical conductivity is approximately one order of magnitude higher than that which characterizes purely ionic conductors even in their fast-ion phase.

3. Owing to the strong interaction with the polar lattice, the supranumerary electrons and holes associated, respectively, with the U^{3+} and U^{5+} ions (formed either by eq.(3) or by stoichiometry deviation) are localized in small-polaron eigenstates. In these states, electrons and holes are associated with local atomic relaxations in the polar lattice and carrier motion takes place by "hopping", the associated mobilities being then activated, as in the case of atomic defects. Whilst from a formal point of view this permits a common treatment, it can, however, give raise to difficulties when it comes to distinguishing the respective contributions to C_p.
4. Uranium dioxide exhibits a significant increase in creep rate above T_t, much more than expected from extrapolation of lower temperature data. The plasticity above 2700K is so high that a high-density sintered UO_2 sample annealed above this temperature for a few hours is subjected to large permanent deformations even in the absence of external applied stresses. (Even the ceramographic grain boundary structure appears to be rounded - similar to that observed by cooling after melting -; the effect is sometimes so striking that early experimenters were induced into the error of taking 2700K as the melting temperature [20]!). The effect is confirmed by a decrease in the rigidity modulus [21], much stronger than that observed in the case of fluorides undergoing superionic transition [22]. It is thus evident that the λ-transition in UO_2 indicates the onset of potentially significant changes in the structural stability of the material.

Theory of the λ-transition

The mean-field models presented here attempt to lay the foundations of an understanding of the behavior of the heat capacity between 1500K and the melting point, simply by describing the temperature dependence of the equilibrium concentration of the above mentioned point defects.

Due to the limitation of space, only the salient aspects of the analysis are discussed here; more details concerning new developments will be published in a separate paper.

Linear model for cooperative Frenkel-defect formation

The simplest model capable of describing the effects associated with the cooperative defect formation in a system is based on the assumption that the free energy of formation of one additional defect decreases linearly with the concentration, n, of the pre-existing defects. The free energy of formation referred to the free energy of the perfect crystal is then:

$$\Delta G = [O_I]\left(\Delta H_0 - \frac{\lambda}{2}[V_L^O] - kT(\Delta S^{c.} + \Delta S^{n.c.})\right) \qquad \text{for} \quad UO_{2-x} \tag{4a}$$

$$\Delta G = [V_L^O]\left(\Delta H_0 - \frac{\lambda}{2}[O_I] - kT(\Delta S^{c.} + \Delta S^{n.c.})\right) \qquad \text{for} \quad UO_{2+x} \tag{4b}$$

where the indices c. and n.c. stand for 'configurational' and 'non-configurational', respectively; ΔH_0 is the enthalpy of formation in the absence of interaction. λ represents a mean attractive energy between complementary defects (oxygen interstitials and vacancies) which, for an isotropic and homogeneous distribution of defects, produces a lowering of the formation energy below the defect-free value ΔH_0. It must be stressed that λ is a purely phenomenological model parameter, which is not necessarily associated with any physically definable interaction configuration (but may, under certain conditions, be identified with the first term of a series expansion of such). The transition model based on eqs. 4a and 4b is in agood agreement with the experiment. The results have been reported in TUAR92, p. 37f.

The classical DEBYE-HÜCKEL model

The results of the phenomenological linear model have been now compared with the predictions of a statistical mechanical model based on a physically well defined interaction - the Coulomb interaction. To this end, we have chosen the original Hückel model because, within the legitimacy limits of the Debye approximation of Boltzmann's formula, it is perfectly self-consistent. We recall that the Huckel model is based on the assumption that the defects interact in an isotropic electric polarization field described by a macroscopic static dielectric constant; the defects are assumed to be rigid spheres with closest distance of approach a.

The defect interaction energy, corresponding to the second term of the r.h.s. of eq.(4) takes now the form: [23]:

$$\Delta G^{el.} = \frac{n\,|ze|^2\,\kappa}{3D}\,\tau(\kappa a) \tag{5}$$

where D is the static dielectric constant, ze the defect charge, and κ is the inverse Debye screening length, defined by:

$$\kappa^2 = \frac{4\pi n\,|ze|^2}{VDkT} \tag{6}$$

where V is the molecular volume and $\tau(y)$ is a function arising from the integration of the electrostatic potential:

$$\tau(y) = \frac{3}{y^3}\left[\log(1+y) - y + \frac{1}{2y^2}\right] \tag{7}$$

Eq.(6) and (7) were then used to replace in eq.(4) the interaction term proportional to λ. Contrary to the linear model, this system of equations has real solutions only for $\Delta H_0 > 4.6$eV; whilst this value is larger than that used in the linear model (3.6 eV), it still falls within the experimental range. Fig.1.30 shows that at the critical temperature the linear model and the Huckel model predict a similar behavior of $C_p(T)$ and $n(T)$. Knowing the critical parameter κ_{crit} and n_{crit} we can solve eq.(6) for the effective dielectric constant; the result is:

$$D = 19.8 \tag{8}$$

which falls in the range of the experimental values ($20 < D_{\exp} < 24$). This result is particularly important in connection with the effects described in the following section.

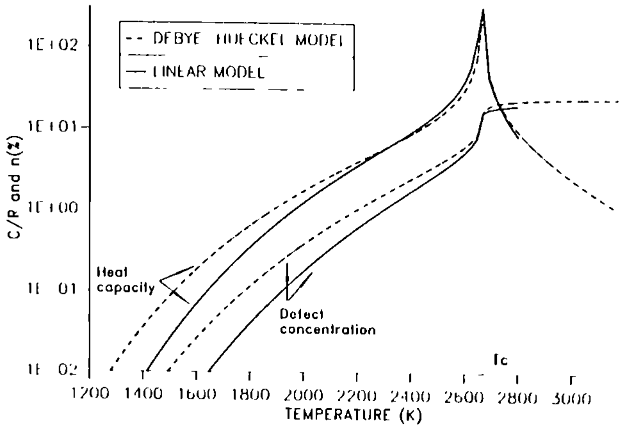

Fig. 1.30 Comparison of the Frenkel defect concentration and heat capacity contribution calculated by using the linear interaction and the classical Debye-Hückel models.

Small polaron contribution to the heat capacity of UO_2

The small polaron C_p contribution associated with the defect equilibrium concentrations predicted by reaction (3) takes the form of a thermally activated process. The experimental basis for the evaluation of the relevant parameters is provided by the d.c. electrical conductivity data, $\sigma = \sigma(T)$, plotted in Fig. 1.31. Customarily, in the analysis of these data the increase in $\sigma(T)$ is interpreted as a single-energy activated process, where the carrier concentration is approximated by an exponential function of T^{-1}, and their hopping mobility involves a factor proportional to $T^{-1.5}$. From this treatment, the contribution of small-polarons to the heat capacity turns out to be far too large to be in any way compatible with the coexisting contribution due to oxygen defects. This problem is reflected by the conclusions of earlier papers where the upswing in C_p at high temperature was attributed either to atomic (e.g. [24]) or to electronic defects (e.g. [25]). Yet, inspection of the conductivity data at high temperatures indicates a significant deviation from a simple exponential dependence of the carrier concentration on T^{-1}, which we have interpreted as evidence for cooperative small-polaron formation. Accordingly, we followed Yoffa and Adler [26] who used a Huckel-type model to describe the temperature-induced transition to the metallic state in Mott-insulators.

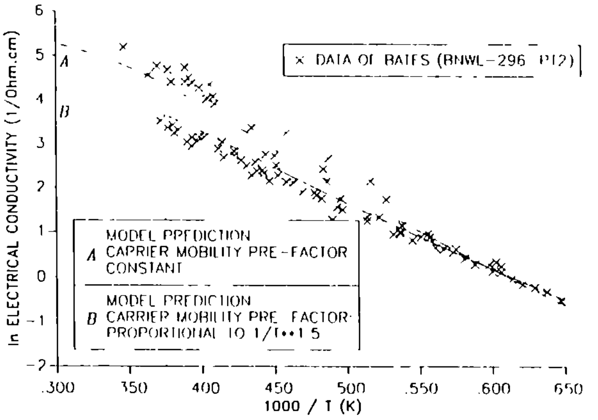

Fig. 1.31 d.c. electrical conductivity measurements and theoretical predictions (crosses) from the interacting polaron model (full lines). The two lines correspond to two different carrier mobility rules.

Quantum-mechanical cooperative model for small-polaron formation

In this model [26], based on the Hubbard Hamiltonian, the on-site Coulomb repulsion, U, between like defects, (the U^{3+} and U^{5+} small-polarons), takes the form:

$$U = U_0 \exp\left(- \sqrt{\frac{8\pi e^2 a^2 \hat{n}}{kTVD}} \right) \qquad (9)$$

where the symbols are the same as in eq. (5). U_0 (the bare intrasite Coulomb repulsion or Hubbard gap) is essentially analogous to the perfect crystal Frenkel formation energy ΔH_0 defined above. It should be noted that n represents the equilibrium concentration of defects and not a free variable. (In their model, Yoffa and Adler faced the well known self-consistency problem and had to introduce this additional "Ansatz". In fact, all the "improved" Huckel solutions are generally not self-consistent (see e.g. [27]). Concerning the problem of conforming the statistical mechanics scheme of assemblies with-temperature dependent energy levels to the demands of thermodynamics, see ref. [28]).

The model was applied to describe small-polaron formation in the presence of electron-hole interaction. U_0 was calculated from the Arrhenius regime of the *intrinsic* conductivity data to be 2.34 eV, whilst the exponent in eq.(16) was adjusted to obtain the best fit of the experimental σ(T) data. As in the preceding models, the effect of the screening is to inflect the curve $n = n(T)$ in a narrow temperature range. For a sufficiently high screening constant and defect concentration the Hubbard-gap collapses and the first-order transition from an insulating to a metallic state realizes. Since this transition is *not* observed in UO_2, the range of variation of the screening constant was relatively small, and the fitting procedure rather unambigous. The results are plotted in Fig. 1.31 as full lines.

The effective dielectric constant was finally evaluated from the screening constant, a value being:

$$D = 18 \pm 1, \qquad (10)$$

which is again in fairly good agreement with the value calculated *in the quite different defect context* of the oxygen Frenkel pair formation, and, of course, with experiment.

The important consequence of including polaron-polaron interaction is that the resulting heat capacity contribution is sufficiently reduced (Fig. 1.32) to be able to be accommodated in the total balance of the other C_p contributions.

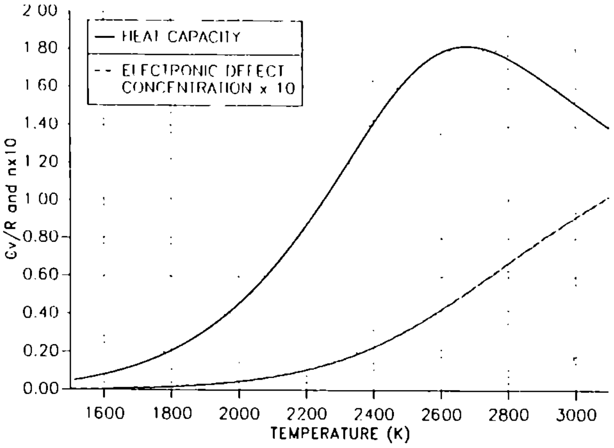

Fig. 1.32 Model prediction of the small-polaron concentration and heat capacity contribution.

Schottky disorder

The simplest variety of cation disorder most likely involves the formation of a trio of vacancies, according to reaction (2). It will be noticed that V_L^0 already occurs in the Frenkel disorder discussed above; the two disordering processes are thus coupled. Given, however, the much higher value of formation energy of Schottky defects, ΔH_0^S, their effect on Frenkel disorder can be practically neglected, as was implicitly done above in our treatment of the λ-transition; the converse does not hold, however.

Whilst the reliability of the value (≃ 6.5eV) currently assigned to ΔH_0^S, is difficult to assess, it is of interest to note that this value does satisfy the empirical relation which holds between ΔH_0^S and T_m of many binary ionic crystals [29]. Accordingly, a mean-field model of the melting transition, based on cooperative Schottky defect formation, is currently under investigation. In this model, the coupling to the existing Frenkel defects (via the common V_L^O species) is included, since in the 450K interval between the λ-transition and melting the degree of anion disorder is appreciable, attaining in $UO_{2.00}$ values around 20%. Pilot calculations neglecting this coupling indicate, however, a small C_p contribution prior to the first-order melting transition at approximately 3120K. The contributions from Schottky disorder included in the synthesis of the following section are therefore only preliminary.

Synthesis of identified contributions to the specific heat of UO_2

Calculations of the C_p contributions from the six sources identified and discussed above are presented in Figs. 1.33a and 1.33b for the case of stoichiometric UO_2, over the temperature range $1000 < T < T_m$. Comparison of the sum of these contributions with the experimental values, given in the final column, reveals that whilst the agreement is good up to 2000K, at higher temperatures the calculated values are apparently in excess. The agreement is significantly better if the theoretical results for a slightly sub-stoichiometric compound are taken, though the calculated transition peak is still broader than that deduced from the experiment. This invites the following comments on the limits of the adopted model:

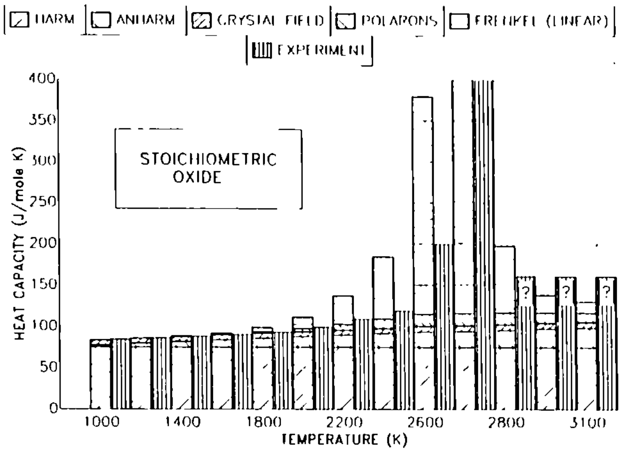

Fig. 1.33a Different elementary contributions to het capacity in stoichiometric urania as calculated from the reported models. The sum of the theoretical contribution is compared with the measured value in nominally stoichiometric samples.

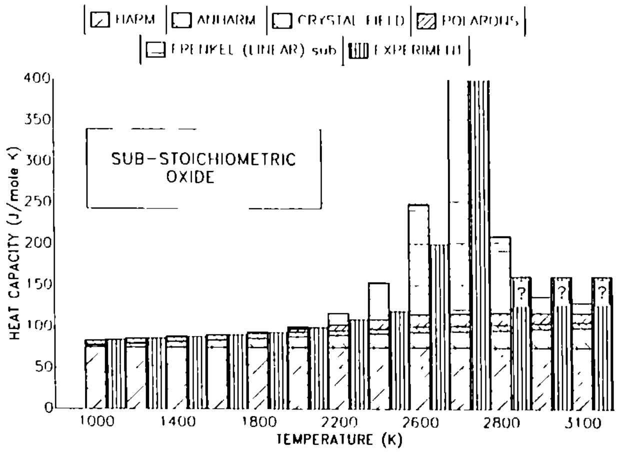

Fig. 1.33b Idem as in (a) but for a slightly sub-stoichiometric sample (O/U = 1.99). The experimental values are the same as in a). The agreement between theory and experiment is here better.

We would hardly expect better quantitative agreement with the λ-transition than is afforded by the adopted "mean-field" model. This has the great merit of correctly reproducing the nature of the transition and its x-dependence. Since it involves only a few parameters, it affords a reasonably simple description, which may, however, be inadequate in a more precise quantitative context. Two possible causes of discrepancy can be advanced:

1. We treated the different contributions as though they were strictly independent : we have already mentioned that this is particularly unrealistic in the case of the Schottky and Frenkel disorder. Now, the small-polaron and Frenkel defect contributions are not independent either. In fact, it should be appreciated that the polaronic nature of the surplus electrons and holes necessarily entail an attendent degree of lattice disorder (polarization field strains), involving, in particular, displacement of oxygen ions to relaxed (interstitial) positions. Although the (unknown) actual position of these atoms may differ from

that of the Frenkel interstitials, an interdependence between polaron and Frenkel pair formation appears to be very likely. (An association between a polaron and a Frenkel pair is also strongly suggested by the structure of the simplest 1:2:2 cluster, whose local crystallographic configuration of uranium and oxygen approaches that found in U_3O_8.). Neglecting this effect entails an over-estimates of the C_p contributions of the two kinds of defects.

2. The assumed formulation of the attractive part of the internal energy: it is well known that the validity of the mean-field approaches based on Debye's approximation is limited to highly dilute systems. At the calculated defect concentrations near the transition (*n* of the order of 0.1) the validity of the approximation is uncertain. Therefore, from a purely phenomenological point of view, terms involving higher powers of *n* should perhaps be included, although this would introduce additional empirical parameters. In the absence of more detailed physical hypotheses on the nature of the defect interactions, however, such a model would be of limited theoretical interest.

References

[1] C. Ronchi, J.P. Hiernaut, R. Selfslag, G.J. Hyland, Nucl. Sci. & Eng. **113** (1993) 1

[2] J.P.Hiernaut, G.J.Hyland, C. Ronchi, Int. J. of Thermophys. **14** (1993) 259

[3] R.A. Hein, P.N. Flagella, US Report GEMP-578, General Electric Company (1968)

[4] J.K. Fink, M.G. Chasanov, L. Leibowitz, US Report ANL-CEN-RSD 80/3 USA (1980)

[5] P. Browning, G.J. Hyland, J. Ralph, High Temp.- High Pressures 15 (1983) 169-178

[6] G.J. Hyland, R.W. Ohse, J. Nucl. Mater. **140** (1986) 149

[7] J.P. Hiernaut, C. Ronchi, High Temp.-High Pressures 21 (1989) 119

[8] M.A. Bredig, Oak Ridge Nat. Laboratory, US Report ORNL 4437 (1969) 103

[9] M.T Hutchings, J. Chem. Soc. Faraday Trans. II **83** (1987) 1083

[10] J.L. Bates et al., J. Amer. Ceram. Soc. **50** (1967)652

[11] G.J. Hyland, J, Nucl. Mater. 113 (1983) 125

[12] O.D. Slagle, J. Amer. Ceram. Soc. **67** (1984) 169-174

[13] E.H. Ranklev, C.A. Hinman, Proc. Int. Conf. on "Fast Breeder Reactor Fuel Performance", Monterey (CA) (1979) 405

[14] J. Ralph, G.J. Hyland, J. Nucl. Mater. 132 (1985) 76

[15] Hj. Matzke, Adv. Ceram., **17** (1986) 1-54

[16] R.A. Jackson et al., Phil. Mag. **A53** (1985) 27

[17] G.J. Hyland, J. Ralph, High Temp.-High Pressures 15 (1983) 179-190

[18] C.R.A. Catlow, Proc. R. Soc. London Ser.A **353** (1977) 533

[19] D.A.McInnes, Proc. Int. Symp. on Thermodynamics of Nuclear Materials, Jülich 1970 (Vienna IAEA) Paper IAEA-SM 236/37

[20] R.J. Ackermann, US Report ANL-5482 (1955) Argonne III.

[21] V.M. Carr et al., J. Phys. C Sol. State Phys. **11** (1978) L637

[22] C.R.A. Catlow et al., J. Phys. C Sol. State Phys. 11 (1978) 3197

[23] P. Debye, E. Hückel, Phys. Z. **24** (1923) 185

[24] R. Szwarc, J. Phys. Chem. Sol. **30** (1969) 705-711

[25] R.A. Young, J. Nucl. Mater. 87 (1979) 283-296

[26] E.J. Yoffa, D. Adler, Phys. Rev. B 20, **10** (1979) 4044

[27] R. Fowler, E.A. Guggenheim, "Statistical Thermodynamics" Cambridge Univ. Press (1965) p.407

[28] G.S. Rushbrooke, Trans. Faraday Soc. 36 (1940) 1055

[29] L.W. Barr, A.B. Lidiard, "Physical Chemistry-An Advanced Treatise", Vol.X Academic Press (1970) New York, p.151

Autoclave melting experiments

Freezing point of UO_2 with simulated burnup

The simulated burnup UO_2 fuel (SIMFUEL) fabricated at Chalk River is probably one of the most representative examples of simulated irradiated structures (see e.g. TUAR90, p.28). In the last years samples of SIMFUEL have been thoroughly characterized at the Institute with the aim of studying the effect of fission product on the relevant fuel physical properties. The variation of the melting point by addition of simulated fission products corresponding to burnups of 3,6 and 8%, respectively was investigated. Small specimens of approximately 1 mm^3 volume have been melted in our laser-heated autoclave and the freezing temperature was determined from the position of the inflection point on the sample cooling curve (a standard thermoanalytical technique which has been successfully applied for the determination of the melting point of a variety of materials).

In the experiment the sample is simultaneously irradiated by four laser beams which, if the sample is spherical, produce a fairly homogeneous surface heating, which provides an accuracy of the measured freezing plateau temperature of better than 10K. The temperature is measured by a six-wave-length pyrometer, whose signal analysis enable both temperature and spectral emissivities to be evaluated with the respective errors. Unfortunately SIMFUEL could not be machined to obtained spherical shapes, so that cubic shaped samples were first cut, and then laser- melted in order to obtain a reasonably rounded shape. Only at this stage could a second laser shot by applied to produce sufficiently homogeneous heating conditions. Therefore, the freezing point measurements were in fact obtained from pre-molten samples, whose chemical composition could possibly be different from the initial one. Furthermore, the material was not very resistent against thermal shocks (especially the batch corresponding to 3% burnup), and crack formation did negatively affect heat propagation, so that finally the spectral pyrometric analysis resulted into much larger inaccuracies (corresponding to approximately ± 50K) of the fractional intensities of the examined colors, which is normally caused by the presence of large temperature gradients in the measured area, i.e., in our case, not simultaneous freezing.

The signals were therefore submitted to the wobbling procedure to compensate for the systematic errors. The temperature precision could be thereafter be increased to approximately 10K. In the absence of a corroboration of the resulting emissivity variations, this value has to be taken as the best expectable (but not the most probable) temperature error.

The results are plotted in Fig. 1.34 and 1.35, where the freezing temperatures and the spectral emissivities at 500 and 960 nm respectively, are plotted versus simulated burnup. For comparison, the melting point of hypo- and hyperstoichiometric uranium dioxide, measured with the same method is also shown in the graph.

A decrease of the freezing temperature with increasing burnup seems to be manifest, the drop being approximatelyh 130K at 8% burnup, that is one order of magnitude larger than the measurement precision of T. The trend of the emissivity is less understandable. If the decrease with respect to pure UO_2 (Fig. 1.35) can be explained by the presence of some percent of metallic phases on the sample surface, the increase of ε with burnup is doubtful, and could be ascribed to a residual systematic inaccuracy of the measurement, which could not be removed by the wobbling correction. Two remarks should be made here: first, if the emissivities are assumed to low, the real melting point of the SIMFUEL would by up to 30K lower than indicated; second, the difference in freezing point between the 3% fuel and the 8% fuel (approximately 50K) could effectively vanish. This point should be further investigated if a reliable empirical function $T_m = T_m(b.u.)$ has to be assessed.

A final word of caution is to be said on the possibility of defining a solidus curve for the SIMFUEL, since different aspects are involved which still escape the present analysis. The main one is the effective stoichiometry of the molten layer after repeated melting in inert atmosphere: systematic measurements under increasing oxygen

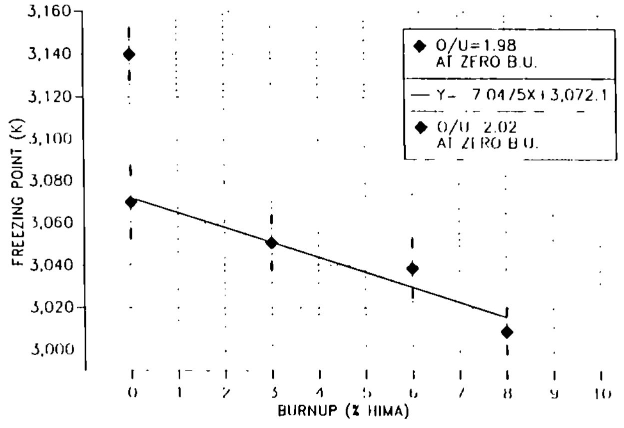

Fig. 1.34 Freezing point of SIMFUEL as a function of simulated burnup. At zero burnup the melting point of $UO_{1.98}$ and $UO_{2.02}$ are respectively indicated at 3140K and 3070K. The curve of Tm in the SIMFUEL is aligned with the superstoichiometric value.

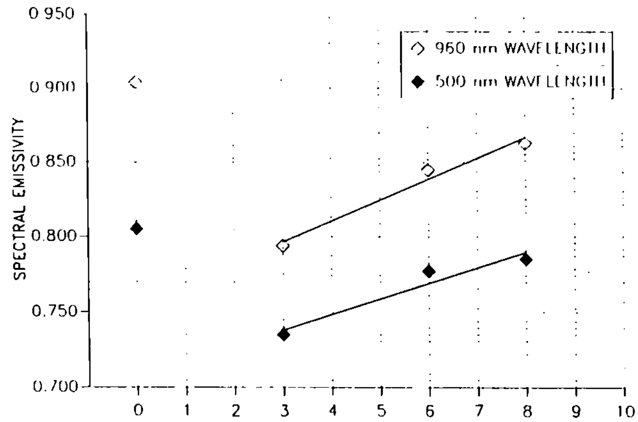

Fig. 1.35 Spectral emissivities of SIMFUEL at 500nm and 960nm as function of simulated burnup.

pressure are in this context recommendable. Furthermore, some elements (Ba, Sr, Ca) rapidly evaporate during heating, so that the residual chemical composition of the molten layer is probably different from the initial one. The establishing of equilibrium, and thus the possibility of detecting a thermodynamic transition, is therefore dependent on these kinetic processes, and not only on the equilibrium $\Delta G(O_2)$.

Thermophysical property measurements

Laser-flash thermal diffusivity

The apparatus for the measurement of the thermal diffusivity of irradiated fuel (LAF.I), designed and constructed in our laboratory, has been recently successfully tested and is now available for implementation in the hot cells. Further measurements will be carried out until spring '94 in order to better determine the performance limits of this instrument, and define the design of a second apparatus (LAF.II) which will be constructed for operation in a glove box.

The apparatus LAF.I is shown in Figs. 1.36a, b with a scheme of the operation principle. The main features of the furnace and of the optical parts have been designed for implementation in a lead-shielded cell where no access will be eventually available for repairs and maintenance except that allowed by two (rather gross) remote-hand manipulators. Three aspects have been especially considered in the design stage:

1. The alignment of the system laser-head /sample/aperture stop/detector has been ensured by a coarse x-y adjustment of the laser head, followed by a micrometric x-y-z displacement of a mirror at the center of which lies the aperture hole corresponding to the measured field of the sample. The center of this aperture is, under the optimum measurement conditions, aligned with the probe laser beam. Based on this initial alignment, the position of the sample, mounted in a graphite holder, can be varied as the latter is fixed to a micrometric x-y table, moved by precision step motors. The whole sample surface can be observed through the mirror, whilst only the area projected onto the hole is seen by the detector. The setup enables the operator to find proper measurements conditions even in cases where the sample platelet has an irreg-

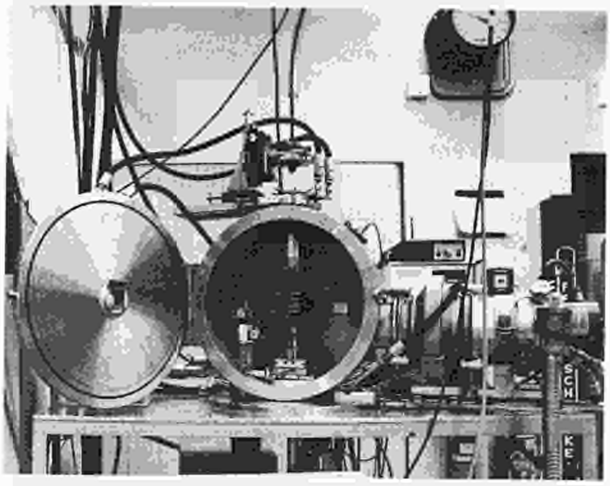

Fig. 1.36a The laser-flash apparatus LAF.I, constructed for implementation in a hot cell with remote manipulation. The picture shows the housing with HF furnace and the micrometric adjustable head, bearing the precision sample viewing mirror and the optical fiber leading to the photodiode detector (H) The instrumentation, including the probe laser, are placed outside the cell.

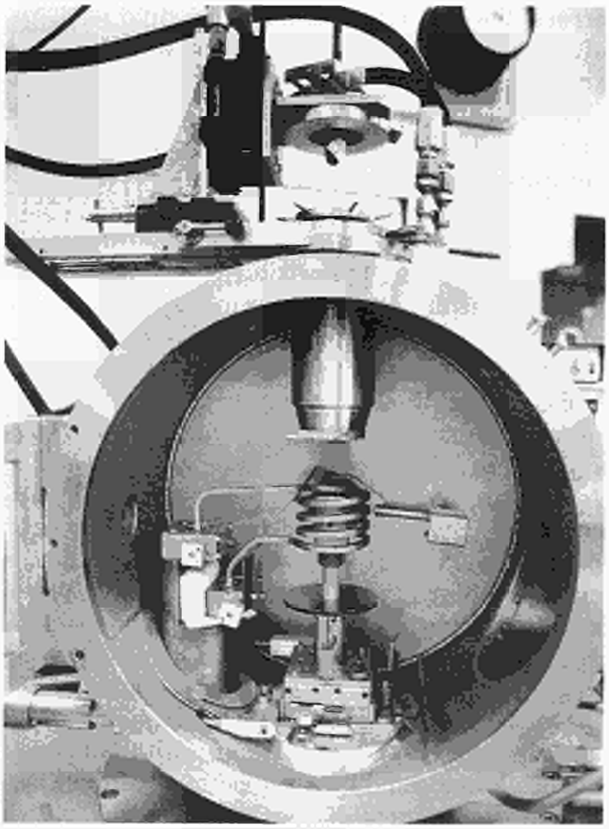

Fig. 1.36b Detail of the specimen holder (S) with the x-y adjustment table (X). The sample is observed through the water-cooled high brightness objective (O).

ular shape, or when the holder cannot be reproducibly positioned in the furnace.

2. The detector and the laser head, which are particularly sensitive to nuclear radiation damage, are placed ouside the cell, the light being transmitted through optical fibers, which can be easily plugged in and out, and thus replaced when they will be exceedingly darkened by the γ radiation. The lenses of the detector objective, placed within the HF furnace housing are protected against direct nuclear radiation of the sample.

3. The system essentially consists of five parts (Fig. 1.36c): laser input block movable holder, HF coil and thermic shields, pyrometer objective, and adjustable viewing head; these are independent mechanical modules which can be readily removed by means of the manipulators, and, in cases of major failures, replaced.

The apparatus is being tested with graphite and ceramic semitransparent zirconia samples. Fig. 1.37 shows the signal detected on the face opposite to that hit by the probe laser. It can be seen that the laser light diffusely reflected during the 1ms pulse produce a significant disturbance; however, this perturbation can be eliminated by inserting a dichroic filter. The used transient recorder provides one measurement per microsecond, so that the high frequency noise can be effectively filtered, obtaining an eventual signal-to-noise ratio of the order of 1000. The characteristics of the instrument are summarized in Tab. 1.4.

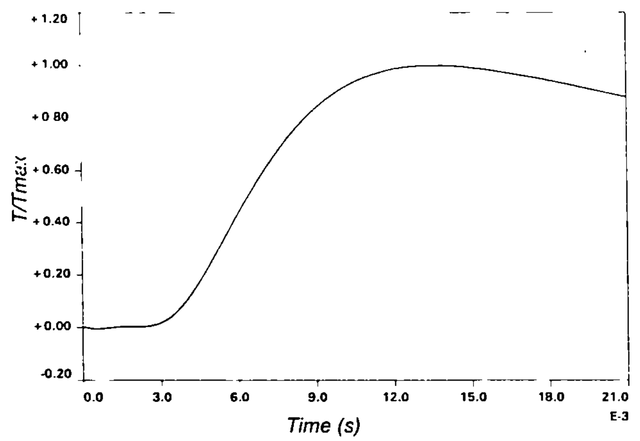

Fig. 1.37 Recorded transient signal from the laser flash on a POCO graphite sample. The laser light was eliminated by using a selecting dielectric mirror. The total temperature raise in approximately 5K, indicating the outstanding prformance of the detector and preamplifier. The instrument presents top level features with regard precision and laser/sample/detector alignment facilities.

New set-ups for diffusivity measurements

Thermophysical properties of reactor materials are often referred to physical conditions (temperature, atmosphere, pressure) which are hardly reproducible in laboratory apparatuses. Therefore, new methods have been studied to enable thermal diffusivity measurements to be carried out under non-conventional conditions. In the first setup the sample is placed in a small chamber with controlled atmophere, and supported by three ceramic pins. The specimen disk is heated from two sides by a CO_2 laser, and a Nd-YAG laser pulse is then applied. The thermal diffusivity is then measured as in the case of the usual laser-flash technique. Very high temperatures can be attained under chemically active atmospheric conditions. Thermal diffusivity of zirconia was measured up to 2500 K in air. It is known that this white translucid material at high temperatures and in vacuo assumes an increasingly dark color, as a consequence of chemical reduction. In our experiments the sample could be maintained stoichiometric during the measurement and the effects due to the variation of the absorbivity and emissivity with temperature could be investigated in the absence of color centers formed by non-congruent vaporisation.

Other advanced techniques for the measurement of the heat transport in heterogeneous systems like, for instance, nuclear fuel rods, are being developed based on high speed CCD cameras and 2D thermography processing. A prototype setup will be constructed in 1994.

Schematic Diagram of The Laser Flash Thermal Diffusivity Measurements of Irradiated Fuels

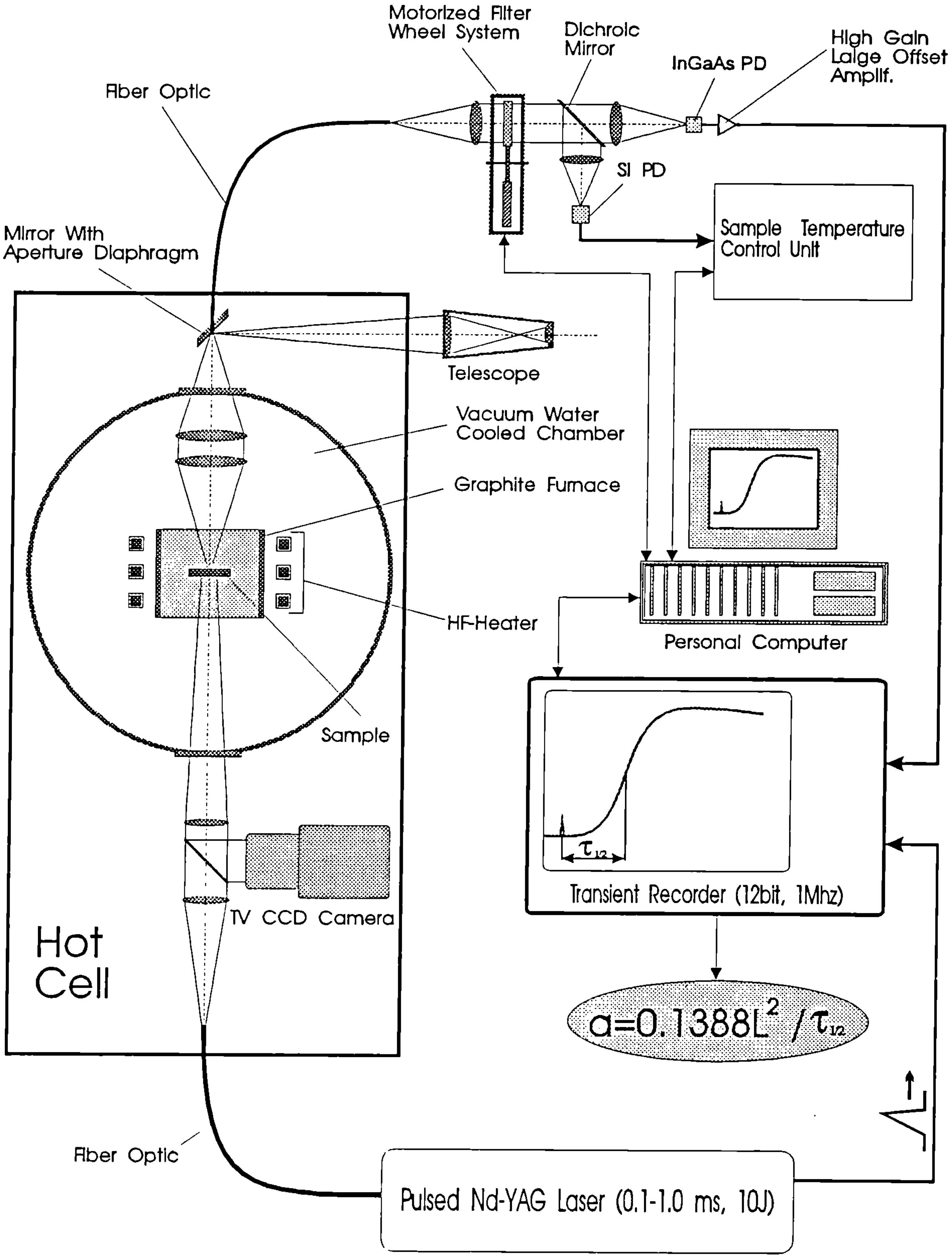

Fig. 1.36c Scheme of LAFI as it will be installed in the hot cell.

Tab. 1.4 Specifications of the Laser Flash Machine.

1. Temperature range: 500-1500 C.
2. Furnace: Graphite with HF heating at 330 kHz frequency.
3. Specimen size: dia. 4-10 mm x 1-2 mm.
4. Specimen holder: graphite, with precise remote X-Y +5mm positioning.
5. Probe laser:
   - Energy: 0-10 J;
   - Pulse length: 100 us - 10 ms continuously variable;
   - Wavelength: 1.06 um;
   - Laser Beam delivery system: Fiber optic with 1 mm core;
   - Beam size: 3 mm (can be reduced to 1.5 mm for the "radial method" operation).
6. Atmosphere - Vacuum or reduced pressure gas at low temperatures.
7. Back Temperature Measurement System:
   - Sensor - InGaAs photodiode;
   - Optical system - Achromatic objective with fiber optic and precision viewing system;
   - Automatic Gray filter changing for covering of the broad temperature range;
   - Spot size of temperature measurements: 1 or .5 mm in dia.;
   - Recording system: Transient Memory with up to 1 us sampling x 256 K Words max.;
   - Amplifier: Bandwidth DC - 3 kHz with background signal subtraction;
   - Precise positioning of the probe spot: X-Y-Z +10 mm.
8. Measuring method: Standard, with 1 mm spatial resolution. Two dimensional.
9. Special features: Possibility of working in the "hot cells" under strong gamma irradiation conditions. Design of the machine permits one to replace specimen, sample holder unit, HF-coil and all optical elements remotely with the aid of manipulators.

Modelling work

Fuel performance code development (TRANSURANUS)

TRANSURANUS is a computer program for the thermal and mechanical analysis of fuel rods in nuclear reactors and was developed at the European Institute for Transuranium Elements [1]. The TRANSURANUS code is fully descibed in the literature and was outlined in previous Annual Reports. The TRANSURANUS code is in use in several european organisations, both research and private industry.

The TRANSURANUS code consists of approximately 200 subprograms which have their own test programs. The total number of files to be maintained is more than 3000. In 1993 many subroutines have been carefully checked, revised and documented. The work on the TRANSURANUS handbook which contains at present 450 pages continued.

The work concentrated on the following items:

Code Release

As in 1992 the TRANSURANUS code was transfered to other parties. Linked with this transfer were training courses and extended user support for the application of the code. The subjects treated in the training courses were basically the same as described in the last annual report.

The revised TRANSURANUS version 1 (modification 2), 1993 was released successfully to interested parties. The installation on different computers did not cause any problems.

New program options

The following options were extended or included

1. *Extended calculation of the inner pin pressure*

   Using this new option allows the user to consider the relocation volume as free volume. The obvious consequence is a lower inner gas pressure.

2. *Extension of convergence limits*

The convergence limits of the thermal analysis, the mechanical analysis and the convergence limits for the coupling of both were carefully revised and extended. It is of interest how the various accuracies determine the computer costs. As can be seen in Fig.1.38, an increase of the accuracy of two orders of magnitude leads to an increase of computer costs by only a factor of 2 to 3. This again proofs the very effective convergence schemes incorporated in the TRANSURANUS code.

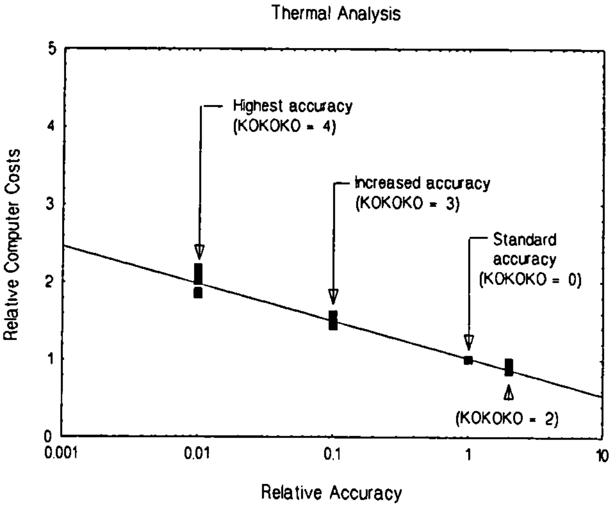

Fig. 1.38 Relative computer costs as a function of the relative accuracy.

3. *Revision and test of thermohydraulic models*

The thermohydraulic models have been extended and carefully tested. Surface boiling is treated. The new options together with the existing standard options allow now the treatment of all different types of flow channels with different hydraulic diameters in a fuel assembly:

a) "normal" subchannels inside the regular lattice
b) those surrounding the control rod guide tubes
c) those between adjacent assemblies in the core and
d) the corner rods of the fuel assemblies.

4. *Statistical Fuel Rod Analysis*

The relevance of statistical analyses was outlined in the previous annual report. Work on the Numerical Noise Analysis and the postprocessor NNOISE continued with low priority. The agreement between the time consuming Monte Carlo technique and the Numerical Noise Analysis is very promising. Fig. 1.39 gives an example of a statistical analysis of a realistic case. The linear rating, the thermal conductivity and the gap conductance were treated as statistical variables. Note that the statistical analysis employing the Monte Carlo technique takes 50 - 100 times longer than the Numercial Noise Analysis.

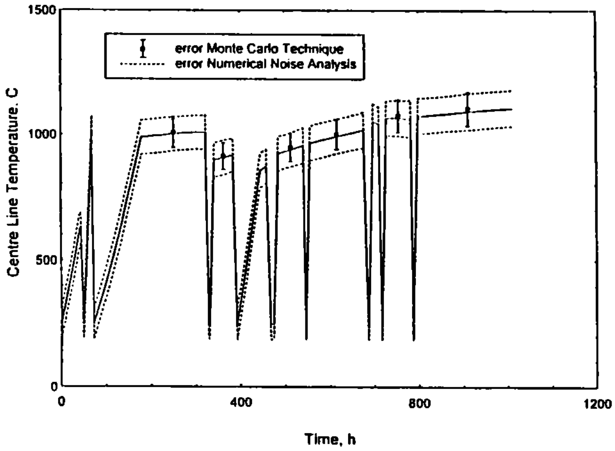

Fig. 1.39 Centre line temperature and error as a function of time; compared are the two statistical analyses of the TRANSURANUS code: the time consuming Monte Carlo technique and the Numerical Noise Analysis. Statistical variables were linear rating (standard deviation ± 5 %), thermal conductivity (± 5 %) and gap conductance (± 15 %).

Analysis of irradiation data

Data cases from the Halden and the Risö project were analysed. A first analysis of the FUMEX cases [2] was performed. The results will be presented after the analyses have been finished.

Specific model development

A model has been developed TUBRNP (Transuranus Burnup Model) which predicts the radial power density distribution as a function of burnup (and hence the radial burnup profile as a function of time) together with the radial profile of uranium and plutonium isotopes [3]. Of particular interest in this model is the description of the marked increase in the concentration of plutonium near the fuel surface at high burnup. This is a result of the capture of epithermal neutrons in the resonances of ^{238}U (with a very large absorption cross-section).

The model predicts the local concentrations of the uranium and plutonium isotopes by solving the following set of equations:

$$\frac{dN_{235}(r)}{dbu} = -\sigma_{a,235}N_{235}(r)A,$$

$$\frac{dN_{238}(r)}{dbu} = -\sigma_{a,238}\overline{N}_{238}f(r)A,$$

$$\frac{dN_{239}(r)}{dbu} = -\sigma_{a,239}N_{239}(r)A + \sigma_{c,238}\overline{N}_{238}f(r)A,$$

$$\frac{dN_j(r)}{dbu} = -\sigma_{a,j}N_j(r)A + \sigma_{c,j-1}N_{j-1}(r)A.$$

where $\sigma_{a,i}$ and $\sigma_{c,i}$ are the absorption and capture cross-sections A is a constant and $N_i(r)$ is the local concentration of isotope i. The local concentration of ^{238}U is written as $N_{238}f(r)$ where f(r) is a normalised radial shape function and N_{238} is the average concentration of ^{238}U. This shape function encapsulates the contribution of the resonance absorption to the plutonium production. It is a function of the form,

$$f(r) = 1 + p_1 \exp\left(-p_2\left(r_{out} - r\right)^{p_3}\right),$$

where p_1, p_2 and p_3 are parameters. The values of these parameters were fitted using some data from the experimental database. Their values were then fixed for all comparisons with measured data.

It has been shown in the previous annual report (TUAR 1992) that there is excellent agreement between the predictions of the TUBRNP model and those of KORIGEN for averaged values.

The TUBRNP model has been verified against a large database of spent fuel measurements for enrichments in the range 1.38% to 8.25% and for burnups between 21000 MWd/t and 72400 MWd/t. Note that there are no free parameters in the model. The input model parameters are the fuel geometry (r_{in}, r_{out}), porosity, enrichment, initial concentration of plutonium isotopes and average burnup. Comparisons of the model predictions and experimental results are illustrated in Fig.1.40: as can be seen the agreement is excellent. The TUBRNP model is at present in use at EdF, FRAMATOME, PSI, ASEA-ATOM and TÜV's. It is envisaged that the model will be applied to the plutonium distribution in high burnup MOX fuels.

Application of the TUBRNP Model

High burnup initiates a process that can lead to major structural changes near the edge of the fuel (Rim effect): grain subdivision, the loss of matrix fission gas and an increase in porosity. A serious consequence of this is a decrease of thermal

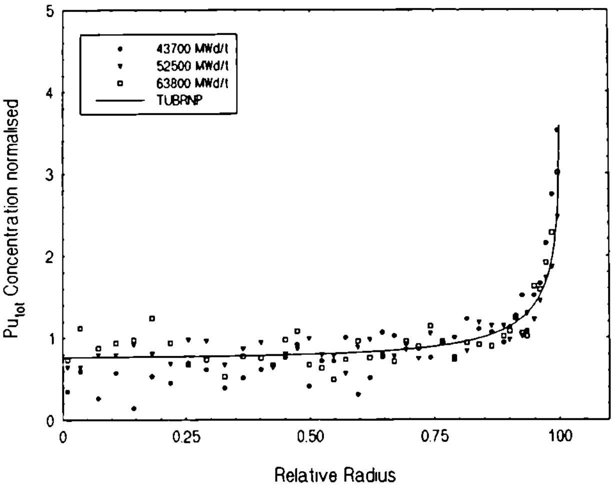

Fig. 1.40a Comparison of the radial total Pu concentration measured in different EPRI fuels (enrichment ^{235}U = 5.75 %) with that calculated by the TUBRNP model for 55000 MWd/t.

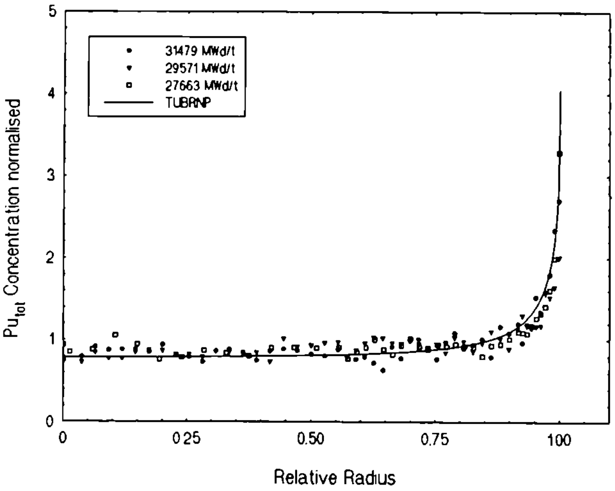

Fig. 1.40b Comparison of the radial total Pu concentration measured in different STRO fuels (enrichment ^{235}U = 2.9 %) with that calculated by the TUBRNP model for 29000 MWd/t.

conductivity near the edge of the fuel. It is assumed the Rim zone corresponds to that region at the edge of the fuel where there is a depletion of Xe from the grains. The TUBRNP model only includes burnup however it can be used as a first step in developing a more comprehensive model within the context of the TRANSURANUS code.

It has been noted experimentally that the Rim effect has an onset threshold local burnup in the range 70,000 to 80,000 MWd/t [4]. A specific value was taken for use in the model as the threshold local burnup. For a given fuel the TUBRNP model predicts the local burnup profile and the depth which corresponds to the threshold value is taken to be the Rim thickness. These theoretical predictions have been compared with experimental data. The data for Rim thickness is derived from the Xe profile using EPMA analysis [4]. In Fig. 1.41 the model prediction for 2% enrichment is compared with measurements (enrichments between 1.38% and 3.2%): as can be seen the agreement is good. This should be seen as a first step in the development of a more detailed model of this phenomenon.

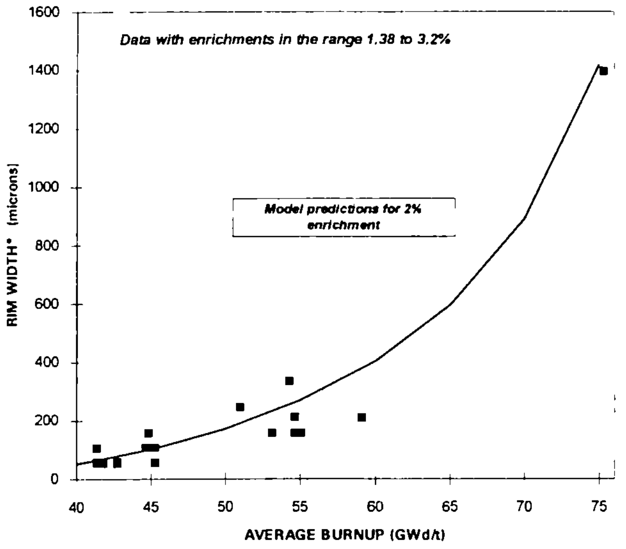

Fig. 1.41 Comparison of the predictions of the Rim thickness with experimental results (EPMA measurements of Xe). The TUBRNP calculation is for a fuel with 2% enrichment radius of 5mm and 5% porosity.

References

[1] K. Lassmann, TRANSURANUS: a fuel rod analysis code ready for use, J. of Nucl. Mater. 188 (1992) 295

[2] IAEA Co-ordinated Research Programme on "Fuel Modelling at Extended Burnup (FUMEX)"

[3] K. Lassmann, C. O'Carroll, J. van de Laar and C.T. Walker, J. Nucl. Mater. 208 (1994) 223

[4] C.T. Walker, T. Kameyama, S. Kitajima and M. Kinoshita, J. Nucl. Mater. 188 (1992) 73

1.2 Safety Aspects of Fuel Operation and Handling

Introduction

The investigations of operational limits for future fuels were continued. The BOL (beginning of life) irradiations of NILOC 3, a fuel pin representing the heterogeneous fuel concept, with $(U,Pu)O_2$ and UN fuel pellets, and NILOC 4, an irradiation of MN fuel pins at high central fuel temperature, were completed. The non destructive analyses of all fuel pins was also completed.

The irradiation of the high burn-up POMPEI experiment was started and has attained 5 cycles in HFR-Petten.

The irradiation of the NIMPHE 1 bis and NIMPHE 2 experiments in the PHENIX reactor is planned to start, respectively to continue end 1994.

An additional destructive examination of selected fuel sections of the 19 carbide-pin bundle, irradiated to 7 $^a/_0$ burn-up in the KNK reactor, was postponed to 1994.

The TRABI experiment, an investigation of the transport of big (> 10 µm) radioactive particles in ducts and chimneys, was completed. Transport of such particles under turbulent conditions was confirmed.

Optimisation of Fuels

Irradiation experiments

BOL-irradiation experiments NILOC 3 and 4

The non destructive analyse of the irradiation experiment NILOC 3, performed at ECN Petten, revealed no anomalies during irradiation up to 1 $^a/_0$ burn-up and a central fuel temperature of 1910 K for both MN pins. In the third pin of the TRIO-capsule, with a heterogeneous arrangement of $(U,Pu)O_2$ and UN fuel stacks, a central fuel temperature of 2470 K was calculated and no severe reaction at the $(U,Pu)O_2$-UN pellet interfaces was observed.

The NILOC 4 irradiation experiment was completed in January 1993 at a planned burn-up of 0.5 $^a/_0$. The irradiation behaviour of the three MN pins, which operated at off normal fuel centre temperature between 2190 - 2515 K, was correct. Both axial gamma scanning and the thermal and epithermal neutron radiography, performed by ECN Petten revealed a normal axial distribution of fission products, no important reaction or sign of fuel decomposition in the fuel centre. In some pellets a cracking in the centre was observed, all pellets were distinguishable from each other.

The transport of both NILOC 3 and 4 to ITU Karlsruhe is planned during 1994. The heterogeneous fuel pin of the capsule NILOC 3 and 1 or 2 pins of NILOC 4, with the highest central temperature will be examined by destructive analysis.

POMPEI mixed nitrides and technetium

In the high burn-up irradiation experiment POMPEI (POM PEtten Irradiation), 20 $^a/_0$ was attained in less than 1 year. The evolution of structure, fission products and the chemical behaviour of (U,Pu)N fuels were investigated (see TUAR-92).

In the same capsule a first irradiation of technetium specimens was included to obtain information on the irradiation behaviour of pure Tc and Tc/Ru alloys. This will give further information on the possibility of Tc transmutation.

The final assembly with inclusion of thermocouples and flux detectors was performed at Petten in May 1993. The irradiation started in the cycle 93-08, 24th September 1993. Actually 4 cycles are achieved since then and with approximately 2.78 $^a/_0$ burn-up per cycle, a burn-up of 11.7 $^a/_0$ has been reached. It is planned to complete the irradiation with another 6 reactor cycles, resulting in a total burn-up of 27.8 $^a/_0$.Unloading is planned for the summer stop of the HFR reactor in 1994.

Aerosol Research

Duct Transport of Big Particles (TRABI)

Introduction

The transport mechanisms of big particles in ventilation exhaust systems with highly turbulent flow conditions were investigated further. The experiments with non-active test aerosols were concluded with the verification by a more precise quantimetric method of a possible agglomeration process during the transport. Investigations with active aerosols were started. Suitable particles of natural uranium oxide were prepared and an autoradiographic method of particle size measurement was tested. The installation of the test duct and monitoring systems in the special glove box has been considerably retarded due to delays in the delivery of box and equipment, so that results with active particles are not yet available.

Agglomeration Process during Duct Transport

On the particle samples deposited on filters after the transport in the highly turbulent flow (Re>100,000), a quantimetric evaluation was carried out with the GALAI CIS-1 Macro-Viewer which was more precise than the method used previously. By comparison with the original particles injected into the inlet of the test channel, the increase in size and number of agglomerates, already suggested in TUAR-92, p.60, is confirmed. Fig. 2.1a and 2.1b show that, after injection of a bismuth oxide powder 30-40 µm in size, respectively 27 % and 28 % of the objects counted on the sampling filters were greater than 40 µm. For comparison purposes, Fig. 2.1c shows the size composition of the original 30-40 µm powder collected on a filter after being transported of a distance of only 50 mm in a turbulent flow (a special device was built for this purpose). It can be seen that the number of agglomerates greater than 40 µm is only 8 % of the total of particles.

Work with Active Aerosols

For the reasons mentioned above, the experimental facility to study the transport of uranium (natural) oxide aerosol was not completed at the end of the reporting period. The equipment is the same as that already used for non-active aerosols. The transport test section, aerosol inlet and the particle monitoring systems were mounted inside a 4.1 m^3 stainless steel glove box provided with the necessary racks for sample conditioning and analysis. A special device allows direct optical examination and quantimetric measurements on samples remaining inside the glove box, using equipment situated outside. The rest of the wind channel facility: fan, HEPA filter unit and preconditioning duct remain outside the glove-box (see TUAR-91, p.61).

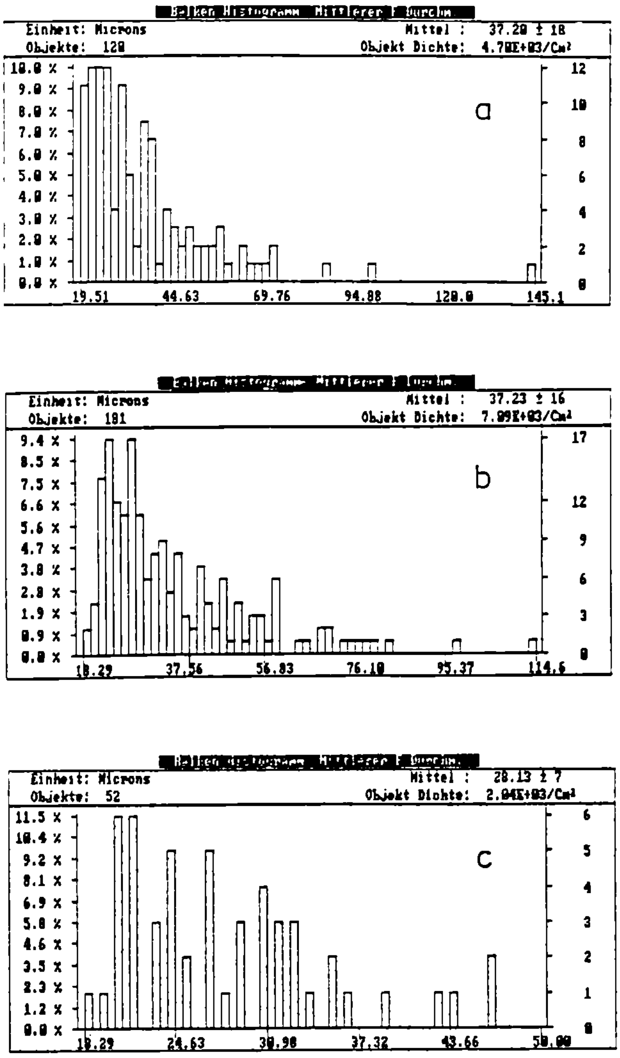

Fig. 2.1 Size distribution of the same bismuth oxide powder collected on sampling filters:
-(a) and (b): after transport in a highly turbulent flow of 15 m/s over distance of 1.20 m,
compared with:
-(c) original powder.
The mean Ferret diameter +/− the standard deviation is indicated on each histogram.

Alpha-autoradiography with the polycarbonate membrane (daylight-insensitive) CN 85 of KODAK was considered at first for the size analysis of uranium particles. Aside from the low investment, the advantages of this method seemed to be evident; thus the sampling filters can be put in contact "in situ" with the detector sheet, that can then be treated uncontaminated outside the glove box: controlled etching in an alkali solution for revealing the alpha particle tracks and subsequent quantimetric measurement of the autoradiographs. Theoretically the size of the radioactive particle is related, by a previous calibration with monodisperse spherical particles (prepared by a sol-gel process), to the size of the "star" formed by the alpha-tracks emitted from this particle. This method was tested using a 30-40 µm fraction of sintered natural uranium oxide particles, separated by ultrasonic sieving.

These experiments showed however that the specific alpha activity of natural uranium is too low and the particle sizes too large for an accurate determination of the diameter. Attempts were carried out increasing the exposition time (up to more than a week) and varying the etching rate, but no satisfactory distribution patterns of the alpha tracks could be obtained, due to the predominance of the matrix effects and the disturbing influence of the beta emission.

For future measurements, a microscope equiped with a video-camera for quantimetric measurements and located outside of the glove box will be used, using the device mentioned above.

The Laser Phase Doppler Anemometer (LPDA), the purchase of which is envisaged by the Aerosol Section for other purposes, would allow direct "in situ" particle size measurements and could also be used for these experiments, provided that the particles are not too far from sphericity.

1.3 Actinide Determination and Recycling

Introduction

Partitioning and transmutation of long-lived nuclear waste constituants was the theme which dominated the activities in the field of actinide determination and recycling during the reporting period.

After the successful conclusion of the first series of pilot experiments to transmute minor actinides - in oxide form - into short-lived fission products in a fast reactor, a thorough analysis of the data thus obtained has been performed in order to compare calculated and measured transmutation rates and to evaluate radiation dosimetry aspects for MA fuel handling.

The present status of research in the field of partitioning and transmutation has been reviewed and the advantages and draw-backs of various transmutation schemes have been compared.

Partitioning studies have been performed with different extractants, and preparations for a second large-scale irradiation (SUPERFACT II) to test the technical feasibility of the concept got under way.

Status of the SUPERFACT Irradiation Experiment

Introduction

Four types of minor actinide containing oxide fuels have been irradiated in the PHENIX fast reactor (TUSR **39**, 52). The post-irradiation examinations of these fuels have provided us the opportunity to investigate the transmutation rate of minor actinides and determine the occupational dose during handling of such material. The experimental findings on the transmutation rates and the radiation dose levels, and their comparison with calculated values will be reported [1].

Experimental

Isotopic analyses of MA fuels

Examinations of isotopic composition were carried out on samples of approximately 1g cut halfway along the active length of the fuel pins. The samples were then dissolved and aliquots taken for chemical analyses. The concentrations of uranium, plutonium, americium and curium isotopes and ^{148}Nd were measured by Isotope Dilution Mass Spectrometry (IDMS). The measurement of ^{237}Np was performed by Inductively-Coupled Plasma Mass-Spectrometry (ICP-MS). The final local burnup (Tab. 3.1) for the samples from each fuel, achieved during irradiation in PHENIX was derived from the number of final heavy metal atoms and ^{148}Nd for each sample. A quantitative analysis of the fission products contributing to the gamma output of the fuels was performed by gamma-spectroscopy relative to ^{137}Cs.

Dosimetry measurements of MA fuels

The gamma dose rates of the four fuel pins were measured during *fabrication* using a portable ionisation chamber and thermoluminescence dosimeters in contact (TUAR-86, p. 82). *After irradiation* (cooling time 57 months), the gamma and neutron dose rates were measured using a passive neutron-gamma interrogation unit developed for spent fuel characterisation inside a hot cell at the Institute (TUAR-86, p. 82),[2].

Theoretical

The program KORIGEN [3] has been used to calculate the actinide and fission product concentrations for each of the SUPERFACT fuels and the neutron and gamma outputs at different cooling times. The fission and capture cross-section libraries were adjusted to those for the PHENIX reactor for the transuranium isotopes. The neutron and gamma outputs were also calculated, for comparison purposes, for a standard FR-MOX fuel containing plutonium of the same isotopic composition as the SUPERFACT homogeneous fuels.

Tab. 3.1 Experimental and theoretical decrease (%) and half-lives in PHENIX

	UPu,2%Np	**U, 20% Am, 20% Np**		**U, 45% Np**	**UPu,2%Am**
	Np-237	**Am-241**	**Np-237**	**Np-237**	**Am-241**
burnup (at %)	6.4	6.1		6.4	6.4
measured TUI	29.6	27.6	33	27.8	28
predicted TUI	24	30.3	26	26.3	26.2
experimental half-life (a)	2.05	2.2	1.8	2.2	2.2

The final burnup achieved by each fuel, as determined experimentally, was used as a normalisation parameter in the calculations.

The neutron and gamma dose rates, were calculated at the Institute for each of the fresh SUPERFACT fuels. The calculations were performed, using the computer program PUDOL [4], on the basis of the charge composition, certain physical properties (such as density and size) and cladding (TUSR-39, p. 52). The program considers self-shielding effects in the fuel itself and attenuation in the cladding. Furthermore, it allows a range of shielding materials for radiation protection purposes.

Results and Discussion

Transmutation rates

The primary information to be confirmed for a given recycling strategy of MA is the change in the MA inventory during an irradiation. The isotope vectors of uranium, plutonium, americium and curium, and ^{237}Np were measured as atom concentration in solution. These results, corrected for decay are converted in % Initial Metal Atoms (%IMA) from which the transmutation rates are deduced. A direct comparison between BOL (begin of life) and EOL (end of life) compositions yields the reduction in ^{237}Np and ^{241}Am through both fission and capture. The experimental and theoretical results on the reduction of ^{237}Np and ^{241}Am for the nominal irradiation period in PHENIX of 375 days are shown in Tab. 3.1.

The agreement between the measurements and theoretical predictions is within 6% except for the recycling scenarios of 2%Np (16%) and 20%Np (20%). The differences observed in the ^{237}Np results, are due to errors in the ICP-MS determination of neptunium and capture cross-sections (the present accuracy of ^{237}Np determination by ICP-MS is about 2% which propagates to 8% for the differences). The ^{238}Pu formed from ^{237}Np is consistently lower for the theoretical results (Tab. 3.2) indicating that the neutron capture cross-section of ^{237}Np is underestimated.

Radiation dosimetry aspects

The inclusion of MA, and in particular ^{241}Am, in a fuel would affect the radiation dose levels of the fuels. A significant increase in the gamma and

Tab. 3.2 Experimental and theoretical % IMA values

		% IMA (exp.)	**%IMA (theor.)**
Upu, 2%Np	**Np237**	1.37	1.49
	Pu238	0.67	0.59
U, 20%Am, 20%Np	**Np237**	14.12	15.9
	Pu238	6.32	5.5
U, 45%Np	**Np237**	32.4	32.9
	Pu238	8.5	7.7
UPu, 2%AM	**Np237**	0.020	0.022
	Pu238	0.42	0.40

neutron outputs has been predicted by KORIGEN for the SUPERFACT fuels over the standard FR-MOX fuel during fabrication (TUAR-92 p. 68). At discharge, the gamma outputs are comparable; however, the SUPERFACT fuels containing ^{241}Am have a significantly higher neutron output due to ^{242}Cm. The neutron outputs decrease with cooling time to that of the FR-MOX fuel at about 5 years after discharge. The total dose rate is now dominated by the gammas. Additional means in order to reduce the occupational dose from the MA fuels would be required certainly during fabrication. The gamma dose rates from the SUPERFACT fuel pins during fabrication are given in Tab. 3.3.

Tab. 3.3 Dose rates at 1 m from a fresh fuel

Fuel	**Measured**	**Predicted**	
	Gamma dose rate (mSv/h)	**Gamma dose rate (mSv/h)**	**Neutron dose rate (mSv/h)**
2% Np	7E-3	8E-3	1.7E-4
20%Am, 20%Np	0.26	0.25	3.3E-4
45% Np	< 0.01	2E-4	1E-7
2% Am	0.04	0.056	2E-4

The availability of computer programs enabling the prediction of EOL composition and dose rate aspects of fuels is essential in view of estimating gains and hazards in fuel cycles. The agreement of our measurements with the KORIGEN predictions for the source term gamma- and neutron-emitting nuclides has been found to be within 20% and 50% for the actinides and fission products respectively. This agreement is sufficient for composition studies associated with dosimetry measurements, but unsuitable for neutron physics calculations. The uncertainties on the cross-section and fission-yield libraries are unknown; however, one of the reasons of PIE isotopics is the improvement of these libraries which is in progress under a separate study.

In order to assess the reliability of the dosimetry computer program, experimental and theoretical dosimetry results were compared for two sets of experiments. The first is based on the dose rates measured during fuel pin fabrication for the SUPERFACT fuels (Tab. 3.3). The level of agreement is within the accuracy required for radiation protection purposes. The 45% Np case is difficult to assess due to the very low gamma component of the fuel. The second comparison is based on the KNK II/b fresh pellets (TUSR-34, p. 52; TUSR-36, p. 57). Calculations have been carried out at 5 cm distance assumed to correspond to the nominal centre of the ionisation chamber used in the measurements. For comparison purposes, the calculations performed (under contract) by UKAEA, Winfrith, UK have been included. The experimental and theoretical results, together with the specifications of the pellets, are shown in Tab. 3.4. The calculations by UKAEA have been based on the sample size and density, and a list of 18-group photon intensities as calculated using KORIGEN. The agreement between the measured and calculated (ITU) dose rates is within 15% which is sufficient for dosimetry purposes. It can be therefore concluded that the ITU dose rate calculations can be considered sufficiently reliable.

Tab. 3.4 Characteristics of fresh actinide pellets and gamma dose rates at 5 cm

Pellet	**Density**	**Gamma dose rates (mSv/h)**		
	g/cm^3	**measured TUI**	**predicted TUI**	**predicted UKAEA**
50%Am, 50%U	9.8	7.8	8.7	11.9
74%U, 24%Pu, 2%Am	9.94	0.37	0.42	0.52
74%U, 24%Pu, 2%Np	9.84	0.074	0.089	0.084
Pellet specifications: radius 0.32 cm; height 0.70 cm; Pu_{fiss}/Pu_{tot} = 0.8				

References

[1] G. Nicolaou, K. Richter, C. Prunier, L. Koch, Technical Committee Meeting on 'Safety and Enviromental Aspects of Partitioning and Transmutation of Actinides and Fission Products', Vienna, Nov. 29 - Dec. 2, 1993

[2] G. Nicolaou, H. Würz, L. Koch, Proceedings Intern. Symp. on Geological Disposal of Spent Fuel and High-level and Alpha-Bearing Wastes, p. 422, Antwerp, Oct. 19-23, 1992

[3] U. Fischer and H.W. Wiese, 'Verbesserte konsistente Berechnung des nuclearen Inventars abgebrannter DWR-Brenstoffe auf der Basis vor Zell-Abbrand-Verfahren mit KORIGEN, Kernforschungszentrum Karlsruhe, KfK-3014 (1983)

[4] M. Schmid, W. Benz, PUDOL 8.4 Dosimetry Computer Program, Siemens AG-KWU, BW Hanau, 1993

Present Status of Partitioning and Transmutation

Comparison of possible partitioning and transmutation schemes when added to the existing nuclear fuel cycle

Introduction

There have been several concepts proposed for partitioning and transmutation: those relying on existing reactors are by far more advanced. For this purpose, fuels are already under development which contain minor actinides and ^{99}Tc. They are being tested under irradiation in fast and thermal neutron fluxes. The status of these experiments is described below.

The partitioning of long-lived radionuclides from the present fuel cycles is being developed and flow sheets are under investigation. A comparison of the present to the expected performance will be made.

So far, accumulated experience allows comparison of partitioning and transmutation schemes with the present conventional reprocessing and the direct storage of spent fuels to be made. An assessment of the possible reduction of the radiological risk - after the release of radiotoxic nuclides from a repository - is given below.

Research for partitioning and transmutation has mainly been focused on the transmutation processes and less attention has been given to the partitioning of radiotoxic nuclides from the waste streams. The development of fuels or targets which can withstand the extreme conditions of a transmutation process and, moreover, can be reprocessed, has been almost disregarded. The oft-proposed "once-through transmutation" scheme, leading to an acceptable reduction of the radiotoxic inventory, is not feasible, because any structural material containing the radionuclides during the process would also be transmuted and rupture.

Comparison of the nuclear fuel cycles

The ongoing discussion on the topic of partitioning and transmutation has brought forward a variety of proposals which are summarised in Fig. 3.1. Processes based on photon-induced reactions or spallation of minor actinides by charged particles are in a stage where it is too early to justify target development except for basic experiments. Other processes, such as certain accelerator-driven reactor concepts and the recently revived proposal of transmutation in fusion reactors, are

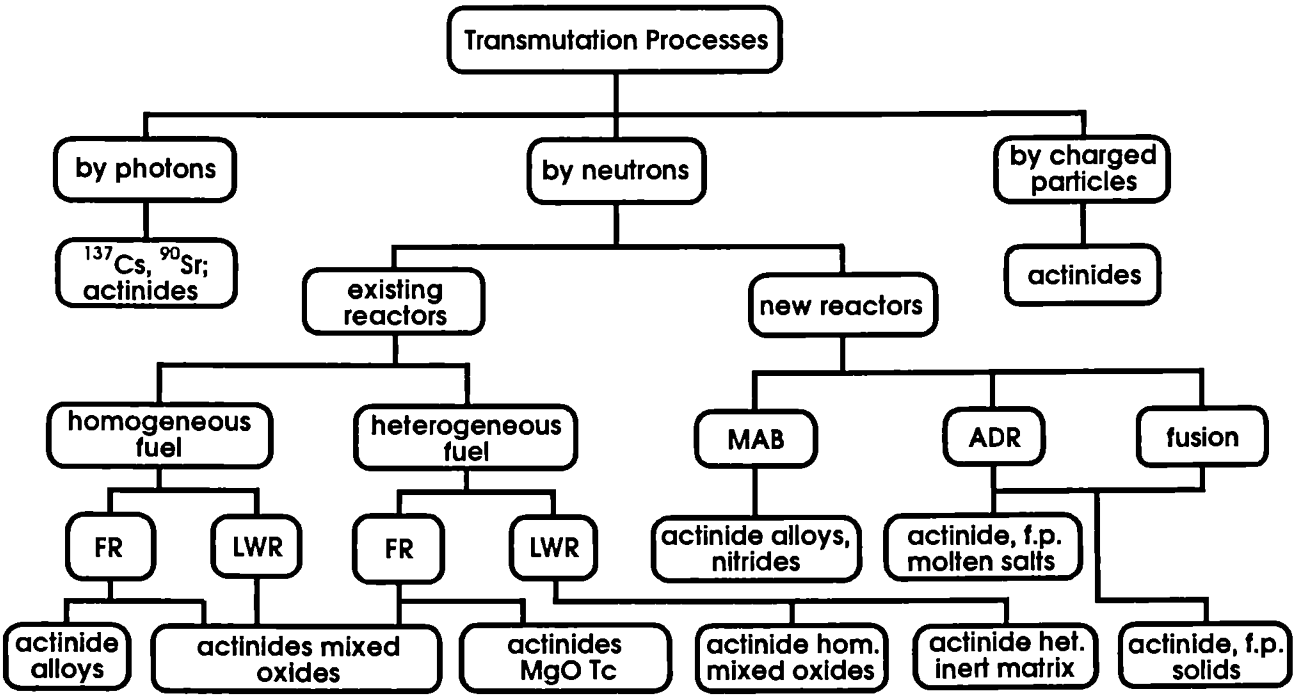

Fig. 3.1 Proposed transmutation schemes

based on similar fuel or target concepts as those proposed for existing reactors.

In the following, fuel cycles in existing nuclear power stations are compared from the point of view of their capabilities to reduce the radiotoxic nuclides in their discharged waste streams. The equilibrium concentrations for the nuclides of Np, Pu, Am, Cm and Tc are given for self-generated nuclide recycling. In order to compare the four concepts, we consider the fuel cycle as a closed system by which energy and radiotoxicity are generated and released, i.e. in the case of the once-through cycle, all nuclides are contained in the fuel, but in the other examples only the losses involved during the remake of the fuel. For clarity, the masses of each discharged nuclide given in Tab. 3.5 have been normalised to the energy output of the fuel.

PWR "once-through" fuel cycle (as a reference case)

Based on the design of the Biblis PWR, the content of Pu and Tc nuclides has been calculated in the spent fuel after a burnup of 50,000 MWd/t and an out-of-pile time of 7 years [2]. The enrichment of ^{235}U was 4 wt% (Tab. 3.5). The discharged concentration after 7y out-of-pile has been normalised to the energy output.

PWR self-generated Pu recycle

For the same reactor and operation conditions as above, the discharge concentration after 7y out-of-pile has been calculated for the case of recycling of the self-generated plutonium. The data refer to an "equilibrium" after 5 cycles [2]. It should be noted that at this stage 75% of the discharged fuel is the same as that in the previous case and 25% consists of recycled plutonium enriched initially to 4 wt%. The values given in Tab. 3.5 are averaged for the total core.

PWR self-generated transuranium recycle

Again for the same reactor and same conditions, all self-generated transuranium nuclides, together with ^{99}Tc are recycled. The values given in Tab. 3.5 are averaged for the total core.

FR self-generated TU recycle

The recycle of TU nuclides in the fast reactor was calculated for the SUPERPHENIX reactor assuming an initial charge of TU nuclides stemming from PWR with the concentrations given (Tab. 3.6). All minor actinides are recycled together with as much of the bred Pu as needed. The concentrations are given after the 16th cycle

Tab. 3.5 Masses of selected radionuclides per MWd discharged from different fuel cycles.

Fuel cycle	(w/o)		MWd/t	mg/MWd
	^{235}UO	$^{239+241}$PuO		
PWR 1300 MWe "once through"	4	–	50.000	^{99}Tc: 24 ^{240}Pu: 55 ^{243}Am: 4 ^{237}Np: 14 ^{241}Pu: 29 ^{244}Cm: 1.4 ^{238}Pu: 7 ^{242}Pu: 18 ^{245}Cm: 0.07 ^{239}Pu: 113 ^{241}Am: 6
PWR 1300 MWe Pu-recycle selfgenerated after 5 cycles	3.75	1	50.000	^{99}Tc: 26 ^{240}Pu: 136 ^{243}Am: 19 ^{237}Np: 12 ^{241}Pu: 56 ^{244}Cm: 8 ^{238}Pu: 19 ^{242}Pu: 92 ^{245}Cm: 0.3 ^{239}Pu: 173 ^{241}Am: 27
PWR 1300 MWe Pu+MA+ ^{99}Tc recycle selfgenerated after 5 cycles	3.75	1	50.000	^{99}Tc: 84 ^{240}Pu: 145 ^{243}Am: 25 ^{237}Np: 15 ^{241}Pu: 57 ^{244}Cm: 26 ^{238}Pu: 32 ^{242}Pu: 96 ^{245}Cm: 3 ^{239}Pu: 177 ^{241}Am: 28
FR 1200 MWe Pu+MA recycle selfgenerated after 16 cycles	–	10	80.000	^{99}Tc: 74 ^{240}Pu: 825 ^{243}Am: 25 ^{237}Np: 9 ^{241}Pu: 115 ^{244}Cm: 26 ^{238}Pu: 42 ^{242}Pu: 89 ^{245}Cm: 9 ^{239}Pu: 1275 ^{241}Am: 38

Tab. 3.6 Initial composition of TU nuclides charged to the SUPERPHENIX-reactor.

ISOTOPES	COMPOSITIONS
Np 237	5.12%
Pu 238	2.15%
Pu 239	52.37%
Pu 240	21.54%
Pu 241	10.15%
Pu 242	3.49%
Am 241	3.95%
Am 242 m	40 ppm
Am 243	1.15%
Cm 244	308 ppm
Cm 245	144 ppm
Cm 246	163 ppm

with a total burnup of 80,000 MWd/t. The out-of-pile-time is two years [3]. Again the discharge concentration for the TU nuclides are normalised to the achieved burnup in Tab. 3.5. For ^{99}Tc heterogeneous recycling is assumed in a thermalised position of the blanket with a transmutation half-life comparable to the 960 fpd of the reactor.

For the four fuel cycles, the corresponding compositions of the fuels are given in Tab. 3.7.

Before the equilibrium concentrations in the fuels are reached, the content of minor actinides will vary. This is especially so in the fast reactor, where minor actinides are charged which have been produced in a thermal flux. In the development, a fuel design should consider an elasticity of the minor actinide content ranging from 1 to 2%.

Instead of having the minor actinides (and Tc) homogeneously distributed in the fuel, one could consider concentrating them in a few fuel assemblies (heterogeneous concept). The latter approach might ease some fabrication problems, but certainly reduces the transmutation rate due to neutron resonance shielding. Since an addition of minor actinides increases the void coefficient (because of the higher fission threshold of most of the MA, a reactivity increase in case of neutron energy hardening would occur), the heterogeneous concept will not allow for significantly higher MA loading to a reactor core.

Tab. 3.7 Fuel compositions for various fuel cycles

"once through" LWR	UO_2
Pu recycle self-generated LWR:	$(U_{0.96}Pu_{0.04})O_2$
TU recycle self-generated LWR:	$(U_{0.95}Pu_{0.04}Np_{0.005}Am_{0.002}Cm_{0.001}Tc_{0.003})O_2$
TU recycle self-generated FR:	$(U_{0.8}Pu_{0.186}Am_{0.007}Cm_{0.006}Np_{0.001})O_2$

Minor actinide-containing fuels or targets

The Institute has been engaged in transuranium element research for 30 years with the main emphasis being placed on the development of fuels and targets. Studies on minor actinide-containing fuels for the purpose of transmutation began in the 70's and led to three irradiation experiments (Tab. 3.8) [4]. Any design of a specific fuel for given reactor type requires full knowledge of basic data [5], such as:

- phase diagram
- melting point of fuel
- oxygen potential
- thermal expansion
- heat capacity
- vapour pressure
- Young's module, etc.

In order to assess the irradiation behaviour, simulation studies are needed, such as:

- fuel restructuring in a thermal gradient by electrical heating
- fuel-cladding interactions
- compatibility of fuel with coolant

To conduct the pertinent experiments with minor-actinide containing samples, the Institute possesses unique facilities which allow the han-

Tab. 3.8 Completed irradiation experiments of MA-containing fuels.

Starting (Reactor)	**Fuel**	
1981 (FR2)	$(U_{0.5}Am_{0.5})O_2$	
1983 (KNKII)	1. NpO_2 2. $(U_{0.5}Am_{0.5})O_{2-x}$	3. $(U_{0.73}Pu_{0.25}Np_{0.02})O_{2-x}$ 4. $(U_{0.73}Pu_{0.25}Am_{0.02})O_{2-x}$
1986 (PHENIX)	5. $(U_{0.74}Pu_{0.24}Np_{0.02})O_{2-x}$ 6. $(U_{0.6}Am_{0.2}Np_{0.2})O_2$	7. $(U_{0.55}Np_{0.45})O_2$ 8. $(U_{0.74}Pu_{0.24}Am_{0.02})O_{2-x}$

dling of bulk quantities of minor actinides [6].

The institute is carrying out an extensive research programme to develop minor-actinide-containing fuels suitable for the existing reactors. Minor actinides added to fast reactor oxide fuels are being tested, together with the CEA, France. In continuation of the above-mentioned SUPERFACT experiment, further irradiations of fuels are planned [7]. The zirconium alloy based fuel concept suited for the IFR is being adapted - under commercial contract with CRIEPI [8] - to minor actinide transmutation. Irradiation experiments in the fast reactor PHENIX will start soon. As in the case of the UO_2 matrix, basic data for thermal conductivity, miscibility of actinides and fission products, fuel cladding compatibility, etc. were obtained from extensive experimental studies [9].

The LWR as a means for transmutation is being studied in the European Union, EU, as well. In spite of obvious disadvantages, the existence of numerous LWR plants is appealing for short-term transmutation applications. In the frame of a cooperation programme with the CEA, the homogeneous concept [7] and in a network collaboration (with KfK, ECN, CEA, EdF) [10] the heterogeneous concept of minor actinide fuels and Tc are being developed.

Partitioning

In the case of the once-through uranium cycle, the total radiotoxic nuclide content is sent to a repository, whereas in the case of the recycling of self-generated plutonium, all of the radionuclides other than plutonium will be discharged (Tab. 3.5). For the two concepts, the difference in the amount of ^{99}Tc and ^{237}Np is not significant. If one takes into account a loss of about 2% of plutonium for reprocessing and MOX fabrication, the plutonium waste from the plutonium fuel cycle amounts to about 5% of the Pu contained in the spent fuel, when directly stored. However, due to the continuous recycling of the plutonium and the subsequent build-up of americium and curium, the amount of the two transplutonium nuclides dramatically increases compared to the direct storage of spent fuel: 460% for americium and 570% for curium. From this it follows that because of the large build-up of transplutonium elements in the plutonium recycle, this concept produces much more radiotoxic TPu-waste than the direct storage of spent UO_2 fuel.

In order to convince the public that partitioning and transmutation is a concept which can reduce the radiotoxic hazards of a repository, a considerable reduction of the radiotoxic inventory must be achieved. In order to assess the separation yields needed by a partitioning scheme, we assume in a first approach, that the radiotoxic hazard would be only 1% of that of the spent fuel of the once-through concept.

The radiotoxicity of a certain nuclide is determined by the ICRP regulations. The radiotoxic hazard, however, must be understood as the probability of radiotoxic nuclides released from a repository to the biosphere. Here, several parameters influence the migration of a nuclide through the lithosphere, moreover, a general agreement on the assessment of the radiotoxicity has not yet been reached. Lacking the data for determining the radiotoxic hazard of each nuclide on one hand, but needing to set targets for the partitioning efficiency for a nuclide, we have resorted to the definition of the maximum decontamination factors, which are needed to reduce the radiotoxic hazard by a factor of 100 compared to the once-through concept. I.e., the two partitioning and transmutation concepts for PWR and FR would discharge only 1% of a nuclide present in the spent fuel of the once-through concept. The figures given in Tab. 3.9 show that for the higher transuranium elements, the required decontamination factors increase due to the stronger built-up of americium and curium during recycling. Again, these targets may be exaggerated, since the radiotoxic hazard is determined only by a few of the radiotoxic nuclides. For example, earlier studies showed that ^{237}Np and ^{99}Tc are the determining nuclides [11]. Under such a condition, the decontamination factors for the other nuclides could be considerably less.

Tab. 3.9 Maximum decontamination factor for single radionuclides by a partitioning process in order to achieve 100 times radiotoxic hazard reduction compared to direct fuel storage.

Decontamination Factors for Partitioning					
	Tc	Np	Pu	Am	Cm
TU recycle in LWR	350	110	230	530	1900
TU recycle in FR	310	64	1060	630	2300

There have been several processes developed to partition minor actinides from spent fuel. In order to assess their potential and compare their performance, we have installed in one of the chemical hot cells of the institute, a battery of centrifugal extractors. From highly active waste resulting from the earlier operation of WAK, minor actinides and residual plutonium have been partitioned [12]. The first results prove that decontamination factors as defined in Tab. 3.9 can be reached.

The studies will be carried on to include newly developed compounds and, with by extending the facility, to study different possibilities to separate lanthanides from the actinides.

References

[1] L. Koch: 'Status of Transmutation', Proceedings of the IAEA Specialists' Meeting on Use of FBRs for Actinide Transmutation, Obninsk, 1992.

[2] H. Wiese, INR; KfK: 'Investigation of Nuclear Inventories of High Exposure PWR MOX-Fuels Including Multiple Recycling of Self-Generated Plutonium', Work performed under ITU contract (unpublished).

[3] J.-P. Grouiller, DRN, CEA: 'Recyclage des actinides mineurs dans un réacteur type SPX'1, Work performed under ITU contract, (unpublished), 1986.

[4] L. Koch, M. Coquerelle, K. Richter: 'Minor Actinide-Containing Fuel for Transmutation Purposes", Proceedings of the IAEA Specialists' Meeting on Use of FBRs for Actinide Transmutation, Obninsk, 1992.

[5] L. Koch: 'Criteria for the Development of Targets and Fuels in Nuclear Transmutation', Proceedings of the OECD/NEA 2nd General Meeting of the International Information Exchange Program on Actinide and FP Separation and Transmutation, Chicago, 1992.

[6] J.-F. Babelot: 'Concept of a Minor Actinide Laboratory", Proceedings of the 3rd Working Group Meeting on Targets and Fuels, Karlsruhe, 1993.

[7] C. Prunier, et al.(CEA) : 'Transmutation of Actinides and Fission Products'. Ibid.

[8] T. Inoue, et al.: 'Recycling of Minor Actinides in Metal Fuel FBR', Proceedings of the OECD/NEA 2nd General Meeting of the International Information Exchange Program on Actinide and FP Separation and Transmutation, Chicago, 1992.

[9] A. Sasahara, M. Kurata: 'Status of Minor Actinide Transmutation Study at CRIEPI', Proceedings of the IAEA Specialists' Meeting on Use of FBRs for Actinide Transmutation, Obninsk, 1992.

[10] J.-F. Babelot:' A European Collaboration in the Field of Transmutation: EFTRA', Proceedings of the 3rd Working Group Meeting on Targets and Fuels, Karlsruhe, 1993.

[11] L. Koch: 'Minor Actinide Transmutation - a Waste Management Option', J. Less-Comm. Metals, 122 (1986) 371-382.

[12] J.-P. Glatz et al.: 'Partitioning of Actinides from HAW in a Continuous Process by Means of Centrifugal Extractors', Proceedings of the Specialists' Symposium on Emerging Technologies in Hazardous Waste Management, Atlanta, 1993.

Working Group Meeting on MA-Containing Targets and Fuels (29 and 30 June 1993)

This was the third in the series of meetings of the Working Group on Targets and Fuels initiated following the Workshop on Partitioning and Transmutation of Minor Actinides held in the Institute in October 1989 (TUAR 90,71). The meeting was attended by 39 participants, including representatives from IAEA, CEC, JRC Ispra, and 11 from the Institute. The following countries were represented: Belgium, Canada, Germany, France, Italy, Japan, Netherlands, Spain and Switzerland.

The idea of this series of meetings is to provide an international platform for the discussion of technical problems. Presentations included national programmes, international cooperations, conceptual studies on different transmutation schemes, partitioning studies, PIE of MA-targets and fuels and different matrices containing MA. The proceedings of the meeting will be published by mid 1994.

The next meeting (4th in the series) of the Working Group will take place in June 1994 at the Institute.

Partitioning Studies with Various Extractants

Introduction

The Institute is involved in several studies concerning the dissolution behavior of high burn-up and other special types of fuel, for instance the MA containing fuels irradiated in the frame of the SUPERFACT experiment (TUAR-92, p. 68). For this reason a study on the capability of the partitioning processes to recover actinides and long-lived fission products from the dissolver solutions was started.

The goal in partitioning actinides from nuclear waste streams with a view to their transmutation is twofold: to reach a large decontamination of the nuclear waste solutions in the extraction step and to achieve a selective and complete recovery (as close as possible to 100%) of the extracted actinides by back-extraction.The highly active waste (HAW) from the PUREX process contains, together with the fission products, significant amounts of actinides, i.e. 0.5 % of U and Pu, a large percentage of the Np and almost all of the Am and Cm. These elements together with some long-lived fission products (i.e. ^{99}Tc) mainly determine the long term radioactive hazard of HAW. Their removal would therefore reduce its radiological hazard considerably. Several extraction processes have been investigated for this purpose, the best known being the TRUEX process [1]. A similar process has been developed recently in the P.R. of China, the so-called TRPO process, which uses a trialkyl (C6-C8) phosphine oxide extractant [2].

Based on the results of a cold test [3] and on the results of preliminary studies of the extraction behavior of TRPO [4], the process was tested by means of an extraction equipment consisting of a battery of 12 centrifugal extractors, installed in our hot cell facility.

A comparison of different types of extractants should give the oportunity to select the best suitable process for the treatment of the above mentioned material. A test was therefore also carried out with CMPO under TRUEX type conditions [5].

In both cases the same genuine HAW, originated from a mixture of dissolver solutions from different LWR fuels was used as feed. The initial composition of the HAW concentrate (500 l/tU) is given in Tab. 3.10.

The use of an extractant for partitioning purposes will only be possible if its radiation stability under realistic conditions is sufficiently high. With an external ^{60}Co source it was found, that up to 10^7 Gy, TRPO has a radiation stability close to that of tri-octyl phosphine oxide (TOPO) and is much better than that of bis (2-ethylhexyl)phosphoric acid (HDEHP) and tributyl phosphate (TBP) [6]. However if the organic phase is loaded with actinides, not only γ- but also β- and α-radiations become relevant for the radiation stability of the organic molecule. The aim of the present work was to concentrate especially on the back-extraction of the extracted species from TRPO after storage times of up to one week.

Radiation stability tests were carried out to study the back-extraction behavior of TRPO for loading periods of up to one week. Six extractions were carried out from 1 M HNO_3 according to the process scheme (TUAR-92, p. 84) followed by back-extractions done after 0, 5, 24, 48, 92 and 164 h.

Tab. 3.10 Composition of the the HAW concentrate (500 l/t U)

Element group	Element	Concentration, g/l
corrosion products	Cr	1.10
	Mn	0.41
	Fe	10.13
	Ni	2.56
	Co	0.01
fission products	Rb	0.53
	Sr	1.18
	Y	0.78
	Zr	0.22
	Mo	2.07
	Tc	1.36
	Ru	2.99
	Rh	0.60
	Pd	0.57
	Cd	4.77
	Sn	0.05
	Te	0.14
	Cs	3.71
	Ba	3.90
	La	2.25
	Ce	4.32
	Pr	2.16
	Nd	7.32
	Sm	1.56
	Eu	0.21
	Gd	0.42
actinides	U	6.82
	Np	0.45
	Pu	0.34
	Am	0.24
	Cm	0.02

The concentration profiles obtained for the 3 back-extraction streams are shown in Fig. 3.2.

Whereas for Np and Pu and also for the extractable light fission products no influence of the storage time can be observed, a slight decrease with time is observed for the concentration of Am, Cm and the lanthanides. At the same time the U concentration in the Na_2CO_3 stream increases considerably. Both observations could be indicators of the presence of some amounts of acidic degradation products building up after several days.

Actinide partitioning from genuine HAW by TRPO in a continuous process

The hot demonstration of a continuous partitioning of actinides from HAW (see Tab. 3.10) was made by means of the centrifugal extractor equipment and the process scheme, both extensively described in TUAR-92, p. 81. The process reached steady state conditions after half an hour. From all stages and process streams samples were taken and analysed by ICP-MS.

The actinide elements are extracted by multistage counter-current contact and back-extracted according to the process scheme. As an example, the concentration profiles (organic and aqueous phase) of Am in the 22 extraction stages are shown in Fig 3.3.

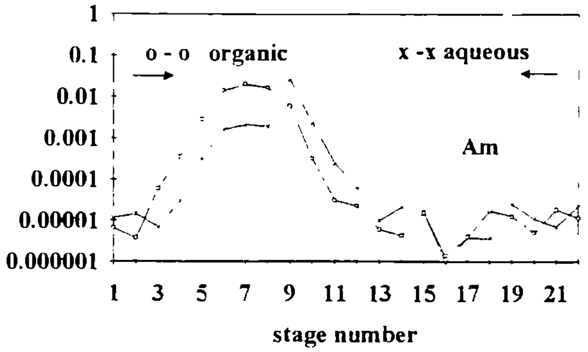

Fig. 3.3 Concentration profiles (organic and aqueous phase) of Am in the 22 extraction stages nitric acid concentration in the feed 0.7 M

After 4 extraction stages the concentration of Am is decreased by 4 orders of magnitude and has reached the detection limit, although the distribution ratio has a value of only about 10. The back-extraction by 5.5 M HNO_3 is also complete after 4 extraction stages.

Similar results were obtained for the other actinide elements, except for Np (see Fig. 3.4).

The distribution coefficient for Np (cf concentrations in the aqueous and the organic phase) is high but appears to decrease after the first extrac-

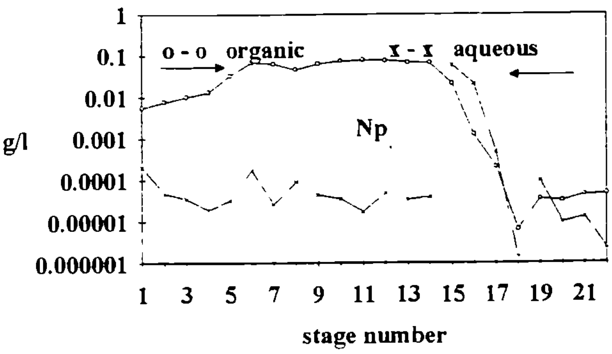

Fig. 3.4 Concentration profiles (organic and aqueous phase) of Np in the 22 extraction stages nitric acid concentration in the feed 0.7 M

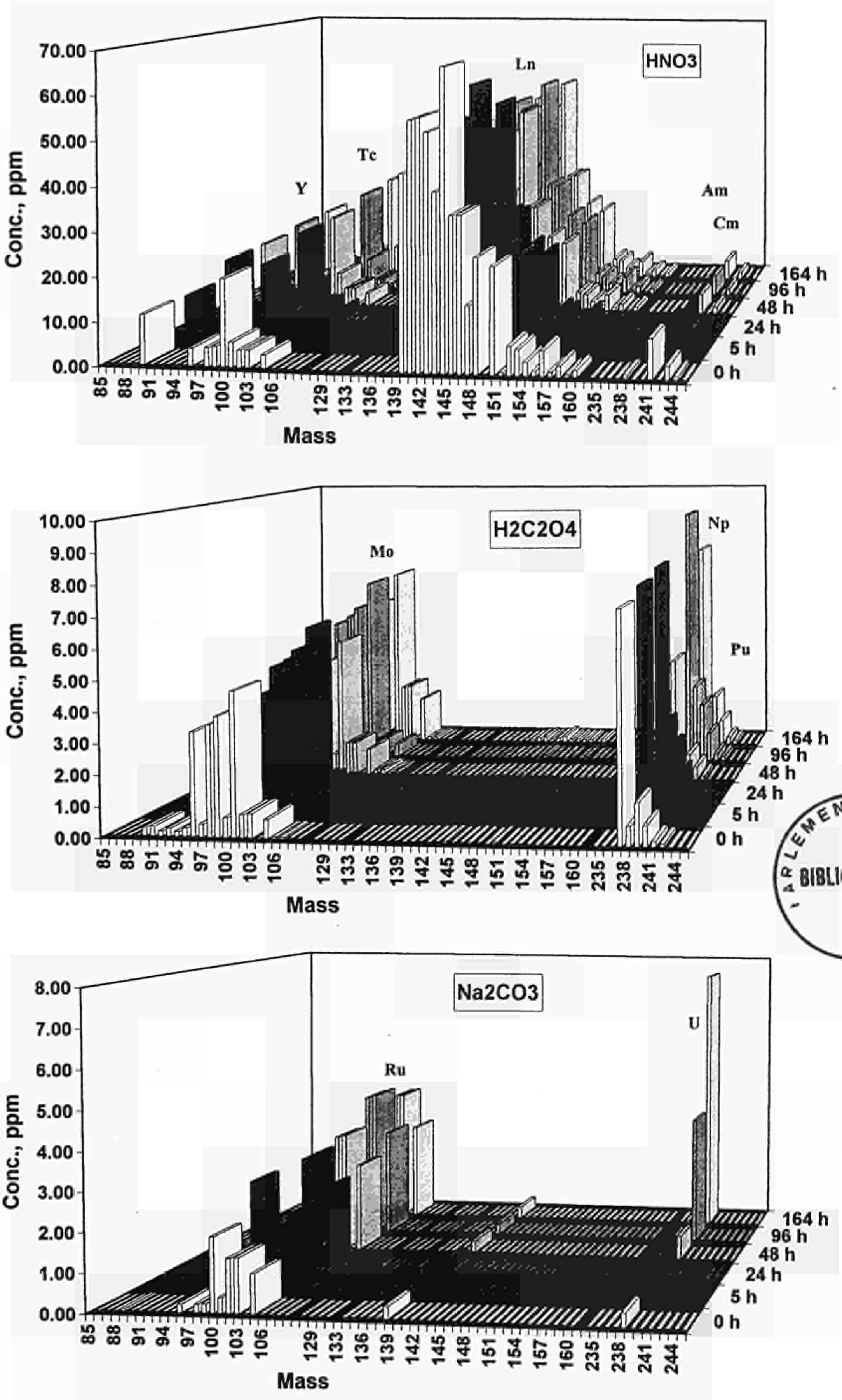

Fig. 3.2 Concentration of the extracted components in the back-extraction streams of the TRPO process for different storage times of the organic phase (HNO3 concentration in the feed 1 M)

tion stages. The back-extraction by oxalic acid on the other hand works well. Thus it is not the extraction but the preliminary reduction which is responsible for the incomplete extraction of Np. Unfortunately the kinetics of this reaction is slow, especially at low nitric acid concentrations [7]. At 0.7 M the reduction was apparently not complete and thus part of the Np remains in the raffinate (Tab. 3.11).

Almost 10 % of Np remain in the raffinate, whereas the other actinides are recovered in a single process stream each with a recovery of better than 99.6%. The Np extraction can be significantly improved if the nitric acid concentration in the feed is increased to 1.36 M (Fig. 3.5). With 1.36 M HNO_3 a good extraction of Np can be obtained after 5 extraction stages, because the reduction is now significantly faster (Tab. 3.12).

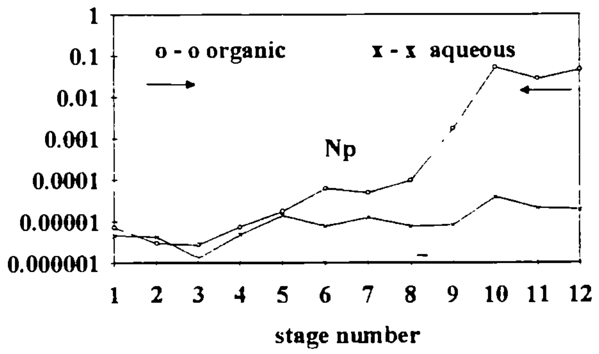

Fig. 3.5 Concentration profiles (organic and aqueous phase) of Np in the 12 extraction stages nitric acid concentration in the feed 1.36 M

Tab. 3.12 Decontamination factors of actinides and Nd

Test No	1		2	
Number of extraction stages	6		10	
HNO_3 concentration	0.7 M		1.36 M	
Nuclide	Effective Stages	DF	Effective Stages	DF
^{144}Nd	5	> 22000	9	> 33000
^{237}Np	6	12.4	5	> 4100
^{238}U	2	> 5400	3	> 7000
^{239}Pu	3	> 760	4	> 950
^{243}Am	4	> 900	6	> 764

In the second test increased decontamination is observed for Nd, U and Pu mainly due the increased number of extraction stages. In the case of Np, the influence of nitric acid is clear: with less effective extraction stages, the DF value is almost 200 times higher. Only for Am is the DF value slightly decreased. It is known from literature, that the extraction of Am, Cm and the lanthanides decreases with increasing nitric acid concentration [8].

Thus a nitric acid concentration of around 1.3 M seems to be a good compromise for an adequate extraction of Am, Cm and Np.

Tab. 3.11 Relative distribution (in %) for the main actinide isotopes

Isotope	Relative distribution					
	raffinate	Am stripping	0.1 M HNO_3	Np/Pu stripping	U stripping	Used TRPO
^{237}Np	9.81	0.02	0.02	89.51	0.10	0.54
^{238}U	0	0	0	0.06	99.85	0.09
^{239}Pu	0.18	0	0	99.58	0.19	0.05
^{241}Am/Pu	0	97.34	0	2.66	0	0
^{243}Am	0	99.69	0.01	0.13	0.14	0.03

Actinide partitioning from genuine HAW in a continuous CMPO process

As mentioned above the TRUEX process is the most investigated process for actinide partitioning. Based on the proposed process scheme developed by Horwitz [1] for a mixer settler battery, a similar scheme was developed for our centrifugal extractors (Fig. 3.6).

All the actinides were completely extracted with the CMPO solvent. In Fig. 3.7 the concentration profiles of Am and Pu in the aqueous phase for both extraction and stripping steps are shown.
Not only the concentrations of Pu and Am but also those of all the other actinides contained in the HAW were below the detection limit in the raffinate. The concentration profiles of Am and Pu at the first stripping section, e.g stages numbers 13 to 16. indicates an accumulation of these nuclides in the equipment. Similar observations were made by Ozawa [9] in his test of the TRUEX process in mixer-settlers.

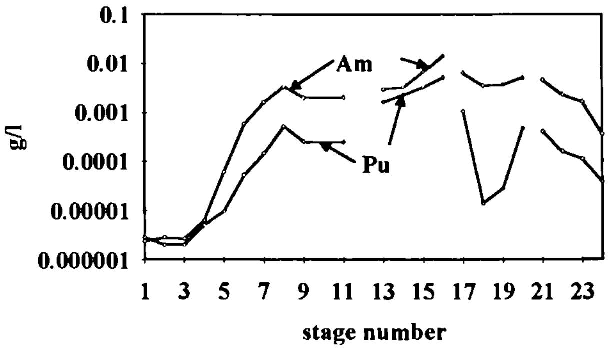

Fig. 3.7 Concentration profiles (aqueous phase) of Pu and Am in the 24 extraction stages

This accumulation was probably caused by the high HNO_3 concentration in the CMPO-TBP solvent: the distribution ratio of Am at stage No. 13 was for instance about 10 because of the high HNO_3 concentration. The decontamination factors for the actinides and for Tc are given in Tab. 3.13.

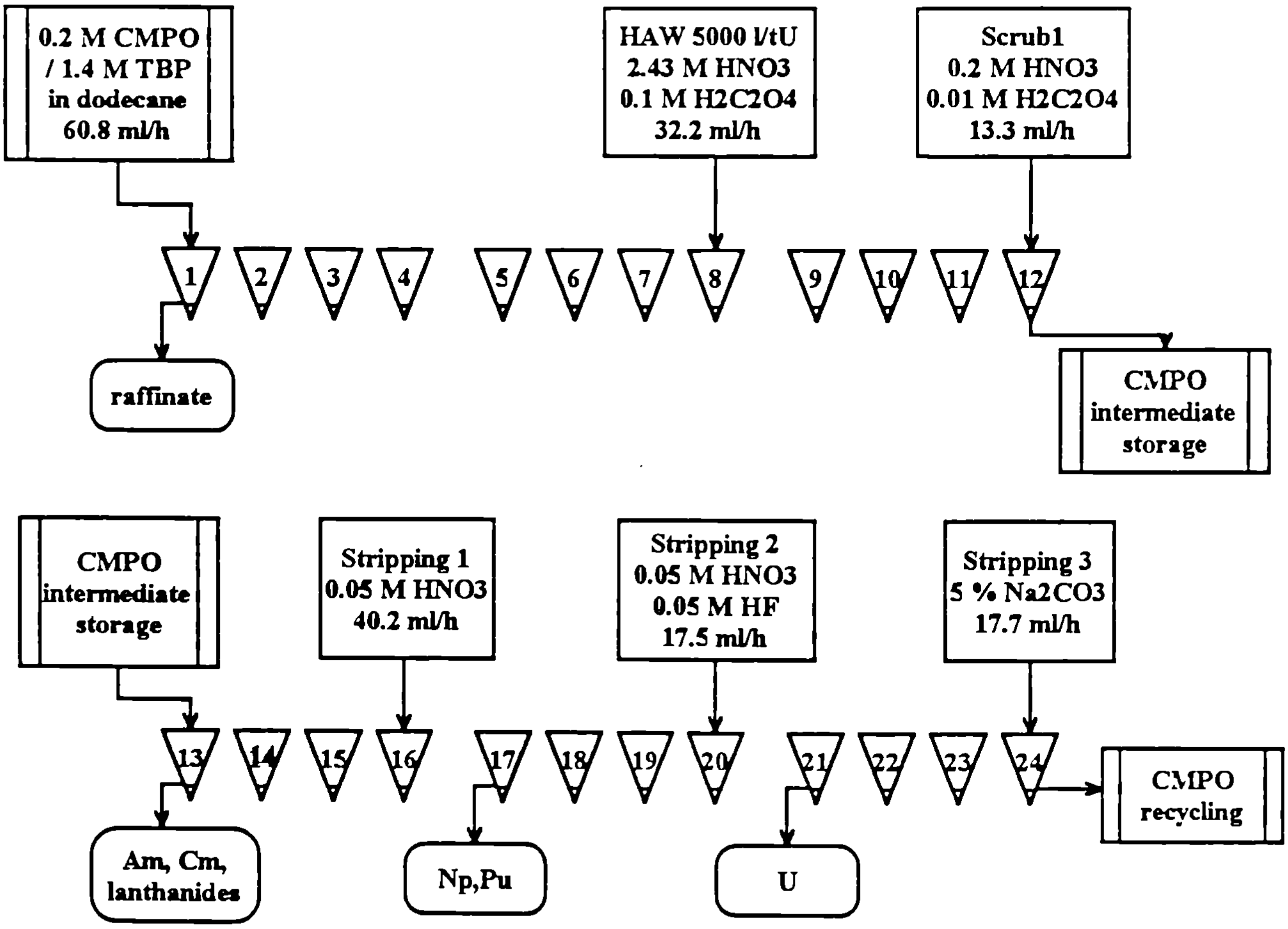

Tab. 3.6 Initial composition of TU nuclides charged to the SUPERPHENIX-reactor.

Tab. 3.13 DF values of Tc, lanthanides and actinides from HAW.

Isotope	Concentration in the feed (g/l)	Effective stages	DF value
^{99}Tc	0.107	8	170
Lanthanides	2.25	7	> 30000
^{238}U	0.859	5	> 100000
^{237}Np	0.0554	5	> 30000
^{239,240}Pu	0.0185	6	> 4000
^{241,243}Am-	0.0566	6	> 15000
^{244}Cm	0.0018	5	> 1000

The TRUEX process showed a very good performance from a viewpoint of decontamination of the HAW from actinides. After reduction of Np to the tetravalent state with Fe^{2+} a high DF value could be achieved for this element as well. However a preferential method would involve a salt-free process. The lanthanides and Y were extracted together with the actinides.

The long-lived fission product Tc was extracted from HAW with a yield of 99.4 %. The yield would be improved by increasing the number of stages for extraction. The distribution of the lanthanides and the actinides on the different streams confirms the accumulation theory (Tab. 3.14).

In the first stripping section, the stripped fractions of Am and Cm were very low, however quite high percentages of Np and Pu were also stripped in this section, although these elements should have been back-extracted only in the second section. From the mass balance it is again evident that a large percentage of the transuranium actinides accumulate in the extractors. The analysis of the organic phase at the exit of each stripping section proves, that the back-extraction is almost complete (Tab. 3.15).

Tab. 3.14 Relative distribution (in %) for lanthanides and actinides in the outlet solutions.

Element	Raffinate	Strip-1 (Am, Cm)	Strip-2 (Np, Pu)	Strip-3 (U)	Used CMPO	Accumulated in the extractors
Ln	0.00	8.63	10.6	3.89	0.35	76.5
U	0.00	0.14	0.43	98.8	1.60	-
Np	0.00	7.66	2.23	2.58	0.11	87.4
Pu	0.02	12.3	3.45	1.34	0.03	82.9
Am	0.01	7.16	6.72	4.89	0.44	80.8
Cm	0.10	13.0	10.3	7.02	0.31	69.4

Tab. 3.15 Relative distribution (in %) for lanthanides and actinides on the stripping sections obtained from the analysis of organic solution at the last stage of each stripping step.

Element	Strip-1	Strip-2	Strip-3	Used
	(Am, Cm)	(Np, Pu)	(U)	CMPO
Ln	31.0	49.1	19.6	0.35
U	4.16	0.24	94.0	1.60
Np	65.6	32.6	1.71	0.11
Pu	68.2	30.4	1.42	0.03
Am	37.5	40.5	21.5	0.44
Cm	34.0	51.2	14.6	0.31

It is quite evident, that the obtained picture does not show the equilibrium state of the process. To avoid the accumulation and thus make possible the recovery of the extracted species, it is necessary to decrease the HNO_3 concentration in the loaded CMPO solvent by changing the conditions of the extraction and the stripping steps.

Conclusions

For the TRPO process, the recovery by back-extraction is almost unchanged even for a loading period of the organic phase of up to one week, indicating a high radiation stability of TRPO to all types of radiation emitted by the HAW constituents. However, the slightly decreasing recovery of Am and Cm with loading time and an increasing amount of recovered U could indicate that increasing amounts of acidic degradation products are formed after several days and that those products would have an influence on the distribution ratios.

The TRPO process for the partitioning of actinides from genuine HAW was successfully tested under real conditions by means of centrifugal extractors operated in a continuous mode. 22 extraction stages are sufficient to achieve high decontamination factors (between 10^3 and 10^5) and recovery rates of 99.6 % or better. Additional efforts will be made to further increase this value and get as close as possible to 100 %.

The Np is generally present in the waste solutions in three different oxidation states (IV, V and VI). The kinetics of the preliminary reduction step, needed to convert the non-extractable Np(V) to Np(IV) is fast enough only if the nitric acid concentration in the feed is higher than 1 M.

The TRUEX process also gave excellent results for the decontamination of HAW. The process parameters selected for the back-extraction part of the process in the present study need to be altered if a reasonably good recovery from the solvent is to be achieved.

In the present process schemes proposed for both extractants (TRPO and CMPO), the separation of Am and Cm from lanthanides is not foreseen. It is well known that these elements always have very similar extraction behaviour and that consequently a separation of these two element groups is very difficult. For transmutation purposes this separation is strongly required, because the lanthanides are contained in a tenfold excess in HAW solutions compared to the actinides and the high neutron capture cross-sections of lanthanides can strongly influence the neutron spectrum of the irradiation source. Thus one of the main goals for future development of actinide partitioning processes should be the implementation of a lanthanide - actinide separation step.

References

[1] Horwitz, E.P., Kalina, D.G., Diamond, H., Vandegrift, G.F., Schulz, W.W., "The TRUEX Process - A Process for the Extraction of the Transuranic Elements from Nitric Acid Wastes Utilizing Modified Purex Solvent", Solvent Extr. Ion Exch., 3(1&2) (1985) 75

[2] Y. Zhu, C. Song, "Recovery of Np, Pu and Am from Highly Active Waste, in Transuranium Elements", L.R. Morss and J. Fuger, eds., ACS, Washington, DC (1992)

[3] C. Song, J.-P. Glatz, X. He, H. Bokelund, L. Koch, "Actinide partitioning by means of the TRPO process", to be published.

[4] C. Apostolidis, R. de Meester, L. Koch, R. Molinet, Y. Liang, Y. Zhu, "New Separation Techniques for Radioactive Waste and other Specific Applications", L. Cecille, M. Casarci and L. Pietrelli, eds., Elsevier Applied Science, London and New York (1991) 80.

[5] Chamberlain, D.B., Leonard, R.A., Hoh,J.C., Gay, E.C., Kalina, D.G, Vandegrift, G.F., "TRUEX hot demonstration", ANL 89/37, (1990)

[6] Y. Zhu, C. Song, J. Xu, D. Yang, B. Lie, J. Chen, Chin. J. Nucl. Sci. Eng. 9(2) (1989) 141

[7] C. Apostolidis, H. Bokelund, M. Ougier, A. Moens, Inorg. Chim. Acta, 140 (1987) 253

[8] Y. Zhu, R. Jiao, Proc. GLOBAL '93, Seattle, Washington, Sep. 12-17, 1993, ANS, Inc. La Grange Park, Illinois USA, 44

[9] Ozawa, Nemoto, S., Togashi, A., Kawata, T., Onishi, K., Solvent Extr. Ion Exch., 10(5) (1992) 829

Means and Materials for the Preparation of Transmutation Targets

Introduction

The fabrication of actinide fuels for transmutation studies is as a step in the fuel cycle sequence placed at the interface between partitioning and transmutation. Under these conditions, the fabrication process is clearly constrained by factors connected to the partitioning and is bound to meet requirements set by the transmutation process. These points are presented in Fig. 3.8.

Constraints from partitioning:

- * Purity of actinides
- * Lanthanides, An/Ln
- * Mixture or individual element

Requirements for transmutation:

- * Type of burner
- * Type of fuel
- * Chemical specifications
- * Composition
- * Impurities, An/Ln
- * Monophasic
- * Stoichiometry

Fig. 3.8 Constraints and requirements for target fabrication

Impurities play a role as neutron absorbers in the actinide destruction device and therefore it is important to specify for which type of burner the fuel is being prepared. Especially, the lanthanides, which in present day partitioning technology would co-extract with the actinides, are important because of their influence on the neutronics of a nuclear reactor. However, the fast reactor is forgiving in this respect and can accept a higher concentration of the lanthanides.

On the fuel side, also a stringent control of the specified impurities, often at the ppm level, is required. Furthermore, only a few percent of lanthanides can be accepted in an oxide fuel, as it has to be monophasic. This interplay of constraints would require a lanthanide/actinide separation factor of more than 1000 in the partitioning step. Dedicated extractants and probably additional separation processes would be needed for this purpose.

Smaller samples of alpha active materials, such as the minor actinides (MA) or their compounds, can be handled in gloveboxes. Larger amounts of MA would however require additional gamma shielding, such as lead glass at the viewing ports or covering main areas of the glovebox, and lead foils of appropriate thickness and size around the remainder of the box.

For the chemical preparation of MA fuels, such as for the Superfact I irradiation, another type of cell arrangement was used [1]: a row of 5 large gloveboxes equipped with manipulators and with sufficient additional shielding against neutrons and gamma-rays. The shielding consisted of water-filled walls placed in front of the operation area. These hybrid type gloveboxes are described elsewhere, e.g. in connection with the discussion of the MA laboratory [2].

The MA to be used in the forthcoming campaigns over the next few years include oxides of ^{237}Np, ^{241}Am and ^{243}Am in quantities of around 20 grammes, either in mixtures or as individual isotopes. The material is currently being purified from oxides or from solutions of scrap material. The purification of ^{241}Am to the ppm level by reduction to the metal and subsequent distillation in high vacuum in an electron beam furnace at 1200 °C can be mentioned as an example. The purity of the americium feed is about 90 %.

Target fabrication by the sol gel process

Considerable experience with the Sol Gel process exists in the Institute. It has been used for the fabrication of $(U,Pu)O_2$ fuels, for the fabrication of fuels containing the MA elements, Np and Am, in concentrations of up to 40% (Superfact I), and for the preparation of inorganic ion-exchange materials, the so-called precursors, for the treatment of medium active waste.

For the studies on transmutation, such as the Superfact II irradiation planned for the coming years in the Institute, many different targets containing MA have to be prepared.

The Sol Gel precipitation is typically placed in front end of the fabrication chain, as it can produce an oxide or mixtures of oxides as feed for the further steps in the fabrication procedure. It was thus a natural choice for the future campaigns with MA.

The process is very flexible: a wide range of mixtures can be produced; rather few impurity elements present with the actinides co-precipitate; the beads resulting from the subsequent calcination are free-flowing; the process is dust-free and has a high actinide yield and can also be rather easily scaled up.

The design of new equipment is based on the extensive experience with Sol-Gel in the Institute: Similar units have been operated for many years in a hands-on glovebox as well as behind the water shielded cells using manipulators. The unit will use the most modern techniques and, considering the limited space in the cell, will be simplified and aim at a minimisation of the amount of ammonia waste arising. A control panel with alarms and instruments is provided, allowing a safe and reliable operation.

Waste considerations

The waste from the co-precipitation is an alkaline solution containing ammonium nitrate. Rather large waste volumes are obtained which is one of the few drawbacks of the method. During the forthcoming fuel fabrication campaigns an effort will be made to account in a representative way for actinides in the waste produced, in order to validate the Sol Gel process. It is believed that the Am losses will be of the order of 0.1 - 0.3 %.

Aspects of the secondary waste are very important in judging the efficiency of the P & T concept: if with the many cycles and process steps the losses can not be kept low, the effect would be to spread the actinides over many secondary waste streams.

Experiments to treat this type of waste have been carried out in the Institute, notably dealing with its denitration [3]. The nitrates should be removed from the raw waste before its solidification by cementation, as these ions make the cement vulnerable for leaching by water. The nitrates can be removed down to the ppm level by a photochemical process, which is particularly efficient in an alkaline medium containing ammonia [3]. This process will also be verified in the future campaigns.

References

[1] H. Bokelund, M. Lebrun, 'Gloveboxes with Manipulators. A Hybrid Laboratory for Handling of Actinides' Meeting on Hot Laboratories and Telemanipulation, Karlsruhe September 1989.

[2] J.-F. Babelot, H. Bokelund, J.-F. Gueugnon, L. Koch and K. Richter, 'Fuel Studies for the Transmutation/Concept of a Minor Actinide Laboratory', Proceedings of the Conference on Future Nuclear Systems: Emerging Fuel Cycles and Waste Disposal Options, Global '93, Seattle, September 1993.

[3] H. Bokelund: 'Denitration of Waste Solutions by a Photochemical Process', (to be published).

1.4 Characterisation of Waste Forms and of High Burn-up fuel

Introduction

The studies on radioactive waste carried out at the Institute for Transuranium Elements are centered on the characterization of waste forms (non-processed spent fuel and vitrified high level waste), with respect to properties relevant to their behaviour under irradiation or under conditions of long term storage.

Within the frame of a contract with Siemens-KWU it became necessary to characterize fuel rods irradiated with the appropriate high enrichment of 3.8 to 4.2 % ^{235}U in highly rated commercial PWR's under realistic conditions. Burn-up as high as 80 MWd/kg(U) were reached at relatively high power levels ranging between 310 and 180 W/cm for the different successive cycles.

Emphasis was put on cladding behaviour, fission gas release, fuel restructuring and fuel-cladding chemical interactions.

After carrying out more than 100 analyses of filling gas after irradiation the following conclusions concerning the influence of the starting enrichment, the initial gap cladding-pellet and the burn-up on the fractional fission gas release can be made.

- As expected the fission gas release of the fuel rods with higher enrichment is generally greater than that of fuel rods with lower enrichment (4 and 8 % fractional fission gas release, respectively, at 60 MWd/kg(U)).
  At low and intermediate burn-up the influence of the diametral gap size is pronounced and decreases at higher burn-up as a consequence of the cancellation of the initial gap due to the combined effects of cladding creep and fuel swelling.

- In spite of decreasing fuel centre temperatures with increasing burn-up, the experimental results indicate a continuous increase in fission gas release (up to 9 % fractional release at 60 MWd/kg(U)).

- An attempt has been made to relate the fission gas release behaviour to fuel microstructure based on optical and scanning electron microscopy, and Xe and Cs radial distribution by EPMA. From this study it results that the major contribution comes from the central part of the fuel when higher atomic mobility favourizes porosity coalescence at grain boundaries. The outer rim ($1 < r/r_0 < 0,98$) shows a high release ratio as well, but its contribution is not determining. From the appearance at high burn-up of a new restructing mode in the zone $0.9 < r / r_0 < 0.8$, consisting of heterogeneous grain growth where greater dense grain are surrounded by small ones with higher porosity and higher fission gas release, it can be anticipated that such a mechanism should progress further by increasing irradiation time and could therefore limit the fuel rod life. This point will be analysed in the next future.

- The neutronic resonance absorption at the fuel pellet periphery leads, as burn-up increases, to a continuous increase of the burn-up at the pellet periphery which reaches a local peak burn-up of 140 MWd/kg(U) corresponding to an average pellet burn-up of 66 MWd/kg(U). At the same position a concentration of 3,2 % Pu was determined by EPMA corresponding to an average pellet Pu build-up of 1.2 %.

- The outer rim zone is also characterized by the formation of a specific microstructure (outer rim with cauliflower structure) with extended porosity; the distance between pores in this zone lies between 1 and 3 µm.
  The extent of this zone is strongly dependent upon the starting enrichment and has 200 µm maximum extent with 3.2 % ^{235}U enrichment. Increase of the enrichment to 3.8 - 4.2 % reduces the maximum extent to 100 µm.

- The presence of metallic fission products (Mo, Tc, Pu, Rh, Pd) at the periphery and pellet centre lets anticipate a fuel stoichiometry in the range $2.00 < O/_M < 2.001$ if equilibrium conditions are assumed. The oxygen excess produced by fission is controlled by gettering the oxygen by Zr at the inner side of the cladding, the formation of U_2CsO_4 and buffer mechanism due to Mo.

An additional study concerns the analysis of UO_2 leached by aqueous solutions in order to model the underground water contamination in a fuel repository, should water accidently leach the fuel.

The latter aspect could be very sensitive to the fuel oxidation state. Therefore, more precise information is necessary concerning the oxidation kinetics of irradiated UO_2 and MOX fuels when in contact with water or vapor.

Results of the oxidation of unirradiated UO_2 at temperatures lower than 500 °C in air and in moist N_2, carried out by thermogravimetry were reported in TUAR-92, p. 106. This study was continued. The results showed that complete oxidation of UO_2 with formation of well crystallised U_3O_8 occurred at 170 °C in 277 days. A new oxidation test was started at 150 °C which will last over a period of 1 year.

In order to carry out similar testing on irradiated UO_2 new equipment had to be developed. First, an autoclave was modified for carrying out controlled oxidation measurement at temperatures lower than 300 °C under moist atmosphere.
Secondly, the characterization possibilities have been extended and a shielded glove box for X-ray diffraction and thermogravimetry has been developed. The mounting of the box should occur in the next future.

Electrochemical testing has been continued with natural UO_2 in 3 % NaCl. Reducing the anodic polarisation shows a thinning of the anodic film. At more cathodic potentials (i.e. below - 480 mV SCE) the capacitance and current rise but become unstable. Although there are a number of other explanations this implies a heterogeneous thinning of the UO_2 surface film.
Modelling of the UO_{2+x} oxide film under reducing conditions has been done with a resistance and capacitor (with losses) in parallel (i.e. a parallel RC circuit) with values of $R \simeq 15\text{-}30\ k\Omega.cm^2$ and $C \simeq 0.4\ nF.cm^2$.
Linear polarisation measurements indicate a higher resistance of $Rp \simeq 150\ k\Omega.cm^2$, however these measurements are only comparable under equilibrium conditions, and the linear polarisation technique is limited in high impedance systems.
Currently some work is being initiated on the oxide layer stability and growth on zircaloy-4 and zirconium electrodes in aqueous media. The aim is to find techniques of increasing or reducing the defectiveness of the ZrO_2 film and thereby increasing its waterside corrosion resistance in service.

Leaching tests on UO_2 powder in an autoclave at 200 °C and short time duration (one month maximum) have been carried out in order to evaluate the influence of different paramaters. From these experiments one can conclude that no actinide transfer occurs when the specimen is leached by vapor. Oxidised UO_2 powder displayed a strong increase of U leaching rate but no modification could be measured for the fission product transfer to the aqueous solutions.

The presence of granite reduces the leaching rate of all measured elements by two orders of magnitude. Preliminary results of leaching tests of the inner side of the cladding showed an increase of the leaching rate of the actinides by two or three orders of magnitude. No visible influence concerning the fission products was noticed.

UO_2 power reactor fuels irradiated to a burn-up of 50.000 GWd/t and more display new aspects of the fuel chemistry. The strong local burn-up increase at the fuel periphery induces fission product accumulation. A reaction between Cs und UO_2 at the cladding / fuel interface was found, resulting in a modification of the fuel cladding mechanical interaction and thermal properties of the outer part of the fuel pellet.

Cs_2UO_4 was synthesized to study its thermal stability and the chemical interaction with ZrO_2. Successful preparation of high density samples allowed the determination of the plasticity, the thermal expansion and the thermal conductivity of Cs_2UO_4.

A non-destructive assay technique was used to characterize individual fuel pins in i.e. the burn-up and the radiotoxicity potential. The present unit for passive neutron and gamma interrogation has been extended to include a miniature semiconductor detector (Cd Te with $3 \cdot 3 \cdot 2\ mm^3$ active volume) for simultaneous spectrometry. The detector which was installed inside an α, γ-hot cell is presently going through extensive tests to check the behaviour in a stringent environment where several spent fuel rods are stored. First findings indicate a good stability of the system during a continuous operation of about one month.

Leaching tests on fuel rod segments with pre-set defects is a part of the programme. These fuel rod segments have to be fabricated from UO_2 and MOX fuel rods irradiated in BR3 at 50.000 MWd/t. The last step of NDT concerning the MOX fuel rods is presently completed and the fabrication of the fuel rod segments will start as early as the defueling machine is in operation.

The outer corrosion of the Zr-y cladding during irradiation is generally considered as the main

limitation factor of the PWR fuel rods. Under current irradiation conditions UO_2 is quite reliable. Nevertheless, this fuel when irradiated in a highly rated reactor, at very high burn-up ($\geq$ 100 MWd/kg(U)) a too high fission gas release could induce internal pressures exceeding the admissible upper strain on the cladding. Consequently, better PWR fuel rod performance could need safer fuels with lower fission gas release. Under this aspect Uranium nitride (UN) is a potential candidate although the thermal instability at 1600 °C and a possible interaction with UO_2 are two points not to be neglected. Experiments were carried out in an autoclave at 200 and 300 °C using irradiated (U, Pu)N since irradiated UN was not available. Presently only experimental results of the low temperature tests are available. Irradiated (U, Pu)N in powder form was submitted to water under vapor conditions at 200 °C during 20 hours. After the test no further fragmentation of the fuel was noticed and the formation of U_3O_8 can be excluded. Periscope examination indicated no alteration of the outer surface.
The analysis of the leachates of the immersed fuel sample gave leaching rates (U, Pu, Np, TPu, f.p.) very similar to those measured for UO_2.
Under vapor conditions no noticeable transfer to the leachate could be measured.

Study of Natural UO_2 in Aqueous Solutions by Electrochemical Techniques

Electrochemical impedance; evaluation of the measuring system

Electrochemical techniques such as current-time or potential-time measurements, polarisation curves (voltage vs. current) and ac impedance measurements (current response to a small imposed ac voltage) enable information to be obtained about the mechanisms and rates of corrosion, the rate-determining steps or intermediate species involved. This information is very important in assessing the stability of UO_2 in final storage and in measuring the conditions and rates of UO_2 and fission product leaching when in contact with groundwater.

The measurement of electrode impedances in an electrochemical cell assumes a knowledge of the resistance characteristics of the measuring system. The necessary equipment consists of a frequency analyser (Voltech TF 2000) and a potentiostat (CAPCIS March Interface). The alternating current measurements are substantially affected by the potentiostat's properties. In the high frequency range there are mainly disturbances of the current measurements from the amplifier.

In order to check these influences, impedance spectra of simple resistance networks are measured. Using a parallel circuit of an ohmic resistance and a capacitor the impedance spectra in Fig. 4.1 are obtained. The deviations from the theoretically expected values are visible above 1 kHz. A fitting routine has been used to adapt the equivalent circuit. The behaviour can be best described by a resistance and an inductance in parallel with a further resistance in series. This model can be used to correct the measured values

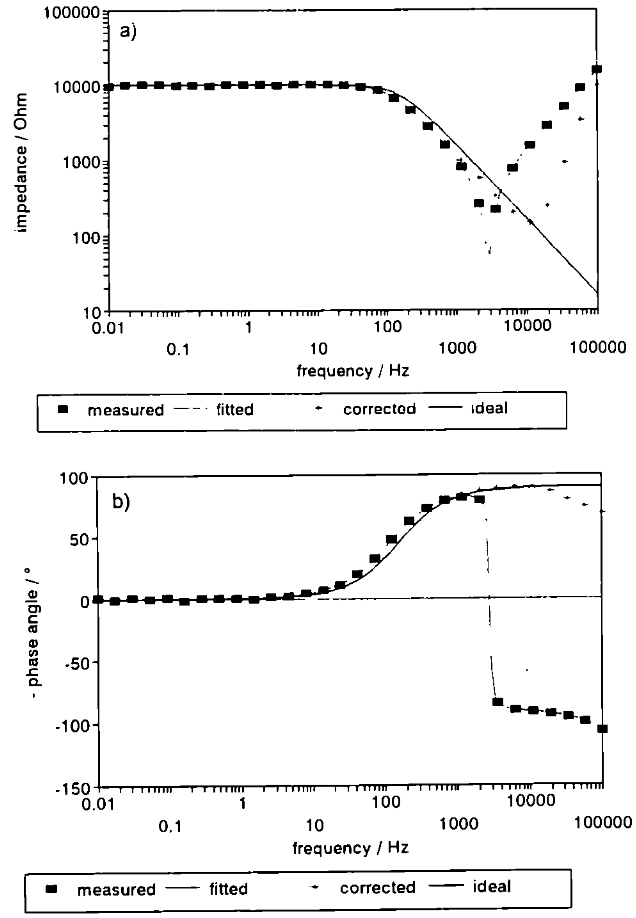

Fig. 4.1 a) Impedance spectrum (Bode Plot) of a resistor and capacitor in parallel (i.e. parallel RC circuit) showing measured values before and after correction for the potentiostat's influence as well as ideal behaviour.
b) Impedance spectrum (Phase angle) of parallel RC circuit showing measured values before and after correction for the potentiostat's influence.

and take the influence of the potentiostat into account. With this the appearance of deviations can be shifted to frequencies one order of magnitude higher.

The spectrum one would expect from an electrode also depends on its construction and geometry. The UO_2 pellet is attached to the metallic specimen holder with conductive glue, and the metal/glue/UO_2 interface will have a contact resistance (Fig. 4.2). The pellet itself will react (in the simplest case) as an ohmic resistance and a capacitor in parallel. At the electrode-solution interface an electrolytic double layer is formed with a capacitance of typically 10-50 $\mu F cm^{-2}$. For an electrode with a 0.5 cm^2 surface area and 2 mm thickness literature values for conductivity and dielectric constants were used to calculate the UO_2 resistance. The other resistance values (e.g. resistance of the solution) were estimated. The charge transfer resistance can then be derived from the measurements and hence an estimation can be made of the electrochemical dissolution rate.

Fig. 4.3 shows a simulated spectrum using the above values. Two time constants become apparent. The physical effects appear in the high frequency range because of the small time constants.

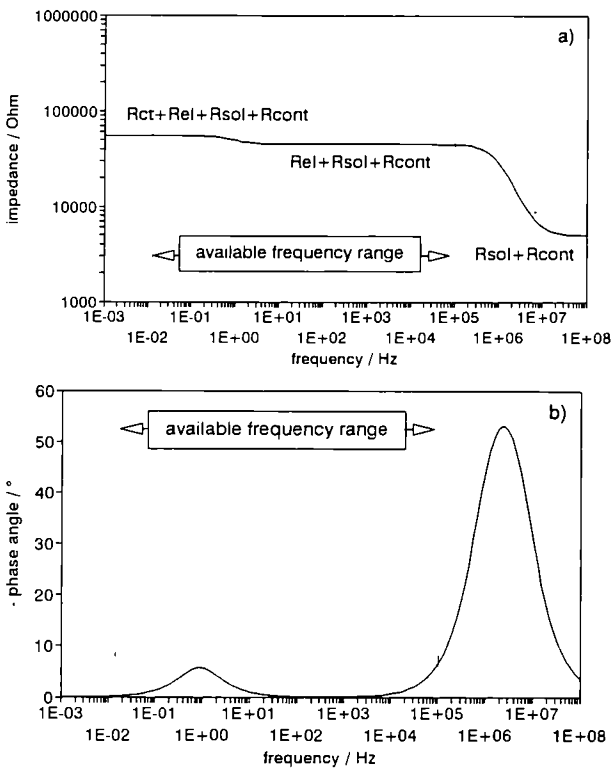

Fig. 4.3 a) Bode plot (impedance) of simulated UO_2 electrode using literature values in the equivalent circuit of Fig.4. 2
b) Bode plot (phase angle) of simulated UO_2 electrode using equivalent circuit of Fig. 4.2

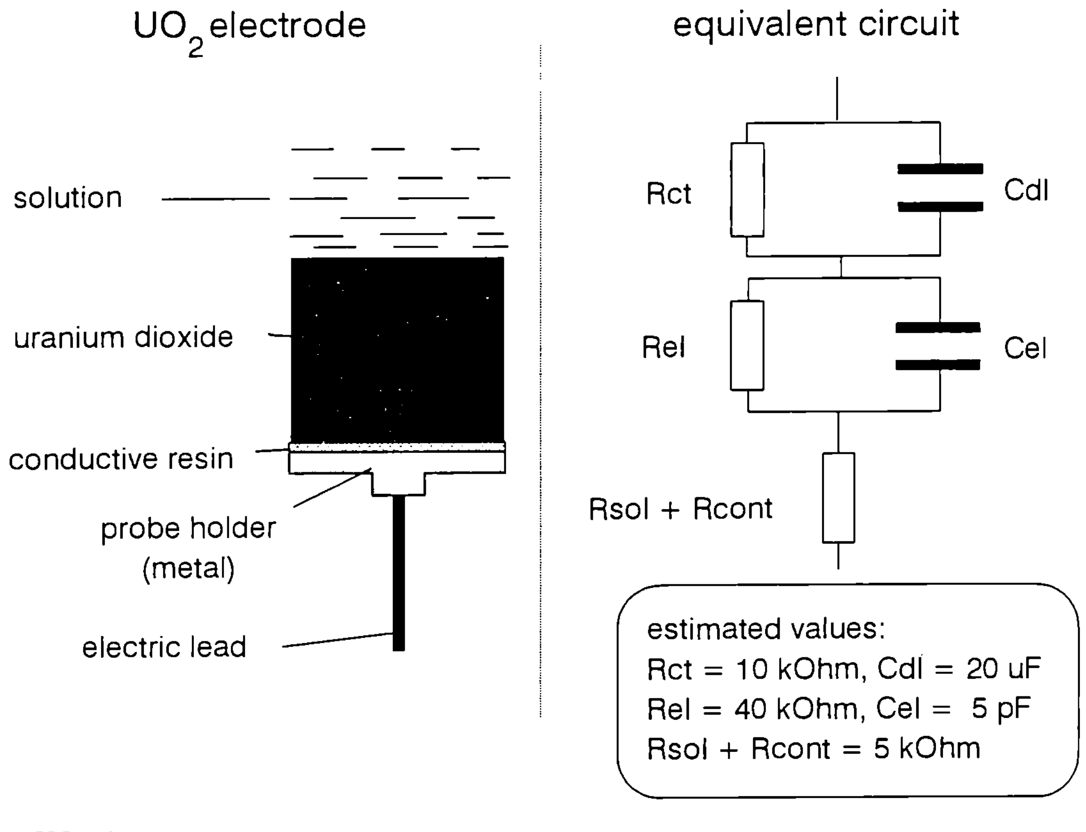

Fig. 4.2 UO_2 electrode construction and equivalent circuit for the electrode

The slower chemical processes influence, by contrast, the low frequency range.

In the Bode plot (impedance (Z) vs. frequency (v) the resistances appear as plateaus; one should however note that only the frequency range of 10 mHz to 100 kHz is measurable (Fig. 4.3). For a specimen at its free corrosion potential in 3 % sodium carbonate solution, the measured impedance spectrum shows generally, a good agreement with the simulated spectrum (Fig. 4.4). The differences that appear can normally be assigned to inhomogeneities and water uptake by the electrode. As impedance (Z) is a vector (with magnitude and phase) it can be represented in complex form $Z = Z_{real} + i\,Z_{imaginary}$ and the spectra displayed as $Z_{imaginary}$ vs. Z_{real} (or Nyquist) plots. In this, RC parallel circuits are displayed as semicircles (see Fig. 4.5).

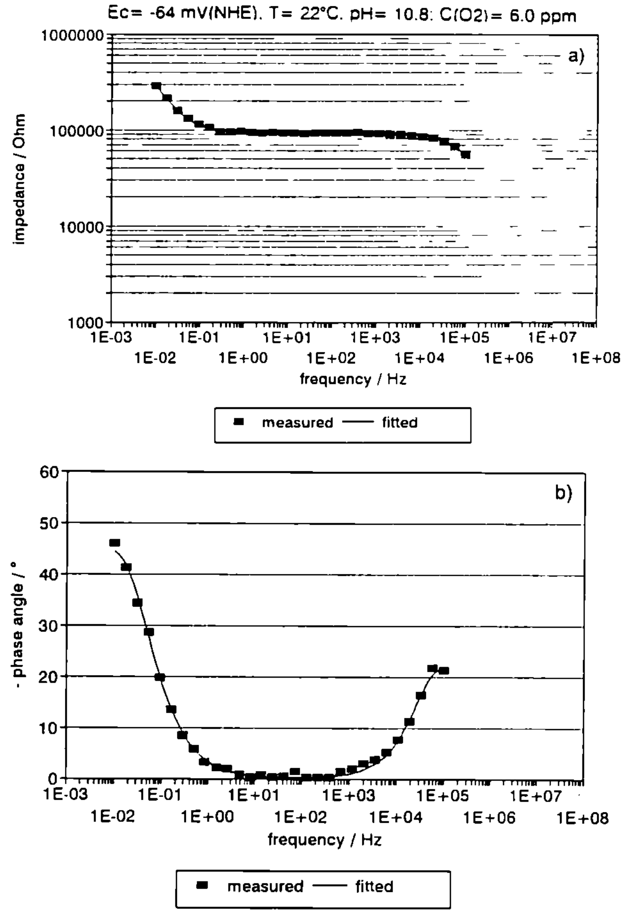

Fig. 4.4 a) Bode plot (impedance) of natural UO_2 electrode polished to 1 µm diamand paste in 3 % Na_2CO_3 solution, measured values and fitted values using equivalent circuit.
b) Bode plot (phase angle) of 1 µm polished natural UO_2 electrode in 3 % Na_2CO_3 solution (measured and fitted values)

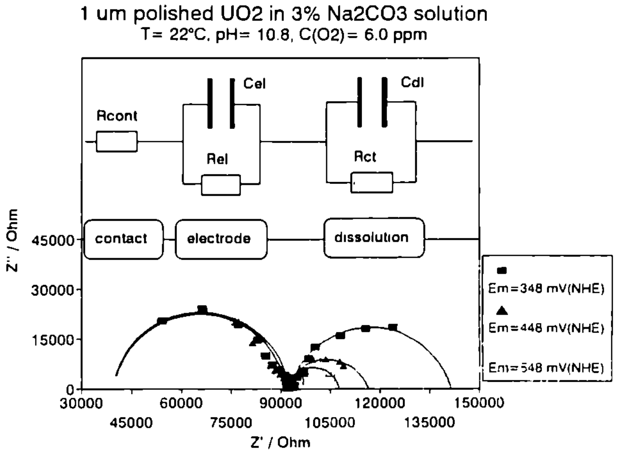

Fig. 4.5 Nyquist (impedance) plot of 1 µm polished natural UO_2 electrode in 3 % Na_2CO_3 at rest potential (+ 348 mV (NHE)), and at + 100 mV and + 200 mV anodic polarisation. The physical component corresponding to each part of the signal and its equivalent circuit is given above the spectrum.

Electrochemical measurements

The measurements in 3 % Na_2CO_3 are shown in Fig. 4.5 for rising anodic potentials of the UO_2 electrode. It is seen that the applied polarisation affects only the charge transfer resistance (R_{ct}); that is the arcs in the lower frequency range.

The charge transfer resistance (R_{ct}) is also seen to be inversely proportional to the current density (i_{corr}) measured during the experiment (Fig. 4.6) and has a slope of 34.5 mV. This linear relationship means that the "Tafel" slope must be valid for all these values, the logarithmic plot of $1/R_{ct}$

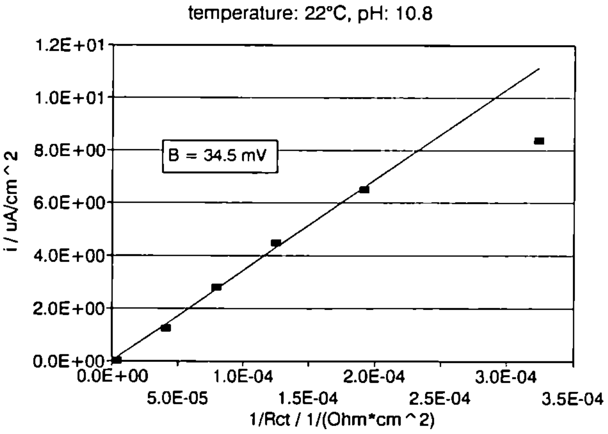

Fig. 4.6 Correlation of measured corrosion currents and the inverse of the charge transfer resistances ($1/R_{ct}$) from the impedance spectra of polished natural UO_2 in 3 % Na_2CO_3 solution

vs potential is therefore also linear. This is further refined in the Stern-Geary equation (1) relating i_{corr} and $1/R_{ct}$:

$$i_{corr} = \frac{1}{2.303}\left(\frac{b_a\, b_c}{b_a - b_c}\right)\frac{1}{R_{ct}} = B\,\frac{1}{R_{ct}} \qquad (1)$$

where b_a, b_c are anodic and cathodic "Tafel" slopes respectively

These are the slopes of the anodic and cathodic arms of the polarisation curve (log|i| vs. potential (E)) for $\pm > 60$ mV around the corrosion (or zero current) potential (E_{corr}).

However the applied potential (or polarisation) must also be corrected for the potential drops across the resistance R_c (contact resistance) and R_{el} (UO_2 electrode resistance).

From the plot of the corrected applied potentials against the R_{ct} values derived from the ac impedance measurements, an anodic Tafel slope of 114 mV was calculated. This slope implies a charge transfer of 2 electrons / molecule. A similar value of 82 mV, after correction of the polarisation , was measured directly from the potential-current curve made in sodium carbonate solution (Fig. 4.7).

For the correlation factor (B) between the reciprocal resistance ($1/R_{ct}$) and current density, a value of 28 mV was derived from the Tafel slopes by using the Stern-Geary equation (Eqn. 1), and a corrosion current density of 0.15 µA.cm^{-2} derived from the polarisation curve. This corresponds, assuming a 100 % dense material, to a corrosion rate of 6 µm p.a.. The corrected current-potential curve for UO_2 in 3 % Na_2CO_3 is seen in Fig. 4.7. The two waves of oxidation in the anodic half of the sweep indicate a two stage oxidation. The return sweep to a higher (more anodic) corrosion potential (at + 200 mV) indicates that the first stage is an irreversible oxidation stage (TUAR-92, p. 93). These facts along with low corrosion rate estimates points to a formation of a passive layer, possibly a uranyl carbonate complex.

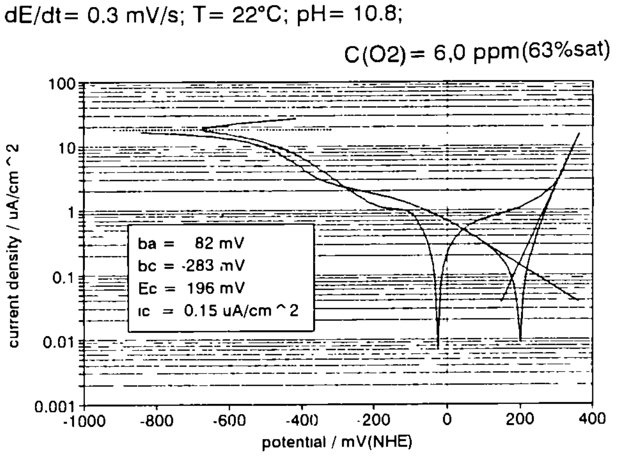

Fig. 4.7 Polarisation curve (log current vs. applied voltage (after allowing for voltage drop)) of polished natural UO_2 in 3 % Na_2CO_3 solution (corrosion potential and current E_c, i_c, anodic and cathodic tafel slopes b_a, b_c are also shown).

In 3 % NaCl solution (Fig. 4.8) it can be seen from the potential-time curve that the free corrosion potential E_{corr} is - 200 mV. In comparison with the carbonate solution it is displaced by 400 mV in the cathodic direction, and in the anodic curve no irreversible oxidation process appears. The corrosion current is correspondingly greater at 2.2 µA.cm^{-2}, which yields a corrosion rate of 90 µm.p.a (under the same assumptions as before).

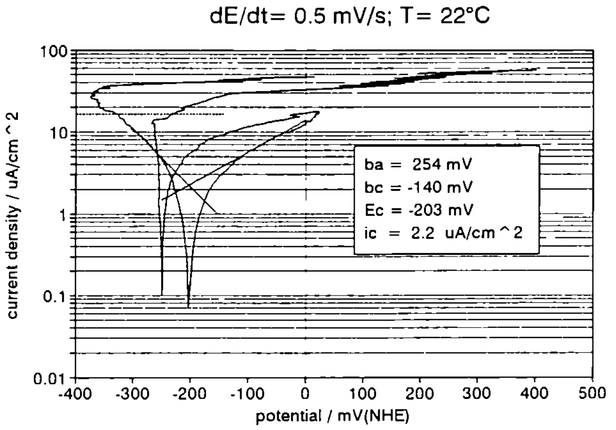

Fig. 4.8 Polarisation curve (log i vs. V) of polished natural UO_2 in 3 % NaCl solution.

At higher current densities of the cathodic curves for both Na_2CO_3 and NaCl solutions overcorrection of the potential is evident. Here the assumption of a constant pellet resistance made for the potential correction is no longer valid. It is explained by its n-type semi-conductive properties so that the UO_2 becomes electrically conducting at strongly cathodic potentials.

A comparison of the normalised impedance spectra for 3 % NaCl and 3 % Na_2CO_3 solutions is made in Fig. 4.9 and again shows a clear difference in the charge transfer resistances. The corrosion rates estimated from these along with the

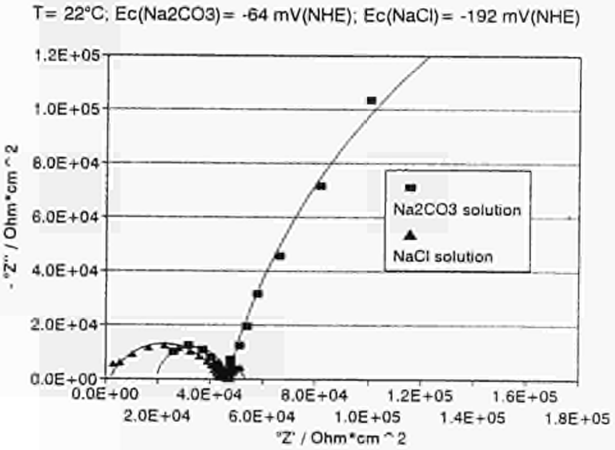

Fig. 4.9 Comparison of Nyquist (Impedance) plots of polished natural UO_2 electrodes at rest (corrosion) potential in 3 % Na_2CO_3 and 3 % NaCl solution.

Tafel slopes from the polarisation curves are 150 µm p.a. for the chloride solution and 4 µm p.a. for the carbonate solution. However there are also large differences between the contact resistances of the two electrodes. In the chloride solution electrode, the UO_2 was glued to the specimen holder with silver glue, whereas for the carbonate solution electrode higher resistance graphite glue was used. Furthermore it can be seen that the internal resistances of the two electrodes differ. The electrode used in carbonate has considerable smaller internal resistance than the other. This is probably attributible to its being thinner.

Finally, scanning electron microscopy of the NaCl electrode after a total of 1200 h in solution (mostly at rest potential Fig. 4.10b) compared to the starting material (Fig. 4.10a - polished to 1 µm diamand paste) indicates the widespread localised attack of the surface. The sodium carbonate electrode is still undergoing testing and has not yet been examined.

Future work will comprise the completion of the sodium carbonate testing and the electrode examination, then the electrode will be repolished and retested in 3 % NaCl with the intention of removing electrode differences from the tests.

Then the apparatus will be set up in the hot cells and this same natural UO_2 electrode will be used to check the apparatus performance under active conditions. Then an irradiated UO_2 electrode will be constructed and the same testing carried out to make the comparison between active and inactive UO_2 samples.

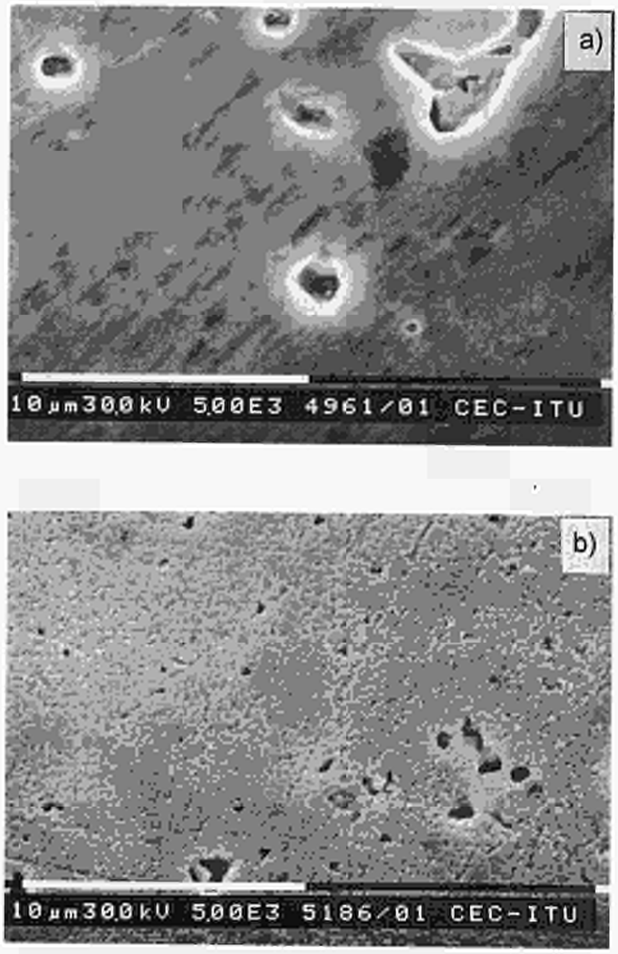

Fig. 4.10 a) Staring material of natural UO_2 electrode polished to 1 µm diamand paste showing smooth initial surface and fabrication porosity (500x)
b) Natural UO_2 electrode polished to 1 µm diamand paste after approximately 1200 h immersion in 3 % NaCl showing localised attack and roughening of the surface (5000x)

Leaching Studies

Influence of granite on the leaching behaviour of spent fuels

In many countries direct storage of spent fuel in granite is considered as an option in waste management strategies. The influence of granite, as one possible host rock material for waste repositories, on the leaching behaviour of nuclear waste glasses has been described in the previous report (TUAR-92, p. 99). In a similar experiment , the influence of granite was tested on two types of spent nuclear fuel, i.e. UO_2 and MOX. The leaching was conducted in soxhlet extractors and the granite was added as powder (grain size 125-250 µm, total amount 1g) to the monolithic fuel samples. The experimental conditions for this test are summarised in Tab. 4.1.

No significant weight loss was measured for each of the 4 samples. At the end of the experiment the leachate was filtered, the heating vessel and the sample container rinsed with 1 M HNO_3, and each solution analysed by ICP-MS. The analytical results are shown in Tab. 4.2.

As already noticed previously by leaching glasses a significant reduction of the leached amounts is observed for all elements, even for Mo, which has been an exception in the experiment with glass (TUAR-92, p. 100). Whereas the relative reduction is limited for Np and Pu, the reduction in the case of U and the fission products is even higher.

Tab. 4.1 Leaching of spent UO_2 and MOX samples with and without granite (experimental conditions). Test duration: 100 d

soxhlet number	sample	weight mg	estimated surface,cm^2	weight loss, mg
1	MOX + granite*	406	0.77	0.002
2	MOX	418	0.79	0.001
3	UO_2 + granite*	329	0.62	0.001
4	UO_2	279	0.53	0.001

*powder: 1 g; grain size 125-250 µm

The adsorption on the equipment walls is very similar to that observed for the glass.

This reduction cannot be due to any saturation effects in the leachate, because in this dynamic leaching test, the total volume of distilled water in contact with the sample and the granite during the test duration of 100 days is about 150 l (flowrate: ca. 1 ml/min). The total amount of elements in the leachate was found to be ca. 2.7 mg, which corresponds with an average molecular weight of 100 to a concentration of 0.2 µmoles/l.

The only possible explanation for the decrease of leaching in the presence of granite must be that the redox conditions of the leachate becoming more reducing when granite is present. From literature it is well known, that reducing conditions

Tab. 4.2 Results of the analysis by ICP-MS in µg

element	MOX	MOX-granite	relative decrease in the presence of granite, %	UO_2	UO_2-granite	relative decrease in the presence of granite, %
Rb	2.59	0.39	92.8	2.44	1.97	18.9
Sr	1.79	0.17	90.6	13.45	0.27	97.9
Zr	8.86	1.01	88.6	8.97	0.49	94.5
Mo	31.53	0.72	97.7	31.21	3.10	90.0
Tc	0.90	0.19	79.3	2.13	0.27	87.1
Cs	67.43	12.60	81.3	68.14	11.54	83.0
Np	0.28	0.09	67.8	0.23	0.08	63.8
U	616.91	149.91	75.7	497.66	61.09	87.7
Pu	2.00	0.57	71.5	0.67	0.59	10.7

decrease considerably the leaching of spent fuel [1].

Furthermore, in the presence of granite the amount of total carbon present in the leachant is increased and should imply an increased leaching according to the literature [1].

A parameter often used to compare leaching results of waste materials, especially spent fuels [2], is the so-called fraction of inventory in the aqueous phase (FIAP). Using the fuel inventories given in TUAR-91, p. 96, leach-rates and FIAP values can be calculated (Tab. 4.3).

The values determined for Cs correspond to the highest values determined by Gray in his leaching experiments on spent fuel in salt brine in static experiments [3]. The U values fit perfectly well with the scatter of values determined by different authors under different test conditions (oxidizing, reducing, sequential, static, dynamic) and our values determined in presence of granite correspond more or less to those reported in the literature under reducing conditions [4]. However no evidence was found for a congruent leaching of Sr and U as claimed by the authors of this overview article.

References

[1] Gray, W.J. Thomas, L. E. Einziger, PNL-SA-20371 (1992)
[2] Grambow, B. SKB 89-13 (1989)
[3] Gray W.J., Mat. Res. Soc. Symp. Proc. 84 (1987) 141
[4] Grambow. B., Werme, L.O., Forsyth, R.S., Mat. Res. Soc. Symp. Proc. 176 (1990) 465

Comparison of the leaching behaviour of spent UO_2, $ThPuO_2$, MOX fuels and unirradiated UO_2

Although commercial reactors are nowadays mainly fuelled with UO_2, an increasing number uses mixed U,Pu oxide fuels to reduce the large stock of fissile Pu. Another possibility considered is the use of Th-fuels in order to reduce significantly the formation of long-lived higher actinides, which are mainly responsible for the long

Tab. 4.3 Leach rates and fractions of inventory in the aqueous phase (FIAP) for Sr, Cs and U.

waste	MOX	MOX + granite*	UO_2	UO_2 + granite*
Sr leach rate µg/cm^2.d	0.022	0.002	0.255	0.004
Cs leach rate µg/cm^2.d	0.854	0.163	1.293	0.186
U leach rate µg/cm^2.d	7.816	1.947	6.298	0.657
Sr inventory µg/g fuel	456		787	
Cs inventory µg/g fuel	2062		1793	
U inventory µg/g fuel	817045		830648	
Sr FIAP	0.00934	0.00091	0.0613	0.00108
Cs FIAP	0.078	0.002	0.136	0.019
U FIAP	0.00181	0.00045	0.00215	0.00022

term radiological hasard of nuclear waste. If these fuels are not reprocessed but directly stored as nuclear waste, it is worthwhile to compare their leaching behaviour with that of UO_2 in order to assess their behaviour in the waste repository.

Similar amounts of monolithic fuel samples of different burn-ups or composition were leached for 1 month in soxhlet extractors and the leachate and rinsing solutions analysed by ICP-MS (Tab. 4.4).

The interpretation of these results is of course limited because a single parameter set was investigated and because the available samples were prepared in different manners (see Tab. 4.4); this affects especially the values obtained for U. The comparison between natural UO_2 and spent fuel reveals a leach rate, which is 20 to 30 times higher for spent fuel, but U leaching is especially low if only a polished surface is in contact with the leachant.

Leach rates of fission products from Th fuel are similar to those of commercial UO_2 and MOX fuels. For the high burn-up fuel a low value for U leaching (see remark above), on the contrary very high values for most of the fission products are

Tab. 4.4 Comparison of leachate compositions of different types of fuel samples in comparison to unirradiated UO_2 (results in µg/cm^2.d)

sample	**nat. UO_2**	**UO_2 (31 GWd/tU)**	**UO_2 (80 GWd/tU)**	**$ThPuO_2$**	**MOX**
sample description	fuel pellet, 8,233 g	fuel particle, 0.459 g	fuel pellet, ca. 9 g	fuel pellet, ca. 9 g 0.22g Pu init.	fuel particle, 0.407 g
surface area cm^2	3.93	0.65	0.95*	0.79*	0.58
Rb	0.000	0.092	0.841	0.048	0.109
Sr	0.001	0.334	0.018	0.084	0.050
Zr	0.014	0.106	0.022	0.019	0.117
Mo	0.042	0.427	0.910	0.052	0.483
Tc	0.000	0.117	0.013	0.001	0.055
Ru	0.000	0.013	0.002	0.001	0.017
Rh	0.000	0.004	0.001	0.000	0.007
I	0.001	0.015	2.647	0.025	0.118
Te	0.000	0.004	0.001	0.001	0.002
Cs	0.001	1.554	93.106	0.970	1.723
Ba	0.009	0.508	5.462	0.284	0.222
La	0.002	0.101	0.018	0.018	0.041
Ce	0.004	0.073	0.022	0.030	0.024
Th	-	-	-	0.025	-
Np	0.000	0.013	0.000	0.001	0.017
U	1.398	27.071	1.202	1.271	37.607
Pu	0.000	0.019	0.002	0.015	0.062
Am	0.000	0.001	0.001	0.001	0.003

*only one polished radial surface was exposed to the leachant found, especially for Cs and I. This is most probably due to the higher concentration of these volatile elements at the periphery of the fuel pellet [1].

Noble metal fission products and especially Tc showed lower leach rates due to the fact that these elements are mainly concentrated in particles as alloy formed during irradiation. In the case of high burn-up fuel for instance more than 80 % of the Tc are found in the metallic particles and are thus in an insoluble and consequently not leachable form[2].

References

[1] T. Tsukada, T. Kamayama, L. Koch, J.-P. Glatz, I. Garcia Alonso, Dissolution Study of High Burnup LWR Fuel (I) - Dissolution Experiments and Analysis of the Residue, 1991 Fall Meeting of the Atomic Energy Society of Japan, Fukuoka, 15-18 Oct. 1991

[2] J.-P. Glatz, J.I. Garcia Alonso, T. Kamayama, L. Koch, G. Pagliosa, T.Tsukada, H. Yokoyama, Dissolution Behaviour of Highly Burnt Fuel, Proc. of the 3d Conf. on Nucl. and Radiochem., Vienna, September 7-11, 1992

Leaching behaviour of irradiated UO_2 under highly oxidising conditions

As a follow-up of the experiment on leaching of spent fuel (burn-up: 51 GWd/tU) under highly oxidising conditions (TUAR-92, 101), three samples of the fuel powder treated (in vapour phase) in the previous tests under different conditions (Tab. 4.5), have been leached for 1 week under static conditions in autoclaves.

The analysis of the leachate by ICP-MS is summarised in Tab. 4.6.

The previous test described in TUAR-92, p. 109 was not conclusive and did not allow a differentiation between leaching under immersion and vapor conditions. In earlier experiments there were problems caused by the presence of Teflon and a possible interference of fluorine in the leaching process. In the current experiment the UO_2 powder was oxidised prior to leaching; the leachate analyses showed an acceleration of fuel dissolution under either H_2O or H_2O_2 conditions. The acceleration due to H_2O_2 is particularly obvious. It is believed that the determining factor in the transfer kinetics is the presence of U partially as U (VI) in the oxidised fuel.

Tab.4.5 Experimental conditions for the leaching of oxidised spent fuel (test duration 1 week)

oxidising agent	H_2O	H_2O_2	H_2O_2
oxidation time, weeks	4	1	4
fuel amount, mg	300	295	398

The leached amounts of the elements sensitive to oxidation such as Tc, U and Np increase with leaching time. Other actinides like Am, Pu and fission products like Cs and Rb are not affected by this parameter.

Although a direct comparison with the results of the soxhlet leaching of fuel is difficult because the surface area of the fuel powder is of course much larger, (50 cm^2/g compared to 2 cm^2/g), the FIAP values determined here are extremely high, especially for Cs, Rb and U and even more for Np and Tc, i.e. those elements which are sensitive to redox reactions.

These results show the high relevance of redox conditions and of the UO_2 oxidation state on the leaching of spent fuel; under highly oxidising conditions in water vapour at high temperature, the spent fuel would certainly not withstand leaching for a very long period of time [1].

Reference

[1] Werme L.O., Forsyth R.S., SKB 98-14 (1989)

Interaction between vapour and nitride fuels

The outer corrosion of the Zr-y cladding during irradiation is generally considered as the main factor limiting the life time of PWR fuel rods. Under current irradiation conditions UO_2 is quite reliable; nevertheless, if this fuel is irradiated in a highly rated reactor, at very high burn-up (≥100 MWd/kg (U)) a too high fission gas release could induce internal pressures exceeding the admissible strain on the cladding. As a potential candidate for substituting UO_2 one could consider uranium nitride as a safer fuel, which has a higher thermal conductivity and therefore a lower centre fuel temperature, along with a lower fission gas release rate.

Tab. 4.6 Composition of the leachates and fraction of inventory in the aqueous phase (FIAP)

element	H_2O 4w* (1)	H_2O_2 1w* (1)	H_2O_2 4w* (1)	content in the fuel, µg/g	H_2O 4w* (2)	H_2O_2 1w* (2)	H_2O_2 4w* (2)
Rb	1.151	3.309	3.813	505	0.00759	0.02219	0.02557
Sr	2.050	4.664	3.994	1045	0.00653	0.01512	0.01295
Y	0.013	0.172	0.102	630	0.00007	0.00093	0.00055
Zr	6.556	1.258	6.041	5395	0.00405	0.00079	0.00380
Mo	6.535	10.497	11.264	5273	0.00413	0.00675	0.00724
Tc	3.836	13.412	19.280	1262	0.01130	0.03603	0.05179
Ru	0.012	0.051	0.161	3752	0.00001	0.00005	0.00015
Rh	0.060	0.022	0.049	562	0.00036	0.00013	0.00029
Pd	0.095	0.032	0.310	5778	0.00006	0.00002	0.00018
I	0.176	0.135	0.131	392	0.00149	0.00117	0.00113
Te	0.002	0.024	0.028	760	0.00001	0.00011	0.00013
Cs	17.708	39.394	34.795	3375	0.01748	0.03956	0.03494
Ba	9.182	4.802	1.950	3191	0.00959	0.00510	0.00207
La	0.031	0.605	0.485	1875	0.00005	0.00109	0.00088
Ce	0.095	1.120	0.779	3730	0.00009	0.00102	0.00071
Pr	0.030	0.642	0.471	1720	0.00006	0.00127	0.00093
Nd	0.106	2.040	1.503	5370	0.00007	0.00129	0.00095
Pm	0.213	4.635	3.352	1558	0.00046	0.01008	0.00729
Sm	0.011	0.423	0.311	1043	0.00004	0.00138	0.00101
Eu	0.008	0.089	0.063	252	0.00011	0.00120	0.00085
Gd	0.004	0.111	0.111	409	0.00003	0.00092	0.00092
U	3601.140	4403.092	9654.314	934129	0.01285	0.01598	0.03503
Np	2.048	8.095	14.139	745	0.00915	0.03679	0.06426
Pu	0.028	0.347	0.220	9373	0.00001	0.00013	0.00008
Am	0.016	0.130	0.104	919	0.00006	0.00048	0.00038
Cm	0.004	0.017	0.016	163	0.00008	0.00035	0.00034

*w: week

(1) total amount in the leachate, µg

(2) fractions of inventory in the aqueous phase (FIAP)

We used irradiated (U,Pu)N from a joint experiment between CEA and ITU, called NIMPHE, (TUAR-92, p. 58) as substitute for irradiated UN, which was not available. An important boundary condition for the use of nitrides is their compatibility with the coolant. This reaction has been simulated by the reaction of nitride fuel particles (up to 7 % burn-up) in autoclaves at 200 °C and 300 °C. Samples were treated in vapour atmosphere and under immersion conditions and for all samples no apparent surface modification could be seen at a magnification of 20x.

At the present time only the results of the tests at 200 °C are available.

For the sample treated under immersion conditions, the leachate components were analysed by ICP-MS (Tab. 4.7).

The leach rate was calculated for two fuel pieces of 170 mg total weight and a geometrical surface of 0.32 cm^2. Compared to UO_2 or MOX fuel the leach rate is about 3 times higher as a consequence of the higher porosity of the nitride fuel, but for a test duration of 1 day compared to 100 days. It is obvious that the leach rate will decrease significantly after several days. From literature values one can expect a decrease of the leach rate by a factor more than 3 [1], so that the leaching behavior of the nitride fuel is probably at least equal if not better compared with oxide fuels.

Tab. 4.7 Analysis of the leachate of nitride fuel leached for 1 d at 200 °C

element	netto concentration, ppb	total amount, µg	leach rate, µg/cm^2.d
Rb	11.86	0.118	0.37
Sr	4.52	0.045	0.14
Y	0.47	0.005	0.01
Zr	0.98	0.010	0.03
Mo	50.72	0.505	1.57
Tc	28.19	0.281	0.87
Ru	0.72	0.007	0.02
Rh	0.56	0 006	0.02
I	1.92	0.019	0.06
Te	0.00	0.000	0.00
Cs	260.86	2.597	8.09
Ba	48.86	0.486	1.52
La	0.75	0.007	0.02
Ce	1.43	0.014	0.04
Np	0.00	0.000	0.00
U	716.29	7.131	22.22
Pu	26.03	0.259	0.81
Am	0.00	0.000	0.00
Cm	0.00	0.000	0.00

Reference

[1] Johnson, L.H., Shoesmith, D.W. "Spent Fuel" in Radioactive Waste Forms for the Future, W. Lutze and R.C. Ewing, eds, North Holland (1988) 635

Non-Destructive Characterisation of Spent Fuel Irradiated in BR3

Introduction

UO_2 and MOX-fuel rods irradiated in the BR3-reactor in Belgium will be used to carry out leaching tests on fuel rod segments with pre-set defects.

The characterisation of the UO_2 has been reported in TUAR-92, p. 103. This report will describe the results of NDT examinations of the MOX fuel rods.

Pre-Irradiation Data

Fuel data

The fuel was fabricated by the company Franco-Belge de Fabrication de Combustible (FBFC) in Dessel, Belgium. The initial enrichment was 6.9 wt % of fissile plutonium.The fuel rods contained also three pellets of natural uranium in the bottom part. The PuO_2-powder was produced by COGEMA. The UO_2-powder was delivered by RBU and produced by the AUC-process. The final powder was prepared by the MIcronized-MASter blend process (MIMAS): a master blend of powder containing a maximum of 30 wt % of PuO_2 was micronized and subsequently mixed with UO_2-powder to obtain the desired enrichment. The main fuel characteristics are given in Tab. 4.8.

Tab. 4.8 Fuel and pellet data

Fuel pellet	Mean diameter (mm) Height (mm) Weight (g)	8.22 - 8.24 11 - 12.5 --
Fuel	Mean density (g/cm^3) (% TD) Boron equivalent (ppm of B) Stoichiometry (O/M) Mean grain size (µm)	-- 94 - 95 % 0.74 1.991 5

Cladding data

The Zry-4 tubes were produced by Mannesmann Röhrenwerke (Germany), from an ingot provided by Teledyne Wah Chang, Albany, Oregon, USA. The tubes were heat treated at 460 °C for 2.4 h. The main characteristics of the cladding are given in Tab. 4.9.

Tab. 4.9 Cladding data

Alloy	Zry-4
Outer diameter [mm]	9.6
Internal diameter [mm]	8.4
Wall thickness	0.56

Irradiation conditions

The 5 MOX-fuels were irradiated in 3 different assemblies during one irradiation cycle (4D2) of the BR3-Reactor, from July 3, 1986 to June 30, 1987, for 6232 effective full power hours (EFPH).

The mean and the maximum calculated burn-ups reached by the 5 rods are given in Tab. 4.10.

Tab. 4.10 Calculated burn-up

Rod No.	Burn-up [GWd/t] (Average)	Burn-up [GWd/t] (Maximum)
F-6565	18.2	23.5
F-6506	18.6	24.2
F-6564	18.6	24.0
F-6501	18.3	23.7
F-6528	18.7	24.3

Post-irradiation examinations

Visual examination

The visual examination of the outer surface of the cladding displayed an uniform adherent black oxide film and the absence of macroscopic defects on all the fuel rods.

Defect determination by eddy current measurements

No cladding defects were detected.

Profilometry

All the rods showed a smooth profile with a slight increase in the mean diameter indicating that fuel cladding mechanical interaction has occurred and lets anticipate a fuel swelling effect. The nominal diameter was 9.5 +/- 0.01 mm. In Tab. 4.11 the creep deformation has been calculated from the outer diameter value and the oxide layer thickness.

Tab. 4.11 Outer diameter variation and creep

Rod No.	Outer diameter variation Δd/d [µm]	Average creep [µm]
F-6565	90	80
F-6506	90	82
F-6564	110	102
F-6501	90	78
F-6528	90	79

Rod length measurements

All the rods presented a slight radiation induced growth. The results of the measurements are gathered in Tab. 4.12.

Tab. 4.12 Rod length and irradiation growth of the cladding

Rod No.	Length [mm]	Growth [%]
F-6565	1137.8	0.16
F-6506	1138.2	0.19
F-6564	1137.8	0.16
F-6501	1137.8	0.17
F-6528	1138.0	0.17

Axial fission product distribution (gamma scanning)

The isotopes detected were: Cs-134, Cs-137, Ru-106 and Ce-144. The axial distribution of burn-up estimated from the Cs-137 distribution agrees well with the calculated values by Belgo-Nucléaire. The axial profile of each rod shows a reduced activity in the neighbourhood of the spacers (central zone). Sometimes the dishing positions appeared not well defined suggesting the migration of fission products to this colder parts.

Oxide layer thickness

All rods showed a uniformly distributed oxide layer whose average thickness is given in Tab. 4.13.

Filling Gas analysis (puncturing)

The results of the elemental and isotopic composition of the released gas are collected in Tabs. 4.14a and 4.14b. The results include helium (also used as filling gas), N_2, O_2 and CO_2 to check if a leakage has ocurred during the test and Ar which is sometimes used in the welding procedure during fabrication.

Tab. 4.13 Oxide layer thickness

Rod No.	Oxide Layer Thickness [µm]
F-6565	18
F-6506	15
F-6564	14
F-6501	23
F-6528	20

As can be seen from Tab. 4.14, the gas release ratio is different for the different pins and can be divided into two groups:

1)High gas release: Pins F-6565, F-6506 and F-6564.
2)Low gas release: Pins F-6501 and F-6528.

Evaluation

- The non-destructive tests performed reveal the absence of cladding defects.
- The gamma scanning indicated the migration of fission products to the interpellet positions.
- The analysis of filling gas reveals a clear difference of the fission gas release indicating two specific thermal behaviours, although the fuel characteristics, the linear power and the radial gap are similar.

  In order to confirm the results obtained from the filling gas analyses more detailed examinations are requested; fuel microstructure analysis, in particular the extent of Pu homogenisation and the determination of the Xe content in the Pu-rich particles and their local burn-up should bring the necessary elements for a better understanding of the thermal behaviour.

Oxidation of Unirradiated UO_2 Pellets below 500 °C

Literature review

The sequential oxidation of UO_2 in air to form oxygen-rich derivatives and then U_3O_8, has been known about 30 years. Nevertheless, this reaction still attracts investigation, mainly because of its importance to dry storage or disposal of irradiated UO_2 fuel. If the UO_2 fuel oxidizes to U_3O_8 associated with the 36 % net volume expansion or the formation of similar low-density phases (including hydrates), fuel swelling could split the cladding and induce a direct contact with the environment [1]. U_3O_8 powder will have a large

Tab. 4.14a Composition of the filling gas

Pin-Nr.	Composition of the filling gas (%)												
	He	N_2	O_2	Ar	CO_2	Kr-83	Kr-84	Kr-85	Kr-86	Xe-131	Xe-132	Xe-134	Xe-136
F-6565	76.9	0.06	0.03	0.1	0.13	0.24	0.41	0.07	0.65	2.72	4.25	5.8	8.64
F-6506	81.1	0.08	0.04	0.08	0.14	0.19	0.35	0.06	0.52	2.19	3.55	4.93	6.78
F-6564	81.25	0.07	0.03	0.07	0.14	0.19	0.33	0.07	0.53	2.24	3.49	4.83	6.78
F-6501	95.2	0.08	0.04	0.04	0.08	0.05	0.08	0.01	0.13	0.55	0.92	1.20	1.58
F-6528	91.7	0.08	0.04	0.06	0.09	0.09	0.15	0.23	0.24	0.98	1.51	2.16	2.87

Tab. 4.14b Normal gas volume of the filling gas, Xe/Kr-ratio, free volume and gas release ratio

Pin-Nr.	Gas Vol. (NTP) [cc]	Xe-Vol. (NTP) [cc]	Kr-Vol. (NTP) [cc]	Xe/Kr ratio	Free volume [cc]	Gas release ratio [%]
F-6565	156,5	33.25	2.15	15.6	6.57	15,1
F-6506	140.7	24.56	1.59	15.5	6.23	11,2
F-6564	145.2	25.17	1.62	15.5	6.3	11,5
F-6501	119.5	5.07	0.33	15.5	6.45	2,3
F-6528	126.8	9.53	0.65	14.6	6.64	4,4

surface area available for leaching of U as U^{+6} and the leaching process would improve the U and fission products transfer to the aqueous solutions.

Oxidation of unirradiated UO_2 at low temperature

The oxidation of unirradiated UO_2 has been intensively investigated and it is generally accepted, that at temperatures up to 250 °C, UO_2 oxidation in air proceeds from the surface inwards by formation of oxygen-rich uranite layers (up to compositions near U_3O_7), followed by surface formation and spallation of U_3O_8 [2-5]. Although the oxidation behavior of unirradiated UO_2 in air at low temperature can be described qualitatively in terms of U_3O_7 and U_3O_8 formation, the mechanism is still far from clear [6]. It was initially thought that the oxidation proceeded by diffusion of oxygen through a UO_{2+x} lattice with the extra oxygen atoms sitting at the cubically coordinated interstitial sites [7,8]. Blackburn et al. [4] then proposed the initial formation of a U_3O_7 layer which grew as oxygen reached the U_3O_7/UO_2 interface. Various other authors [9,10,11] have since suggested that a critical thickness of U_3O_7 is required prior to the nucleation and growth of U_3O_8. Tyler et al. [6] studied the mechanism of UO_2 to U_3O_8 transformation by sequentially oxidizing planchets of Commercial Advanced Gas-cooled Reactor (CAGR) UO_2 fuel pellets in air at 230 and 270 °C and have observed the linear growth of a U_3O_7 layer several microns thick prior to any U_3O_8 nucleation and growth. Teixeira et al. [12], who studied the oxidation of UO_2 sintered plates at 170-275 °C, accepted that the oxidation of UO_2 was followed up to the U_3O_7 phase and proceeds in the sequence $UO_2 \rightarrow U_4O_9 \rightarrow U_3O_7$ with a parabolic form. Taylor et al. [13] investigated the oxidation of unused (CANDU) UO_2 fuel in air-steam mixtures at 200 and 225 °C and he demonstrated that UO_2 is oxidized to UO_3 hydrates but he did not quantify the rate of this reaction. The same author [14] studied the early stages of U_3O_8 formation on unirradiated CANDU UO_2 fuel oxidized in air at 200-300 °C and he tried to determine the time-temperature relationships for the appearance of U_3O_8 and the dependence of U_3O_8 formation on individual UO_2 grain orientation.

Oxidation of irradiated UO_2 at low temperature

During the last years many studies have revealed significant differences in oxidation behavior between unirradiated and irradiated UO_2 fuel. Unlike unirradiated, UO_2 spent fuel at temperatures between 140 and 220 °C oxidizes by rapid advance of U_4O_9 along grain boundaries and growth of U_4O_9 into the UO_2 grains. At tests performed above 250 °C the oxidation goes on with a second reaction step which leads to U_3O_8 formation (a much less dense phase) [1,15-17]. Various authors have already started investigations for the low-temperature oxidation of spent fuels. Einziger et al. [16] tried to determine the oxidation rate of spent fuel during the post containment period when low temperature (110-175 °C) low radiation field strength and high dew point air conditions exist. The same author [17] tested also at temperatures between 140-225 °C several pressurized water reactor (PWR) spent fuel samples to determine the release of fission gas and used a simplified model for the oxidation mechanism to describe the kinetic data. The effect of fission products on the oxidation of light water reactor (LWR) spent fuel has been tested by Thomas et al. [15] and the most important result of this work is that the U_4O_9 formed by air oxidation is apparently stabilized by fission products in solid solution in the UO_2 matrix.

Questions to be answered

Although the problem of the low temperature oxidation of spent fuels is intensively treated, there are still a lot of questions about the effects of variations in burn up, gas release and grain size on oxidation. There is only little concern about the moisture influence of the oxidizing atmosphere and the effect of impurities on the structural stability of UO_2 and stabilization of U_4O_9 by impurities concentrations. In the last two years have been performed in our Institute the first experiments with nonirradiated reactor grade UO_2 pellets below 500 °C [see TUAR-92, p. 104; and TUAR-92, p. 106]. The identified oxidation products were UO_2 , U_4O_9 and U_3O_8, whereas the final product was U_3O_8 powder. This is not in agreement with some literâture reports about the appearance of the uraninite phase U_3O_7 as an intermediate oxidation product. Test with light water reactor (LWR) spent fuel showed no formation of U_3O_8 after the exposure to air at 180 °C during 1 week; only U_4O_9 has been indentified and the amount formed is strongly depended upon the fuel porosity. This result indicates the determining influence of the fuel restructing on the oxidation kinetics of irradiated UO_2. A systematic study of oxidation tests in autoclaves at temperature lower than 500 °C has started and aims for a better determination of the influence of following parameters:

- burn-up
- fuel restructuring
- moisture content in the oxidizing atmosphere

Future experimental set-up to study the oxidation of irradiated UO_2

Methods

The study of the oxidation of irradiated UO_2 at low temperatures (500 °C) needs an experimental set up including basic methods such as the X-ray diffractometry (XRD) and the thermogravimetric analysis (TG) together with optical microscopy (OM), scanning electron microscopy (SEM) and density determination; these latter are already available for examination of irradiated materials, but not XRD and TG analysis.

Irradiated materials require for their examination shielded hot cells or glove boxes. We selected the latter technical option and as illustrated in Fig. 4.11 the X-ray diffractometer (goniometer), as well as the thermobalance (for the TG analysis) will be placed in a glove box with 50 mm lead shielding. The irradiated samples under study will be placed in the high temperature chamber of the goniometer and in the thermobalance oven (Figs. 4.11 and 4.12).

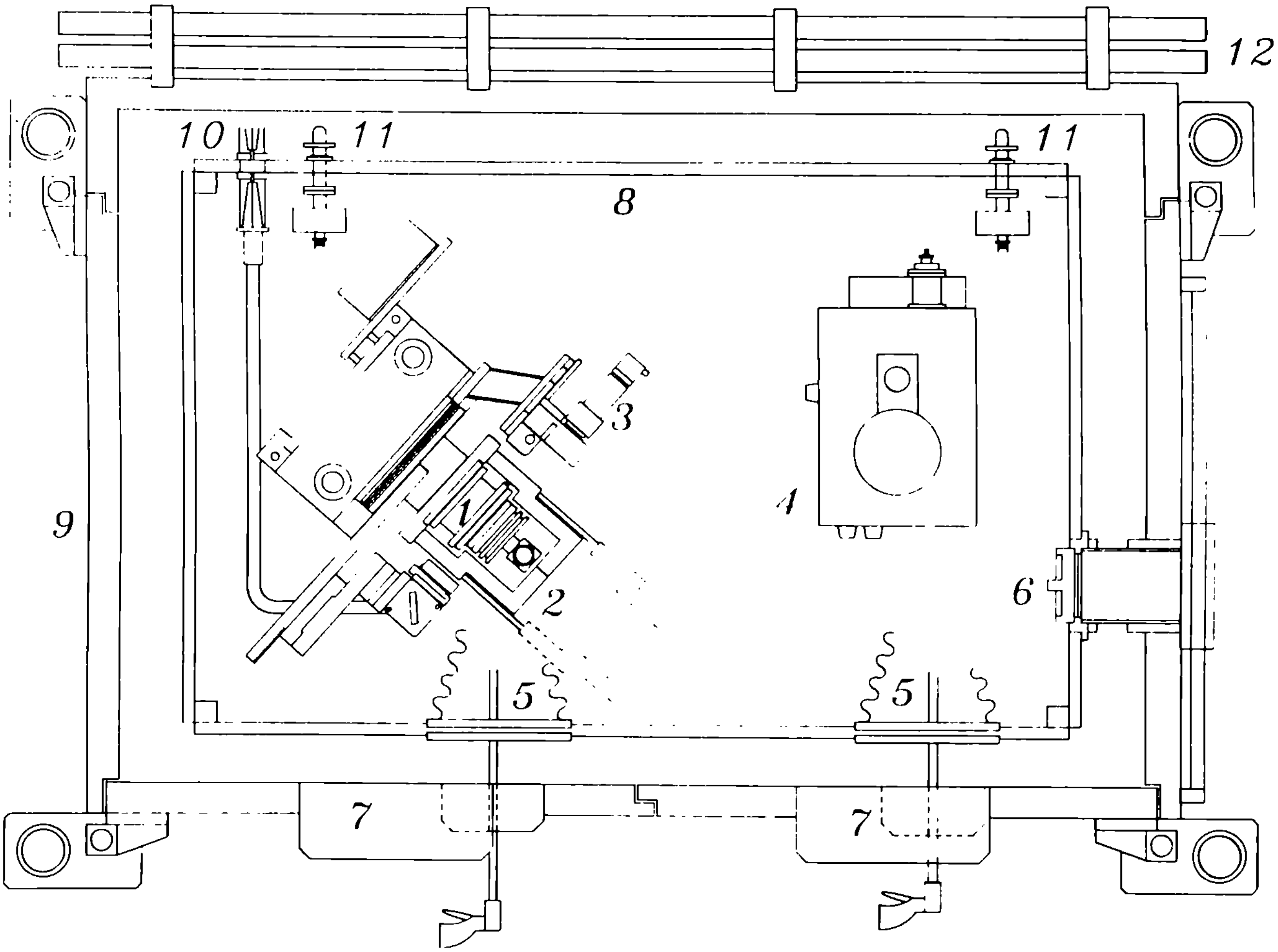

Fig. 4.11 Cross sectional plan of the lead shielded glove box with the goniometer and the thermogravimetric balance.
1. High temperature chamber; 2. Shielding shell; 3. Detector; 4. Thermobalance; 5. Manipulator; 6. La Calhene system; 7. Lead glass window; 8. Glove box; 9. Lead shielding; 10. High voltage; 11. Vacuum; 12. Lead rolling doors

Shielding of the high temperature chamber

In Figs. 4.11 and 4.12 is shown the high temperature chamber shielding as suggested by the manufacturer (Seifert). The outer shell (Nr.2 in Figs. 4.11 and 4.12) could be made from Denal and moved along rails; this complicated construction would weigh 100 Kg. We developed a new design for the shielding of the high temperature chamber consisting of a new chamber body with the same form as the original, but made from Densimet, with a wall thickness of 33 mm. That would be also served as a chamber body. This new chamber body with only 17 Kg weight will be screwed on to the round base plate of the goniometer and opened and closed by a "door"-system. This solution is lighter and more practical than the first one and will solve several problems, for example removing the necessity for a rail sytem for the shielding.

Detector shielding

The detector shielding (30 Kg) proposed by the manufacturer consists of a tetragonal plate screwed out the round theta plate of the goniometer and a 30 mm thick Denal tube for the detector's protection. Our design is reduced to a simple Densimet tube (also 30 mm wall thickness) as one piece with the detector support. It is estimated that this will be not more than 5 Kg, reducing the weight problem for the motor drive and offering the same shielding. It should be noted that our designs about the high temperature chamber and the detector shielding have been agreed by the technicians of the constructor.

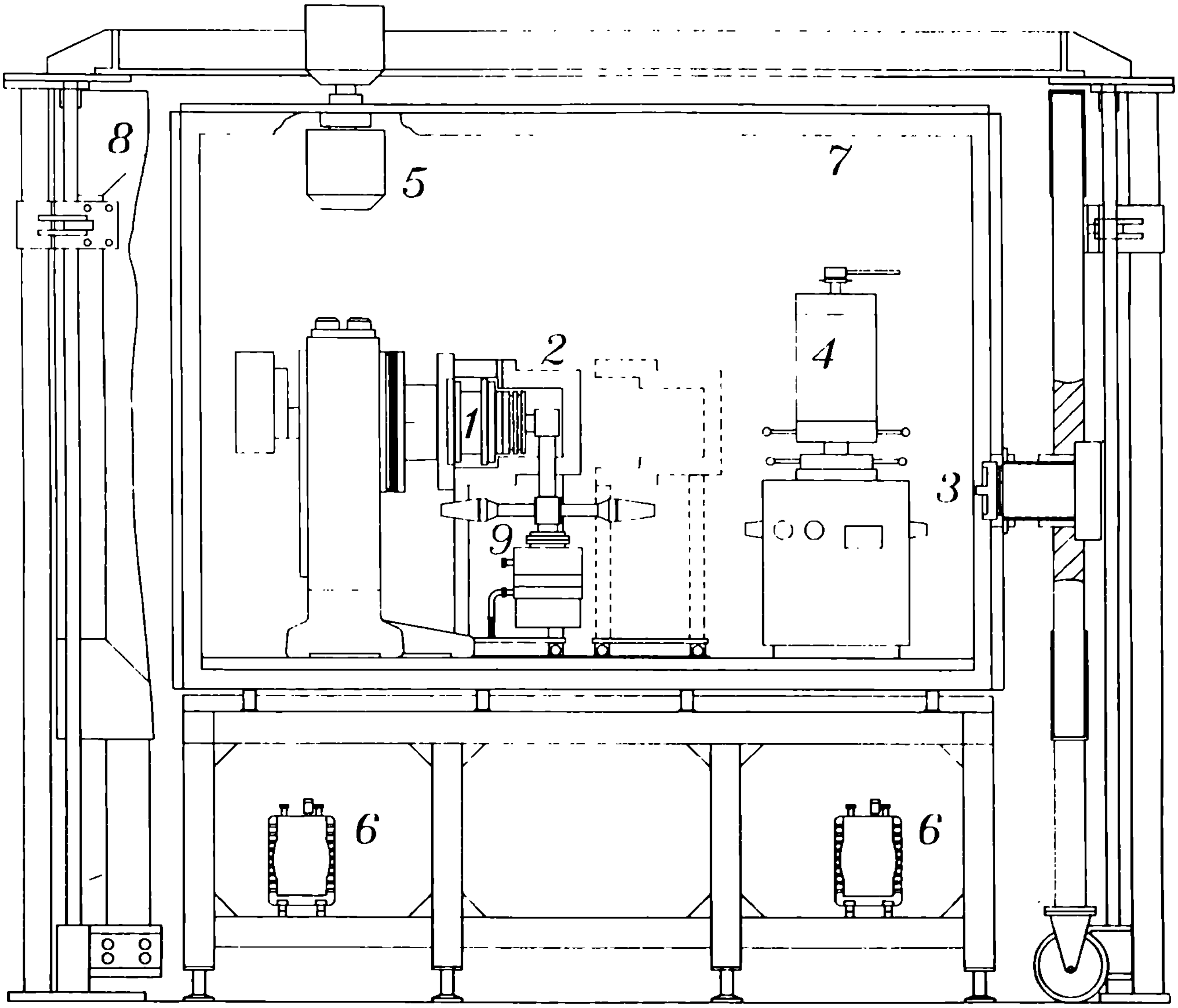

Fig. 4.12 Front view of the lead shielded glove box.
1. High temperature chamber; 2. Shielding shell; 3. La Calhene system; 4. Thermobalance oven; 5. Filter; 6. Vacuum pump; 7. Glove box; 8. Lead shielding; 9. High vacuum pump

Shielding of the thermobalance oven

In order to avoid a too high γ-backround due to the specimens of the thermogravimetric analysis and to prevent damage of the goniometer electronics, it is necessary to shield the thermobalance oven. This will be made externally by using a Densimet tube shielding a central lengh of about 100 mm from the total height of the oven.
The shielding of the high temperature chamber, the protection of the detector and the shielding of the thermobalance oven, as described above, are only a part of the whole construction. As shown in Figs. 4.11 and 4.12 the glove box will be equipped with two different vacuum and cooling systems, for the goniometer and the thermobalance respectively, two manipulators, a crane, a La Calhene system etc., which will be mounted in the near future.

References

[1] R.E. Einziger, L.E. Thomas, H.C. Buchanan and R.B. Stout, J. Nucl. Mater. **190** (1992) 53-60

[2] D.G. Boase and T.T. Vandergraaf, Nucl. Technol. **32** (1977) 60

[3] T.K. Campbell, E.R. Gilbert, C.K. Thornbill and B.J. Wrona, Nucl. Technol. **84** (1989) 182

[4] L.E. Thomas, R.E. Einziger and R.E. Woodley, J. Nucl. Mater. **166** (1991) 243
[5] L.E. Thomas, O.D. Slagle and R.E. Einziger, J. Nucl. Mater. **184** (1991) 117
[6] P.A. Tempest, P.M. Tucker and J.W. Tyler, J. Nucl. Mater. **151** (1988) 251-268
[7] K.B. Alberman and J.S. Anderson, J. Chem. Soc. London 2 (1949) 303
[8] S. Aronson, R.B. Roof, Jr. and J. Belle, J. Chem. Phys. **27** (1957) 137
[9] T. Smith, Atomics International North American Aviation Report NAA-SR-4677 (1960)
[10] K.T. Harrison, C. Padgett and K.T. Scott, J. Nucl. Mater. **23** (1967) 121
[11] P. Taylor, E.A. Burgess and D.G. Owen, J. Nucl. Mater. 88 (1980) 153
[12] S.R. Teixeira and K. Imakuma, J. Nucl. Mater. 178 (1991) 33-39
[13] P. Taylor, D.D. Wood, A.M. Duclos and D.G. Owen, J. Nucl. Mater. **168** (1989) 70-75
[14] P. Taylor, D.D. Wood, M. Duclos, J. Nucl. Mater. 189 (1992) 116
[15] L.E. Thomas, R.E. Einziger, H.C. Buchanan, J. Nucl. Mater. **201** (1993) 310
[16] R.E. Einziger, S.C. Marschman and H.C. Buchanan, Nucl. Techn. **94** (1991) 383
[17] R.E. Woodley, R.E. Einziger and H. Buchanan, Nucl. Techn. 85 (1989) 16

Hot Cell Annealing Tests for Fission Gas Release Studies

Modifications of equipment and technique

In the previous year considerable testing had been done on fission gas release from high burn-up fuels during annealing treatments as part of the international High Burn-up Chemistry Project managed by Belgonucleaire [1]. These results were reported in the previous annual report TUAR-92, p. 103.

This year's work continued with annealing tests of irradiated fuel in contact with reactor structural materials (304 stainless steel, Ag-In-Cd absorber alloy and zircaloy-4), at temperatures up to 1600 °C using mostly a lightly reducing atmosphere ($H_2O:H_2 = 1:10\ ^{v}/_{v}$). Work has shown that both PWR [2] and BWR [3] materials have low temperature interactions if fuel and certain structural materials are in contact (e.g. Inconel-Zry and B_4C-Zry systems). A first series of experiments is being carried out according to the conditions given in Tab. 4.15, using a medium burn-up fuel U627 (29.5 GWd/tU) with one high burn-up fuel BN3-241 (58 GWd/tU) test to examine the possible material interactions at this temperature and their influence on fission gas and volatile release. A 50-200 mg fuel sample and the chosen combination of materials in the form of shavings were placed in an inner ZrO_2 crucible and packed down. This was then placed in a tungsten crucible and this, in turn, in the holder of the induction furnace for filling with the H_2O/H_2 gas at 550 ml.mn^{-1} flow rate.

The sample was slowly heated up in approximately 30 °C steps per 10 min. up to 1500 °C to 1600 °C (depending upon release behaviour). After maintaining the maximum temperature for 10 min. the furnace power was cut to effect a rapid cooling from temperature compared to the controlled slow cooling of the HBC programme. As before ^{85}Kr fission gas release rates and total releases were continuously monitored. The ^{85}Kr release rates signals were collected and analysed using a new PC system and software (Interspec) from Intertechnique. The total ^{85}Kr release accumulated in the cold trap was monitored as before by a ratemeter that was output onto a flat-bed recorder. In order to estimate the releases from the fuel of fission products (especially volatiles such as Cs) a cartridge composed of a baffle then 20 µm, 10 µm and 3 µm filters was introduced below the crucibles containing the fuels which would capture the aerosols and condensing vapours (Fig. 4.13). This cartridge would be in the approximate temperature range 700 °C down to below 250 °C, during the tests at 1500 °C.

After the experiment the sample and materials were examined by SEM-EDX to see the interaction between fuel and structural materials. Thereafter the sample could be embedded and polished for optical ceramography of the cross-section.
The filters and baffle were dismantled from the cartridge and the first filter was placed in the micro γ-scanning apparatus for analysis of the impacted particles. After γ-analysis of the filters, selected filters could be analysed by SEM-EDX to determine the morphology and the composition of the particles on the filter. Although EDX is not as sensitive as γ-spectroscopy for active isotopes nevertheless it also analyses inactive elements and enables point analyses.

Tab. 4.15 Test conditions and ^{85}Kr releases during irradiated fuel-structural material interactions with heating to 1500 °C in reducing atmospheres.

Fuel (burn-up/ GWd/tu)	Material added	Heat	Atmosphere Treatment	Temperature of releases °C	Cumul. release of ^{85}Kr imp.s^{-1}g^{-1}
BR3 U 627 (29.3)	Abs./St. st./Zry	to 1505 °C in 30 °C step (5h 45 min.)	H_2O:H_2 = 1:10	1st 1240 °C regularly from 1505 °C	41.830
BN 3-241 (58)	Abs./St. st./Zry	to 1580 °C in 30 °C step (5h 28 min.)	H_2O:H_2 = 1:10	1st 1350 °C regularly from 1420 °C	12.195
BN 3-241 (58)	Abs./St. st./Zry	to 1505 °C in 30 °C step (5h 50 min.)	N_2 - 2 % H_2	1st 670 °C regularly from 1135 °C	37.992
BN 3-241 (58)	Abs./-/Zry	to 1494 °C in 30 °C step (6h 20 min.)	H_2O:H_2 = 1:10	1st 670 °C regularly from 1135 °C	15.765
BN 3-241 (58)	Abs./St. st./-	to be repeated			
BN 3-241 (58)	Abs.	to be repeated			
BN 3-241 (58)	--	to be repeated			

1) Abs. = Absorber alloy, Ag-15 In - 5 Cd, St.St. = 304 stainless steel, Zry4 = zircaloy
2) rapid cooldown was done by switching off the furnace:
3) flow rate = 560 - 600 ml.mn^{-1}

Results

The results available to date for the test matrix are given in Tab. 4.15. It can be seen that the total releases varied most clearly between the samples with lightly reducing H_2O/H_2 and strongly reducing (N_2/H_2) atmospheres in contact with structural materials and imply that slight surface oxidation of the zircaloy or stainless steel will have a big influence on the extent of interaction. Both the total release was greater under strongly reducing atmospheres and there was an earlier onset of release ~700 °C compared to 1350 °C. This is in direct contrast to results obtained in the HBC programme where oxidising atmospheres clearly caused greater releases than reducing atmospheres. This may be due either to structural metal oxide layer formation or intermetallic formation (e.g. Zr transfer to U). A further anomaly was the higher burn-up fuel (BN 3-241) which gave a lower fission gas release than the moderate burn-up fuel (U627) in contact with structural materials. No comment can be made about the influence of just one or two structural materials in contact with the fuel until the series is completed.

Specimen and filter analysis

γ-Spectroscopy

Analysis and examinations are in the initial stages with results only to date on the first sample and one set of filters. γ-spectroscopy has also been carried out on filters from 2 tests.
γ-spectroscopy of the filter from BN 3-241 heated alone in H_2O/ H_2 atmospheres shows a strong

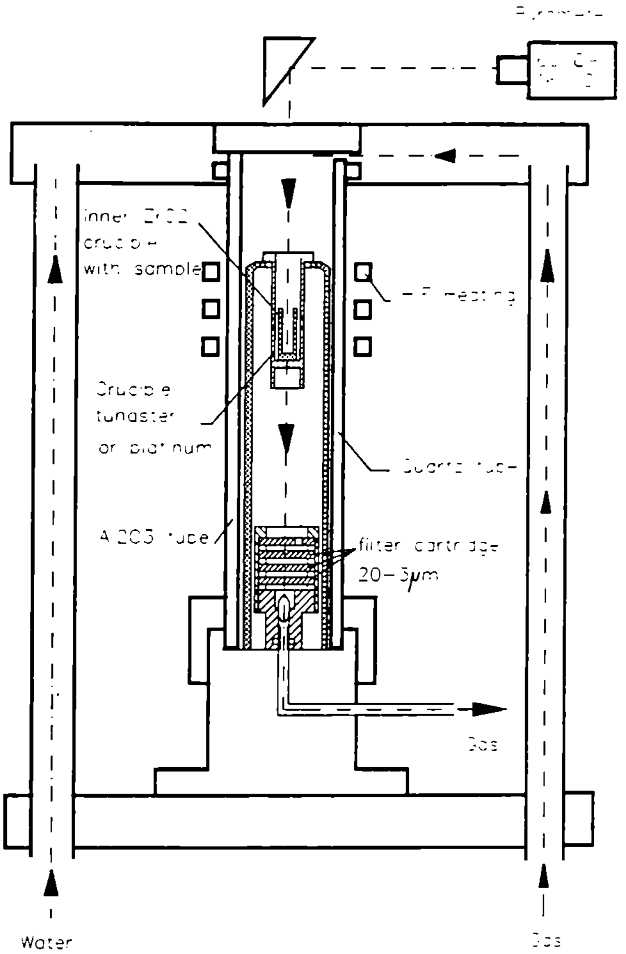

Fig. 4.13 Modified induction furnace for annealing experiments showing filter cartridge for analysis of volatile fission products.

^{137}Cs peak as well as ^{125}Sb (Fig. 4.14); the ^{241}Am peak is likely to be background. This indicates considerable Cs release occurs alongside the fission gas release even when no structural materials were present.

Filter microscopy

SEM-EDX analysis of the filter after BN3-241 was fuel heated in contact with Ag-15In-5Cd, zircaloy 4 in H_2O/ H_2 atmospheres showed small spherical particles of UO_2 (Fig. 4.15) and Ag/In as well as Zr. In addition traces of Ba were detected (this may be the daughter of ^{137}Cs), and if so this indicates Cs is also released when fuel is in contact with structural materials. However γ-spectroscopy of the filters will be able to confirm whether Cs release is increased by the structural materials. The presence of non-volatiles and even UO_2 on the filter suggests that some transport of the fuel as aerosol particles is also occurring. In addition there appeared to be various impurities in the spectrum, such as Na_2SiO_3 or similar compounds which seemed to come from the ZrO_2 or Al_2O_3 ceramics, and also feathers of W or WO_3 that have come from the outer W crucible. As the filter was made of poral stainless steel it is difficult to distinguish between particles of the 304 stainless and the base material of the filter.

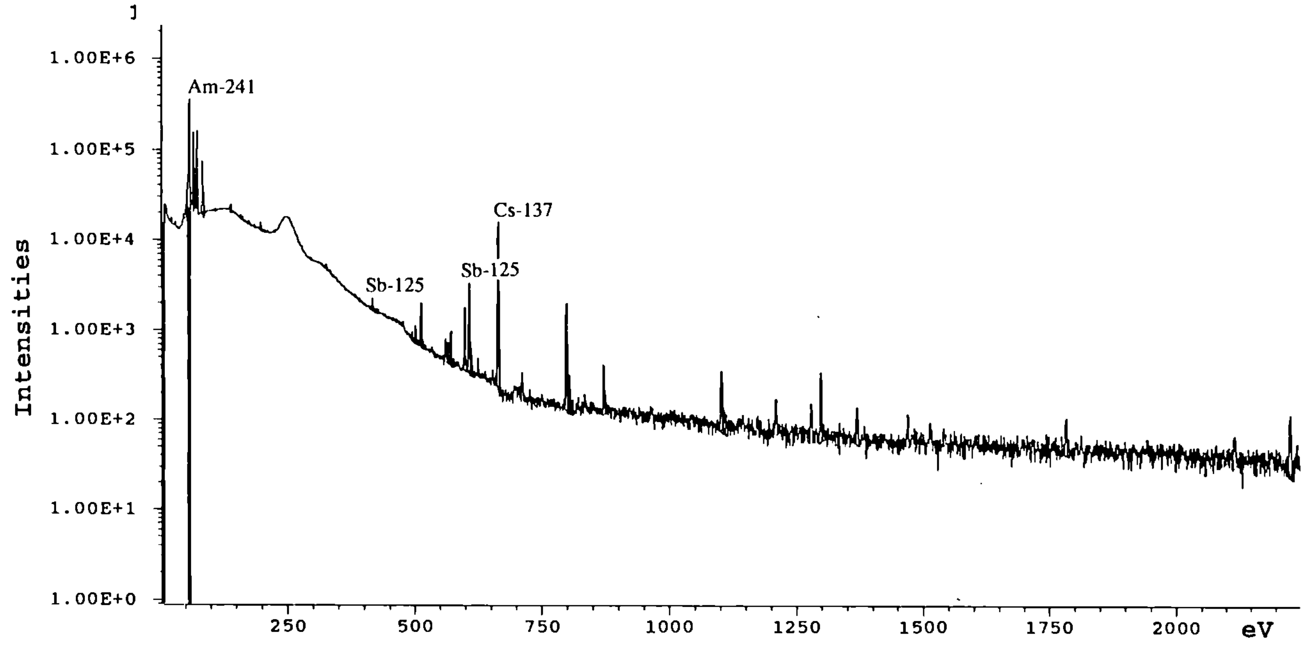

Fig. 4.14 γ-spectrum of 18 μm filter from annealing test of BN 3-241 alone in reducing H_2O/H_2 = 1:10 atmosphere upto 1500 °C

1) Fe > Cr,Si,Na,Zr > Ni

2) Si > Zr > Fe

3) Fe,Si > Cr > Ni,Ag,In

4) Fe,Si,Na > Cr > Ba,Ni,Ag

5) Zr > Si,Na

6) W,Si

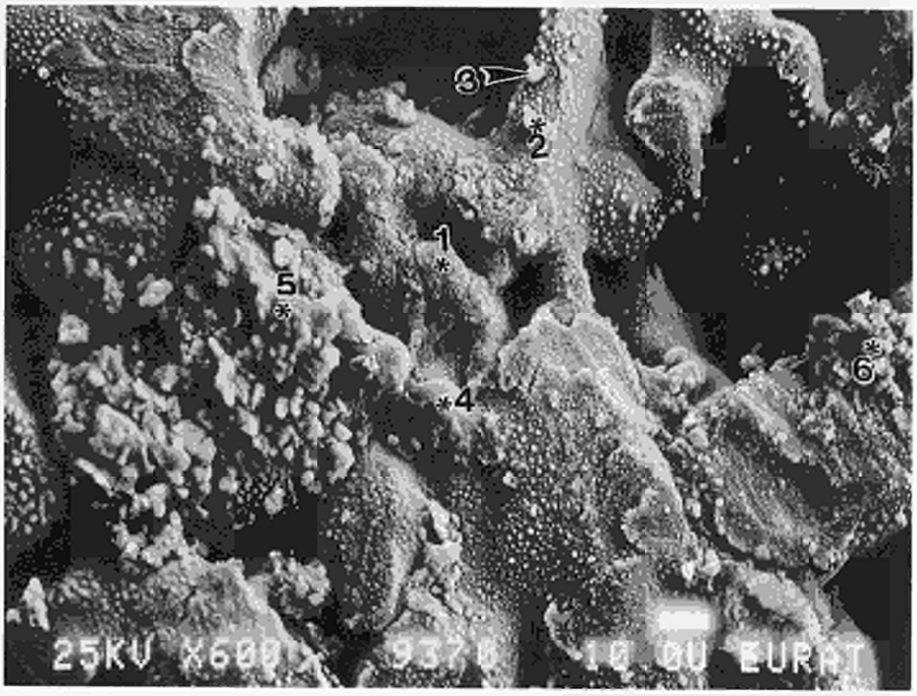

Fig. 4.15 SEM Micrograph of filter after annealing of BN3-241 fuel with Ag absorber and zircaloy-4 in H_2O/H_2 atmosphere upto 1500 °C

Sample microscopy

The SEM-EDX examination of the fuel sample heated in H_2O/ H_2 atmosphere with 304 stainless steel and Ag absorber and zircaloy-4 shavings showed remarkable changes in the structure compared to the starting material (Fig. 4.16a and b). Areas of the fuel sample appeared to be much more porous than previously, while other zones appeared to have many frozen droplets of the structural materials adhering to the surface. Where an interior surface is visible, considerably increased intergranular porosity is evident.

Analysis of the droplets on the external surface showed these to be mainly stainless steel. A closer view of a large stainless steel sphere showed a small spot of silver-indium material within it indicating both materials were molten (Fig. 4.17). Fused pieces of zircaloy were also seen occasionally (Fig. 4.18a). The material spheres appeared to slowly dissolve the fuel and left small imprints on the fuel surface where they had been dislodged. EDX analysis noted traces of Fe in the UO_2 fuel indicating iron uptake by the UO_2. (Fig. 4.18b) Often the spheres appeared to sit on or even in, the enlarged grain boundaries. Fig. 4.19a shows an internal surface and the considerable intergranular porosity. Certain zones of intragranular porosity are also seen at the edges of the grain and implies that intragranular bubble growth is also enhanced. Fig. 4.19b shows a close up of transgranular / intergranular facet of this surface in which many stainless steel spheres are present on the grain boundaries. Some of these liquid droplets also contain metallic fission products (e.g. analysis point Nr. 5 included Mo, Ru), which would normally be precipitates at the grain boundary; Tc was also detected in one sphere. Clearly the penetrating molten droplets of stainless steel had reacted or dissolved those precipitates. The metallographic cross-section yielded an estimated penetration depth of about 10 µm for the liquid metallic droplets (principally Ag and Fe-Ni-Cr).

Discussion

The greater fission gas release under strongly reducing conditions may be due to the fact that there is no oxidation at the zircaloy and stainless steels so that they melt and flux the UO_2 grains faster than under H_2O/H_2 atmospheres where oxide films can form that restrict the fluxing action. The liquid silver and stainless steel seen on the surface appear to slowly attack the fuels' outer surface giving it a smoothed appearance. However they most rapidly penetrate at the grain

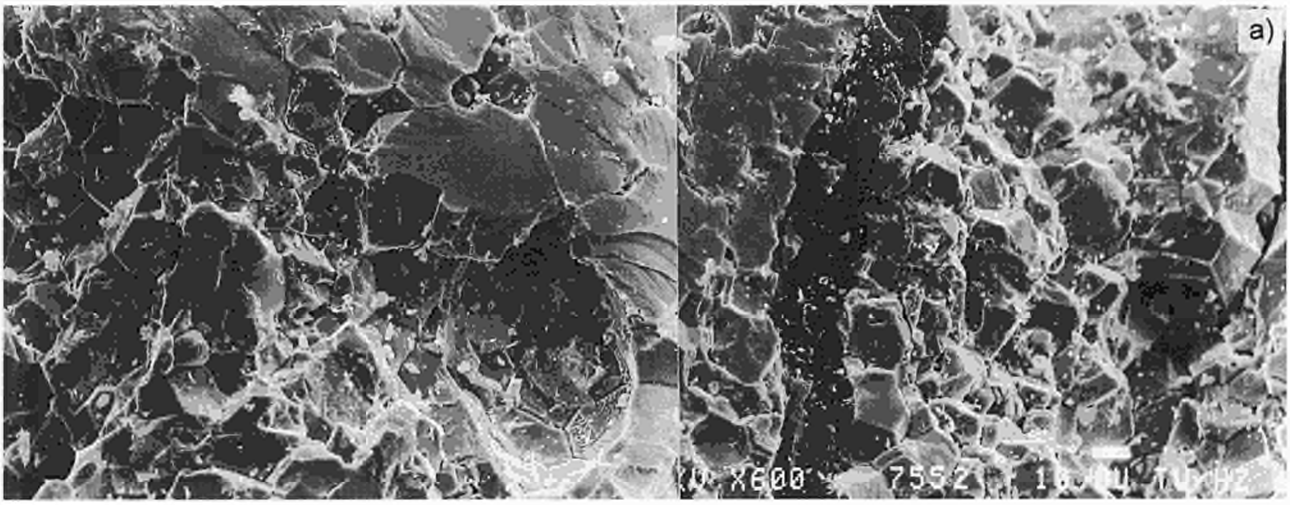

1850 µm
$r/r_0 = 0.54$

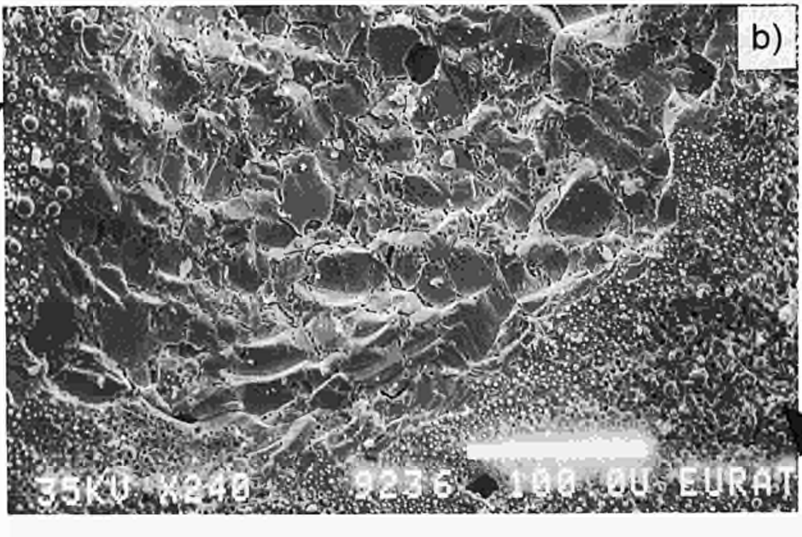

fracture surface showing porous grain boundaries

lightly attacked surface covered with metallic sphere

more attacked fuel surface with metallic spheres

Fig. 4.16 U627 fuel sample after annealing in contact with Ag absorber, zircaloy 4 and 304 stainless steel in H_2O/H_2 (1:10) atmosphere upto 1500 °C. a) starting material 600× b) after annealing 240×

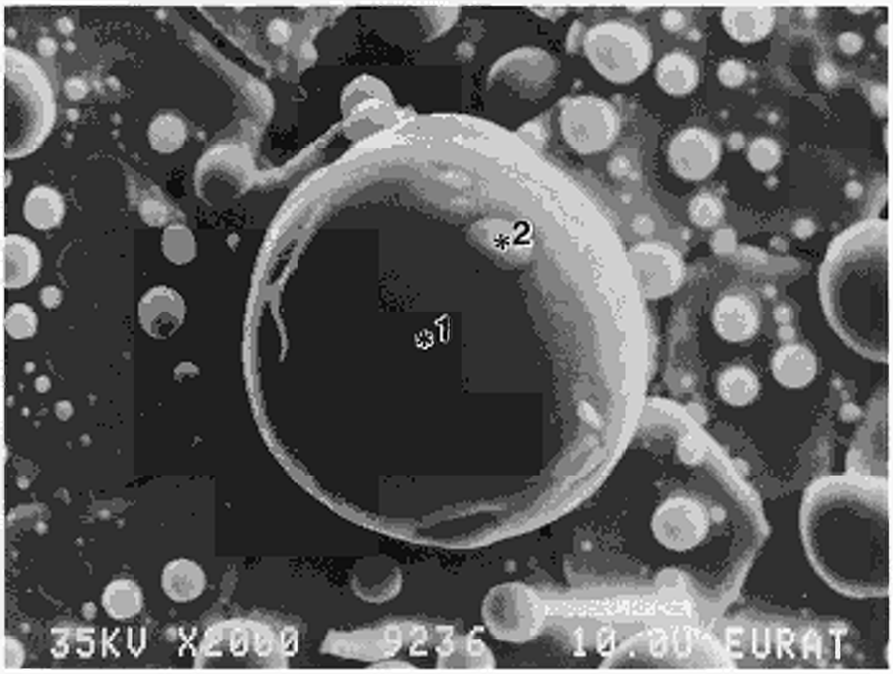

* 2 silver
globule in stainless st. sphere
Ag > In, Fe
> Ni, Cr

* 1 stainless
steel sphere
Fe ≫ Ni, Cr

Zone A Stainless steel sphere with silver absorber globule

Fig. 4.17 Molten stainless steel sphere with Ag absorber alloy spot found on the U627 fuel sample after annealing with structural materials in H_2O/H_2 *(1:10) atmosphere upto 1500 °C (2000 ×)*

boundaries with increased area of attack and by connecting between preexisting intergranular porosity (elongated pores of up to 5 μm length were observed on the grain boundary).

This greatly increased pore interconnection will lead to greater fission gas release. From this result it could be argued that higher porosity fuels would have a greater fission gas release. Cs and other volatiles may also be released as no Cs was seen on the sample but was observed on the filters. The Cd of the absorber alloy Ag-In-Cd also appears to have volatilised.

The outer 2 μm of the UO_2 grains are microporous with an average pore diameter of about 0.3 μm. This indicates considerably enhanced bubble growth either through increased gas diffusion or bubble coalescence. This may be due either to the Fe, Ni, Cr dissolution in the grain increasing the fission gas diffusion coefficients or that surface oxidation of the UO_2 grains by the H_2O/H_2 atmosphere is augmenting the fission gas mobility, a further possibility is Me-U intermetallic formation. This matter may be resolved in subsequent examinations. Nevertheless it is clear that at longer time durations increased release levels would be expected.

Although 304 stainless steel and absorber alloy do not interact, their conjoint attack as liquid phases at 1500 °C appears to be the main fluxing agent; the zircaloy also seems to have fused locally, probably by interaction with stainless steel (Fe-Zr or Ni-Zr eutectics form at 1100-1200 °C).

Nevertheless some direct Zr-UO_2 interactions appears to have taken place while Zr alone was detected in certain EDX analyses of the UO_2 grains. This interaction may take place via formation of a Zr-U intermetallic. This U removal would result in superstoichiometric UO_{2+x} formation. If this caused a phase change then it may be one cause of the microporosity seen in the fuel grains' outer edges.

Interactions of zircaloy with absorber alloy (Ag-Zr eutectics) are known but were not observed with this sample. It seems that when chemical interactions between UO_2 and structural materials are established they can hide the influence of atmosphere on the UO_2 fission gas release.

Conclusions

The phenomenon needs more investigation but from the results to date the following preliminary conclusions can be drawn:

SEM Analyses

* 7 fused Zry
Zr ≫ U
traces of Cr, Fe

* 8 stainless piece
on Zry
Zr > Fe > Cr

* 9 stainless st.
sphere
Fe > Ni, C

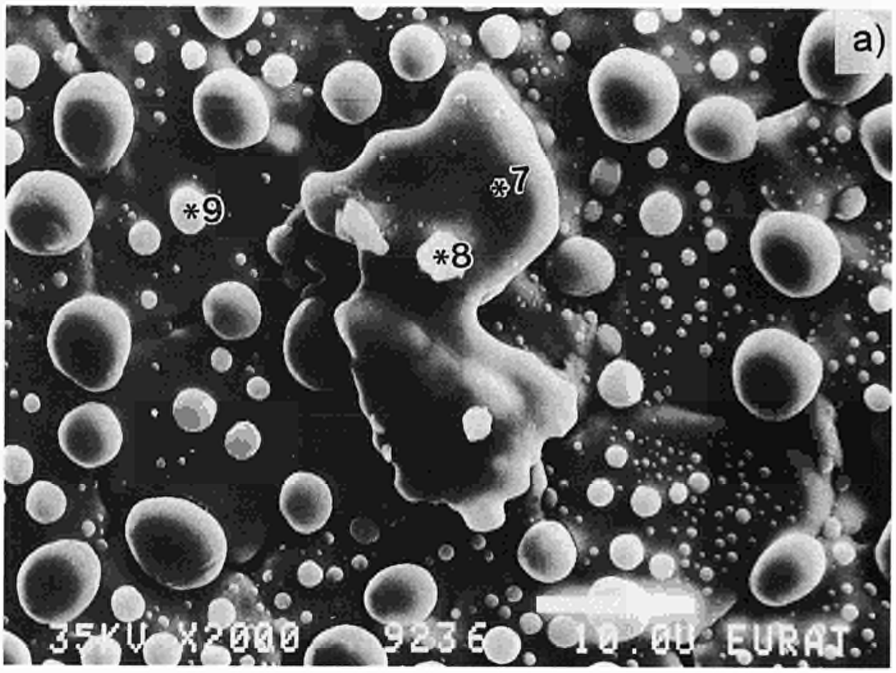

Zone A Fused Zirconium and stainless st. sphere on fuel surface

* 13 grain surf.
U > Fe

* 14
U ≫ Fe

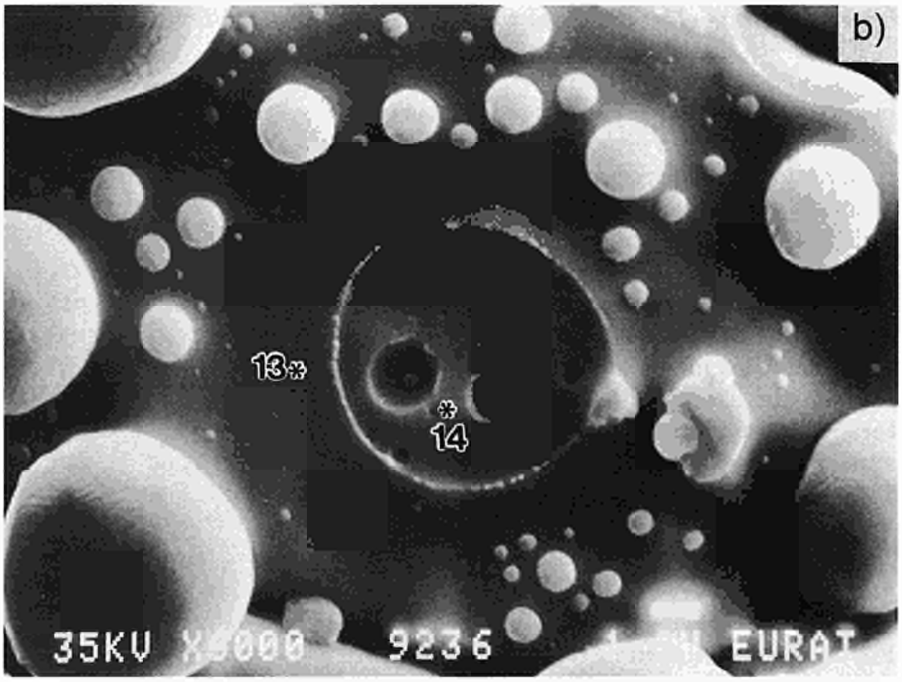

Zone A Fuel surface showing circular contact points between melted metal and fuel

Fig. 4.18 a) Fused zircaloy piece on the surface of the U627 fuel sample after annealing in contact with structural materials in H_2O/H_2 *1:10 atmosphere upto 1500 °C (2000×). b) Surface of heat-treated U627 fuel which stainless steel spheres have been dislodged. Fe is detected in the underlying* UO_2 *by EDX (6000×)*

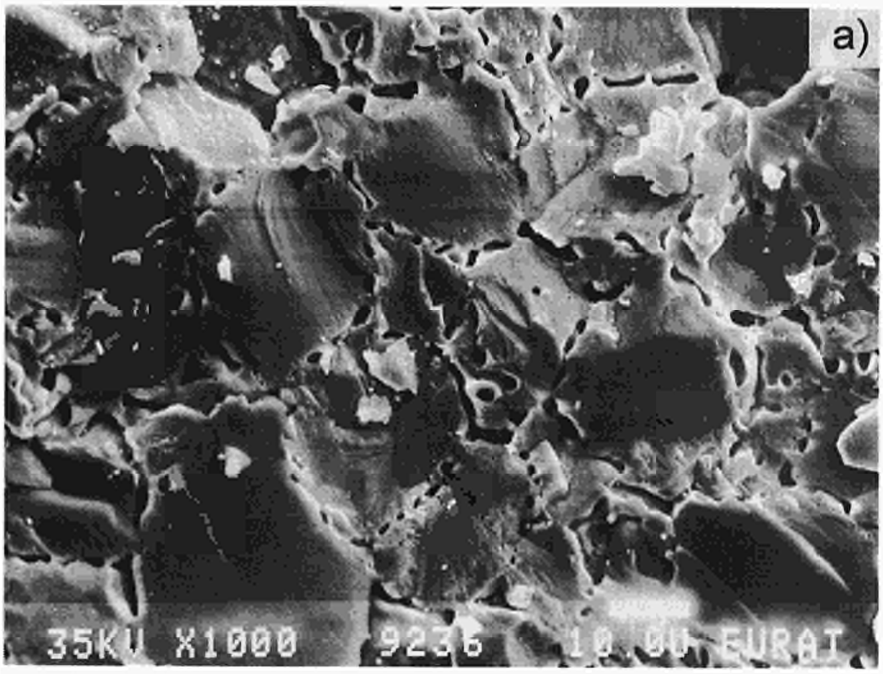

Zone C Internal fracture surface with considerable macro porosity at grain boundaries and micro-porous zones around the grain edges (SEM - 1000 x).

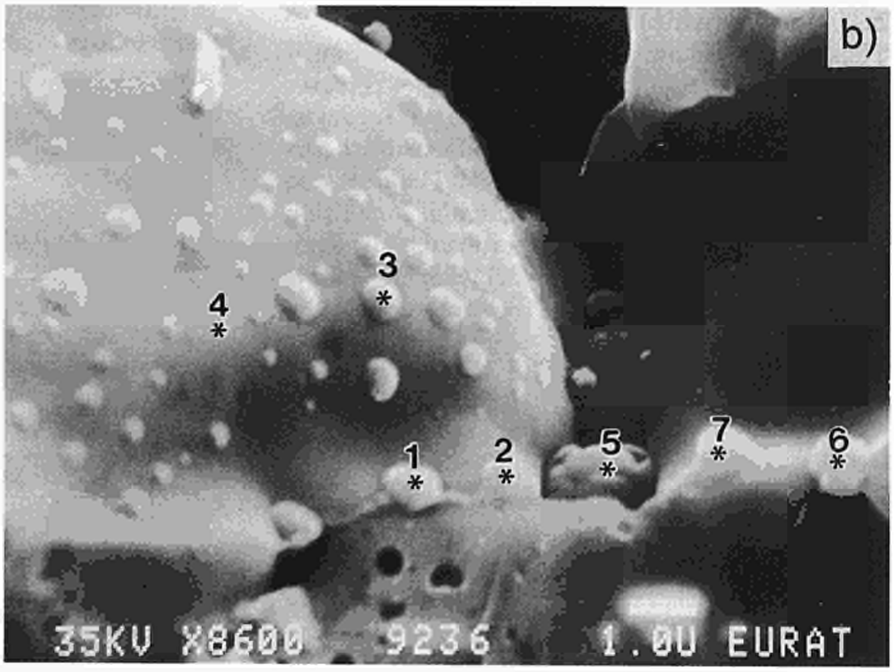

* 1 stainless sphere
on grain b.
Fe, U ≫ Ni, Cr + Mo

* 4 grain surface
U (traces of Fe)

* 5 stainless sphere
(with f. ps.)
Fe > U > Ni, Cr
- traces of Mo, Ru

Zone C Junction of transgranular and intergranular fracture surface. Showing
(i) metallic spheres sitting on the grain boundary and
(ii) surrounding micro-porous zone. SEM - 8600 x.

Fig. 4.19 a) Internal surface of U627 fuel, sample after annealing with structural materials showing the considerable porosity at the internal grain boundaries (2000 ×). b) Mainly stainless steel spheres (some containing fission products) at an internal grain boundary of the U627 fuel sample after annealing with structural materials (8600 ×).

Fission gas releases

Materials in combination result in only slight increases in the first 5 hours of testing up to 1500-1600 °C but sometimes low temperature releases (~600 °C) are seen that may be aided by silver in the mixture melting. The main releases appear at 1350-1400 °C - that is similar to heating without additives. Strongly reducing conditions appear to help fission gas release.

SEM-EDX

SEM reveals a very considerable effect of material - fuel interaction, with liquid stainless steel, silver and zircaloy spheres reacting with the fuel surface (U is present in zircaloy; Fe is in UO_2). In addition to the smoothed surfaces there is grain boundary dissolution causing enlarged intergranular porosity and penetration of metals into the grain boundary to about 10 µm depth and dissolution of the fission product precipitates there. Finally the fuel grains show porous outer zones which is speculated may be a result of Me-U (e.g. Zr-U) intermetallic formation.

These results show a considerable interaction is occurring and that greater fission gas releases would be expected in the longer term. Inconsistencies in some results are attributable to the variation in fuel-structural material contact due the order of addition to the crucible. Repetition with premixed filings of the materials, although less realistic, will avoid this variation and enable a more precise assessment of the interaction.

References

[1] IAEA Technical Committee Meeting "Fission gas release and fuel rod chemistry related to extended burn-up", Pembroke (CA), April 28 - May 1 (1992)

[2] S. Hagen, P. Hofmann, G. Schanz and L. Sepold "Interactions in zircaloy / UO_2 fuel rod bundles with Inconel spacers at temperatures above 1200 °C" (KfK 4378) Sept. 1990

[3] F. Nagase "High temperature interaction of control material for BWR" in Conf. Proc. "Severe Accident Research in Japan, (SARJ-93)", 4-6 Nov. '93, Tokyo, Japan

Fuel Rod and Spent Fuel Behaviour at Extended Burnup

Introduction

In the past decade the discharge burnup of fuel assemblies has steadily been increased and in the meantime has reached maximum assembly average values of 55 MWd/kgU. In order to reach such high burnups with complete reloads, higher fuel enrichments than those being previously used for fuel reloads are necessary. As a consequence of the high enrichment fuel rods are operated at higher average power over a longer period of time and hence higher fuel temperatures. Siemens-KWU has irradiated fuel assemblies with the appropriately high enrichment of 3.8 to 4.2 w/o U-235 in a highly rated commercial pressurized water reactor (PWR) under realistic power conditions. In order to even extend the burnup beyond the target burnup of these fuels assemblies, a number of fuel rods were withdrawn from the assemblies and reinserted into fresh assemblies for further irradiation. By such procedures peak pellet burnups of about 85 MWd/kgU where reached at relatively high power levels. Typical power histories for those fuel rods to be discussed in this paper are given below in Tab. 4.16.

Tab. 4.16 Typical Fuel Rod Power Histories

Cycle	Cycle Average LHGR W/cm	Cycle Average Burnup MWd/kgU	Cumulative Average Burnup MWd/kgU
1	270-310	15.0-16.5	15.0-16.5
2	230-270	13.0-14.5	29.5-30.0
3	210-230	11.5-12.5	41.5-43.0
4	180-200	10.5-11.0	51.5-54.5
5	170-180	9.5-10.5	60.5-64.0

LHGR = Linear Heat Generation Rate

Destructive Testing

The initial step of the destructive testings is the determination of the fission gas release into the free volume of the rods applying standard puncturing techniques. Fig. 4.20 shows the fractional fission gas release of the higher enriched fuel rods as a function of rod average burnup. For compari-

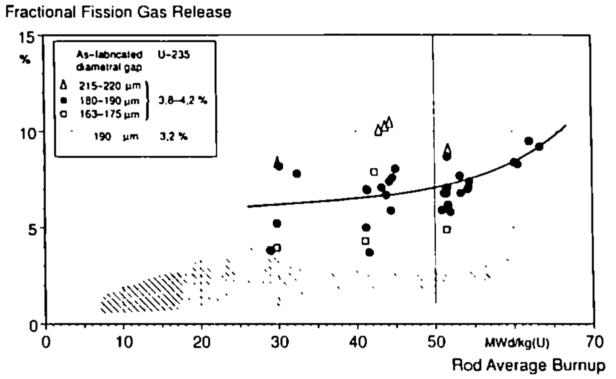

Fig. 4.20 Fractional fission gas release of PWR fuel rods with U-235 enrichments of 3.8 w/o to 4.2 w/o as a function of burn-up

son the shadowed band shows the fractional fission gas release of standard rods of lower enrichment from a large number of fuel rods irradiated in several commercial pressurized water reactors [1]. As expected the fission gas release of the fuel rods with higher enrichment and operated at higher fuel temperatures is generally greater than that of fuel rods with lower enrichment and operated at lower fuel temperatures. In addition the data obtained on the highly enriched fuel rods show a distinct dependence of fission gas release on the initial diametrical fuel/clad gap. This pronounced influence of the diametrical gap size on fission gas release must be discussed in terms of fuel pellet center temperatures. At a given linear power the fuel pellet center temperature depends on fuel conductivity and the temperature gradient across the effective fuel/clad gap which in turn depends on the initial gap size. This influence of the gap size is most pronounced at low and intermediate burnups and decreases at higher burnups, a fact that is not surprising, since the initial gap decreases in size due to the combined effects of cladding creep and fuel swelling under irradiation [2]. As shown in Fig. 4.21 the decrease in gap size, as measured by a compression technique after irradiation at room temperature is more pronounced for fuel rods with large initial gaps than for fuel rods with smaller ones. At operating temperature the gap is closed in high burnup rods independent of initial gap size. Consequently, initial differences in gap size diminish at higher burnups and fuel surface respectively fuel center temperatures approach each other at the lower level. However, in spite of decreasing fuel center temperatures the experimental results do clearly indicate a continuous increase in fission gas release with increasing burnup.

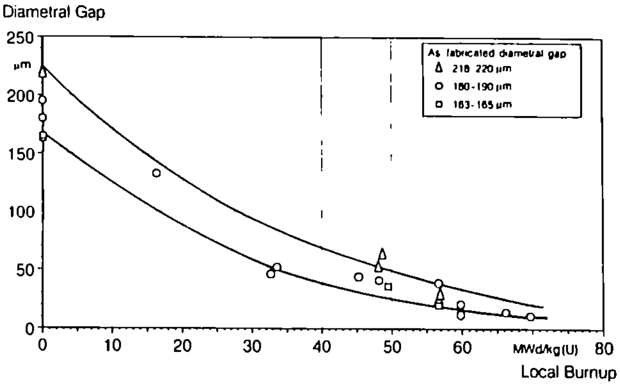

Fig. 4.21 Diametral gap between fuel and cladding as function of local burn-up (measured at room temperature by a non-destructive compession technique)

An attempt has been made to relate the fission gas release behaviour to fuel microstructural features. The microstructure analysis was based on the following examinations:

a) The determination of the radial distribution of xenon and ceasium by means of electron probe microanalysis (EPMA) on representative ceramographic cross sections.

(b) Optical microscopy examination and, in particular, the study of the grain growth and fuel restructuring on the same specimens.

(c) Scanning electron microscopy (SEM) analysis either of the etched specimen as used in b) or a fractography prepared from the specimens.

The radial concentrations of xenon and ceasium retained in the individual UO_2-grains are shown in Figs. 4.22 and 4.23 for two different burnup

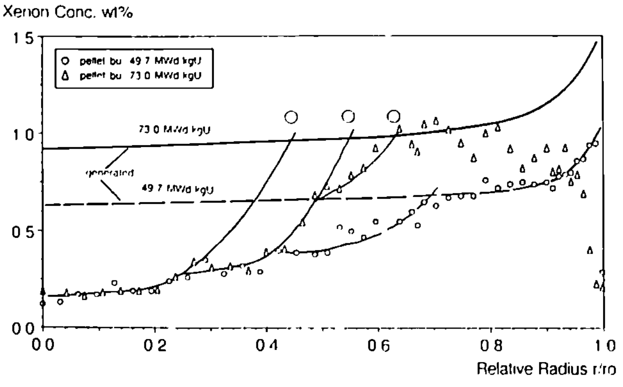

Fig. 4.22 Radial Xe distribution in PWR fuel pellets as function of relative radius determined by EPMA

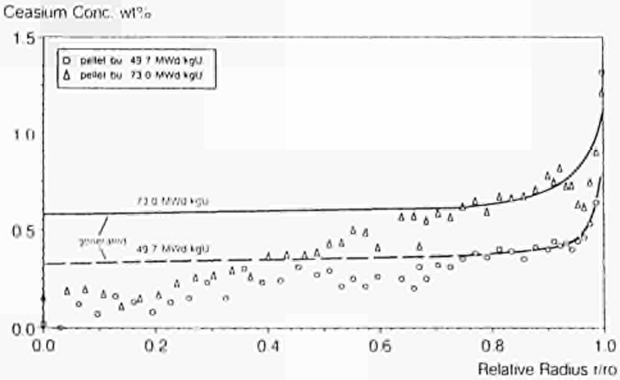

Fig. 4.23 Radial Cs distribution in PWR fuel pellets as function of relative radius determined by EPMA

levels of 49.7 MWd/kgU and 73 MWd/kgU, respectively. The EPMA results clearly indicate three different regions along the radius of the pellets.

At both burnup levels the EPMA shows a significant xenon release from the central region of the pellet. The release starts at a relative radius r/r_0 of about 0.7 and increases towards the center. This increase is not a monotonous function of r/r_0 but shows steps with different slopes. These steps are associated with consecutive steps in power history, for instance due to reshuffling. They mark regions of fission gas release at certain time intervals of operation [3] als also indicated by the dark rings in the optical microscopy, shown in Fig. 4.24. Furthermore some cesium is released from the center region of the pellet.

Fig. 4.24 Typical cross section of PWR fuel rod (pellet burn-up 73 MWd/kgU)

For the region between $0.7 < r/r_0 < 0.96$ the EPMA reveals differences for the two burnup levels. At a burnup of 49.7 MWd/kgU the xenon concentration in that region was found to be equivalent to the amount of xenon generated; consequently no fission gas release has occured. In contrast, the EPMA of the pellet of 73 MWd/kgU burnup indicates some fission gas release with the tendency of increasing release towards the pellet periphery. Noteworthy is the scatter in the local xenon measurements. That is specific for this region which must be discussed in view to the particular fuel structure there. The concentration of cesium is not affected and does not deviate from the theoretically calculated values in that region.
At the pellet periphery between $0.96 < r/r_0 < 1.0$ (pellet rim) the EPMA indicates a high xenon release, similar for both burnup levels. The cesium concentration in this region corresponds to the theoretically calculated one.

The radial distribution of xenon can be related to the fuel restructuring by means of optical microscopy and scanning electron microscopy. A precise correlation between the xenon release and the fuel microstructure can be established. At high burnup three basic restructuring regions are present (Fig. 4.25) and can be described from the pellet periphery towards the fuel center as follows:

(a) the usual porous region (cauliflower microstructure) where the initial grain boundary structure has disappeared and seems to be substituted by a very small grain structure (1 µm size). The pore density is very high and pore separation ranges between 1 and 3

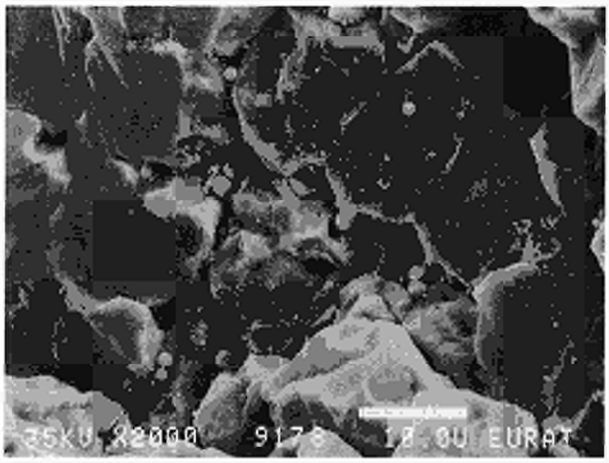

Fig. 4.25 Characteristic fuel microstructures of a PWR fuel rod after a pellet average burn-up of 73 MWd/kgU

µm (initial grain size 6 µm). This is typical for the region $1 > r/r_0 > 0.96$. By increasing temperature the pore density decreases and the distance between pores can reach 5 to 10 µm.

(b) A region ranging from $0.88 > r/r_0 > 0.74$ where the fuel structure is heterogeneous and is a mixture of dense grains surrounded by small porous areas of the same type described just before.

(c) The region from $r/r_0 = 0.70$ up to the center is characterized by two mechanisms indicating a higher atomic and bubble mobility, i.e., grain growth and formation besides intragranular porosity - of intergranular porosity whose degree of coalescence increases with temperature.

It has already earlier been established that the small pores visible in the micrographs contain fission gas which is not completely detected by EPMA [1].

Apart from the outer rim a distinct chemical interaction zone between fuel pellet and cladding develops at high burnup. This zone consists of compounds of U-(Pu)-Cs-O or U-Zr-Cs-Te-O. In this case the fuel pellet is strongly bonded to the cladding resulting in a strong fuel/cladding mechanical interaction. This implies that any dimensional changes of the pellet (thermal expansion and swelling) are transmitted directly to the cladding tube, and finally determine the dimensional changes of the fuel rod. Diameter measurements on fuel rods with various types of cladding tubes have shown that the initial decrease in diameter is followed by an increase in fuel rod diameter at burnups in the range of 40 to 50 MWd/kgU. Nevertheless, the fuel rod diameters stay still below the initial diameter up to fuel rod average burnups of 65 MWd/kgU. However, this creep and hence stress reversal in the cladding affects the hydride precipitation near the cladding inner surface and causes the hydrides to realign radially.

Conclusion

The fission gas release of these fuel rods was found to be generally higher than that of the lower enriched standard rods. The fractional fission gas release increases with burnup. Microstructural examinations and EPMA have confirmed that the fission gases released stem mainly from the center region at the pellet. The diameter of that region and the amount of fission gases released is determined by the local fuel temperature. With increasing burnup more and more pellet regions at lower temperature become saturated with fission gases. Exceeding the saturation temperature in the course of burnup will result in an additional release of fission gases. Such a stepwise release has clearly been confirmed by EPMA.

The central zone with higher gas release is followed by a zone characterized by heterogeneous grain growth where greater dense grains are surrounded by smaller grain with higher porosity. The dependance of porosity concentration upon the grain size is known and this new microstructural at local burnup at 70 MWd/kgU contains the potential for a further increase in fission gas release when burnup increases.

At the fuel periphery the porous outer rim increases in thickness with burnup. The fission gases have partly been released from the grains but seem still to be confined in small bubbles and evidence is growing that these fine bubbles are precipitated in subgrains and on subgrain boundaries.

In general, the overall fuel rod behaviour at extended burnup has been very satisfactory. In the burnup range investigated no exponential changes in fuel rod behaviour and no burnup limiting phenomena have been experienced.

At high burnups a strong interaction between fuel and cladding occurs resulting in creep reversal. After an initial decrease in diameter the fuel swelling causes the fuel rod diameter to increase again but at a rate where cladding properties can accomodate.

In the same zone neutronic resonance absorption leads, as burnup increases, to a continous increase of the burnup at the pellet periphery which reaches a local peak burnup of 140 MWd/kgU corresponding to an average pellet burnup of 66 MWd/kgU. At the same position a concentration of 3.2 % Pu was determined by EPMA, corresponding to an average pellet Pu build-up of 1.2 %. This outer rim zone is also characterized by a specific microstructure (cauliflower structure) with extended porosity; the distance between pores in this zone lies between 1 and 3 µm.

The extend of this outer porous zone is strongly dependent on the starting enrichment and has a maximum value of 200 µm for an enrichment of 3.2 % U-235. Increase of the enrichment to 3.8-4.2 % reduces the maximum extent to 100 µm.

The presence of metallic fission products (Mo, Te, Pu Rh, Pd) at the fuel periphery and pellet centre indicates a fuel stoichiometry in the range $2.00 < O/M < 2.001$ if equilibrium conditions are assumed. The oxygen excess produced by fission is balanced by gettering the oxygen by Zr at the inner side of the cladding, the formation of oxide(s) involving Cs, U(VI) or Cs, Te and zircaloy-4 and by a buffer mechanism due to the presence of Mo.

References

[1] R. Manzel, F. Sontheimer and H. Stehle, "Fission gas release of PWR fuel under steady and transient conditions up to high burnup", Proceedings of the ANS Topical Meeting on Light Water Reactor Fuel Performance, Orlando, Florida, April 21-24 (1985)

[2] R. Manzel, R.P. Bodmer and G. Bart, "Fission gas release of high burnup fuel", Proceedings of a Technical Committee Meeting on Fission Gas Release and Fuel Rod Chemistry Related to Extended Burnup, Pembroke, Ontario, April 28-May 1, published as IAEA-TECDOC-697 (1991)

[3] R. Manzel and R. Eberle, "Fission gas release at high burnup and the influence of the pellet rim", Proceedings of the ANS Topical Meeting on Light Water Reactor Fuel Performance, Avignon, France, April 21-24 (1991)

[4] J.A. Turnbull et.al., "The diffusion coefficients of gaseous and volatile species during the irradiation of uranium dioxide", J. Nucl. Mat. **107** (1982) 168-184

[5] C. Forat et.al., "Fission gas release enhancement at extended burnup: experimental evidence from French PWR irradiations", Proceedings of a Technical Committee Meeting on Fission Gas Release and Fuel Rod Chemistry Related to Extended Burnup, Pembroke, Ontario, April 28-May 1, published as IAEA-TECDOC-697 (1991)

[6] M. Bain, W.A. McInteer and T.P. Papazoglou, "Release and migration of fission products in high burnup fuel"
S.R. Pati and A.M. Grade, "Fission gas release from PWR fuel rods at extended burnup"
R.A. Weiner, "Evaluation of high burnup fission gas release data", Proceedings of the ANS Topical Meeting on Light Water Reactor Fuel Performance, Orlando, Florida, April 21-24 (1985)

[7] H. Zimmermann, "Untersuchungen zum Schwellen und Spaltgasverhalten in oxidischem Kernbrennstoff unter Neutronenbestrahlung", KfK-Report 2467 (1977)

[8] C. Ronchi and P.T. Elton, "Radiation re-solution of fission gas in uranium dioxide and carbide", J. Nucl. Mat. **40** (1986) 228-244

[9] R.C.Daniel, M.L. Bleiberg, H.B. Meieran and W. Yeniscavich, "The Effect of High Burnup on Zircaloy", Clad Bulk UO2 Plate Fuel Samples, US Report WAPD-263 (1962)

[10] D.S. Wood, "High deformation creep behaviour of 0.6-in.-diameter zirconium alloy tubes under irradiation", Zirconium in Nuclear Applications, ASTM STP 551, (1974) 274-291

Non-Destructive Assay for Spent Fuel Characterisation

Spent fuel is characterised in terms of burn-up and radiotoxicity potential by passive neutron and total gamma interrogation complemented by isotopic correlations. A semi-cylindrical array of three neutron and one GM detectors, embedded in a polyethylene moderator are used for the measurement of neutrons and gammas emitted by the fuel (TUAR-91 p. 108, TUAR-93 p. 128).

The neutron and gamma distribution profiles were measured within a number of applications: First on BR3 UO_2 and MOX spent fuels, secondly on the PWR high burnup and MOX fuels used in the CRIEPI project concerned with spent fuel characterisation for interim dry storage (see this report). The profiles will be used for the verification of the average burnup declared by the operators. Furthermore, the axial distribution of the local burnup will be determined since all information obtained from the destructive studies on pellets is a function of burnup. The neutron and burnup distributions will be used as a normalisation parameter on calculations performed on the fuel evolution during irradiation.

The present unit for passive neutron and gamma interrogation has been extended to include a miniature semiconductor detector (CdTe with 3x3x2 mm^3 active volume) for simultaneous gamma spectrometry. The detector and the preamplifier circuit board are situated inside a collimated housing made of an Pb-W alloy. The amplifier, a unit specifically designed for signal-to-noise improvement by the firm EURORAD (France) is situated 10 m from the detector. The gamma spectrometry unit has been tested in a low background environment for operation characteristics and calibrations. The detector was then installed inside a β- γ hot cell at the Institute and is presently going through extensive tests on spent fuel for operation behaviour in an environment where several spent fuel rods are stored (estimated dose rate on the detector 1 Sv/h). First findings indicate a good stability of the system for a continuous operation of about one month and well resolved photopeaks of Cs-137 and Cs-134 (whose presence is cooling-dependent).

Chemistry of the UO_2 Fuel Periphery - Properties of Cs-U-O Compounds

Introduction

The investigations on U-Cs-O compounds, reported in TUAR-92, p. 124, were continued and aimed especially at the determination of the mechanical and thermal expansion properties of Cs_2UO_4. The pure Cs_2UO_4 specimens in the form of pellets, 6 mm in diameter, 3 or 10,5 mm in length, had a theoretical density of about 90 %.

Results

Deformation under compression.

Experiments of deformation under compression were carried out at temperatures up to 800 °C. The results are collected and represented in Fig. 4.26.

- The plasticity of Cs_2UO_4 seems to be relatively important even below 600 °C. The deformation of the samples before rupture reached values around 30 %.
- The overall deformation before rupture is a function of the temperature.
- A contribution of the viscosity appears at temperature around 800 °C and, together with the plasticity, causes the deformation of the specimens. The viscosity coefficient will be determined in the near future by applying different compression rates at 800 °C.

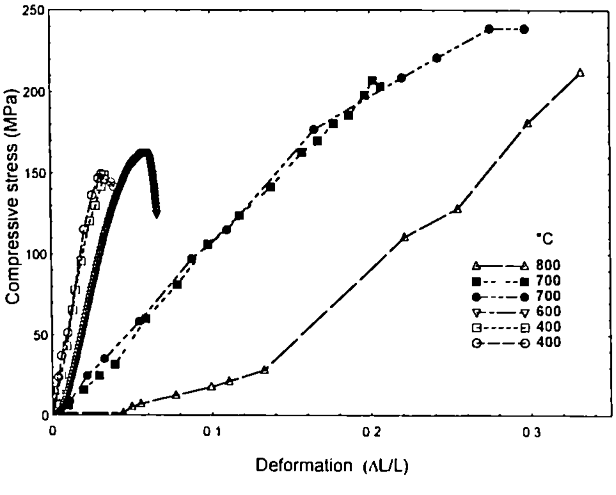

Fig. 4.26 Deformation of Cs_2UO_4 pellets as a function of compressive stress and temperature.

Thermal expansion.

The thermal expansion of Cs_2UO_4 pellets, 10,5 mm long, was investigated using a differential dilatometer. Reference materials were Al_2O_3, UO_2, Pt and Cu. The measurements were carried out under argon atmosphere at a heat rate of 3°C/min.

Fig. 4.27 shows the values of the thermal expansion of Cs_2UO_4 determined with various reference materials. The expansion curves reported in the literature for the reference materials are also plotted for comparison.

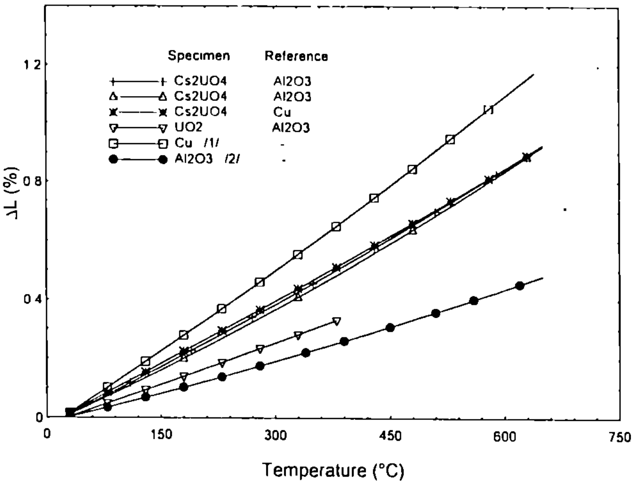

Fig. 4.27 Thermal expansion curves of Cs_2UO_4 and UO_2 obtained using Cu and Al_2O_3 as reference materials.

The values of the calculated expansion coefficients are given in Tab. 4.17. The results of Cs_2UO_4 range between those of UO_2 and of Cu.

Tab. 4.17 Expansion coefficients of Cs_2UO_4, Al_2O_3, UO_2 and Cu.

Materials	Cs_2UO_4	Cs_2UO_4	Al_2O_3/2/	UO_2/3/	UO_2	Cu/1/
References	Cu	Al_2O_3	-	-	Al_2O_3	-

Temperature (°C)	Expansion coefficient (10^{-6}/°)					
300	14,2	14,1	6,89	8,07	9,14	18,7
400	14,4	14,3	7,13	8,28	9,34	19,35
500	14,5	14,6	7,34	8,47	9,49	20,1
600	14,6	14,9	7,53	8,66	9,62	20,97
700	14,7	15,1	7,71	8,84	9,75	22,06

Conclusion

The results obtained so far improve the knowledge of the mechanical properties of the cesium uranate. Both values of thermal expansion and deformation under compression can be used in the modelling of pellet-cladding mechanical interaction.
It can be anticipated that the plasticity of cesium uranate is high enough to ensure a more favourable distribution of the mechanical stresses.

References

[1] Touloukian, Kirby, Taylor, Desai, Thermal Expansion, IFI/PLENIUM-N.Y:-Washington, vol. 12 (1975) 77

[2] Touloukian, Kirby, Taylor, Lee, Thermal Expansion, IFI/PLENIUM-N.Y:-Washington, vol. 13 (1975) 76

[3] Touloukian, Kirby, Taylor, Lee, Thermal Expansion, IFI/PLENIUM-N.Y:-Washington, vol. 13 (1977) 413

Leaching Test of the Inner Side of Zircalloy Cladding Material

Introduction

The leaching of the components resulting from the fuel-cladding chemical interaction has been studied from samples prepared from 5 mm thick cross sections. The examination of the inner side of the cladding, after fuel removal, revealed a layer of reaction products in the order of a few tens of a micrometer. In order to characterise the components before and after each leaching step, the following operations were performed:

- examination of the original sample by SEM-EDX
- leaching of the sample with cold water for 1 day
- leaching at 100 °C for different test durations in soxhlet equipment (reflux ± 1 ml / min)
- examination of the leached specimen by SEM-EDX
- selective leaching with nitric acid of different molarity
- examination of the digested sample by SEM-EDX
- complete dissolution of the layer by HF/HNO_3 digestion at 200 °C in autoclaves
- similar dissolution of the corresponding fuel
- analysis of the leachates and the dissolver solution by ICP-MS

SEM examination of the unleached sample by SEM and EDX

From the SEM examinations the fuel-cladding chemical interaction (FCCI) is compared for the three successive layers: a ZrO_2 layer with a modular structure, an intermediate layer resulting from the interdiffusion of Zr into the fuel and finally an outer layer of UO_2. The intermediate layer appears as a microcrystalline glassy compound (Figs. 4.28, 4.29).

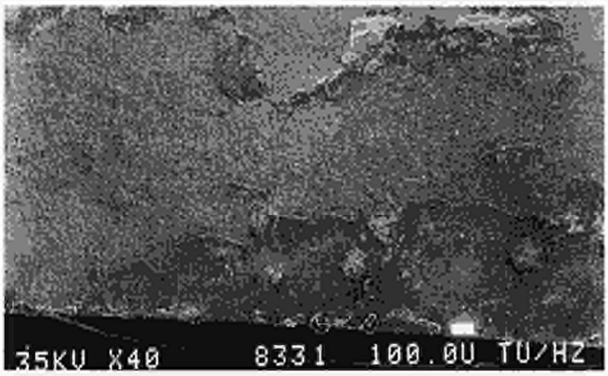

Fig. 4.28 Cladding inner surface (magnification 40x)

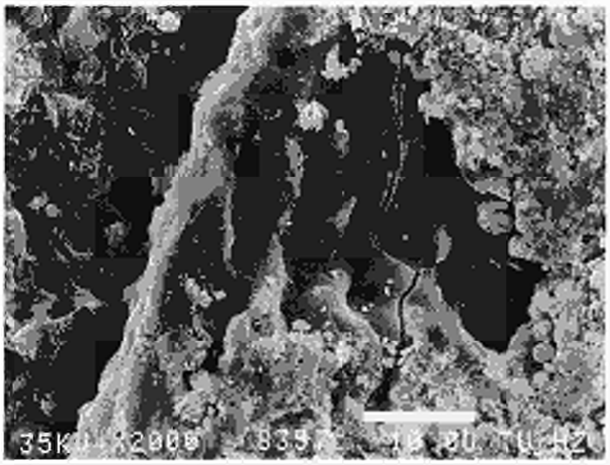

Fig. 4.29 Cladding inner surface (magnification 720x)

EDX analyses of this intermediate layer indicate as main elements Zr (60 - 90 %) and U (10 - 40 %). These elements are associated with large amounts of Cs (up to 40 %) and Te (up to 20 %).

Leaching test of the inner side of the cladding with distilled water and digestion with HNO_3

A cladding specimen was leached in a soxhlet extractor (100 °C) up to 4 weeks; intermediate examinations were carried out after 1 day and 3 weeks. A second specimen was treated with 50 ml of nitric acid in series with 0.1 M HNO_3 and with 1 M HNO_3 for 1 day respectively.

From the inventories of the fuel and the layer stuck to the inner side of the cladding, a comparison of the corresponding leach rates can be made.

The complete dissolution of the FCCI layer and of the corresponding fuel matrix (35 mg) was made by HF/HNO_3 digestion at 200 °C in autoclaves. Tab. 4.18. shows the quantitative results obtained by ICP-MS. After normalisation to the same amount of material, a ratio Rn cladding layer/fuel can be calculated.

Tab. 4.18 Quantitative results (mg) of the analysis of the dissolver solutions of fuel and cladding obtained by ICP-MS

element	FCCI layer amount	fuel amount	Rn FCCI layer / fuel
Rb	0.010	0.009	2.34
Sr	0.022	0.015	2.81
Mo	0.000	0.000	1.97
Tc	0.103	0.104	1.50
Ru	0.021	0.028	0.74
Rh	0.030	0.080	1.58
Pd	0.011	0.013	1.58
I	0.064	0.080	0.60
Te	0.008	0.006	2.77
Cs	0.224	0.167	2.67
Ba	0.163	0.136	2.37
La	0.076	0.055	2.77
Ce	0.158	0.142	2.20
Pr	0.083	0.087	1.90
Nd	0.259	0.294	1.75
Sm	0.094	0.083	2.25
Eu	0.016	0.015	2.16
Gd	0.022	0.021	2.11
Np	0.013	0.021	1.23
U	12.496	26.429	0.94
Pu	0.288	0.247	2.32
Am	0.023	0.016	2.75
Cm	0.005	0.003	4.21
total	14.192	28.176	1.00

* normalised with respect to the same amount of material (Zr not included)

Rn values >1 correspond to an enrichment of the corresponding element in the cladding layer, values < 1 mean depletion (only observed in the case of Ru). Unfortunately these results can only give a global answer corresponding to the three successive layers observed in the FCCI layer by SEM but no specific information concerning the intermediate layer is obtained.

As expected an increased leaching in nitric acid compared to water leaching (n.b. that the duration for the acid digestion was only 1 day) is observed. About 1.5 % of the layer was leached after 1 month in water (dynamic conditions) and after two days in nitric acid (static conditions) about 7 %, i.e. ca. 5 times more. This factor is valid for all fission products analysed but increases in the case of Np and especially I, Pu and Am up to 10 to 60 times. This could mean, that these elements are present in a water-insoluble form.

Based on the cladding inventory, the leach-rate (in l/m^2 d) of the cladding can be compared to the leach rates of a MOX and a UO_2 fuel (Tab. 4.19).

Tab. 4.19 Leach rates in l/m^2 d of the cladding in comparison to those of a MOX and an UO_2 fuel

element	clad-soxhlet 1 month	MOX 1 month	UO_2 1 month
Rb	7.02	15.74	18.97
Sr	21.87	4.49	44.03
Zr		4.63	7.68
Mo	21.54	18.13	33.15
Tc	7.26	2.04	8.74
Ru	0.93	0.73	1.33
Rh	2.29	0.58	0.87
Pd	1.12	1.73	1.73
Te	3.74	n.m.	n.m.
Cs	30.45	37.5	97.88
Ba	19.71	4.98	32.17
La	4.00	0.75	4.80
Ce	8.36	0.41	4.00
Nd	5.06	0.27	1.07
Np	3.37	1.31	1.24
U	6.90	0.87	1.54
Pu	0.58	0.09	0.23
Am	1.09	0.91	0.28
total	7.39	0.91	1.78

For fission products the values lay in-between those of MOX and UO_2. Only for actinides the leach rates of the cladding piece are significantly higher.

SEM-EDX examination after leaching with distilled water and digestion with HNO_3

After leaching in water the morphological aspect of the sample has not changed except that some crystals (probably uranate formed with the humidity during storage of the sample), which were observed on the fuel surface before leaching, have disappeared. In the EDX spectrum Cs has disappeared, the Te and also the U content in the intermediate layer are lower, up to 10% (20 % before leaching) for Te and up to 15% (10-40% before leaching) for U.

After digestion in nitric acid, especially the fuel became porous, and plenty of cracks were formed. Also the intermediate layer shows degradation in form of holes in the micron range (Fig. 4.30).

Cs is again no longer detected and U and Te values are still lower in the layer compared to water leaching.

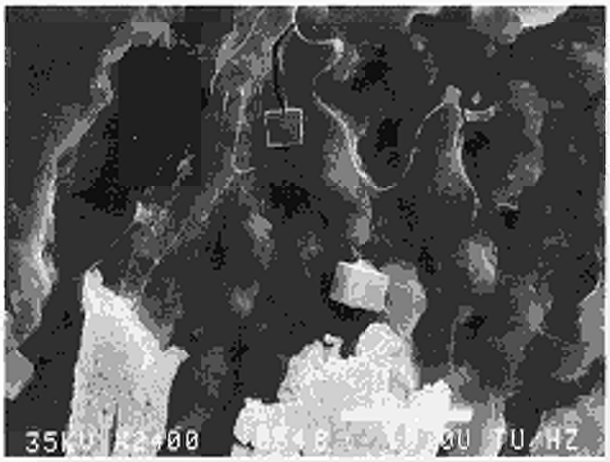

Fig. 4.30 Cladding inner surface after digestion in nitric acid (magnification 240x)

Conclusions

The layer formed during irradiation at the interface between the cladding and the fuel has a glassy aspect and should have grown in from the inner surface of the cladding. It looks as if this layer has a nodular structure towards the fuel.

SEM-EDX examination showed that the layer is mainly composed of Zr (60-90%) and U (10-40%) associated with Cs (up to 40%), Ba (up to 30%) and Te (up to 20%). The layer could be a ZrO_2 matrix loaded with U and also the most important fission products.

A complete dissolution of the layer by HF/HNO_3 digestion at 200 °C in an autoclave, revealed that in comparison to the bulk fuel, the concentration of the main fission products and transuranium actinides is 2 to 3 times higher than in the matrix and results from the neutronic resonance adsorption in the first 100 µm at the fuel pellet periphery.

Leaching of the cladding at 100 °C for different test durations in soxhlet equipment (reflux ±1ml/min) showed, that the leach rate in water decreases considerably with time and is after 1 month similar to that of the bulk fuel. For fission products the leach rates lie between those of MOX and UO_2 fuel. Only for the actinides the leach rates of the cladding piece are 3 to 4 times higher and allow to anticipate the existence of these elements as a component or with a valency promoting this dissolution.

Investigation of the Np-Zr and U-Np-Zr systems

Introduction

The investigation of the U-Zr-Np ternary system was undertaken in the frame of the work for the determination of the properties of U-Pu-Zr metallic fuels containing minor actinides (Cm, Np and Am) and rare earth elements (Y, Nd and Ce) [1-3]. These alloys are foreseen for irradiation tests aimed at studying the transmutation of the long-lived elements Am, Np and Cm into short-lived fission products in order to reduce the long-term hazard of high level waste storage [4, 5].

No information existed concerning the influence of additions of Zr to the binary low-melting temperature U-Np alloys. Moreover, only U-Np [6, 7] and U-Zr [8-11] of the three binary systems at the boundary of the ternary U-Zr-Np system are well known, but very little has been published about Np-Zr alloys [12].

Starting materials and experimental conditions

The alloys used for this investigation were prepared by the arc melting procedure of exactly weighed amounts of U, Zr and Np. The purity of the metals was better than 99.95 wt%. Composition inhomogeneities were removed by turning the bead over and remelting.

The solid-state transformations of the alloys were determined by dilatometry using rods, 3 mm in diameter and about 7 mm in length, prepared by casting. The melting points were determined by means of a vertical dilatometer using small spheres about 3 mm in diameter.

The structure of the specimens at several temperatures was obtained by annealing and quenching. Annealings were carried out using specimens enclosed in quartz capsules and quenching after annealing was done by ejecting the capsule from the furnace by means of a pneumatic system, and breaking it in water. No reaction between the alloys, quartz and water was observed. After annealing and quenching the specimens were submitted to microscopic examination and electron probe microanalysis.

Results and discussion

The Np-Zr system

The solid-state transformation temperatures of three alloys of Np and Zr were determined by dilatometry. Only one transformation at about 530 °C was detected for the specimen with 50 wt% of Zr, whereas the specimens containing 20 and 80 wt% underwent two transformations. The three alloys have also been annealed for one week and then quenched in water from 520, 595 and 700 °C. After quenching from 520 °C two phases were detected in samples containing 20 and 80 wt% Zr and one phase in the specimen containing 50 wt% Zr. Two phases were detected in the samples containing 80 wt% Zr after quenching from 595 and 700 °C, whereas the specimens with 20 and 50 wt% Zr were single phase.

The composition of the phases were determined by electron probe microanalysis. The results obtained were used to draw the tentative Np-Zr phase diagram represented in Fig. 4.31. This shows that Np is partially soluble in α-Zr, the maximum amount being about 17 wt% at 520°C, and is soluble in all proportions in β-Zr. The solubility value of Zr in β-Np is probably below 10 wt% at 530 °C. One intermediate phase probably extends from 42 to 58 wt% Np and is stable up to 530 °C and then transforms into the high temperature γ-phase. The δ-phase extends from about 42 to 58 wt% Np.

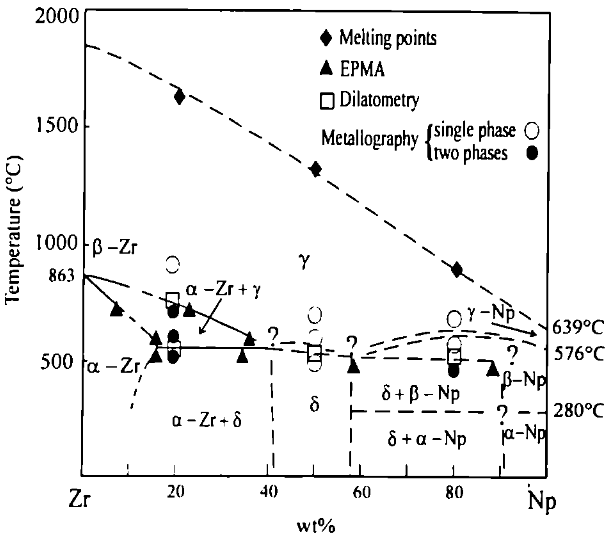

Fig. 4.31 Tentative Np-Zr phase diagram

The U-Zr-Np system

The solid state transformation temperatures of a series of U-Zr-Np alloys were measured by dilatometry. The dilatometric curves show that the specimens underwent phase transformations at temperatures between 500 and 600 °C and between 600 and 700 °C. At temperatures above 700 °C no further transformations were observed besides that caused by melting. Metallographic analysis of the specimens quenched from 520, 595 and 700 °C showed that the specimens were either single or two phases depending on the temperature and composition. The composition of these phases was determined by electron probe microanalysis. Isothermal sections of the U-rich corner of the ternary system covering the temperature range 520 to 700 °C have been constructed using the data obtained by dilatometric measurements, electron probe microanalysis, by metallographic examination and by combining the three boundary binary systems. (see Fig. 4.32 and 4.33) For the identification of the phases of the ternary system the same nomenclature of the common phases of the limiting binary systems was used. The transformation temperatures of the ternary alloys were lower than those of the corresponding transformations determined for the binary U-Zr and U-Np systems. The solubility of Zr in α- and β-U was favourized by the addition of Np; nevertheless, the maximum value was below 12 wt% at 700 °C. The values of the melting points of the samples ranged between 955 and 1170 °C depending on composition. Above 900 °C the alloys were single phase and melting occurred congruently.

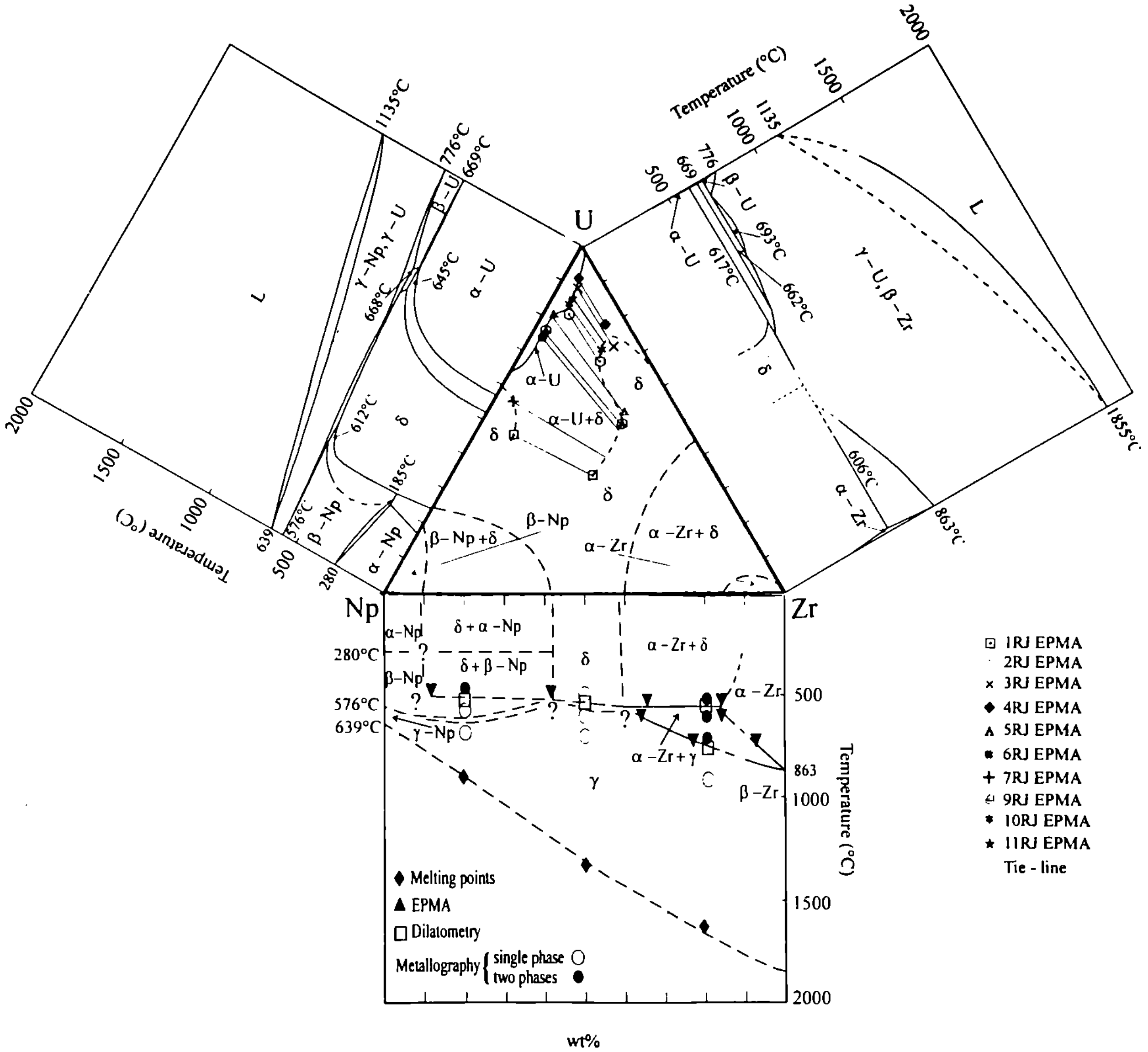

Fig. 4.32 System U-Zr-Np. Isothermal section at 520 °C. The points represent the compositions of the different phases and matrices determined by EPMA.

Conclusion

The Np-Zr system is characterized by the complete mutual solubility of β-Zr and γ-Np in the range of temperatures up to the melting point. The solubility of Np in α-Zr decreases with decreasing temperature. Zr and Np form an intermediate phase (called δ) stable from room temperature to about 530 °C.

The investigation of the U-rich corner of the U-Zr-Np ternary diagram shows that the γ-phase is stable above 700 °C and that the solubility of Zr in the α-and β-phases of the binary U-Np compounds is limited to a maximum of 11 wt%. No ternary compounds were found.

References

[1] L. Koch, K. Richter and C. Sari, Trans. Amer. Nucl. Soc., 64 (1991) 551

[2] M. Kurata, T. Inoue, C. Sari and J.C. Spirlet, Trans. Amer. Nucl. Soc., 64 (1991) 552

[3] M. Kurata, T. Inoue and C. Sari, J. Nucl. Mater. in press

[4] L. Koch, J. Less-Common Met., 122 (1986) 371

[5] S. Pilate, "Some aspects of the transmutation of minor actinides in Fast Reactors", Proc. of the workshop on partitioning and transmutation of minor actinides, Karlsruhe 16-18 October 1989, EUR-13347

[6] P.G. Mardon and J.H. Pearce, J. Less-Common Met., 1 (1959) 467

[7] M.W. Chase, Bull. Alloys Phase Diagrams, 4 (1), (1983) 124

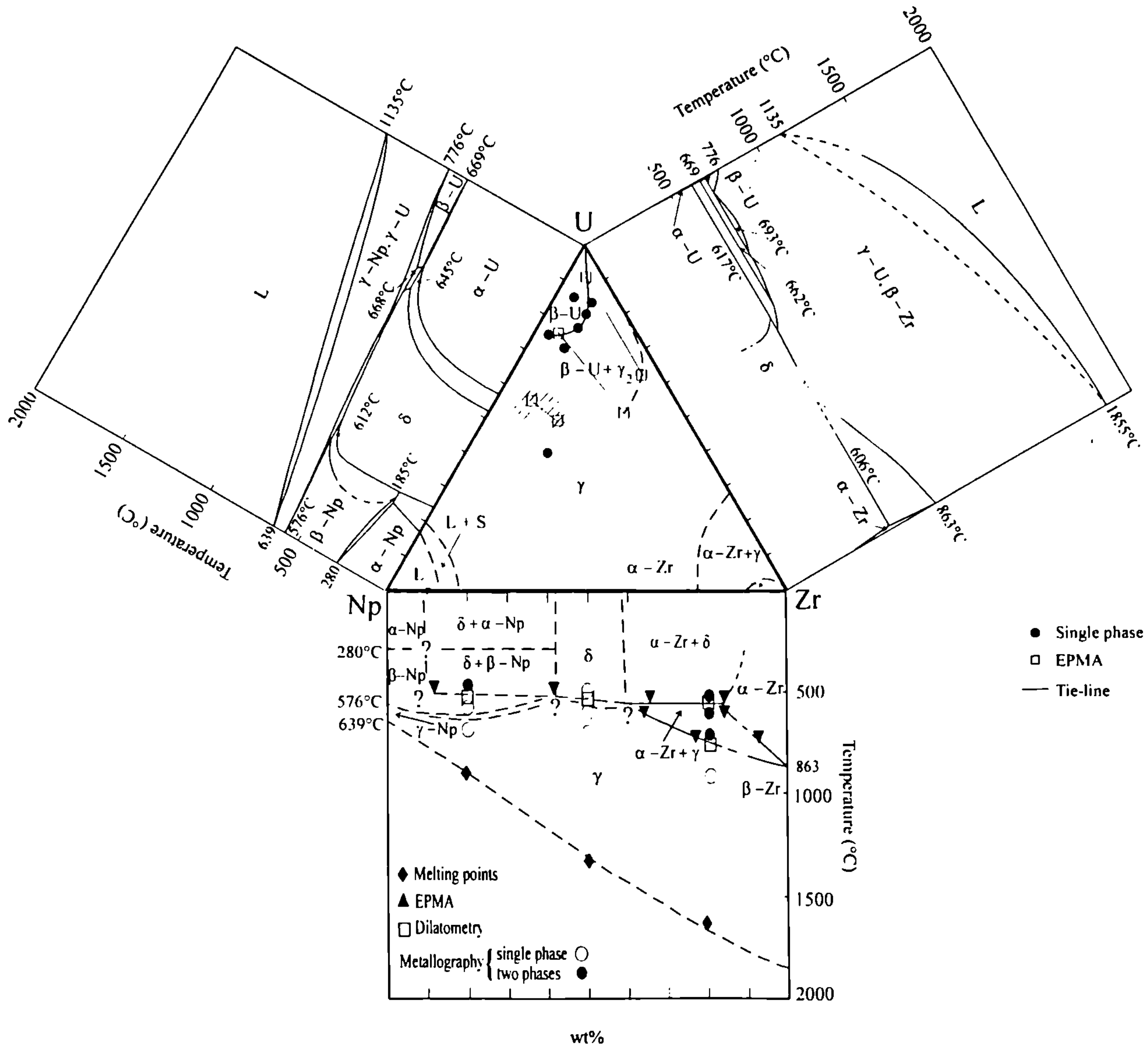

Fig. 4.33 System U-Zr-Np. Isothermal section at 700 °C. The □ points represent the compositions of the different phases and matrices determined by EPMA. The ● points represent single phase structures.

[8] D. Summers-Smith, J. Inst. Met., **83** (1955) 277

[9] E.R. Boyko, Acta Cryst., **10** (1957) 712

[10] A.N. Olden and W.E. Seymour, Trans. A.I.M.E., **209** (1957) 515

[11] S.T. Ziegler, "The Uranium Rich End of the Uranium-zirconium system" ANL-6065 (1962)

[12] J.K. Gibson and R.G. Haire, J. Nucl. Mater. 201 (1933) 225

1.5 Actinide Research

Introduction

The central objective of actinide research in ITU and in its numerous collaborations is the elucidation of the electronic structure of actinide metals and actinide compounds, in particular of the behaviour of the 5f electrons. The dualism between localized and itinerant characteristics as it is particularly clearly demonstrated in the actinide series, is a key problem in these studies.

These goals are approached by experiment and theory. Experimental studies are either selective investigations on the basis of theoretical or other experimental information which indicates that a particular material and method are promising, or they can involve a systematic approach to a whole class of compounds. Theoretical calculations can indicate to the experimentalist where he can expect to find important results, and theory can on the other hand try to combine experimental evidence from different sources into a general picture. An important basis for the experimental study is the preparation of polycrystalline and single crystal samples of actinides of high specific activity, and their careful characterization by x-ray diffraction, chemical, and electron microprobe analysis. As far as possible, study of physical properties concentrates on the most interesting of the available actinide compounds, and an attempt is made to study them by several different methods to obtain a maximum of information on their physical behaviour.

Preparation and Characterization of Actinide Metals and Compounds

Research on actinide-containing materials requires new and well characterized samples. To respond to the request of the international Actinide Community, work on preparation, crystal chemistry and physical properties of large families of isostructural compounds continued during the reporting period. Progress in the following groups of materials will be reported:

- Magnetic compounds with the $ThMn_{12}$ structure
- Compounds with the 1:13 composition
- Compounds with the 1:1:1 composition
- Compounds with the 2:2:1 composition

In addition, a study on binary technetium alloys was carried out.

Characterization by Mössbauer spectroscopy of compounds with the 1:2:3 composition, $NpNi_2Al_3$, $Np_{0.5}U_{0.5}Pd_2Al_3$ and $Np_{0.3}U_{0.7}Pd_2Al_3$ was performed and results are reported below in the paragraph on Mössbauer studies; the investigation of the AnX_3 compounds with the $AuCu_3$ structure type was continued by the preparation and characterization of $NpAl_3$, $NpGa_3$, $NpIn_3$, $Np(Ge_{0.05}Sn_{0.95})_3$, $NpSn_3$, $Np(Ge_{0.1}Sn_{0.9})_3$, $Np(Ge_{0.2}Sn_{0.8})_3$, $NpGe_3$ and $Np(Ge_{0.5}Sn_{0.5})_3$ for which some results are summarized below in the paragraph on Mössbauer studies. New samples of USn_3, $UIn_3U(Sn_xIn_{1-x})_3$, $U(Ge_xGa_{1-x})_3$ and UGe_3, were prepared for μ-SR studies.

The compounds prepared and encapsulated for physical property measurements during 1993 are listed in Tab. 5.1.

The new intermetallic compounds prepared and characterized in the reporting period are listed in Tab. 5.2 and 5.3.

Magnetic compounds of the $ThMn_{12}$ structure type

Continuing the work started during 1992 in cooperation with the Chemical Department of the ICEN-LNETI in Portugal, to study uranium intermetallic compounds with the $ThMn_{12}$-type structure, the $UFe_{12-x}Ge_x$, $UFe_{12-x}Mo_x$ and $UFe_{12-x}Ru_x$ systems were explored in detail. The samples were prepared by arc or induction melting of stoichiometric amounts of the pure elements, examined by SEM-EDS, and characterized by X-ray diffraction.

In the $UFe_{12-x}Ge_x$ system a congruent melting compound UFe_6Ge_6 was found. This composition was confirmed by single crystal X-ray diffraction and observed to crystallize in a hexagonal YCo_6Ge_6-type structure, space group P6/mmm, with cell parameters a = 512.7(1) pm and c = 405.1(1) pm. Magnetization was measured in single phase polycrystalline UFe_6Ge_6 samples in the temperature range 4-400K and under fields up to 5 Tesla. At 322(5)K there is a small anomaly in the M(T) dependence suggesting an antiferromagnetic transition. Mössbauer measurements confirm that the iron atoms become magnetically ordered at 322 K. At 230(10) K the system under-

Tab. 5.1 Samples prepared, characterized and encapsulated in 1993 for the indicated measurements.

Resistivity	CEN Grenoble	NpSb	M-SC
Hall Effect	CEN Grenoble	NpSb NpTe NpSe	M-SC M-SC M-SC
Mössbauer Spectroscopy	CEN Grenoble	NpTe $Np_xY_{1-x}Pd_3$ x=0.75,0.5,0.25 Np_2T_2Sn T= Co, Ni, Rh, Pd, Pt, Ru $NpAl_2$	M-SC AcM-P AcM-P AcM-P
	TU München	$NpAl_3$ $Np(Sn_{1-x}Ge_x)_3$ x=0.05,0.10,0.50 $NpBe_{12}$ $NpBe_{13}$ $NpBe_{14}$ $Np(C_{32}H_6N_8)_2$	AcM-P AcM-P AcM-P AcM-P AcM-P P
Neutron Scattering	CEN Grenoble	U_2Ni_2Sn U_2Pt_2Sn	Cz-SC Cz-SC
	Los Alamos National Laboratory	U_2Pd_2In U_2Pd_2Sn UCoGa	AcM-P AcM-P AcM-P
X-Ray Scattering	Brookhaven National Laboratory	PuSb PuBi	M-SC M-SC
Specific Heat Magnetism	Univ. Amsterdam	U_2T_2Sn (T = Rh, Pd, Ir, Ru) U_2T_2In (T= Ni, Pd, Pt) U_2Ru_2Sn U_2Ni_2Sn U_2Ir_2Sn	AcM-P AcM-P AcM-P AcM-P AcM-P
μ-Sr	TU München	UO_2 UGe_3 USn_3 UIn_3 $U(Ge_xGa_{1-x})_3$ x=0.25,0.5,0.75 $U(In_{0.4}Sn_{0.6})_3$	AcM-P AcM-P AcM-P AcM-P AcM-P AcM-P

AcM = Arc Melting M= Mineralisation SC: Single Crystals
P= Powders, Polycrystalline sample Cz= Czochralsky Method

Tab. 5.2 Crystallographic data of new intermetallic compounds.

Compounds	Space Group	Structure Type	Lattice Parameters (pm)	Z
$(Np_{0.75}Y_{0.25})Pd_3$*	Pm3m	$AuCu_3$	409.0(1)	1
$(Np_{0.5}Y_{0.5})Pd_3$*	Pm3m	$AuCu_3$	408.1(2)	1
$(Np_{0.25}Y_{0.75})Pd_3$*	Pm3m	$AuCu_3$	407.7(1)	1
$Np(Sn_{0.5}Ge_{0.5})_3$*	Pm3m	$AuCu_3$	442.5(1)	1
$Np(Sn_{0.9}Ge_{0.1})_3$*	Pm3m	$AuCu_3$	459.5(1)	1
$Np(Sn_{0.95}Ge_{0.05})_3$*	Pm3m	$AuCu_3$	406.8(1)	1
$NpBe_{12}$	Fm3c	$NaZn_{13}$	1025.6(1)	8
$NpBe_{13}$	Fm3c	$NaZn_{13}$	1025.5(1)	8
$NpBe_{14}$	Fm3c	$NaZn_{13}$	1025.6(1)	8
Np_2Pd_2In*	P4/mbm	U_3Si_2	764.5(2) 380.0(1)	2
Np_2Co_2In*	P4/mbm	U_3Si_2	733.1(1) 350.7(1)	2
Np_2Ir_2In*	P4/mbm	U_3Si_2	756.9(2) 362.4(1)	2
Np_2Ru_2Sn*	P4/mbm	U_3Si_2	742.4(2) 362.6(1)	2
U_2Ru_2Sn*	P4/mbm	U_3Si_2	749.7(2) 354.2(1)	2
U_2Ni_2Sn*	P4/mbm	U_3Si_2	726.3(1) 369.1(1)	2
U_2Pt_2Sn*	P4/mbm	U_3Si_2	749.7(2) 354.2(1)	2
U_2Co_2Sn*	P4/mbm	U_3Si_2	728.9(1) 350.5(1)	2
U_2Rh_2Sn*	P4/mbm	U_3Si_2	752.4(1) 363.0(1)	2
$TcAl_2$*	C2/m	$TcAl_2$	1297.6(1) 329.6(1) 649.3(2) ß= 112.13°(2)	6
Tc_4Al_{11}*	P-1	Tc_4Al_{11}	515.7(2) 898.1(3) 515.9(2) 90.17°(2) 99.73°(2) 105.17°(2)	2

*From X-Ray Single Crystals analysis

Crystallographic data of new intermetallic compounds.

Tab. 5.3 Lattice parameters, atomic positions and interactinide distance of An_2T_2X compounds obtained up to now.

Compound An_2T_2X	Lattice parameters		Atomic position An 4h x, x+0.5,0.5 T 4g y, y+0.5,0 X 2a 0,0,0		Interactinide distance	
	a (pm)	c (pm)	x	y	$d_{An\text{-}An'}^{(1)}$	$d_{An\text{-}An'}^{(2)}$
$U_2Ru_2In^*$	750.5(3)	354.5(1)	-	-	-	-
$U_2Co_2In^{**}$	736.1(2)	343.1(1)	0.1695	0.3697	343.1	353.1
$U_2Rh_2In^{**}$	755.3(2)	360.5(1)	0.1707	0.3667	360.5	364.7
$U_2Ir_2In^*$	759.6(9)	358.2(5)	-	-	-	-
$U_2Ni_2In^{**}$	737.4(2)	357.2(2)	0.1727	0.3761	357.2	360.2
$U_2Pd_2In^{**}$	763.7(1)	375.2(1)	0.1744	0.3716	375.2	376.6
$U_2Pt_2In^{**}$	765.4(2)	372.5(1)	0.1727	0.3701	372.5	373.8
$U_2Fe_2Sn^*$	730.0(2)	344.5(1)	-	-	-	-
$U_2Ru_2Sn^{**}$	748.2(2)	355.8(1)	0.1683	0.3656	355.8	356.2
$U_2Co_2Sn^{**}$	728.9(1)	350.5(1)	0.1713	0.3706	350.5	353.1
$U_2Rh_2Sn^{**}$	752.4(1)	363.0(1)	0.1740	0.3702	363.0	370.3
$U_2Ir_2Sn^{**}$	756.6(1)	360.1(1)	0.1732	0.3692	360.1	370.7
$U_2Ni_2Sn^{**}$	726.3(1)	369.1(1)	0.1743	0.3756	369.1	358.0
$U_2Pd_2Sn^{**}$	760.3(2)	378.5(1)	0.1757	0.3726	378.5	377.8
$U_2Pt_2Sn^{**}$	767.0(5)	369.8(2)	0.1728	0.3703	369.8	374.8
$U_2Co_2Al^*$	713.6(6)	346.3(3)	-	-	-	-
$U_2Co_2Ga^*$	707.6(5)	347.6(3)	-	-	-	-
$U_2Ni_2Zn^*$	725.2(5)	368.8(2)	-	-	-	-
$Np_2Co_2In^{**}$	733.1(1)	350.7(1)	0.1693	0.3702	350.7	351.1
$Np_2Rh_2In^{**}$	752.4(2)	364.9(1)	0.1687	0.3657	364.9	359.4
$Np_2Ir_2In^{**}$	756.9(2)	362.4(1)	0.1688	0.3655	362.4	361.3
$Np_2Ni_2In^{**}$	736.4(2)	359.0(1)	0.1722	0.3747	359.0	358.6
$Np_2Pd_2In^*$	764.5(2)	380.0(1)	0.1734	0.3716	380.0	374.9
$Np_2Pt_2In^{**}$	767.5(2)	371.6(2)	0.1718	0.3698	371.6	372.8
$Np_2Ru_2Sn^{**}$	742.4(2)	362.6(1)	0.1688	0.3656	362.6	354.5
$Np_2Co_2Sn^{**}$	726.2(2)	356.5(1)	0.1723	0.3715	356.5	356.5
$Np_2Rh_2Sn^{**}$	750.2(3)	366.8(1)	0.1717	0.3667	366.8	364.3
$Np_2Ni_2Sn^{**}$	729.3(2)	366.1(1)	0.1740	0.3759	366.1	358.9
$Np_2Pd_2Sn^{**}$	762.2(4)	381.6(2)	0.1753	0.3706	381.6	377.9
$Np_2Pt_2Sn^{**}$	765.6(2)	373.0(1)	0.1737	0.3705	373.0	375.8

** on single crystal, *on polycrystalline sample goes a ferromagnetic-like transition. No reordering of the iron atoms can be observed from the Mössbauer spectra suggesting that the second transition corresponds to ordering of the U-sublattice [1].

In the $UFe_{12-x}Mo_x$ system, no congruent melting compound was found. However, the $ThMn_{12}$-type phase is present, reaching 80% of the material for $UFe_{9.9}Mo_{1.6}$ compositions. By long term annealing (~ 2 weeks at 1200°C) of a sample with nominal composition $UFe_{9.9}Mo_{1.6}$ it was possible to obtain an almost single phase material with secondary phases less than 5%. A small single crystal was separated from this material and the cell parameters were determined by x-ray diffraction (a = 848.2(1) pm, c = 474.5(1) pm). ^{57}Fe Mössbauer studies indicate a paramagnetic state at room temperature with ordering of yet unknown nature between 160-200 K.

In the $UFe_{12-x}Ru_x$ system no $ThMn_{12}$-type structure or other low uranium content phases were found.

High temperature A.C. susceptibility measurements were performed in a single phase $UFe_{9.2}Si_{1.8}$ polycrystalline sample previously identified as a congruent melting compound. A transition reminiscent of ferromagnetic ordering was observed at 650 (10)K. Single crystals of this composition were grown by the Czochralski method [2], oriented and prepared for the measurement of physical properties.

In the UFe_4Al_8 single crystals previously grown, magnetization and magnetoresistance measurements, parallel to the c axis, have been made in the temperature range 4-300 K and under fields up to 8 Tesla (Fig. 5.1). The $ThMn_{12}$-structure type was confirmed by neutron diffraction experiments performed on UFe_4Al_8 single crystal at Risø. The cell parameters were found to be a = 874.0(1) pm and c = 503.6(1) pm, R(F) = 2.18%. All the iron was found to be in the 8f position, within the experimental error. In this system it was observed that the ab plane is of easy magnetization and c is the hard axis. Neutron experiments are under progress.

References

[1] A.P Gonçalves, J.C. Waerenborgh, G. Bonfait, A. Amaro, M.M. Godinho, M. Almeida and J.C. Spirlet, J. Alloys Comp., in press

[2] A.P Gonçalves, M. Almeida, C.T. Walker, J. Ray and J.C. Spirlet, Mater. Lett., in press.

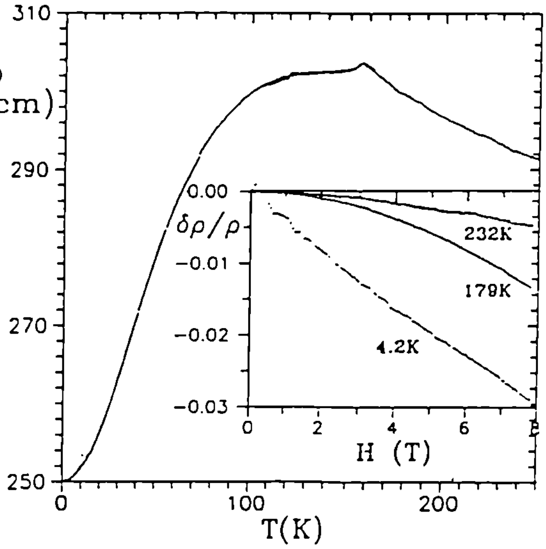

Fig. 5.1 Resistivity and magnetoresistance curves of UFe_4Al_8.

Compounds with the 1:13 composition

Extended studies of the physical properties of $NpBe_{13}$ have been planned and are a subject of interest for the international Actinide Community. The magnetic properties of this compound are sensitive to the Be content and thus preparation of high quality samples is of utmost interest.

As reported in TUAR-92, Mössbauer measurements of a sample produced in Los Alamos revealed two phases at 1.3 K. These phases exhibit different magnetic hyperfine interactions. Only one of the two phases orders magnetically. According to reference [1], the existence of a magnetic phase is dependent on the Be content. To study this question, we have prepared and characterized three new samples with nominal stoichiometry $NpBe_{12}$, $NpBe_{13}$ and $NpBe_{14}$. X-ray diffraction performed on polycrystalline samples shows that those three samples have the same structure and lattice constant (Tab. 5.2) within experimental accuracy. Characterization by means of Mössbauer spectroscopy shows for all samples a magnetic splitting below 2.5 K. However, each spectrum had to be analysed with two slightly different magnetic hyperfine fields. The ordering temperatures were nearly equal. The previous observation of two different magnetic phases at 1.3 K remains unexplained. According to our preliminary results, the Be content does not seem to play a drastic role in magnetic properties of $NpBe_{13}$. The serious deviation in magnetic properties of three different batches of nominally the same composition $NpBe_{13}$, made in Beer Sheva, Los Alamos and in the present work seems to indicate that slight crystal defects or strains, which cannot be observed by X-ray diffraction, exert an effect. Further characterizations and studies of long time annealed samples are necessary to reach a better understanding of the properties of $NpBe_{13}$.

Reference

[1] J. Gal, F.J. Litterst, W. Potzel, J. Moser, U. Potzel, G.M. Kalvius, S. Fredo and S. Tapuchi, Phys. Rev. **B 36** (1987) 2457

Compounds with the 1:1:1 composition

In the reporting period, the main efforts for this family of compounds were on the synthesis and study of single crystals. Single crystals of UCoGa, UNiGa and UPdGa were obtained by the Czochralski method and by mineralisation.

Magnetic properties of UCoGa single crystal show a small ordered moment of 0.78 μ_B/U, T_C= 47 K, and a large magnetocrystalline anisotropy [1]. However, there were some doubts about the nature of the ground state. Besides the ferromagnetic ground state, in which the hysteresis loop is affected by pinning of very narrow domain walls, we could not exclude antiferromagnetism with small critical field of moment re-orientation. Therefore we undertook neutron diffraction experiments both on UCoGa single crystals and powder (both prepared in ITU), which proved that the ground state is really ferromagnetic.

The very complicated magnetic phase diagram of UNiGa [2] in which details can be dependent of the degree of perfection of the crystal, was studied. Besides a crystal of UNiGa prepared in the Van der Waals-Zeeman Laboratory, University of Amsterdam, a new single crystal was produced in our laboratory by a zone melting technique. SQUID magnetic measurements showed only a minor difference in properties of the two crystals. Essentially there is only an influence on the width of the hysteresis loop at helium temperature, which is affected by crystal imperfections. The range of stability of high-temperature phases seems to be identical for both crystals. Further experiments are still under progress.

All this work was a subject of collaborative research between ITU Karlsruhe, Charles University, Prague, and Van der Waals-Zeeman laboratory, University of Amsterdam. The neutron work was done in collaboration with Los Alamos National Laboratory.

References

[1] H. Nakotte, F.R. de Boer, L. Havela, P. Svoboda, V. Sechovsky, Y. Kergadallan, J.C. Spirlet and J. Rebizant, J. Appl. Phys. **73** (1993) 6554

[2] V. Sechovsky, L. Havela, F.R. de Boer, E. Brück, T. Suzuki, S. Ikeda, S. Nishigori and T. Fujita, Physica **B 186-188** (1993) 775

Compounds with 2:2:1 composition

In TUAR-92 we first reported on the synthesis and preliminary physical property studies of a new family of compounds of the type An_2T_2X. Those isostructural compounds allow systematic study that can contribute to better understanding of the behaviour of 5f electrons. In 1993 we extended our research to An_2T_2X with An= U or Np, T= Fe, Co, Ni, Ru, Rh, Pd, Ir, Pt and X= In, Sn, Ga, Al, in order to determine the limits of stability of 2:2:1 phases with various transition metals and metalloids and to improve the quality of the samples by new methods of synthesis or by thermal treatment. We achieved single crystal growth of U_2Ni_2Sn and U_2Pd_2Sn by the Czochralski method and by a zone melting technique, we continued the characterization of all samples obtained in polycrystalline or single crystal form, and performed physical property studies.

Polycrystalline samples were prepared by arc melting stoichiometric amounts of metals under purified argon atmosphere, checked by metallography and X-ray diffraction on powder, the structure determinations on single crystals were performed on an Enraf-Nonius CAD-4 four circle diffractometer.

All compounds investigated were found to crystallize in the U_3Si_2-type (space group P4/mbm). The atomic positions are the following: An in 4h (x,x+0.5,0.5), T in 4g (y,y+0.5,0) and X in 2a (0,0,0) with x and y of average value respectively 0.17 and 0.37, depending on the various constituents. Tab. 5.3 gives the lattice parameters, atomic positions and An-An distances of all compounds obtained.

For X= In or Sn and T belonging to the Co and Ni group, all U_2T_2X compounds were obtained in single phase samples, however U_2Ir_2In presents a second phase UIr that thermic treatment could not eliminate. For U_2Pt_2Sn the X-ray diffraction pattern presents some superlattice peaks which are not belonging to the U_3Si_2 structure type. In the case of the Fe group, U_2Ru_2Sn, U_2Ru_2In and U_2Fe_2Sn only could be obtained.

Structural and basic magnetic properties were investigated for An = U and Np (using ^{237}Np Mössbauer spectroscopy). For U compounds we have found out that an onset of magnetic ordering can be observed when moving to the right in the long transition metal series, and Sn-containing compounds have a stronger tendency to magnetism than the respective In-compounds. Thus ordering (exclusively the AF type) was up to now found in U_2Ni_2Sn, U_2Ni_2In, U_2Rh_2Sn, U_2Pd_2Sn, U_2Pd_2In and U_2Pt_2Sn, with T_N from 14 K to 41 K, whereas U_2Co_2Sn, U_2Co_2In, U_2Rh_2In, U_2Pt_2In and U_2Ir_2Sn present a fundamental state characterized by Pauli paramagnetism. All Np compounds studied up to now were found magnetic (Np_2Co_2In, Np_2Ni_2In, Np_2Rh_2In, Np_2Pd_2In, Np_2Pt_2In), but Np magnetic moments increase with a particular d-band filling, which gives the impression that the 5f-d hybridization is responsible for the tendency observed in the U and Np series. The latter one shows, however, a stronger tendency to magnetism. The initial stage of investigation was reported in the Ref. [1].

Two points make these compounds specially intriguing:

- *first,* systematic occurrence of enhanced γ-values of the low temperature specific heat (heavy-fermion phenomena), reaching the maximum of 900 mJ/mol.K^2 in U_2Pt_2In, which has a non-magnetic ground state. Magnetically ordered compounds display somewhat lower γ-values (400 mJ/mol.K^2 for U_2Pd_2In, 131 mJ/mol.K^2 for U_2Rh_2Sn, 200 mJ/mol.K^2 for U_2Pd_2Sn, 330 mJ/mol.K^2 for U_2Pt_2Sn) and similar values were also observed in some paramagnets (270 mJ/mol.K^2 for U_2Rh_2In) where strong spin fluctuations exist. Such a large isostructural group of compounds with pronounced γ enhancement is unique. We believe that further investigations can help to understand the origin of heavy fermion state.
- *second,* a crystal structure that allows to modify a spacing between different nearest An neighbors. This gives an excellent possibility to test theories, considering the type of magnetic anisotropy, influenced mainly by the arrangement of An atoms, which leads to an easy-magnetization direction perpendicular to the nearest An-An spacing $d_{An\text{-}An}$. In the smallest $d_{An\text{-}An}$, within the basal plane, magnetic moments should be confined to the c-axis. This is indeed the case of U_2Ni_2Sn, as shown recently by neutron diffraction [2]. We have chosen for our neutron diffraction studies U_2Pd_2Sn and U_2Pd_2In. The first one has a similar relation of $d_{An\text{-}An}$ as U_2Ni_2Sn, only the difference of the two different $d_{An\text{-}An}$ is much smaller; U_2Pd_2In has the smallest $d_{An\text{-}An}$ along the c-axis. However, the neutron experiment showed the same magnetic structure in both cases. The moments are within the basal plane (1.4 μ_B in U_2Pd_2In and 1.9 μ_B in U_2Pd_2Sn). A closer inspection of the crystal lattice in U_2Pd_2Sn revealed however that this does not indicate failure of the theory. Due to anisotropy of thermal expansion the interuranium spacing along c really becomes the smaller parameter at low temperatures (below approx. 200 K). Thus we have actually confirmed the validity of theoretical explanations on a very fine scale.

This work was a subject of collaborative research between ITU Karlsruhe, Charles University, Prague and Van der Waals-Zeeman Laboratory, University of Amsterdam. The neutron work was done in collaboration with Los Alamos National Laboratory.

References:

[1] M.N. Peron, Y. Kergadallan, J. Rebizant, D. Meyer, S. Zwirner, L. Havela, H. Nakotte, J.C. Spirlet, G.M. Kalvius, E. Colineau, J.L. Oddou, C. Jeandey, J.P. Sanchez and J.M. Winand, J. of Alloys and Compounds **201** (1993) 203

[2] F. Bourée, B. Chevalier, F. Mirambet, T. Roissel, V.H. Tran and Z. Zolnierek, to be published.

Synthesis of binary technetium alloys

Technetium forms as a fission product in nuclear power reactors. It is a ß emitter of relatively low intensity. Nevertheless, due to the high mobility and toxicity of the pertechnetate ions (TcO_4^-) it presents a significant health risk in terms of long time storage. ^{99}Tc is transformed into the stable ^{100}Ru isotope by neutron capture. For this reason, its possible transmutation on the industrial scale in high flux thermal reactors is being studied in different laboratories.

Pure technetium metal has a hexagonal structure. Materials with the hexagonal crystal structure have the tendency to anisotropic swelling under neutron irradiation which can lead to the destruction of the cladding. Technetium rich alloys with a cubic crystal structure would be preferred to pure technetium metal for transmutation feasibility studies. In our laboratory, binary and ternary technetium alloys are investigated for their potential use as targets for particle accelerators or as fuel for transmutation experiments.

Technetium is commercially available as ammonium pertechnetate. The ammonium pertechnetate is reduced into metal powder in a resistance furnace under a hydrogen atmosphere at 800 °C. The metallic powder is remelted several times into small spheres by arc melting to improve the purity of the metal by evaporation of impurities. The melting point of technetium metal is 2435 ± 45 K. 150 g of technetium metal were produced by the reduction of 30 g batches of ammonium pertechnetate. The spheres obtained subsequently by arc melting were analyzed by glow discharge mass spectroscopy. The results are given in Tab. 5.4.

Tab. 5.4 Analysis of Tc samples by glow discharge mass spectrometry (GDMS).

Element	Sample 1 Concentration in ppm	Sample 2 Concentration in ppm
C	60.72	208
N	1.2	18.7
O	54.12	131
Na	0.24	< 10 ppb
Al	13.43	3.2
Si	22.6	0.16
S	1.52	0.3
Cl	28.25	1.46
Cr	0.47	0.5
Fe	10.81	1.81
Ni	1.32	1.83
Cu	0.75	< 10 ppb
Zn	1.17	< 10 ppb
Pu	< 10 ppb	< 10 ppb
Np	0.007	< 10 ppb
U	18.5	2.18

Technetium rods of 4.8 mm in diameter and 2.5 cm long were prepared for their irradiation in the high flux reactor in Petten. These rods were obtained by casting in a cold copper mold. The equipment is a modified mini-arc melting system of the Bühler company, shown in Fig. 5.2. Rods of 2.5 cm obtained are shown in Fig. 5.3. The metallographs of a transversal and longitudinal cut of the rods are shown on Figs. 5.4 and 5.5. The measured densities of the 6 rods are respectively 11.43, 11.47, 11.49, 11.46, 11.47 and 11.47 g.cm^{-3}. The measured density reported in the literature is of 11.492 g.cm^{-3}. The density calculated from X-ray measurements is varying from 11.464 to 11.492 g.cm^{-3}.

Fig. 5.2 Modified mini-arc melting apparatus used for preparation of Tc-rods.

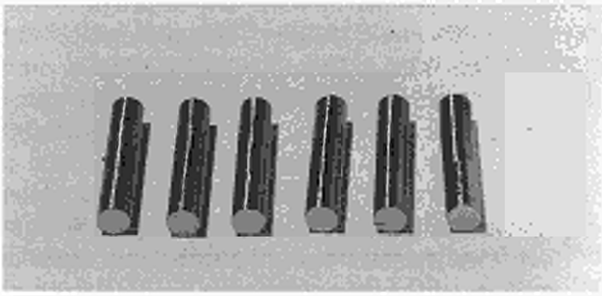

Fig. 5.3 Technetium metal rods obtained in this work.

Alloys of technetium and ruthenium were produced for the preparation of disks of 9 mm in diameter and 1 mm thickness for neutron irradiation. Technetium and ruthenium metals are isomorphic. The crystal structure is hexagonal. They are forming a solid solution from 0 to 100 %.

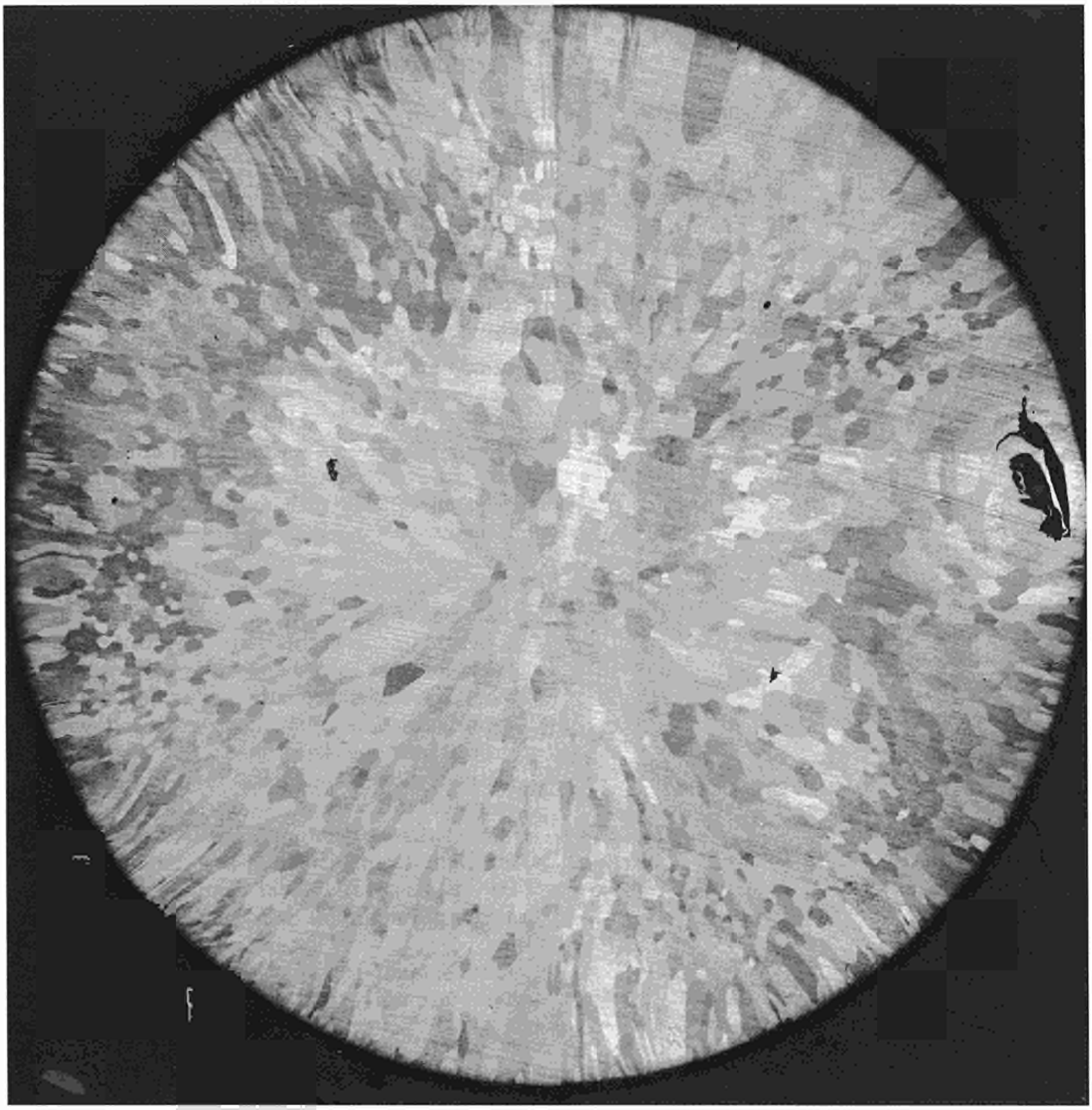

Fig. 5.4 Metallograph of a transversal cut of Tc metal rods.

Ingots of $Tc_{20}Ru_{80}$, $Tc_{50}Ru_{50}$ and $Tc_{80}Ru_{20}$ composition were prepared by arc melting the pure elements in stoichiometric ratio. Rods of 9 mm in diameter were obtained by casting in a water cooled copper mold and disks were cut with a high speed diamond saw. The disks were encapsulated and are irradiated in the high flux reactor in Petten.

The technetium aluminium alloys are interesting for the preparation of targets for accelerators of particles. Samples of $TcAl_6$, $TcAl_4$, $TcAl_3$,$TcAl_2$, Tc_2Al_3, and TcAl were prepared and investigated by X-ray diffraction and metallography to study the binary Tc-Al phase diagram. From our preliminary results, we can conclude that $TcAl_2$ and Tc_4Al_{11} are congruently melting while the other compounds are forming peritectically or peritectoidically. In our sample of nominal composition $TcAl_3$, instead of the expected phase, we could identify Tc_4Al_{11}, and its structure was determined by X-ray diffraction on single crystal. In the Al rich part of the Tc/Al binary system, ascast samples consist of a mixture of aluminium and Tc_4Al_{11}. The crystallographic structure and parameters of obtained compounds are summarized in Tab. 5.2.

Fig. 5.5 Metallograph of a longitudinal cut of Tc metal rods.

Solid State Physics Studies on Actinide Systems

Calculated optical properties of thorium, protactinium and uranium metals

Self-consistent energy band calculations for the ground states of the actinide metals, both scalar relativistic [1] and fully relativistic [2], yield approximate agreement with experiment for the lattice constants of the elemental metals. More recently, full potential calculations have been used to calculate the total energies of different lattice structures as a function of volume [3] and, again, good agreement with experiment has been obtained.

One of the fundamental questions concerning the actinides is whether their f-states are localized or itinerant and from this point of view it is of interest to compare theory and experiment for spectroscopic as well as ground state properties. Optical spectroscopy, like photoelectron spectroscopy and Bremsstrahlung Isochromat Spectroscopy, is a method which allows one to probe the states (both occupied and vacant) around the Fermi energy [4,5]. The most thorough spectroscopic studies of the light actinide metals are for thorium [6-9]. Data is also available for uranium metal [10] but not for protactinium.

The conductivity tensor is obtained from the Kubo formula [11,12]

$$\sigma_{ij}(\mathbf{q}, w) = \left[\frac{iNe^2}{m\omega}\right] +$$

$$\frac{1}{\hbar\omega}\int_{-\infty}^{0} dt < \left[j_j(\mathbf{q}, 0), j_j(-\mathbf{q}, t)\right] > \exp^{-i\omega t} \quad (1)$$

and, for optical properties, the $q = 0$ limit is appropriate. The conductivity and dielectric tensors are related by

$$\varepsilon_{ij}(\omega) = \delta_{ij} + \left[\frac{4\pi i\sigma_{ij}(0, \omega)}{\omega}\right]. \quad (2)$$

The intraband contribution is

$$\varepsilon^{intra}(\omega) = 1 - \frac{\omega_p^2}{\omega(\omega + i\gamma)} \quad (3)$$

where the free electron plasma frequency is given by the Drude relationship

$$\omega_p^2 = 4\pi n e^2 / m^*$$

and γ is the relaxation frequency. The only available data for the intraband contribution is given by Weaver and Olson [7] for Th, who give σ_{DC} = 1.79 Ry, γ = 0.0073 Ry. We find that the Drude contribution is negligible above 0.5 eV, as is generally the case for metals with strong interband transitions.

Fig. 5.6 shows a comparison between the calculated results and experiment for Th metal. At low energy the agreement is good, and at higher energies the general decrease is reproduced but there are two shortcomings. The first is the experimental feature at 9 eV and the second is the broader feature at 19 eV. It is impossible to find calculated features from the conduction bands that could correspond to the broad 19 eV feature. However, X-ray photo emission places the Th $6p_{3/2}$ states 16.8 eV below the Fermi energy [13,14]. We have made two self-consistent calculations for free atoms to check this feature at 19 eV. Firstly, for a normal Th atom we found that the $6p_{3/2}$ states lie about 20 eV below the centre of the $6d_{3/2}$ and $6d_{5/2}$ states. Secondly we made a transition state calculation [15], by taking one half of an electron out of the $6p_{3/2}$ core state and placing in the $6d_{3/2}$ and $6d_{5/2}$ states, weighted according to their degeneracy - thus allowing for relaxation. In this case the $6d_{3/2}$ states lie 19.9 eV below the centre of the $6d_{3/2}$ and $6d_{5/2}$ states. This feature is therefore due to $6p \rightarrow 6d$ transitions. The breadth arises due to the width of the 6d (band) final states. The lower feature, at 9 eV is not given by theory.

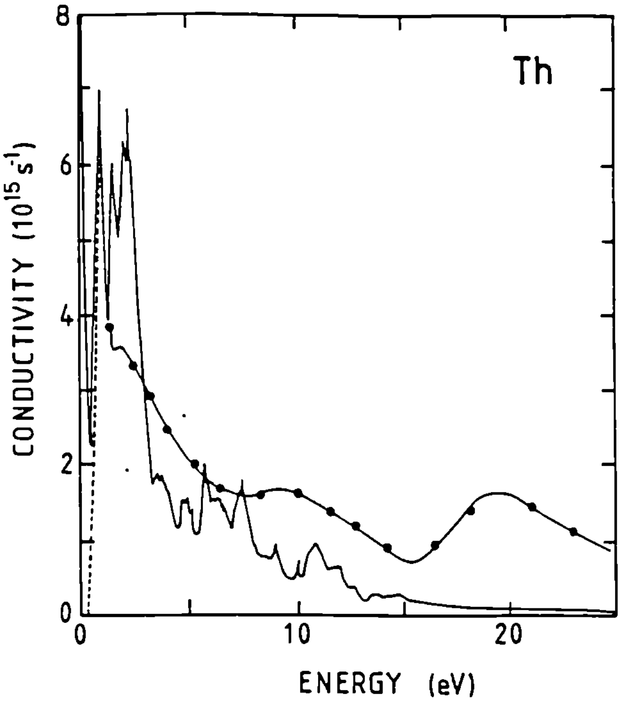

Fig. 5.6 Calculated and measured (full line with points) optical conductivity of thorium metal

While $d \rightarrow f$ transitions are allowed, the oscillator strength is found to be nearly zero. The feature at 1.1 eV arises from $p, f \rightarrow d$ transitions. The 2 eV feature arises from transitions into 5f bands [9] which contain d-character through hybridization.

There is no data for Pa but one would expect the same features at high energy as for Th. The calculated conductivity is shown in Fig. 5.7. For the fcc structure there are two noticeable features, at 2 and 4 eV, in contrast to the bcc and bct structures which are relatively flat.

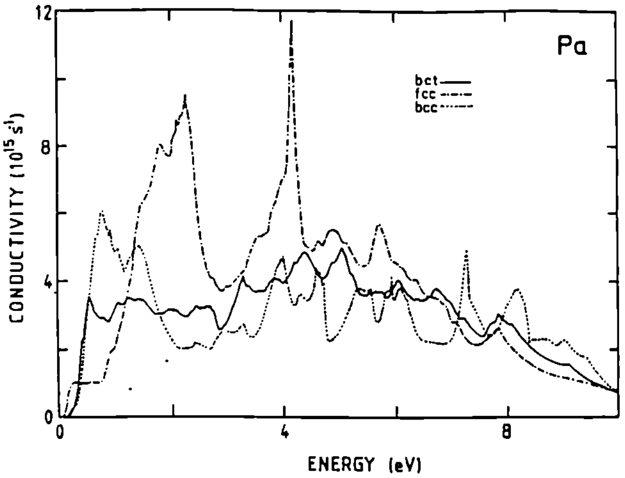

Fig. 5.7 Calculated optical conductivity of protactinium for three structures

The calculated conductivity for uranium is shown in Fig. 5.8. As for Th and Pa, the $d \rightarrow p, f$ oscillator strength is extremely low and it is the $f \rightarrow d$ transitions which dominate. The conductivity for the fcc structure has two optical features, at 2.2 and 4.5 eV. The conductivity for alpha-U is much more smeared out. Over this background there are increases in intensity at 0.3, 1.5 and 5.0 eV. Compared with experiment [10] there is good agreement for the features at 0.7, 1.4 and 3.8 eV although the intensity is too low for the first two features.

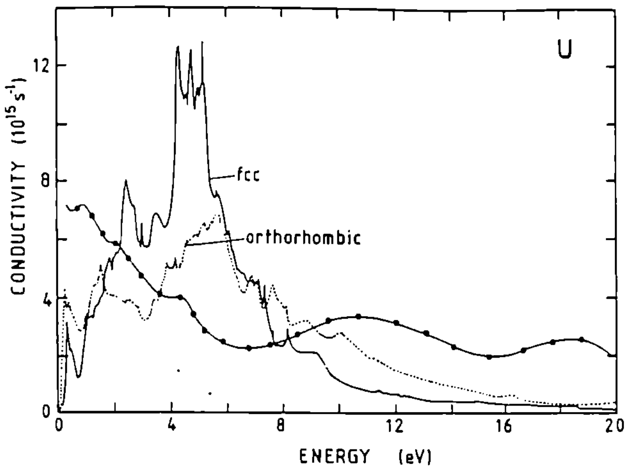

Fig. 5.8 Calculated (for two structures) and measured (full line with points) optical conductivity of uranium metal

Crystal structure has a surprisingly large effect upon the optical properties of Pa and U. This is due to the near zero *d* → *f* oscillator strength which means that the small differences in the distribution of d final states are important. It would therefore be interesting to measure the optical properties of these actinides under pressure. Either a change of crystal structure or a change in the *d* → *f* oscillator strength could result in a marked change of the optical properties.

These results imply that the 5f states in the early actinides are itinerant. This is similar to the conclusions of X-ray photoemission and Bremsstrahlung Isochromat Spectroscopy [16].

References

[1] H.L. Skriver, O.K. Andersen and B. Johansson, Phys. Rev. Letts., **41**, 42 (1978)

[2] M.S.S. Brooks, J. Phys. F13 (1983) 103

[3] J.M. Wills and O. Eriksson, Phys. Rev., **B45** (1992) 13879

[4] Y. Baer, in *Handbook on the Physics and Chemistry of the Actinides*, (North Holland, Amsterdam) eds. A. Freeman and G. Lander, Vol. **1**, Chapter **4**

[5] see, e.g., the review by J. Schoenes, in *Handbook on the Physics and Chemistry of the Actinides*, (North Holland, Amsterdam) eds. A. Freeman and G. Lander, Vol. 1, Chapter 5

[6] B.W. Veal, D.D. Koelling and A.J. Freeman, Phys. Rev. Lett. **30** (1974) 1061

[7] J.H. Weaver and C.G. Olson, Phys. Rev. B **15** (1977) 4602

[8] C. Alvani and J. Naegele, J. Physique Coll. 40 C4 131

[9] Å. Fäldt and P.O. Nilsson, Phys. Rev. B **22** (1980) 1740

[10] Å. Fäldt and P.O. Nilsson, J. Phys. F : Metal Phys. **10** (1980) 2573

[11] R. Kubo, J. Phys. Soc. Japan, **12** (1957) 570

[12] J. Callaway, *Quantum Theory of the Solid State*, Academic Press, New York, 1976

[13] J. Fuggle, A. Burr, W. Lang, L. Watson and D. Fabian, J. Phys. F 4 (1974) 335

[14] B.W. Veal and D.J. Lam, Phys. Rev. B **10** (1974) 4902

[15] J.C. Slater, *The Self-consistent Field in Molecules and Solids: Quantum Theory of Molecules and Solids, Vol. 4*, McGraw Hill, New York, 1974

[16] Y. Baer and J.K. Lang, Phys. Rev. B **21** (1980) 2060

Magnetic moments, exchange interactions and ordering temperatures of gadolinium and curium under pressure

The rare earth and heavy actinide metals are characterized by their localized f shell. The magnetism of these metals is local in origin but is mediated by the conduction electrons through the RKKY interaction [1,2]. In the local spin density approximation (LSDA) to density functional theory, the spin density of the localized states polarizes the spin up and spin down conduction electron states via *local* exchange interactions. The exchange split conduction electron states interact with the localized f states at other sites, thus acting as the medium for the indirect *f* - *f* interaction. Both Van Vleck (localized-f) and Slater (itinerant) magnetism, both of which are essential for the correct modelling of the magnetic properties, coexist [2]. Theory has advanced enough for attempts to be made to calculate the local, or *s* - *f* [1], exchange interaction and to estimate the effects of the entire RKKY interaction upon Curie temperatures from *ab-initio* calculations.

Cm is the actinide analogue of Gd with, as far as is known, the same ground state configuration. These elements both have half filled f states with a total spin of 7 μ_B and zero orbital moment.

Exchange integrals between the f states and conduction band states have been calculated from first principles for Gd and Cm. The d-f exchange integral is 50 per cent larger in Cm (9.7 mRy) than in Gd (6.6 mRy) due to larger d-f overlap. The d-d exchange integrals (38 mRy) in the two metals are about the same.

The calculated conduction electron moment of Gd is in good agreement with recent experiments [3,4]. The conduction electron moment is approximately proportional to the product of the state density at the Fermi energy and the d-f exchange integral. The state density at the Fermi energy in Cm is a little over half the state density at the Fermi energy Gd. The calculated conduction electron moments are, however, about the same since the d-f exchange integral is larger in Cm. The volume dependence of the state density at the Fermi energy was found to be much less than would be expected from a rigid band model, and the volume dependence of the conduction electron moment correspondingly smaller in both metals.

The exchange interactions and calculated conduction electron moments were used to estimate the volume dependence of the Curie temperatures of Gd and Cm, in ferromagnetic ground states. With normal mean field theory the calculated volume dependence of the Curie temperature,

$$\frac{d\ln T_C}{d\ln V} = 0.26 \ ,$$

for Gd was far less than the measured volume dependence of

$$\frac{d\ln T_C}{d\ln V} = 2.2 \ .$$

This indicates that Gd must have disordered local moments above its Curie temperature and therefore that only the intersite susceptibility governs the ordering temperature. When it is assumed that the local susceptibility is relatively large and has a smaller volume dependence that the intersite susceptibility the calculated value of

$$\frac{d\ln T_C}{d\ln V} = 1.8$$

for Gd in reasonable agreement with measurements. The corresponding theory for Cm yields

$$\frac{d\ln T_C}{d\ln V} = 0.7 \ .$$

References

[1] M.A. Ruderman and C. Kittel, Phys. Rev. **96** (1954) 99

[2] For a review see: J. Jensen and A.R. Mackintosh *Rare Earth Magnetism, Structures and excitations*, Oxford Science Publications, Clarendon Press, Oxford, 1991

[3] L.W. Roeland, G.J. Cock, F.A. Muller, C.A. Moleman, K.A.M.McEwen, R.C. Jordan and D.W. Jones, J. Phys., F5 (1975) L233

[4] R.M. Moon, W.C. Koehler, J.W. Cable and H.R. Child, Phys. Rev., B5 (1972) 997

Neutron and synchrotron X-ray scattering

Introduction

We have continued to make use of the neutron sources in Grenoble (Siloë) and Saclay (Orphée) during the shutdown of the ILL. The latter is expected to operate again in late 1994. We are concentrating our neutron efforts on single-crystal experiments on intermetallic compounds. The goal of this work is to characterize the response function S(**Q**, w) in elastic and inelastic scattering of both uranium and transuranium materials. A major effort is being made on UFe_2, although the magnetic response is proving difficult to establish. A new effort on URhAl is just starting.

The magnetic X-ray scattering (all performed at the Brookhaven Synchrotron) went well this year with the completion of the study of the complex phase transitions in NpAs, and $USb_{0.8}Te_{0.2}$, and a series of experiments on specially prepared (at ITU) UO_2 crystals. We hope to start experiments at the ESRF in Grenoble on uranium samples in early 1994. A new initiative was started on multilayers containing uranium that we obtained from IBM.

Neutron studies of intermetallic compounds

A) Structural studies

In an extension of our work on the 1:1:1 compounds we have performed two experiments on small single crystals of the new heavy-fermion material UPd_2Al_3 that were obtained from Sendai, Japan. The first experiment (at Saclay) was to test whether the susceptibility was centered totally at the U site in the paramagnetic case. An additional goal was to test whether the large change predicted theoretically in the ratio of the orbital to spin components of the moment, as compared to the free-ion value, was present. Fig. 5.9 shows a maximum entropy plot of the magnetiz-

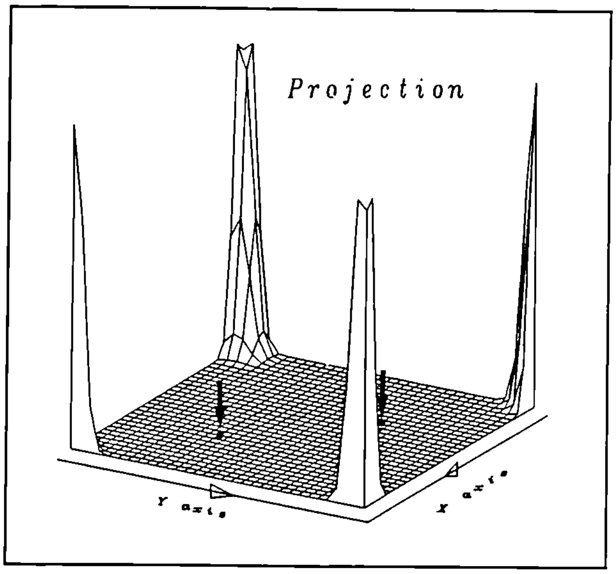

Fig. 5.9 Maximum entropy reconstruction of the magnetization density projected on the basal plane of the UPd_2Al_3 structure. The high values at the corners are associated with the uranium atoms. The arrows indicate the positions of the palladium atoms. No induced spin density is found at the Pd sites.

ation density as measured in an applied field of 5 T just above the antiferromagnetic ordering temperature of 15 K. Clearly there is n̲o̲ induced moment associated with the palladium site, the total susceptibility arises from the response at the U site. Moreover the ratio μ_L/μ_S was found close to that expected for a U^{4+} ion. The apparent lack of hybridization between the U and Pd ions is in strong contrast with the situation in the 1:1:1 compounds, but can be understood on the assumption that the 4d̲ band of Pd is filled and the hybridization between the 4d̲ Pd and U 5f̲ electrons is reduced to a minimum. A consequence of this is that the easy axis of magnetization (this time in the **ab** plane of the hexagonal structure rather than along the unique **c** axis as in the 1:1:1 compounds) is determined by exchange and crystal-field effects rather than by hybridization.

In a second experiment (at CEN-Grenoble) we have determined the magnetic structure as a function of applied field. This experiment was undertaken because of the unusual magnetic phase diagram proposed from bulk measurements. In fact, our studies show that, at least in the normal state (T>2K), the magnetic phase diagram is relatively simple. The moments lie in the **ab** plane of the hexagonal structure and the effects observed when a field is applied are related to the re-orientation of the domains. The preferred direction is such that the antiferromagnetic moments are perpendicular to the field direction. The results of the experiments are shown in Fig. 5.10. They show the re-orientation of the domains when the field is applied. No evidence for any incommensurate or non-collinear magnetic structures, both of which had been proposed, was found.

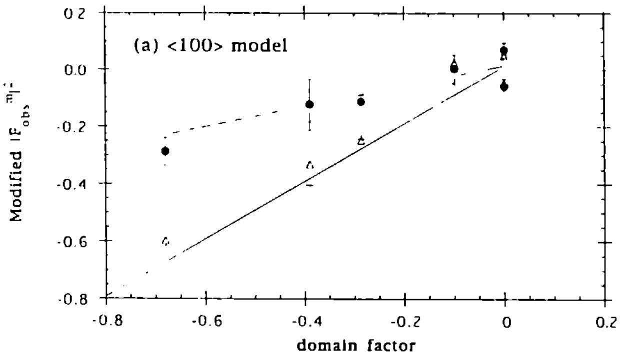

Fig. 5.10 The observed intensities in the experiments on UPd_2Al_3 are proportional to the quantity plotted along the y axis. The domain factor (x axis) is a quantity relating to the sensitivity of the reflections to the domain population. The solid points correspond to the zero-field (H=0) experiment. The slope of the dashed line is 1/3 corresponding to a random orientation of the 3 possible domains. For H=2 T (open triangles) and H=4.7 T (crosses) the intensities fall on a line close to a slope of 1. This indicates a preferential occupation of the domain perpendicular to the applied field.

B) Dynamical studies

UFe_2 is a ferromagnet with a strong hybridization between the U 5f̲ and Fe 3d̲ electrons, as shown by the magnetic form factor which was examined by us some years ago. We are presently engaged in a series of experiments aimed at measuring the inelastic response function on a large single crystal. Since the anisotropy of UFe_2 is small, we expect a small anisotropy 'gap', and thus the possibility that there is mixing between the magnetic and vibrational spectra. Experiments have been performed at the PRISMA spectrometer at the ISIS spallation source, and at a triple axis spectrometer at the Siloë reactor. The low-energy phonon dispersion curves are shown in Fig. 5.11. It is known from a number of experiments reported by a Russian group that there are large anomalies in the elastic constants of UFe_2 when the material orders ferromagnetically at ~170K. The elastic constants are measurements at

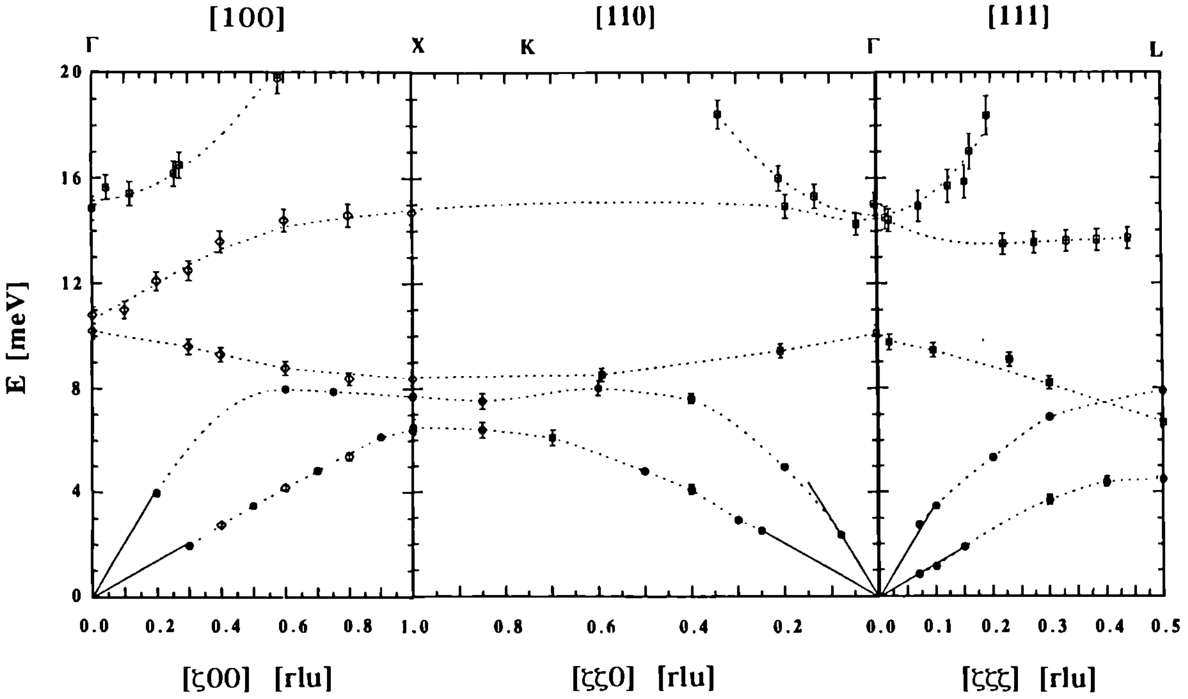

Fig. 5.11 Phonon dispersion curves (only modes with energies below 20 meV are shown) in the three principal directions at 293 K as measured from a single crystal of UFe_2. The x-axis gives the reduced wavevector in reciprocal lattice units [rlu]. The y axis gives the frequency (energy) of the mode. The different symbols correspond to different measuring conditions and the dotted lines are guides to the eye.

essentially q = 0 in Fig. 5.11, whereas the neutrons measure at a finite wavevector in the Brillouin zone. To study the comparison between the two sorts of measurements, we have followed the phonons as a function of temperature. The important change of the TA[100] phonon is shown in Fig. 5.12. The neutron experiments are in excellent agreement with those from the elastic constants. These effects are large, showing strong magneto-elastic coupling. Further measurements on UFe_2 are in progress; in particular we would like to use polarization analysis to be able to separate the purely vibrational and magnetic parts of the response function.

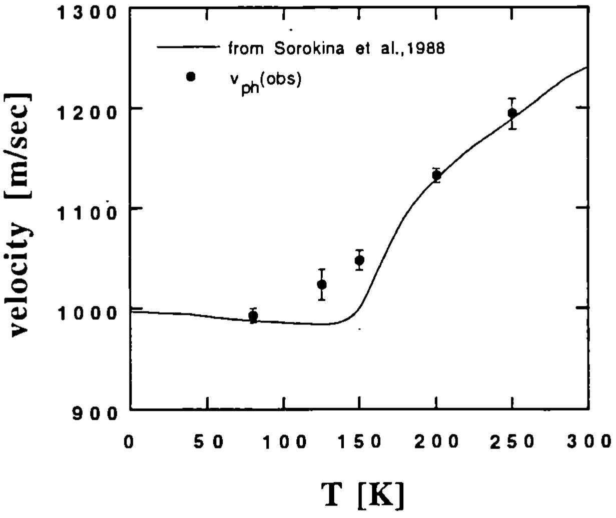

Fig. 5.12 The velocity of the transverse acoustic phonon in the [100] direction of UFe_2 as determined by measurements of the elastic constants (solid line) and the results deduced from the present neutron experiments.

Resonant X-ray magnetic scattering

A) Studies of NpAs single crystals

The initial experiments on the NpAs crystal at the National Synchrotron Light Source (Brookhaven Nat. Lab.) were reported last year (TUAR-92, p. 144). The data analysis has now been completed. Here we highlight two aspects of the study.

The first is the unusual *domain* effects that are observed in these experiments because of the limited penetration depth and extreme sensitivity to the near-surface (~1200 Å) layers. We show in Fig. 5.13 a schematic figure of the crystal, with its antiferromagnetic domains A, B, and C. It will be noticed that C domains are different from the other two domains in that, at the surface, the moments are perpendicular to the surface. From dipole anisotropy arguments this is an energetically unfavourable situation in a *ferromagnet.* But does this have any effect on an antiferromagnet where the bulk moment is zero? The NpAs experiments confirm that it does. We show in Fig. 5.14 the population of the fraction of the C domains as a function of temperature in NpAs as measured in the near-surface region by resonant magnetic x-ray diffraction. A random domain population would correspond to 0.3333 on this plot. There are 3 regions of interest: (a) Near T_N. If the signal was observable at higher temperature presumably it would attain the value of 1/3. However, as the correlations develop above T_N the fraction of C domains *decreases* because the moments rotate into the A and B domains. This is a consequence of the dipolar anisotropy discussed above. It shows that, although the overall bulk moment is zero, the surface layers are defining the domain fraction, and the behaviour is thus similar to that found in ferromagnets. (b) Below T_N there is a small increase in the C domain fraction, but at the lock-in transitions T_{IC} there is no strong discontinuity. However, at 138 K an almost first-order transition takes place to (c) a *single domain* state with only C domains. This may be understood on the basis of elastic strain energy, given that the crystal symmetry below T_N is tetragonal. Again, it is an effect which requires relaxation at the surface. Note that below T_0 the structure is different and the domain arguments no longer apply.

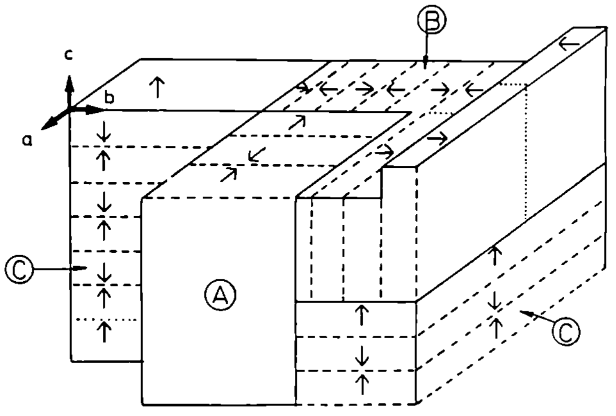

Fig. 5.13 Schematic drawing of the NpAs crystal showing the different types of magnetic domains. The top plane represents the surface of the crystal. Each arrow represents 4 magnetic moments (i.e. 2 unit cells). Solid lines represent domain boundaries, dashed lines are changes of moment direction within one domain, and the dotted lines are other possible antiphase domain boundaries.

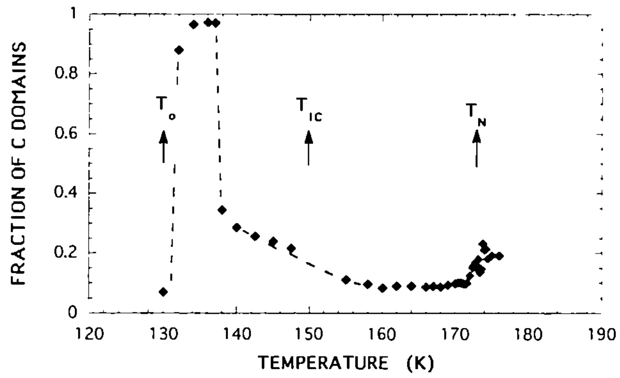

Fig. 5.14 Calculated fraction of C domains in the near-surface region of the crystal as observed by resonant x-ray magnetic scattering from NpAs as function of temperature.

A second interesting aspect is the region near T_N and the length scales of the short-range order that are extracted by a detailed analysis of the lineshape, suitably deconvoluted with the instrumental resolution function. In this work it became apparent that the lineshapes could not be fitted by assuming a single Lorentzian function, as one finds in the textbooks on critical phenomena. What this means is that there is more than one length scale in the region where the fluctuations are driving the system towards magnetic order. Such a situation has been found recently in similar experiments on holmium, and by analogy with that material and other examples in phase transition studies, we have used an analytical fit consisting of a Lorentzian and a Lorentzian-squared function. The fits to the data are greatly improved by this method, and the respective half-widths give two correlation lengths, $\kappa_{\parallel}$ for the Lorentzian, and $\kappa'_{\parallel}$ for the Lorentzian-squared function. They are shown in Fig. 5.15 as a function of the reduced temperature $t = (T-T_N)/T_N$. From this figure we see that the length scale corresponding to $\kappa_{\parallel}$ is essentially the same as determined by neutron experiments; however, the length scale corresponding to $\kappa'_{\parallel}$ has no analog in

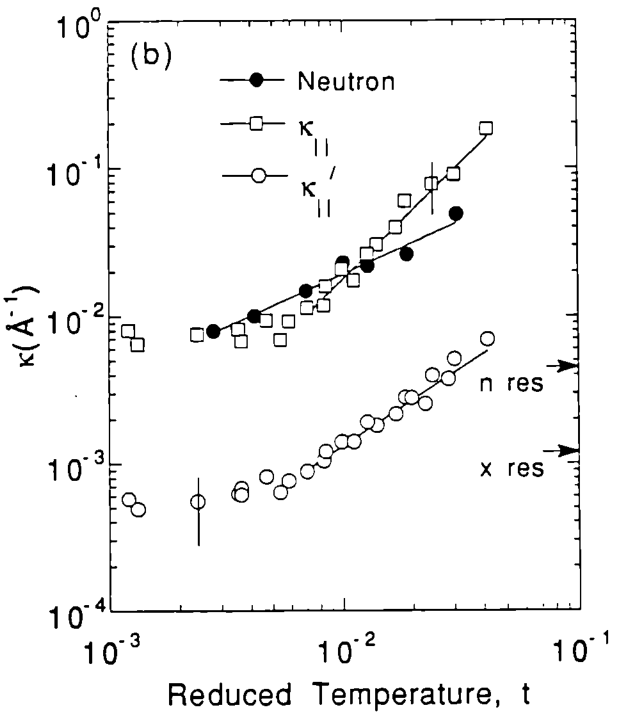

Fig. 5.15 Deconvoluted inverse correlation lengths using the two component model described in the text as a function of the reduced temperature $t = (T-T_N)/T_N$. The instrumental resolution widths are indicated on the vertical scale.

the neutron experiments. One reason might be that the resolution of the x-rays is considerably better than that of the neutrons (see indications of the resolution in the figure), but the reason could also be due to the small depth probed by the resonant x-ray experiments. The neutrons, of course, probe the whole crystal. The $\kappa'_{\parallel}$ correlations are shorter by a factor of almost ten in reciprocal space (they correspond to very sharp peaks) than those of the $\kappa_{\parallel}$ correlation. This means that in real space the new correlations are on a much *longer* spatial scale. What these are remains an interesting and unsolved point.

B) Experiments on UO_2 'surface crystal'

The above study of NpAs has shown that the experiments with resonant x-rays are sensitive to the magnetism at the surface. To further investigate this point, we have prepared (at ITU) a highly polished single crystal of UO_2. The ultimate aim of these experiments is to perform grazing incidence x-ray experiments to examine the magnetism of the surface layer. Since the antiferromagnetic transition (near 31 K) is known to be first order in UO_2 the amount of critical scattering (see the text above with respect to the experiments on NpAs) is anticipated to be small. Indeed, experiments on the smooth surface, Fig. 5.16a showed that no measurable critical scattering was present. A small part of the crystal surface was then intentionally roughened causing damage down to ~ 0.5 µm. Scans from this region are shown in Fig. 5.16b. The Néel temperature (T_N) is not affected by this roughening, but the form of the scattering near T_N is completely changed. Strong short-range fluctuations are now associated with the antiferromagnetic ordering. A key aspect of these fluctuations is that they take place on a lattice slightly larger than the bulk UO_2 lattice. This is obtained from scans in the perpendicular direction [H, H, 0] which are not shown here. It is the damaged surface that is apparently able to sustain these variations in the lattice parameter, and thus leads to regions in which critical fluctuations occur. This is the first time such a microscopic quantity as the short-range fluctuations has been found to depend on the surface preparation; other experiments to characterize this phenomenon are in progress.

X-ray and high resolution UV photoemission study of 5f electron localization in α- and δ-Pu

Introduction

The electronic properties of the actinide metals vary widely along the series due to a cross-over of 5f electron behaviour from itinerant to localized [1]. Previous photoemission data have in fact demonstrated that this transition takes place between monoclinic α-Pu and dhcp Am [2]. Recently Pu has again attracted particular interest [3,4] because of its complicated phase diagram with six different structures. fcc δ-Pu (320 C < T < 450 C) shows particular interesting properties like lowest density of all the six allotropes, large electronic specific heat with $\gamma = 53$ mJ/mole·K^2 [5] and no magnetic moment. It has been claimed to represent the first occurrence of localized 5f electrons [6].

To investigate in more detail differences of the electronic properties between α- and δ-Pu, X-ray photoemission (XPS) measurements of the 4f core levels and high-resolution UV photoemission (HRUPS) measurements of the conduction band have been performed.

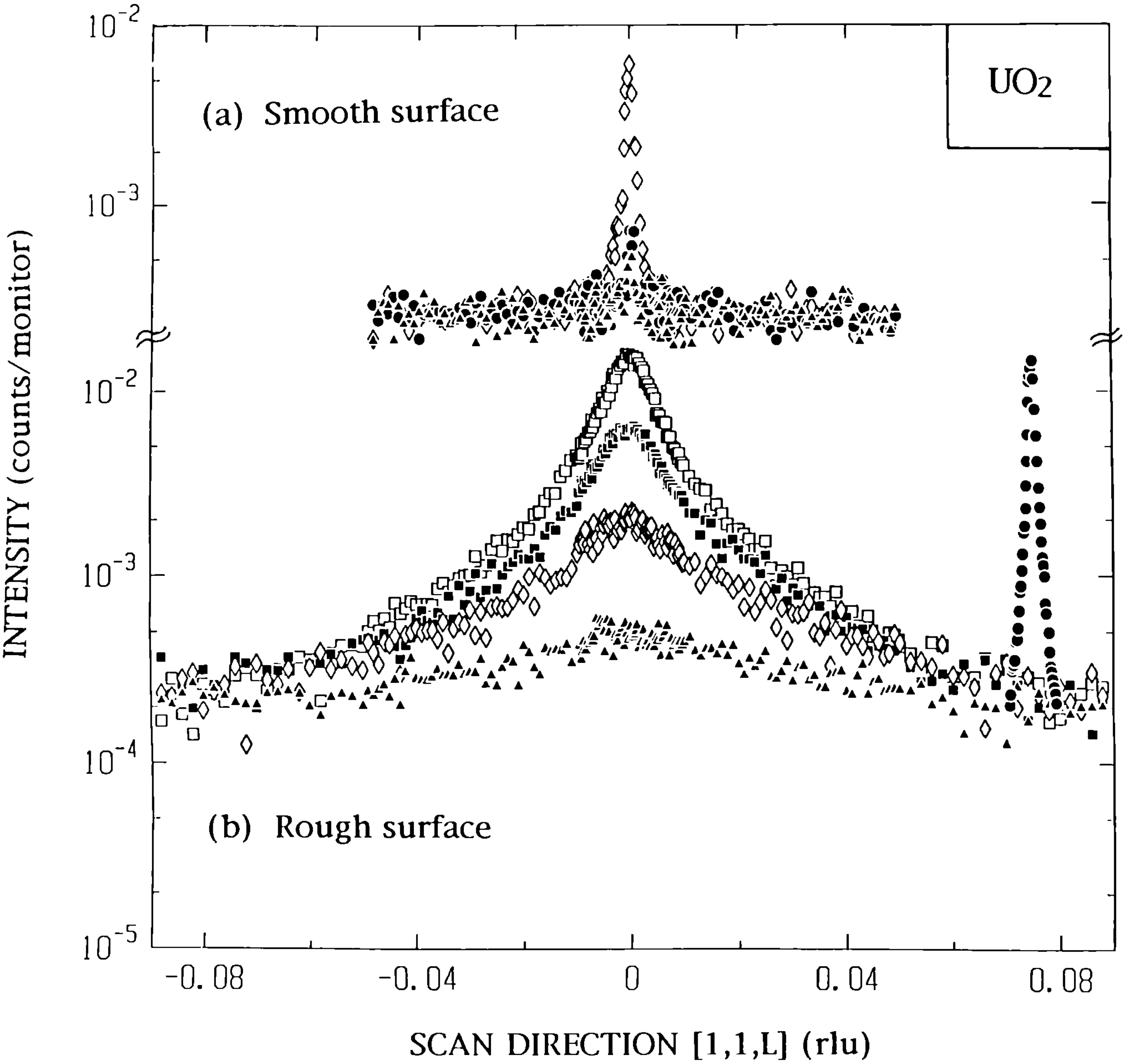

Fig. 5.16 The x-ray scattering near T_N from a UO_2 crystal, (a) on the smooth and (b) on the rough surface. The data on the smooth surface are taken at $T=30.64$ K (open diamonds), 30.72 K (solid points) and 40.0 K (closed triangles). These, and other, data establish T_N = 30.75 (2) K and show that there is no observable critical scattering near T_N. The data on the smooth surface are taken at T = 30.8 K (open squares d), 32.1 K (solid squares), 34.1 K (open diamonds), 37.0 K (solid triangles). Separate scans show that T_N is the same as on the smooth surface (=30.75 K). The (110) magnetic peak at 10 K (with its intensity divided by 50) has been plotted, but offset for clarity to appear at L=0.08. The peak is clearly much sharper than the critical scattering observed just above T_N.

Experimental

The photoemission measurements were performed in a Leybold-Heraeus LHS-10 spectrometer modified to work on highly radioactive samples as described previously [7]. A recent modification facilitated sample cooling with liquid He resulting in enhanced energy resolution of ΔE ≈ 30 meV. 4f core level and conduction band spectra were recorded at liquid N_2 (T ≈ 75 K) and liquid He (T ≈ 15 K) with energy resolutions of 1.0 eV (XPS, AlK_α: 1486.6 eV) and between 45 meV (liquid N_2) and 30 meV (liquid He) for HRUPS (He I: 21.22 eV, He II: 40.82 eV). The base pressure was in the medium 10^{-9} Pa range.

Samples used in this study were high-purity double electrorefined α-Pu and Ga stabilized δ-Pu. The surface Pu_2O_3 layer was removed "in-situ" by repeated cycles of Ar^+-ion sputtering and annealing at 130 C; δ-Pu was additionally scraped to produce a Ga containing δ-Pu surface. Surface oxygen was monitored by XPS (O1s level) as well as by UPS of higher sensitivity (O2p level at 5.5 eV below E_F). The sputter-annealing cycles were continued until no O2p signal was detectable at T = 75 K for at least 15 minutes, a typical time to record a 4f core level spectrum; conduction band spectra were recorded within 5 minutes. The δ-stabilizer Ga was monitored by recording its 3p levels. In a previous study [3] Ga was neither detected in Ar-ion sputtered (i.e. Ga depleted) Pu considered to represent mainly α-Pu, nor for the sample annealed briefly at 225 C, considered to represent δ-Pu. In this study we succeeded by time extended XPS scans over the Ga 3p core level range to detect a small amount of Ga even in the surface of heavily sputtered Pu. For scraped Pu we detected an about 3 times bigger Ga signal; the scraped surface of δ-Pu is therefore considered to represent δ-Pu, whereas the sputtered surface mainly represents α-Pu.

Results and discussion

Conduction-band spectra of "in-situ" scraped δ-Pu recorded at T = 15 K for 21.22 eV (He I) and 40.82 eV (He II) excitation energies are shown in Fig. 5.17. A comparison of the conduction-band spectra for scraped δ-Pu and α-Pu for 40.82 (He II) excitation energy is presented in Fig. 5.18. To show in more detail the structures just below E_F, Fig. 5.19 displays the conduction band spectra of δ-Pu and α-Pu in a narrow binding energy range from 2.0 eV to E_F.

The spectra for δ-Pu are dominated by a resonant-like narrow (FWHM: 80 meV) emission just at E_F never reported previously for any actinide material. In addition, two side maxima at 0.5 and 0.9 eV binding energy are observed. Further, a shoulder is found around 2 eV; the overall conduction band width is about 3.8 eV.

The spectra for α-Pu are also dominated by a strong emission at E_F but considerably broadened (FWHM: 180 meV) and nearly completely covering the 0.5 eV structure. The maximum at 0.9 eV is less pronounced but still existent at T = 15 K (at room temperature only a shoulder is seen as previously reported [2]). The overall conduction band width is not changed; the shoulder seen for δ-Pu at 2 eV is shifted to about 2.5 eV.

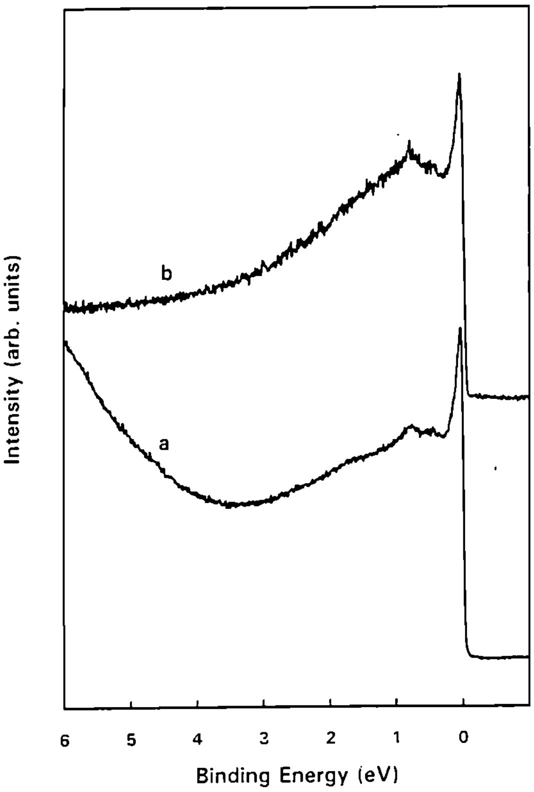

Fig. 5.17 High resolution UPS conduction band spectra of scraped δ-Pu for He I (a: 21.22 eV) and He II (b: 40.82 eV) at T = 15 K.

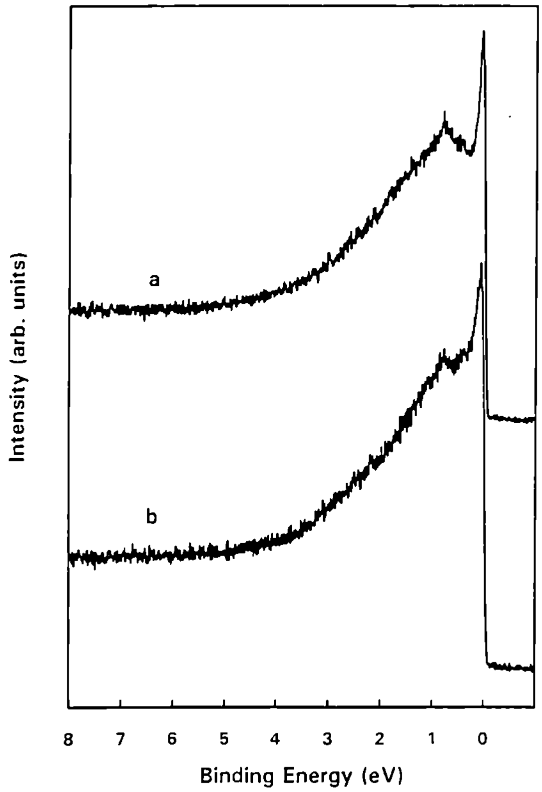

Fig. 5.18 High resolution UPS conduction band spectra of scraped δ-Pu (a) and α-Pu (b) for He II excitation (40.82 eV) at T = 15 K.

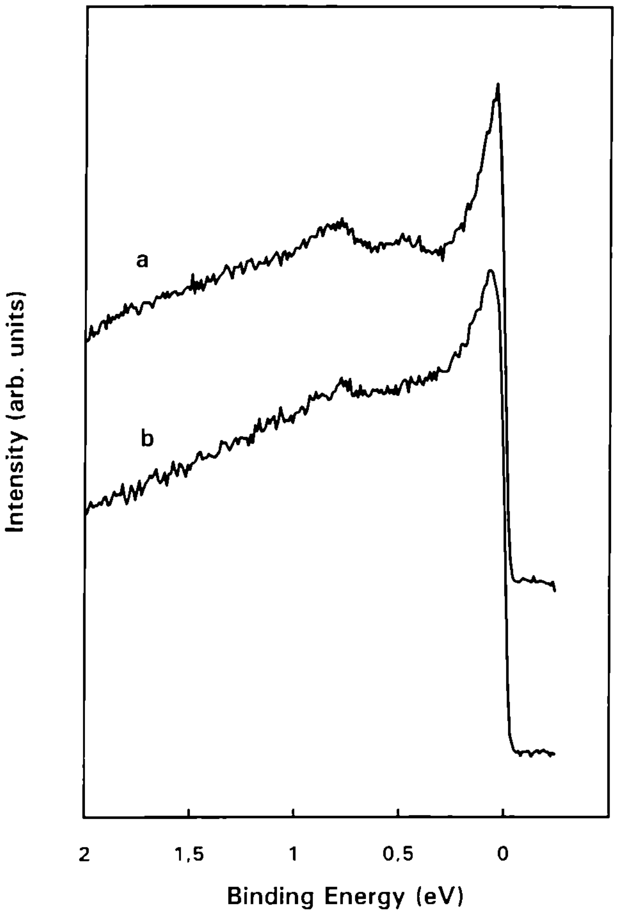

Fig. 5.19 High resolution UPS conduction band spectra of scraped δ-Pu (a) and α-Pu (b) from 2 eV binding energy to E_F recorded at T = 15 K.

Due to the high partial 5f photoemission cross section for 40.82 eV excitation energy compared to the 6d and 7s ones [8], the related conduction band spectra are dominated by 5f derived electron emission. In particular, the maximum at 0.9 eV for δ-Pu is becoming more pronounced for the higher excitation energy, a clear indication for the 5f character of this emission. The sharp emission at E_F for δ-Pu does not show such a clear behaviour. But also here, the relative increase to the background is clearly observed at higher excitation energy. The shoulders at 2 eV (δ-Pu) and 2.5 eV (α-Pu) behave just in the opposite way and are thus attributed to predominantly 6d - 7s states. *Final state multiplets as observed [2] for the localized 5f system of Am and expected here around 2 eV in case of a localized $5f^5$ state (at least in δ-Pu) are neither found for α- nor δ-Pu.* Thus no signs of predominant 5f electron localization are evident. On the contrary, comparison with recent advanced fully relativistic band structure calculations on δ-Pu including simultaneously spin polarization [9] give excellent agreement. The experimentally observed emission maxima at 0.9 and 0.5 eV are described by calculated predominantly 5f derived density of state (DOS) maxima at 0.9 and 0.4 eV. At E_F a very narrow 5f derived DOS is found, again in perfect agreement with the presented experimental finding, and consistent with the high γ-value [5]. The fact that the calculated DOS at E_F is slightly smaller than the one at 0.9 eV is easily explained by life time broadening becoming more pronounced with increasing binding energy. The calculated ds DOS extend from nearly 4 eV to E_F, peaking around 2 eV, also in complete agreement with the experiment. This is, perhaps, surprising, because one would expect pronounced 5f correlation/-localization effects. Therefore the main change from α-Pu to δ-Pu is the considerable narrowing of the 5f electron band indicating increasing 5f electron correlation/localization but not full localization like in Am.

The narrowing of the 5f electron band is equivalent to an increased 5f electron band mass that might lead to an alternative interpretation based on the Anderson impurity model [10]. This model results in a resonant-like enhanced emission in the vicinity of and at E_F, the so-called Kondo Resonance (KR) with crystal-field (CF) and spin-orbit (SO) side bands [11]. Since at present no calculations of the KR for the Pu $5f^5$ system are available we can only tentatively propose the 0.9 and 0.5 eV structures in δ-Pu being SO and CF side bands of the Kondo Resonance at E_F. The width of the emission at E_F of 80 meV would relate to a Kondo temperature T_K of about 950 K, which is a high, but not unreasonable value. Considering δ-Pu being a Kondo system with high T_K explains in addition in a natural way why magnetic measurements show paramagnetic behavior in contrast to band structure calculations: The magnetic moments are just screened in a Kondo system. The major drawback of this model is the missing ionisation or final-state multiplet structure that should be present at 2 to 3 eV below E_F. Temperature dependent HRUPS measurements particular at T > 500 K will clarify the situation because the emission at E_F should decrease much stronger than expected from temperature induced Fermi edge broadening. In addition a multiplet structure at 2 to 3 eV below E_F should start to develop indicating the transition to a localized 5f electron Pu system. First measurements succeeded only at about T = 400 K; at higher temperatures the oxygen segregation was too fast. Further sputter-annealing cycles have to be performed for depleting bulk δ-Pu of oxygen.

The Pu 4f core levels also reflect the 5f electron properties [2,3] by the screening mechanism of the core hole. Fig. 5.20 shows the XPS 4f core level spectra for α-Pu and scraped δ-Pu. In both cases the surfaces were completely oxygen free as monitored afterwards by UPS measurements. δ-Pu shows clearly a satellite on the high binding energy side of the main peak in contrast to α-Pu. The satellite intensity is considerably smaller than reported previously [3]. The apparence of a satellite in δ-Pu also invokes an increased 5f electron localization if the satellite is attributed to 6d-like screening, but the degree of localization turns out to be smaller than previously assumed [3]. This is in agreement with HRUPS results since δ-Pu shows increased 5f electron correlation / localization as demonstrated by the dramatic narrowing of the 5f electron band at E_F; it even explains the missing final state multiplet because of strong screening by 5f electrons at E_F i.e. predominantly itinerant 5f electrons.

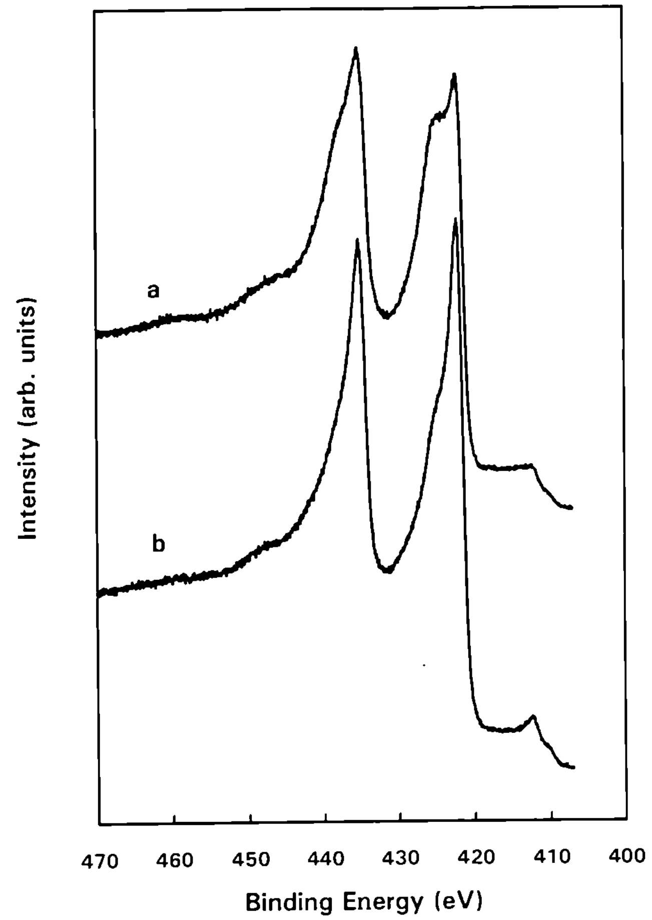

Fig. 5.20 XPS 4f core level spectra for scraped δ-Pu (a) and α-Pu (b) (heavily sputtered δ-Pu) at $T = 75\,K$.

References

[1] See articles in: "Handbook on the Physics and Chemistry of Actinides" Eds. A.J. Freeman and G.H. Lander (Elsevier Science Publishers, Amsterdam, 1984).

[2] J.R. Naegele, L. Manes, J.C. Spirlet, and W. Müller, Phys. Rev. Letters **52** (1984) 1834.

[3] L.E. Cox, Phys. Rev. **B 37** (1988) 8480.

[4] L.E. Cox, O. Eriksson, and B.R. Cooper, Phys. Rev. **B 46** (1992) 13571.

[5] G.R. Stewart and R.O. Elliot, Actinides Rev. **81** (1981) 206.

[6] J.L. Smith and E.A. Kmetko, J. Less-Common Metals **90** (1983) 83.

[7] J.R. Naegele, J. Phys. C2 (1984) 8411.

[8] J.J. Yeh and I. Lindau, Atomic Data and Nuclear Data Tables **32** (1985) 1.

[9] I.V. Solovyev, A.I. Liechtenstein, V.A. Gubanov, V.P. Antropov and O.K. Andersen, Phys. Rev. **B 43** (1991) 14414.

[10] P.W. Anderson, Phys. Rev. **124** (1961) 41.

[11] O. Gunnarson and K. Schönhammer, Phys. Rev. **B 31** (1985) 4815.

Mössbauer and μSR studies

Recently three Mössbauer spectrometers have been installed in ITU by Physik-Department E15, Technische Universität München. All studies described below have been performed in a cooperation of E15 Munich with ITU.

Mössbauer investigations of NpNi$_2$Al$_3$, Np$_{0.5}$U$_{0.5}$Pd$_2$Al$_3$ and Np$_{0.3}$U$_{0.7}$Pd$_2$Al$_3$

Recently we have studied NpPd$_2$Al$_3$ [1,2], the Np analogue of the isostructural (hexagonal PrNi$_2$Al$_3$ structure) heavy fermion superconductor UPd$_2$Al$_3$ [3] by means of Mössbauer spectroscopy.

We have extended our investigations to Np$_{0.5}$U$_{0.5}$Pd$_2$Al$_3$, Np$_{0.3}$U$_{0.7}$Pd$_2$Al$_3$ and NpNi$_2$Al$_3$ [4], the latter being the isostructural Np analogue of the heavy fermion superconductor UNi$_2$Al$_3$ [5]. Fig. 5.21 shows Mössbauer transmission spectra recorded at 4.2 K. The hyperfine parameters evaluated from the Mössbauer spectra taken at 4.2 K and the ordering temperatures are listed and compared to NpPd$_2$Al$_3$ in Tab. 5.5.

Contrary to UNi$_2$Al$_3$ the Np compound NpNi$_2$Al$_3$ shows magnetic order (below 23 K). The Mössbauer spectrum taken at 4.2 K could be fitted by assuming a distribution of at least three magnetic hyperfine fields with a slight additional line broadening, similar to NpPd$_2$Al$_3$ [1]. The values

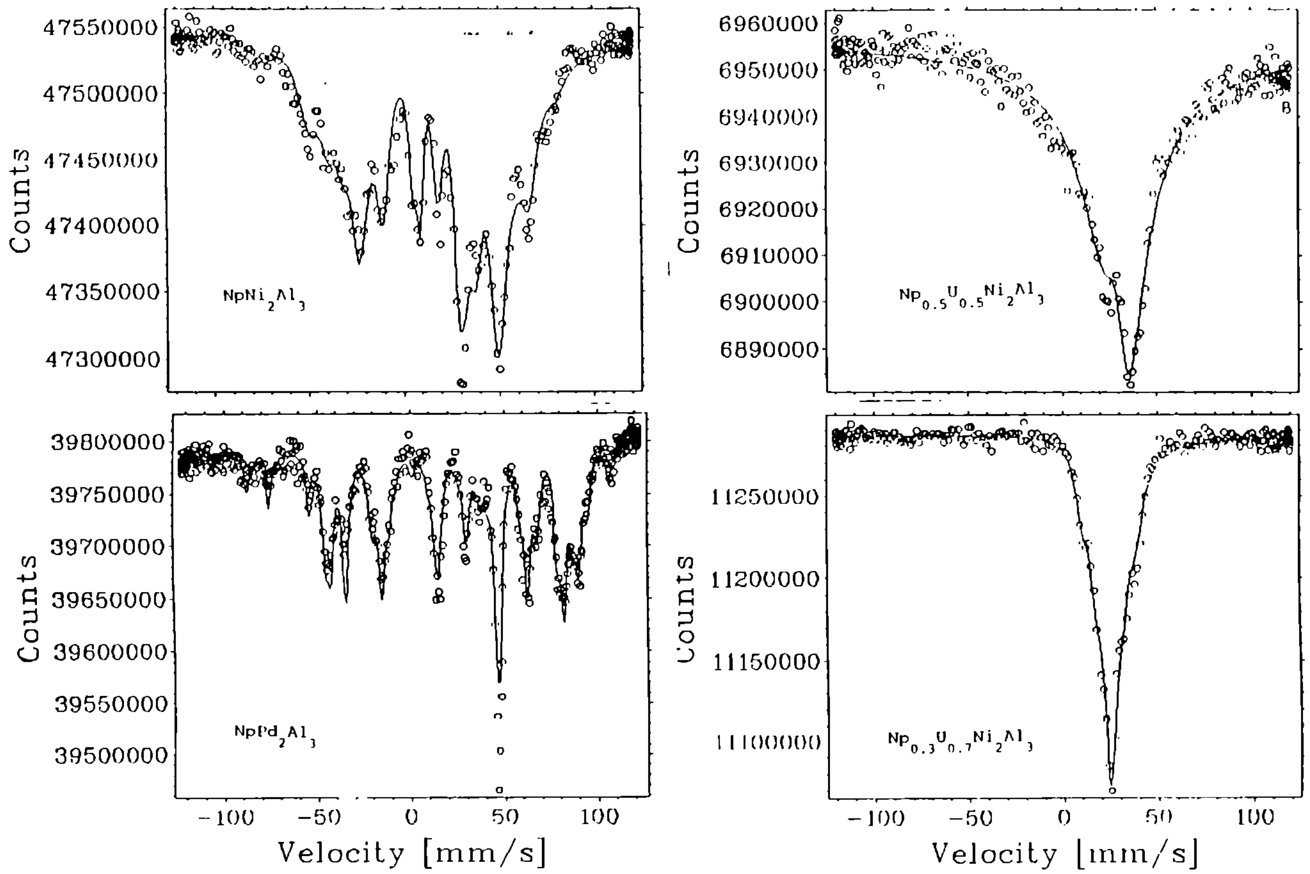

Fig. 5.21 Mössbauer spectra at 4.2 K of AnX_2Al_3 compounds (An = Np or Np, U; X = Ni or Pd)

Tab. 5.5 Hyperfine parameters and ordering temperatures of 4 neptunium compounds

Compounds	T_{ord} [K]	B_{Hf}^1 [T]	I_1 [%]	B_{Hf}^2 [T]	I_2 [%]	B_{Hf}^3 [T]	I_3 [%]	e^2qQ [mm/s]	IS[a] [mm/s]
$NpPd_2Al_3$	38(1)	360(1)	37(3)	316(1)	55(3)	121(3)	8(2)	48(1)	23.5(5)
$NpNi_2Al_3$	23(1)	298(2)	38(3)	228(2)	35(3)	200(2)	27(3)	38(1)	13.5(5)
$Np_{0.5}U_{0.5}Pd_2Al_3$	<6	150(5)	100	-	-	-	-	49(1)	24.7(5)
$Np_{0.3}U_{0.7}Pd_2Al_3$	-	-	-	-	-	-	-	48(1)	23.8(5)

[a] Isomer Shift is given relative to Am metal.

for the quadrupole coupling constant e^2qQ and magnetic hyperfine fields B_{hf} were obtained by assuming a common quantization axis for the magnetic and electric hyperfine interactions. This is different in the U compounds with the same structure [7]. According to the values of the isomer shift the charge state of both Np compounds is close to a Np^{3+} state (J = 4).

To investigate the difference of the magnetic anisotropic coupling and of the charge state between the U and the Np ions, we measured the isostructural solid solutions $Np_{0.5}U_{0.5}Pd_2Al_3$ and $Np_{0.3}U_{0.7}Pd_2Al_3$. For both compounds isomer shift and quadrupole splitting hardly deviate from the values found for $NpPd_2Al_3$, i.e. the Np^{3+} charge state and the electric field gradient are not affected by the alloying partner.

References

[1] S. Zwirner, J.C. Spirlet, J. Rebizant, W. Potzel, G.M. Kalvius, C. Geibel and F. Steglich, Physica **B 186-188** (1993) 681-683.

[2] TUAR-92, p. 151.

[3] C. Geibel et al., Z. Phys. **B 84** (1991) 1.

[4] S. Zwirner, J.C. Waerenborgh, J.C. Spirlet, J. Rebizant, W. Potzel, G.M. Kalvius (1994) to be published.

[5] C. Geibel et al., Z. Phys. **B 83** (1991) 305.

[7] A. Krimmel et al., Z. Phys. **B 86** (1992) 161

Mössbauer high pressure studies of NpX_3

The NpX_3 Mössbauer high pressure studies reported recently [1-2] were extended to $NpGa_3$ in the pressure range between ambient pressure and 9.2 GPa, and for $NpIn_3$ up to pressures of 10 GPa. The complex distribution of magnetic hyperfine fields observed in $NpIn_3$ at ambient pressure has been transformed at 10 GPa into a simple magnetic hyperfine pattern with a slightly enhanced field B_{hf}. The ordering temperature rises from 17 (2) K at ambient pressure to 32 (3) K at 10 GPa (Fig. 5.22).

According to earlier work [2,5,6] on $NpGa_3$, a larger hybridization between the 5f-electrons and the ligand conduction electrons is expected. Resistivity data showed a Kondo type behaviour [7]. However, the Kondo mechanism hardly seems to suppress the ordered moment, if a crystal field state T_5 is assumed. At ambient pressure $NpGa_3$ is ferromagnetic below 52 (2) K and antiferromagnetic between 52 K and 67 (2) K (Fig. 2). According to our high pressure data the antiferromagnetic phase disappears under pressure and only the ferromagnetic phase is left in the ordered temperature range: T_{ord} increases from 67 (2) K at ambient pressure to 105 (2) K at 9.2 GPa. The magnetic hyperfine field decreases only very slightly (less than 1 %). However, the decrease is nonlinear and possibly indicates an enhanced 5f-mixing with the conduction band, which on the one hand leads to an increase of the 5f delocalization, but causes on the other hand a stronger exchange interaction between the 5f moments [8]. It is planned to check by means of high pressure resistivity measurements, whether the increase of T_{ord} is accompanied by a gradual suppression of the Kondo mechanism. Furthermore the possibility to achieve pressures up to 20 GPa with this method [9], enables us to study whether the nonlinear decrease of the magnetic hyperfine field is an indication of a weakening of the magnetic exchange at higher pressures (between 10 GPa and 20 GPa).

References

[1] G.M. Kalvius, S. Zwirner, U. Potzel, J. Moser, W. Potzel, F.J. Litterst, J. Gal, S. Fredo, I. Yaar, J.C. Spirlet, Phys. Rev. Lett. **65** (1990) 2290

[2] S. Zwirner, W. Potzel, J.C. Spirlet, J. Rebizant, J. Gal and G.M. Kalvius, Physica **B 190** (1993) 107-113

[5] M.R. Norman and D.D. Koelling, Phys. Rev. **B 33** (1986) 3803

[6] J. Gal, I. Yaar, S. Fredo, J. Halevy, W. Potzel, S. Zwirner and G.M. Kalvius, Phys. Rev. **B 46** (1992)

[7] M.N. Bouillet, T. Charvolin, A. Blaise, P. Burlet, J.M. Fournier, J. Larroque and J.P. Sanchez, J. Magn. Mater. 125 (1993) 113-119

[8] B.R. Cooper and Q.G. Sheng, 23^{iemes} Journées des Actinides Bühlerhöhe, Hrtmsnx, Sptil 20-23, 1993, O2.1

[9] P. Link, Dissertation, Universität Karlsruhe (1993)

µSR studies of uranium compounds with $AuCu_3$ structure

We carried out µSR experiments on USn_3, UIn_3 and $U(Sn_{0.5}In_{0.5})_3$ in a 220 G transversal field, zero field and 2, 5, and 10 G longitudinal field and at temperatures between 300 K and 13 K. USn_3 behaves analogous to the well known spin-fluctuator UAl_2. UIn_3 exhibits in its antiferromagnetic state (T_N = 88 K) a Lorentzian Kubo-Toyabe pattern of the type seen in other simple cubic uranium compounds like UAs. $U(Sn_{0.5}In_{0.5})_3$ does not order magnetically. Its µSR spectra at low temperatures suggest that this material should be considered a spin glass like system with disordered spin freezing setting in at around 30 K.

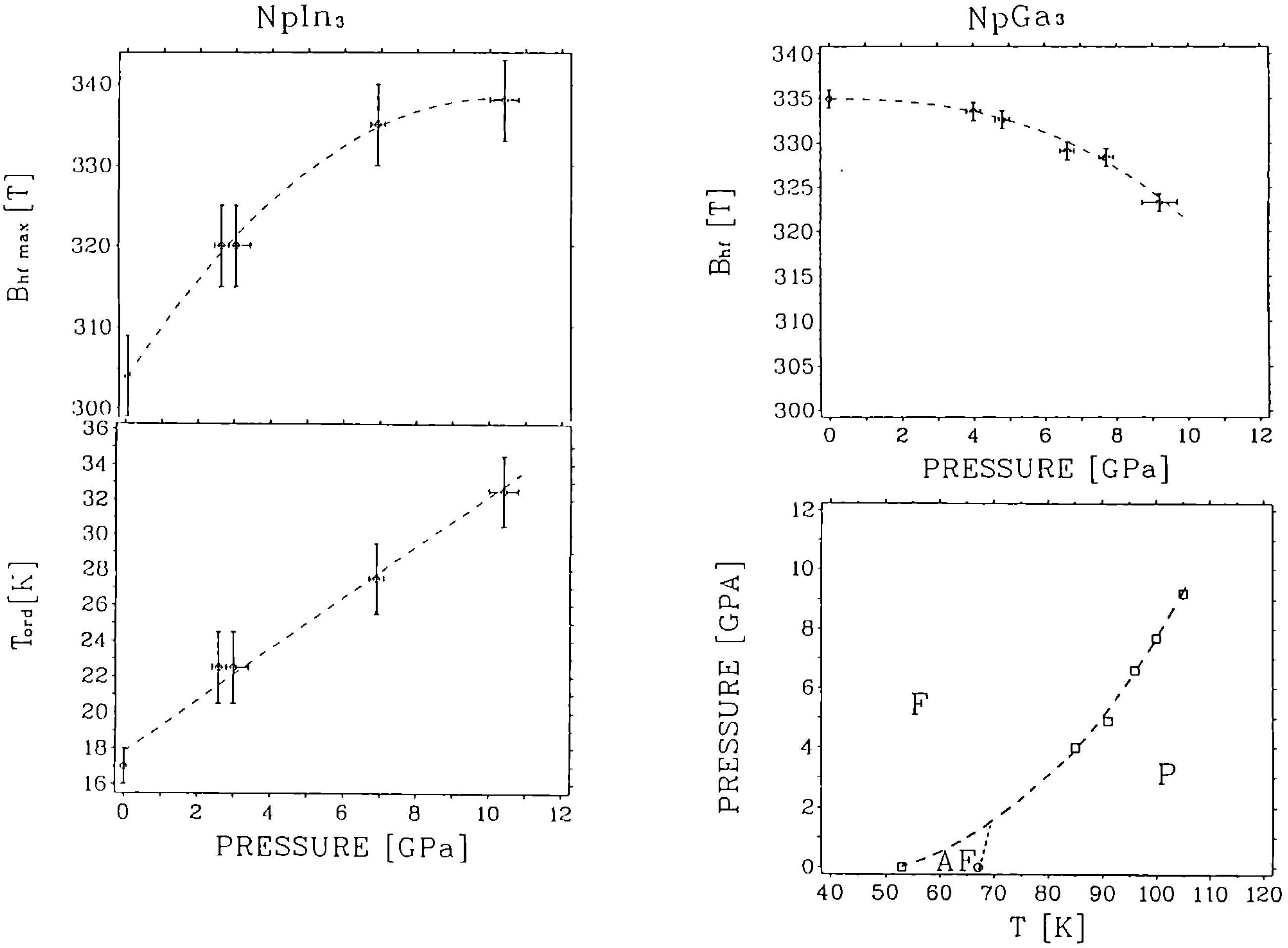

Fig. 5.22 Pressure dependence of the ordering temperature and the magnetic hyperfine field of $NpIn_3$ *and* $NpGa_3$*. For* $NpIn_3$ *the maximum values of the complex distribution of magnetic hyperfine fields are shown. For* $NpGa_3$ *there exist a ferromagnetic (F), an antiferromagnetic (AF) and a paramagnetic (P) phase. The dotted line between the phases AF and P is an extrapolation of the pressure behaviour of (antiferromagnetic)* $NpSn_3$*.*

To approach a more systematic understanding of UX_3 compounds we have started further measurements on $U(Sn_{0.25}In_{0.75})_3$, $U(Sn_{0.75}In_{0.25})_3$ and $NpGa_3$. Furthermore the investigation of $U(Sn_{0.6}In_{0.4})_3$, $U(Ge_{0.25}Ga_{0.75})_3$, $U(Ge_{0.5}Ga_{0.5})_3$ $U(Ge_{0.75}Ga_{0.25})_3$ and UGe_3, is under way.

High Pressure Studies on Actinide Systems

Electrical and magnetic properties of actinide materials under pressure

Resistivity and superconductivity of americium metal under pressure up to 25 GPa

We report here the high-pressure resistance of the dhcp and fcc form of americium as a function of temperature down to 1.3 K and up to pressures of 25 GPa. The most significant finding in this study was the considerable rise of the superconducting transition temperature for both the dhcp and fcc form of americium under pressure. In Fig. 5.23a the T_c versus p dependency of the dhcp-americium is shown together with the transition widths. Under increasing pressure T_c initially increases with a slope of about 0.45 K/GPa, if the onset at normal pressure is taken at 0.79 K as reported [1]. The T_c increases monotonously up to a value of 2.3 K at 6.5 GPa. It then decreases until a secondary maximum (or at least a clear shoulder) appears at about 10 GPa. The T_c decreases steadily again dropping below our temperature limit of 1.3 K at 13 GPa. Surprisingly enough, the dhcp-americium sample's T_c becomes measurable at 17 GPa again and rises to 1.6 K at 19 GPa. The T_c decreases once again and no indication of the superconductivity was seen above 21 GPa.

Fig. 5.23b shows the critical temperature determined for the fcc form of americium. We first observed the transition to superconductivity for the fcc sample at a pressure of 4.7 GPa. Taking into account the T_c of 1.05 K at ambient pressure [1], the T_c of the fcc sample had to increase strongly to the maximal value of 1.83 K we observed at 4.7 GPa. At higher pressures T_c decreases and becomes undetectable around 10 GPa, to reappear at 16 GPa and disappear again for the highest pressures.

The superconducting transition of americium was sharp and with a slow scanning of the temperature, totally reversible. The lowest-pressure resistance curves agree very well with previous, normal pressure measurements on thin samples [2]. In figure 5.24a we show a compiled diagram of the resistance of dhcp-americium versus pressure and temperature. A broad maximum in the low temperature resistance occurring at pressures be-

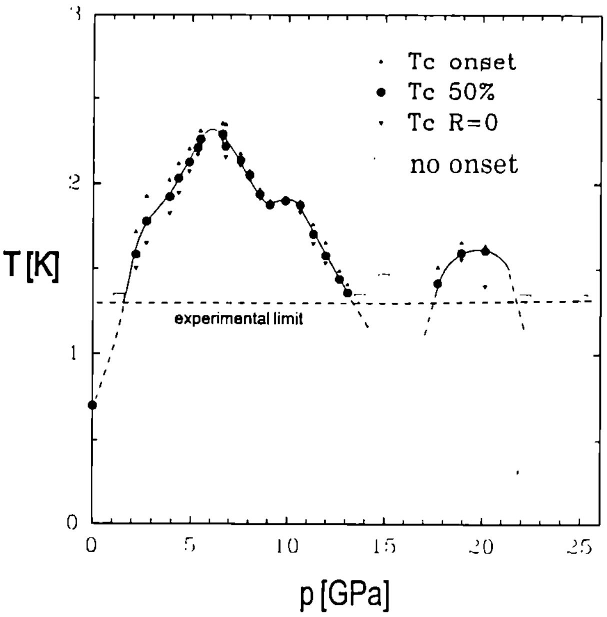

Fig. 5.23a Variation of the superconducting transition temperature, T_C, of dhcp-americium with pressure. The different symbols show the onset, midpoint and zero resistance temperatures. The hatched line shows the experimental limit with open triangles indicating that no onset of the superconductivity was observed.

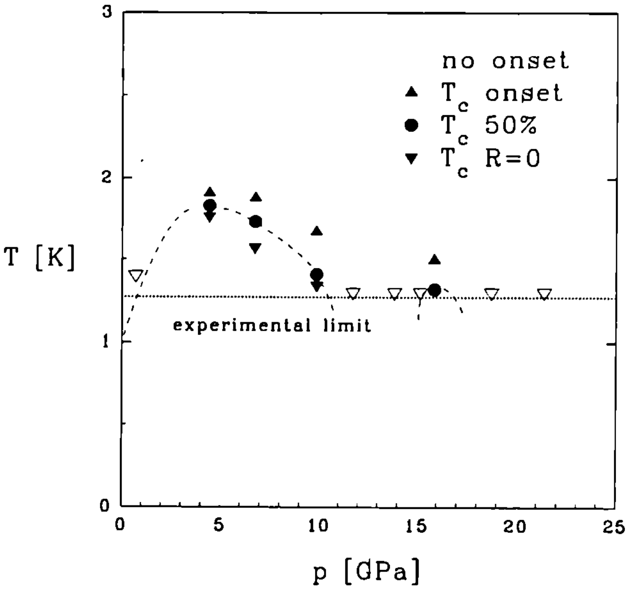

Fig. 5.23b Variation of the superconducting transition temperature, T_C, of fcc-americium with pressure. The different symbols show the onset, midpoint and zero resistance temperatures. The hatched line shows the experimental limit with open triangles indicating that no onset of the superconductivity was observed.

tween 6.6 GPa and 10 GPa is one and a sharp pronounced peak at 20 GPa most pronounced at higher temperatures another remarkable feature exhibited by this view. The resistance-vs.-pressure curves of the fcc sample are w-shaped (Fig. 5.24b). For pressures above 10 GPa, they exhibit a similar shape as those of the dhcp sample shown in Fig. 5.24a. The resistance of the fcc sample decreases first to a minimum around 4.5 GPa, increases then to maximum at 9 GPa for ambient temperature. At low temperatures the maximum is shifted to lower pressures. Further the resistance decreases again to a minimum around 15 GPa. Finally there is a pronounced maximum around 18 GPa.

Comparing the Figs. 5.24a and 5.24b of the dhcp- and fcc-americium respectively, the main differences appear at low pressures, where the phase transition AmI-AmII should not occur in the case of fcc-americium. In the neighbourhood of 20 GPa we find for both a pronounced maximum, which we attribute to the phase transition to the Am IV phase.

The Am III-Am IV transition was previously associated with the onset of the itinerancy of the 5f-electrons [3]. We believe our measurements provide some, admittedly faint, support for this notion. The sharp drop in the superconducting critical temperature above 20 GPa may be taken as a sign of a "magnetic behaviour", when the $5f^6$ configuration starts breaking up. Further investigation of $T_c(p)$ dependence in this pressure region is of considerable interest, but clearly outside of the present experimental possibilities.

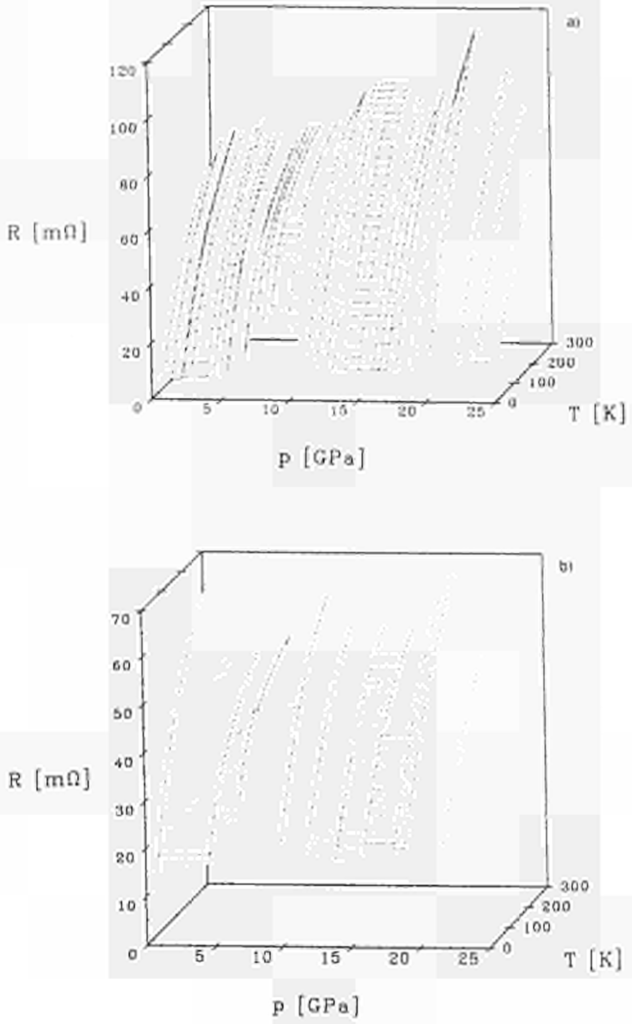

Fig. 5.24 Resistance versus pressure and temperature for a) dhcp-americium and b) fcc-americium. The isobaric lines represent the pressures where the measurements were made. The isothermal lines are guidelines to the eye.

References

[1] J.L. Smith and R.G. Haire; Science **200** (1978) 535.
[2] R. Schenkel and W. Müller; J. Phys. Chem. Solids **38** (1977) 1301.
[3] U. Benedict, J.P. Itié, C. Dufour, S. Dabos and J.C. Spirlet; in N. Edelstein, J.D. Navratil and W.W. Schulz (eds.), *Americium and Curium Chemistry and Technology* (1985) 213.

The electrical resistance of PuSb under high pressure

We measured the resistance of PuSb in the temperature range from 300 K down to 1.3 K at pressures up to 25 GPa. Fig. 5.25 shows that the temperature dependence of the resistance at the lowest pressures is in good agreement with the ambient pressure resistivity curve given by Blaise et al. [1]. With increasing pressure, the maximum of the resistance is shifted to higher temperatures and the decrease of the resistance with increasing temperature becomes less pronounced (Fig. 5.25). As seen from Fig. 5.26 the temperature derivative of the resistance features, two maxima in agreement with the ambient pressure behaviour. The broader maximum at higher temperatures indicates the Néel temperature, which increases from 82 K to 112 K at 8 GPa. The sharp peak is associated with the temperature of the transition from the incommensurate antiferromagnetic phase to the ferromagnetic ground state, which increases from 65 K to 80 K. Above 8 GPa this phase transition disappeared.

In the pressure range from 10 - 15 GPa the elec-

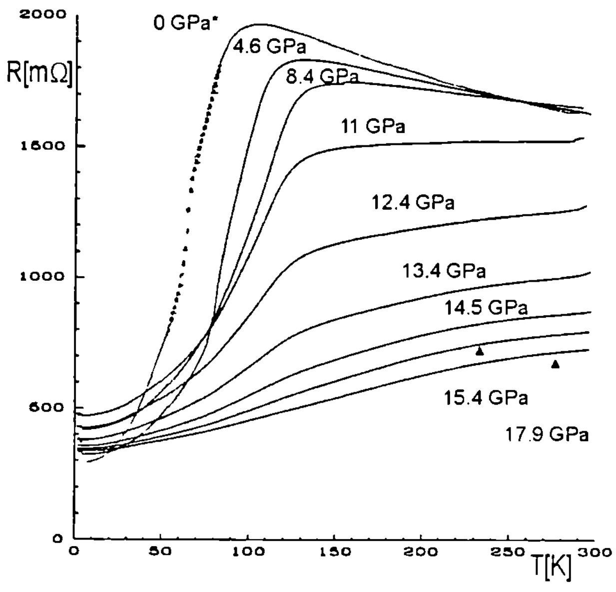

*Fig. 5.25 The electrical resistance of PuSb at selected pressures up to 18 GPa. * The rescaled 0 GPa data is taken from Blaise et al. [6].*

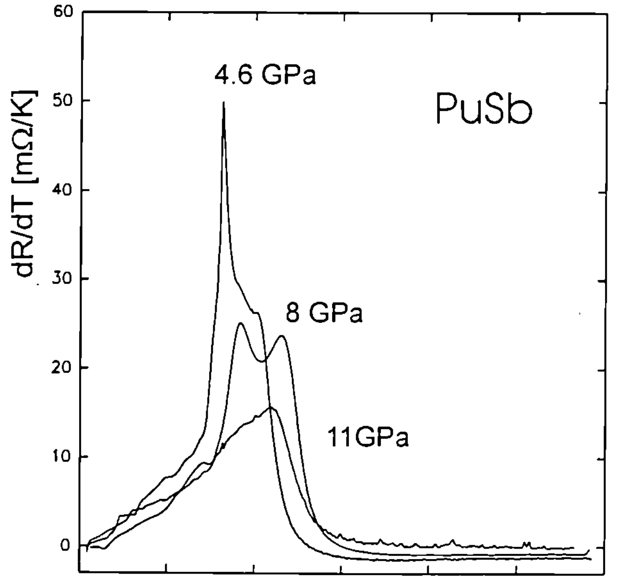

Fig. 5.26 Typical dR/dT curves of PuSb at selected pressures

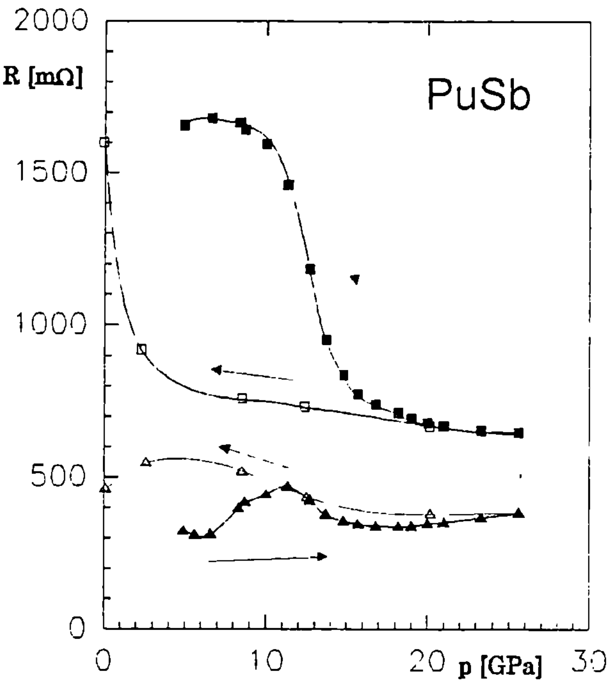

Fig. 5.27 The resistance of PuSb vs pressure at 273 K ■ and 4.2 K ▲; (open symbols for decreasing pressures)

trical resistance at the higher temperatures decreases strongly, as shown by the isobars at 11 GPa to 14.5 GPa in Fig. 5.25. The resistance at 4.2 K has a maximum at 12 GPa, almost coinciding with the pressure where the resistance at 273 K decreases most steeply (Fig. 5.27). In the same pressure range the maximum in dR/dT (related with the Néel-temperature) disappears. The temperature dependence of the resistance above 15 GPa shows no sign of magnetic ordering, most obviously displayed in the resistance at 25 GPa. Upon release of pressure, the resistance increases slightly (Fig. 5.27). Below 2.5 GPa the resistance increased sharply to the ambient pressure value (Fig. 5.27).

The high pressure behaviour of PuSb determined by our resistance measurements is dominated by the pronounced changes found above 8 GPa. These changes might be related to a crystallographic phase transformation, as will be discussed later.

In the low pressure region up to 8 GPa mainly three properties derived from our results call for an explanation. Firstly, there is a strong increase of the Néel-temperature from 82 K to 112 K at 8 GPa; secondly there is the shift of the maximum of the resistance to higher temperatures (Fig. 5.25); and in the third place, there is the weakening of the 'Kondo'-like resistance decrease at higher temperatures (Fig. 5.25). All these features are very reminiscent of the high pressure behaviour of UTe [2]. In UTe, suppression of the Kondo behaviour with pressure leads to a strong increase of the Curie-temperature. We propose that the increase of the ordering temperature in PuSb can be understood in the same way.

Above 10 GPa the 273 K-resistance of PuSb decreases rapidly to a value of about 40 % at 15 GPa (Fig. 5.27). Upon releasing pressure the resistance only returns to the original value at pressures below 2.5 GPa. The resistance at 4.2 K has a pronounced maximum at 12 GPa (Fig. 5.27) which is absent during the release of the pressure. This hysteretic behaviour of the resistance is reminiscent of that reported from high-pressure x-ray diffraction (HPXRD) [3]. The high-pressure phase (CsCl-structure) remains metastable with decreasing pressure down to 2 GPa. This feature, together with the maximum in the 4.2 K resistance around 12.5 GPa, which can then be explained by the formation of lattice defects (i.g. grain-boundaries) during the phase transition, supports our interpretation that the profound changes in the resistance between 10 GPa and 15 GPa are caused by the crystallographic phase transition.

The temperature dependence of the resistance at the highest pressures is exponential at temperatures below 20 K, and, quite remarkably, almost linear at higher temperatures. Hence, an indication for magnetic ordering could not be detected. During the crystallographic phase transition the plutonium-plutonium distance decreases from 417 pm to 366 pm. The decrease of the Pu-Pu-distance might cause the 5f-electrons to delocalise at the phase transition by means of increased 5f-5f-overlap, and/or 5f-6d hybridisation and could lead to the absence of magnetic ordering in the high pressure phase.

The magnetic ordering temperatures, obtained from the temperature dependence of the resistance at high pressures, allow us to suggest a magnetic phase diagram for PuSb as shown in Fig. 5.28.

References

[1] A. Blaise, J.M. Collard, J.M. Fournier, J. Rebizant, J.C. Spirlet and O. Vogt; Physica **130B** (1985) 99.

[2] P. Link, U. Benedict, J. Wittig and H. Wühl; J. Phys.: Condens. Matter **4** (1992) 5585.

[3] S. Dabos-Seignon, U. Benedict, S. Heathman and J.C. Spirlet; J. Less-Common Met., **160** (1990) 35.

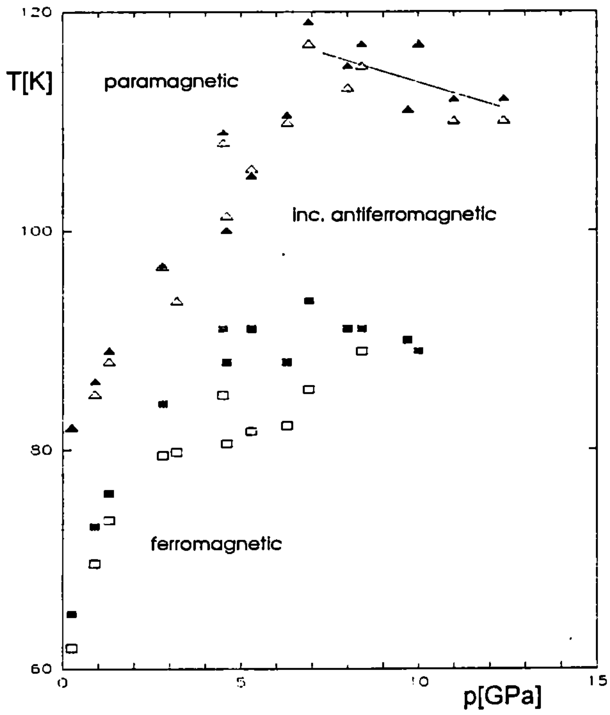

Fig. 5.28 Magnetic phase diagram of PuSb, derived from measurement of the electrical resistance as a function of pressure and temperature.
Néel-temperature T_N ▲
and transition temperature T_{IC} ■
- two independent cells
- open symbols represent decreasing temperatures

Improvements to the resistivity under pressure experiment

The purchase of a scanner and high precision programmable current source brought the following improvements:

- The sample and the Pb manometer can be measured simultaneously. By systematically recording the resistance of the lead versus temperature we can see any accidents that may happen during cooling or warming the cell (i.e. sudden change of pressure, movement of wires, change in measuring current due to a grounded wire, ...). We can therefore have more confidence in any real anomalies in the sample resistance.
- The thermometer measuring current is now programmable and is automatically adjusted for each temperature range. It will also be possible to use lower currents than before which will be important at very low temperatures.

Further improvements are planned, including a He^3 insert which will enable measurements to be made down to a temperature of about 300 mK (the present limit is 1.3 K) to continue the recent work on the superconductivity under pressure of americium and possibly other actinide metals or compounds.

Theory of pressure effects and the correlated-electron behavior of uranium monochalcogenides

Experimentally, hydrostatic pressure experiments provide a very sensitive way to probe the development of magnetic ordering in correlated-electron systems. The recent high-pressure experiments of Link et al. [1] on UTe provide extremely interesting results. With applied pressure, the Curie temperature (T_C) for UTe increases from 104 K to a maximum of 181 K at 7.5 GPa and then decreases to 156 K at 17.5 GPa. This experimental behavior is qualitatively what we expect on the basis of our theory of the correlated-electron behavior. Basically, increasing pressure causes increased hybridization which causes an increase of coupling between the moments associated with the relatively localized part of the f spectra density at each lattice site. However, as the pressure increases further, the loss of localized f spectra density caused by the increased merger with the non-f band density causes a decrease of ordered moment and hence a decrease in T_C. We have performed calculations quantifying the above picture for UTe. First we calculate the pressure dependence of the lattice constant, in reasonable agreement with experiment. Next, at calculated lattice constants we calculate T_C using correlated-electron theory for magnetic ordering. These results capture the initial increase in T_C resulting from increased hybridization as well as the reversal of this initial increase caused by the loss of localized f-density (Fig. 5.29).

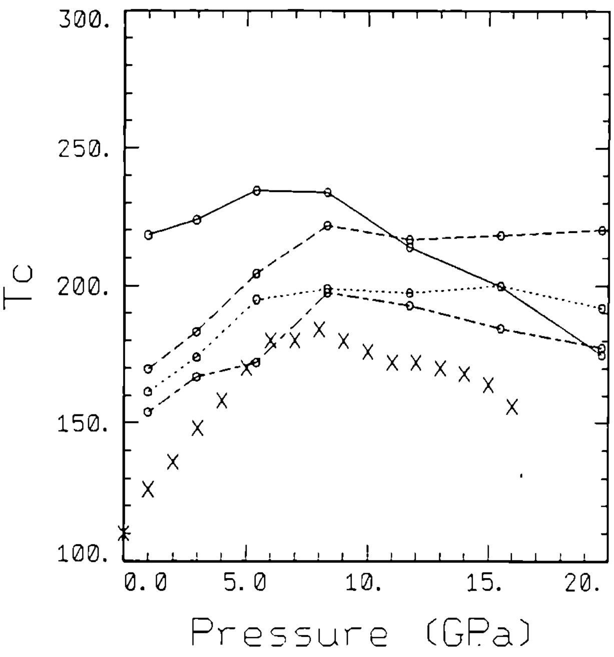

Fig. 5.29 T_C of UTe versus pressure. The solid line is calculated for $\rho_{cutoff} = 15\%\rho_{max}$; the long dashed line for $\rho_{cutoff} = 20\%\rho_{max}$; the short dashed line for $\rho_{cutoff} = 25\%\rho_{max}$; the long-short-dashed line for $\rho_{cutoff} = 28\%\rho_{max}$. The crosses are experimental data from Link et al. [2].

Reference

[1] P. Link, U. Benedict, J. Wittig, and H. Wühl, J. Phys: Condens. Matter 4 (1992) 5585

Structural versus physical properties of actinide materials at high pressure

In a first approach, one was tempted to associate the changes in crystal structure, i.e. the phase transitions, with synchronous changes in other properties. Electrical resistance and optical properties were expected to undergo relatively abrupt changes at the pressure of the structural phase transition. Such a situation was found to exist in the variation of optical reflection of some B1 type compounds with pressure: For 10 uranium and thorium compounds, variation of reflectivity with pressure and with the energy of the incident light was measured [1]. Peaks in the reflection spectrum correspond to electronic excitations in the solid by the incident light. Many of these peaks could be correlated with either the high-pressure or the ambient-pressure phases of the compounds studied, supplying indications on the electronic structures of these phases. The optical reflection spectra of UAs for different pressures are given in Fig. 5.30 as an example. Maxima A and C in reflectivity around 1.2 and 3.5 eV seem to be characteristic of the B1 type phase since they disappear at pressures above 18 GPa where the transition to the B2 type phase occurs.

Another example are phase transitions in UC and UP to less symmetric high-pressure structures which are accompanied by a shift of the L_{III} x-ray absorption edge [2].

But in other cases the changes in electrical, magnetic and optical properties are not synchronous with the crystallographical phase transitions.

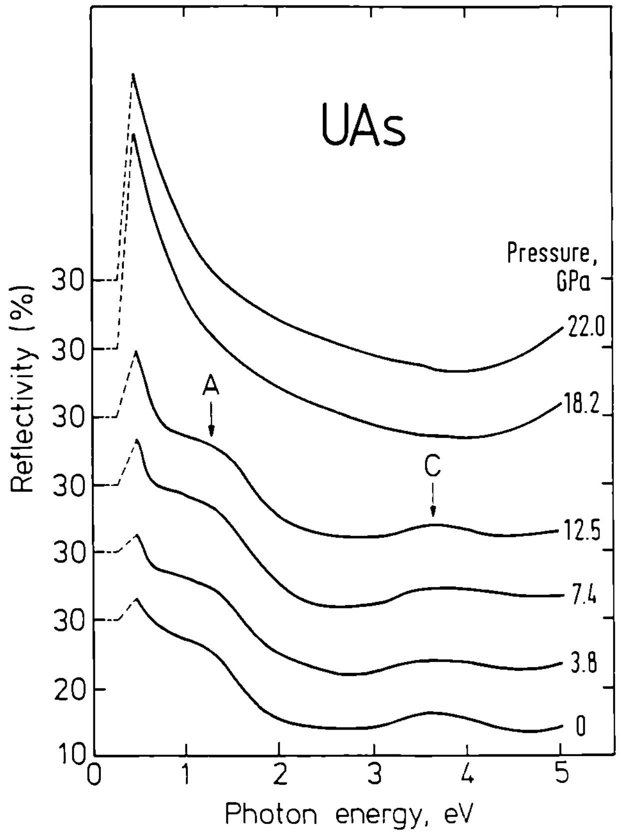

Fig. 5.30 Optical reflectivity of UAs for different pressures. The figures for reflectivity (%) only apply to the 0 GPa curve; all other curves are shifted by a constant amount with respect to the curve of next-lower pressure. Note disappearance of maxima A and C above the structural phase transition which occurs around 18 GPa.

Certain physical properties can start to change at pressures where no indication is yet observed of a structural phase transition. On the other hand, a physical phenomenon such as magnetic order can persist **through** a structural phase transition. We shall see from a few selected examples that each material has to be discussed separately, and that even inside the same family of compounds, e.g. the B1 type compounds, the relationship between the structural phase transition and other physical changes may vary considerably. We shall successively discuss the results obtained on UTe, USe, PuSb, Th_3P_4, UO_2 and Am metal.

Uranium monotelluride

UTe was observed to successively transform from the B1 to the B2 structure type in the pressure range 10-20 GPa, at room temperature [3]; TUAR-91, p. 154-157. This phase transformation is indicated in Fig. 5.31a by the narrow shaded zone around 298 K.

The derivative dR/dT of the electrical resistance of UTe has a sharp maximum at the ferromagnetic ordering temperature T_C [4,5]. This allows us to plot in Fig. 5.31a the upper limit of the ferromagnetic area of the magnetic phase diagram. In the pressure range 11.5 to 16.5 GPa, the maximum in dR/dT corresponding to T_C successively disappears, but another maximum grows up at lower temperature (about 80 K) and persists up to the upper pressure limit reached in this experiment. The temperature variation of this second maximum with pressure is shown by the lower line in the left part of Fig. 5.31a. The second maximum was tentatively interpreted as corresponding to magnetic ordering too. This will have to be confirmed by direct determination of magnetic properties under pressure, and in particular we do not know *which kind* of magnetic order may exist below this line in the diagram.

The transition between the two regimes of assumed magnetic order takes place in the same pressure range where the structural transition from B1 to B2 was observed. Although the structural transition was only studied at room temperature and could in principle occur at a different pressure (or even not at all) at lower temperatures, the agreement between the two pressure ranges suggests the best interpretation is the following: also at temperatures below 200 K, the B1 type phase transforms to the B2 type in roughly the same pressure range as at room temperature, but the structural change does not destroy magnetic order as could be expected. The only effects on magnetic behaviour induced by the structural phase transition are a large decrease in the ordering temperature, and, possibly, a transition to a different type of order. Thus UTe seems to be a case where magnetic order is not independent from structure, but survives the structural phase transition.

Another strong argument for the selected interpretation is based on the hysteresis observed for the structural transition of UTe. The backward transition B2 to B1 does not occur on pressure release at room temperature. The analogous hysteresis observed in the assumed magnetic ordering very clearly shows that in the case of UTe the two **different ordering temperatures correspond to the two different crystallographic structures, NaCl (B1) type and CsCl (B2) type.**

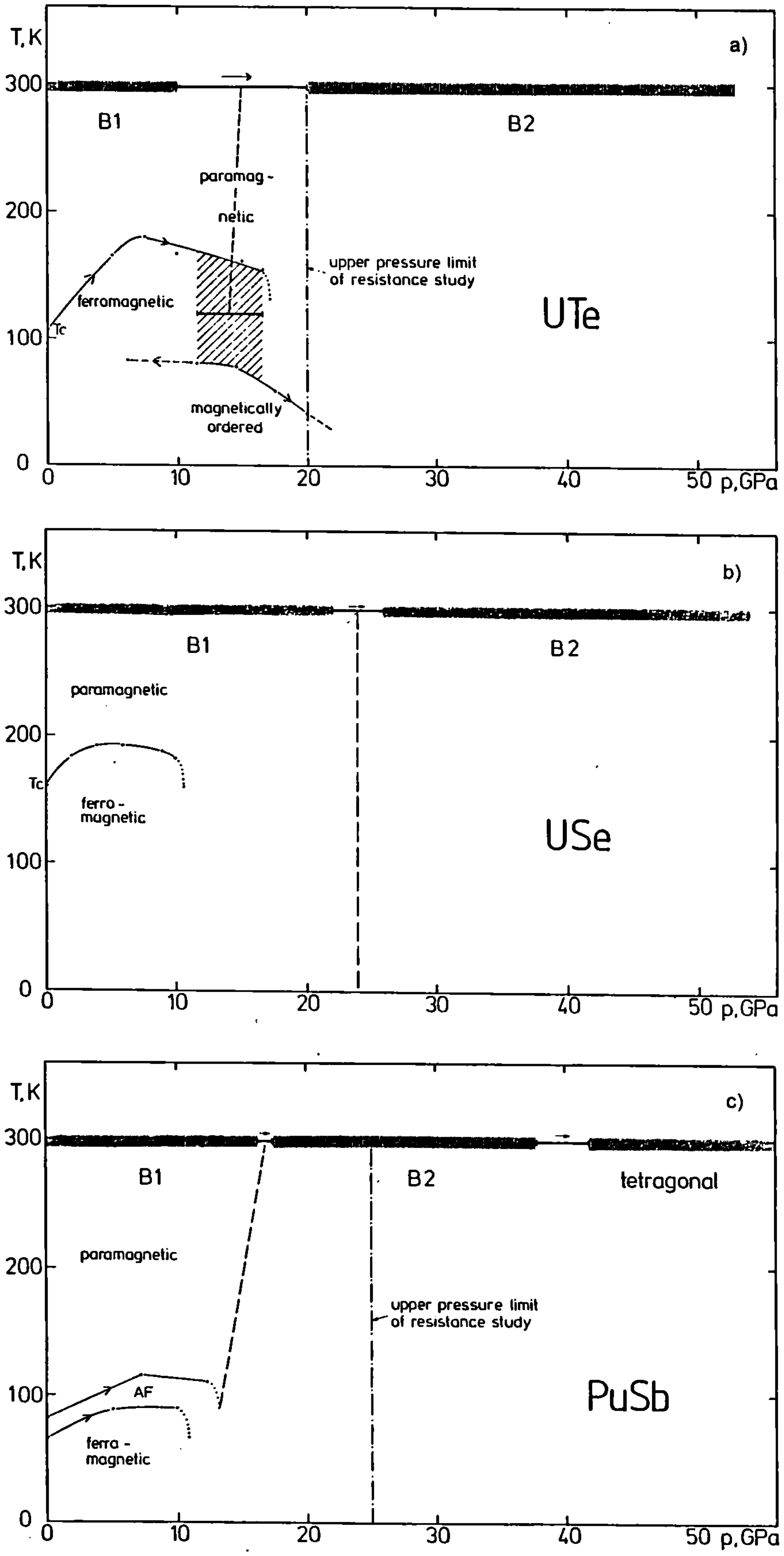

Fig. 5.31 Known elements of structural and magnetic phase diagrams for UTe (Fig. 5.31a), USe (Fig. 5.31b) and PuSb (Fig. 5.31c). Arrows indicate direction of pressure variation. AF: antiferromagnetic

Uranium monoselenide

Fig. 5.31b is a representation of the known results of the pressure behaviour of USe analogous to that given in Fig. 5.31a for UTe. USe has been studied up to 54 GPa by x-ray diffraction at room temperature [3; TUAR-92, 154-156]. The same B1 to B2 transition as in UTe was observed, but it occurred at higher pressure, in the pressure range 22 to 26 GPa (narrow shaded zone at room temperature in Fig. 5.31b). The ferromagnetic transition of USe, deduced from the dR/dT curve in the same way as for UTe [6], is shown as the curved line between 160 and 192 K in the left part of Fig. 5.31b. Although the variation of electrical resistance in USe was followed up to 22 GPa, no indication for magnetic order was obtained from these measurements above 10 GPa.

Two interpretations are possible: Either the disappearance of ferromagnetism above 10 GPa indicates that the structural transition from B1 to B2 takes place around 10 GPa in the temperature range of ferromagnetic ordering, and there is no magnetic order in the high-pressure B2 type phase. This would mean a quite oblique limit between B1 and B2 in the structural phase diagram, as shown in Fig. 5.31b by the thin dashed line. Or we assume that the pressure range of the structural phase transition, as in the case of UTe, undergoes only small variation when temperature is lowered (thick dashed line), and magnetic order is destroyed by volume effects only, without any influence of crystal structure.

In view of the very good coincidence in pressure ranges for the structural and electrical/magnetic changes in UTe, indicating a nearly vertical line in the phase diagram for the B1 to B2 transition, we tend towards the second explanation.

Plutonium antimonide

Two successive magnetic transitions are observed in this compound as a function of temperature. At ambient pressure, PuSb is ferromagnetic below 65 K and antiferromagnetic between 65 and 82 K. Fig. 5.31c shows, on the basis of recent measurements of the electrical resistance under pressure [5,7,8], how the temperatures of the two magnetic transitions vary with pressure. As in the two cases of UTe and USe described above, the magnetic ordering temperatures appear as clear maxima in the derivative dR/dT. No maximum corresponding to an antiferro-ferro transition is observed any longer above 10 GPa, and the maximum associated with the para-antiferro transition also disappears at a somewhat higher pressure, i.e. above 12.5 GPa.

Ref. 8; see also this report, pp. 150-152 gives good arguments to correlate the disappearance of the maxima in dR/dT with the structural phase transition from the B1 to the B2 type that was observed earlier [9]. This view is presented in Fig. 5.31c by the thick dashed line which would mean that 1) the B1 to B2 phase transition is accompanied by the loss of magnetic order and 2) the transition pressure for the B1 to B2 transformation decreases slightly with decreasing temperature.

Summary for the B1 type compounds

The three examples seem to show that magnetic order, which has certainly strong links to crystal structure, is nevertheless more independent from structure than one may think. In these three compounds, if our hypotheses are definitely confirmed, we have one example (USe) where within the same crystal structure, we have magnetic order or not, only depending on volume and interatomic distances, and we have one case (UTe) where even with a severe structural change, magnetic order survives the phase transition.

Trithorium tetraphosphide

This compound and the isostructural U_3P_4 were studied by x-ray diffraction up to 40 GPa [10; TUAR-90, p.127]. No structural phase transition was observed in this pressure range for either of these two compounds. The evolution of optical reflectivity, optical conductivity and dielectric constant with pressure was determined for Th_3P_4 and U_3P_4 [11,12; TUAR-92, 153-154]. In the thorium compound, which is a semiconductor at ambient pressure, indications for the appearance of metallic character were obtained at a pressure of 38 GPa, whereas the x-ray diffraction spectra did not show any sign of a structural phase transition up to 40 GPa. This means again that an important physical process, i.e. metallization, occurs without an accompanying change in crystal structure, but only seems to depend on volume and interatomic distance.

Uranium dioxide

The optical response of UO_2 was studied up to 36 GPa [13]. At pressures above about 15 GPa, excitations within the $5f^2$ multiplet of UO_2 became observable in reflection and seem to indicate an increasing admixture of presumably d-like character to the $5f^2$ ground state configuration. In addition, the optical reflectivity of UO_2 at 0.5 eV was found to increase sharply above 20 GPa (Fig. 5.32). An x-ray diffraction study of UO_2 up to 38 GPa [14] showed that cubic fluorite-type UO_2 successively transformed to an orthorhombic structure in the pressure range 29 to 38 GPa.

The above mentioned intra-band transitions and the sharp increase in reflectivity appear at pressures much below that of the structural phase transition. They seem to be more or less structure-independent and a consequence of the volume compression and the accompanying band overlap. The fact that the reflectivity of ThO_2 does not exhibit similar features [12] may confirm that the excitations in UO_2 are 5f-related.

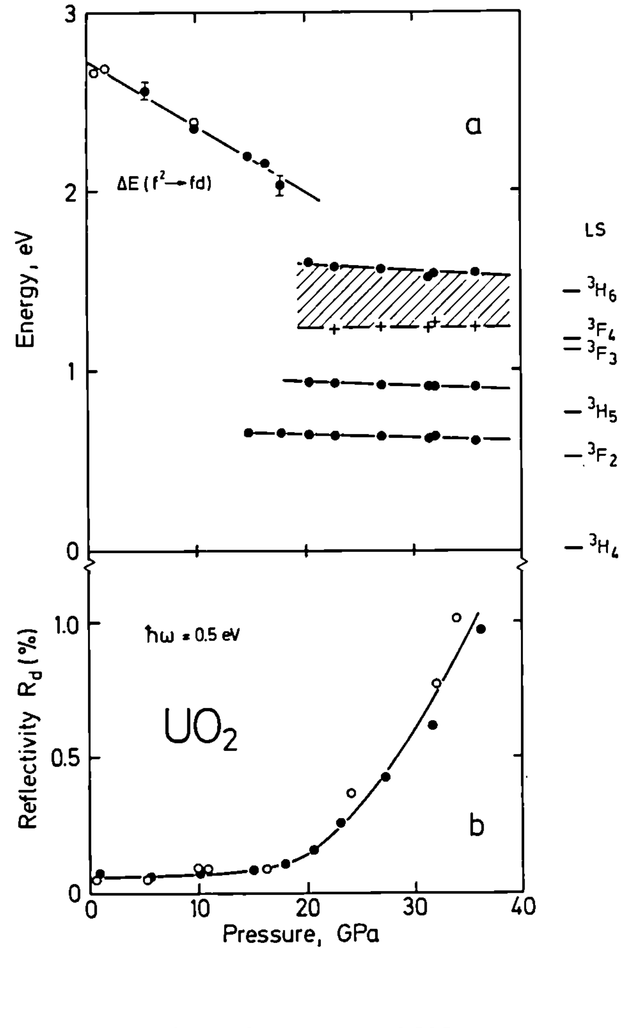

Fig. 5.32 Optical response of UO_2 vs. pressure up to 36 GPa [14]
a. Energy of reflectivity maxima
b. Reflectivity at 0.5 eV

Americium metal

X-ray diffraction study under pressure was made on Am by three different groups at room temperature. In addition to the ambient-pressure room-temperature dhcp phase, 3 high-pressure phases were observed. A review on these results has been given elsewhere [15].

Recently, the electrical resistance of Am was determined up to a pressure of 25 GPa and down to temperatures of 1.3 K [8 (see also this report, pp. 149-150)]. It was observed that the superconducting transition earlier observed around 0.8 K at ambient pressure by Smith and Haire [16] was shifted to temperatures above 1.3 K in two separate pressure ranges (2-13 and 17-21 GPa for an initially dhcp sample, and about 3-10 and 15-18 GPa for a sample with quenched fcc as initial structure). An attempt to associate either maxima or minima of the superconducting T_c, as well as other particular features of the resistance-vs.-pressure curves with the pressure-induced structural phase transitions observed by x-ray diffraction is made in Fig. 5.33.

Fig. 5.33a and d represent the two most complete published data sets on volume decrease and phase transitions of americium with pressure [17,18]. From both, the reported pressure ranges of structural phase transitions project as hatched zones into Figs. 5.33b and c which show the variation of T_c and R with pressure, at the same pressure scale [19,20]. (It should be noted that the pressure ranges for the phase transitions differ between the two sets of data.)

Comparing with Fig. 5.33a, we see that the reported transition from dhcp to ccp (= fcc) occurs in the range where a) T_c is close to a minimum b) R(100) has a maximum (this maximum persists at the same pressure when temperature drops below 100 K). The range of transition from the trigonal to the orthorhombic phase coincides with a steep drop in T_c and R.

Comparing then with Fig. 5.33d, the three reported pressure ranges of structural phase transitions coincide approximately with extrema of the T_c curve, best agreement being observed between the transition Am II --> Am III and the second maximum in T_c. But there is no correspondence with particular features of the resistance curves.

Can we give any physical significance to these correspondences, or are they merely fortuitous? There is one first argument: can we assume that a

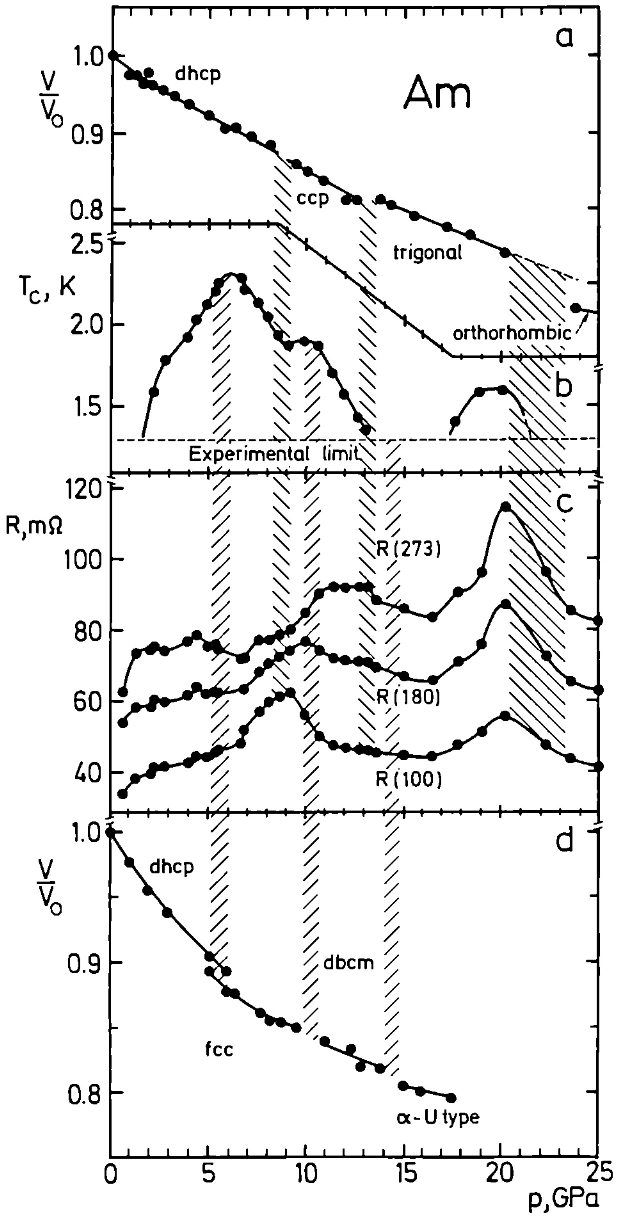

Fig. 5.33 Variation of electrical and structural properties of americium with pressure.
a. Relative volume and structural phase transitions according to ref. 17
b. Superconducting transition temperature T_c according to ref. 20
c. Electrical resistance at three selected temperatures (273, 180 and 100 K) according to refs. 19 and 20
d. Relative volume and structural phase transitions according to ref. 18

structural phase transition observed at room temperature occurs at the same pressure when the temperature is down to, say, 100 K, or even 1.5 K? If not, there is no base at all for the comparisons made in the two preceding paragraphs.

If in contrast we assume that lowering the temperature does not essentially affect the pressure ranges of the structural transitions in Am, in a similar way as we have proposed above in connection with magnetic properties of B1 type compounds, then we have to find a plausible physical interpretation of the observed correspondences, and also of the fact that we have correspondences with some of the features, but not with other similar features in the same group of curves.

Let us try to explain why two maxima and one minimum in the T_c curve correspond approximately with the phase transitions as reported in ref. [18] (compare Figs. 5.33b and d). An obvious way would be to say that the T_c vs. pressure characteristic of each phase of Am is different. Then two other extrema (a minimum around 9 GPa and a maximum around 20 GPa) and a marked shoulder around 2 GPa in the T_c curve remain unexplained. No known structural phase transitions can be associated with these features. But ref. 20 gives strong argument for associating the first maximum of $T_c = 2.3$ K with the dhcp phase and the second maximum ($T_c = 1.8$ K) with the fcc phase. In this reference, in addition to the results described above for the compression of an initially dhcp sample, T_c (p) and R(p) for an initially fcc sample are reported: only one maximum with $T_c = 1.8$ K was observed. This could also mean that only in the dhcp phase T_c can reach 2.3 K, while it can only increase to 1.8 K in the fcc phase.

If, on the other hand, we compare with Fig. 5.33a (ref. [17]), the maximum in R(100) around 9 GPa (Fig. 5.33c) could tentatively be explained by some mechanical stress induced by the dhcp --> ccp phase transition reported at the same pressure. But why then does this maximum not exist at the same pressure when resistance is measured at room temperature, where the structural results were obtained? The second correspondence with Fig. 5.33a, the sharp drop in T_c and R at the reported phase transition Am III --> Am IV, may tentatively be associated (as done in ref. [20]) with the delocalization of the 5f electrons which is assumed to occur when the low-symmetry orthorhombic structure is formed.

It is felt that, as was already shown in the examples given above for the compounds, also for americium metal

1) we can not expect that a given physical property abruptly changes when a structural phase transition takes place

2) a physical property can undergo a marked change *within* the area of stability of a given crystal structure. In the case of Am, an additional complication is the disagreement between different groups of authors on the pressures at which certain phase transitions take place, and on the crystal structure of some of the high-pressure phases.

References:

[1] H. Luo, K. Syassen, U. Benedict, O. Vogt, poster presented at the 18èmes Journées des Actinides, Paris, April 20-22, 1988

[2] J.P. Itié, U. Benedict, S. Dabos, E. Dartyge, A. Fontaine, G. Tourillon, J. Staun Olsen, Inorg. Chim. Acta 140 (1987) 193-195

[3] L. Gerward, J. Staun Olsen, U. Benedict, S. Dabos, O. Vogt, High-Pressure Research 1 (1989) 235-251

[4] P. Link, U. Benedict, J. Wittig and H. Wühl, J. Phys.: Condens. Matter 4 (1992) 5585-5589

[5] P. Link, Diss. Univ. Karlsruhe, Feb. 1993

[6] P. Link, U. Benedict, J. Wittig and H. Wühl, Physica B 190 (1993) 68-71

[7] P. Link, U. Benedict, J. Wittig, H. Wühl, J. Rebizant and J.C. Spirlet, oral communication at 23èmes Journées des Actinides, Bühlerhöhe, Germany, April 20-23, 1993

[8] P. Link, U. Benedict, J. Wittig, H. Wühl, J. Rebizant and J.C. Spirlet, J. Alloys Comp. (1994) (in print)

[9] S. Dabos-Seignon, U. Benedict, S. Heathman, J.C. Spirlet, M. Pagès, J. Less-Common Metals 160 (1990) 35-52

[10] L. Gerward, J. Staun Olsen, U. Benedict, H. Luo, F. Hulliger, High Pressure Research 4 (1990) 357-359

[11] M. Gensini, K. Syassen, U. Benedict and F. Hulliger, to be published

[12] TUAR-92, Annual Report for 1992, CEC-JRC, Institute for Transuranium Elements, Karlsruhe, Germany, 1993, 153-154

[13] K. Syassen, H. Winzen, U. Benedict, Physica 144B (1986) 91; K. Syassen, H. Winzer, private communication (internal report) 1985

[14] U. Benedict, G.D. Andreetti, J.M. Fournier, A. Waintal, 1982, J. Phys. Lett. 43 (1982) L171-L177

[15] U. Benedict, in: Handbook on the Physics and Chemistry of the Actinides, vol. 5, eds. A.J. Freeman, G.H. Lander, North Holland Amsterdam 1987, pp. 227-269

[16] J.L. Smith and R.G. Haire, Science 200 (1978) 535

[17] U. Benedict, J.P. Itié, C. Dufour, S. Dabos, J.C. Spirlet, pp. 213-224 of: Americium and Curium Chemistry and Technology, ed. N.M. Edelstein, J.D. Navratil, W.W. Schulz, D. Reidel Publ. Co. Dordrecht/Boston 1985

[18] R.B. Roof, Z. Kristallogr. B 15 (1982) 307-312

[19] P. Link, D. Braithwaite, U. Benedict, J. Wittig and R.G. Haire, poster communication at 23èmes Journées des Actinides, Bühlerhöhe, Germany, April 20-23, 1993

[20] P. Link, D. Braithwaite, J. Wittig, U. Benedict and R.G. Haire, J. Alloys Comp. (1994) (in print)

The optical response of NpSb and PuSb under pressure

Optical reflection is a well known technique to obtain information about the electronic structure of a material. When used in combination with high pressure, it is possible to investigate the changes in the electronic structure due to a changed lattice parameter without changing the chemical composition. For this purpose, different monopnictides and -chalcogenides of neptunium and plutonium were studied at room temperature up to maximum pressures of about 60 GPa.

To obtain high pressures inside the actual pressure chamber, a gasket hole of about 200 μm diameter, two diamonds with culets of ~ 0.5 mm diameter are pressing against it [1,2]. A solid but soft pressure medium (CsCl) inside the hole ensures a close contact of the sample surface and the diamond, while on the same time providing nearly hydrostatic pressure conditions. The pressure was determined by the ruby fluorescence method [3].

The normal incidence reflection measurements were recorded with a confocal microscopic imaging system in the energy range of 0.5 eV to 5 eV. To obtain the normalized reflectivity R_N for each energy $E = \hbar\omega$, the reflected light intensity I_S of the sample was corrected by a prerecorded diamond-air reference measurement I_R and an energy dependent diamond reflectivity R_D [4].

$$R_N(\hbar\omega) = R_D(\hbar\omega)\,\left.\frac{\textit{sample intensity } I_S}{\textit{reference intensity } I_R}\right|_{E=\hbar\omega}$$

Two examples shall be given to illustrate the effect of pressure on the reflectivity spectra of actinide compounds. Figure 5.34 shows the reflectivity of NpSb for pressures up to 60 GPa.

At low pressures, the sample has a very low overall reflectivity, corresponding to the fact, that NpSb is a semimetallic system [5]. Around 3 eV a small and very broad oscillator of unknown origin is observed. With increasing pressure, the overall reflectivity shows a strong and steady increase, especially pronounced at very low energies. Fi-

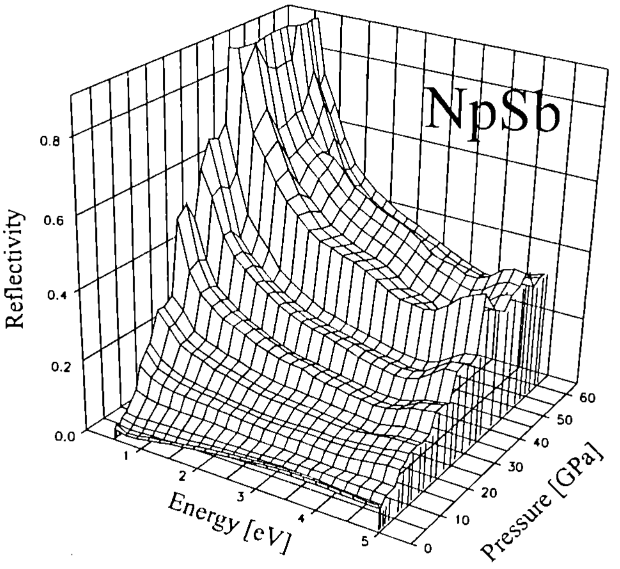

Fig. 5.34 Various reflectivity spectra of NpSb at different pressures, obtained with a diamond anvil cell at room temperature.

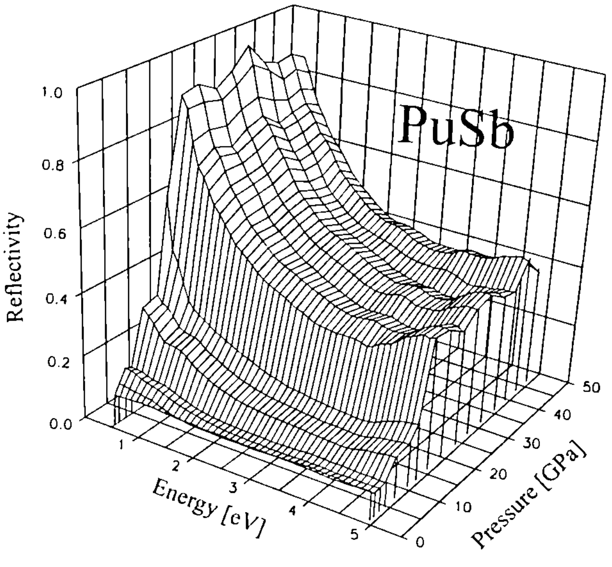

Fig. 5.35 Room temperature reflectivity spectra of PuSb for different pressures.

nally, at the highest pressures obtained, the low-energy reflectivity reaches a remarkable value of about 90 %. This might be seen as an indication for an increasing number of practically free electrons at higher pressures.

An interesting aspect can be gained by looking at the structural behaviour at elevated pressures. X-ray experiments reveal a sudden phase transition at 12 GPa from the NaCl-structure at ambient pressure to a tetragonal high pressure structure [6]. Correlating this change in structure with the steady increase of the overall reflectivity in Fig. 5.34, it can be concluded, that in terms of the electronic structure, this phase transition seems to be a very sluggish process.

A somehow similar behaviour during a structural phase transition can be observed in the reflectivity spectras of PuSb (Fig. 5.35).

At very low pressures, the overall reflectivity is quite small as in the previous case, eventually rising with increasing pressure. And again, the low-energy parts of the spectra rise much faster than the rest. But approaching the transition pressure of the NaCl-to-tetragonal phase transformation at ~20 GPa, the reflectivity increase continously accelerates, whilst reflectivity eventually becomes constant at more elevated pressures.

These examples prove, that even in spite of the still prevailing problem of possibly oxidized surface layers, optical experiments can help to understand the electronic structure of actinide compounds. Therefore one of the major goals of the future is to obtain a closer theoretical explanation for the observed phenomena.

References

[1] A. Jayaraman. Diamond anvil cell and high-pressure physical investigations. Rev. Modern Phys. 55 (1983) 65

[2] A. Jayaraman. Ultrahigh pressures. Rev. Sci. Instrum. 57 (1986) 1013

[3] H.K. Mao, J. Xu, and P.M. Bell. Calibration of the ruby pressure gauge to 800 kbar under quasi-hydrostatic conditions. J. Geoph. Res. 91 (1986) 4673

[4] Landolt-Börnstein, O. Madelung, H. Weiss, and M. Schulz. *Numerical data and functional relationships in science and technology, new series*, vol. **17**, Springer Verlag, Heidelberg, 1982

[5] J.M. Fournier, E. Gratz, pp. 409-537 of: *Handbook on the Physics and Chemistry of Rare Earths*, K.A. Gschneidner, LeRoy Eyring, G.H. Lander, G.R. Choppin, eds., North Holland, Amsterdam 1993

[6] S. Dabos-Seignon, U. Benedict, S. Heathman, J.C. Spirlet, and M. Pages, J. Less-Common Met. **160** (1990) 35

Recent study of actinide materials under pressure by synchrotron X-ray diffraction

High pressure phase transformations in $Ce_{0.5}Th_{0.5}$ alloy to 253 GPa

Ce (localized f-shell) and Th (itinerant f-band) form two extremes in f-electron behaviour. We report ultra high pressure phase transformations caused by changes in f-character and its occupation. Splat-cooled $Ce_{0.5}Th_{0.5}$ alloy was studied in diamond anvil cell with platinum as pressure standard up to 253 GPa by synchrotron x-ray diffraction at X-17C, NSLS. The ambient pressure fcc γ-phase (a = 5.089 Å) showed anomalous compressibility below 5 GPa (γ → α transformation). We report a phase transformation to a body centered tetragonal (bct) phase above 20 GPa. The tetragonal distortion (c/a) increases with increasing pressure and the bct phase is stable up to the highest pressure of 253 GPa ($V/V_0 = 0.402$). Experimental results are under evaluation and will be discussed inview of the prevailing theoretical Kondo model and orbital polarization model.

High-pressure X-ray diffraction studies of ThS_2, US_2 and other AnX_2 and AnXY compounds

A majority of binary and ternary compounds of actinides (An) and nonmetallic elements (X, Y) with composition AnX_2 or AnXY crystallizes under normal condition in the tetragonal Fe_2As or PbFCl type structures [1]. Many of them transform to the orthorhombic $PbCl_2$ type structure at high pressure. On the other hand, several actinide compounds, including ThS_2 and US_2, have the $PbCl_2$ type structure already at normal pressure.

A phase transformation occurs in ThS_2 at about 50 GPa. It is impossible to determine the crystal structure of the high-pressure phase from the present data. From the V(p) curve, we obtain B_0 = 195(15) GPa and B_0' = 2(1). US_2 crystallizes in three distinct phases: high-temperature tetragonal α-US_2, orthorhombic β-US_2 and low-temperature hexagonal γ-US_2 [2]. In the present work we have studied orthorhombic β-US_2 (space group *Pbnm*). The bulk modulus B_0 = 155(20) GPa has been obtained from the experimental pressure-volume data. Above 10-15 GPa new lines of a high-pressure phase are observed. Only two diffraction lines are observed for the high-pressure phase and its structure therefore remains unknown.

In previous work we have studied several binary and ternary compounds with the composition AnX_2 and AnXY, where An = Th, U and X, Y are non-metallic elements from the IIIA-VIA groups of the periodic table. Tab. 5.6 summarizes the experimental results so far. It is seen that a majority of the compounds either transforms to the orthorhombic $PbCl_2$ type structure, or does not transform at all in the measured pressure range (mostly up to 60 GPa). UC_2 is a notable exception, the high-pressure phase being hexagonal [3]. For the tetragonal structures it is of interest to note the pressure dependence of the c/a ratio. As shown in Fig. 5.36, this ratio decreases with pressure up to the transition pressure. The experimental data for UAs_2 indicate that the transition pressure is 18 GPa rather than 15 GPa as quoted in Ref. [4].

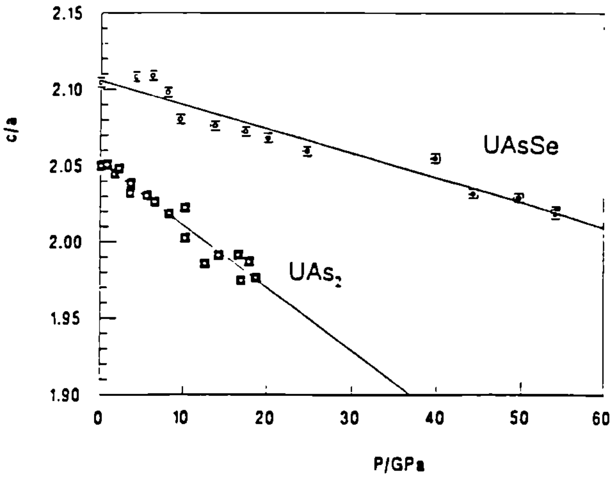

Fig. 5.36 The c/a ratio as function of pressure for tetragonal UAs_2 and UAsSe. UAs_2 transforms to the orthorhombic phase at 18 GPa. UAsSe remains tetragonal in the whole pressure range indicated. Data from Ref. [4].

References

[1] U. Benedict, *J. Less-Common Met.* **128** (1987) 7-45

[2] *Gmelin Handbook of Inorganic Chemistry*, 8th Ed., Uranium, Supp. Vol. **C10**, Berlin: Springer Verlag, 1984f, p. 54.

[3] J.-P. Dancausse, S. Heathman, U. Benedict, L. Gerward, J.S. Olsen and F. Hulliger, *J. Alloys Comp.* **191** (1993) 309-312

Tab. 5.6 High-pressure results for AnX_2 and $AnXY$ compounds; P_{tr} = transition pressure

Compound	Crystal system	B_0 (GPa)	B_0'	P_{tr} (GPa)	High-pressure structure
ThS_2	orthorhombic	195(15)	2(1)	50	unknown
US_2	orthorhombic	155(20)	-	10-15	unknown
UP_2	tetragonal	124(15)	9(2)	22	orthorhombic
UAs_2	tetragonal	101(8)	4.7(7)	18	orthorhombic
UAsS	tetragonal	105(7)	3.7(5)	46	orthorhombic
UAsSe	tetragonal	99(6)	3.8(5)	-	-
ThOS	tetragonal	201	3.0	-	-
UOSe	tetragonal	154	1.8	-	-
ThO_2	cubic	262(4)	6.7(5)	40	orthorhombic
UO_2	cubic	207(10)	7(2)	35	orthorhombic
UB_2	hexagonal	225(12)	2.6(1)	-	-
UC_2	tetragonal	216(10)	2.2(1)	18	hexagonal

[4] L. Gerward, J.S. Olsen, U. Benedict, S. Dabos-Seignon and H. Luo, *High Temp. - High Pressures* **22** (1990) 523-532

Other actinide compounds

Samples of UGa_3, UGe_3 and USn_3 were studied up to pressures of 55 GPa during two beam periods at Hasylab DESY and $NpGa_3$ was studied up to 40 GPa using the active glove box set-up in Karlsruhe. No crystallographic phase transitions were observed with these samples but the uranium compounds showed unusual variations in their pressure - volume curves as can be seen in Fig. 5.37. The $NpGa_3$ sample did not show the same variations as those of uranium and gave a normal smooth compressibility curve. Theoretical calculations are being carried out on some of these compounds to determine the nature of these variations. A similar behaviour has been noted in pressure studies of YbTe which has been attributed to a 4f-5d electronic collapse.

ThC was studied up to 81 GPa using a High Pressure Diamond Optics inc. Super Pressure cell and extends previous measurements on ThC from 50 GPa. The sample remained in the NaCl structure *Fm-3m* over the whole pressure range investigated. This is in contrast to the corresponding uranium compound UC which undergoes a first order phase transition to an orthorhombic structure at 27 GPa. The bulk modulus and its pressure derivative was determined as Bo = 109 and Bo' = 3.0 in good agreement with the previous determination.

Other series of measurements have dealt with the study of EuTe and EuO up to 54 and 62.5 GPa respectively. EuTe undergoes a B1-B2 phase transition at between 12 and 14 GPa and in the case of EuO as shown in Fig. 5.38a B1 B2 transition was observed starting at 47 GPa accompanied by a volume collapse of 8 % with some B1 phase still present at the highest pressure. Bo was determined as 116 GPa with Bo' = 2.5. No indication of an isostructural phase transition at lower pressures was observed.

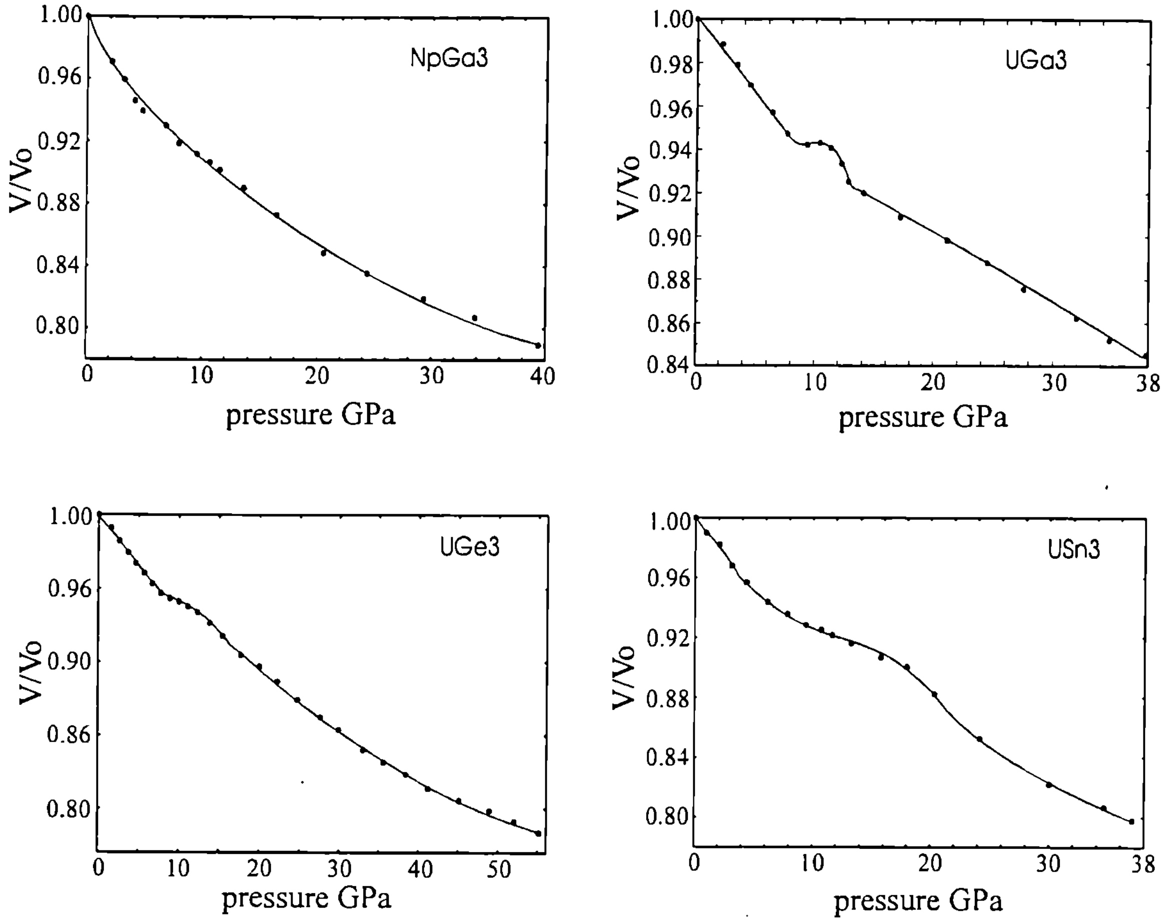

Fig. 5.37 Relative volume vs. pressure for $NpGa_3$*,* UGa_3*,* UGe_3 *and* USn_3

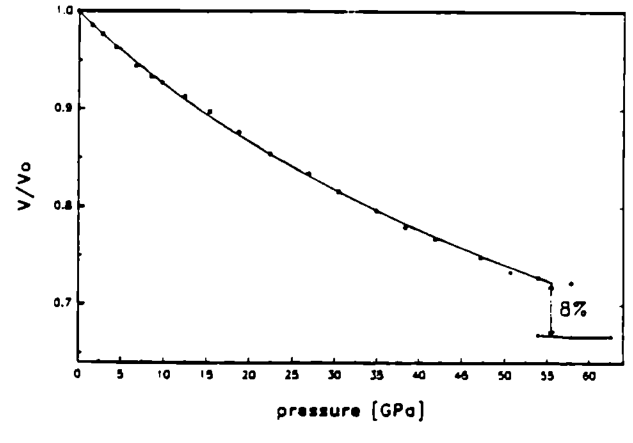

Fig. 5.38 Relative volume vs. pressure for EuO

HPXRD study on transuranium materials

New high pressure X-ray diffraction study of Am

After recent high pressure resistivity measurements on Am (this report, pp.149-150) difficulties have been encountered in interpreting these results partly arising out of discrepancies in previous x-ray experiments.

It was tried to resolve some of these discrepancies by high pressure x-ray measurements on part of the same Am sample as used for the resistivity studies. In addition, by very careful cleaning of the glove box used for HPXRD, th γ background of the energy-dispersive diffraction spectra could be considerably reduced. By careful alignment of the double cone system very clear X-ray spectra can be collected with both the 5 and 7 degree diffraction angles used.

Previous X-ray studies have yielded different results as regards the transition pressures in Am and the structure of Am III. Also some groups have been unable to confirm the proposed high pressure α-uranium type structure of Am IV due to poor fits of the data. Another discrepancy is the lack of agreement between experimental and theoretical studies whereby a 34% volume collapse is predicted by Eriksson and Wills (1993) [1] at 11 GPa but not observed.

Am I and II

The ambient pressure dhcp structure has been observed by all groups and the present study confirms those results. About 60% of the fcc structure was present at 6 GPa and only fcc present at 6.3 GPa. We obtain :

Bo = 28.5 Bo' = 3.0 Birch and Bo = 28.8 Bo' = 2.7 Murnaghan for the 5° angle.

Bo = 30.1 Bo' = 3.2 Birch and Bo = 30.3 Bo' = 2.9 Murnaghan for the 7° angle.

This gives an average value of 29.4 GPa for Bo and 3 for Bo'.

Am III

The structure of Am III has caused problems for previous authors and has led them to propose 3 different possibilities. This structural change also occurs at the beginning of the pressure range where a volume collapse is predicted by theory. Roof and Akella both proposed different monoclinic structures which have been shown to be related to each other by Roof. Benedict and Dabos found that their spectra did not fit the proposed monoclinic structure but instead a trigonal distorted fcc one as found in some of the lanthanides. Roof found the transition to Am III at 10 GPa whereas Benedict and Dabos found it at 13.5 GPa. It was one of the aims of this present study to obtain pure spectra of both Am III and Am IV without extra lines to confuse fitting to possible structures.

We found about 20% Am III to be present at 8.1 GPa, 80% at 9.1 GPa and only Am III at 10.0 GPa. No gasket or extra lines are observed except for the Am Lγ1 fluorescence line at 22.12 Kev and Am γ at 26.36 Kev and 43.53 Kev particularly in the 7 degree spectra. The pure Am III spectra at 11 GPa seem quite simple and do not fit either the monoclinic structure or the distorted fcc structure. The monoclinic structure simply has too many diffraction lines to fit these spectra and although the trigonal distorted fcc structure can be fitted to some lines other important strong lines remain unobserved. Another very recent proposed structure for the distorted fcc phase was given by Hamaya et al [2] . In their study of praseodymium under pressure they identified a crystal structure in the trigonal space group R-3m occurring between the fcc and α uranium phases at 7 to 15 GPa. They derived the trigonal structure from the fcc structure. In this proposed structure the 200 reflection must remain as a single peak which is the case for Pr but clearly not for Am III where the 200 reflection disappears completely. Consequently it was not possible to fit Am III to this structure either.

By trying to fit the Am III spectra to an orthorhombic structure based on that of α-uranium but with 2 atoms in the standard position 4c a remarkably good fit is obtained compared to the other structures. Unfortunately although this structure would mean a volume collapse of about 30% as predicted by theory [1] the resulting volume would be too low to allow an α uranium structure for Am IV. As an orthorhombic type pattern fits best to the data an α"-Ce type monoclinic structure I 2/m with 2 atoms at 0,0,0 and $\frac{1}{2},\frac{1}{2},\frac{1}{2}$ was tried [3]. This is described as a pseudocubic monoclinic body centered structure whereby if the β angle were 90° and the axial ratios $\sqrt{2}:1:1$ it would become fcc. The α" phase is formed in Ce at high pressure from the fcc phase and an α-uranium type structure called α' Ce has also been observed. As these phases are also present in Am it was logical to try fitting the α" Ce structure to Am III as well. After refinement using Am III data the best fit is obtained when the 92° β angle falls close to 90° and is then basically the same as an orthorhombic structure. The refined cell parameters for Am III at 11 GPa using this structure are a= 4.907 b= 3.154 c= 2.880 β= 90.0 ± 0.4 giving a volume decrease of about 2% from the fcc phase.

Am IV

Roof found the structure of Am III to be stable between 10 and 15 GPa with Am IV appearing at 16 GPa. Benedict and Dabos found this transition at 23 GPa. This study found about 10% Am IV to be present at 13 GPa and Am IV to be exclusively present at 17.5 GPa and above. 2 different α uranium structures with slightly different cell parameters could be fitted to the Am IV spectra at 24.7 GPa (Fig. 5.39).

Upon releasing pressure Am IV was stable down to 10.7 GPa, an equal mixture of Am III and Am IV was present at 5.9 GPa and the **fcc structure remained at ambient pressure** for both samples. A very small amount of the dhcp structure was observed with the fcc but even after one week

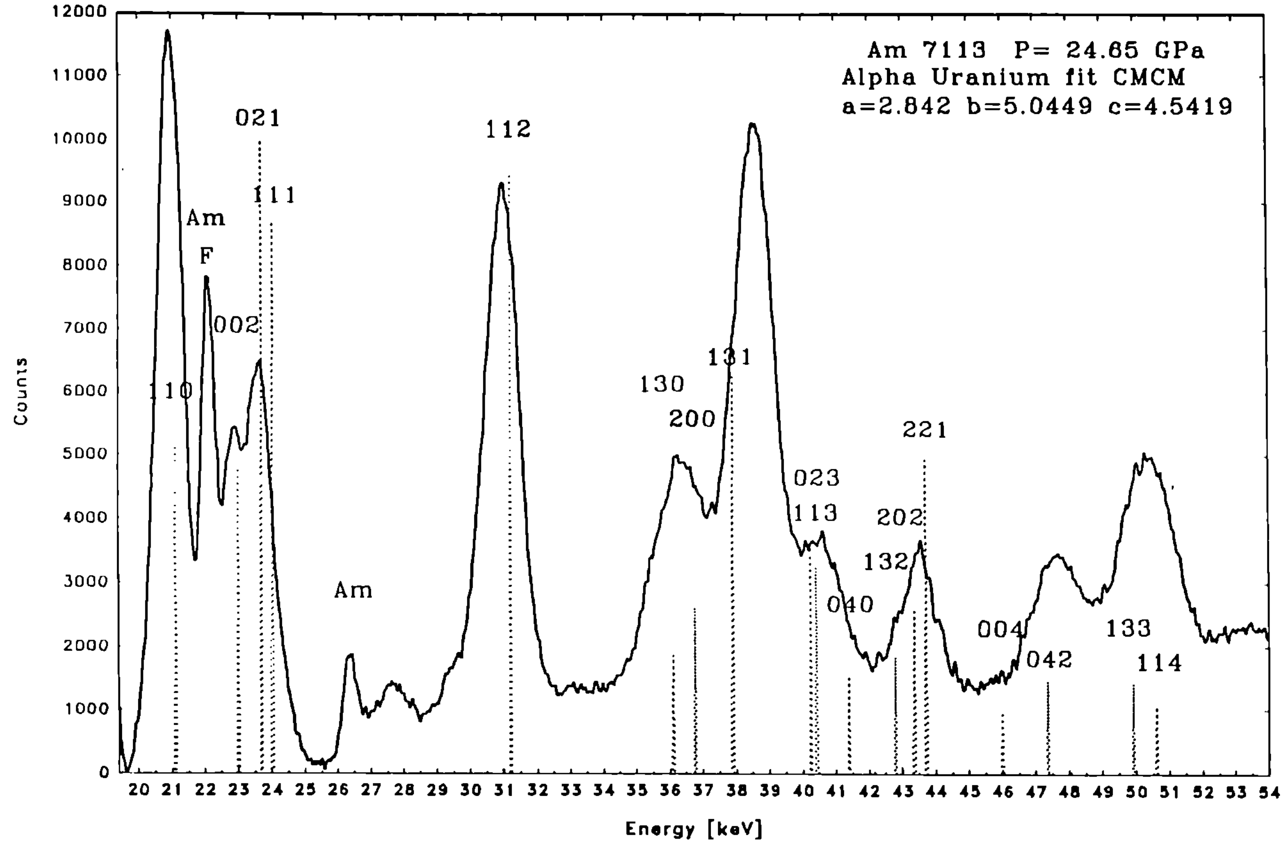

Fig. 5.39 Fit of Am-IV spectrum at 24.7 GPa to α-U with a = 2.842, b = 5.0449, c = 4.5419 Å

at ambient pressure the samples remained basically cubic fcc. Akella et al. also noted that when taken above 10 GPa Am retains the fcc structure upon releasing pressure.

Conclusion

The transition pressures in this study agree reasonably well with those found by Roof and Akella although Am III cannot be indexed using their proposed structures or that proposed by Benedict et al.[6]. Am IV can be indexed using the α-uranium structure and this may be a confirmation.

Taking the α-uranium structure at 10.7 GPa we would obtain a volume difference of about 22% compared to the dhcp, fcc, α" monoclinic pressure volume curve. At 14.5 GPa the volume collapse would be about 15% and at 17.5 GPa about 12% due to the different slopes of the curves. Taking the proposed orthorhombic Am III structure at 11 GPa we would obtain a volume collapse of about 30%. As the calculated volume of the proposed orthorhombic Am III structure at 11 GPa is 62 Å^3 and that of the α-uranium at 24.7 GPa is 64-65 Å^3 this would mean a slight volume increase which is impossible. Only if a different structure for Am IV with a lower volume were found would orthorhombic Am III be a viable structure, and could a 30 % volume decrease at 10 GPa be assumed, as theoretically calculated.

The present study has led to

1) clearer diffraction spectra of Am under pressure, owing to reduced background, less parasitic lines, and very careful alignment of the double cone-collimator-pressure cell system
2) better definition of the phase transition pressures
3) new proposals for the structures of Am III and Am IV
4) a combination of structures for Am III and Am IV where the volume decreases by the order of 15 % from III to IV.

A combination of structures which would confirm the theoretically predicted volume collapse, of the order of 35 % around 10 GPa, was not found up to now.

References

[1] O. Eriksson ,J.M. Wills, Phys. Rev. B 45 (1992) 3198

[2] N. Hamaya , Y. Sakamoto , H. Fujihisa , Y. Fujii , K. Takemura , T. Kikegawa , O. Shimomura, *J. Phys. Condens. Matter* 5 (1993) L369-L374.

[3] W.H. Zachariasen , F.H. Ellinger, Acta Cryst. A33 (1977) 155-160.

[4] U. Benedict , J.P. Itié , C. Dufour , S. Dabos , J.C. Spirlet, in: *Americium and Curium chemistry and technology* (1985) 213-224, D. Reidel, Dordrecht.

Comparison between LnX and AnX compounds of the B1 type

Systematic trends in the nature of the high-pressure phases, the transition pressures and the compressibility have become evident through recent studies in the B1 type compounds, the largest group of compounds formed by lanthanides and actinides. The B1 → B2 phase transition is the dominating mechanism in the high-pressure structural behaviour of these compounds.

The lanthanide monochalcogenides LnX of the B1 type are of metallic character, with the exception of those with a divalent metal (Sm, Eu, Yb, and, to some extent, Tm) which are semiconductors. Semiconducting LnX can undergo transition to a metallic state under pressure. That is why divalent Ln chalcogenides have been extensively studied under pressure. Several semiconductor → metal transitions, for instance in SmS, SmSe, SmTe, EuO, TmTe, YbO, YbS, YbSe, and YbTe, were observed.

Isostructural volume collapses accompanying "electronic transitions" under pressure were observed for monochalcogenides of Ce, Sm, Eu, Tm and Yb, and for CeP and SmBi. Pressure-induced structural transitions were observed for monopnictides of La and Ce, for the monochalcogenides of Eu, and for the monotellurides of Ce, Pr, Sm, Eu and Tm. Not all of the remaining Ln monopnictides and monochalcogenides have been studied under pressure up to now.

In the AnX compounds, the B1 → B2 transition is accompanied by a volume decrease of the order of 10 %. Sb as an anion favours tetragonal high pressure structures. Monocarbides, -nitrides, -phosphides and -sulfides of Th and U either did not transform in the pressure range studied (ThC, ThN) or transformed to structures of relatively low symmetry (UC, UN, UP, US, ThS) which could possibly point to an f contribution. In this group of Th and U compounds with light anions, only ThP exhibits the B1 → B2 structural transition.

In UTe, USb and UBi, re-transformation to the B1-type phase on pressure release does not occur at room temperature. The B2-type high-pressure phase is maintained in a metastable condition at ambient pressure. This is an example of pressure-induced preparation of a new polytype of material. It should be recalled, too, that ThBi and ThTe have a *stable* B2-type phase at ambient pressure, or otherwise expressed, they have a theoretical B1 → B2 transition at negative pressure.

In contrast to the lanthanide compounds, isostructural volume collapses were not detected until recently in the AnX compounds. This situation may change owing to recent high pressure X-ray diffraction studies of certain AnX compounds. Recent work on the monobismuthides of U, Np and Cf [1] revealed a negative curvature of the *V(p)* curves for these compounds. This phenomenon had been taken in lanthanide compounds, such as SmS and SmSe as a sign of the commencing of a 4f participation in the bonding, or otherwise expressed, of a so-called electronic transition, which was often thought to be linked to an increase of the valence of the cation. On the basis of these results, one should consider the possibility that an electronic transition also takes place in UBi, NpBi and CfBi. However, it is difficult to give definite proof for this assumption from the data available up to now, because, if the electronic transition occurs in these compounds, it is immediately followed and in part masked by the structural B1-to-B2 transition.

Fig. 5.40 gives the dependence of transition pressures from the cation-anion radius ratio at ambient pressure. This ratio is in general between 0.41 and 0.73 for B1-type compounds. In the actinide monopnictides and monochalcogenides, as well as in the lanthanide monotellurides, the transition pressure is seen to increase with decreasing r_C/r_A. This even includes a few of the transitions to structures different from B2. Some of the Th compounds (ThAs, ThSb) do not follow this rule. The general trend can be explained by anions being more compressible than the cations. With increasing pressure, the ratio r_C/r_A thus increases up to a critical value, which induces the phase transition. Lower initial radius ratios need higher pressure to reach this critical value.

In the f metal compounds, f delocalization seems to be only a minor aspect of the structural phase transitions. Geometrical factors have to be considered as one of the major reasons for inducing

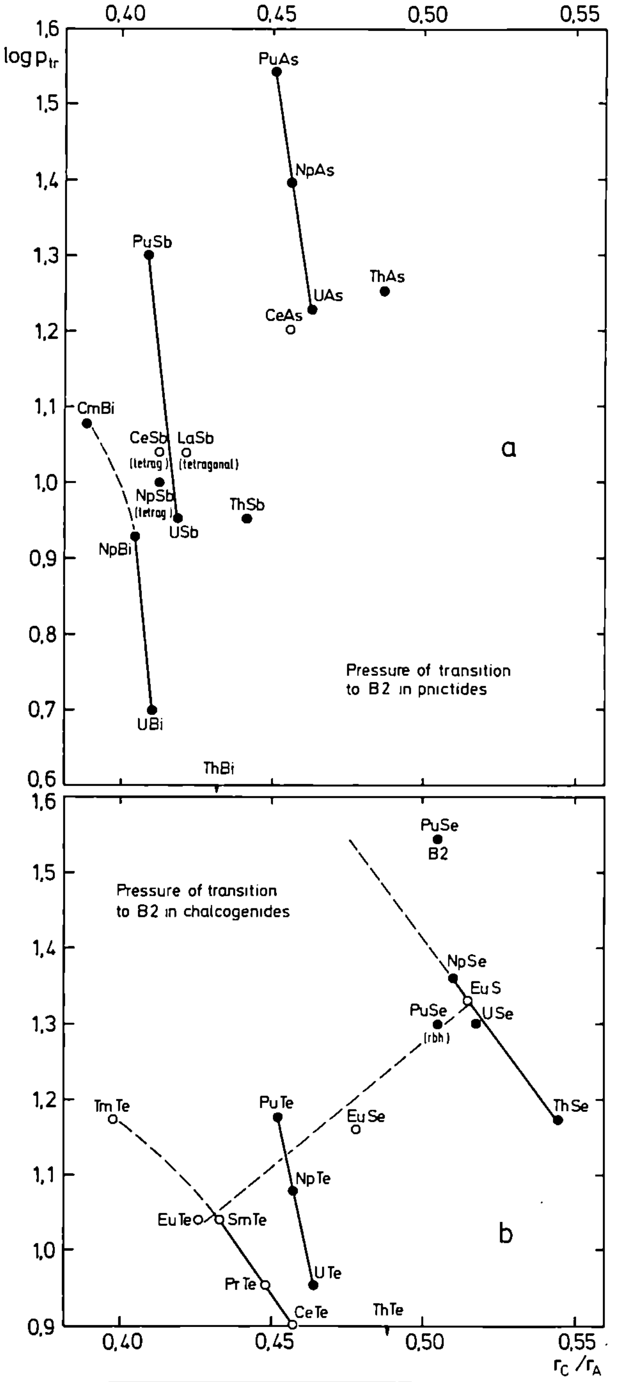

Fig. 5.40 Logarithm of upstroke transition pressure vs. cation-anion radius ratio for the B1-to-B2 transition in lanthanide and actinide compounds. Trivalent ionic radii are used for all cations. Some transitions to other high pressure structures are included for comparison and have been marked as such in the graphs. (a) Monopnictides with As, Sb and Bi. Isolated data for the phosphides CeP and ThP are not included. No mononitrides have been observed to transform to the B2-type under pressure. (b) Monochalcogenides with S, Se and Te. The EuO transition is outside the graph.

phase transitions. Systematics in the compounds are less advanced than in the metals, and this is due in large part to lack of high pressure study on most of the numerous lanthanide compounds with the B1-type structure. Only those which were expected to exhibit electronic transitions have received major attention from experimentalists, and it will be extremely useful to restart an effort in high pressure study of the remaining B1-type lanthanide compounds.

References

[1] U. Benedict and W.B. Holzapfel, in: K.A. Gschneidner and L. Eyring (eds.), *Handbook on the Physics and Chemistry of Rare Earths, Lanthanide/Actinide*, special volumes, in press.

Actinide Information Centre

THERSYST-ACT, a thermophysical data base for actinides and actinide compounds

The development of a thermophysical database for actinides and actinide compounds, THERSYST-ACT, was continued. THERSYST-ACT is an important tool of the Institute's Actinide Information Centre, which collects systematically, evaluates, and keeps readily available bibliographical references on the physics and the chemistry of uranium and transuranium elements and their compounds.

During the reporting period 42 publications on the thermophysical properties of actinide compounds were evaluated. The contents of these publications have been stored in 320 data sets, which brings the total number of data sets collected in THERSYST-ACT to about 1400. The present content of THERSYST-ACT (status November 24, 1993) is given in Tab. 5.7.

A thorough literature review brought to light another 140 articles and reports on the thermophysical properties of actinides which had been published between 1952 and 1970 and which might be of interest for historical reasons. 70 more relevant papers on actinide metals and alloys from 1971 to 1993 are ready for evaluation, and 40 sources on actinide carbides, nitrides, sul-

Tab.5.7 List of materials and properties stored in THERSYST-ACT
THC: thermal conductivity; THD: thermal diffusivity; CP: specific heat at constant pressure
ENT: enthalphy; ELR: electrical resistivity; LEX: linear thermal expansion coefficient,
DEN: density; EMI: emissivity

SHORT	MATERIAL NAME	PROPERTIES								
		THC	THD	CP	ENT	ELR	LEX	DEN	EMI	SUM
AMPU	plutonium	-	-	-	1	-	1	-	-	2
AMTH	thorium	-	-	1	1	-	-	-	-	2
AMU	uranium	-	-	1	1	-	-	-	-	2
B0GAPU00	gallium-plutonium alloy	-	-	3	6	-	-	-	-	9
K0AL2O3	aluminum oxide	-	-	1	1	-	-	-	2	4
K0AMO2	americium dioxide	-	-	-	-	-	5	-	-	5
K0BKO2	berkelium dioxide	-	-	-	-	-	1	-	-	1
K0MGO	magnesium oxide	-	-	-	-	-	-	-	2	2
K0ND2O3	neodymium oxide	-	-	-	-	-	-	-	1	1
K0NPO2	neptunium dioxide	-	-	-	-	-	1	-	-	1
K0PUO2	plutonium dioxide, plutonia	13	8	3	3	4	8	-	-	39
K0THO2	thorium dioxide, thoria	3	3	2	2	3	4	-	5	22
K0U3O8	uranium oxide	10	-	4	-	1	-	-	-	15
K0U4O9	uranium oxide	1	1	-	-	2	3	-	-	7
K0UO2	uranium dioxide, uranium oxide, urania	104	32	19	11	21	16	4	5	212
K0UO3	uranium oxide	-	-	-	-	6	-	-	-	6
M0AMUQ00	americium-uranium dioxide	4	2	-	-	-	-	-	-	6
M0CRUQ00	chromium-uranium oxide	-	-	-	-	3	-	-	-	3
M0EUUQ00	europium-uranium dioxide	6	6	2	-	2	-	-	-	16
M0GDUQ00	gadolinum-uranium oxide	12	21	7	2	3	3	3	-	51
M0LAUQ00	lanthanum-uranium oxide	-	-	3	-	3	-	-	-	6
M0NBUQ00	niobium-uranium oxide	-	-	1	-	10	-	-	-	11
M0NDPU00	neodymium-plutonium dioxide	8	8	-	-	-	-	-	-	16
M0NDUQ00	neodymium-uranium dioxide	6	6	-	-	-	-	-	-	12
M0NPUQ00	neptunium-uranium dioxide	4	3	-	-	-	-	-	-	7
M0PUTH00	plutonium-thorium dioxide	1	-	-	-	-	-	-	-	1
M0PUUQ00	plutonium-uranium dioxide	107	54	34	10	28	15	9	-	257
M0PUYQ00	plutonium-yttrium dioxide	8	8	-	-	-	-	-	-	16
M0SCUQ00	scandium-uranium oxide	-	-	1	-	1	-	-	-	2
M0SMUQ00	samarium-uranium dioxide	6	6	-	-	-	-	-	-	12
M0THUQ00	thorium-uranium dioxide	7	6	7	7	18	2	-	-	47
M0TIUQ00	titanium-uranium dioxide	-	-	1	-	3	-	-	-	4
M0UQYQ00	uranium-yttrium dioxide	6	6	-	-	20	-	-	-	32
N0AMUQ01	americium-uranium-neptunium dioxide	2	1	-	-	-	-	-	-	3
N0PUUQ01	plutonium-uranium-neodymium oxide	4	4	-	-	-	-	-	-	8
N0PUUQ02	plutonium-uranium-europium oxide	4	4	-	-	-	-	-	-	8
N0PUUQ03	uranium-plutonium-titanium dioxide	1	-	-	-	-	-	-	-	1
N0PUUQ04	plutonium-uranium-zirconium dioxide	-	-	-	-	-	3	-	-	3
PCUQ01	uranium oxycarbide	8	-	-	-	-	-	-	-	8
QAUQ01	uranium arsenide	-	-	1	-	-	-	-	-	1
QCCEUQ01	uranium-cerium carbide	4	4	-	-	1	-	-	-	9
QCMOUQ01	uranium-molybdenum dicarbide	2	2	-	-	-	-	-	-	4
QCPU01	plutonium monocarbide	1	1	12	4	1	3	-	-	22
QCPU02	plutonium sesquicarbide	-	-	4	2	-	3	-	-	9
QCPU03	plutonium dicarbide	-	-	-	-	-	1	-	-	1
QCPUUQ00	plutonium-uranium carbide	13	3	1	2	3	4	-	-	26
QCPUUQ01	uranium-plutonium-cerium carbide	2	2	-	-	1	-	-	-	5
QCPUUQ02	uranium-plutonium-zirconium carbide	3	3	-	-	3	-	-	-	9
QCPUUQ03	uranium-plutonium-molybdenum carbide	6	-	-	-	2	-	-	-	8
QCRHUQ01	uranium-rhodium dicarbide	1	1	-	-	-	-	-	-	2
QCRUUQ01	uranium-ruthenium dicarbide	1	1	-	-	-	-	-	-	2
QCTA01	tantalum carbide	-	-	-	-	-	-	-	1	1
QCTH01	thorium dicarbide	1	-	-	-	1	-	-	2	4
QCUQ01	uranium monocarbide	42	12	8	4	29	13	-	3	111
QCUQ02	uranium sesquicarbide	1	1	2	2	-	2	-	-	8
QCUQ03	uranium dicarbide	4	3	4	4	2	-	-	8	25
QCUQZR00	uranium-zirconium carbide	-	-	-	-	1	-	-	1	2
QFPU01	plutonium trifluoride	-	-	1	1	-	-	-	-	2
QFPU02	plutonium tetrafluoride	-	-	1	1	-	-	-	-	2
QNPU01	plutonium mononitride	5	5	4	3	1	2	-	-	20
QNPUUQ00	plutonium-uranium nitride	2	3	1	1	1	3	-	-	11
QNTH01	trithorium tetranitride	-	-	-	-	1	-	-	-	1
QNUQ01	uranium mononitride	14	7	11	8	17	2	-	-	59
QNUQ02	uranium sesquinitride	-	-	3	3	-	-	-	-	6
QPPU01	plutonium monophosphide	-	-	-	-	1	-	-	-	1
QPUQ01	uranium monophosphide	6	5	8	3	2	-	-	-	27
QPUQ02	triuranium tetraphosphide	-	-	1	1	-	-	-	-	2
QQUQ01	uranium monoselenide	-	-	2	1	-	-	-	-	3
QRPU01	plutonium monosulfide	-	-	-	-	1	-	-	-	1
QRTH01	thorium monosulfide	-	-	2	-	1	-	-	-	3
QRTHUQ00	thorium-uranium monosulfide	-	-	6	-	3	-	-	-	9
QRUQ01	uranium monosulfide	4	3	6	2	7	-	-	-	19
QSUQ01	uranium silicide	-	-	1	1	-	-	-	-	2
QTUQ01	uranium monotelluride	-	-	1	-	-	-	-	-	1
QUUQ01	uranium antimonide	-	-	2	-	-	-	-	-	2
QYCQNQ01	uranium carbonitride	16	16	-	-	22	1	-	-	55
QYCQNQ02	uranium-cerium carbonitride	-	-	-	-	-	1	-	-	1
WCUQUQ01	uranium carbide-uranium system	1	-	-	-	-	1	-	-	2
WOPUFE01	plutonium dioxide/AISI 304 steel system	-	-	-	-	-	2	-	-	2
VCFUEL	simulated fuel from carbon	24	-	-	-	4	18	-	-	46
		478	251	172	88	234	118	16	30	1386

fides, and fluorides are available and will be prepared for input into THERSYST-ACT.

The THERSYST data bank system was originally designed for use with a VAX computer. In the meantime, personal computers (PC's) have become available which are more convenient to use than large computing facilities and which have sufficient memory and power to handle a complex data handling system as it is used in THERSYST. Furthermore, the exchange of data between different institutions by means of diskettes is much simpler than by magnetic tape. It was therefore decided to develop a PC-version of THERSYST with features identical to the VAX-version.

The input to the PC-version uses Clipper programming tools in connection with a dBase data bank system. The retrieval is accomplished with the YACC-tool (in C). Using the programming language C has the advantage of producing a language-independent object code. For the graphic representation of the results by means of a PC, the Fortran library PICASSO is being used which creates a postscript file that can be output on a typical printer.

The PC-version of the THERSYST management system employs the X-Windows interface. In an X- environment the user has access to advanced Windows management and event handling. For example, instead of specifying input paramaters by typing them into the command line, dialog boxes can be used.

The input programme of the PC-version of THERSYST has successfully been demonstrated at the 13th European Conference on Thermophysical properties in Lisboa (30 August to 3 September, 1993). Retrieval and graphics systems are presently undergoing testing.

RADONN (RAdioactive Decay Of Nuclides and Neutronics) A Software Tool for PCs

Background

For many scientist and technologists working in the nuclear field, the original 'Chart of the Nuclides' [1] is an indispensable tool for obtaining data on radionuclides and working out qualitatively decay schemes and nuclear reaction paths. Since the publication of the original chart, others have appeared [2, 3] which include more recent data and different colour schemes to indicate possible physical processes. In all cases, however, one has to process the information contained in these charts to obtain quantitative information (e.g. to obtain the activities, or the alpha, beta, gamma, intensities of a given daughter product, starting from an initial mass or activity of the parent nuclide).

This was the primary reason for developing the RADONN software package. In addition to providing the basic data and working out the decay schemes and reaction paths, it should also allow quantitative evaluation of the decay scheme or the nuclear reaction path by solving the differential equations. In addition, it should be user friendly and run on standard PC's. In the present version of the program, the data base contains information on over 2700 radionuclides. Such information consists of type of decay (α, β-, β+, EC, IT, etc.), half-lives, branching ratios, the ALI values for inhalation and ingestion, the average alpha, beta, and gamma energies, etc. The present version of RADONN includes, in addition to decay schemes and reaction path evaluations, radiotoxicity and dosimetry calculations.

Nuclide Database

The nuclide database NUKLID.dbf used in RADONN contains nuclear data for over 2700 radionuclides. For each isotope the data [4, 5] consists of the half-life, the modes of decay (α, β-, β+, EC, IT, etc.), branching ratios for different modes, the ALI values for inhalation and ingestion, the average alpha, beta, and gamma energies per decay, the energies and emission probabilities of the ten strongest emissions. At present the nuclear reaction cross sections [6] for most of the actinides are contained in CROSSECT.dbf database. It is intended to extend this cross section data (where known) to all nuclides. Another database BUILDUP.dbf contains the data for the dosimetry calculation. This consists of the mass attenuation coefficients (MAC), the mass energy absorption coefficients (MEAC), the densities, and the build up factors (as a function of the number of mean free paths in the shielding material) for a selection of shielding materials which at present include air, water, lead, and iron.

Decay Schemes

A demonstration of the decay scheme is shown in Figs. 5.41 and 5.42 for the nuclide ^{253}Es . In Fig.

5.41 the entire scheme is shown and in Fig. 5.42 only the main chain. The colour scheme adopted is that used in the original 'Chart of the Nuclides' i.e. yellow - α-emitter, blue - β-emitter, etc. Starting from the original nuclide, ^{249}Bk is produced by alpha emission and is shown vertically below the ^{253}Es. This isotope, in turn, decays by β-emission to ^{249}Cf situated to the right of ^{249}Bk in the diagram. A β+ emission would result in the daughter product situated to the left of the parent nuclide.

Calculations

All 'chains' of the radioactive decay of a nuclide are described by linear first order kinetics shown below where N_1, N_2 etc. are the amounts of species 1, 2, etc. in a particular chain.

$$\frac{dN_1}{dt} = P_1 - k_1 N_1$$

$$\frac{dN_2}{dt} = P_2 + k_{(1,2)} N_1 - k_2 N_2$$

$$\vdots$$

$$\frac{dN_i}{dt} = P_i + k_{(i-1,i)} N_{i-1} - k_i N_i$$

$$\vdots$$

$$\frac{dN_n}{dt} = P_n + k_{(n-1,n)} N_{n-1} - k_n N_n$$

N_i is the amount of species i present at time t, K_i is the decay constant for species i, $k_{(i,i+1)}$ is the partial decay constant which is related to the branching fraction $f_{(i,i+1)}$ through the relation $k_{(i,i+1)} = f_{(i,i+1)} k_i$ and P_i is the constant rate of production of species i. An elegant solution to this system of equations has been given by Skrable et al. [7] i.e.

$$N_n = \sum_{i=1}^{i=n} \left[\left(\prod_{j=1}^{j=n-1} k_{(j,j+1)} \right) \sum_{j=i}^{j=n} \left\{ \frac{N_i^0 \exp(-k_j t)}{\prod\limits_{\substack{p=i \\ p \neq j}}^{p=n} (k_p - k_j)} + \frac{P_i [1 - \exp(-k_j t)]}{k_j \prod\limits_{\substack{p=i \\ p \neq j}}^{p=n} (k_p - k_j)} \right\} \right]$$

If there are convergent or divergent branches then the above equation can be applied to all applicable chains. In the present version of RADONN only one chain is solved for. This is usually the main chain and is for most purposes sufficient. How good this approximation is made can be seen in the list of branching fractions seen alongside the main chain. In some cases, however, this is not the case and the main chain is not the most interesting. An example is the radioactive decay of ^{232}U in which the main daughter product of ^{212}Bi is ^{212}Po (with a branching fraction of 0.64). The secondary chain passing from ^{212}Bi to ^{208}Tl is much more important because of the strong gamma emission from the ^{208}Tl. This is, however, easily achieved in RADONN by 'switching on' the alpha emission in ^{212}Bi the database.

Evaluation of the Results

Once the amounts (expressed either in mass or activity units) of the various species have been calculated at any time, the program calculates the α, β-, and γ intensities, the radiotoxicities for inhalation and ingestion. In addition the spectral gamma intensities for various energy bins between 40 keV and 10 MeV are given. Finally, in the dosimetry section of the program, one can calculate the dose rates at a given distance from the source using a given shield thickness assuming point source geometry. The mass attenuation and energy-absorption coefficients have been taken from Hubble [8] and the buildup factors from Chilton et al. [9].

References

[1] W. Seelmann-Eggebert, G. Pfennig, H. Münzel, H. Klewe-Nebenius, "Chart of the Nuclides", Gersbach & Sohn Verlag, München, 5th edition, 1981

[2] F. William Walker, Josef R. Parrington and Frank Feiner, "Chart of the Nuclides",General Electric Company, Nuclear Energy Operations, 175 Curtner Avenue, M/C 397, San Jose, California 95125 (USA), 14th Edition, 1989

[3] M.S. Antony, "Chart of the Nuclides" - Strasbourg 1992, Centre de Recherche Nucléaires et Université Louis Pasteur, Strasbourg, 1992

[4] Edgardo Browne and Richard B. Firestone, "Table of Radioactive Isotopes", Editor Virginia S. Shirley, John Wiley & Sons, 1986

[5] Decay Data of the Transactinium Nuclides, Technical Reports Series No. 261, IAEA, Vienna 1986

[6] Handbook of Chemistry and Physics, 73 rd Edition 1992-1993, Ed. D.R. Lide, CRC Press, 1992

[7] K. Skrable et. al., Health Physics **27** (1974) 155-157

[8] K. J.H. Hubble, Int. J. Appl. Radiat. Isot. **33** (1982) 1269-1290

[9] A.B. Chilton, J.K. Shultis, and R.E. Faw, "Principles of Radiation Shielding", Prentice-Hall, Englewood Cliffs, NJ 07632, USA

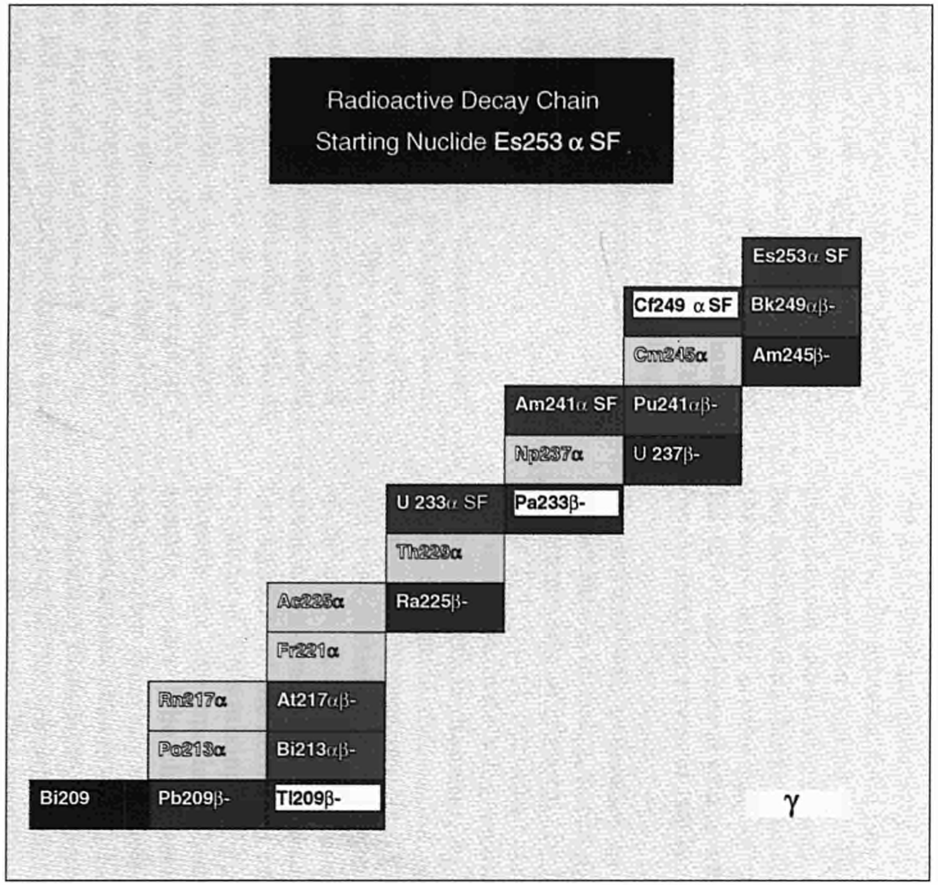

Fig. 5.41　*Radioactive decay scheme for ^{253}Es*

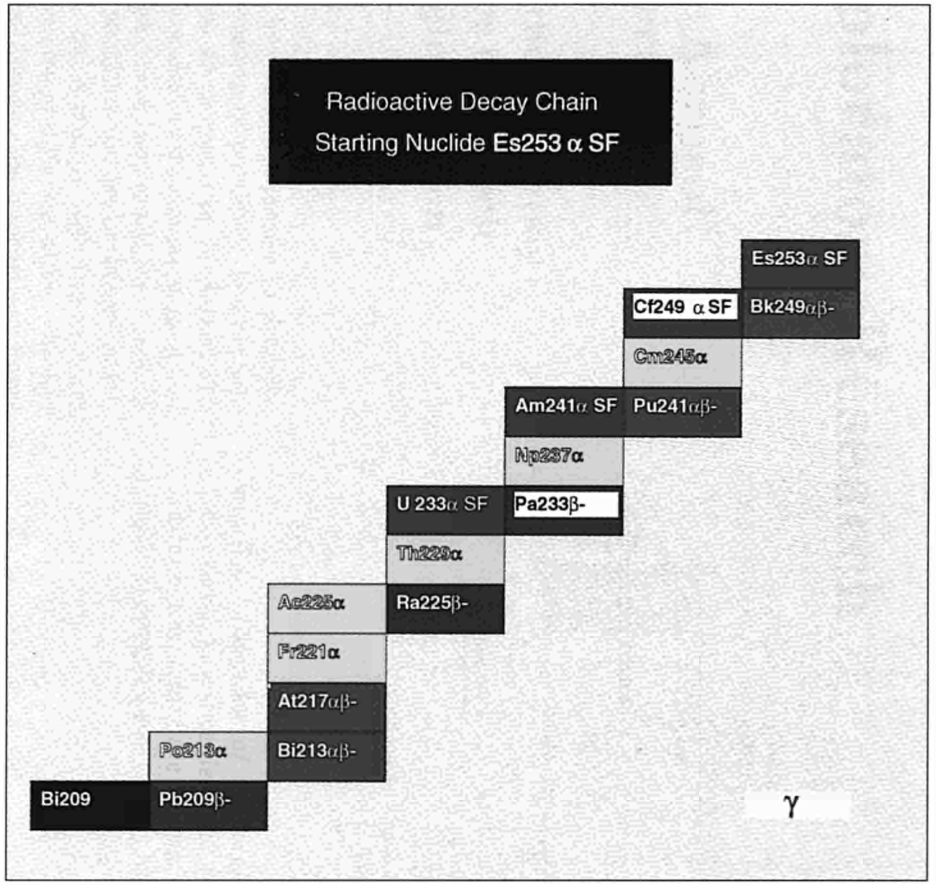

Fig. 5.42　*Radioactive decay scheme for ^{253}Es; main decay chaim.*

2. Exploratory Research

Acoustic Aerosol Agglomeration

Scaling of the frequency dependence of acoustic aerosol agglomeration

Introduction

Various models have been proposed to describe acoustic agglomeration of particles. The orthokinetic mechanism, as proposed by Mednikov [1], invokes the differential entrainment velocity of particles in the wave as a function of their size. In this way, small particles impact on larger particles. This model deals mainly with the interaction between particles of different sizes. The hydrodynamic effect [2] takes the interaction of particles with the same size into account. Other mechanisms such as turbulence [3,4,5] and Brownian diffusion also influence the acoustic agglomeration process. In this study, the effect of different acoustic frequencies on the agglomeration of a glycol fog are compared. The experimental observations are discussed within the framework of the orthokinetic and hydrodynamic effects. A detailed analysis of the evolution of the size distribution of the aerosol particles undergoing acoustic agglomeration is also presented.

Experimental facility

Acoustic aerosol agglomeration measurements were performed in a cylindrical plexiglas chamber (0.70 m in diameter and 2.0 m in length), shown schematically in Fig. 6.1. The acoustic source was mounted axially at one extremity of the chamber. In order to reduce the amplitude of acoustic standing waves in the chamber, sound absorption material was installed at both ends. The acoustic sources consist of a piezo-electric transducer, a mechanical amplifier and a radiating plate [6,7]. The 21 kHz source was fitted with a 480 mm radiating plate constructed from titanium and can be operated at powers up to 400 Watts. The 10 kHz source was fitted with an aluminium plate with a diameter of 670 mm and has a maximum power input of 250 Watts. Given the experimental geometry of the chamber and sources, the acoustic field has the characteristics of the near-field regime [8]. This means that the distribution of acoustic energy in the chamber is not homogeneous. Maximum values of the sound pressure level on the axis of the chamber were 150 dB for each sound source when operated at an input electrical power of 100 W.

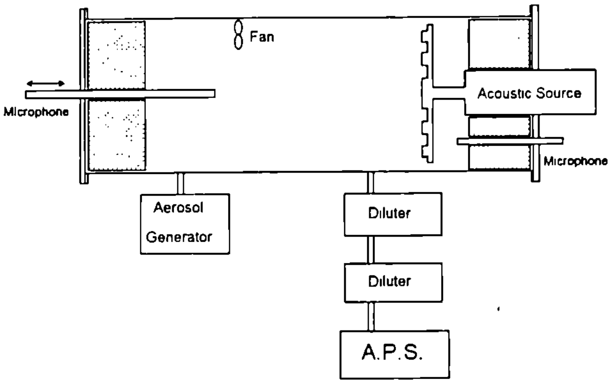

Fig. 6.1 Diagram of the experimental facility. The sound pressure level is monitored by two microphones, while the aerosol (after dilution by 10000) is sampled every 5 s by the APS.

The aerosol was generated by evaporation and condensation of Safex, a commercial liquid consisting mostly of glycerol. In the measurement range (0.4 - 5 µm), the initial aerosol size distribution is approximately log-normal with a geometric mean particle diameter, d_g, of 0.85 µm and a geometric standard deviation, σ_g, of 1.3. The mass loading was approximately 1 g.m^{-3}, and the initial total particle concentration was of the order of 10^6 cm^{-3}. A fan located near the top of the chamber ensured efficient mixing, so that spatial homogeneity of the aerosol at any given time was maintained. This mixing is also necessary to compensate for the spatial inhomogeneity of the acoustic power. The characteristic mixing time was smaller than any characteristic time of the agglomeration phenomenon (i.e. < 5 s). All agglomeration tests were performed in a standard way so that the resulting data sets were synchronised in time. The sound source was operated continuously at the desired power (100 Watts), so that steady conditions were reached. The aerosol was injected in a 4 to 5 s burst, 120 s after data collection had been started. The chamber was flushed with clean air between experimental runs which typically lasted between 10 and 15 minutes.

Evolution of the size distribution of glycol fog during acoustic agglomeration

Series of size distributions were measured as a function of agglomeration time at both frequencies. In order to improve statistics, particularly in the 2-6 μm diameter range (which corresponds to 2% of the initial size distribution), it was necessary to average the size distributions of three separate runs at each frequency. As the total particle concentration decreases in an approximately exponential way, further improvement in statistics was achieved by averaging several size distributions, in time intervals corresponding roughly to a geometrical progression. Processing of the data in this way gives a good statistical convergence of the measurements.

The experimental results for acoustic agglomeration of the glycol fog at 10 and 21 kHz are shown in Fig. 6.2. At 21 kHz (see Fig. 2a) a peak centred at 2.8 μm forms with time. Initially the number of particles in the 2-5 μm range increases. Production of these particles originates from collision of particles with diameters outside the 2-5 μm range. After 240 s, this peak begins to decrease in number, without significantly changing its shape or mean diameter. Concurrently, the peak due to the small particles, which is initially centred at 0.75 μm slowly drifts to the left (i.e. smaller diameters). A very large decrease in particle concentration is observed in this region of the size distribution. The behaviour at 10 kHz is similar, although the peak due to large particles is centred at 4 μm. It is also noteworthy that, in this latter case, particles in the small size range (< 2 μm) are still present at the end of the experiment.

The similar agglomeration behaviour observed at both frequencies indicates that a characteristic diameter can be introduced to scale the size distributions. A characteristic scale, d_f, is given by

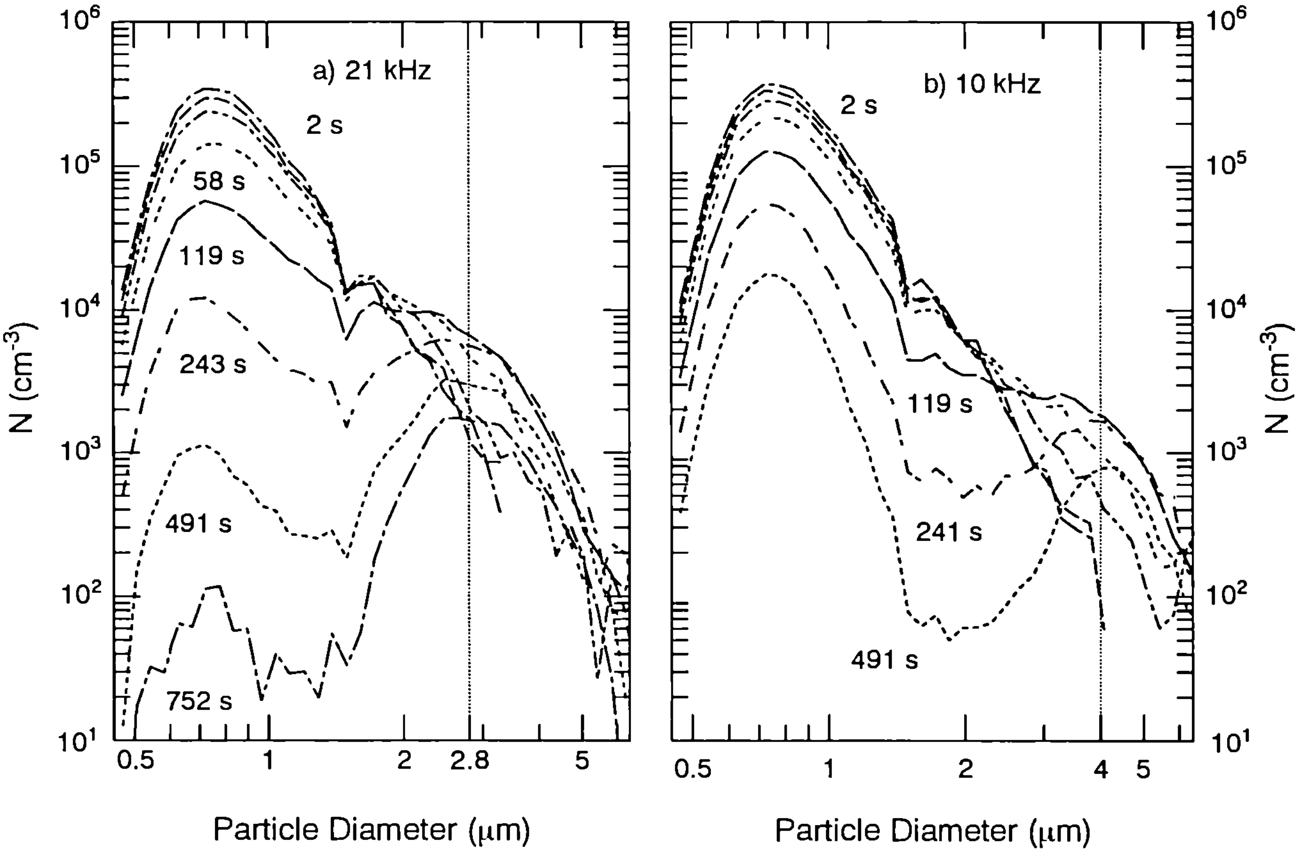

Fig. 6.2 Size distribution of the glycol fog, during an acoustic agglomeration at 21 kHz (a) and 10 kHz (b). The electrical power of the sources was 100 W.

$$d_f = \sqrt{\frac{9\mu}{\rho\pi f}} \qquad (1)$$

where μ is the dynamic viscosity of air, ρ the droplet density and f the acoustic frequency. The entrainment factor, α, of the particles in the wave is then given by

$$\alpha = \frac{1}{\sqrt{1+\delta^4}} \qquad (2)$$

where the reduced diameter, δ, is given by d/d_f.

The initial and final size distributions for measurements made at both frequencies have been plotted as a function of δ in Fig. 6.3. By means of this non dimensionalising procedure, both peaks due to the large particles are centred on $1.8 \cdot d_f$. As these peaks correspond to particles with relaxation times, τ, greater than the period, T, of the wave, these particles are inertial. The scaling by d_f permits discrimination between two zones in the size distribution. The first zone corresponds to the peak of inertial particles which is centred at $1.8 \cdot \delta$ and extends from δ to $4 \cdot \delta$. Such particles are 5-70 % (30 % at $1.8 \cdot \delta$) entrained in the wave. The second zone ($\delta < 1$) corresponds to particles with an entrainment factor greater than 70 % i.e. they are almost completely entrained in the periodic flow.

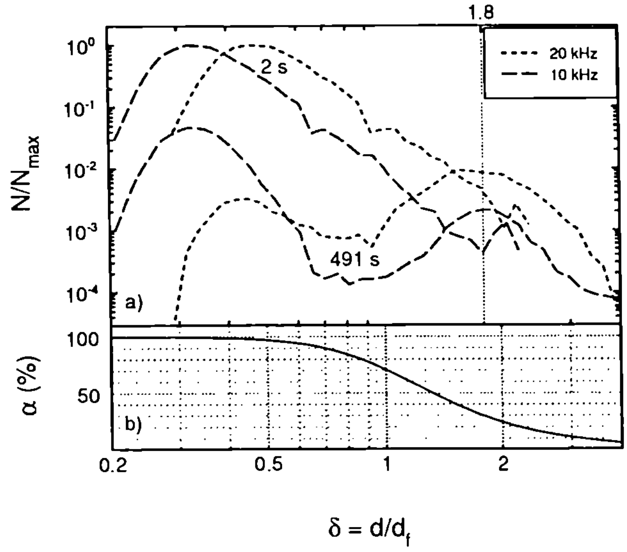

Fig. 6.3 (a) Initial and final size distributions for sound treatment of a glycol fog at 10 and 21 kHz, as a function of the non-dimensional parameter, δ. (b) Entrainment factor, α, as a function of δ.

Further insight can be gained by studying the evolution of the mass in both zones of the size distribution. The mass in the inertial zone (M_I) and in the smaller particle mode (M_s) have been integrated in experiments performed at each frequency. These masses and the total mass (M_T) are plotted in Fig. 6.4. Two phases corresponding to the increase and decrease of M_I are clearly identified. The main region of interest in the initial period of evolution (t < 200 s) has been plotted in greater detail in Fig. 6.5. At 21 kHz, the initial value of M_s is 3 times greater than M_I. As M_I increases with time, the rate of decrease, $K_s^M = d\,M_s/(M_s\,dt)$, of M_s also increases (i.e. the slope of $\ln(M_s)$ *versus* t in Fig. 6.5a increases). The total mass, M_T, remains roughly constant during this first phase. The evolution of mass at 10 kHz is quite similar. Initially M_s is 4 times greater than M_I. In this latter case, the increase of K_s^M with M_I is more evident, and the disappearance of the total mass (M_T) more pronounced.

Comparison of the evolution of mass at longer treatment times where M_I is decreasing reveals different behaviours at 10 and 21 kHz (see Fig. 4a and 4b). In both cases the rate, K_s^M, is reduced after the maximum in M_I has been reached. However, the decrease in M_s parallels the decrease in M_I in the case of 10 kHz. Indeed, the ratio M_s / M_I (see Fig. 6.6) reaches an asymptotic constant value at 10 kHz, while at 21 kHz it decreases steadily. This difference in behaviour is correlated with the survival of a fine particle mode at 10 kHz, where a peak centred at 0.65 µm (see Fig. 6.2b) remains even after long acoustic treatment times.

As acoustic agglomeration corresponds to transfer of mass between particles of different size, mass should be conserved during the entire experiment. Another phenomenon, inertial impaction on the walls of the acoustic chamber, also influences the evolution of the size distribution with time. Other investigations [4] have shown that this removal process is both frequency and particle size dependant. This phenomenon has not yet been characterised in detail in the present investigations, but evidence for its presence is found in Fig. 6.4, where a decrease in total mass is observed at both frequencies. At 21 kHz this effect is somewhat less pronounced.

Conclusion

A number of important conclusions can be drawn from these experimental studies. The use of the scaling diameter, d_f, allows rigorous comparison

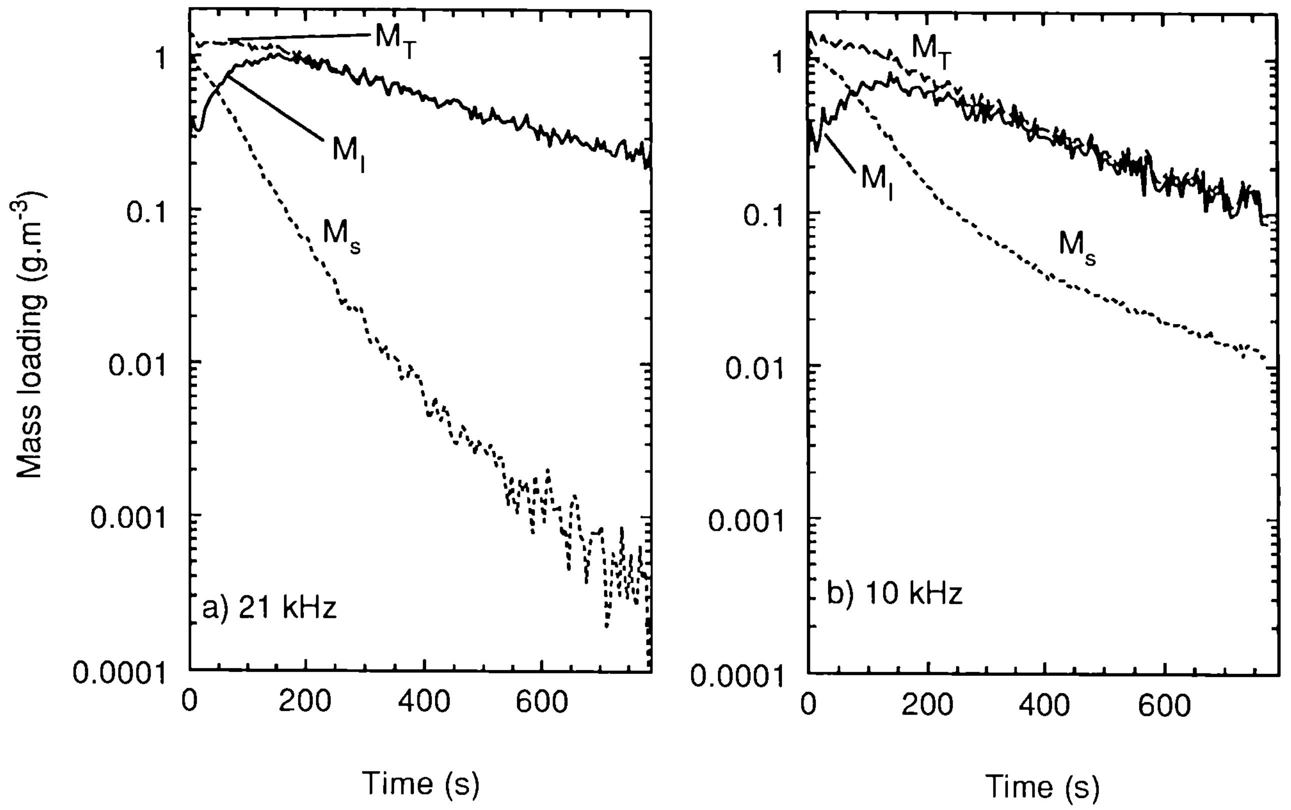

Fig. 6.4a & b: Time evolution of the mass in the fine particle mode (M_S) and in the inertial mode (M_I) during acoustic agglomeration at frequencies of 21 kHz (a) and 10 kHz (b). The total mass M_T is also shown.

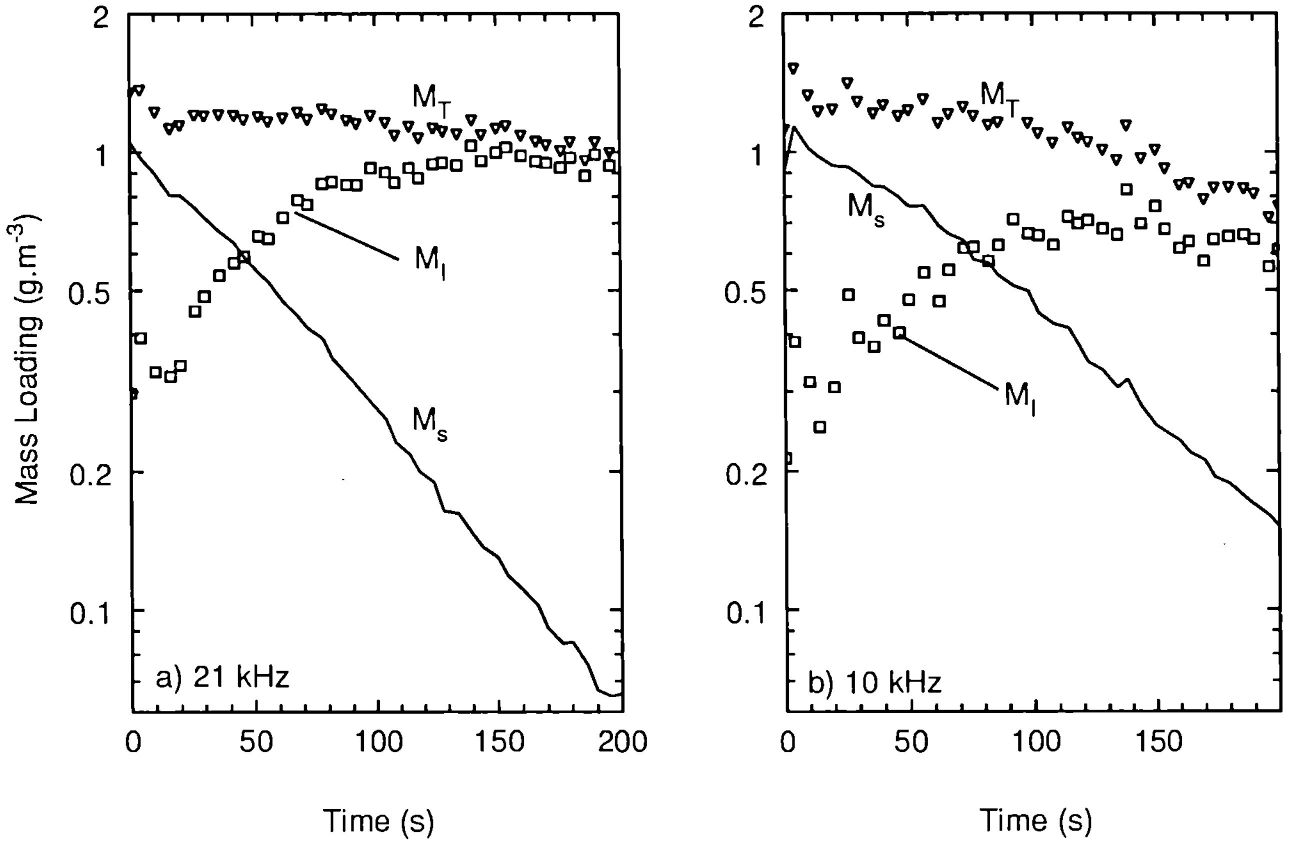

Fig. 6.5a & b: Evolution of the mass in the fine particle mode (M_S) and in the inertial mode (M_I) during the first phase of the acoustic agglomeration process at 21 kHz (a) and 10 kHz (b).

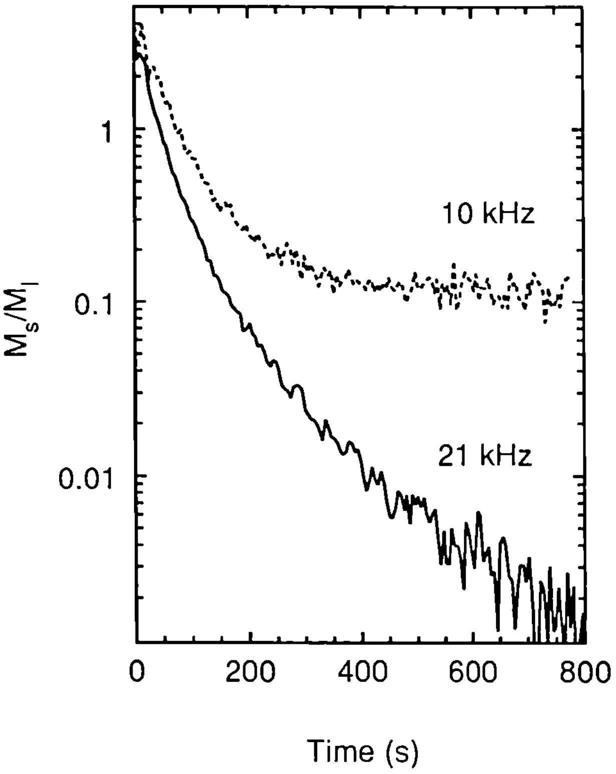

Fig. 6.6 Time evolution of the ratio of particle mass in the fine particle mode to that in the inertial mode, (M_s/M_I), at 10 and 20 kHz.

of the effect of different frequencies in the acoustic agglomeration process. The increase in the number of inertial particles in the initial agglomeration phase means that small particles collide amongst themselves to produce inertial particles. The main mechanism responsible for this effect is that of hydrodynamic interaction. However, the observed dependance of K_s^M on M_I indicates that the orthokinetic agglomeration mechanism increases in importance and may even dominate the process. In later stages of the agglomeration process, loss of particles to the wall is evident.

References

[1] E.P. Mednikov, *Acoustic Coagulation and Precipitation of Aerosols*, translated from Russian by Larrick, C.V., Consultants Bureau, New York (1965).

[2] N.L. Shirokova, in *Physical principles of Ultrasonic Technology* **2**, (ed. L.D. Rozenberg), translated from Russian by J.S. Wood, Plenum, New-York (1970) 477.

[3] P.G. Saffman and J.S. Turner *J. Fluid Mech.* 1 (1956) 16.

[4] M. Barbe-Le Borgne, D. Boulaud , C. Malherbe, A. Renoux, and A. Boutier, *J. Aerosol Sci.* 19 (1988) 3.

[5] C. Malherbe, Rapport CEA-R-5365, CEN, Saclay, France (1985).

[6] G. Rodriguez, J.A. Gallego, E. Riera and F. Montoya (1981) *Ultrasonic International*, (1981) 77.

[7] J.A. Gallego, G. Rodriguez and L. Gaete, *Ultrasonics* **16** (1978) 267.

[8] S. Temkin, *"Elements of Acoustics"*, John Wiley & Sons (1981).

3. Scientific-Technical Support to Community Policies

Introduction

In 1993, S/T-support to the services of the European Commission concerned the transfer of technologies developed in ITU laboratories to external industrial users (DG XIII) and supporting work for the analysis of fissile materials (DG XVII).

In order to develop the acoustic aerosol scavenging technique for industrial air cleaning application experiments were made to investigate the effect of "inertial" particles on the agglomeration efficiency. As one would expect for acoustic agglomeration via the orthokinetic mechanism, the agglomeration coefficient increased linearly with the humber of inertial particles added. It could also be shown that hydrodynamic interactions also contribute significantly to the agglomeration process.

Work has started to adapt a six-wavelength pyrometer, which was originally designed for measurements of high temperatures (> 1400 K), to a lower temperature range, which should make it more attractive for a wide range of industrial applications.

Field testing of equipement for on-site sample conditioning by robots in the Gatchina pilot facility was continued. Comparative analyses of samples, which had been prepared with improved techniques, were carried out at the Khlopin Radium Institute in St. Petersburg (Russia), in the IAEA Safeguards laboratories in Seibersforf (Austria) and at ITU. The final evaluation of the results is foreseen for 1994.

Components for the Safeguards analysis at the on-site laboratory in Sellafield (OSL) were tested under reaslistic conditions, and various non-destructive analytical methods were adapted for use in the reprocessing plant.

A number of improvements were necessary to optimize the expert system used at ITU for the evaluation of analytical results, and the main VAX installation had to be upgraded.

Training of staff for the on-site laboratory at the Sellafield plant was continued with three teams of four operators each, working under simulated realistic conditions.

Analytical techniques for safeguards applications were developed and further refined. Isobaric interferences could be eliminated by the use of ion-chromatography in combination with mass spectrometry for the determination of Pu and Nd in spent fuel. Laser ablation combined with ICP-MS has successfully been employed for measuring the spatial distribution of fission products across a spent fuel rod section. The glow discharge mass spectrometer underwent hot testing with isotope abundance studies and trace metal analysis in uranium metal, and from total evaporation mass spectrometry data ^{238}Pu/^{239}Pu ratios could be determined with a precision adequate for routine analyses.

Following a request from the International Atomic Energy Agency, methods of monitoring undeclared Pu and HEU production were suggested : Further testing will be carried out in a specially designed "clean room"

3.1 Support to DG XIII

Acoustic Aerosol Scavenging

Introduction

Many industrial processes produce large quantities of off gas which must be cleaned of both particulate and toxic gas content before it can be emitted to the atmosphere. Electrostatic filters and cyclones are devices widely used in industry to remove particulate matter from gas streams. While they exhibit a high efficiency for removal of particles with aerodynamic diameters greater than a few microns, they are much less efficient in removing smaller particles. This deficiency is even more pronounced when one considers that the latter particles are respirable and thus pose greatest health risk. An improvement in the separation efficiency for such particles is clearly desirable.

This project has been concerned with the use of high intensity sound waves to agglomerate these fine particles so that the diameter of the agglomerates is large enough that they can be separated more efficiently by a conventional particle separation device. There are a number of parameters which can influence the efficiency of the acoustic agglomeration process. Measurements of the influence of one of these parameters, the concentration of inertial particles, on the agglomeration process are presented and discussed below.

During the year the "Technische Vereinigung der Großkraftwerkbetreiber" (VGB-Forschungsstiftung) agreed to fund partially a proposal for the continuation of this project. As their support was made dependent on a contribution of the same magnitude from the filtration plant construction companies, an information seminar was held in Karlsruhe in October so that a decision could be reached in January 1994.

Throughout the year, a number of visits to these laboratories was made by representatives of a variety of companies. One of these, KEMA (Arnheim), have shown interest in a collaborative project.

Influence of the concentration of inertial particles in the acoustic agglomeration process

The role of inertial particles, which are stationary or near stationary in an acoustic wave field, on the acoustic agglomeration of a glycol fog, was first highlighted by Mednikov [1]. These particles act as impaction centres for the smaller, almost fully entrained particles. This so called orthokinetic mechanism is not the only effect active in the acoustic agglomeration process [2,3]. Indeed, recent experimental results, reported elsewhere in this report [4] provide evidence for the formation of inertial particles by coagulation of smaller particles. This process is probably due to hydrodynamic interaction. These results [4] also show that the diameter, d, of the inertial particles lies in the range $d_f < d < 4 \cdot d_f$. The parameter d_f scales with the acoustic frequency, f, as

$$d_f = \sqrt{\frac{9\mu}{\rho\pi f}} \qquad (1)$$

where μ is the dynamic viscosity of air and ρ the droplet density. In order to evaluate the influence of the concentration of inertial particles on the agglomeration efficiency, the ratio of inertial particles to fine particles must be varied. This has been achieved by using the agglomeration process to manipulate the aerosol size distributions.

Experimental procedure

The experiments were performed in an agglomeration facility described in greater detail elsewhere in this report [4]. The aerosol was generated by the evaporation and condensation of glycerol, and the size distributions were monitored continuously by an aerodynamic particle sizer (APS). The sound sources (10 or 21 kHz) were operated continuously at an electrical power of 100 W, while constant quantities of fresh aerosol were injected, in three second bursts, into the agglomeration chamber at constant time intervals. In this way, the concentration of large particles gradually increases, while that of the small particles was periodically brought back approximately to the starting concentration.

Results

Five successive size distributions, measured directly after injection of the aerosol, are plotted, as a function of the reduced diameter $\delta = d/d_f$, in Fig. 7.1. The number of inertial particles ($\delta > 1$) increases from one injection to the next, while the overall shape of the fine particle mode ($\delta < 1$) is reproduced identically at each injection. The total particle concentration, N_T, the concentration of inertial particles, N_I, and total mass loading, M_T,

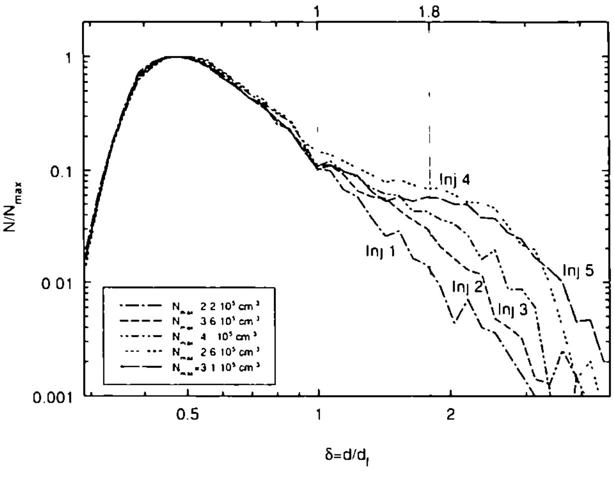

Fig. 7.1 Size distributions, in terms of the reduced diameter, δ (= d/d_f), immediately after fog injection (21 kHz, 100 W). After the fifth injection, a drift of the inertial particles towards higher sizes is observed.

are shown in Fig. 7.2 as a function of acoustic (21 kHz, 100 Watts) agglomeration time. The evolution of the total mass loading, M_T, was step-wise with an increase by approximately 2 g.m^{-3} at each injection. Between injections, N_T decreases dramatically while N_I and M_T remain constant. Comparisons of the agglomeration process at consistent initial conditions was achieved by only considering data from injections in which N_I or M_T increased step-wise.

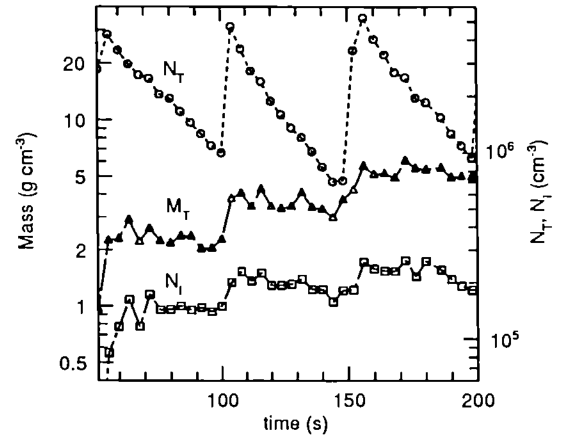

Fig. 7.2 Concentrations of all particles, N_T, of inertial particles, N_I, and total mass, M_T, during three injections of the aerosol. Agglomeration was achieved by a 21 kHz source operating at 100 W.

Plots of the acoustic agglomeration coefficient, K (=$dN_T/N_T dt$), which was evaluated immediately following each injection, are shown as a function of concentration of inertial particles in Figs 7.3a and 7.3b for acoustic agglomeration at 21 and 10 kHz, respectively. At 21 kHz, these results clearly indicate that there is a linear relationship between K and N_I, as would be expected in the case of the orthokinetic agglomeration mechanism. The finite value of K extrapolated to zero inertial particle concentration, ($N_I = 0$), corresponds to coagulation of small particles, ($\delta < 1$), by means of the hydrodynamic interaction mechanism. The 10 kHz data exhibit a similar tendency. There is an increase in the scatter in the experimental points, as compared to the 21 kHz data. This is due to the increase in d_f at lower frequencies which means that for a given size distribution, the concentration of inertial particles decreases with frequency.

Conclusion

These investigations have shown that the number of inertial particles, with diameters such that $d > d_f$, influences the efficiency of the acoustic agglomeration process directly. This is particularly the case for combinations of aerosol size distribu-

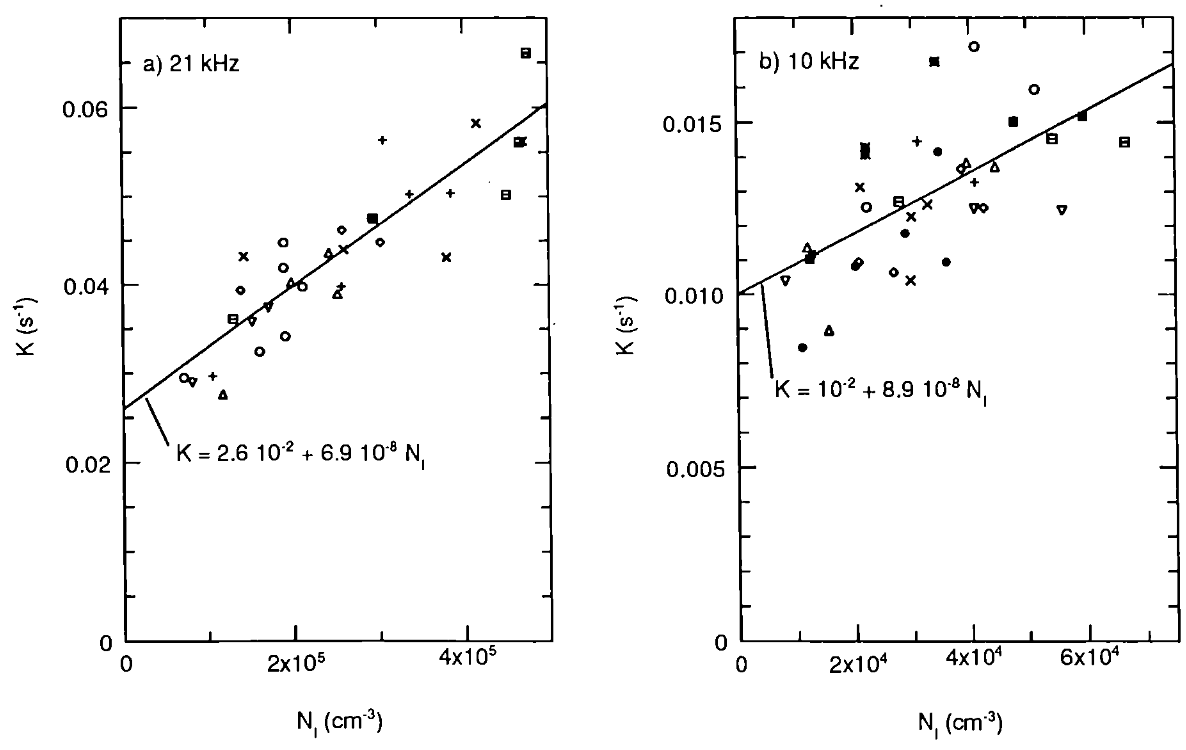

Fig. 7.3 Agglomeration rate coefficient, K, as a function of N_I, for 21 kHz (a) and 10 kHz (b). Both K and N_I were determined immediately after injection of the aerosol. The electrical power of both sources was 100 W.

tion and acoustic frequency which favour the orthokinetic mechanism of acoustic coagulation. The results also show that hydrodynamic interaction also contributes significantly to the agglomeration process. In an industrial application, the running costs of the process can be minimised by careful choice of operating conditions. Further research and development are required if this goal is to be reached.

References

[1] E.P. Mednikov , *Acoustic Coagulation and Precipitation of Aerosols*, translated from Russian by Larrick, C.V., Consultants Bureau, New York (1965).

[2] N.L. Shirokova, in *Physical principles of Ultrasonic Technology* **2**, (ed. L.D. Rozenberg), translated from Russian by J.S. Wood, Plenum, New-York (1970) 477.

[3] M. Barbe-Le Borgne , D. Boulaud , C. Malherbe , A. Renoux , A. Boutier , J. Aerosol Sci. **19** (1988) 3.

[4] TUAR 93 p. 173

Advanced Pyrometry

The initial objective of the project was to design and construct a six-wavelength pyrometer for high temperature measurements with:

1. An effective measurement range T < 1400K (this required a considerable improvement of the sensitivity of the laboratory instrument PL1).
2. A simultaneous measurement of the six wavelength channels (entailing a new design of the available data acquisition system).
3. A detection time of less than 2 ms.
4. A substantial reduction of the component costs with respect to PL1 (comprising the three preceding improvements). In this respect, an indicative upper bound for the instrument prime cost was set to be approximately 5000 UC, excluding the microcomputer for data processing.

The construction of a modular pyrometer (PX1) complying with these specifications was started according to the following scheme:

- Pyrometer objective: Two standard achromatic lenses (80 mm), with an object focusing field of 70-110 cm. The radiating surface was assumed to be of approximately 10 mm diameter.
- Beam splitting: A bundle of 1000 glass fibers randomly subdivided into seven sub-bundles (six measurement channels plus a viewfinder) was adopted.
- Channel monochromators: Six interference filters of 40 nm band-width.
- Spectral range: 550-1050 nm (upper limit for Si-detectors).
- Detectors: 6 Silicon photodiodes ($1 mm^2$).
- Preamplifiers: Linear, with low noise and variable amplification factor.
- Digital conversion: Six parallel A/D converters.
- Data processing: a commercial AT.

Following the results of a marketing study, it was decided to extend the temperature range down to 700 K. This makes it necessary to work in a spectral range up to approximately 1.7 μm wavelength where the following limitations, in order of importance, have to be considered: a) the silicon photodiodes are insensitive to infra-red (IR) light with $\lambda > 1050$ nm, and, hence, other detectors have to be adopted, b) above 1000 nm the available commercial lenses exhibit increasing chromatic aberrations, and c) the IR absorbing glass fibers have to be replaced by more transparent (but considerably thicker) quartz fibers.

After preliminary tests, we were able to propose solutions for the problems under points 1., 2. and 3.

- by using silicon detectors for two wavelengths (900, 1050 nm) and Indium-Gallium Arsenide for the others (1200, 1350, 1500, 1650 nm), and

- by constructing a bundle of approximately 100 quartz fibers.

Point 4. is still under study.

3.2 Support to DG I

Gatchina: Field Test for On-Site Sample Conditioning by Robot

The field test continued with the conditioning of two series of input samples which were reprocessed in the Gatchina pilot facility. The conditioned samples were sent for analysis to the Khlopin Radium Institute in St. Petersburg, to the IAEA Safeguards Laboratory in Seibersdorf (Austria) and to our institute. Most of the campaigns have now been measured. The evaluation is foreseen for 1994.

The main objective of this field testing was to check the reliability of the robot under routine condition away from our laboratory with its easy access to support. In general, the performance of the robot was very satisfactory. Following our Russian colleagues, the following observations and improvements were made [1]:

- In order to exclude the hazard of main power supply interruption and to obtain reliable performance from the robot system, it was decided to equip the system with a computer regulator and standby power source. This equipment was supplied by us and was installed by the specialists of the Khlopin Radium Institute.

- Occasionally, the balance showed instabilities during the process. For the second part of the field test, a correction of the main programme was made and the balance was also replaced.

- The syringe in the hydroxylamine chloride solution line was damaged as a result of corrosion. The syringe was replaced.

- It was noted that, after a long interval between operations of the robot system, oxidation of the pin contacts in the robot manipulator occurred. It was found that this problem can be solved by means of switching on the robot manipulator periodically for a short time according to computer programme written by specialists of the Khlopin Radium Institute.

After the evaluation of the final experiment, the trilateral field test will be concluded in the summer of 1994. The bilateral contract with the Khlopin Radium Institute, which foresees further studies with the instruments will then have to be defined in detail.

Reference

[1] G.A. Akopov, B.N. Beljaev, L.S. Buljanitsa, A.V. Lovtsus, A.V. Stepanov, N.V. Shuljak, V.G. Khlopin Radium Institute: 'Field Test of On-Site Sample Conditioning by Robot', St. Petersburg, June 1993.

3.3 Support to DG XVII (On-Site Labs)

On-site Laboratory, Sellafield

Introduction

A large amount of development work has been carried out this year, preparing for the installation in Sellafield of the on-site laboratory. The work has included the following areas:

- Testing of components, including the IDMS glovebox under realistic conditions
- Development of the titration glovebox
- Updating of the VAX computer system for data storage and calculation of end results
- Testing of the non destructive components (n-counter, gamma counting of Pu, K-edge absorptiometer, COMPUCEA)
- Training of OSL operators

These topics are discussed more fully below.
The HAZOP procedure for Sellafield was completed (TUAR-92, p. 182). In effect the design and working procedures have been accepted by BNFL as forming the basis of the Pre-construction Safety Case. A quality assurance program has been started for the project under contract by NNC. It only became clear late in the HAZOP procedure that QA (ISO 9001) would be required for the on-site project. This has led to extra difficulties, firstly because the Institute has no QA certificate and secondly because the quality assurance program has had to be started late in the course of the project.

Development of components

Construction of a transportable compact K-edge absorptiometer

Following a request from DCS Luxembourg, a transportable glovebox for a compact K-edge apparatus was designed (TUAR-92, p. 184) and constructed according to their specification. Problems were found during testing with microphony of the germanium detectors. This degraded the gamma and X-ray spectra and produced unacceptable results.

To overcome this problem, the counter table and stand was redesigned with rubber foam isolation pads. The effect could not be totally removed but was highly attenuated.

The glovebox has been accepted for installation in La Hague and will be transferred there early next year.

Construction of a test glovebox for the product K-edge

To test the K-edge densitometer, including the gamma spectrometer under active conditions (i.e., with Pu), it was necessary to install the system in a glovebox. A slightly contaminated glovebox was used for this purpose: the box was thoroughly decontaminated and installed on a new metal support. The high level of decontamination was necessary in order to be able to construct a metal finger in the floor of the glovebox in which the sample cuvettes could be inserted. The finger is illuminated by the collimated X-ray beam and a LEGe (low-energy germanium detector) is positioned to view the transmitted beam, and a second at the side to view the passive emitted gamma rays from the Pu. Shielding was done with tungsten, with cadmium liners to absorb X-rays induced from the tungsten.

The glovebox has now been installed in the product measurement laboratory at the Institute. Electrical and water supplies have been connected and it is expected that optimisation work can be carried out early next year.

Testing of components for the OSL

The IDMS glovebox has been installed in the laboratory in the Institute and is being utilised for routine analyses.

Certain modifications were found necessary for the MS filament preparation unit:

- The electrical contacts on the mass-spectrometer turrets were found to give problems in the glovebox atmosphere. These have now been replaced with silver contacts

- When the turret is rotated to permit the next filament to be prepared, some of the liquid was occasionally spilled, causing contamination. A small 12V resistance heater has been installed which is switched on under robot control after dispensing a drop onto a filament and dries the solution before the turret is turned.

New Design and exchange of the alpha chamber

Improvements have also been made to this apparatus:

- The motor drive to the alpha chamber turntable has been replaced: the turntable is now turned either by the robot directly, or by the operator manually.
- The vacuum dead volume inside the alpha chamber has been reduced to lower the pumping time
- The planchette loading/unloading mechanics have been improved to obviate planchettes being dropped

Titration glovebox

The titration glovebox was successfully tested using a robot with Fe as substitute for Pu. The microwave oven was received, and after testing and modification was installed in the glovebox. The glovebox has been transported to a hot laboratory in the Institute where test titrations on U solutions (using depleted U) will begin next year.

Non-destructive methods for the OSL

Introduction

It is expected in the present planning, that the vast majority of samples arriving at the OSL, Sellafield will be measured using non-destructive techniques. These include:

- K-edge absorptiometry in conjunction with high resolution gamma-spectrometry for the concentrations and isotopic abundances of Pu nitrate solutions
- Compact K-edge in conjunction with a well gamma detector for the concentrations and enrichment of uranium nitrate samples
- Neutron coincidence counter in conjunction with high resolution gamma-spectrometry for total amounts and isotopic abundances of Pu oxide samples

All of these techniques have been applied elsewhere; in this sense they are not new. However the combination of the techniques, together with the particular constraints of the OSL constitute the problem areas.

None of the methods exists at present in the final version to be applied in the OSL. Adaptation and tests presently being carried out will be described for each of the techniques. Common to all the methods is development needed for the data aquisition and transfer to the central computer laboratory.

Product K-edge

The K-edge apparatus has been routinely used for a large number of quality control samples. The results of these samples and the comparison with other techniques will be reported elsewhere. The X-ray generator and the apparatus head needed to be changed to comply with new safety regulations and to accomodate the gamma detector for passive gammas: for the determination of the Pu isotopic vector and ^{241}Am concentration. A new K-edge head has been constructed from tungsten and is being installed around a finger of a new glovebox, where the measurements can be made and controlled. Special attention has been given to the shielding around the head to eliminate possible stray-beams of X-rays. An electrical safety trip is also being installed on the shielding which prevents the X-ray tube being operated without the shielding in place. This precaution is required for the OSL.

Compact K-edge (COMPUCEA)

Although a glovebox has been constructed with the head of the compact K-edge, the series of measurements hoped to be carried out this year have not been made because of problems in the delivery of a ^{57}Co source. This excitation source is being constructed together with a uranium foil at Amersham, England.

Neutron coincidence counter

The counter was tested in 1992 as part of an international experiment (TUAR-92, p. 188). Many further measurements have been carried out since then to determine the optimal mode of operation and in particular the interaction with the in-built gamma detector and its associated shielding.

Problems were experienced with the software for this counter. The software packet, 'NCC' controls the NIM module (JSR 12) with ASCII strings sent via the serial port of the control PC. At an upgrade of the software, it was found that the JSR 12 module would not switch on under program control. The problem was eventually resolved by the equipment manufacturer, but as a result the apparatus could only be used to some extent throughout the year. Hardware problems with the in-built gamma detector meant also that during the time this detector was away being repaired, the neutron counter was effectively out of action because the efficiency of neutron counting is dependent on the gamma detector being in position. A substitute for the gamma detector was also not possible because of the unique geometry of the detector.

A new plutonium oxide standard has been prepared for the calibration of the detector with plutonium of a different isotopic abundance. This is reported below. The intention is to test the response curve of the instrument with well-characterised plutonium oxide samples having different isotope vectors. It is hoped these measurements can be carried out at the beginning of the next year.

HPGe gamma counter

The Pu isotopics will be determined by a high performance pure germanium gamma detector which is mounted on a cold finger which fits into the neutron coincidence counter from below. A description of the apparatus was given previously (TUAR-92, p. 189). The spectra are evaluated using the program MGA. A HPGe gamma detector will also be employed on the K-edge apparatus. This detector is mounted more conventionally than that used with the neutron coincidence apparatus and will be tested on standard solutions when the glove-box is installed for testing the K-edge absorptiometer.

During the international experiment, the gamma counting side was not pursued. However, when the experiment was completed, many Pu spectra of a standard PuO_2 material obtained from IRMM were accumulated under various conditions. The size of the detector (500 mm^2), means that spectra from typical PuO_2 samples of 2-5g size are accumulated within a relatively short time, 20-30 mins. At the same time, Compton scattering from the low atomic weight neutron shielding produces peaks in the spectra which disturb the evaluation process (the background determination during peak deconvolution in particular is sensitive to such effects during multiple peak fitting). Some cadmium shielding was also necessary to reduce the relative size of the ^{241}Am peak in the spectra. The effect of this shielding on the neutron counts has also to be determined. To minimise the effect of this shielding, Sn was used instead of Cd because of its much lower neutron absorption.

Biases of between 0.3 and 0.5% relative to the certified isotopic abundance of ^{240}Pu were found for a range of counting conditions. As part of the determination of the characterisation of the detector, standard Pu oxide samples were counted with the detector situated in the open laboratory, well away from possible sources of scattering. During these counts, instabilities in the detector were noticed and as a result the detector was returned to the manufacturer (Canberra) for repairs. The fault was finally diagnosed to be a contact problem between Ge crystal and preamplifier. As a result of these hardware problems, the counting series have not been completed and a definitive statement cannot be made on the accuracy of the Pu isotopics determination by gamma spectrometry in the combined n-coincidence / gamma detector instrument.

A second detector is expected to be delivered in the coming year and this will allow comparison measurements to be made. The following parameters will be investigated:

1. The comparison between the isotopic abundances for the IRMM PuO_2 standard and the new PuO_2 standard (see below) counted on each detector under ideal conditions, i.e. with no shielding, a dead-time of about 20% and no collimation.
2. The effect on the evaluation, counting each standard with the gamma detector installed in the neutron coincidence counter. Both detectors will be used and compared.
3. The effect of absorption shielding (Sn) on and round the detector and the amount needed to optimise the count conditions for the 2 standard materials.
4. Possible effects of a collimator placed between detector and well of the glove-box into which the samples are inserted.

Preparation of a Second PuO_2 Standard Material (SM2)

Introduction

For the international experiment reported previously (TUAR-92, p. 188), a standard PuO_2 material was prepared and sealed under carefully controlled conditions into plastic and stainless-steel vials. The material was prepared and certified by IRMM, Geel [1].

This material was made from low burnup plutonium and thus had a ^{239}Pu content of 93.5 at. %. The relatively low amount of ^{241}Pu was favourable for a standard material because the certified isotopic values change little with time. One disadvantage, however, is that typical plutonium to be expected in the OSL will have much lower abundances of ^{239}Pu and it could be that the calibration of the neutron counter, using the IRMM standard material for this purpose, cannot be applied to materials with very different ^{239}Pu abundances. It appeared that other plutonium material could be prepared and certified in this Institute which could be used as secondary standard material for this purpose.

Plutonium is available in the Institute with isotopic characteristics closer to those expected in material in the OSL. A batch of plutonium was therefore taken, purified and dried and samples were weighed quantitatively into plastic vials of the same type as those used for the OSL counter. (It appears now that stainless-steel vials will be used at Sellafield, however these were not available at the time this standard material was prepared and the material in the plastic vials can be compared directly with the IRMM standard material).

The Pu was supplied in the form of oxide (ca 13g). It was to be purified by anion exchange, precipitated as oxalate and finally calcined to PuO_2. The powder would then be weighed into polycarbonate vials similar to those of the IRMM samples. Amounts of about 1,2,3 and 6 grams were required. An aliquot of the powder would also be dissolved for titration.

Description of method

The Pu oxide was dissolved in concentrated HNO_3 + 0.1 M HF in an Erlenmeyer flask. The solution was diluted with water to obtain a concentration of approximately 100g Pu/l in 8 M HNO_3. The Pu was converted to the 4-valent state by the addition of 10 ml H_2O_2 (30%); the excess H_2O_2 was destroyed by stirring. An anion exchange column was prepared containing about 150g DOWEX 1x8 anion exchange resin. The resin was washed with 8M HNO_3 to remove chloride ions and then brought into the glove-box.

The Pu solution was put on the column and the column washed with 900 ml 8 M HNO_3. The Pu was visible as a dark green layer. The Pu was stripped with 0.5 M HNO_3. After 1 litre of the stripping solution, part of the Pu remained fixed on the column. The rest of the Pu was eluted with 90 ml 0.2 M hydroxylamine chloride. The Pu left the column as lilac-coloured Pu^{III}. The solution containing Pu^{III} was evaporated to about 50 ml and 20 ml concentrated HNO_3 was added to destroy excess hydroxylamine reagent and to convert the plutonium to Pu^{IV}. The solutions were combined.

250 ml saturated oxalic acid solution in 1M HNO_3 were added and the Pu allowed to precipitate. The precipitate was collected on a filter paper, washed with 500 ml of 10% oxalic acid and allowed to dry in an oven at 100°C. The Pu oxalate precipitate was transferred to a crucible and placed in an oven where it was slowly dried and then calcined at 1000°C for 16 hours followed by 1050°C for 6 hours.

The material was allowed to cool under a N_2 atmosphere and was then weighed into plastic vials in a glove-box under N_2. The vials had been allowed to equilibrate with the N_2 atmosphere for 24 hours before weighing.
4 vials were made up, of nominal weights: 1,2,3 and 6 grams. About 1/2 g was weighed into 2 Erlenmeyer flasks for titration. Aliquots of each dissolved Pu solution were diluted to yield ca. 15 mg Pu/g solution for mass-spectrometry. 2 filaments were prepared from each solution, using ca. 0.7 ml and the mass-spectra measured using a VARIAN 261 thermal-ionisation mass-spectrometer. The sample weights are given in Tab. 7.1 and the results of the measurements in Tab. 7.2.

Tab. 7.1 Weights of PuO_2 standards 'SM"'

Sample identity	Weight PuO_2(g)
SM2-01	1.00085
SM2-02	2.00121
SM2-03	3.00035
SM2-04	5.50009

Tab. 7.2 Atom percent abundances of PuO_2 standard material, SM2. Measurements made 29.4.93

Isotope	Atom percent
238	0.40
239	70.87
240	24.54
241	2.54
242	1.66

Expert System and Data Transfer

Expert system

The expert system was designed and built to check the analysis results from the routine DCS analyses (TUAR-92, p. 184-185). This year's work consisted of testing the system with the data from our routine analyses. These tests have shown some deficiencies in the set of rules used up to now by the expert system. In certain cases all sources of possible error were not always foreseen and the system could not produce an answer. A few rules had to be added to take these cases into account. In addition, it was also found necessary to redefine or split up rules to get better diagnostics.

Another improvement which was implemented in the expert system was to speed up the response time. For a single analysis the system needed 2 to 3 minutes to produce an answer. This was due to the fact that an expert system is very time consuming in terms of processor time. Nevertheless, it is possible to write the rules in order to increase the speed. The system avoids for example the inspection of a set of rules which is not relevant for the given data and, as a consequence, saves time. A gain of a factor of 3 in the response time was achieved with this method. Moreover, the installation of a new VAX, 20 times faster than the previous one, again increased the speed. The expert system now produces the diagnosis within seconds.

A control charts utility has been added to the expert system. The measured results on a standard material are compared with the specified value and standard deviation. If a measurement on a standard material is found by the system to lie outside the set limits on the control chart, sample measurements in the same batch will automatically be repeated. This feature is still in development.

A further facility was included to ease the addition of new analytical methods to the expert system. Menu-driven functions to define new methods, including all the information needed by the expert system (instruments, measured elements, errors limits), can be used. This information is then loaded in the expert system. Another benefit of this feature is the ability for the user to adjust or modify parameters without any knowledge of how the expert system is constructed.

Upgrades to the main VAX installation

The VAX computer calculates the results from data transmitted from the laboratory instruments and holds the repository of all measured data. By the beginning of the reporting period the transfer of the programs for the data calculations, previously held on the main-frame IBM computer, had been completed and the comparison tests had shown that the programs on the VAX were entirely satisfactory. The link to the IBM was therefore closed down and since this time all calculations have been carried out on the VAX.

The rising demands on the VAX also showed clearly that a hardware upgrade was needed. A VAX 3100-90 was purchased and is now in use as the central laboratory computer for all Safeguards measurements. This gives a much higher performance than the previous Micro VAX II and is also considerably more reliable.

The following additions or improvements were carried out to the data analysis software on the VAX:

1. The necessary programs for the calculation of spikes for IDMS were written and tested.
2. The programming of the propagation of measurement errors has been started. This is considered essential for the prediction of the final errors of a measurement series and will be used in the expert system (see above for a description of the present state of this system).
3. A handbook containing the error messages of the data processing system has been written.
4. An automatic weekly reporting system for measurements has been written. This gives a direct overview of the work carried out during the week for the laboratory manager.
5. General improvements in the data processing system brought to light during routine use have been included.

Training of Personnel

The theoretical training for the "Laboratoria In Situ (LIS)" personnel which started in 1992, was continued in 1993.

In 1992 a basic revision of topics concerning fuel cycle, reprocessing treatments, general inorganic, analytical and nuclear chemistry of plutonium and uranium was made. During 1993 analytical techniques such as titration, mass-spectrometry, K-edge and hybrid K-edge absorptiometry, α- and γ- spectrometry and high level neutron coincidence counting were revised from a basic instrumental and theoretical point of view. Attention was given to the specific analytical procedures used. The technical characteristics and performance of the instrumentation employed in the LIS have been also considered.

Lectures on health physics and radioprotection have been held in house as well.

For the practical training, during the first trimester of 1993, in the Institute the work for three LIS teams, each composed of four operators, has been organised simulating the actual operational situation in the on-site laboratories.

The two French language courses, at two different levels of knowledge, which started in-house for LIS personnel on October 1992, were continued during 1993.

Maintenance of the Hybrid K-edge Absorptiometer at La Hague

Following the arrangement reported last year, the hybrid K-edge apparatus, installed at the reprocessing plant at La Hague for on-site verification measurements, has been maintained by personnel of this Institute on a one-week-per-month basis.

During the year various problems occurred:

Three separate breakdowns of the X-ray generator led to the generator being replaced by the firm from whom it was purchased. A series of tests was requested by the firm to try and determine the cause of the problem, but the information was not conclusive and it is to be feared that further breakdowns will occur.

A new software package was installed based on a menu system. This was requested by DCS, Luxembourg. The package contains the K-edge/XRF program for the hybrid K-edge operation, the K-edge program, a semi-automatic calibration program and a program designed for low Pu and low U concentration solutions.

An extension to this packet was later installed, which allows the X-ray unit to be controlled by the program.

It was observed during the year that the calculated concentration of the uranium reference capsule showed a steady increase with time, indicating possible concentration effects. A new set of reference standards was quickly prepared at the Institute in the middle of the year. At the same time the holder for the reference cuvettes was improved to allow the cuvettes to be replaced using the hot-cell manipulators at La Hague. This includes also the cuvette with a solid MOX sample which is used to calibrate U/Pu ratios.

A systematic negative bias was observed between the measured U and Pu concentrations and the (operator) declared values. For this reason it was decided to recalibrate the machine and for this purpose a set of standard solutions (U, Pu, U-Pu) was ordered from IRMM, Geel. The calibration was carried out in the second half of the year. The new calibration for U differed by less than 0.2% from the initial calibration performed in July 1990. This suggests that the observed measurement bias must have a different cause. The new calibration for the U/Pu ratio was not completely satisfactory however because it was based on a set of reference solutions with the same ratio (100:1). Further standard solutions with different U/Pu ratios are needed to complete the calibration.

The above problems have caused some disturbance in the flow of measurements and illustrate the difficulties of maintaining such a complex instrument at a remote station like La Hague. These were exacerbated by software errors in the delivered programs and also by delivery problems when sending the reference materials to La Hague both from IRMM and from this Institute which caused major hold-ups in the calibration program. Part of these delivery problems arose from tougher transport regulations but also partly because of bureaucratic difficulties in and out of house.

3.4 Support to DG XVII (Analytical Techniques)

Determination of Fission Products and Actinides by Isotope Dilution - Ion Chromatography - ICP-MS

Introduction

The direct determination of many fission products and actinide isotopes in nuclear samples by ICP-MS is hindered by the presence of isobaric interferences. As an example, ^{238}Pu is interferred by the presence of ^{238}U in most nuclear samples. For the fission products, the isobaric interferences arise from the β-decay of short-lived isotopes or from neutron capture reactions during fuel irradiation and natural element impurities can also be a source of isobaric interferences in the measurement of the long-lived isotopes (e.g. in the analysis of vitrified HAW). These isobaric interferences cannot be resolved by conventional Mass Spectrometry and therefore a chemical separation of the interfering nuclides is necessary.

Three important areas of activity have been identified:

1. The separation of the actinides by ion chromatography for the determination of low levels of Pu in the presence of U, Np, Am and Cm.
2. The separation of the lanthanides for the determination of fuel burn-up based on the ^{148}Nd method.
3. The separation of Cs and Ba for the determination of low levels of Cs in leaching samples. (see previous chapter)

The separations were done by Ion Chromatography coupled on-line with the ICP-MS. Quantification will be carried out by isotope dilution analysis.

Experimental

Instrumentation

The instrument used was an ELAN 5000 (Sciex, Canada), modified for glove box work and coupled to a Dionex ion chromatography system. Details of the glove box installation were presented previously (TUAR-92, p. 191).

Chromatographic conditions

The separation of the actinides was performed using a cation exchange CS10 column, Dionex, using 1M nitric acid as eluent. The eluent flow was 1 ml/min and the injected volume was 200 µl. Prior to injection the sample is treated with a few mg of solid Ag(II) oxide in order to convert quantitatively the Pu to Pu(VI). Under these conditions the elution order is Np-Pu-U-Cm-Am.
The separation of the lanthanides was achieved using a mixed-bed ion-exchange column (CS5 from Dionex) using a oxalic acid - diglycolic acid gradient. As in the previous case the eluent flow was 1 ml/min and the injected volume was 200 µl. No sample pre-treatment was necessary for the separation of the lanthanides. The elution order followed that of increasing atomic number [1].

Isotope dilution analysis procedure

For the determination of uranium, ^{233}U was used as spike. For Pu, ^{244}Pu was used. The results obtained were compared with the standard procedure using TIMS. For the determination of Nd two spikes were used: enriched ^{150}Nd and natural Nd. The final results were compared to previously obtained burn-ups for the same type of sample.

Results and discussion

Determination of Pu in spent fuel

Fig. 7.4 shows the separation of the actinides in spent nuclear fuel solutions and detection by ICP-MS. All masses from 232.5 to 244.5 were measured consecutively in order to produce a three dimensional graph. Each scan of the mass range took about 3 seconds. The total separation time including the elution of Cm and Am took less than ten minutes. This particular sample was

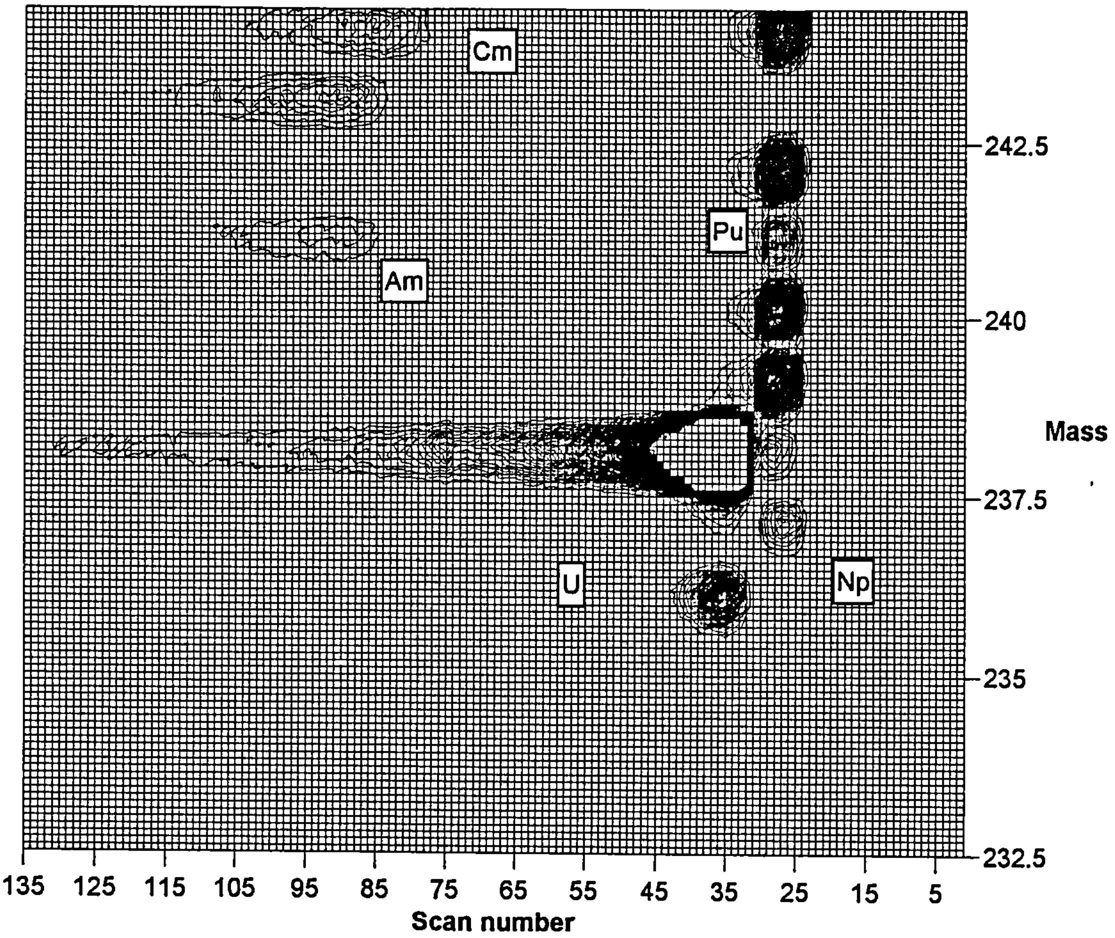

Fig. 7.4 Separation of actinides in spent fuel by Ion Chromatography and on-line detection by ICP-MS

spiked with ^{244}Pu in order to perform the isotopic dilution analysis. As can be observed, Np and Pu co-elute practically but they are well separated from U, Am and Cm. The co-elution of Np and Pu has no effect in their determination as there are no isobaric interferences between those elements. After separation the determination of Pu by isotope dilution analysis is facilitated. As can be seen, ^{238}Pu is not overlapped by ^{238}U and also ^{241}Pu is well separated from ^{241}Am. The use of ^{244}Pu as spike for the isotope dilution procedure requires the separation of Pu and Cm. This is also obtained in our present conditions.

The concentration of Pu obtained for this sample was 2.42 ppm for the dissolver solution. The data obtained by ID-TIMS was 2.47 ppm.

Determination of Nd in spent fuel

Fig. 7.5 shows the chromatogram obtained for the separation of the lanthanides in the same fuel shown in Fig. 7.4. As can be observed, the elution follows the expected order: La-Ce-Pr-Nd-Pm-Sm-Eu-Gd. All Nd isotopes are now free from isobaric interferences (^{142}Ce, ^{148}Sm and ^{150}Sm) which allows the determination of total Nd by isotope dilution analysis. The result obtained using the ^{150}Nd enriched spike was 2.111 ppm which agreed quite well with that obtained using natural Nd spike (2.205 ppm).

Determination of fuel burn-up

Based on the data obtained for the determination of U, Pu and Nd in the fuel dissolver solution the fuel burn-up can be calculated according to the equation:

$$\text{B.U. (at\%)} = \frac{100 \cdot A}{A + U_f + Pu_f}$$

where A = Total actinides fissioned (nmol)
U_f = Total U final (nmol)
Pu_f = Total Pu final (nmol)

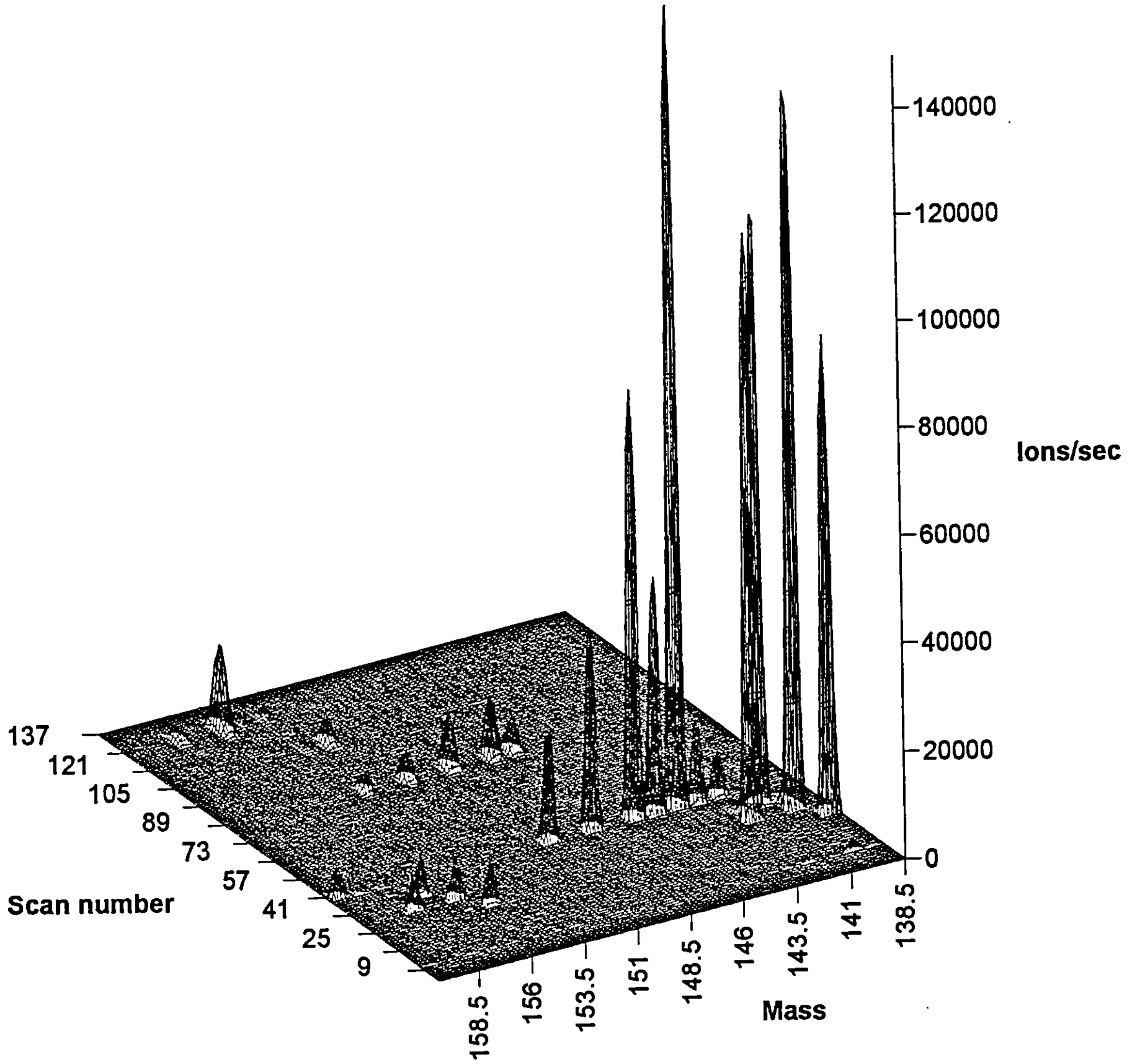

Fig. 7.5 Separation of the lanthanides by Ion Chromatography and on-line detection by ICP-MS

Tab. 7.3 summarises the results obtained for this particular sample.

Tab. 7.3 Determination of fuel burn-up

U total (nmol/g)	1008.2
Pu total (nmol/g)	10.07
Nd total (nmol/g)	14.87
^{148}Nd (nmol/g)	1.39 (based on isotopic composition)
^{148}Nd fission yield	1.693%
Total actinides fissioned (nmol/g)	82.10
Burn-up (at%)	7.46%

Detection of medium-lived fission products

Thanks to the separation of isobars from β-decay pairs the determination of medium-lived fission products is possible by IC-ICP-MS. Fig. 7.6 shows the separation of ^{147}Pm from its decay product ^{147}Sm by selective detection at mass 147. The cooling time of this particular fuel was 11 years at the time of measurement and the dilution factor ca. 30000.

As can be observed, even at high dilution factors and long cooling times the detection of medium-lived fission products is possible. In the same sample ^{151}Sm and ^{154}Eu were detected in the presence of stable nuclides (see Fig. 7.7).

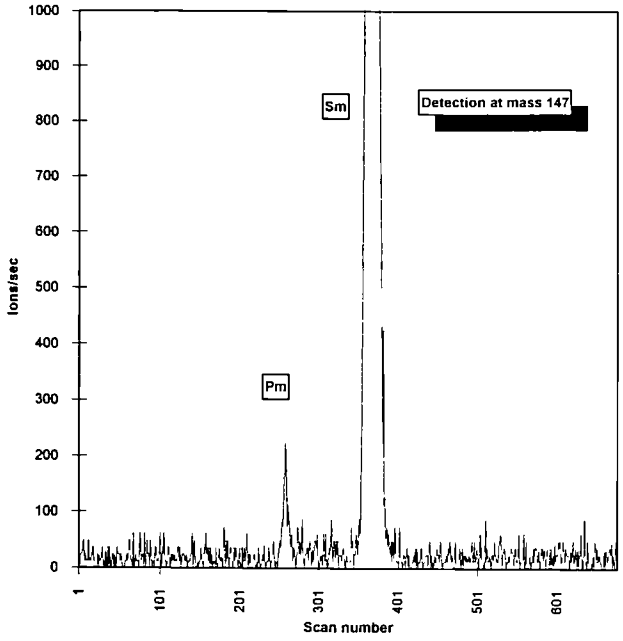

Fig. 7.6 Selective detection of ^{147}Pm and ^{147}Sm after ion chromatographic separation.

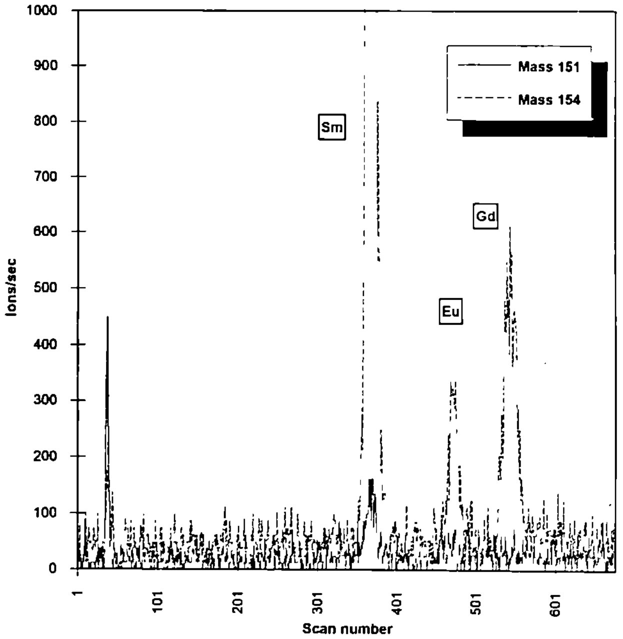

Fig. 7.7 Selective detection of ^{151}Sm and ^{151}Eu after ion chromatographic separation.

Conclusions

The coupling of an Ion Chromatograph on-line with an ICP-MS for the analysis of nuclear samples opens new possibilities of applications for the characterisation of nuclear materials. The determination of U and Pu after separation, the determination of fuel burn-up based on ^{148}Nd and the detection of medium-lived fission products are only some of the applications of this novel technique.

References

[1] S.S. Heberling, J.M. Riviello, M. Shigen and A.W. Ip, Res./Dev., 9 (1987) 74

Laser Ablation - ICP-MS on Spent Nuclear Fuel

Introduction

The analysis of fission products and actinides is carried out normally after dissolution of the fuel in 7M nitric acid (PUREX type conditions). U and Pu are preferentially determined by isotope dilution employing TIMS [1], while fission products and minor actinides can be analysed by ICP-MS [2]. However, the dissolution of spent nuclear fuel in nitric acid and posterior dilutions for analysis require extensive sample preparation in a hot cell provided with master-slave manipulators. Also, the gaseous and volatile fission products (Kr, Xe, I) are lost during dissolution while an insoluble residue containing noble fission metals as well as U and Pu traces is formed.

It is clear that the elemental and isotopic analysis of spent nuclear fuels would be simplified if the solid samples could be analysed directly in a hot cell without any chemical conditioning. Furthermore, spatial information for radionuclide concentrations could be gathered which otherwise would be lost when dissolving the sample. Current methods for the spatial analysis of solid highly active samples mainly include Electron Microprobe Analysis (EMPA) and Gamma Spectrometry. Electron microprobe analysis offers high spatial resolution but lacks enough sensitivity to detect low concentrations of fission products and minor actinides and does not give isotopic information. On the other hand, gamma spectrometry can be applied only to radioactive isotopes (e.g. ^{137}Cs). In this context, Laser Ablation coupled to ICP-MS could offer an alternative or complementary solution for these type of studies. However, the spatial resolution would not be comparable to electron microprobe analysis. Also, quantification of fission products and actinides in spent nuclear fuel by laser ablation ICP-MS would be a difficult task due to the non-existence of available reference materials containing all fission products and actinides. The use of SIMFUEL ('simulated nuclear fuel') [3] as reference could aleviate some of the problems for selected fission products but one has to bear in mind that SIMFUEL is not an elemental reference material.

A commercial uranium oxide (UO_2) fuel contains ca. 85% of uranium of which typically 3.2% is ^{235}U before irradiation. During irradiation between 3 and 5% of fission products are produced both from the original ^{235}U and from ^{239}Pu formed by neutron capture of ^{238}U. Plutonium and other transuranium elements (Np, Am, Cm) are also produced as a result of successive neutron capture reactions. The formation of ^{239}Pu is known to be preferential at the rim of the fuel pellet [4] due to the absorption of epi-thermal neutrons by ^{238}U in this area (which is the origin of the so-called rim effect). As a result, fission products are also enriched in the cladding-fuel boundary.

Due to the high temperature gradient between the centre and the exterior of the fuel pellet, migration of volatile fission products can also be observed (e.g. Cs). The net result of the rim and of diffusion effects is a large increase in the concentration of fission products and transuranium elements in the pellet-to-cladding boundary with a decrease in the grain size and the appearance of a porous microstructure [4]. When we consider the direct deposition of spent fuel in deep geological formations the concentrations of fission products and actinides in the fuel rim should have to be taken into account in the computer predictions of the long-term stability of the fuel. All the effects previously described have been observed by electron microprobe analysis and microscopy [4]. However, for some low-yield fission products, like iodine, EMPA is not sensitive enough and nothing is known about spatial changes in the isotopic abundances of fission products and actinides. The application of Laser Ablation ICP-MS to spent nuclear fuel could answer some of these questions.

Experimental

Instrumentation

The ICP-MS used is an Elan 250 from Sciex, Canada, which was modified in order to analyse radioactive samples in a glove box. Details of the modified ICP-MS instrument have been presented elsewhere [5]. The plasma torch and sliding interface, with the sampler and skimmer cones, are installed inside the glove box while the mass-spectrometer and associated electronics are outside. The Laser Ablation instrument is a Laser Sampler 320 from Perkin Elmer which was also modified for the analysis of radioactive samples in a hot cell.

Fig. 7.8 shows a schematic diagram of the final set-up. The ablation stage takes place inside the hot cell (alpha, beta and gamma protection). The laser (IR, Nd-YAG) has been installed on the wall opposite the hot cell and the light beam is sent into the cell through a series of two IR mirrors and one IR lens installed in a periscope connecting the control room with the hot cell. The periscope is fitted with two optical paths, one used for the laser and the other for a video camera to observe the sample and position it for ablation. The ablation cell was installed inside the hot cell with the original x-y-z translation stage and was modified to handle the ablation stage by master-slave manipulators. The ablated aerosol is carried with an argon flow of, typically, 1 l/min through a PVC tubing of 8 m in length, 4 mm i.d., to the ICP-MS instrument situated behind the hot cell. Under standard operating conditions the ablated aerosol takes 6 seconds to reach the plasma.

Operating conditions

The spent fuel pellet was cut and embedded in Araldite and then polished. The uranium oxide fuel diameter was 9.1 mm and surrounded by a 1 mm thick Zircalloy cladding. Sampling was performed along the diameter of the pellet including the cladding every 0.5 mm: approximately, 20 measurements were performed for spatial studies.

The laser is operated in Q-switch mode at 65 mJ per pulse and a repetition rate of 4 Hz. A flow of 1 l/min Ar carries the ablated aerosol to the plasma operating at 1400 watt forward power. For a qualitative examination of the fuel a 5 minute ablation is performed on one spot and the data are collected in scanning mode in high resolution (20 measurements per peak). For spatial studies the data are collected in peak jumping mode at low resolution (1 measurement per peak). In this case, the total ablation time is 60 seconds while the first 40 seconds are used for pre-ablation and then 5 scans are acquired in the remaining 20 seconds. Other operating conditions used are summarised in Tab. 7.4.

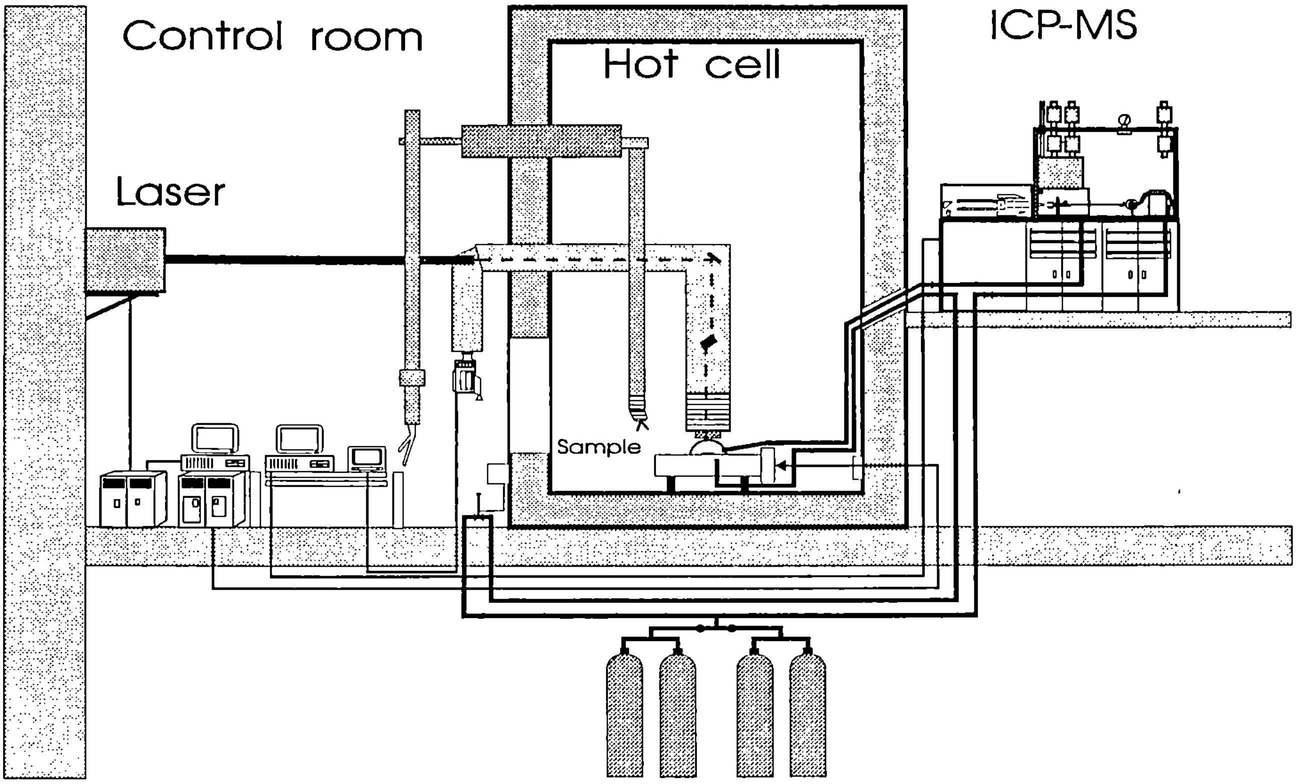

Fig. 7.8 Schematic diagram of the Laser Ablation ICP-MS set-up installed in the hot cell

Tab. 7.4 Operating conditions

RF power	1400 watt
Reflected power	<5 watt
Argon cooling	12 l/min
Argon auxiliary	1.4 l/min
Argon carrier	1 l/min
Load coil/Sampler cone distance	25 mm (fixed)
Interface pressure	2 Torr
Quadrupole working pressure	2 x 10^{-6} Torr
Sampler cone	Nickel, 1 mm orifice
Skimmer cone	Nickel, 0.7 mm orifice
Laser power	65 mJ
Repetition rate	4 Hz
Dwell time (spatial studies)	20 ms
Integration time (spatial studies)	200 ms/amu
Integration time (qualitative)	2 s/amu (20 meas.)
Total scan time (spatial studies)	2.5 s
Mass range (qualitative)	80-160 and 230-245
Mass range (spatial studies)	91-100,119,127-150,234-237,239-244,254

Peaks at mass 119 ($^{238}U^{2+}$) and 254 ($^{238}U^{16}O^{+}$) were measured and used as internal standards as the concentration of ^{238}U varies only slightly along the pellet diameter.

Results and discussion

Characterisation of spent fuel

In Fig. 7.9 the intensity vs time profile for four selected isotopes in spent fuel is shown. The total ablation time was 2 minutes. As can be observed, adequate signals can be obtained both for actinides and fission products. ^{136}Xe, which is not present in the pellet surface, appears later than the other isotopes once the external layers of the fuel have been ablated. No important memory effects have been observed and the signal decays to background levels within 1 minute after finishing the ablation. In some cases, residual Xe peaks have been detected even 5 minutes after ablation which can be used to study fission Xe isotopic abundances in the absence of Cs and Ba isobaric interferences.

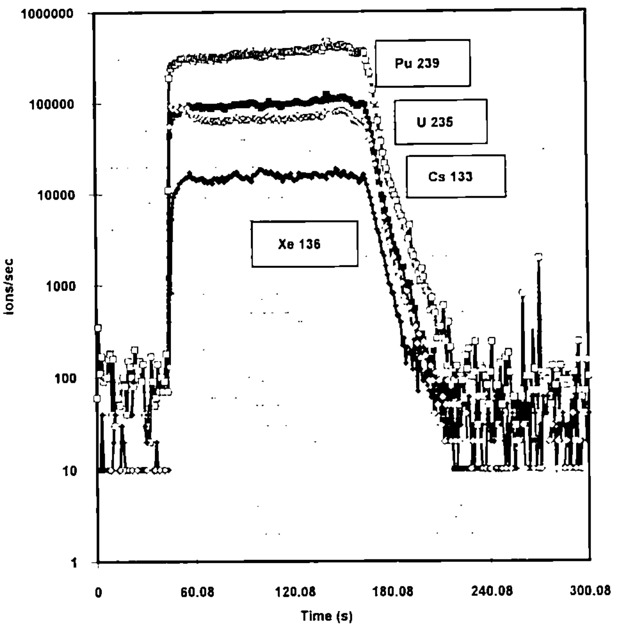

Fig. 7.9 Intensity vs time profile for 2 minutes ablation of spent nuclear fuel

The fission product distribution of the spent fuel as detected with the laser ablation system is shown in Fig. 7.10. Except for Kr (masses 83, 84, 85 and 86) all other fission products can be detected. Peaks at masses 85 and 87 correspond to Rb, 88 and 90 to Sr, 89 to Y, 90, 91, 92, 93, 94 and 96 to Zr, 95, 96, 97, 98 and 100 to Mo, 99 to Tc, 100, 101, 102 and 104 to Ru, 103 to Rh, 104, 105, 106, 107, 108 and 110 to Pd, 109 to Ag, 110, 111, 112, 113 and 114 to Cd. The peak at mass 119 corresponds to $^{238}U^{2+}$ which shows the symmetry of the fission process. For the other half of the fission products, peaks at masses 126, 128 and 130 correspond to Te, 127 and 129 to I, 131, 132, 134 and 136 to Xe, 133, 134, 135 and 137 to Cs, 134, 136, 137 and 138 to Ba, 139 to La, 140, 142 and 144 to Ce, 141 to Pr, 142, 143, 144, 145, 146, 148, 150 to Nd, 147 to Pm, 147, 148, 149, 150, 151, 152 and 154 to Sm, 151, 152, 153, 154 and 155 to Eu and 154, 155, 156, 157, 158 and 160 to Gd. As can be observed some of the peaks can be assigned to more than one element due to beta decay or neutron capture reactions during fuel irradiation. Also peaks at masses 154 to 160 could be attributed partially to the oxides of Ba, La, Ce and Nd. When the spent fuel is dissolved in nitric acid for analysis, all I and Xe peaks disappear and the peaks for Zr, Mo, Tc, Ru, Rh and Pd are reduced significantly as they partially form insoluble residues. In this context laser ablation produces a more complete picture of the fission product inventory. The lack of reference materials, however, prevents the acquisition of quantitative results at present. The use of simulated spent fuel (SIMFUEL) [3] for calibration will be tested for future studies.

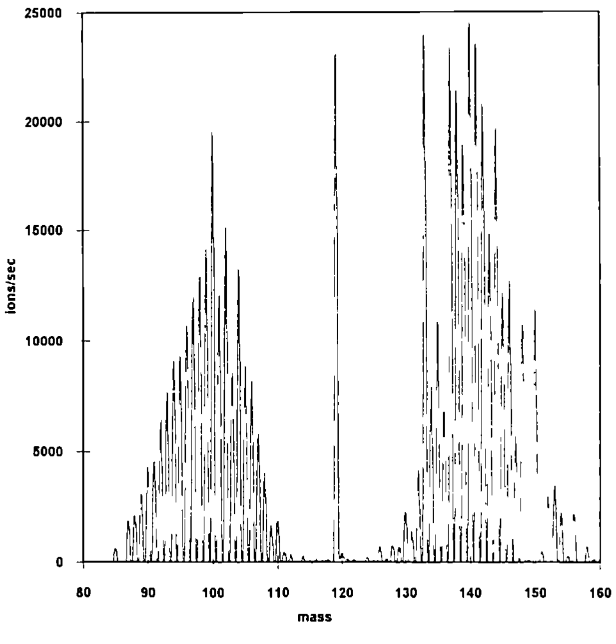

Fig. 7.10 Fission product distribution of spent nuclear fuel obtained by laser ablation sampling

Spatial distribution of fission products and actinides

For the study of the spatial distribution of fission products and actinides in spent fuel, 20 points along the pellet diameter, including the cladding, were measured under the conditions described above. Five scans of the mass ranges 91-100, 119, 127-150, 234-237, 239-244 and 254 were obtained in each point and the ratios to the peaks at masses 119 ($^{238}U^{2+}$) and 254 ($^{238}U^{16}O^{+}$) used to study relative concentration changes. No other internal standard can be used for this type of sample. The radial distribution of uranium, neptunium and plutonium isotopes normalized to the $^{238}U^{16}O^{+}$ peak are shown in Fig. 7.11. As can be observed the concentration of ^{235}U (Fig. 7.11a) decreases gradually approaching the rim of the pellet while the concentration of ^{236}U (formed by neutron capture of ^{235}U) increases at the pellet rim. The ^{235}U to ^{236}U isotopic ratio varies from 0.62 at the pellet rim to 0.78 at the centre which shows a symmetrical non-homogeneous distribution of isotopic abundances. ^{237}Np, formed from ^{236}U by neutron capture, is also enriched at the rim. Similar results are observed for Pu isotopes in Fig. 7.11b. The "rim effect" is clearly observed as all Pu isotopes are formed by successive neutron capture from ^{238}U. The large increase of ^{239}Pu concentration in the rim of the fuel would

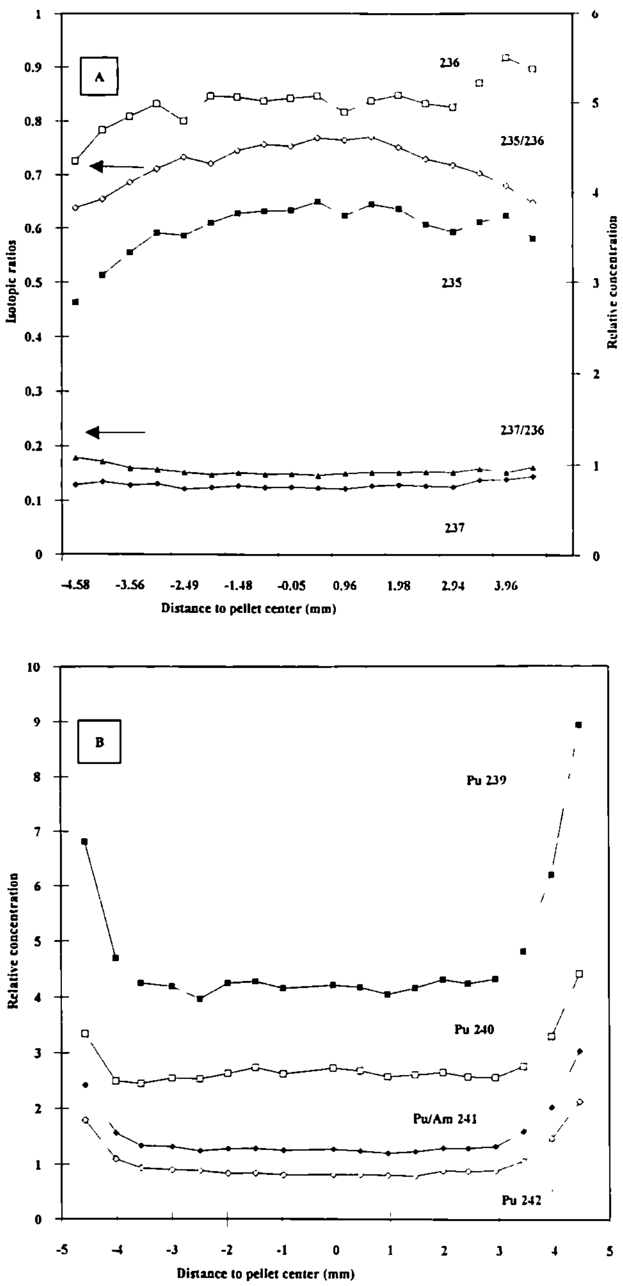

Fig. 7.11 Relative concentrations of U, Np and Pu isotopes referred to the $^{238}U^{16}O^{+}$ *peak. a) U and Np isotopes including isotopic ratios. b) Pu isotopes*

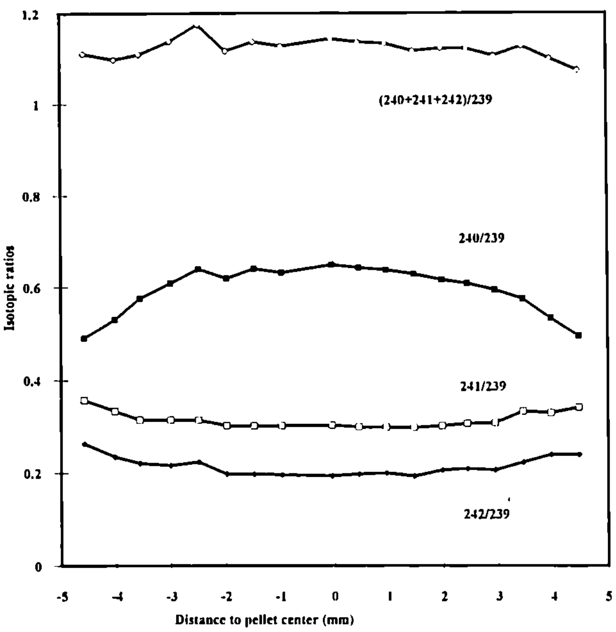

Fig. 7.12 Isotopic ratios for Pu with the distance to the centre of the pellet

give rise also to an increase in the concentration of the fission products (see below). Fig. 7.12 shows the observed Pu isotopic ratios with the distance to the pellet centre. The peak at mass 241 corresponds both to ^{241}Pu and its beta decay product ^{241}Am. As can be observed ^{239}Pu has a constant isotopic abundance with respect to the sum of all other Pu isotopes while ^{240}Pu is reduced at the pellet exterior where ^{241}Pu and ^{242}Pu increase. The relative increase in ^{241}Pu and ^{242}Pu at the pellet rim with respect to the total Pu concentration will have to be considered for waste disposal purposes as ^{241}Am and ^{237}Np will build up as successive decay products from ^{241}Pu.

On the other hand, no changes in isotopic abundances for fission products have been observed across the pellet diameter. The isotopic ratios obtained for Zr are shown in Fig. 7.13. The natural

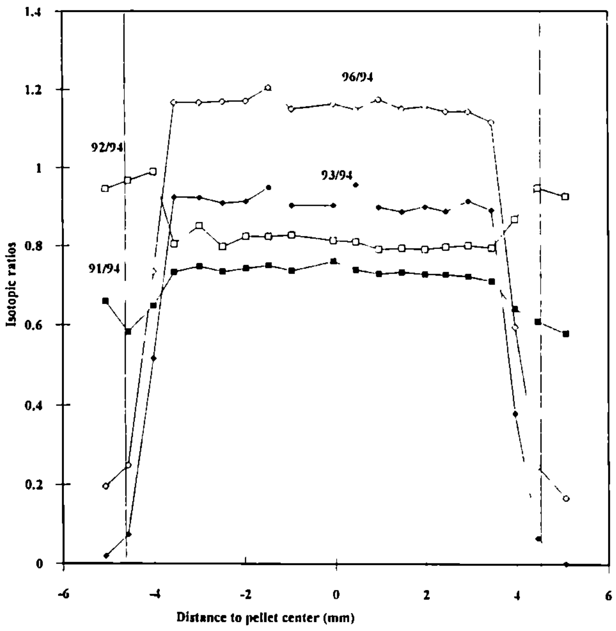

Fig. 7.13 Isotopic ratios for Zr with the distance to the pellet centre including the cladding containing natural Zr (vertical lines show the cladding-fuel boundary).

abundances of Zr in the cladding allows the contribution from cladding and fuel to be distinguished. The fission yields for Zr isotopes from ^{235}U and ^{239}Pu are also clearly different. As can be observed there is a big change in the Zr isotopic abundances at the pellet edges but no changes are observed inside. These constant isotopic ratios were observed also for Mo,Te, I, Cs, Xe, Ce and Nd, i.e. all multi-isotopic elements measured. The conclusion of these findings is that the fission yield contribution of ^{239}Pu and ^{235}U should be independent of the distance to the pellet centre except for the rim zone where isotopic ratios can not be determined precisely because of the wide crater diameter of the laser pulses.

The cumulative fission yields for selected Zr and Nd isotopes obtained from ^{235}U and ^{239}Pu fission[6] are given in Tab. 7.5. In order to compensate for neutron capture reactions in the reactor (e.g. formation of 92Zr from 91Zr), composite isotopic ratios are used to study fission yield contributions. The observed isotopic ratios for the Zr 91 + 92/93 + 94 and Nd 143 + 144/145 + 146 are illustrated in Fig. 7.14 and the mean values for the fuel introduced in Table 7.4. As can be observed the isotopic ratios for the fuel are constant and lie between the ^{235}U and ^{239}Pu fission values. Based on the Zr ratios, it can be calculated that ca 45% of the fission comes from ^{239}Pu and 55% from ^{235}U . The Nd ratios can not be used for these calculations because of the similar fission yields from both nuclides. The computer code KORIGEN [7] was also used to calculate isotopic ratios for Zr and Nd given the irradiation history of the fuel, the final burn-up (53 GWd/tU), the reactor type (PWR) and its neutron spectrum. The fission yield contribution calculated from the KORIGEN results was 51% for ^{235}U and 49% for ^{239}Pu. As can be observed, there is a good agreement between the experimental data and the theoretical calculations for fission yield contributions of ^{235}U and ^{239}Pu.

Tab. 7.5 Comparison between the experimental isotopic ratios obtained and those predicted by the cumulative fission yield data [6] of 235U and 239Pu

Isotope or isotope ratio	Cumulative fission yield (%) from:		Ratio found	KORIGEN prediction
	^{235}U	^{239}Pu		
Zr-91	5.9174	2.4317		
Zr-92	5.9924	3.9266		
Zr-93	6.4128	3.7796		
Zr-93	6.4539	4.2960		
Nd-143	5.9933	4 4586		
Nd-144	5.4492	3.7746		
Nd-144	3.9534	3.0160		
Nd-146	2.9989	2.4807		
Zr (91+92)/(93+94)	0.9256	0.6635	0.8078	0.8221
Nd (143+144)/(145+146)	1.6458	1.4978	1.5118	1.5749

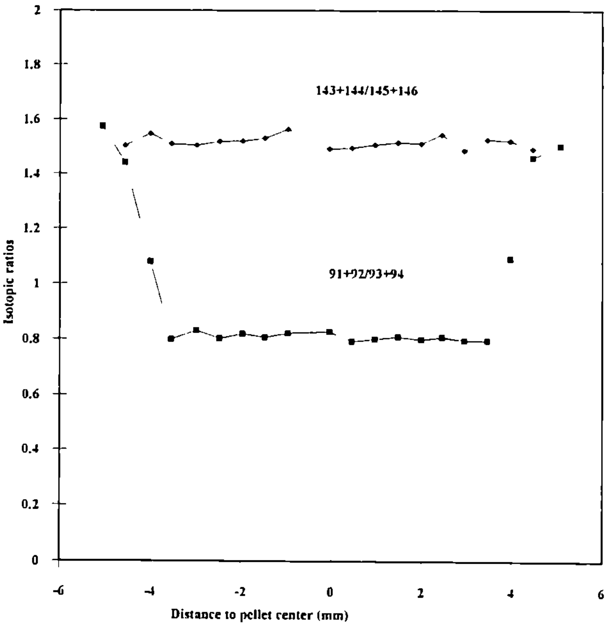

Fig. 7.14 Composite isotopic ratios for Zr and Nd used to calculate fission yield contributions.

Finally, relative concentration changes for fission products were determined relative to the ^{238}U^{2+} peak (m/e = 119). In all cases enrichment at the pellet rim was observed as illustrated in Fig. 7.15 for selected Mo, Tc, Ba, Ce and Nd isotopes. These elements give an indication of the relative fuel burn-up as they do not migrate with the temperature gradient. As can be observed, a constant concentration is obtained at the centre of the pellet with increasing concentrations at both sides due to the rim effect. The width of the rim has been observed to be only about 100 to 200 µm by EMPA [4], depending of the fuel burn-up. However, in our results this area is not well defined and the observed concentration changes are smoothed by the wider crater diameter of about 0.5 mm.

Elements like Cs and I do migrate due to the temperature gradient in the fuel pellet. In order to study migration effects the ratio to a non-migrating element, such as Nd, will give an indication of the magnitude of this effect. The relative

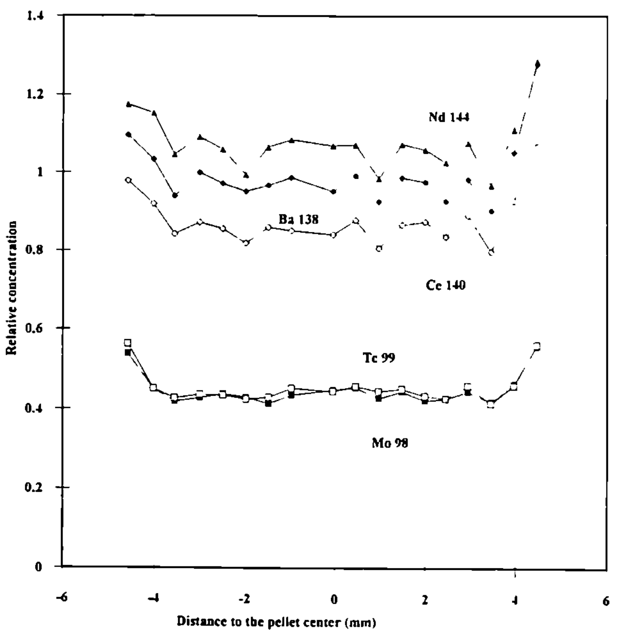

Fig. 7.15 Relative concentration changes of non-migrating fission products in spent fuel.

concentration changes of ^{135}Cs and ^{129}I relative to 144Nd are shown in Fig. 7.16. As can be observed, Cs and I migrate to the pellet rim. The migration of readily soluble elements, like Cs and I, with long-lived beta-emitting isotopes, such as those illustrated in Fig. 7.16, should be kept in mind in planning studies for the direct repository of spent fuel.

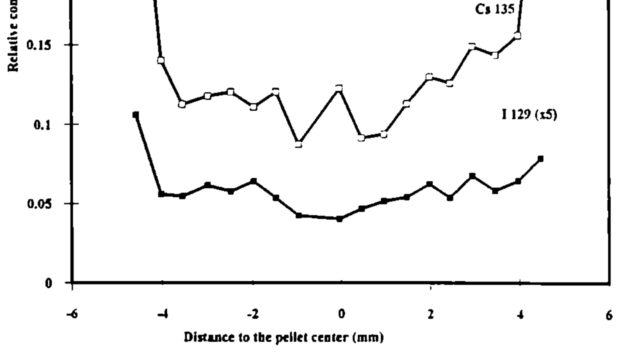

Fig. 7.16 Migration of Cs and I in the fuel pellet relative to the fuel burn-up (^{144}Nd used as fuel burn-up indicator)

Conclusions

The technique of Laser Ablation ICP-MS has been applied to the characterisation of spent nuclear fuels and to study elemental and isotopic distributions of fission products and actinides in the fuel pellet. Changes in the isotopic abundances for the actinides have been observed for the first time and these results could be used to study neutron capture reactions in relation to the rim and self-shielding effects. On the other hand, isotopic abundances for fission products do not change in the fuel pellet but changes in relative concentrations have been observed. Migration of elements such as I and Cs could be demonstrated but the extent of these migration effects and their relation to the fuel temperature gradient have still to be studied.

References

[1] M. Wantschik, B. Ganser and L. Koch, Int. J. Mass Spectr. Ion Physics, 48(1983) 405

[2] J.I. García Alonso, J.-F. Babelot, J.-P. Glatz, O. Cromboom and L. Koch. Radiochim. Acta, 62 (1993) 71

[3] P.G. Lucuta, R.A. Verrall, Hj. Matzke and B.J. Palmer, J. Nucl. Mater., 178 (1991) 48

[4] Hj. Matzke, J. Nucl. Mater., 189 (1992) 141

[5] J.I. Garcia Alonso, D. Thoby-Schultzendorff, B. Giovanonne, L. Koch and H. Wiesmann, J. Anal. Atom. Spectrom., 8 (1993) 673

[6] M.E. Meek and B.F. Rider, "Compilation of Fission Product Yields". General Electric Company. Vallecitos Nuclear Center. Pleasanton, California (1972)

[7] U. Fischer and H.W. Wiese, "Verbesserte konsistente Berechnung des nuklearen Inventars abgebrantes DWR-Brennstoffe auf der Basis von Zell-Abbrand-Verfahren mit KORIGEN", KfK-3014 (1983)

Installation and First Results with the Glow Discharge Mass Spectrometer (GDMS)

As previously reported (TUAR-92, p. 195), in October 1992 after a four-week testing of the GDMS, its installation in a glove-box started and was finished during April 1993. The instrument, after a testing in the workshop, was moved to the hot lab in May for testing.
In the following, some details concerning the modifications made for the installation of the machine in a glove-box and the results obtained during 1993 are given.

Introduction

Glow discharge mass spectrometry (GDMS) has found use in the trace element analysis of a wide range of inorganic materials [1-5]. Conducting samples such as metals, alloys and semiconductors can be analysed directly by a DC (direct current) glow discharge. Electrical insulators require indirect means to convert them into conductors [1, 2] or the use of a RF (radio frequency) powered glow discharge [3-5] for direct analysis.

A priori, the glow discharge mass spectrometer is an analytical tool which would be ideally suited for the analysis of solid samples of nuclear origin, requiring minimum chemical treatment. The elemental and isotopic capabilities of GDMS could be fully applied to materials having non-natural isotopes and/or non-natural isotopic abundances. Other advantages of GDMS are: i) virtually all elements can be determined; ii) the wide dynamic range of the detector allows the determination of both major components and trace constituents within the same analytical cycle; iii) decoupling of the atomisation and ionisation processes results in uniform sensitivities for many elements and also minimum matrix effects.

For the analysis of nuclear materials difficulties arising from the radioactive nature of the sample have to be overcome. Firstly, the operator has to be protected from the material, which means that the use of glove-boxes (alpha, beta protection) and/or hot cells (alpha, beta and gamma protection with master-slave manipulators) is a necessity. Secondly, in order to avoid contamination of the working area, the analytical instruments have to be modified in order that containment is assured and no radioactive material leaks either to the laboratory or to the environment. Complete instruments cannot be introduced into a glove-box because electronics are very sensitive to radiation. In practice, electronics and parts that might need special maintenance are kept outside the glove-box and only samples and the corresponding sampling stage are contained in the box.

From the experience gained from other instrumentation [6], for GDMS measurements, the glove-box should enclose the ion source chamber, sample interlock and associated pumping system. All supplies to the ion source (argon discharge support gas and liquid nitrogen for cryogenic cooling of the discharge cell) and pumping ports should be fitted with absolute filters to eliminate any external contamination.

The ion source itself has been designed to minimise the number of operations and to simplify routine maintenance inside the glove-box area. This has been achieved through the use of simple plug-in components and by reducing the number of screw connections.

Experimental

Mass spectrometer

The VG 9000 glow discharge mass spectrometer has been described in detail previously [7]. The instrument consists of a glow discharge ion source coupled to a double-focusing mass spectrometer of reverse (Nier-Johnson) geometry. This provides high transmission and sensitivity whilst operating at high resolving power (typically 5000, 10% valley definition, >75% transmission). Ion detection is accomplished by a dual detection system comprised of a Faraday cup for the measurement of large (typically $> 10^{-13}$ A) ion currents and a transverse mounted Daly detector [8] for the detection of lower signals.

Source housing

For the analysis of nuclear samples, the glow-discharge ion-source housing and the associated pumps are placed within a glove-box. The glove-box is provided with an extraction system and filters for all gas lines. Absolute filters (> 99.99% efficiency, SOLFILTRA, Lagarenne, France) are situated both inside and outside the glove-box which is kept at a lower pressure than the exterior (20 mm water column). In Fig. 7.17 a schematic

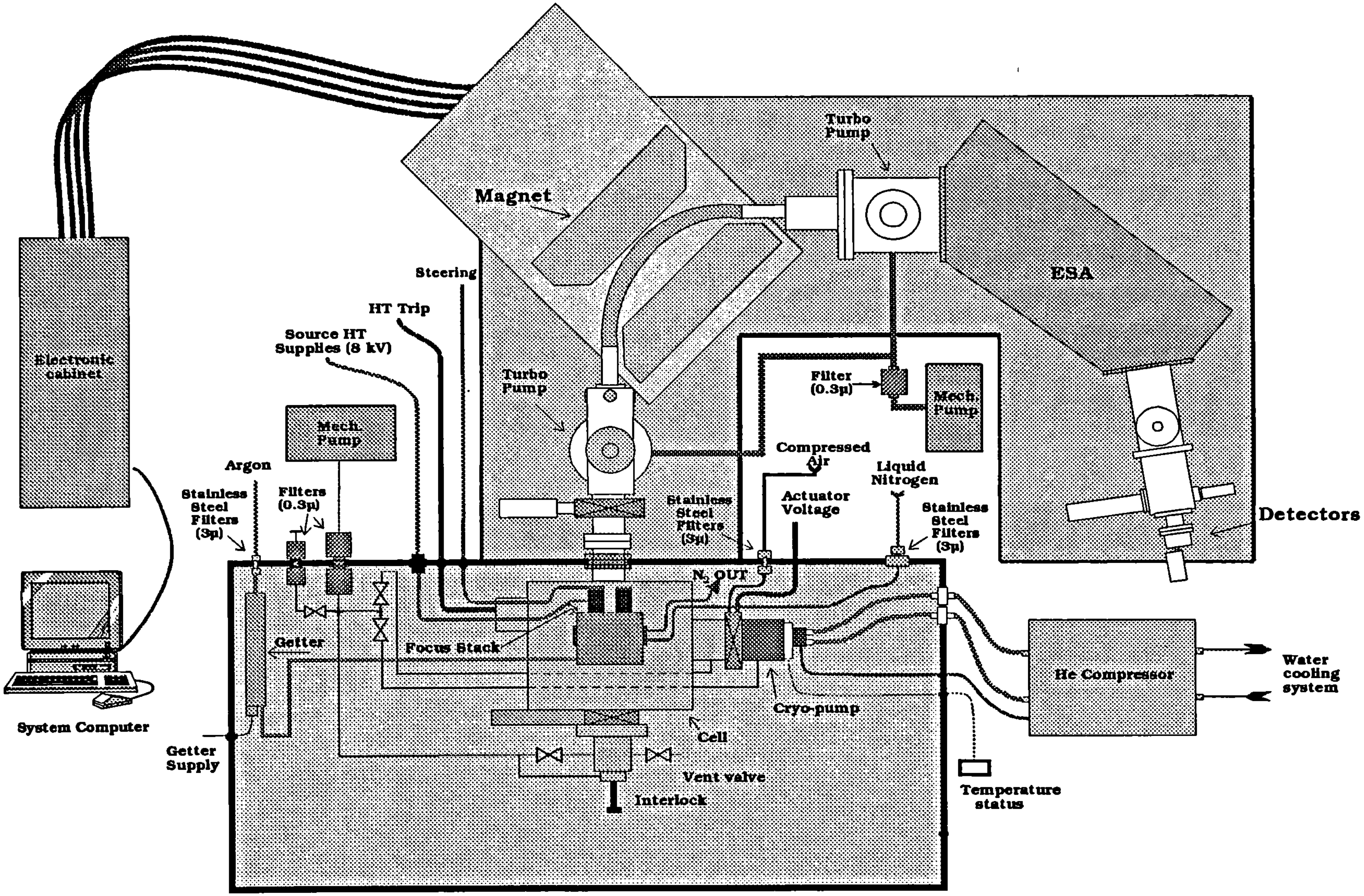

Fig. 7.17 Scheme of the installation of the discharge source housing in glove-box.

diagram of the installation of the glow-discharge source housing in a glove-box is given showing all connections to the glove-box. Stainless-steel filters (3µm porosity) are installed in the argon, compressed air and liquid nitrogen inlets, and absolute filters (0.3µm porosity) in the vacuum line to prevent any radioactive contamination. The cryogenic pump is installed in the glove-box and the absolute filters are connected with the pump. In Fig. 7.18 the instrument is shown in the hot lab, after the closing of the glove-box for radioactive material handling.

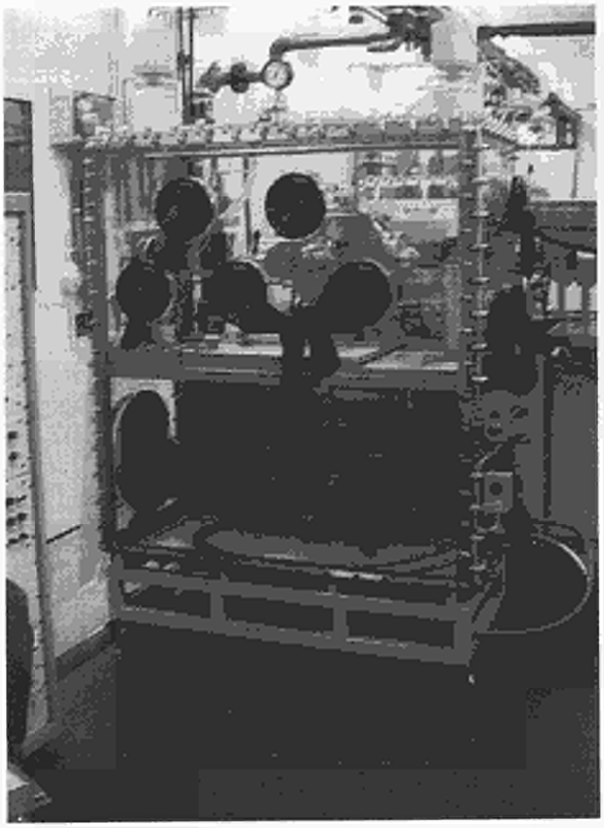

Fig. 7.18 Complete view of the instrument in glove-box after closing the glove-box for nuclear material handling.

Ion source

The probe and sample interlock have been shortened to give easier access to the ion source within the glove-box. The source chamber door opens by a sliding mechanism to give easier access to the ion source. The Wilson-seal can assembly provides a vacuum interlock region so that sample changes may be performed with the ion source maintained at high vacuum (Fig. 7.19).

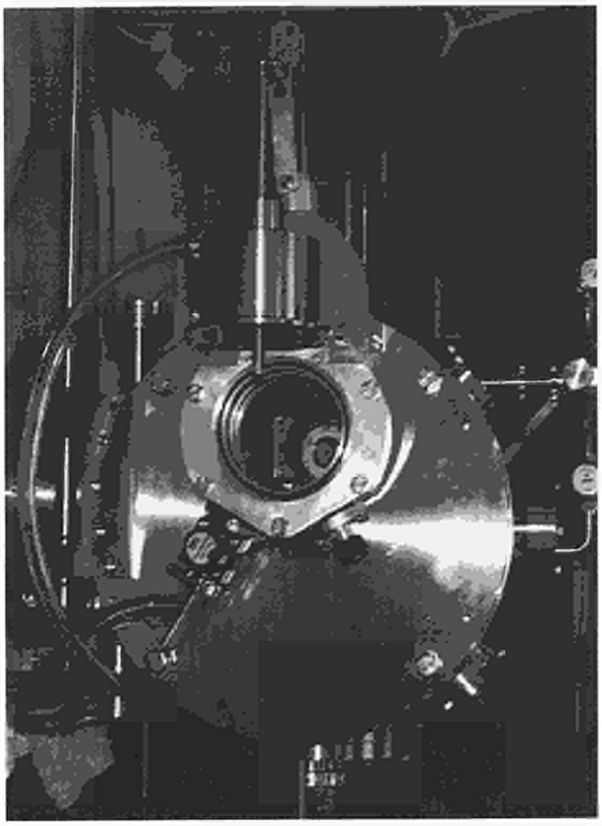

Fig. 7.19 Modified probe and sample interlock.

The ion source itself has been designed to minimise the number of operations performed within the glove-box area and to simplify routine maintenance. This has been achieved by utilising a "universal" cell for the analysis of both pin and flat samples; and a "plug-in" focus stack. The source itself (Fig. 7.20) is split up into various components, comprising a mounting plate with removable cell and focus stack assemblies. The source mounting position remains fixed to the back wall of the source housing chamber. The focus stack then plugs into a recess in the mounting plate and is held in place by four fixing rods. Electrical contact to the plates of the focus stack is made by a series of copper/beryllium contacts. This eliminates the need to disconnect any wires when removing the focus stack, thus simplifying its removal. The contact assembly is connected to the high tension feed-through by Kapton-coated wire (Dupont, France).

The focus stack assembly consists of a series of tantalum plates, separated by PEEK spacers, mounted onto a base containing the source-defining slit for the mass spectrometer. The focus stack provides for deflection and focusing of the ion beam in the y- and z- directions to give the

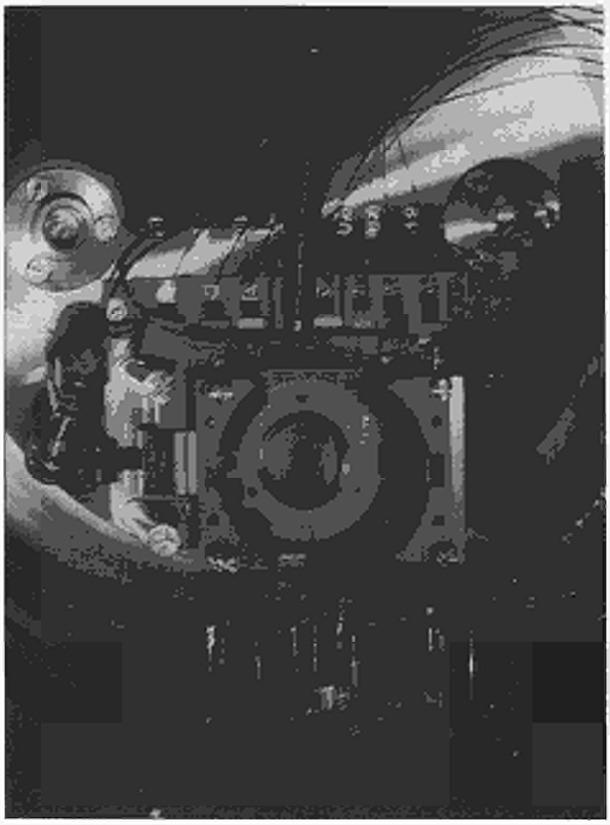

Fig. 7.20 Modified source and its housing chamber.

best object on the source defining slit. The plates are shaped so that, when the focus stack is in position, they make electrical contact with the appropriate connector on the contact assembly. The focus stack assembly also contains a mounting bracket for firing the location of the cell and sample holder.

The "universal" cell has been designed to accommodate a range of pin and flat samples. The cell itself consists of a universal body that plugs into the focus stack. This cell body, based around the existing flat geometry [9], then remains located in position. The "universal pin holder" can be used for the analysis of a wide range of pin samples.

In Fig 7.21a a sample pin assembled in the holder (left side) and the different parts used for the assemling (right side) are shown respectively. The use of a combination of cathode plates (A), anode chamber bodies (B) and sample chucks (C) allows analysis of pin and rod samples (D) up to 7mm in diameter. With the appropriate sample holder combination, the sample is held in position in the chuck with a screw. The chuck is then placed in the sample holder with the tapered end mating with the appropriate cathode plate. The spring ensures that a tight reproducible gas seal is maintained. Electrical insulation between the anode and cathode components is achieved by using a ceramic ring, and nylon screws (F) are used to provide a gas-tight seal.

The analysis of flat samples is performed using the flat sample holder as described previously [9]. In Fig 7.21b the different parts used for the assembling of flat sample in the holder are in detail shown.
The sample (A) is held in the holder against an insulating disk (B) to provide electrical isolation from the front plate (C) of the sample holder which is at anode potential. Sample size can vary from approximately 10 to 38 mm in diameter and from wafer thin to a thickness of 20mm. To cope with different sample sizes, a range of front plates and insulating disks are available. In Fig 7.21b, the points where the sputtering took place can be also clearly seen.

Changing the sample geometry from pin to flat simply requires changing the appropriate sample holder when loading the sample. It is no longer necessary to break the vacuum to do this, thus reducing the number of operations required inside the glove-box.

Materials

The argon discharge gas (BOC 99.9999%) enters the discharge cell via a heated getter inlet system (SAES GP50). The pressure is regulated using a leak valve (Vacuum Generators) and monitored using an ion gauge situated above the cryogenic pump (Edwards Coolstar 1500) serving the source housing. The discharge cell is cooled using a flow of liquid nitrogen to reduce background gases such as water vapour.

A certified reference material, CRM 115 depleted uranium metal (uranium and uranium-235 standard), obtained from New Brunswick Laboratory (U. S. Department of Energy) was used.

Once optimisation of the discharge parameters has been performed, a discharge voltage of 0.9 kV with a corresponding current of 0.6 mA is used throughout unless otherwise specified.

The samples were pre-sputtered prior to analysis for 2 minutes with a 1mA current.

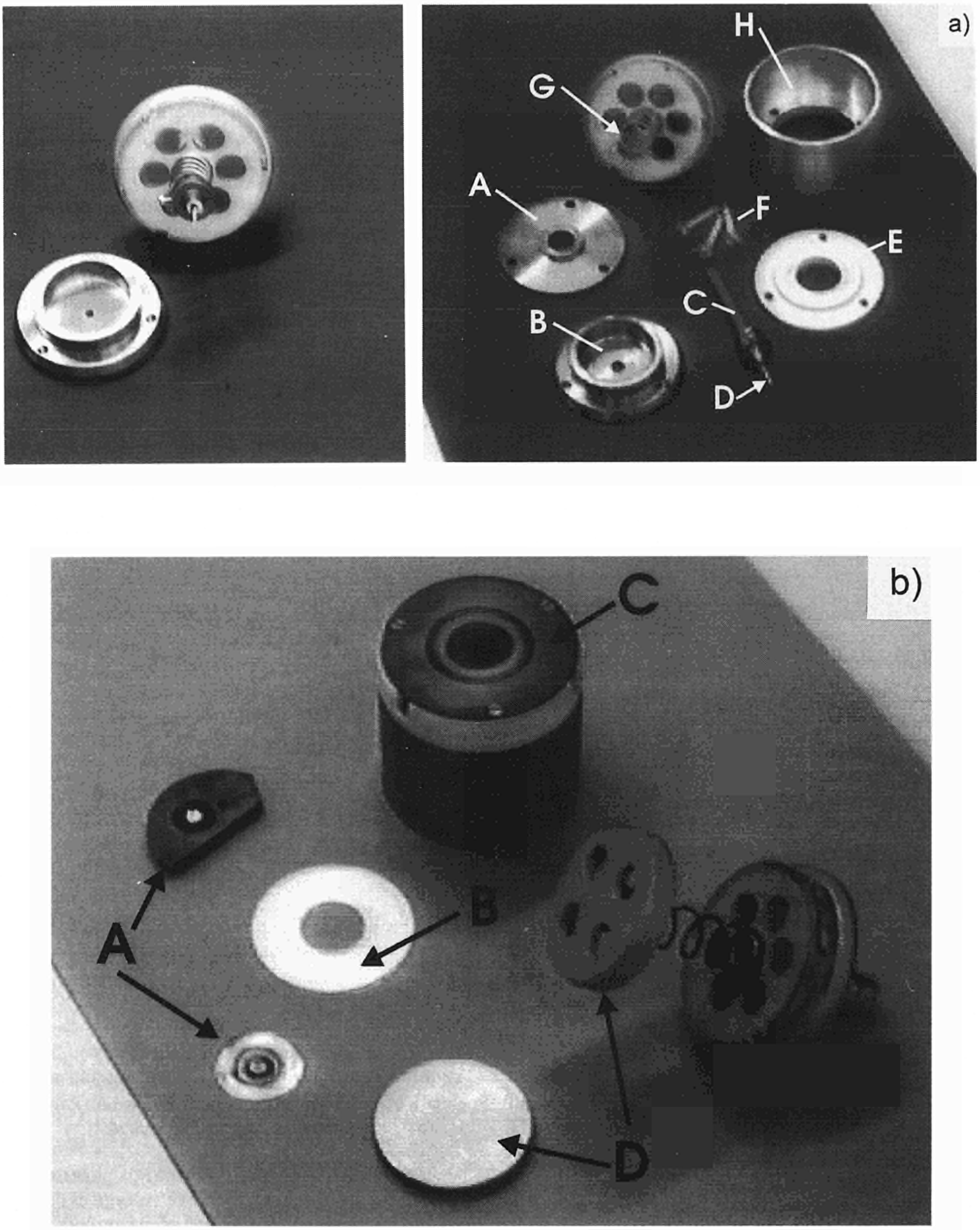

Fig. 7.21 (a) Pin sample mounted in the proper holder (left side) together with the different parts used for the assembling (right side): (A) cathode plate, (B) anode chamber body, (C) sample chuck, (D) pin or rod sample, (E) ceramic ring, (F) Nylon screws, (G) spring, (H) assembly holder.
(b) Flat samples together with the proper holder. (A) samples, (B) insulating disk, (C) front plate of the sample holder (anode), (D) loaded sample fixation.

Results and discussion

GDMS performance at various stage of its installation in a glove-box

As described above, for the installation of the GDMS in a glove-box, many modifications of the source housing and of the ion source were necessary. Attention was given that the instrumental specifications would not be affected and in the case that some of those changed, it was important to know to which extent the modifications could influence the performance of the instrument..

From this point of view, the specifications of the GDMS were checked throughout the technical modifications for its installation in a glove-box.

In Tab. 7.6 the specifications tested at various stages are summarised. As it appears the modifications carried out to allow the installation of the GDMS in a glove-box did not affect its performance.

Isotope abundance studies in uranium metal

The isotopic analysis of uranium is important to determine the enrichment of the sample and thus its potential use as a nuclear fuel. Of primary interest is the ratio 235:238.

Tab. 7.6 Comparison of GDMS instrumental specifications at various stages of its installation in a glove-box. A: before modifications and installation in glove-box; B: after modifications and before installation in glove-box; C: after modifications and after installation in glove-box.

Specification	A	B	C
Analyser vacuum	3.0E-8 mbar	1.8E-8 mbar	2.4E-8 mbar
Mass resolution - Al	5384	6940	6174
- Cu	4562	6626	5624
- Au	4139	5466	6744
Matrix current	4.9E-10 A	6.2E-10 A	8.4E-10 A
Transmission	70 %	75 %	67 %
Stability (10 min)	2.94 % RSD	2.52 % RSD	1.32 % RSD
Stability (30 min)	4.22 % RSD	3.87 % RSD	4.68 % RSD
Peak position stability	9 ppm	13 ppm	24 ppm
Mass Calibration	7 mmu	8 mmu	5 mmu
Mass Marking	234 ppm	100 ppm	180 ppm
Ion counting efficiency	76.0 %	80.7 %	76 %
Abundance sensitivity	0.43 ppm	0.38 ppm	0.21 ppm
Reproducibility - Major	0.8 % RSD	1.6 % RSD	1.0 % RSD
Minor	1.2 % RSD	2.6 % RSD	3.7 % RSD
Traces	3.5 % RSD	1.8 % RSD	1.0 % RSD
Accuracy - Major	1.0 % RSD	2.5 % RSD	1.5 % RSD
Minor	4.0 % RSD	2.7 % RSD	4.4 % RSD
Traces	3.9 % RSD	2.1 % RSD	2.8 % RSD
Gas background - N	0.5 ppm	4.3 ppm	0.4 ppm
C	0.3 ppm	3.6 ppm	0.9 ppm
O	0.5 ppm	0.7 ppm	2.4 ppm

In this investigation isotopic abundances were measured in uranium metal samples.

A certified reference material (CRM 115) uranium metal depleted in ^{235}U was measured. Three samples of this standard were analysed. The results of these measurements are shown in Tab. 7.7, where the signal intensities (expressed in Amperes) measured for the three isotopes of uranium, ^{234}U, ^{235}U and ^{238}U , are reported.

Each result represents the mean of 10 measurements with each measurement lasting 5 s. The grand mean (in Amperes and in concentration units), RSD, CRM values and bias are shown at the base of each isotope column. The internal precision [% Standard Error (SE)], reported in parentheses for each isotope in each sample, describes the reproducibility of each measurement of the individual isotopes tested for a single sample, and is defined as:

$$\%SE\,(1\sigma) = 100/x_m * \left\{\left[\sum_{i=1,n} (x_m - x_i)^2\right]^{1/2}\right\} / [n(n-1)]$$

where x_m is the mean value and n is the number of measurements performed.

The RSD values (external precision) reflect the reproducibility of the isotopic concentration measurements from different specimens of the same original sample. This reproducibility is typically 0.2% or better, even for ^{234}U at a measured concentration of 8.26 ppm. This suggests that GDMS could be used to measured isotopic abundances at trace levels.

In Tab. 7.8 results obtained for another uranium metal sample are shown. The abundance value measured for ^{235}U in the CRM115 reference material was used to produce a mass bias correction factor. This factor was used to correct the ^{235}U abundance in a uranium sample with unknown isotopic composition. This correction gives an abundance which is accurate to within 0.12% of the natural abundance. No such correction was performed for the isotope ^{234}U.

From data of Tab. 7.7 and 7.8, it is clear however that CRM115 is also depleted in ^{234}U.

Both the CRM115 depleted uranium and the natural uranium metal samples were analysed in the flat sample form. The relative standard deviations obtained for both samples, over 10 and 5 runs respectively, indicate very good stability of the discharge and homogeneity of the sample surface.

Comparison with other techniques

The CRM115 reference depleted uranium sample was also analysed using isotope dilution analysis mass spectrometry (IDMS) and inductively-coupled plasma mass-spectrometry (ICP-MS).

When analysing CRM115 by IDMS, an accuracy of 0.1 % was achieved. This represents an improvement in accuracy over GDMS, mainly due to the fact that an internal standard is used. The accuracy of GDMS is improved when the mass bias is accounted for. When this correction is made,

Tab. 7.7 Analysis of CRM 115 depleted uranium reference sample. Signal intensities in Amperes. Values in parantheses are the standard error (%).

Sample	^{234}U	^{235}U	^{238}U
1	$4,626\ 10^{-15}$ (1.8)	$1.072\ 10^{-12}$ (1.23)	$5.253\ 10^{-10}$ (0.7)
2	$4,638\ 10^{-15}$ (1.6)	$1.075\ 10^{-12}$ (0.88)	$5.273\ 10^{-10}$ (0.4)
3	$4,630\ 10^{-15}$ (1.7)	$1.070\ 10^{-12}$ (1.0)	$5.273\ 10^{-10}$ (0.6)
Mean(Amperes)	$4,6314\ 10^{-15}$	$1.0724\ 10^{-12}$	$5.266\ 10^{-10}$
RSD %	0.132	0.235	0.219
mean (conc)	8.26 ppm	0.1973 %	99.770 %
CRM 115 value	not certified	0.2008(7) %	99.776 %
Bias %	not applicable	- 1.7	- 0.006214

Tab. 7.8 Analysis of uranium metal sample. Isotope values expressed in concentration units.

Measurement	^{234}U (ppm)	^{235}U (w%)	^{238}U (w%)
1	57.950	0.7031	99.2730
2	59.090	0.7064	99.2745
3	59.150	0.7070	99.2736
4	59.330	0.7145	99.2729
5	59.331	0.7122	99.2740
mean	59.9702 ppm	0.7086 %	99.2736 %
s. d.	0.5803 ppm	0.005 %	0.0007 %
RSD %	0.98	0.65	0.0007
literature data [10]	55 ppm	0.72 %	99.2745 %
bias %	9	- 1.6	- 0.0009

the accuracy obtained by GDMS for the natural sample is 0.12 %. Without this correction the precision and accuracy of GDMS is comparable to that measured using ICP-MS.

The major advantage of GDMS is the very quick and straightforward sample preparation. Both IDMS and ICP-MS require sample dissolution, dilution and, for IDMS, further preparation of spiked aliquots. GDMS simply requires a flat surface of metal. As for handling of radioactive samples all techniques require the use of a glove-box.

Consequently, the ability of GDMS to perform direct analysis of uranium provides an accurate and rapid isotopic screening process in preliminary investigations.

Trace element analysis in uranium metal

The VG9000 is capable to analyse the whole mass range, and can thus determine the concentrations of many other elements such as the transition metals and rare earths.

Trace element analysis in uranium metal is important in the specification of the material.

In Tab. 7.9 the elements observed in the CRM115 sample are listed. After the rapid complete survey, the sample was analysed only for the trace elements observed.

Tab. 7.9 Trace element analysis of CRM 115 uranium metal. Concentrations expressed in ppm.

Element	Measured concentration	Standard deviation	% RSD (n=5)
B	0.021	0.001	5.9
Na	0.064	0.003	4.0
Mg	11.0	0.3	3.1
Al	19.6	0.5	2.7
Si	43.3	1.0	2.2
Cr	0.17	0.007	3.7
Mn	12.4	0.4	3.1
Fe	73.8	1.2	1.6
Ni	15.0	0.4	2.6
Cu	6.5	0.3	4.7
Zr	0.070	0.003	4.3
Mo	0.56	0.02	3.5
Ru	0.11	0.006	5.5
Ag	0.85	0.03	3.8
I	0.044	0.008	17.4
Pb	17.7	0.2	1.3
Th	0.062	0.002	3.5

Among the elements listed in Tab. 7.9, some of particular importance are those elements with high neutron capture cross-sections such as lithium, boron, cadmium, etc., for which a precise and accurate determination is required.

Boron for instance, cannot be easily measured in diluted solutions at ppb-levels (which correspond to ppm levels in the solid) by ICP-MS because of low ionisation efficiency, low sensitivity and blank contaminations. In GDMS, Boron can easily be detected at low concentration levels directly in the solid sample. In Fig. 7.22 the peaks of ^{10}B (6a) and ^{11}B (6b) isotopes are shown, measured on the same sample, at a concentration level of 20 ppb in a uranium matrix .

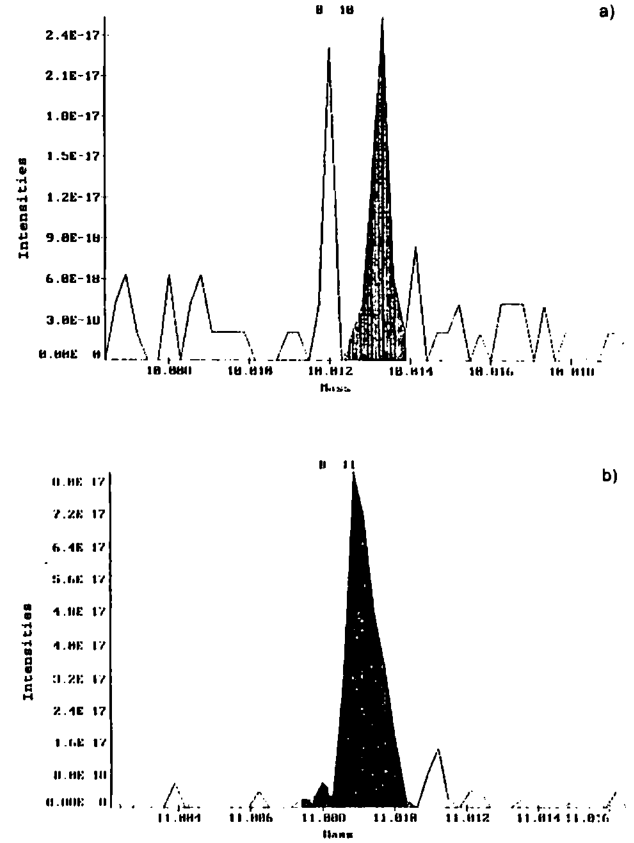

Fig. 7.22 GDMS spectra for ^{10}B (a) and ^{11}B (b) isotopes obtained in the analysis of an uranium metal sample. Concentration of boron was 20 ppb.

Another example, showing the power of GDMS for trace detection is reported in Fig. 7.23. Here the peak of ^{52}Cr, which is often requested to be analysed as impurity in uranium, is very well separated from the peak of ^{40}Ar^{12}C$^+$. The sample contained 540 ppm of C and the ^{52}Cr has been determined at a level of 170 ppb.

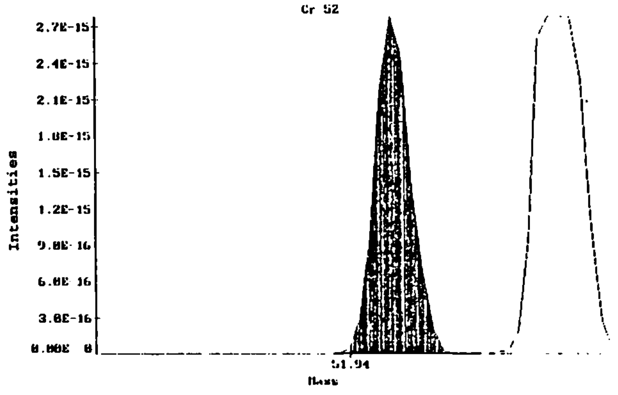

Fig. 7.23 GDMS spectrum obtained when analysing ^{52}Cr (170 ppb) in an uranium metal sample in presence of carbon (540 ppm). On right the peak due to $^{40}Ar^{12}C^+$, the mass resolution necessary to resolve ^{52}Cr from $^{40}Ar^{12}C^+$ is 2400.

For the analysis of trace elements in uranium metal, five different runs were performed. In Tab. 7.9 the mean concentration values and the internal precision obtained over the five runs are reported for all elements found. The imprecision in the analysis is typically 5% RSD or less even at ppb level. The exception is iodine which may be inhomogeneously distributed in the sample.

Detection limits

In GDMS, the detection limit depends on the number of points measured, the integration time and the resolution used.

The data relevant to the elements of Tab. 7.9 were collected by measuring 200 points for an integration time of 100 ms for the Daly detector and using high resolution (5000) to overcome potential molecular and isobaric interferences. This resulted in typical detection limits of 3 to 10 ppb for most elements. Using low (1500) resolution, measuring the same number of points and for the same integration time as for high resolution measurements, the detection limits can be lowered. The detection limit for thorium in uranium determined this way was 0.2 ppb.

Conclusions

The modifications made to the glow discharge source of a VG9000 GDMS for its installation in a glove-box did not alter the instrument specifications significantly. Elemental and isotopic capabilities of glow discharge mass spectrometry can be successfully applied to the characterisation of samples of unknown isotopic composition, such as uranium metal. GDMS has a precision and accuracy comparable to ICP-MS and for preliminary investigation, the GDMS technique can give information on the isotopic abundance composition faster than IDMS analysis.

References

[1] F. L. King and W. W. Harrison, Mass Spectrom. Rev., 9 (1990) 285

[2] W.W Harrison, in 'Inorganic Mass Spectrometry', Eds., Adams, F., Gijbels, R., and van Grieken, R., Wiley, New York, 1988

[3] J. W. Coburn and E. Kay, Appl. Phys. Lett., 18 (1971) 435

[4] D. L. Donohue and W. W. Harrison, Anal. Chem., 47 (1975) 1528

[5] D. C. Duckworth and R. K. Marcus, Anal. Chem., 61 (1989) 1879

[6] J.I. Garcia Alonso, D. Thoby-Schultzendorff, B. Giovannone and L. Koch, J. Anal. At. Spectrom., 8 (1993) 673

[7] J. E. Cantle, E. F. Hall, C. J. Shaw and P. J. Turner, Int. J. Mass Spectrom. Ion Process., 46 (1983) 11

[8] N. R. Daly, Rev. Sci. Instrum., 31 (1960) 264

[9] D. M. P. Milton, R. C. Hutton and G. A. Ronan, G. A., Fresenius J. Anal. Chem., 343 (1992) 773

[10] P. De Bievre and I. L. Barnes, Int. J. Mass Spec. Ion Proc., 65 (1985) 211

Analysis of ^{238}Pu/^{239}Pu Ratios from Total Evaporation Mass-Spectrometry Data

Introduction

The measurement of ^{238}Pu by thermal-ionisation mass-spectrometry (TIMS) is problematic because interferences from ^{238}U are very difficult to eliminate. ^{238}U is usually present in burnt fuel solutions at concentrations 100 times that of Pu - and the ^{238}Pu isotope is typically only a few percent of the total plutonium. Separation coefficients of at least 10000, of plutonium from uranium, are required if the interference from ^{238}U is to be kept low so as not to interfere in the measurement of ^{238}Pu. Moreover, separations in the mass-spectrometer process which rely on the different atomisation and ionisation efficiencies between plutonium and uranium cannot be applied when the isotope ratios are measured using the technique of total evaporation [1,2].

Because of the interference of uranium at the 238 mass peak, ^{238}Pu is routinely determined in our laboratory by alpha spectrometry, i.e. planchettes are prepared with the separated plutonium fraction and by alpha spectrometry the activity ratio of ^{238}Pu to the sum of ^{239}Pu and ^{240}Pu, is measured. From this ratio, the atom ratio of ^{240}Pu/^{239}Pu (measured by mass-spectrometry) and the half-lives of the isotopes, the atom ratio of 238/239 in the plutonium can be calculated. Although with care, 238/239 ratios can be measured to between 1-2 % accuracy, in practice the accuracy lies between 2 - 5%: a value acceptable for Safeguards analysis and most other purposes.

However the method has disadvantages: time and effort are required to make planchettes, and more solution is needed for the planchettes than for filaments for mass-spectrometry. The presence of β/γ-emitting fission products in the solution can also effect the alpha spectrometry and consequently the results.

In the course of the total evaporation process, the ion currents at all masses of interest are accumulated as a function of time in parallel. The development of these currents is determined by the behaviour of the element in question in the evaporation process in the mass-spectrometer. This process can be followed for each mass, and as expected is identical for masses 239 and 240, which arise only from plutonium but is different for mass 235, for instance, which arises from uranium. At mass 238 there are contributions from both U and Pu and the relative contribution of each is dependent on the amounts of U and Pu in the sample. (Although the sample measured is a chemical fraction containing mainly Pu, it is found in practice that there are variable levels of uranium in the fraction.)

The purpose of the investigation reported here was to see if it is possible to strip out the pure Pu and U information from the mass 238 current data, thus giving directly ratios of $^{238/239}$Pu.

Method

Instrumentation

All samples were measured using a Varian MAT 261 or 262 TIMS with multiple Faraday cups to simultaneously measure ion currents at preset masses. For plutonium the masses were 235,238,239,240,241,242,244, whereby the 235 mass was used to monitor uranium and 244 was the mass of the spike isotope. The channel with the highest current is also monitored independently by the control program. This allows the heating current to be optimally applied so that a sharp rise to a plateau value of the current is obtained and this plateau held as long as possible until the sample is exhausted. Depending on sample size (normally several nanograms of Pu), the evaporation and measurement process takes between 10 minutes and 1 hour. During the initial heating phase, the mass-spectrometer focus is adjusted and during this time a small amount of information is lost. The computer-controlled filament heating, however, ensures that the sample is totally evaporated in a reasonable time; that no tailing of heavier isotopes occurs at the end of the evaporation.

The evaporation data were transferred to diskette and then to a PC where after initial data treatment, they were imported into an EXCEL spreadsheet and analysed.

Theory

If we apply multicomponent theory [3] to the process, expressed as:

$$y = K \cdot c \qquad (1)$$

where y is the observation vector (in this case the vector of current values with time at mass 238),

> K is the response matrix for the two elements at this mass, and
> c is the concentration vector for the two elements,

then applied to this particular restricted case of 2 components, we can substitute the matrix of the 2 current vectors at masses 235 and 239 for the K matrix. The resulting vector, c, contains the values of the 238/235 ratio for uranium, and the 238/239 ratio for plutonium.

The equation is solved using standard techniques:

$$c = (K' \cdot K)^{-1} \cdot y \qquad (2)$$

The variance of the concentrations is given by:

$$V(c) = s^2_e (K' \cdot K)^{-1} \qquad (3)$$

where s^2_e = SSe / (n-m) and SSe the sum of squares of calculated and measured y, and (n-m) the number of degrees of freedom.

The variance on the 238/235 and 238/239 ratios calculated is:

$$V(c_1) = s^2_e \cdot c_{11} \qquad (4)$$

$$V(c_2) = s^2_e \cdot c_{22} \qquad (5)$$

Results

Calculations following the above scheme have been made for a series of samples to compare the results with those already obtained by alpha-spectrometry and to try and determine the practical limits of the method. The first set of results is given in Tab. 7.10. For each sample the ratio of the values obtained by this method to that by alpha-spectrometry is given as well as the calculated standard deviation (eqs. 4,5 above) and the chi-square of fit. The calculated percentage contribution of uranium to the response at mass 238 in the mixture is also given. A feature of these results (Tab. 7.10) is that the chi-square values are very low. This reflects the fact that the signal at the 238 peak is predicted extremely well by the signals at the 235 and 239 peaks.

Tab 7.10 Data calculated from mass-spectrometry

Sample	Pu-ratio	st devn Pu-ratio	%U in 238	ratio ms/alpha	Chisq
1	0.023405	0.05%	11.50%	1.026548	2.6E-06
2	0.023433	0.33%	23.02%	1.027785	1.3E-03
3	0.018525	0.24%	76.99%	0.97807	6.7E-06
4	0.016284	0.09%	14.92%	1.022844	8.8E-05
5	0.016233	0.19%	7.20%	1.019691	6.7E-05
6	0.089001	56.03%	98.50%	1.0775	1.0E-02
7	0.022318	10.49%	95.36%	1.166061	5.5E-02
8	0.024355	11.09%	97.05%	1.272446	5.5E-03
9	0.037246	0.20%	0.64%	1.033755	1.3E-05
10	0.037008	0.21%	0.84%	1.027145	3.4E-06
11	0.016075	5.03%	96.54%	0.846036	4.1E-03
12	0.019805	5.31%	97.32%	1.042375	2.7E-04
13	0.046023	0.12%	0.64%	1.023409	4.0E-04
14	0.046021	0.12%	0.22%	1.023371	1.9E-05

It can be seen that when the uranium contributions to the 238 mass are more than 90%, the calculated 238/239 ratios are considerably different to those found by alpha spectrometry. The predicted standard deviations are also high. Sample 3, with a 77% U contribution to the 238 peak appears to be unusual: an acceptable value of the standard deviation is found, but the calculated 238/239 ratio is lower than that found by alpha spectrometry. It is encouraging that poor results are flagged by the large calculated standard deviations, and also to some extent by the chi-square values.

It can be seen also that the analysis system is in principle favourable over a wide range of uranium contents. Samples with small amounts of uranium will have a low 235 mass signal, but the error thus introduced in the fitting is applied only to a small correction, and on the other hand, samples with a large amount of uranium will also have a strong 235 mass signal and a corresponding low error contribution to the deconvolution process.

A selection of these results is shown in Fig. 7.24. The ratios of the mass-spectrometry calculated values to alpha spectra determinations are shown with a bar indicating the calculated standard deviation in each case. The counting errors of the alpha spectrometry have not been included. Apart from one value (ms/alpha = 0.97), the mass-spectrometry to alpha-spectrometry ratios for these samples show the mass-spectrometer calculations are about 2% higher than the alpha-spectrometry results. This agreement is very satisfactory.

It is possible that the alpha-spectrometry has a bias. However the two main causes of bias in alpha-spectrometry of ^{238}Pu - peak overlapping and incomplete separation of ^{241}Am - work in a positive direction and the bias observed is difficult to explain as coming from the alpha-spectrometry. A more likely cause is the mass effect in the mass-spectrometer, whereby the lighter masses tend to evaporate earlier than the heavier masses. In the initial heating period, the ^{235}U will preferentially evaporate and the assumption of the method as described, that the evaporation patterns of ^{235}U and ^{238}U are identical is thus not absolutely correct. By extending the method to other cases: for instance at mass 241, where isobars of americium and plutonium are found, this point can be investigated.

Conclusions

The method of stripping the Pu and U contributions from the data output of the total evaporation measurement of Pu solutions containing some uranium has shown that results close to the alpha-spectrometry values can be obtained. The method appears promising and if brought into routine use could replace much of the alpha spectrometry at present carried out. A clear signal at mass 235 is essential for the fitting process. This is not a problem for most Safeguards samples, but it is conceivable that in some cases, a small amount of enriched ^{235}U can be added to the sample before depositing on the filament.

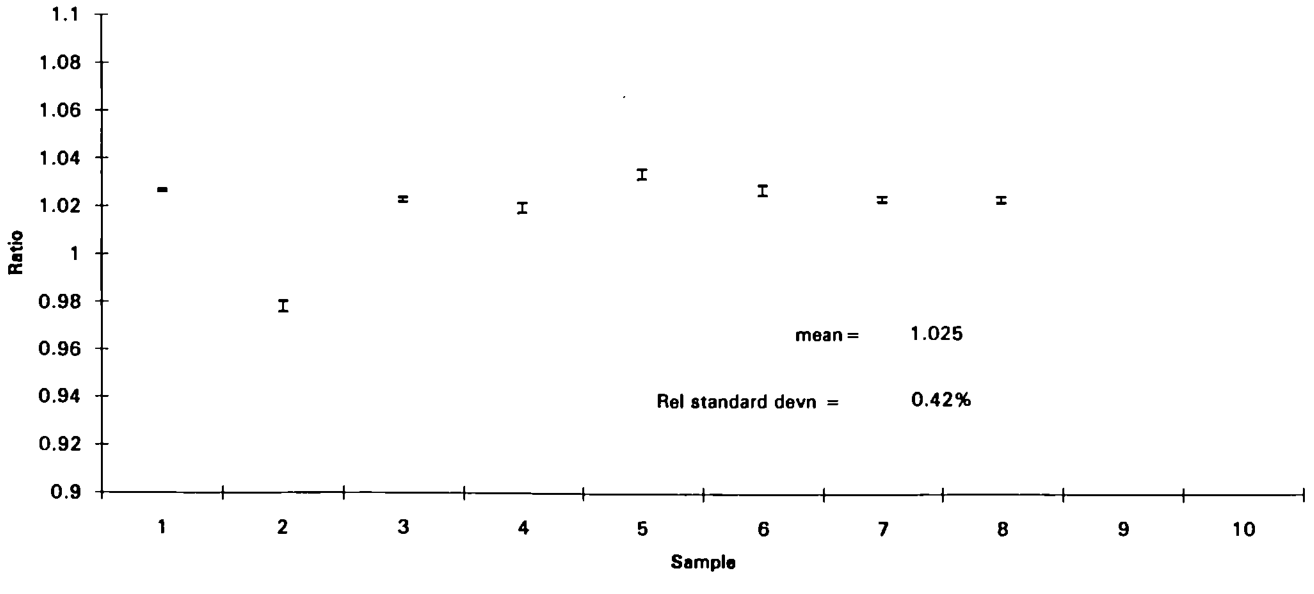

Fig. 7.24 Comparison of alpha and mass-spectrometry methods for ^{238}Pu

An extension of the method to other problems is also possible. The measurement of uranium ratios, *without* prior chemical separation of plutonium, can be made using the same method. Also, the determination of ^{241}Pu in the presence of ^{241}Am using another Pu isotope (e.g. ^{240}Pu) and ^{243}Am as comparisons should be feasible. In this case, addition of ^{243}Am to the solution before deposition on the mass-spectrometer filament may be needed.

It is intended to apply the method regularly and compare the results of a larger number of samples with the results from alpha spectrometry, whereby the calculation algorithms will be incorporated directly in the mass-spectrometer evaluation program. A series of accurately known mixtures of Pu and U is also being made up and the results of the described methods will be tested against these values.

Reference

[1] M. Romkowski, S. Franzini, L. Koch, Mass-Spectrometric Analysis of Sub-Nanocurie Samples of Uranium and Plutonium, 9th International Symposium on Safeguards and Nuclear Material Management, London, 12-14 May 1987

[2] H. Kuehn, Total Flash Evaporation for U and Pu, 12th International Mass Spectrometry Conference, Amsterdam, 26-30 August 1991

[3] D.L. Massart, B.G.M. Vandeginste, S.N. Deming, Y. Michotte , L. Kaufmann, 'Chemometrics: a textbook', Elsevier, 1988

Safeguards Monitoring for Detection of Undeclared Pu and HEU Production

Introduction

The IAEA is examining technical methods which could be used to support a possible broadened safeguards regime. In particular, there is recent emphasis on enhancing the Agency's ability to detect undeclared nuclear activities which should have been declared under the terms of a comprehensive safeguard agreement. Approaches are being considered which can give assurance that there are no undeclared spent fuel reprocessing and/or enrichment activities in a country covered by a comprehensive safeguards agreement.

The IAEA convened a Consultants Group meeting, held between 30 March and 2 April 1993. The Agency was interested in collecting information relevant to the following topics:

(i) the most sensitive and selective analytical methods for measuring the chemical, elemental or isotopic signatures associated with the undeclared production of high-enriched uranium (HEU) or plutonium,

(ii) the appropriate sampling methods and quality assurance requirements for a programme of environmental monitoring aimed at the detection and characterisation of the above signatures, including the effects of concealment methods,

(iii) the most appropriate methods which are available for handling and evaluating data resulting from such measurements,

(iv) the availability of expertise in the IAEA's Member states which could be utilised in the areas of training, provision of analytical services or the development of enhanced analytical capabilities within the IAEA itself.

Detection of uranium enrichment activities

Uranium enrichment processes used for production of low-enriched uranium (LEU) for commercial uses are also capable of producing nuclear weapons grade material in the form of highly enriched uranium (HEU). Activities involving enriched uranium can leave unique signatures in the environment that may be detectable in samples of soil, vegetation, or water by applying sufficiently sensitive analytical techniques.

Uranium with isotopic abundances different from that of natural uranium is the primary signature for HEU production activities. In any separation technology some enriched uranium will inevitably be released to the environment. Environmental samples taken at or near an enrichment facility can contain some of the enriched material thus altering the uranium isotopic abundance.

The isotopic content of natural uranium is constant at values of 0.72% for ^{235}U and 0.0055% for ^{234}U. Any change in these values can be easily detected by sensitive isotopic analysis techniques, in samples of different origin such as soils, vegetation and water. This variation of the isotopic ratios from their natural abundances is unequivocal evidence that enriched uranium processing activities have been or are being carried out in the vicinity of the sampling place. As well as this, the presence of ^{236}U would also indicate that the uranium in the sample had been exposed to a neutron flux.

Detection of undeclared plutonium production

Undeclared reactor operations.

Detection of an undeclared reactor by environmental sampling is possible by sampling short-lived atmospheric radioactive gases and radionuclides transported in surface water (streams, rivers, lakes, oceans). The effectiveness of detection techniques decreases with the distance from the reactor. On-site and short-range sampling of short-lived fission gases is the key to the detection of an undeclared reactor. However, the reactor must be operating. Aqueous effluents containing trace activation and fission products are also excellent sources for effective on-site and short-range detection. Aqueous effluents also have the advantage of long range detection because of their traceable mechanism of transport. Furthermore the reactor does not have to be presently operating because many effluent signatures will remain in the stream sediments for several years gradually migrating downstream where they concentrate in deposited sediments and aquatic biota.
On the basis of these considerations, a variety of signatures and the associated sampling and detection technologies have to be considered. Here the reactor signatures are reported. Their importance is dependent on the reactor type:

Reactor signatures released to air during normal reactor operation:
^{41}Ar, ^{88}Kr, ^{85m}Kr, ^{87}Kr, ^{133}Xe, ^{133}Xe, ^{14}C, ^{3}H (HTO)

Reactor signatures released to air due to fuel failure:
^{132}I, ^{133}I, ^{131}I, ^{129}I, ^{85}Kr, ^{103}Ru, ^{106}Ru

Reactor signatures released to water.
^{3}H

Short-lived (<30 days) activation products (quantities depending on the reactor type):
^{24}Na, ^{56}Mn, ^{64}Cu, ^{76}As, ^{51}Cr, ^{72}Ge, ^{56}Fe, ^{32}P, ^{239}Np

Long-lived (>30 days) activation products (quantities depending on the reactor type):
^{60}Co, ^{58}Co, ^{57}Co, ^{65}Zn, ^{54}Mn, ^{46}Sc, ^{63}Ni, ^{55}Fe, ^{56}Fe.

Fuel rod storage failure:
^{134}Cs, ^{135}Cs, ^{137}Cs, ^{132}I, ^{133}I, ^{131}I, ^{129}I, ^{103}Ru, ^{106}Ru, ^{95}Zr, ^{95}Nb, ^{141}Ce, ^{144}Ce, ^{140}Ba, ^{140}La, ^{230}Np, ^{238}U, ^{234}U, ^{235}U, ^{236}U, ^{239}Pu, ^{240}Pu, ^{241}Pu, ^{242}Pu, ^{238}Pu.

Undeclared reprocessing of irradiated fuel

Recovery of Pu from irradiated fuel will, potentially, give rise to environmental signatures, from both the radioactive and non-radioactive operations. It is assumed at this stage that environmental signatures will primarily arise from gaseous, rather than from aqueous discharges. It is thought that for small-scale weapons manufacture liquid wastes will be stored and not discharged. However, if liquid wastes are discharged, the fission and activation products, as well as the actinides may find way into the aqueous discharges.

Signatures arising from reprocessing.

Reprocessing operations are likely to give clear environmental signatures which should, in principle, be easily distinguishable from reactor operation and Pu recovery for fuel purpose. The release of ^{85}Kr/^{133}Xe and ^{129}I/^{131}I during reactor operation will be distinctly different from that occurring during reprocessing. The β, γ/α activity ratio will also be different. Operations to produce Pu for nuclear fuel and Pu for weapons purposes will give markedly different Pu isotopic signature (from the conversion process).

The reprocessing term is process-dependent and will therefore encompass a wide range of active and inactive components. The environmental signatures will depend on the release fraction, plume transport and dispersion and, in the case of organic materials, their reactivity in the environment.

Environmental signatures may consist of the radioactive and non- radioactive species listed below:

Radioactive:

- gaseous and volatile products: ^{85}Kr, ^{133}Xe, ^{3}H, ^{14}C, $^{103/106}Ru$;
- fuel derived particulates: ^{95}Zr, ^{95}Nb, $^{134/133/137}Cs$, ^{144}Ce, ^{99}Tc;
- 2 years cooling will effectively remove ^{133}Xe and ^{131}I by decay;
- conversion-derived particulates: characteristic Pu isotopic, ^{241}Am and ^{99}Tc.

Non-radioactive:

- NO_x from aqueous dissolution;
- secondary/tertiary amines with C chains C_8-C_{12};
- organo-phosphorus compounds (phosphates, phosphonates) with C chains C_4-C_6;
- diluents, such as ^{12}C alkanes, aromatic hydrocarbons, brominated/chlorin-ated hydrocarbons;
- reducing agents such as sulphonate, hydroxylamine,
- HF, H_2O_2, $(C_2O_4)_2$-, I_2 from conversion.

Present situation

In 1993 we began to adapt the analytical procedures and instrumentation for the detection of some of the above signatures at background concentration levels. Some samples of different environmental origin have been collected and chemical treatments tested. It was found that soil samples could be directly analysed by GDMS after drying and pellet compacting. A procedure for the isotopic ratio $^{235}U/^{238}U$ determination was developed and some results have been already obtained. In the soil samples collected an isotopic ratio $^{235}U/^{238}U$ coresponding to the natural isotopic abundance was measured. The procedure is still under development and it will be continued during 1994.

In 1994 different procedures for the extraction of the above signatures from solid samples will be investigated and compared.

A liquid scintillator counter for the low-level detection of tritium and ^{14}C has been purchased and it will be delivered and installed in the first trimester of 1994.
A clean room and cleaning/protection facilities for sample handling and storage have been designed and are being installed.

4. Work for Third Parties

Introduction

In 1993, new contracts with third parties worth 1.670 kECU have been signed. This brings the total volume of contracts under execution at ITU on December 31, 1993, to roughly 23 million ECU. By the end of 1993, additional contracts totalling 412 kECU were ready for signing.

Among the main achievements of the reporting period was the in-vitro demonstration of cell killing with specific ^{213}Bi-labelled antibodies. These results justify the continuation of preclinical studies with ^{225}Ac- and ^{213}Bi-immunoconjugates for application in the treatment of cancer.

Preparations for the fabrication of minor actinide-containing metallic test fuel for irradiation in the PHENIX reactor were concluded.

Irradiated fuel rods from the BR3 reactor in Mol were characterised by several methods for the PHEBUS-PF in-pile fission product release experiments to be performed in Cadarache. The thermal conductivity of the ceramic shroud material of the PHEBUS-PF in-pile set-up was measured and its structural and chemical stability during typical thermal treatments tested.

Post-irradiation examination of power reactor fuel rods by destructive and non-destructive techniques was continued according to schedule.

182 UO_2-based fuel specimens were fabricated and shipped to Halden, Norway, for an irradiation experiment designed to investigate and evaluate the effect of microstructural changes (RIM-effect) in the outer regions of LWR fuel pellets on fuel rod performance.

4.1 Radio-Therapeutical Work for AKZO/ Alpha Medical

Interaction of ^{213}Bi and ^{225}Ac with Human Cells.

Before a radionuclide can be applied for therapeutic purposes [1] the interaction with human cells must be investigated. The investigations reported here were directed at the specific problems of the mechanisms of the binding of the radionuclides ^{213}Bi; and ^{225}Ac to human cells.

Cytotoxicity investigations

Experiments with ^{213}Bi

The labelling conditions for antibody-chelator-complexes were established last year and following this a series of cytotoxicity experiments on monolayers of human tumour cells has been started. In view of the maximum attainable specific activities of the ^{213}Bi-antibody conjugates, we selected the A431-cell line (epidermic tumour), which has a high antigen-density (the Ag being the EGF-receptor) and the matching α-LEWIS IgG (murine) while MOPC-antibody (irrelevant IgG) was used as control. Some typical results are shown in Fig. 8.1.

From these experiments, it can be concluded that specific cell-killing can be achieved with ^{213}Bi-immunoconjugates: from the amount of radioactivity bound to the cells, it can be calculated that approximately 25 α-particles/cell are needed for >90% morbidity.

Experiments with ^{225}Ac

A difficulty in the application of ^{225}Ac was the preparation of immunoconjugates and the stability of these products. In 1993, reaction conditions were established under which ^{225}Ac-antibody

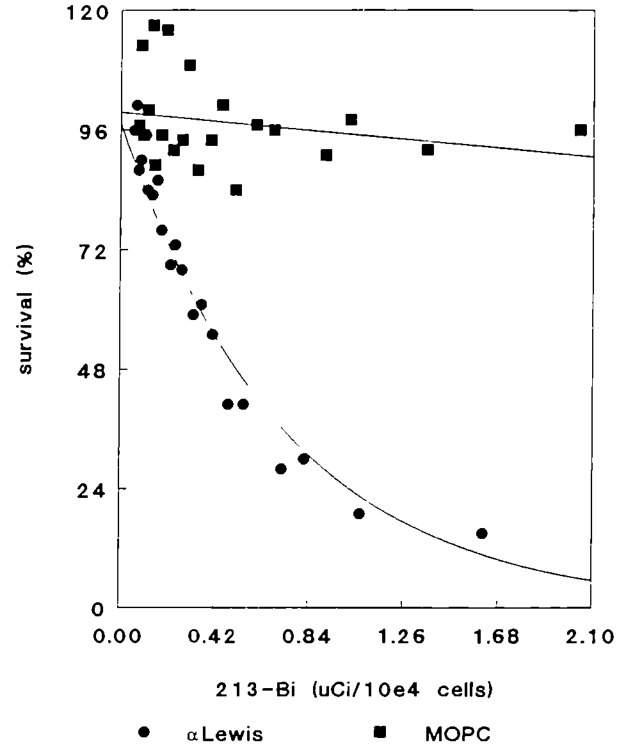

Fig. 8.1 Cytotoxicity of ^{213}Bi-Ab-conjugates on A431-cells. Cells were incubated with the conjugates for 48 hours: survival was measured by vital-staining procedure

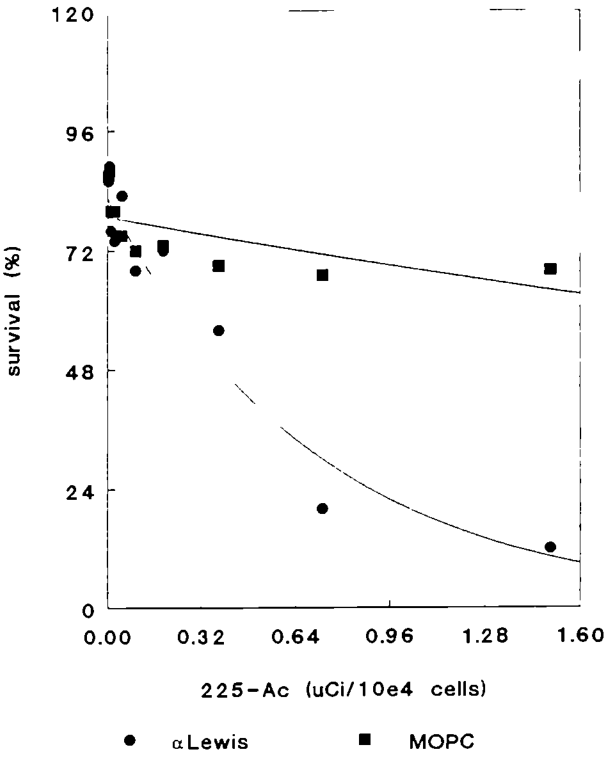

Fig. 8.2 Cytotoxicity of ^{225}Ac-conjugates on A431-cells using ^{225}Ac-a-LEWIS (specific) and ^{225}Ac-MOPCS (non-specific) conjugates. For conditions, see Fig. 8.1

conjugates could be prepared in high yields, but a kinetically stable Ac-chelator is still lacking. The present conjugates release (trans-chelation) ^{225}Ac in the presence of biological fluids. Nevertheless, we were able to prove specific cytotoxicity with these suboptimal conjugates as shown in Fig. 8.2.

From the results, it is concluded that the daughter isotopes of ^{225}Ac do not contribute to the specific cytotoxicity of the conjugates in this system. The lower cytotoxicity of ^{225}Ac in comparison with ^{213}Bi is in agreement with the release of the ^{225}Ac from the chelator-Ab-conjugate.

These cytotoxicity experiments justify continuation of the preclinical studies with ^{225}Ac and ^{213}Bi-immunoconjugates for application in the treatment of cancer.

Reference

[1] M.W. Geerlings, F.M. Kapersen, C. Apostolidis, R. van der Hout: "The Feasibility of Actinium-225 as Soource of α-particles in Radioimmunotherapy" Nucl. Med. Comm. (1993) 14, 121-125.

4.2 Preparation and Characterisation of MA Containing Alloys (CRIEPI)

Based on the fuel concept for the Integral Fast Reactor in the United States, minor actinides in varying quantities are added to the standard U, Pu, Zr alloy fuel. During the reporting period, preparations were completed to fabricate the test fuels for irradiation in PHENIX. The minor actinide-containing fuel will be located in the centre of eight PHENIX standard pins. The remaining space is filled with the standard U, Pu and Zr alloy fuel. The equipment for the production of Am and Cm metal was set up and successfully tested. Am metal batches have first been produced. It appears that the casting of fuel in Y_2O_3 moulds will be the preferable technique for the minor actinide-containing fuel production.

4.3 Characterisation of Highly Burnt UO_2 and MOX Fuel (CRIEPI)

In order to verify predictions for the interim storage behaviour of highly burnt UO_2 fuels and spent MOX fuel, extensive analyses are under way, which will be compared to results obtained by Japanese calculations. The work is sponsored by MITI.

4.4 Work for the PHEBUS-PF Project

Characterisation of Lots 3 and 4 of BR3 Fuel Rods

The characterisation of 125 irradiated fuel rods is being performed at ITU as part of the work for the Phebus PF project. The characterisation of the fuel rods delivered by SKN/CEN Mol from the BR3 reactor is necessary in order to check their condition and the composition of the fuel. The cladding must be in good condition so that it does not fail prematurely during the Phebus test ramp and knowledge of the composition of the fuel is required for burn-up determination.

Non-destructive testing

The main characterisation is carried out by means of non-destructive testing (NDT). This comprises of the following tests on all rods :

- Eddy current defect testing
- γ scanning (total, $^{137,134}Cs$, $^{106}Ru/Rh$, ^{144}Ce)
- length determination
- visual examination (macrograph)

On 3 rods selected out of each batch of 25 rods these additional measurements are made:

- Eddy current oxide thickness measurements
- Profilometry

Finally on 1 rod per batch a

- filling gas analysis (puncturing)

is being performed.

Destructive testing

Thereafter on the rod selected as most typical of the batch (and which was used for puncturing) the destructive testing (ceramography) is carried out, with the aim to determine and analyse the fuel structure. Cuts are made at the maximum and mean power position as determined from the total γ scanning of the fuel rod.

Preparation for ceramography

3 mm sections are taken from each cut for mounting and polishing. These are then examined and micrographs taken at rim, mid-radius and central positions. For the cut at the maximum power position the micrographs are also made on etched samples to show the grain boundaries. With these micrographs image analyses are performed (with a Cambridge Quantimet) to determine:

- grain size distribution
- porosity percentage
- pore size distribution

of the fuel and to see if any changes (grain growth or increased grain boundary porosity) have occurred during the irradiation. The size of the fuel gap and any fuel-cladding interactions were also observed.

Fuel Chemical Analysis

A 12 mm long piece of fuel (~ 1 pellet) from the maximum power position is dissolved in 8 M nitric acid, and then quantitative chemical analysis of the heavy metal atoms is performed (by isotope dilution mass spectroscopy) for fissile material determination. Certain fission products (^{137}Cs, ^{134}Cs, ^{148}Nd) are also analysed by inductively coupled plasma-mass spectroscopy (ICP-MS) for burn-up determination. These values are required as accurate input data for codes simulating the effects of an accidental ramp.

Results of lots 3 and 4

As with the results from the lots 1 and 2, the fuel rods from lots 3 and 4 appeared from the non-destructive testing to be in good condition. Visual examination (Fig. 8.3) and eddy current testing

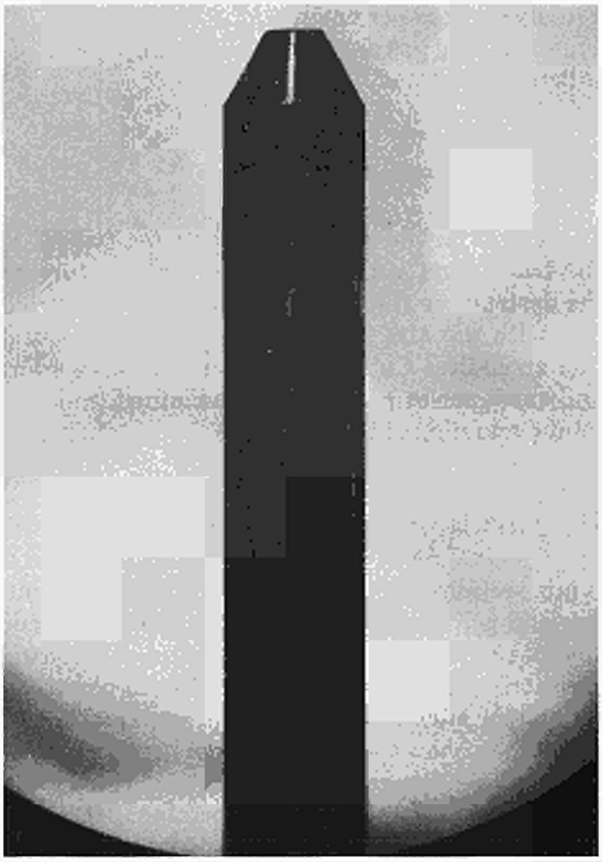

Fig. 8.3 Phebus PF - Visual Inspection of U570 (Lot 4) (2.2x)

showed no defects and only one rod out of 56 showed some thickening of the oxide scale (at the spacer grid position).
The oxide layer was approximately 15 µm thick, while profilometry and length measurements demonstrated a 0.05 mm (0.3 %) shrinkage of the diameter and a 5 mm (0.5 %) increase in length (Fig. 8.4).
From the total γ-spectroscopy the usual power arc with a small depression in the centre due to the spacer grid could be derived. This profile was reflected in the isotopic profiles of ^{137}Cs, ^{134}Cs, ^{106}Ru/Rh, and ^{144}Cs (see Fig. 8.5 for the ^{137}Cs profile).

Puncturing

The filling gas had an increased pressure (20 bar ⇒ 24 bar) and the analysis showed that about 0.05 cm^3 of total Kr isotopes and 0.4 cm^3 of total Xe isotopes had been released; the Xe/Kr ratio was thus 7-8 (Tabs. 8.1 and 8.2).
Using a calculated Kr and Xe inventory (Mitra + Korigen) this yielded a fission gas release of not more than 0.2 %. This is a reasonable fraction for the chosen fuel rods with burn-ups of 24.5 and 27.8 GWd/t U from lot 3 and lot 4 rods, respectively.

Ceramography

Micrographs of rods U568 from lot 3 at the outer edge, and at center positions are showen in Figs. 8.6a-b and 8.7a-b for the mean and the maximum power position sections. The fuel-cladding gap and the outer oxide of the cladding is shown in Figs. 8.8 and 8.9. The image analysis of U568 and the examination of lot 4 (U570) is yet to be done however, it is seen that the outer oxide layer is approximately 5 µm thick which is only a third of the value given by the Eddy current testing. Similar discrepancies were also observed in the previous examinations of lots 1 and 2. In addition the mean grain size appears to be of the order of 15-20 µm in diameter and a low porosity of 1-2 %. For reference, the previous batch examined (lot 2) had a mean grain diameter of 17-19 µm and a porosity of 1-2 %. There is no evidence of grain growth at the centre of the U568 rod (i.e. for excessive fuel centreline temperatures). This data is tabulated along with the nominal starting or specified values of the fuel rods in Tab. 8.3.

The outer cladding is covered only with a thin and protective oxide film; the cladding has also undergone a slight creepdown (0.4%) but became slightly thicker with irradiation. The fuel has swollen with a diameter increase of 11-14 %; this has lead to a considerable reduction in the fuel/cladding gap by 25 ± 10%. Here the gap reduction is significantly larger at the maximum power position (-84%) compared to the mean power position (-64%), but no gap closure occured. These values are measured at cold conditions; the gaps will be much smaller at operating temperature. Only a slight fuel-cladding interaction at the maximum power position was observed.

Conclusions

The non-destructive testing shows the rods from lots 3 and 4 from the BR3 reactor to be in good condition with no defects and a thin protective oxide layer. The fission gas release is low, with 0.2 % maximum, as estimated from puncturing. The ceramography performed on U568 (lot 3) indicates low porosity with pores of small average size, similar to previously examined batches (lots 1 and 2). No grain growth is apparent, thus the rods have not been subjected to high linear pow-

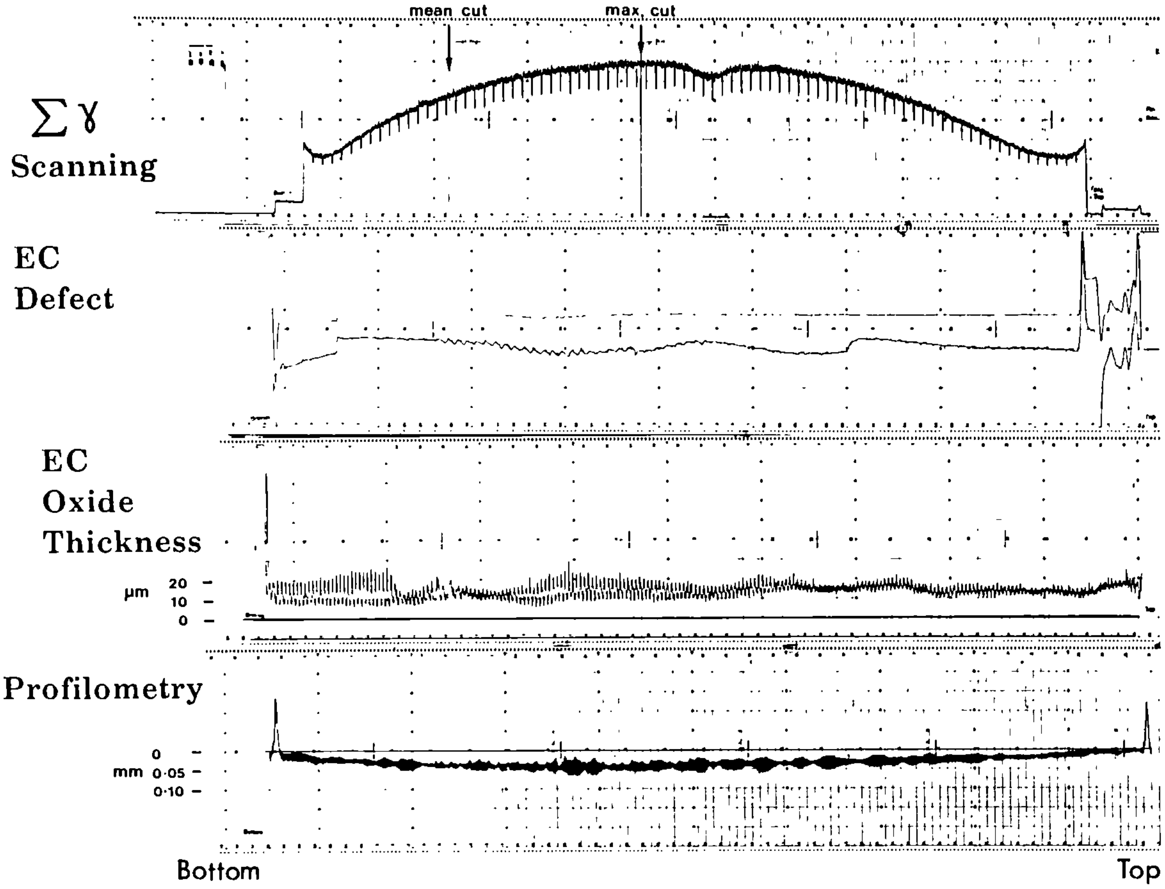

Fig.8.4 Phebus PF - Non-destructive testing results of U570 (Lot 4)

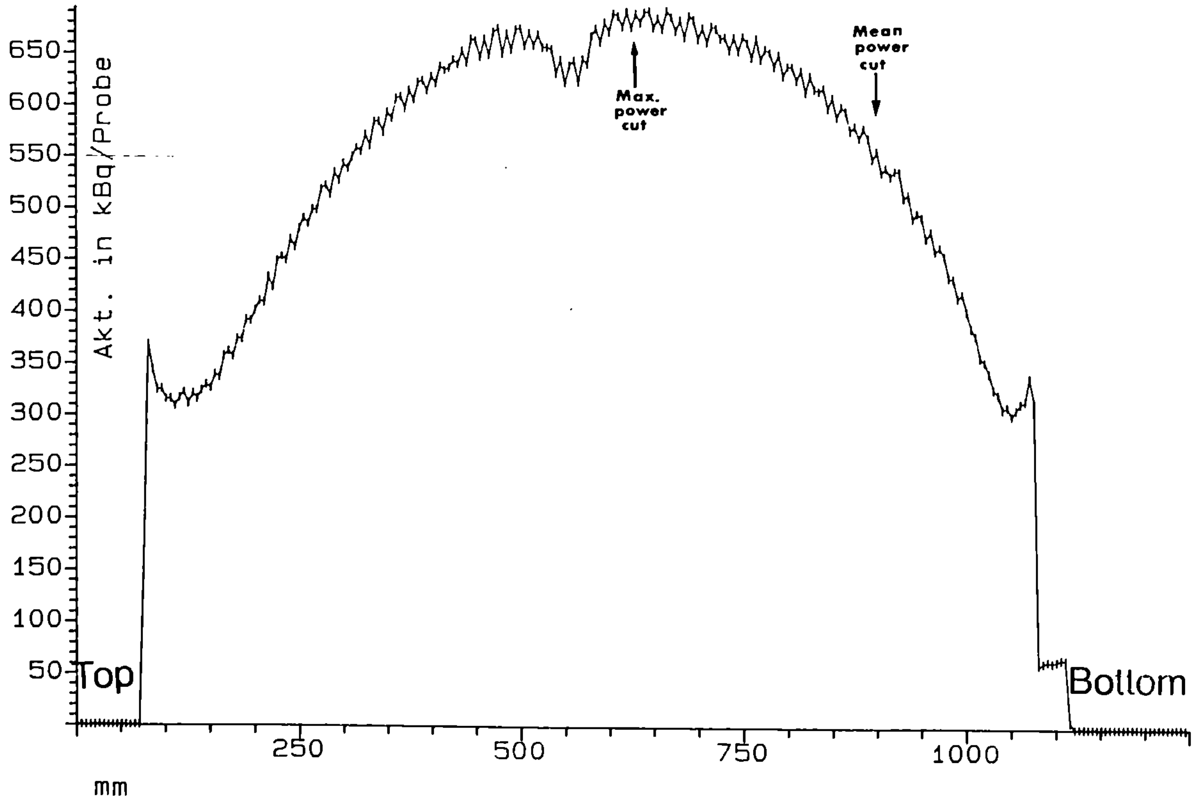

Fig. 8.5 Phebus PF - Axial Cs-137 γ-spectrum profile for U570 (Lot 4)

	1 U627 (Lot 2)	2 U568 (Lot 3)	3 U570 (Lot 4)	% Release of Inventory (KORIGEN / MITRA)
Mean Burn-up (GWD.tU^{-1})	23.4	24.5	27.8	
Krypton Isotopes	(cm^3)	(cm^3)	(cm^3)	
^{83}Kr	0.01	0.01	0.01	0.15
^{84}Kr	0.02	0.01	0.02	0.16
^{85}Kr	0.01	0.00	0.00	-
^{86}Kr	0.03	0.02	0.03	0.14
Total Kr	**0.08**	**0.04**	**0.05**	~ 0.15 %
Xenon Isotopes	(cm^3)	(cm^3)	(cm^3)	
^{131}Xe	0.07	0.04	0.04	0.16
^{132}Xe	0.12	0.07	0.09	0.16
^{134}Xe	0.18	0.10	0.11	0.14
^{136}Xe	0.23	0.13	0.15	0.14
Total Xe	**0.59**	**0.33**	**0.39**	~ 0.16 % (0.20 % max.)

Note: U568 and U570 are more accurate than the 1st meas. of U627

Tab. 8.1 Phebus PF-fission gas releases determined by puncturing of U568 and U570 compared to U627 (1st.measurement)

	1 U627 (Lot 2)	2 U568 (Lot 3)	3 U570 (Lot 4)	% Release of Inventory (KORIGEN / MITRA)
Mean Burn-up (GWD.tU^{-1})	23.4	24.5	27.8	
Ratio Xe/Kr	7.82	7.48	7.18	12
relative error of vol. meas. (and calibration)		< 5 %	< 5 %	
Pin pressure prior to test	24.1 bar		24.1 bar	-

Note: Model Inventory on g.b. is ~ 0.3 - 0.75 %

Tab. 8.2 Phebus Pf-Ratios of Xe/Kr determined by puncturing of U568 and U570 compared to U627 (1st.measurement)

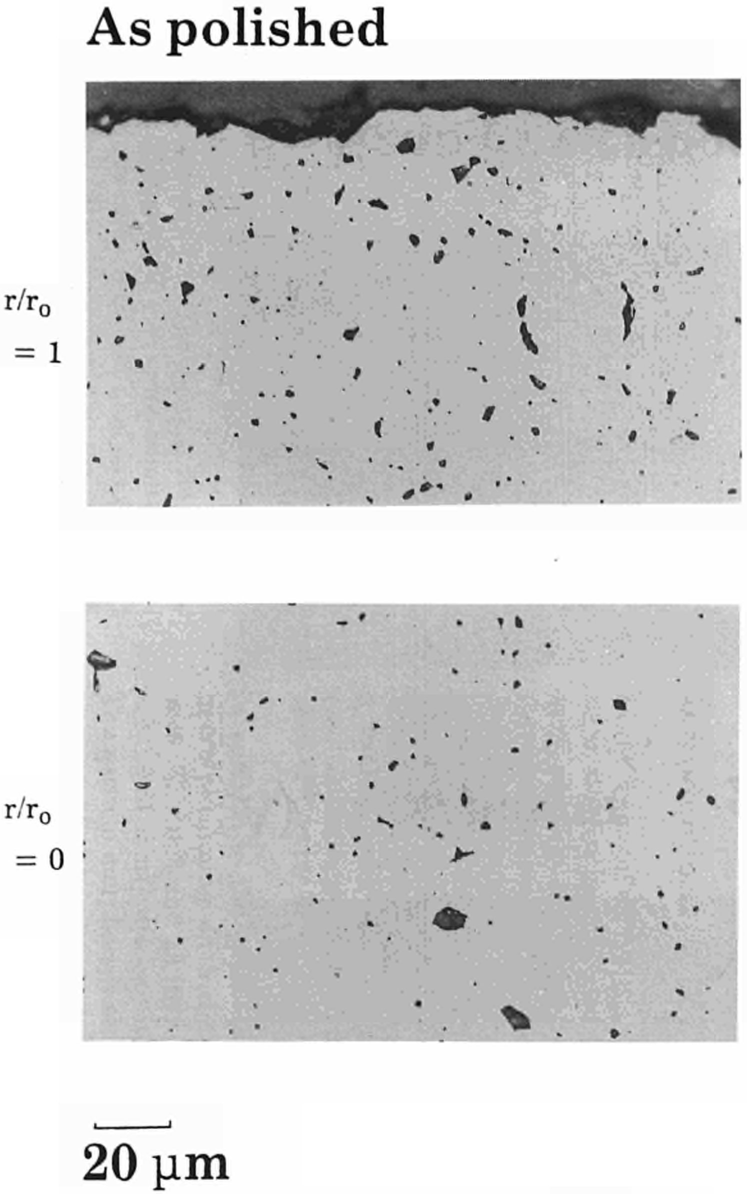

Fig. 8.6 Phebus PF - Fuel structure of U568 (Lot 3) at mean power position (600×)

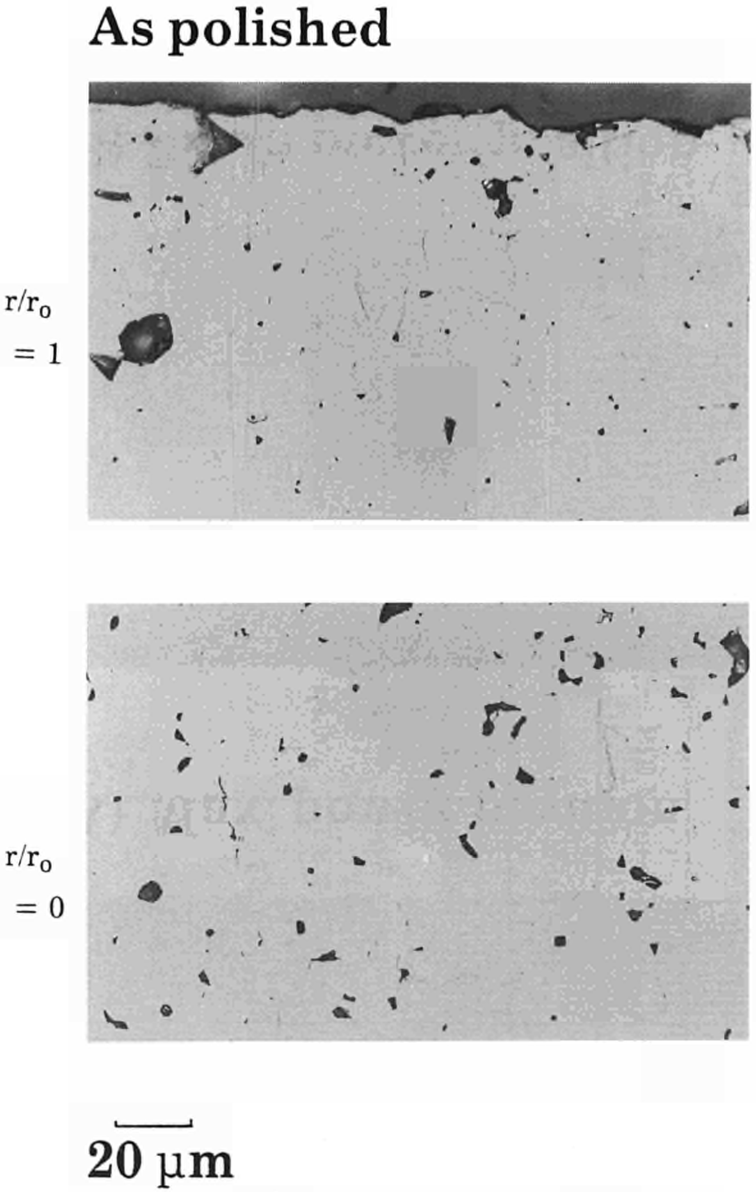

Fig. 8.7 Phebus PF - Fuel structure of U568 (Lot 3) at max power (600×)

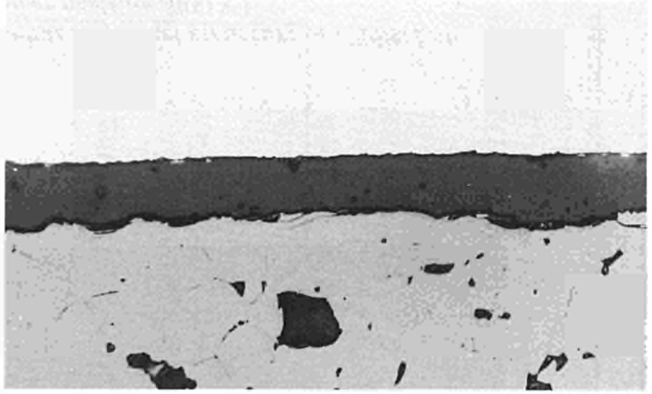

A) Max. power

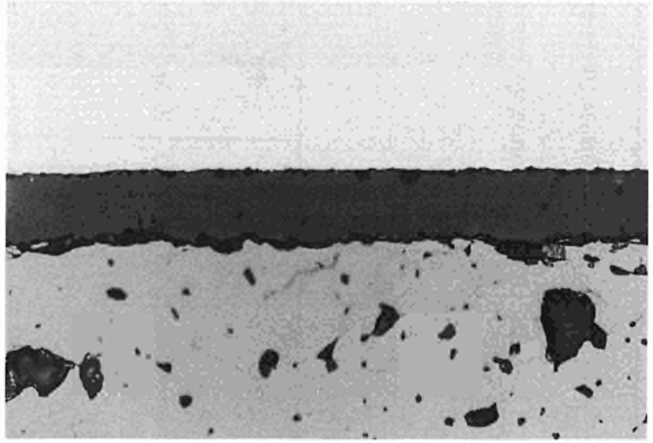

B) Mean power position

Fig. 8.8 Phebus PF - Fuel cladding gap and internal corrosion of U568 (600 ×)

A) Max. power position

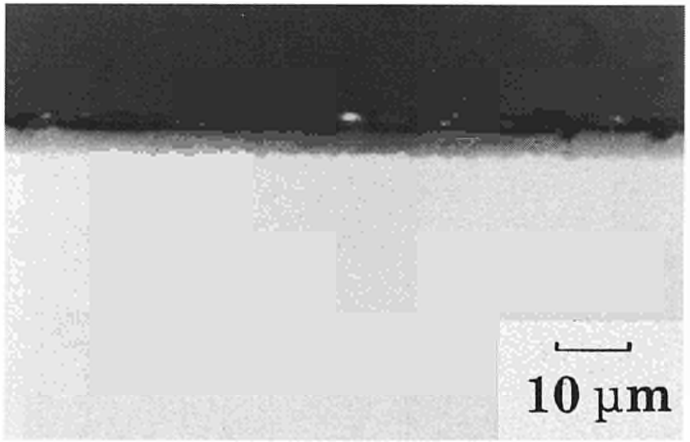

B) Mean power position

Fig. 8.9 Phebus PF - Fuel cladding oxidation of U568 at max and mean power position (1200 ×)

Tab. 8.3 Phebus PF-fuel cladding dimensions for U568(Lot3) - 6.85 % ^{235}U

Parameter	Nominal values (pre-irradiation)	PIE Values		Variation (%)	
		Max power	Mean power	Max	Mean
cladding					
Ø ext (mm)	9.485 - 9.493	9.461 ± 0.007	9.462 ± 0.005	- 0.3	- 0.3
Ø int (mm)	8.24 (spec.)	8.193 ± 0.004	8.201 ± 0.004	- 0.6	- 0.5
Thickness (mm)	0.58 (spec.)	0.634 ± 0.007	0.631 ± 0.004		
outer oxide layer (μm)	-	3.4 ± 0.3	2.8 ± 0.7		
Fuel/cladding gap width (μm)	98 ± 6	16 ± 5	35 ± 14	- 84	- 64
Fuel Ø mean (mm)	8.039 - 8.051	8.161 ± 0.006	8.130 ± 0.031	+ 1.4	- 1.1

U568 Burn-up: max 30.9 GWd/tU U568 cuts: max 495 mm (from bottom end)
mean 24.5 GWd/tU mean 225 mm (from bottom end)

ers, at the fuel centre temperatures did not exceed 1800 °C.

The burn-up given by γ-scanning reflects the axial power distribution expected for this reactor and the ^{137}Cs scans show no signs of Cs displacement.

The good condition of the rods makes them suitable for use in the Phebus PF experiments with a minimal risk of premature failure and for a non-typical fission product release behaviour.

Future work

The ceramography on U570 (lot 4) and the radiochemical analysis of the maximum power section of two destructively tested fuel rods from lots 3 and 4 remain to be carried out. These are expected to be completed by end-February '94 (ceramography) and end-april '94 (radiochemical analysis). Previous radio-chemical analysis (on lots 1 + 2) showed little deviation from the calculated values.

PHEBUS-Round Robin Test

Introduction

In the frame of the PHEBUS PF project a round robin test has been carried out for qualifying the most suitable analytical methods. ITU has received and examined the punch number 4 (out of 5) of the impactor plate 5 from an experiment conducted within the frame of the VERCORS project. The sample supplied by SECC/Grenoble was a disc of about 20 mm diameter mounted (glued) on a small cylinder. This sample was examined according to the proposed flowsheet for the PHEBUS FPT tests.

In addition to the gross γ-scanning, a detailed micro-γ-scanning on 5 different zones (surface area: 25 mm^2) and 13 individual points (surface area: 0.81 mm^2) was carried out on the sample. The particle morphology and the elemental composition of the individual particles were determined by SEM-EDX. Finally, the sample was successively leached with water and nitric acid, followed by the complete dissolution of the sample in a mixture of concentrated fluoric and nitric acid, and analysed by ICP-MS to determine the overall elemental and isotopic composition.

At 1 cm distance from the sample shown in Fig. 8.10, a dose level of 0.5 mSv β γ was measured.

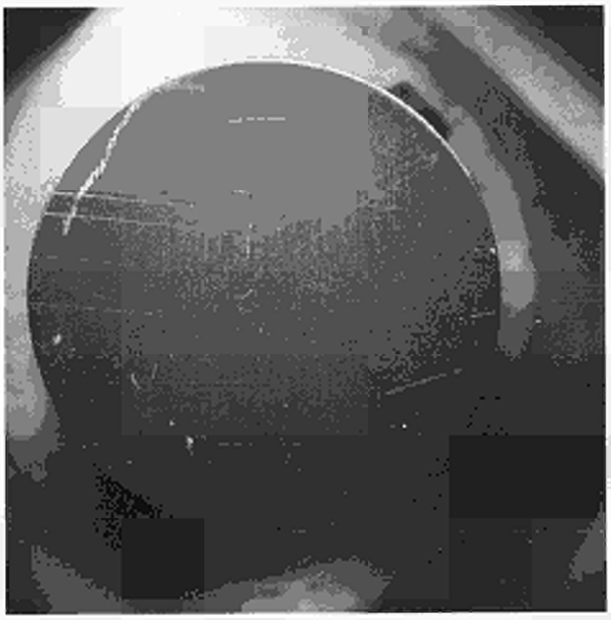

Fig. 8.10 Photograph of the sample (magnification 10x)

Experiments

The sample was taken as received and placed on a specially prepared sample holder of the micro γ-scanning apparatus. The measurements were carried out for 18000 s (dead time 0.62 %), the detector was calibrated against a standard point source. Fig. 8.11 shows the positions for the different measurements.

The calibration of the detector was made with a ^{152}Eu point source outside the hot cell. The slightly different geometry of the sample inside of the hot cell had of course an influence on the accuracy of the values given in Tab. 8.4 below. This was especially true for zone and point measurements where separate calibrations would be needed. Furthermore, up to now only 1 zone and 2 point measurements were evaluated (Tab. 8.4).

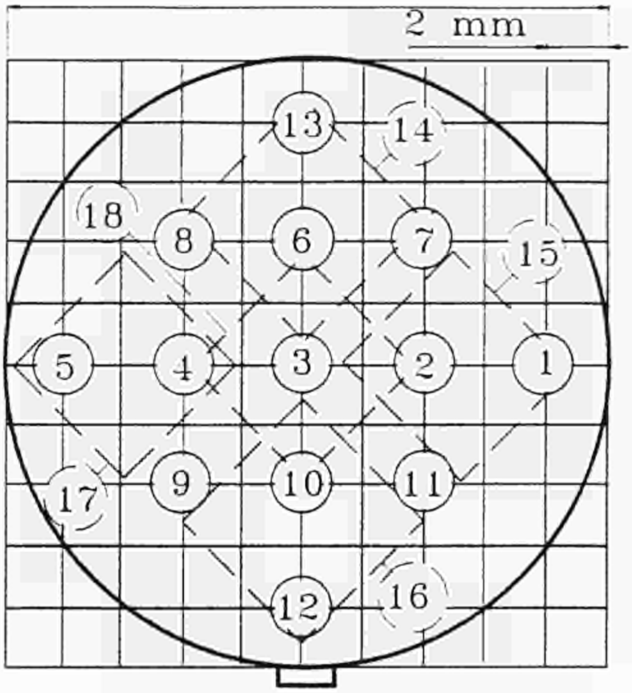

Fig. 8.11 Schematic drawing of the sample showing the positions for the different measurements

Tab. 8.4 γ-activities in mCi

Position	meas. type	surface area mm^2	^{137}Cs	^{134}Cs	^{125}Sb	^{60}Co
	global	314	$3.19 \cdot 10^{-1}$	$1.96 \cdot 10^{-2}$	$2.97 \cdot 10^{-3}$	$5.899 \cdot 10^{-5}$
16	zone	25	$6.01 \cdot 10^{-3}$	$7.33 \cdot 10^{-4}$	$9.80 \cdot 10^{-5}$	$9.18 \cdot 10^{-6}$
2	point	0.81	$2.04 \cdot 10^{-4}$	$2.92 \cdot 10^{-5}$		
10	point	0.81	$1.82 \cdot 10^{-5}$	$1.53 \cdot 10^{-5}$		

** calculated for the reference date 13.4.1992*

The main γ emitter was ^{137}Cs. The other isotopes measured by γ-spectroscopy were ^{134}Cs, ^{125}Sb and ^{60}Co; the latter was detected at very low concentration and thus may not originate from the sample.

SEM pictures showed a light deposit of particles on the zircaloy disc (Fig. 8.12).

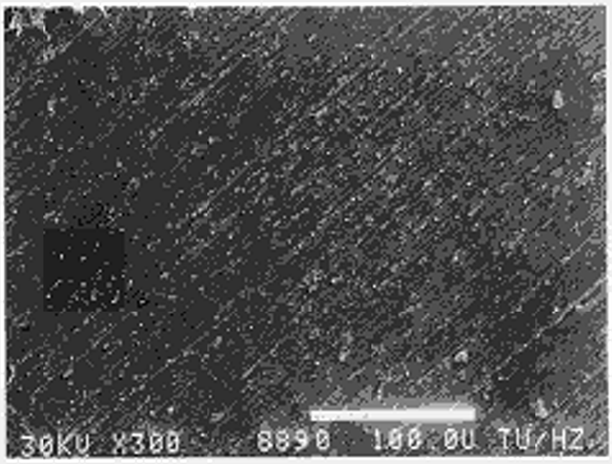

Fig. 8.12 SEM micrograph of the sample

The particles were mostly spherical, suggesting their transport as liquid droplets. At a lower concentration, plate and needle shaped particles were observed. Particle sizes varied from about 0.05 µm to 3 µm diameter.

Most of the EDX spectra exhibited large Zr- and often weaker Sn-signals coming from the substrate. However Sn-rich spheres were also observed. In addition, ferrous (Ni, Fe, Cr) and silicate (Si, Al, Ca) particles were found. Plate-like needle-shaped particles were characterised by the presence of Cs.

EDX spectra of 93 particles were analysed and the elements present were divided into major and minor constituents (trace elements were ignored). Tab. 8.5 shows the frequency with which the elements occured in the different particles.

After examination by SEM/EDX, the specimen was submitted to a sequence of washing, leaching and dissolution procedures to determine its elemental composition:

1. washing of the cylindrical specimen support
2. leaching of the sample (together with its cylindrical support) in distilled water at 50 °C
3. leaching with 4 M HNO_3 at 80 °C (after removal of the strongly corroded cylinder)
4. leaching with 8 M HNO_3 at 80 °C
5. dissolution in conc. HF/ HNO_3 at 180 °C in an autoclave.

Tab. 8.5 Statistical evaluation of the EDX spectra

element	elemental content (percentage of particles analysed*)	
	major	minor
Zr	98	1
Sn	30	20
Si	2	15
Al	3	5
U	2	-.
Cs	2	28
Fe/Cr/Ni	2/1/-	13/7/3
Ca (Te)	2	-
Mo	1	-

**a total of 93 particles were analysed*

The qualitative mass spectra obtained by ICP-MS for the different procedure steps are shown in Fig. 8.13.

As expected, Rb and Cs were mainly detected in the water rinsing solution. Acid rinsing and especially dissolution in HF/HNO_3 gave a large excess of elements from the sample support. The specimen as delivered was glued on a cylindrical specimen holder. For the leaching in water and 4 M nitric acid the sample was treated as such. As a consequence the acid leachate had a dark brown color and large amounts of corrosion products (Fe, Cr, Ni) and also natural Mo were detected by ICP-MS, making a detection of fission product Mo impossible. For the following leaching and dissolution steps the sample holder had been removed and now a small amount of fission product Mo was found in the leachate, but of course a quantitative determination of Mo was not possible.

A quantitative evaluation for those elements which were deposited during the VERCORS experiment gave the result shown in Tab. 8.6.

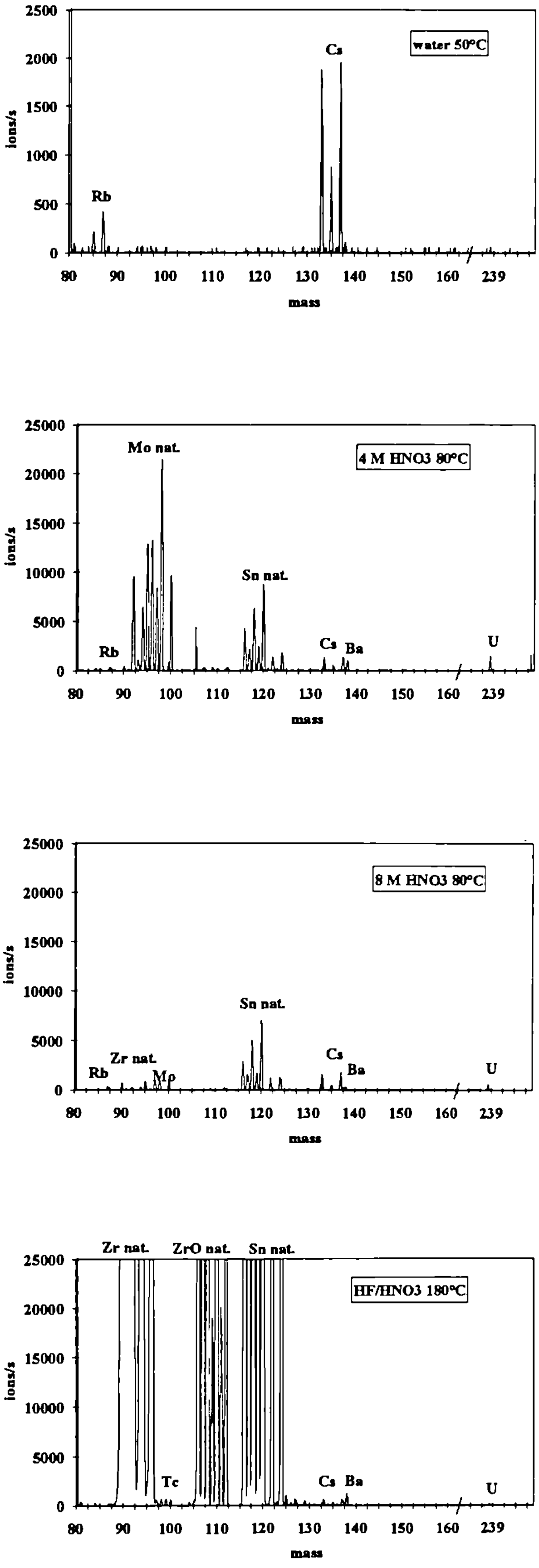

Fig. 8.13 Qualitative mass spectra of the different process streams by ICP-MS

Tab. 8.6 Elemental composition (in ng) of the deposit by ICP-MS

element	elemental composition (ng)
Rb	1970
Tc	632
Sb	536
I	312
Te	717
Cs	12496
Ba	3003
La	37
Ce	173
Pr	23
Nd	60
Np	9
U	4178
Pu	38

Discussion and conclusions

The total amount of fission product elements detected on the sample by ICP-MS was 24 µg. The main elements are Cs, Ba and U. Other elements were detected with lower concentrations: Rb, Tc, Sb, I, Te, La, Ce, Pr, Nd, Np, Pu. Possibly some traces determined were due to a contamination of the low activity sample during handling in contaminated hot cells. This seems particulary true for Rb, Np, Pu and the lanthanides, which show an inconsistent chemical behavior during the sample treatment.

The gold coating of the sample limited its dissolution in water, the subsequent acid dissolution drove out most of the iodine.

Despite the slightly different geometry used for calibration and measurement in the case of γ-spectroscopy, the total amounts of ^{137}Cs observed by γ-spectroscopy and by ICP-MS were similar (3.82 µg versus 5.10 µg, respectively).

The main signals in the EDX spectra were from Zr and Sn contained in the substrate. However also spheres were observed with a large Sn content of unknown origin . Cs signals were seen on plate-like and needle-shaped particles. This may indicate that two different chemical forms of Cs are present. However none of them corresponds to CsI (since no I was detected by EDX).

Measurement of the thermal conductivity of zirconia

According to a request from the PHEBUS project management, the ceramic shroud material (low-density yttrium-stabilized zirconia) for the in-pile set-up was characterised. Aim of this work was to measure a set of properties related to the thermal behavior of this material and to the vapor species which this ceramic might release during the reactor transient experiments. The following properties were investigated:

1. Thermal diffusivity from 700 to 2500 K, including hysteresis effects due to thermal restructuring of the sintered ceramic,
2. Structural and chemical stability during thermal treatments pertinent to the PHEBUS reactor test,
3. Melting point under different atmospheres,
4. Spectral and total emissivity as a function of temperature and relation of the latter to color changes due to chemical reduction,
5. Knudsen cell effusion rate of approximately 20 contaminant species present in the as-fabricated zirconia, and evaluation of the equilibrium vapour pressure of the main components.

The results of these investigations were summarized in three reports. The circulation of these is restricted to ITU and to the PHEBUS Project.

4.5 Post-Irradiation Examination of LWR Fuel Rods

In the framework of the contract with Siemens AG - Bereich Energieerzeugung (KWU), non-destructive and destructive examinations of power reactor fuel rods are to be carried out (see TUAR-91 and TUAR-92).

In 1993, 5 fuel rods from the Isar reactor (KKI) were received for analysis at the Institute, 28 fuel rods from the Neckarwestheim reactor (GKN-II) were conditioned and transported back to the reactor pool.

A list of the numbers and types of examinations carried out on different fuel rods in 1993 is given in Tab. 8.7.

4.6 Fabrication of Fuel Discs for the High Burnup Rim Project

182 UO_2-based fuel discs were fabricated for irradiation in the test rig IFA 601 of the Halden reactor for a project conducted by the Central Research Institute of Electric Power Industry, CRIEPI, Tokyo. The purpose of the programme is to investigate and evaluate the effect of microstructural changes (RIM-effect) in the outer regions of Light Water Reactor UO_2 fuel. To achieve this aim, CRIEPI has started an irradiation in the Halden reactor to study the influence of temperature, burnup, pressure and type of fuel on fuel surface restructuring during irradiation. The irradiation will be performed at four temperatures (600, 800, 1000, 1200 °C), to four different burnups (55, 70, 85 and 100 MWd/kg M), at two pressures (0.1 and $>$ 10 MPa) and with four types of fuel: standard UO_2 and UO_2 containing some additives.

Extensive tests were performed to define the fabrication conditions necessary to achieve the required homogeneity, density and densification behavior during post-sintering anneals. The final fabricated material was characterized by optical and electron microscopy, chemical and X-ray analysis as well as by electron probe microanalysis.

The specimens were transported to Halden, Norway in July 1993 and the irradiation was started in December 1983.

Tab. 8.7 Contract Siemens AG-KWU examinations carried out

Type of analyisis	KWO	KKGg-VI	MTS-6	GKN1-II	KKGg-VII	MTS-2	GKN1-III	KKGg-VII	MTS-III	EM& Met	KK12-I	TOTAL
Visual examination								6				6
Fuel rod length							5	4				9
Profilometry							5	4				9
Defects							2	2				4
Oxide layer thickness								4	3			7
Gamma Scan.							2	4			3	9
Gap					6		5	4				15
Fission Gas analysis					1		27	5				33
Free volume					1		27	5				33
Metallography				2	4							6
Ceramography				10	2							12
Density	9	6		7								22
H_2-Determin.		5										5
TEM										3		3
Dismantling							7					7
Weighing			13									13

5. Scientific Infrastructure

5.1 Guest scientists, visitors, training opportunities at ITU

During the exercise under review, the Institute has welcomed 5 new doctoral grantees, from France, Germany, Portugal, and Spain. In the frame of the Human Capital and Mobility Programme of the European Commission 10 postdoctoral grantees were offered the possibility to work at ITU. They came from Belgium, Germany, Greece, Italy. Potugal, and the United Kingdom.

During the same period, 4 visiting scientists (from Greece, Germany, and China) worked in the Karlsruhe laboratories of the Joint Research Centre and a visitor from Russia who was supported through a contract between DG XII, Brussels, and the Institute for High Temperatures (IVTAN) of the Russian Academy of Sciences in Moscow.

Two "stagiaires visitors" came from France and Japan. They were entirely payed by their organization of origin.

Three doctoral grantees from the Institute have obtained their PhD in 1993 at the University of their choice:

- J.A. de Carvalho Paixao, Estudo por Diffracão de Neutroës de Magnetismo do Compostos Intermetalicos de Urânio, Universidade de Coimbra (Portugal),

- Y. Kergadallan, Synthèse, croissance et études (cristallochimie, magnetochimie) de composés et d'alliages intermétalliques de stoechiometrie 1.1.1 à base d'actinides, Université de Paris XI, Orsay (France),

- P. Link, Der elektrische Widerstand von Urantellurid, Uranselenid und Plutoniumantimonid bei hohem Druck und tiefen Temperaturen, Universität Karlsruhe (Germany)

5.2 Installation of a Minor Actinide Laboratory

The Institute for Transuranium Elements is equipped for the preparation of irradiation experiments, as well as for post-irradiation examinations, and can rely on a long experience in the field. The studies on fresh fuels are performed in glove boxes, while the examination of irradiated fuels has to be done in hot cells. First devoted to the development of fuels based on uranium/plutonium, ITU has seen in recent years its centre of gravity shifted from Pu toward the minor actinides (MA). MA containing samples were produced and studied in the existing installations, either for the determination of their basic properties, or for transmutation related irradiation experiments. Small samples were handled in glove boxes, with additional lead windows when required ; for larger amounts of MA, like for the preparation of Am and Cm, of for the fabrication (chemistry) of the fuel, water-shielded cells were used.

With a view on the latest, more stringent regulations for radioprotection and the increasing demand for minor actinides-containing fuels for transmutation studies, it was decided to install a Minor Actinides Laboratory at the Institute. The purpose of this laboratory is to strengthen the tools for the fabrication and the characterisation of samples containing Am, Np, and/or Cm. The new laboratory should be highly flexible, making use of the most modern technologies, and provide for a high degree of safety for the operators (e.g. by trying to work dust-free).

For a systematic and coherent approach, three working groups were formed (planning, concept, design). A plan of the work to be performed in the MA laboratory was prepared, based on the planned irradiation experiments, and the corresponding needs for properties of the fuels and for fabrication and characterisation. By nature, the MA laboratory will not correspond to one given place in the Institute, but concern several existing laboratories, all along the fabrication and characterisation chain. Three different types of activity, each one with its specific problems, have to be considered.

- the chemistry, concerning big quantities of MA;
- the fuel pin preparation, the fabrication of samples or targets, and quality control (severe specifications);
- the analysis and the study of the materials, possibly on small samples, but according to the requirements for application.

For the first step, a sol-gel preparation technique will be used, as described in this report. The equipment is under construction, and will be installed in the available water-shielded cells.

The up-grading of existing installations for treating larger quantities of MA-fuel has started. The design for a fabrication chain is under way. It is based on the press-sinter technique, and will consist of a sequence of water-shielded cells, arranged around a modern computer-controlled and remotely operated press (Fig. 9.1).

Concerning the study and the characterisation of MA-containing fuel material, appropriate improvements of available equipment are foreseen, depending on the size of the samples and the potential dose risks for the operators.

ITU is already equipped for the chemical analysis of very small quantities of MA-containing samples, with a robotized sample preparation technique.

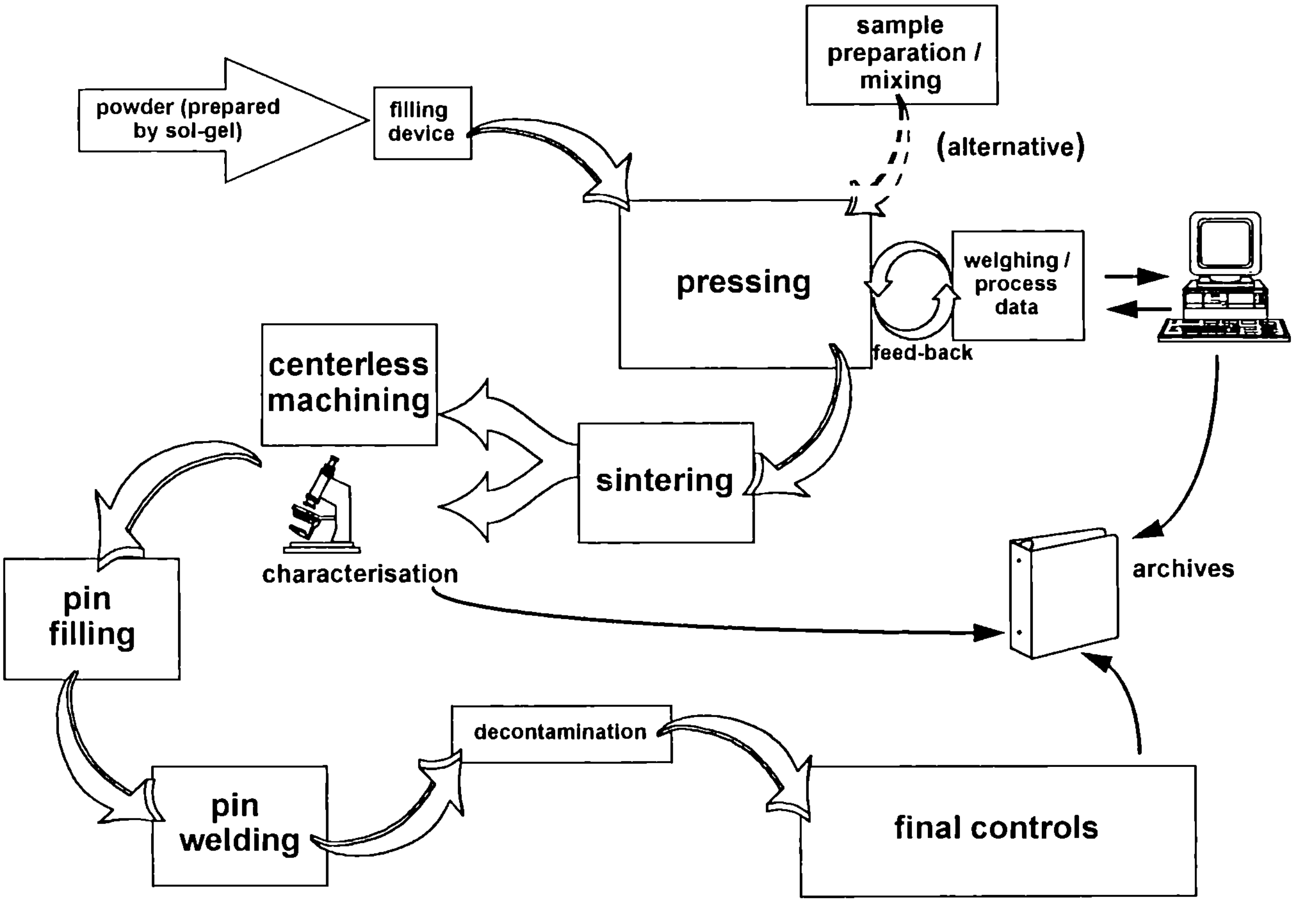

Fig. 9.1 Schematic representation of the fabrication chain for the fabrication and control of minor actinides containing fuel pins.

5.3 Quality Assurance

Rules have been established in recent years on an international level which, when rigorously applied, should guarantee a product or a service delivered by a commercial enterprise to be of consistently good quality. These rules (e.g. the EN 29000 standards) might equally well be applied to procedures and tools operative in a research laboratory.

In fact, the compliance with these standards has been requested in certain cases by customers for whom the Institute performs contract work. This compliance is verified by an accredited independent institution and/or by the customer by performing audits to check the accordance of the applied procedures with the standards and the efficiency with which these procedures are followed.

The advantages of such a quality assurance system for the customer are obvious. But also the laboratory may profit from it: The gain in transparency of working conditions as a consequence of clear definitions of competences, responsibilities, and working rules leads eventually to an increase in motivation and efficiency.

Therefore, in 1993, the decision was taken for a stepwise introduction of a quality assurance system at the Institute for Transuranium Elements.

This introduction is being pursued on two levels:

A long-term programme foresees that all production- and service-related units are subject to a well-defined quality assurance system. For this purpose, a quality manual is being written and procedures of principle and working instructions are being defined. As a consequence, some, or all, of the units concerned may have to be more or less re-organized. This process may take several years.

To satisfy immediate needs for quality assurance arising from requests of several customers, detailed quality plans are drawn up for specific tasks and procedures on a short-term basis. They concern post-irradiation examinations of fuel rods from commercial nuclear power plants and the installation of on-site laboratories for safeguards analyses in two large European reprocessing plants. These short-term plans are foreseen to become operational before the end of 1994, whereby care is being taken that they fit into the final Institute's overall quality assurance system.

ANNEXES

Annex I

Publications 1993

1. Conferences

Conference papers published in 1993 in journals or special conference proceedings volumes may appear also under paragraph 2 (Books and Periodicals)

European Winter Conference on Plasma Spectrochemistry
January 10-15, 1993, Granada (ES)

Betti, M., Garcia Alonso, J.I., Koch, L.
Determination of Selected Fission Products in Spent Nuclear Fuel by On-Line Coupling of Ion Chromatography and ICP-MS

Garcia Alonso, J.I.
ICP-MS for the Analysis of Nuclear Materials

Garcia Alonso, J.I., Betti, M., Arbore, Ph., Koch, L., Wiesmann, H.
Installation of an Elan 5000 ICP-MS Coupled to an Ion Chromatograph in a Glove Box for the Analysis of Nuclear Materials

Garcia Serrano, J., Garcia Alonso, J.I., Babelot, J.F., Closset, J.C., Koch, L., Criado, A.J.
Installation of a Laser Ablation System in a Hot Cell Coupled to a Glove Box ICP-MS for the Characterization of Solid Nuclear Samples

Conference on Neutrons and X-Rays in Magnetism
January 20 -22, 1993, Grenoble (F)

Brooks, M.S.S., Eriksson, O., Severin, L., Johansson, B.
Spin and Orbital Magnetization Densities in Itinerant Magnets

Waste Management '93
February 28-March 4, 1993, Tucson, Arizona (USA)

Nicolaou, G., Koch, L.
Radiation Dose Levels in the Handling of Minor Actinide Fuels

5th International Symposium on Advanced Nuclear Energy Research
March 10-12, 1993, Mito (J)

Lander, G.H.
Prospects for Neutron Probes in the 21st Century
Proceedings JAERI 93-228 vol. 1 (1993) 17-24

International Symposium on Nuclear Material Safeguards
March 14-18, 1993, Vienna (A)

Betti, M., Garcia Alonso, J.I., Koch, L.
Capabilities of Trace Analyis to Reveal Unknown Nuclear Activities

Brandalise, B., Ougier, M., Wagner, H.G., Wojnowski, D., Koch, L.
Robotised Equipment for the On-Site Analysis of Fissile Material

23. Journées des Actinides
April 20-23, 1993, Bühlerhöhe (D)

Almeida, T., Cox, L.E., Ward, J.W., Naegele, J.R.
Comparison of Adsorption Studies on Pu and U Metals by Photoemission Spectroscopy

Amanowicz, M., Rebizant, J., Spirlet, J.C., Vogt, O.
Transport Properties of NpP Comparison with the other Np-Monopnictides

Athanasiou, N., Politis, C., Spirlet, J.C., Ray, I., Sari, C., Moens, A., Lebrun, M., Lefbvre, P., Thiele, H., Huber, W. et al.
Synthesis and characterization of quasicrystalline materials

Bottomley, P.D.W.
Reactor Core Degradation - A Study of TMI-2 Samples at ITU Karlsruhe

Bouillet, M.N., Colineau, E., Blaise, A., Jeandey, C., Oddou, J.L., Sanchez, J.P., Rossat-Mignod, J., Spirlet, J.C., Rebizant, J.
Magnetic Behaviour of $NpPt_3$

Bourdarot, F., Burlet, P., Bouillet, M.N., Sanchez, J.P., Rossat-Mignod, J., Rebizant, J., Spirlet, J.C., Vogt, O.
Magnetic Properties of NpTe

Brooks, M.S.S., Gasche, T.
Density Functional Theory of Optical and Magneto-Optical Transitions in Actinides

Cooper, B.R., Sheng, Q.G., Benedict, U., Link, P.
Theory of Pressure Effects and the Correlated-Electron Behavior of UTe

Dabos-Seignon, S., Dancausse, J.P., Gering, E., Heathman, S., Benedict, U.
The High Pressure Phase of Plutonium

Goncalves, A.P., Waerenborgh, J.C., Henriques, R.T., Bonfait, G., Almeida, M., Spirlet, J.C.
Growth and Characterization of $UFe_{9.2}Si_{1.8}$ and UFe_6Ge_6 Single Crystals

Havela, L., Sechovsky, V., Nakotte, H., Prokes, K., de Boer, F.R., Spirlet, J.C., Kergadallan, Y., Seret, A.
Magnetic Properties of U_2T_2X Compounds

Kergadallan, Y., Peron, M.N., Meyer, D., Rebizant, J., Spirlet, J.C., Winand, J.M.
Preparation and Structural Study of new Ternary Intermetallic Compounds An_2T_2X (An = U,Np; X = In, Sn;T = Co,Ir,Ni,Pd,Pt,Rh)

Kergadallan, Y., Bednarczyk, E., Moens, A., Rebizant, J., Rijkeboer, C., Spirlet, J.C., Zwirner S.
Relations between the Localisation of the 5f Electrons and the Structure in AnTAl Compounds (T Element from the VIIIth Group)

Kergadallan, Y., Rebizant, J., Spirlet, J.C., Zwirner, S., Blaise, A., Jeandey, C., Odou, J.L., Sanchez, J.P.
Complex Behaviour of the Magnetism of the NpTAl Compounds with ZrNiAl Structure (T Element from the VIIIth Group)

Lander, G.H., Shapiro, S.M.
Observation of a Phase Transition within the ordered State of USb

Langridge, S., Stirling, W.G., Lander, G.H., Rebizant, J., Spirlet, J.C., Gibbs, D., Vogt, O.
X-Ray Resonant Magnetic Scattering from NpAs:- Observation of Critical Effects near T_N

Link, P., Braithwaite, D., Benedict, U., Wittig, J., Haire, R.G.
Resistivity and Superconductivity of Americium Metal Under Pressure up to 25 GPa

Link, P., Benedict, U., Wittig, J., Wühl, H., Rebizant, J., Spirlet, J.C.
Recent Results of High-Pressure Resistance Measurements of Actinide Compounds

Marmeggi, J.C., Lander, G.H., Ghering, P.M., Gibbs, D.
Comparison of X-Ray Synchrotron and Neutron Scattering from an Alpha-Uranium Crystal at low Temperature under Pressure

Naegele, J.R., Cox, L.E., Ward, J.W.
The Electronic Structure of Pu-Metal: An X-ray and High Resolution UV Photoemission Study

Paixao, J.A., Rebizant, J., Blaise, A., Delapalme, A., Sanchez, J.P., Nakotte, H., Burlet, P., Bonnet, M., Lander, G.H.
Magnetic Properties of U_5Sb_4

Zwirner, S., Potzel, W., Spirlet, J.C., Rebizant, J., Gal, J., Kalvius, G.M.
NpX_3 Compounds under High Pressure

4th International Conference on Nuclear Fuel Reprocessing and Waste Management RECOD '94
April 24-28, 1993, London (UK)

Glatz, J.P., Koch, L., Garcia Alonso, J.I., Pagliosa, G., Matsumura, T., Tsukuda, T.
Characterisation of Residues and Reprecipitates from Dissolver Solution of Highly Burn LWR Fuel

Workshop on Diffusion in Metals
April 26-30, 1993, Porto Alegre (BR)

Péres, R.A., Dyment, F., Abriola, D., Somacal, H., Bérmudes, G.G., Behar, M., Matzke, Hj.
Measurements of Diffusion in α-Ti Using Ion Beam Analysis

15th Annual Symposium on Safeguards and Nuclear Material Management
May 11.-13, 1993, Rome (I)

Davidson, D., Verplancke, J., Vermeulen, P., Menlove, H., Wagner, H.G., Brandalise, B., Stutz, H.
A New High-Accuracy Combined Neutron/Gamma Counter for In-Glove Box Measurements of PuO_2 and MOX Safeguards Samples (OSL - Counter)

Garcia Alonso, J.I., Thoby, D., Koch, L.
ICP-MS for Fissile Material Analysis in Highly Radioactive Samples

Leitner, E., Weh, R., Nicolaou, G.
A Passive Neutron Detector for Nuclear Material Measurement in a Pilot Conditioning Facility

Li, T.K., Parker, J.L., Wagner, H.G., Goerten, J., Wellum, R., Kammerichs, K.
Plutonium Analysis of High-Burnup Spent Fuel Dissolver Solutions by Low-Energy Gamma-Ray Spectrometry

Matussek, P., Michel-Piper, I., Wagner, H.G., Brandalise, B., Cromboom, O.
First In-Field Experience with "COMPUCEA". A Portable Assay System for the Combined Determination of Uranium Concentration and ^{235}U Abundance in Uranium Solutions by NDA methods

Menlove, H., Wellum, R., Ougier, M., Wagner, H.G., Goerten, J., Mayer, K.
Performance Test of the High-Accuracy Combinded Neutron/Gamma Detector (OSL-Counter)

Sena, F., Cromboom, O., Koch, L.
Application of the Microwave Dissolution Method to Safeguards Samples

Wagner, H.G., Riemer, G., Kiewit, K., Ottmar, H., Eberle, H., Baumann, S., Kuhn, E., Cromboom, O., Ougier, M., Berg, R.
Performance Evaluation of the K-Edge Densitometer for Reprocessing Product Solutions - 8 Years of Operation

7th Annual Conference of the Aerosol Society
June 29-3., 1993, Bristol (UK)

Capéran, Ph., Somers, J., Magill, J., Richter, K., Fourcaudot, S., Barraux, P., Lajarge, P., Riera, E., Rodriguez, G., Gallego, J.A.
The Attenuation of Sound Energy in Soot and Fog Aerosols

Caperan, Ph., Somers, J., Richter, K., Fourcaudot, S.
Acoustic Agglomeration of a Fog Aerosol: The Influence of the Particle Concentration, and of the Frequency and Intensity of the Sound Field

13th ISNA International Symposium on Nonlinear Acoustics
June 28- July 2, 1993, Bergen (N)

Magill, J.
The Effect of Fluid Forces on Acoustic Aerosol Agglomeration

3rd Working Group Meeting on Targets and Fuels
June 29 - 30, 1993, Karlsruhe (D)

Babelot, J.F., Bokelund, H., Gueugnon, J.F., Koch, L., Richter, K.
Concept of a Minor Actinides Laboratory

Babelot, J.F., Fuger, J., Koch, L.
A European Collaboration in the Field of Transmutation: EFTTRA

Bokelund, H.
Actinide Fuels by the Sol-Gel Technique

Glatz, J.P., Pagliosa, G.
Dissolution of Spent Nuclear Fuels in View of Transmutation Studies

Glatz, J.P., Song, C.
Partitioning Studies

Julian Rodriguez, R., Sari, C., Criado Portal, A.J.
Study of the Phase Diagram U-Zr-Np

Koch, L.
Evaluation of P&T Research

Koch, L.
Specifications of MA Fuels

Matzke, Hj.
Inert Matrix Targets: Radiation Damage Effects

Nicolaou, G.
The Superfact Irradiation Experiment

Walker, C.T.
EPMA Investigation of Targets Irradiated in the Superfact Experiment

14th Int. Conf. of the International Association for the Advancement of High Pressure Science and Technology (AIRAPT)
June 28.- July 2 ,1993, Colorado Springs, CO (USA)

Benedict, U.
Updated Diagrams of High-Pressure Phase Relations in f-Metals

Gerward, L., Staun Olsen, J., Benedict, U., Dancausse, J.P., Heathman, S.
High-Pressure X-Ray Diffraction Studies of ThS_2, US_2, and other AnX_2 and AnXY Compounds

XXVIII CSL Post-Symposium on Analytical Applications of Glow Discharges in Optical and Mass Spectrometry
July 4-7, 1993, York (UK)

Betti, M., Rasmussen, G., Dockendorf, G., Schrodt, H., Koch, L., Milton, D.M.P.
Adaptation of a Glow Discharge Mass Spectrometer in a Glove-Box for Nuclear Sample Analysis

Milton, D.M.P., Hutton, R.C., Betti, M.
Design Considerations for a Glow Discharge Ion Source Housed inside a Glovebox

Swiss Summer-School on Neutron Scattering
August 15-21, 1993, Zuoz (CH)

Lander, G.H.
Magnetic Excitations
Proc. PSI-Report 93-01 (1993) 235 - 252

13th European Conference on Thermophysical Properties
August 28-September 1, 1993, Lisbon (P)

Hiernaut, J.P., Ronchi, C.
Recent Developments in Multichannel Pyrometry

7th International Conference on Radiation Effects in Insulators (REI-7)
Sepember 6-10, 1993, Nagoya (J)

Matzke, Hj., Turos, A., Linker, G.
Polygonization of Single Crystals of the Fluorite-Type Oxide UO_2 due to High Dose Ion Implantation

International Conference on Future Nuclear Systems: Emerging Fuel Cycles and Waste Disposal Options (Global '93)
September 12-17,1993, Seattle, Washington (USA)

Babelot, J.F., Bokelund, H., Gueugnon, J.F., Koch, L., Richter, K.
Fuel Studies for the Transmutation - Concept of a Minor Actinides Laboratory

Prunier, C., Boussard, F., Koch, L., Coquerelle, M.
Some Specific Aspects of Homogeneous Am and Np Based Fuels Transmutation through the Outcome of the Superfact Experiment in the Phenix Fast Reactor

van Geel, J., Schmidt, H.E., Matzke, Hj., Nicolaou, G., O'Carroll, C.
European Research and Development Work on the Safety of the Nuclear Fuel Cycle

5th Meeting of the European Severe Accident Chemistry Group on High Temperature Chemistry
September 23, 1993, Winfrith (UK)

Bottomley, P.D.W., Coquerelle, M.
High Temperature Chemical Interactions observed in the TMI-2 Reactor Accident

International Conference "Actinides '93"
September 19-24,.1993, Santa Fe, NM (USA)

Axe, J.D., Grübel, G., Lander, G.H.
Structure and Phase Transformations in Uranium Metal

Benedict, U.
Structural and Physical Properties of Actinide Materials at High Pressure

Brooks, M.S.S., Gasche, T., Eriksson, O., Severin, L.Johansson, B.
Density Functional Theory of Spin and Orbital Magnetization Densities in Actinide Magnets

Gensini, M.
Modeling of the High Pressure Behavior of the Actinide Monopnictides and Monochalcogenides

Goffart, J., Jemine, X., Wastin, F., Fuger, J.
Organo-f-Element Thermochemistry

Lander, G.H., Stirling, W.G., Langridge, S., Tang, C.C. Gibbs, D.
Resonant Magnetic X-Ray Scattering - A New Probe for Actinides

Leal, J.P., Marcalo, J., Pires de Matos, A., Marshall, A.G., Spirlet, J.C.
Gas Phase C-C and C-H Bond Activation in Arenes by Uranium and Thorium Ions

Link, P., Benedict, U., Wittig, J., Wühl, H., Rebizant, J., Spirlet, J.C.
The Electrical Resistance of PuSb under High Pressure

Link, P., Braithwaite, D., Benedict, U., Wittig, J., Haire, R.G. (invited)
Resistivity and Superconductivity of Americium Metal Under Pressure up to 25 GPa

Mayer, K., Kanellakopoulos, B., Naegele, J.R., Koch, L.
On the Valency State of Americium in $(U_{0.5}Am_{0.5})O_{2-x}$

Naegele, J.R., Cox, L.E., Ward, J.W.
X-Ray and High Resolution UV Photoemission Study of 5f Electron Localization in α-and δ-Pu

Paixao, J.A., Rebizant, J., Blaise, A., Delapalme, A., Sanchez, J.P., Nakotte, H., Burlet, P., Bonnet, M., Lander, G.H.,
Magnetism of a new U-Sb-Phase: U_5Sb_4

Ronchi, C., Hyland, G.J.
Analysis of Recent Measurements of the Heat Capacity in Uranium Dioxide

Sheng, Q.G., Cooper, B.R., Benedict, U., Link, P.
Theory of Pressure Effects and the Correlated-Electron Behavior of Uranium Monochalcogenides

Zwirner, S., Kalvius, G.M., Potzel, W., Spirlet, J.C., Rebizant, J., Geibel, Ch., Steglich, F.
Electron Configuration and Magnetism of $NpPd_2Al_3$

Zwirner, S., Potzel, W., Kalvius, G.M., Gal, J., Rebizant, J., Spirlet, J.C.
High-Pressure Mössbauer Study of NpX_3 Compounds

Spent Fuel Workshop '93
September 27-29, 1993, Santa Fe, NM (USA)

Coquerelle, M.
Characterisation of Spent Fuels irradiated at high burn-up. Overview of the Studies developed at ITU

Matzke, Hj.
Leaching of UO_2 and of SIMFUEL with up to 8 at. % Simulated Burnup

I&EC Special Symposium, American Chemical Society
September 27-29, 1993, Atlanta, GA (USA)

Glatz, J.P., Song, C., He, X., Bokelund, H., Koch, L.
Partitioning of Actinides from HAW in a continuous Process by Means of Centrifugal Extractors

Conference on the Technical Basis for Measuring, Modeling and Mitigating Toxic Aerosols
September 26 - October 1, 1993, Albuquerque, New Mexico (USA)

Magill, J., Werner, P., Schmidt, H.E.
Toxic Aerosol Mitigation using High-Intensity Sound

6th International Conference on Fusion Reactor Materials
(ICFRM-6)
September 27-October 1, 1993 Stresa (I)

Dalle Donne, M., Scaffidi, F., Ferrero, C., Ronchi, C.
Modelling of the Swelling and Tritium Release in Irradiated Beryllium

Int. Workshop on "Fusion Materials"
October 4 - 6, 1993, Karlsruhe (D)

Dalle Donne, M., Scaffidi, F., Ferrero, C., Ronchi, C.
Computer Simulation of Tritium Retention and Release in Irradiated Beryllium

Dalle Donne, M., Scaffidi, F., Ferrero, C., Ronchi, C.
Modelling He-Induced Swelling in Beryllium During Fast Neutron Irradiation

European Aerosol Conference
October 4 - 8,1993, Duisburg (D)

Capéran, Ph., Somers, J., Richter, K., Fourcaudot, S.
Acoustic Agglomeration of Sub-Micron Particles
Proceedings J. Aerosol Sci. **24** Suppl. 1 (1993) pp. 593-594

Somers, J., Caperan, Ph., Richter, K., Fourcaudot, S.
The Influence of Particle Size Distribution on the Acoustic Aerosol Agglomeration Rate
Proceedings J. Aerosol Sci. **24** Suppl. 1 (1993) pp. 595-596

XIX Annual Meeting of the Spanish Nuclear Society
October 6 - 8,1993, Caceres (ES)

Garcia Serrano, J., Garcia Alsonso, J.I., Koch, L., Criado Portal, A.J.
Aplicaciones de la tecnica de LA-ICP-MS a la caracterizacion de combustibles nucleares irradiados

Julian Rodriguez, R., Sari, C., Criado Portal, A.J.
Estudio del sistema U-Zr-Np

E-MRS 1993 Fall Meeting
October 17 - 21,1993, St. Petersburg (Russia)

Babelot, J.F., Koch, L., Inoue, T., Kurata, M.
Determination of the Thermal Conductivity of an Experimental Nuclear Fuel

'93 Workshop on Severe Accident Research in Japan
November 1 - 2, 1993, Tokyo (J)

Bottomley, P.D.W., Coquerelle, M.
Fission Gas Release from Irradiated Fuels in Contact with Mixed Reactor Materials

22nd International Thermal Conductivity Conference
November 7 - 10, 1993, Tempe, Arizona (USA)

Babelot, J.F., Gaal, P.S., van Geel, J., Schmidt, H.E.
A Heat Flow Comparator for Measuring the Thermal Conductivity of Highly Radioactive Materials

Lucuta, P.G., Matzke, Hj., Verral, R.A., Klemens, P.G.
Analysis of SIMFUEL Thermal Conductivity

Matzke, Hj., Lucuta, P.G., Verrall, R.A., Hiernaut, J.P.
Thermophysical Properties of UO_2 and SIMFUEL - Simulated High Burn-Up Fuel

Schmidt, H.E., Richter, J., Matzke, Hj., van Geel,J.
The Effect of Self Irradiation on the Thermal Conductivity of Plutonium- and Americium Oxides

Frontiers in High Magnetic Fields 1993
November 10 - 12, 1993, Tokyo (JA)

Nakotte, N., Prokes, K., Brück, E., Svoboda, P., Sechovsky, V., Havela, L., Winand, J.M., Seret, A., Rebizant, J., Spirlet, J.C.
High-Field Magnetization of U_2T_2X Compounds ($T = Co, Ni, Rh, Pd, Ir, Pt$, and $X = In, Sn$)

38th Annual Conference on Magnetism and Magnetic Materials
(MMM-38)
Novemvber 15 - 18, 1993, Minneapolis (USA)

Solanki, A.K, Kashyap, A., Auluck, S., Brooks, M.S.S.
Band Structure Calculations of Heavy Fermion YbPdSb and YbNiSb

Nautiyal, T., Auluck, S., Brooks, M.S.S.
Electronic Structure and Stoner-Parameter for RPd_3 Compounds (R = La, Ce, Pr, and Nd)

XVIII Simposio Annual da Academia de Ciencias
do Estado di Sao Paulo, ACIESP
November 16 - 19, 1993, Sao Paulo (BR)

Arico, E.M., Apostolidis, C., Dornberger, E., Rebizant, J., Kanellakopulos, B., Zinner, L.B.
Methanesulfonates of Trivalent Lanthanoids: New Starting Compounds for Ln(III) Organometallics

IAEA Technical Meeting on Safety and Environmental Aspects of Partitioning and Transmutation of Minor Actinides and Fission Products
November 29 - December 2, 1993, Vienna (AU)

Nicolaou, G., Richter, K., Prunier, C., Koch, L.
Experience with Fast Reactor Fuels Containing Minor Actinides: Transmutation Rates and Radiation Doses

10. Journées sur les Aerosols
November 30 - December 1, 1993, Paris (F)

Capéran, Ph., Somers, J., Richter, K., Fourcaudot, S.
Evolution et rôle des particules stationnaires lors de l'agglomeration d'un broulliard en chambre acoustique

4th Int. Conf. on Chemistry Migration Behaviour of Actinides
and Fission Products in the Geosphere
(MIGRATION '93)
December 12 - 17, 1993, Charleston, SC (USA)

Merli, L., Fuger, J.
Thermochemistry of a few Lanthanide and Actinide Hydroxides and Carbonates

2. Books and Periodicals

(including publications which had been submitted or presented at conferences in 1992 and which appeared in print in 1993)

Almeida, T., Cox, L.E., Ward, J.W., Naegele, J.R.
Gas Adsorptions Studies on Pu Metal by Photoemission Spectroscopy
Surf. Sci. 287/288 (1993) 141-145

Bauer, M., Brooks, M.S.S., Dormann, E.
Orbital Polarization of the Electrons in Ferromagnetically Ordered $GdAl_2$
Phys. Rev. B 48 (1993) 1014-1021

Benedict, U., Holzapfel, W.B.
High-Pressure Studies - Structural Aspects Chapter 113 of the Handbook of the Physics and the Chemistry of Rare Earths, Vol.17 (1993) 245-300; K.A.Gschneidner, L.Eyring, G.H.Lander, G.R.Chopin (Eds.), Elsevier Science Publishers,

Benedict, U.
Pressure Induced Phase Transitions in 5f and 4f Metals and Compounds
J. Alloys Comp. 193 (1993) 88

Betti, M., Rasmussen, G., Hiernaut, T., Koch, L. Milton, D.M.P., Hutton, R.C.
Adaptation of a Glow Discharge Mass Spectrometer in a Glove Box for the Analysis of Nuclear Materials
J. Anal. At. Spectrom. (submitted)

Bottomley, P.D.W., Coquerelle, M.
Electrochemical Experiments on UO_2 corrosion in aqueous solutions
Corrosion Science 35 (1993) 377

Bottomley, P.D.W., Daguzan-Lemoine, F.
An electroanalytical examination of gas retention in a ramped $(U,Pu)O_2$ irradiated fuel
Inst. Phys. Conf. Ser. 130, 2 (1993) 243

Brooks, M.S.S.
Pressure Effects upon the Magnetization of Actinide Compounds
Physica B 190 (1993) 55-60

Brooks, M.S.S., Johansson, B.
Density Functional Theory of the Ground-State Magnetic Properties of Rare Earths and Actinides. Chapter 3 of the"Handbook of Magnetic Materials, vol. 7 (1993) 139 - 230
ed. Buschow, K.H.J., Elsevier Science Publishers

Chkuaseli, V.F., Matzke, Hj.
Fission Gas Bubble Behaviour in Uranium Dioxide
J. Nucl. Mater. 201 (1993) 92-96

Dabos-Seignon, S., Dancausse, J.P., Gering, E., Heathman, S., Benedict, U.
Pressure-induced Phase Transition in α-Pu
J. Alloys Comp. 190 (1993) 237-242

Dancausse, J.P., Heathman, S., Benedict, U., Gerward, L., Staun Olsen, J., Hulliger, F.
High Pressure X-ray Diffraction Study of UC_2 Using Synchrotron Radiation
J. Alloys Comp. 191 (1993) 309-312

Delapalme, A., Raison, P., Schweiss, P., Lander, G.H., Rebizant, J., Kanellakopulos, B.
Studies of $U(C_5H_5)_3Cl$: II - Temperature Dependence of the Configurations
Z. Kristallogr. (submitted)

Delapalme, A., Raison, P., Lander, G.H., Kanellakopulos, B.
Studies of UCp_3Cl: IV - Magnetisation Density
Mol. Phys. (submitted)

Farthing, I., Love, G., Scott, V.D., Walker, C.T.
A versatile computer program for improving the precision of quantitative electron probe microanalysis results
Inst. Phys. Conf. Ser. 130, 2 (1993) 145

Fuger, J., Haire, R.G., Peterson, J.R.
Molar Enthalpies of Formation of $BaCmO_3$ and $BaCfO_3$
J. Alloys Comp. 200 (1993) 181-185

Garcia Alonso, J.I.
Four Years of Experience with Nuclearized ELAN ICP-MS at the Institute for Transuranium Elements
Interface 6 (1993) 3-4

Garcia Alonso, J.I., Thoby, D., Giovannone, B., Koch, L., Wiesmann, H.
Performance Characteristic of a Glove Box Inductively Coupled Plasma Mass Spectrometer for the Analysis of Nuclear Materials
J. Anal. At. Spectrom. 8 (1993) 673-679

Garcia Alonso, J.I., Babelot, J.F., Glatz, J.P., Cromboom, O., Koch, L.
Applications of a Glove-Box ICP-MS for the Analysis of Nuclear Materials
Radiochim. Acta 62 (1993) 71-79

Geerlings, M.W., Kaspersen. F.M., Apostolidis, C., van der Hout, R.
The Feasibility of ^{225}Ac as a Source of α-Particles in Radioimmunotherapy
Nucl. Med. Commun. 14 (1993) 121-125

Gensini, M., Haire, R.G., Benedict, U., Hulliger, F.
High-Pressure Behavior of CmBi and UBi
Physica B 190 (1993) 75-83

Gensini, M., Benedict, U., Rebizant, J.
High-pressure Phase and Compressibility of NpSe
J. Alloys Comp. 201 (1993) L19 - L20

Hiernaut, J.P., Hyland, G.J., Ronchi, C.
Premelting Transition in Uranium Dioxide
Int. J. Thermophys. 14 (1993) 259-283

Hocking, W.H., Verrall, R.A., P.G. Lucuta, Matzke, Hj.
Depth Profiling Studies of Ion-Implanted Cesium and Rubidium in SIMFUEL and Uranium Dioxide
Radiat. Eff. Defects Solids 125 No. 4 (1993) 299-321

Holland-Moritz, E., Lander, G.H.
Neutron Inelastic Scattering from Actinides and Anomalous Lanthanides. Chapter of the "Handbook on the Physics and Chemistry of the Rare Earths". Eds.:Gschneidner,K.,Lander,G.H. "Rare-Earth Handbook" Series Vol. 19

Joachim, J.E., Apostolidis, C., Kanellakopulos, B., Maier, R. Marques, N., Meyer, D., Müller, J., de Matos, A.P., Nuber, B., Rebizant, J. et al.
Metallorganische Chemie des Technetiums. VIII. Technetium(I)-carbonyl-Komplexe mit Polyprazol-1-yl-borato-Liganden im Vergleich mit seinen Mn- und Re-Homologen
J. Organomet. Chem. 448 (1993) 119-129

Joachim, J.E., Apostolidis, C., Kanellakopulos, B., Maier, R., Ziegler, M.L.
Synthese, Charakterisierung u. Untersuchung der Verbindungen Hydrotris(1-pyrazolyl)borato-technetium(VII)trioxid u.Hydro-tris (3,5-dimethyl-1-pyrazolyl)borato-technetium(VII)trioxid
Z. Nat.forsch. B: Anorg. Chem., Org. Chem. 48b (1993) 227-229

Joachim, J.E., Apostolidis, C., Kanellakopulos, B., Maier, R.Meyer, D., Rebizant, J., Ziegler, M.L.
Synthese, Charakterisierung und Röntgenstrukturanalyse von μ-Distickstoff-bis[hydrotris (3,5-dimethylpyrazolyl)-borato-technetium-dicarbonyl], $[L^*Tc(CO)_2]_2(\mu\text{-}N_2)$
J. Organomet. Chem. 455 (1993) 137-141

Joachim, J.E., Apostolidis, C., Kanellakopulos, B., Meyer, D., Raptis, C., Rebizant, J., Ziegler, M.L.
Synthese, Charakterisierung und Röntgenstrukturanalyse von 5-Tetramethylazacyclopentadienlytechnetiumtricarbonyl $(Me_4C_4N)Tc(CO)_3HNC_4Me_4$ und seinen Mn- und Re-Homologen
J. Organomet. Chem. (submitted)

Johansson, B., Brooks, M.S.S.
Theory of Cohesion in Rare Earths and Actinides Chapter 112 of the Handbook of the Physics and the Chemistry of Rare Earths, Vol.17 (1993) 149 - 244; K.A.Gschneidner, L.Eyring, G.H.Lander, G.R.Chopin (Eds.), Elsevier Science Publishers

Julian Rodriguez, R., Sari, C., Criado Portal, A.J.
Investigation of the Np-Zr and U-Zr-Np Systems
J. Alloys Comp. (submitted)

Kern, S., Lander, G.H., Soderholm, L., Loong, C.K. Trouw, F., Cort, B., Welp, U.
Neutron Inelastic Scattering Studies of UF_4 and NpF_4
J. Chem. Phys. (submitted)

Kitazawa, H., Kwon, Y., Ohe, Y., Amanowicz, M., Ayache, C., Rossat-Mignod, J., Rebizant, J., Spirlet, J.C., Suzuki, T., and Kasuya, T.
Low-Temperature Magnetoresistance and Magnetic Phase Diagram of the Intermetallic Actinide Compound $NpPt_3$
Physica B 186 - 188 (1993) 694

Kurata, M., Inoue, T., Sari, C.
Redistribution Behavior of Various Constituents in U-Pu-Zr Alloy and U-Pu-Zr Alloy Containing Minor Actinides and Rare Earths in a Temperature Gradient
J. Nucl. Mater. (submitted)

Lander, G.H.
Resonant Magnetic Scattering from 5f Magnetic Materials
J. Appl. Phys. 73 (1993) 6877-6882

Lander, G.H.
Neutron and Synchrotron X-Ray Scattering Experiment son Actinides
Physica B 186-188 (1993) 664-669

Lander, G.H.
Neutron Elastic Scattering of Actinides and Anomalous Lanthanides,
Chapter 117 of the Handbook of the Physics and the Chemistry of Rare Earths, Vol.17 (1993) 635-709; K.A.Gschneidner, L.Eyring, G.H.Lander, G.R.Chopin (Eds.)Elsevier Science Publishers

Lander, G.H. and Aeppli, G.
Neutron Scattering Studies of Magnetic Properties of Actinide Systems, in "Selected Topics in Magnetism", eds. L.C. Gupta and M.S. Multani, World Scientific, Singapore, 1993, p. 233 - 36

Langridge, S., Stirling, W.G., Lander, G.H., Rebizant, J.Spirlet, J.C., Gibbs, D., Vogt, O.
X-Ray Study of the Critical Magnetic Scattering in NpAs
Europhys. Lett. 25 (1993) 1994

Langridge, S., Stirling, W.G., Lander, G.H., Rebizant, J., Gibbs, D.
Resonant Magnetic X-Ray Scattering Studies of NpAs. I - Magnetic and Lattice Structure
Phys. Rev. B Condensed Matter (submitted)

Langridge, S., Stirling, W.G., Lander, G.H., Rebizant, J., Gibbs, D.
Resonant Magnetic X-Ray Scattering Studies of NpAs. II - The Critical Regime
Phys. Rev., B Condensed Matter (submitted)

Lassmann, K., O'Carroll, C., van de Laar, J., Walker, C.T.
The Radial Distribution of Plutonium in High Burn-Up UO_2 Fuels
J. Nucl. Mater. (submitted)

Lausch, J., Berg, R., Koch, L., Coquerelle, M., Glatz, J.P., Walker, C.T., Mayer, K.
Dissolution Residues of Highly Burned Nuclear Fuels
J. Nucl. Mater. (submitted)

Link, P., Benedict, U., Wittig, J., Wühl, H.
The Electrical Resistance of USe under High Pressure
Physica B 190 (1993) 68

Maier, R., Kanellakopulos, B., Apostolidis, C., Meyer, D., Rebizant, J.
Molecular Structure and Charge Distribution in Organometalics of the 4f and 5f Elements V: Crystal and Molecular Stucture of Tetrakis(5-Cyclopentadienyl)-Thorium(IV)
J. Alloys Comp. 190 (1993) 269-271

Maier, R., Apostolidis, C., Müller, J., Kanellakopulos, B., Domingos, A., Marques, N., Pires de Matos, A.
Molelecular Structure and Charge Distribution in Compounds of the 5f-Elements. VI: 1:1 Adducts of Uranium(IV)-Hydrotris(3,5-Dimethylpyrazol-1-yl)Borate-Trichloride with Lewis Bases
Polyhedron (submitted)

Marmeggi, J.C., Lander, G.H., Brückel, T.
Progress Towards Producing a Monodomain in the Charge-Density-Wave State of Alpha-Uranium
Solid State Commun. 87 (1993) 837-841

Matzke, Hj.
Ceramics for Energy Production and Environmental Applications with Emphasis on Nuclear Energy
Ceram. Acta (submitted)

Matzke, Hj.
Oxygen Potential in the Rim Region of High Burnup UO_2 Fuel (RIM Contr. No 3)
J. Nucl. Mater. (submitted)

Matzke, Hj.
Ion Beam Analyses of Ceramics and Glasses in Nuclear Energy
Surf. Interface Anal. (submitted)

Mendik, M., Wachter, P., Spirlet, J.C., Rebizant, J.
The Intermediate Valent Pu Monochalcogenides : Negative Elastic Constants, Physica B 186 - 188 (1993) 678

Mogensen, M., Bagger, C., Walker, C.T.
An Experimental Study of the Distribution of Retained Xenon in Transient-Tested UO_2 Fuel
J. Nucl. Mater. 199 (1993) 85-101

Mogensen, M., Bagger, C., Toftegaard, H., Knudsen, P., Walker, C.T.
Observations of Athermal Gas Release from Water-Reactor Fuel at Extended Burnup
J. Nucl. Mater. 202 (1993) 199-209

Monachesi,. P., Domanski, Z., Brooks, M.S.S.
Optical and Magneto-Optical Properties of PrSb
Phys. Rev. B (submitted)

Naegele, J.R., Cox, L.E., Ward, J.W.
Nature of the 5f electrons in Ga-stabilized δ-Pu: A high revolution photoemission study
Phys. Rev. Letters (submitted)

Nakotte, H., de Boer, F.R., Havela, L., Svoboda, P., Sechovsky, V., Kergadallan, Y., Spirlet, J.C. Rebizant, J.
Magnetic Anisotropy of UCoGa
J. Appl. Physics 73 (1993) 6554

Nordström, L., Johansson, B., Brooks, M.S.S.
Calculations of the Electronic Structure and the Magnetic Moments of $Nd_2Fe_{14}B$
J.Phys. Condens. Matter 5 (1993) 7859-7870

Paixao, J.A., Lander, G.H., Tang, C.C., Stirling, W.G., Blaise, A., Burlet, P., Brown, P.J., Vogt, O.
Magnetization, Neutron-, and Resonant X-Ray Diffraction Studies of $U_{0.85}Th_{0.15}Sb$
Phys. Rev. B 47 (1993) 8634-8645

Paixao, J.A., Delapalme, A., Paulus, W., Brück. E.
Structure of URuAl by Single-Crystal Neutron Diffraction at 120K
Z. Kristallogr. (submitted)

Paixao, J.A., Lander, G.H., Delapalme, A., Nakotte, H., de Boer, F.R., Brück, E.
Hybridization Effects in Uranium Compounds - Evidence for strong Anisotropy
Europhys. Lett. 24 (1993) 607-611

Paolasini, L., Paixao, J.A., Lander, G.H., Delapalme, A., Sato, N., Komatsubara, T.
Magnetization Density in the Heavy-Fermion UPd_2Al_3
J. Phys., Condens. Matter 5 (1993) 8905-8910

Paolasini, L., Paixao, J.A., Lander, G.H., Burlet, P., Sato, N., Komatsubara, T.
Field Dependence of the Magnetic Structure of UPd_2Al_3 in the Normal State
Phys. Rev. B (submitted)

Peron, M.N., Kergadallan, Y., Rebizant, J., Meyer, D., Zwirner, S., Havela, L., Nakotte, H., Spirlet, J.C.Kalvius, G.M., Colineau, E. et al.
A New Family of Actinide Ternary Intermetallic Compounds
J. Alloys Comp. (1993) 203-208

Peterson, J.R., Heathman, S., and Benedict, U.
Energy Dispersive X-ray Diffraction of $NdBr_3$ at Pressures up to 52 GPa,
J. Alloys comp. 193 (1993) 306

Raison, P., Delapalme, A., Kiat, J.M., Schweiss, P., Kanellakopulos, B., Rebizant, J., Apostolidis, C., Gonthier-Vassal, A., Lander, G.H., Brown, P.J.
Studies of $U(C_5H_5)_3Cl$: I - Evidence for Structural Phase Transitions below Room Temperature
Z. Kristallogr. (submitted)

Raison, P., Lander, G.H., Delapalme, A., Williams, J.H., Kahn, R., Carlile, C.J., Kanellakopulos, B.
Studies of $U(C_5H_5)_3Cl$: III - Reorientational Motions of Cyclopentadienyl Rings
Mol. Phys. (submitted)

Ronchi, C., Hiernaut, J.P., Selfslag, R., Hyland, G.J.
Laboratory Measurement of the Heat Capacity of Urania up to 8000 K;
I. Experiment
Nucl. Sci. Eng. 113 (1993) 1-19

Sari, C., Walker, C.T.
Interaction of Stainless Steel with Metallic Alloys of U-Pu-Zr Containing Minor Actinide and Rare Earth Elements
J. Nucl. Mater. (submitted)

Severin, L., Gasche, T., Brooks, M.S.S., Johansson, B.
Calculated Curie Temperatures for RCo_2 and RCo_2H_4 Compounds
Phys. Rev. B48 (1993) 13547-13549

Severin, L., T., Brooks, M.S.S., Johansson, B.
Relationsship between the Coulomb Integral U and the Stoner Parameter I
Phys. Rev. Lett. 71 (1993) 3214-3217

Somers, J., Capéran, Ph., Magill, J., Richter, K., Fourcaudot, S., Barraux, P., Lajarge, P., Riera, E., Rodriguez, G., Gallego, J.A., et al.
Verbesserung der Effektivität von elektro statischen Filtern mittels akustischer Aerosol Vorbehandlung
Staub Reinh. Luft (submitted)

Spirlet, M.R., Rebizant, J., Liegeois-Duyckaerts, M.
Structure of Lithium Copper Pyrophosphate, $Li_2CuP_2O_7$
Acta Crystallogr. C49 (1993) 209-211

Spirlet, M.R., Rebizant, J., Apostolidis, C., Kanellakopoulos, B.
Structure of Tris(µ5-cyclopentadienyl)uranium Thiocyanate
Acta Crystallogr. C49 (1993) 929-931

Spirlet, M.R., Rebizant, J., Bettonville, S., Goffart, J.
The Crystal Structure of Tris(Indenyl) UraniumTrifluoroacetate
J. Organomet. Chem. (submitted)

Spirlet, M.R., Rebizant, J., Bettonville, S., Goffart, J.
Tris[(1,2,3-n)-1-ethylindenyl]-methylthorium (IV)
Acta Crystallogr. C49 (1993) 1138-1140

Staun Olsen, J., Gerward, L., Dancausse, J.P., Gering, E.
Developments and New Possibilities in High Pressure Powder Diffraction with Synchrotron Radiation Results for Cerium Metal and U_6Fe
Phys., B Condens. Matter 190 (1993) 92-97

Stirling, W.G., Lander, G.H.
Resonant Magnetic Scattering from 5f Magnetic Materials
J. Appl. Physics 73 (1993) 6877

Wastin, F., Rebizant, J., Spirlet, J.C., Fuger, J., Kanellakopulos, B., Sechovsky, V.
Magnetic Study of New Pu (Mt: 3d, 4d, or 5d Transition Metal)$_2$Si$_2$ Intermetallic Compounds
J. Alloys Comp. 193 (1993) 119

Wastin, F., Rebizant, J., Spirlet, J.C., Sari, C., Walker, C.T., Fuger, J.
New Transuranium Intermetallic Compounds with $ThCr_2Si_2$-and $CaBe_2Ge_2$-Type Structures
J. Alloys Comp. 196 (1993) 87-92

Wastin, F., Rebizant, J., Sanchez, J.P., Blaise, A., Goffart, J., Spirlet, J.C., Walker, C.T., Fuger, J.
New Actinide Ternary Intermetallic Compounds: Synthesis, Characterisation, and Physical Properties
J. Alloys Comp. (submitted)

Zwirner, S., Potzel, W., Spirlet, J.C., Rebizant, J., Gal, J., Kalvius, G.M.
NpX_3 Compounds under High Pressure
Physica B 190 (1993) 107

Zwirner, S., Spirlet, J.C., Rebizant, J., Potzel, W. Kalvius, G.M., Steibel, Ch. Steglich, F.
Mössbauer Spectroscopy of $NpPd_2Al_3$
Physica B 186 - 188 (1993) 681

Zwirner, S., Spirlet, J.C., Munch, K.H., Kratzer, A., Asch, L., Kalvius, G.M.
A USR Study of UIn_3, and U $(Sn_{0.5}\,In_{0.5})_3$
Physica B 186 - 188 (1993) 798

3. Reports

Capéran, Ph.
The Attenuation of Sound in Fog and Soot Aerosols
K0293167 (1993)

Glatz, J.P., Bottomley, D., Coquerelle, M.
Phebus PF Round Robin Test - Analysis of Sample OV1-315 (24) (0) Impactor Plate 5 Punch 4/5
K0293176 (1993)

Lassmann, K., O'Carroll, C., van de Laar, J., Walker, C.T.
Radial Distribution of Plutonium in High Burn-up Fuels
K0293171 (1993)

Matzke, Hj., Tebaldi, V.
Oxygen Potential Measurements on a Fuel Piece from the
BR3 Fuel for the PHEBUS FP Tests
K0293170 (1993)

Nicolaou, G., Koch, L.
Proceedings of the Working Group Meeting on Target and Fuels
Karlsruhe, Institut for Transuranium Elements, 23.-24.6.1993
K0293169 (1993)

Pereira, T.M.
Sound Wave Analysis and Flow Master Control from a Personal Computer - Reference Manual
K0293172

Richter, K., Gueugnon, J.F., Fuchs, C., McGinley, J.
Experience d'irradiation POMPEI
K0293166 (1993)

Richter, K., Gueugnon, J.F., Fuchs, C., McGinley, J.
Standards (U,Pu)O2 pour densitomètre hybride K-edge
K0293175 (1993)

Ronchi, C., Hiernaut, J.P., Hyland, G.J.
X-Points in the Spectral Emissivity of Solid and Liquid Refractory Transition Metals Measured by Multichannel Pyrometry
EUR 14220 EN (1993)

Schmidt, H.E., Richter, J., Ruczka, L. (eds)
Institute for Transuranium Elements Annual Report 1992
EUR 15154 EN (1993)

Somers, J., Capéran, Ph.
An Investigation of the Influence of Acoustic Agglomeration
on the Efficiency of an Electrostatic Precipitator
K0293168 (1993)

Tasman, H.A., Pellottiero, D., Introvigne, B.
Thermomètre à ultrason: conception, fabrication, étalonnage
K0293165 (1993)

Tasman, H.A.
Design of Multiple-Section Sensors for Ultrasonic Thermometry
K0293173 (1993)

Tasman, H.A.
Black Box Mark 3: Control and Evaluation Electronics and Software for Ultrasonic Thermometry
K0293174 (1993)

4.0 Patents

a) Patents granted in 1993

van Geel, J., Fuger, J., Koch, L.
Verfahren zur Erzeugung von Aktinium-225 und Wismut-213
Patent Nr.:635619; Granting date: 25.03.93
Country: AU (WO)

Koch L., Apostolidis, C., Babelot J., Molinet R., Kehoe R.
Verfahren zur Trennung von Stoffgemischen durch Lösungsmittelextraktion in wässsrig / organischer Phase in Gegenwart von Laserstrahlung
Patent Nr.: 88031; Granting date: 17.05.93
Country: LU

Magill, J.
Fremgangsmåde og udstyr til kontrolleret nedbrydning af en aerosol
Patent Nr.: 166484; Granting date: 01.06.93
Country: DK

Hiernaut, J.-P., Werner, P.
Verfahren und Vorrichtung zum Herstellen eines Pulvers von amorphen Partikeln einer keramischen oder metallischen Substanz
Patent Nr.: 0361396; Granting date: 18.08.93
Country: AT BE CH DE ES FR GB GR IT LI LU NL SE (registered at the OEB (Office Européen des Brevets)

van Geel J., Werner, P., Hiernaut, J.-P., Magill, J.
Vorrichtung zum Herstellen amorpher Keramikstoffe oder Metallegierungen
Patent Nr.: 167215; Granting date: 20.09.93
Country: EP

Ronchi, C., Hiernaut, J.P., Beukers, R., Heinz., W., Selfslag R.
Multi-Wavelength Pyrometer
Patent Nr.: 639029; Granting date: 09.11.93
Country: AU (WO)

b) Patent applications in 1993

Demars, P., Brandalise, B.
Smart Interface for Video Titrator VIT90 (P/2411)

van Geel, J., Matzke, Hj.
Brennstoff für Leichtwasserreaktoren (P/2412)

Ronchi, C.
A method for evaluating the channel signals of a multichannel pyrometer (P/2422)

Magill, J., Werner P.,
Fahrbare Maschine zur Beseitigung von toxischen Aerosolen aus Gasatmosphären (P/2423)

Matzke, Hj., Kinoshita, M.
Modifizierter Kernbrennstoff zur Verzögerung der Entstehung des RIM-Effekts (P/2429)

Annex II

Collaborations with External Organisations

Argentina

CNEA Buenos Aires: Diffusion in solids (F. Dyment)

Austria

International Atomic Energy Agency, Vienna: Evaluation and Automation of techniques for safeguards analysis

Belgium

University of Liège: Single crystal growth, X-ray diffraction, and analysis (J. Goffart, L. Martinot, M.R. Spirlet)

Canada

AECL Chalk River: Gas release, SIMfuel production and property studies (I. Hastings, P. Lucuta, R. Verrall)

AECL Whiteshell: Behaviour of Rb and Cs in SIMfuel (W. Hocking)

McMaster University, Hamilton: Synchrotron X-ray scattering (B. Gaulin)

China

University of Beijing, Beijing: TRPO separation scheme development (C. Song)

Czech Republic

University of Prague: Magnetic and electrical measurements (V. Sechovsky, L. Havela); Gas release measurements (V. Balek)

Denmark

Risø National Laboratory: Neutron scattering (B. Lebech)

Technical University Lingby: High-pressure X-ray diffraction (L. Gerward)

University of Copenhagen: High pressure X-ray diffraction (J. Staun-Olsen)

France

CEA, Cadarache: Transmutation of actinides - irradiation experiments: DEC (J.L. Faugère, R. Ginier, Y. Guerin, C. Prunier, D. Warin); DER (A. Lanquille, J. Rouault); DRN (M. Salvatores);

CEA, Cadarache: TRANSURANUS fuel pin development (J.P. Pages)

CEN, Grenoble: Neutron diffraction, magnetic studies, transport properties and Mössbauer studies (A. Blaise, P. Burlet, J.M. Fournier, and J.P. Sanchez)

CEN, Saclay: Neutron diffraction (A. Delapalme)

CNRS (Lab. de Cristallographie), Grenoble: Crystallography of phase transitions (J.C. Marmeggi)

CNRS, Orsay: Basic studies on spent UO_2 fuel (J.C. Dran)

COGEMA, SGN, La Hague: On-site laboratories

Electricité de France, Paris: TRANSURANUS fuel pin code development (B. Salles)

ESRF, Grenoble: Synchrotron studies on actinides (C. Vettier, G. Grübel)

FRAMATOME, Paris: TRANSURANUS fuel pin code development (P. Blanpain)

ILL, Grenoble: Polarized neutron diffraction and neutron inelastic scattering (P.J. Brown, C. Zeyen)

Germany

Apparatebau Rothemühle, Wenden: Acoustic aerosol scavenging (W. Niggeschmidt, N. Seyfert)

Hahn-Meitner-Institut, Berlin: Ranges of ions in solids, B-profiles in leached glasses (D. Fink, J. Biersack)

Hahn-Meitner-Institut, Berlin: High-energy ion implantation (S. Klaumünzer)

TECHNOMAR: Fast multichannel pyrometry (H. Dippelhens)

KfA Jülich, Inst. für Festkörperforschung: Electrical resistivity under pressure (J. Wittig)

KfA Jülich, Institut für Chemische Technologie: Sample characterization (A. Solomah)

KfK, Karlsruhe, Inst. für Heisse Chemie: Susceptibility and crystal preparation (B. Kanellakopulos); reprocessing (H.J. Bleyl)

KfK, Karlsruhe, INE: Waste characterisation (L. Kahl)

KfK, Karlsruhe, INFP: Radiation damage studies, RBS analyses, channeling, ion implantation (O. Meyer, G. Linker)

KfK, Karlsruhe, Institut für Kernphysik III: On-site laboratory training

KfK Karlsruhe, Institut fürNeutronenphysik und Reaktortechnik: Neutron collar development

KfK Karlsruhe, Institut für Kernphysik III: K-edge densitometry

Max Planck Institut für Festkörperphysik Stuttgart: High-pressure reflectivity studies (K. Syassen)

Siemens/KWU, Erlangen: Post-irradiation fuel element examination (R. Manzel)

Technischer Überwachungsverein Bayern, München: TRANSURANUS fuel pin code development (G. Sauer)

Technischer Überwachungsverein Hannover/Sachsen-Anhalt: TRANSURANUS fuel pin code development (D. Märtens)

Technischer Überwachungsverein Norddeutschland, Hamburg: TRANSURANUS fuel pin code development (H. Schmidt)

Technischer Überwachungsverein Südwest, Mannheim, Karlsruhe: TRANSURANUS fuel pin code development (I. Brestrich)

Technische Universität München: Mössbauer and μSR studies (M. Kalvius, W. Potzel, L. Asch, S. Zwirner)

Universität Stuttgart, IKE: Source term studies (H. Hocke)

Universität Stuttgart, IKE: Data bank system THERSYST (G. Neuer, G. Jaroma-Weiland)

Univ. München, Inst.Anorg.Chem.:Single crystal growth and X-ray diffraction (F. Lux, M. Böhme)

Italy

Centro Ceramico Bologna: Leaching studies, Indentation techniques (L. Esposito)

Centro Legnaro/Padova: RBS, Ion implantation, H-analysis on leached waste matrices (G. Della Mea, V. Rigato)

University of Padova: Analysis of glass surfaces (P. Mazzoldi)

University of Trento: Indentation techniques (R. DalMaschio)

University of Ancona: Neutron and bulk magnetization studies (R. Caciuffo)

Japan

Central Research Institute of Electricity Producing Industries (CRIEPI), Tokyo: Preparation and characterisation of minor actinide alloys; Dissolution studies on high burn-up fuel (CRIEPI,T.Ohe)

JAERI, Tokai Mura: Basic studies on nitride fuels (T.Ohmichi); Inductively-coupled plasma mass spectrometry; DIDPA actinide separation process (Y. Morita)

Netherlands

AKZO n.v., Arnhem: Production of alpha-emitting nuclides (M. Geerlings)

BCMN, JRC Petten: HFR Division, irradiation experiments (L. Debarberis, R.L. Moss)

University of Amsterdam: Low temperature magnetization and resistivity (F. R. de Boer, J. Franse, H. Nakotte)

Poland

Nuclear Institute, Warszawa: Channeling techniques, Radiation damage studies (A. Turos)

Portugal

LNETI, Sacavem: Physical chemistry of actinides (A. Piros de Matos, M. Almeida)

University of Coimbra: Neutron and X-ray studies (J.A. Paixão)

Russia

Academy of Sciences, IVTAN, Moscow: Studies on high-melting materials (A.E. Sheindlin)

Radium Khlopin Institute, St.Petersburg: Installation and field testing of a robotized system for safeguards analysis (N. Shulyak)

Spain

CIEMAT, Madrid: TRANSURANUS fuel pin code development (J. Lopez Jimenez)

Instituto de Acústica, Madrid: Acoustic aerosol scavenging (J.A. Gallego-Juarez)

Sweden

University of Uppsala: Solid state theory of actinides (B. Johansson, O. Eriksson)

Infrasonik AB, Årista: manufacture of infraphones (M. Olsson)

Switzerland

ETH, Zürich: Single crystal growth, magnetic, optical and transport properties, preparation of U and Th compounds (O. Vogt, P. Wachter, F. Hulliger, K. Mattenberger)

Paul-Scherrer-Institut, Würenlingen: TRANSURANUS fuel pin code application (C. Ott); Post-irradiation structural investigations by electron microscopy

United Kingdom

Birkbeck College: neutron and magnetization studies (K. McEwen)

Royal Institute, London: Calculation of fission products in UO_2

University of Birmingham: Preparation of high purity single crystals (D. Fort)

University of Keele: X-ray and neutron scattering (W.G. Stirling, W.J. Nuttall, S. Langridge)

University of Warwick: Compton scattering (M.J. Cooper); Radiative properties at high temperatures (G. Hyland)

University of Salford: Solid gas precipitates (S. Donnelly)

USA

Argonne National Laboratory: Neutron scattering (C.K. Loong; L. Soderholm, S. Kern, G. Goodman)

Brookhaven National Laboratory: High-resolution and magnetic X-ray scattering (D. Gibbs, J. Axe)

Lawrence Livermore National Laboratory: Surface reactions (C. Colmenares)

Los Alamos National Laboratory: Materials preparation and photoemission (B. Cort, J. Ward, L. Cox)

Oak Ridge National Laboratory: Material preparation, high pressure X-ray and optical studies (R.G. Haire, J.R. Peterson)

University of W. Virginia, Morgantown, W.-Virginia: Actinide theory (G.J. Hu, B.R. Cooper)

Purdue University, West Lafayette, Indiana: Magnetisation and sample preparation (G. Honig)

Annex III

Human Resources

1. Institute's Staff

The evolution of the staff situation in 1993 is given for three reference dates on the table below:

Date	A2-A4	A5-A8	B	C	D	total
01.01.	22	23	80	67	1	193
01.10.	23	22	79	68	1	193
31.12.	23	22	79	69	1	194

2. Visiting Scientists and Scientific Fellows

30 graduate sectorial grantees from the following countries spent in 1993 prolonged periods of time at the Institute:

D (3)
ES (3)
F (6)
GR (3)
I (3)
P (3)
UK (3)
B (3)
China (2)
(CS (1)

3. Secondment from other laboratories

2 experts were delegated from other European research establishments to carry out specific tasks at the ITU in 1993, i.e. from CEA Cadarache (F) and CEA Saclay (F).

Annex IV

Organisational Chart

Institute Director	Jacques VAN GEEL
Adviser, acting as Institute Deputy Director	Jean FUGER
Adviser (Programmes)	Hans Eberhard SCHMIDT
Personnel and Administration	Paul BLAES
S/T Services:	
- Technical Physics	Michel COQUERELLE
- Applied Physics	Hansjoachim MATZKE
- Nuclear Technology	Karl RICHTER
- Nuclear Chemistry	Lothar KOCH
- Actinide Research	Ulrich BENEDICT
S/T-Support:	
- Radiation Protection	Klaas BUIJS
- Technical Services	Gérard SAMSEL

Annex V

Glossary of Acronyms and Abbreviations

ABB: Asea Brown Bovery
ASCII: American Standard Code for Information Interchange
AUC: Ammonium Uranyl Carbonat
BN: BelgoNucléaire
BNL: Brookhaven National Laboratory
BNFL: British Nuclear Fuels plc
BOL: Beginning Of Life (of a fuel pin)
BWR: Boiling Water Reactor
CANDU: CANadian Deuterium Uranium reactor
CCD: Charge Coupled Device
CEA: Commissariat à l'Energie Atomique (F)
CEC: Commission of the European Communities
CEF: Crystalline Electric Field
CEN: Centre d'Etudes Nucléaires
CENG: Centre d'Etudes Nucléaires, Grenoble
CF: Crystal-Field
CHEMIF: code to calculate the chemical behaviour of high burn-up fuel
CMPO: Carbonyl-Methyl-Phosphine Oxide
COGEMA: COmpagnie GEnerale des MAtières nucléaires
CRIEPI: Central Research Institute of the Electric Power Industry (Japan)
DCS: Division Contrôle de Sécurité
DESY: DEutsches Elektron-SYnchrotron
DG I: Directorate General "External Relations" of the Commission of the European Communities, Brussels
DG XII:Directorate General "Science, Research, and Development" of the Commission of the European Communities, Brussels
DG XIII: Directorate General "Telecommunication, Information Industry, and Innovation" of the Commission of the European Communities, Brussels and Luxembourg
DG XVII: Directorate General "Energy" of the Commission of the European Communities, Brussels and Luxembourg
DOS: Density of States
DSC: Differential Scanning Calorimetry
DTA: Differential Thermal Analysis
ECN: Energie Centrum Nederland (Petten, NL)
ECSAM: European Commission's Safeguards Analytical Measurements
EDAX: Energy-Dispersive Analysis with X-rays
EDF: Electricité de France
EDS: Energy-Dispersive Spectroscopy
EOL: End Of Life
EDX: Energy-Dispersive X-ray spectroscopy
EFPH: Effective Full Power Hours
EMPA: Electron MicroProbe Analysis (also EPMA)
EPMA: Electron Probe Micro-Analysis
ESRF: European Synchrotron Radiation Facility
ETH: Eidgenössische Technische Hochschule (Zürich, CH)
EURATOM: EURopean ATOMic energy community
FBFC: Compagnie Franco-Belge de Fabrication de Combustible
FCCI: Fuel Cladding Chemical Interaction

FIAP: Fraction of inventory In the Aqueous Phase
FIMA: Fissions per Initial Metal Atom
FR: Fast Reactor
FRG: Federal Republic of Germany
FUMEX: FUel Modelling at EXtended Burnup research programme
FUTURE: code for fuel transient calculations
FWHM: Full Width at Half Minimum
GDMS: Glow Discharge Mass Spectrometer
GKN: GemeinschaftsKernkraftwerk Neckar GmbH (D)
HAW: Highly Active Waste
HAZOP: HAZards of OPeration study
HBC: High Burn-up Chemistry
HEPA filter: High Efficiency Particulate Air filter
HEU: Highly Enriched Uranium
HFR: High Flux Reactor (Petten, NL)
HPXRD: High-Pressure X-Ray Diffraction
HRUPS: High Resolution Ultravilet Photoelectron Spectroscopy
IAEA: International Atomic Energy Agency (Vienna, A)
IBM: International
ICEN:Instituto de Ciencia e Energia Nucleare (Savacem, P)
ICP-MS: Inductively Coupled Plasma Mass Spectrometry
ICRP: International Commission on Radiological Protection
IDA: Isotope Dilution Analysis
IDMS: Isotope Dilution Mass Spectrometry
ILL: Institut Max von Laue - Paul Langevin (Grenoble, FR)
IMA: Initial heavy Metal Atoms
INETI: Instituto Nacional de Engenharia e Technologia Industrial (Savacem, P)
IRMM: Institute for Reference Materials and Measurements
ISO: International Standards Organization
ITU: Institute for Transuranium Elements
JAERI: Japan Atomic Energy Research Institute
JRC: Joint Research Centre
KEMA: N.V. tot Keuring van Electrotechnische Materialien (Arnhem, NL)
KfK: Kernforschungszentrum Karlsruhe (Karlsruhe, D)
KKI: KernKraftwerk Isar
KORIGEN: KfK development of the ORIGEN Code
KR: Kondo Resonance
KWU: KraftWerk-Union (D)
LAF: LAser-Flash apparatus
LEU: Low-Enriched Uranium
LHGR: Linear Heat Generation Rate
LNETI: Laboratorio Nacional de Engenharia e Tecnologia Industrial (Savacem, P)
LPDA: Laser Phase Doppler Anemometer
LSDA: Local Spin Density Approximation
LWR: Light Water Reactor
MA: Minor Actinides (Np, Am, Cm)
MIMAS: MIcronized-MASter blend process
MITI: Ministry of International Trade and Industry
MITRA: code to calculate the release of radio-nuclides
MOX: Mixed OXide fuel
μ-Sr: Muon Spin Rotation spectroscopy
NDA: Non-Destructive Analysis
NDT: Non-Destructive Testing
Nd-YAG: Neodymium-Yttrium Aluminium Garnet laser
NILOC: Nitride Irradiation with LOw Carbon content
NIMPHE: NItrures Mixtes dans PHenix à joint HElium
NNC: National Nuclear Corporation (Knutsford, GB)

NRC: Nuclear Regulatory Commission (USA)
NSLS: National Synchrotron Light Source
OM: Optical Microscopy
ORIGEN: Oak Ridge Isotope GENeration and depletion code
ORNL: Oak Ridge National Laboratory
OSL: On-Site Laboratory
PHEBUS: French test reactor (Cadarache, F)
PHEBUS-FP: Programme to study fission product release and their distribution in the primary circuit
PHENIX: French prototype fast reactor
PIE: Post Irradiation Examination
PNC: Power reactor and Nuclear fuel development Corporation
POMPEI: POM PEtten Irradiation experiment to study the structure of nitride fuel
PUDOL: Dosimetry computer program
PUREX: Plutonium and Uranium Recovery by EXtraction
PWR: Pressurized Water Reactor
QA: Quality Assurance
RADONN: RAdioactive Decay Of Nuclides and Neutronics
RBS: Rutherford Backscattering Spectroscopy
RBU: Reaktor Brennelemente Union
RSD: Relative Standard Deviation
RUMP: Computer code to evaluate RBS Spectra
SCE: Saturated Calomel Electrode
SCK: Studie Centrum voor Kernenergie
SECC: Service d'Etudes de Cycles de Combustibles (Grenoble, FR)
SEM: Scanning Electron Microscopy
SIMFUEL: SIMulated high burn-up UO_2 FUEL (with major non-volatile fission products)
SO: Spin-Orbit
SUPERFACT: Minor Actinide Irradiation in Phenix
TBP: TriButyl Phosphate
TEM: Transmission Electron Microscopy
TG: Thermo Gravimetric analysis
THERSYST -ACT: THERmophysical database SYSTem for ACTinides and Actinide Compounds
THORP: THermal Oxide Reprocessing Plant (Sellafield, UK)
TIMS: Thermal Ionization Mass Spectrometry
TOPO: Tri-Octyl Phosphine Oxide
TRABI: project to study TRAnsport of BIg particles
TRANSURANUS: Fuel behaviour code (ITU Karlsruhe)
TRIO: Irradiation capsule, HFR Petten
TRPO: TRialkyl Phosphine Oxide
TRU: TRansUranium elements
TRUEX: TRansUranium EXtraction
TU: TransUranium nuclides
TUAR: Annual Report, Institute for Transuranium Elements (ITU, Karlsruhe)
TUBRNP: Trans-Uranus BuRN- uP model
TUCOP: Transient UnderCooled OverPower
UKAEA: United Kingdom Atomic Energy Agency
UPS: Ultraviolet Photoelectron Spectroscopy
VGB: Vereinigung der Grosskraftwerk-Betreiber (D)
WAK: WiederAufbereitungsanlage Karlsruhe
XPS: X-ray Photoelectron Spectroscopy
XRD: X-Ray Diffraction

Annex VI

List of Contributors to this Document

1. Specific Programmes

Basic Safety Research on Nuclear Fuels
*Hj. Matzke, J.P. Hiernaut, K. Lassmann, C. O'Carroll,
I. Ray, C. Ronchi, H.A. Tasman, C.T. Walker*

Safety Aspects of Fuel Operation and Handling
K. Richter, K. Buijs, B. Chavane, J.F. Gueugnon

Actinide Determination and Recycling
L. Koch, H. Bokelund, J.P. Glatz, G. Nicolaou

Characterisation of Waste Forms and of High Burn-Up Fuel
*M. Coquerelle, D. Bottomley, J.P. Glatz, Hj. Matzke, G. Nicolaou,
S. Sari, E. Toscano, C.T. Walker, D. H. Wegen*

Actinide Research
*U. Benedict, M. Brooks, G. Lander, J. Magill, J. Naegele, J. Rebizant, J.C. Spirlet,
H.E. Schmidt, F. Wastin*

2. Exploratory Research (Acoustic Aerosol Scavenging)

K. Richter, P. Capéran, J. Somers

3. Scientific-Technical Support to Community Policies

Support to the Directorate General for External Relations DG I
L. Koch, M. Betti, I. Garcia Alonso, R. Wellum

Support to the Directorate General for Innovation and Technology Transfer DG XII
K. Richter, P. Capéran, J. Somers

Support to the EURATOM Safeguards Directorate DG XVII

L. Koch, M. Betti, R. Wellum

4. Work for Third Parties

C. Apostolidis, D. Bottomley, M. Coquerelle, J.P. Glatz, L. Koch, H.J. Matzke, K. Richter, C. Ronchi, E. Toscano

5. Scientific Infrastructure

J. Fuger, J. F. Babelot, W. Bartscher

Annex VII

Previous Progress Reports of the Institute for Transuranium Elements

TUSR	Period	COM-Nr	EUR-Nr
1	Jan - Jun 1966	1580	
2	Jul - Dec 1966	1522	
3	Jan - Jun 1967	1745	
4	Jul - Dec 1967	2007	
5	Jan - Jun 1968	2172	
6	Jul - Dec 1968	2300	
7	Jan - Jun 1969	2434	
8	Jul - Dec 1969	2576	
9	Jan - Jun 1970	2664	
10	Jul - Dec 1970	2750	
11	Jan - Jun 1971	2833	
12	Jul - Dec 1971	2874	
13	Jan - Jun 1972	2939	
14	Jul - Dec 1972	3014	
15	Jan - Jun 1973	3050	
16	Jul - Dec 1973	3115	
17	Jan - Jun 1974	3161	
18	Jul - Dec 1974	3204	
19	Jan - Jun 1975	3241	
20	Jul - Dec 1975	3289	
21	Jan - Jun 1976	3358	
22	Jul - Dec 1976	3384	
23	Jan - Jun 1977	3438	6475 E
24	Jul - Dec 1977	3484	7209 E
25	Jan - Jun 1978	3526	7459 E
26	Jul - Dec 1978	3582	7227 E
27	Jan - Jun 1979	3657	7483 E
28	Jul - Dec 1979	3714	7509 E
29	Jan - Jun 1980	3822	7857 E
30	Jul - Dec 1980	3846	8230 E
31	Jan - Jun 1981	3898	8447 E
32	Jul - Dec 1981	3927	8777 E
33	Jan - Jun 1982	3990	9581 E
34	Jul - Dec 1982	4048	10251 E
35	Jan - Jun 1983	4094	10266 E
36	Jul - Dec 1983	4117	10454 E
37	Jan - Jun 1984	4150	10470 E
38	Jul - Dec 1984	4165	11013 E
39	Jan - Jun 1985	4201	11835 E
40	Jul - Dec 1985	4263	11836 E

TUAR			
86	Jan - Dec 1986	4302	12233 E
87	Jan - Dec 1987		11783 E
88	Jan - Dec 1988		12385 E
89	Jan - Dec 1989		12849 E
90	Jan - Dec 1990		13815 E
91	Jan - Dec 1991		14493 E
92	Jan.-Dec.1992		15154 E
93	Jan.-Dec. 1993		15741 E

Previous Programme Progress Reports were confidential for a period of two years. Since 1977 they are made freely accessible after that period as EUR-Reports. They can be ordered from the Office for Official Publications of the European Communities, 2 rue Mercier, L-2985 Luxembourg, Tel. 499 28-1, Telex 1322 PUBOF LU

European Commisson

EUR 15741 — Institute for Transuranium Elements — Annual report 1993

H. E. Schmidt, J. Richter, L. Ruczka

Luxembourg: Office for Official Publications of the European Communities

1994 — 270 pp., — 21.0 x 29.7 cm

ISBN 92-826-4367-0

Venta y suscripciones • Salg og abonnement • Verkauf und Abonnement • Πωλήσεις και συνδρομές
Sales and subscriptions • Vente et abonnements • Vendita e abbonamenti
Verkoop en abonnementen • Venda e assinaturas

BELGIQUE BELGIË

Moniteur belge / Belgisch staatsblad

Rue de Louvain 42 / Leuvenseweg 42
B-1000 Bruxelles B-1000 Brussel
Tél. (02) 512 00 26
Fax (02) 511 01 84

Jean De Lannoy

Avenue du Roi 202 / Koningslaan 202
B-1060 Bruxelles B-1060 Brussel
Tél. (02) 538 51 69
Télex 63220 UNBOOK B
Fax (02) 538 08 41

Autres distributeurs/
Overige verkooppunten:

Librairie européenne/ Europese boekhandel

Rue de la Loi 244 Wetstraat 244
B-1040 Bruxelles B-1040 Brussel
Tél. (02) 231 04 35
Fax (02) 735 08 60

Document delivery:

Credoc

Rue de la Montagne 34 / Bergstraat 34
Bte 11 Bus 11
B-1000 Bruxelles B-1000 Brussel
Tél. (02) 511 69 41
Fax (02) 513 31 95

DANMARK

J. H. Schultz Information A/S

Herstedvang 10-12
DK-2620 Albertslund
Tlf. 43 63 23 00
Fax (Sales) 43 63 19 69
Fax (Management) 43 63 19 49

DEUTSCHLAND

Bundesanzeiger Verlag

Breite Straße 78-80
Postfach 10 05 34
D-50445 Köln
Tel. (02 21) 20 29-0
Telex ANZEIGER BONN 8 882 595
Fax 202 92 78

GREECE ΕΛΛΑΔΑ

G.C. Eleftheroudakis SA

International Bookstore
Nikis Street 4
GR-10563 Athens
Tel. (01) 322 63 23
Telex 219410 ELEF
Fax 323 98 21

ESPAÑA

Boletín Oficial del Estado

Trafalgar, 27-29
E-28071 Madrid
Tel. (91) 538 22 95
Fax (91) 538 23 49

Mundi-Prensa Libros, SA

Castelló, 37
E-28001 Madrid
Tel. (91) 431 33 99 (Libros)
431 32 22 (Suscripciones)
435 36 37 (Dirección)
Télex 49370-MPLI-E
Fax (91) 575 39 98

Sucursal:

Librería Internacional AEDOS

Consejo de Ciento, 391
E-08009 Barcelona
Tel. (93) 488 34 92
Fax (93) 487 76 59

Llibreria de la Generalitat de Catalunya

Rambla dels Estudis, 118 (Palau Moja)
E-08002 Barcelona
Tel. (93) 302 68 35
Tel. (93) 302 64 62
Fax (93) 302 12 99

FRANCE

Journal officiel
Service des publications des Communautés européennes

26, rue Desaix
F-75727 Paris Cedex 15
Tél. (1) 40 58 77 01/31
Fax (1) 40 58 77 00

IRELAND

Government Supplies Agency

4-5 Harcourt Road
Dublin 2
Tel. (1) 66 13 111
Fax (1) 47 80 645

ITALIA

Licosa SpA

Via Duca di Calabria 1 1
Casella postale 552
I-50125 Firenze
Tel. (055) 64 54 15
Fax 64 12 57
Telex 570466 LICOSA I

GRAND-DUCHÉ DE LUXEMBOURG

Messageries du livre

5, rue Raiffeisen
L-2411 Luxembourg
Tél. 40 10 20
Fax 49 06 61

NEDERLAND

SDU Overheidsinformatie

Externe Fondsen
Postbus 20014
2500 EA 's-Gravenhage
Tel. (070) 37 89 911
Fax (070) 34 75 778

PORTUGAL

Imprensa Nacional

Casa da Moeda, EP
Rua D. Francisco Manuel de Melo, 5
P-1092 Lisboa Codex
Tel. (01) 69 34 14
Fax (01) 69 31 66

Distribuidora de Livros Bertrand, Ld.ª

Grupo Bertrand, SA

Rua das Terras dos Vales, 4-A
Apartado 37
P-2700 Amadora Codex
Tel. (01) 49 59 050
Telex 15798 BERDIS
Fax 49 60 255

UNITED KINGDOM

HMSO Books (Agency section)

HMSO Publications Centre
51 Nine Elms Lane
London SW8 5DR
Tel. (071) 873 9090
Fax 873 8463
Telex 29 71 138

ÖSTERREICH

Manz'sche Verlags- und Universitätsbuchhandlung

Kohlmarkt 16
A-1014 Wien
Tel. (1) 531 610
Telex 112 500 BOX A
Fax (1) 531 61-181

SUOMI FINLAND

Akateeminen Kirjakauppa

Keskuskatu 1
PO Box 218
FIN-00381 Helsinki
Tel. (0) 121 41
Fax (0) 121 44 41

NORGE

Narvesen Info Center

Bertrand Narvesens vei 2
PO Box 6125 Etterstad
N-0602 Oslo 6
Tel. (22) 57 33 00
Telex 79668 NIC N
Fax (22) 68 19 01

SVERIGE

BTJ AB

Traktorvgen 13
S-22100 Lund
Tel. (046) 18 00 00
Fax (046) 18 01 25
30 79 47

SCHWEIZ / SUISSE / SVIZZERA

OSEC

Stampfenbachstraße 85
CH-8035 Zürich
Tel. (01) 365 54 49
Fax (01) 365 54 11

BĂLGARIJA

Europress Klassica BK Ltd

66, bd Vitosha
BG-1463 Sofia
Tel./Fax 2 52 74 75

ČESKÁ REPUBLIKA

NIS ČR

Havelkova 22
CZ-130 00 Praha 3
Tel. (2) 235 84 46
Fax (2) 235 97 88

MAGYARORSZÁG

Euro-Info-Service

Európa Ház
Margitsziget
H-1138 Budapest
Tel./Fax 1 111 60 61
1 111 62 16

POLSKA

Business Foundation

ul. Krucza 38/42
PL-00-512 Warszawa
Tel. (22) 621 99 93, 628-28-82
International Fax&Phone
(0-39) 12-00-77

ROMÂNIA

Euromedia

65, Strada Dionisie Lupu
RO-70184 Bucuresti
Tel./Fax 0 12 96 46

RUSSIA

CCEC

9,60-letiya Oktyabrya Avenue
117312 Moscow
Tel./Fax (095) 135 52 27

SLOVAKIA

Slovak Technical Library

Nm. slobody 19
SO-812 23 Bratislava 1
Tel. (7) 220 452
Fax : (7) 295 785

CYPRUS

Cyprus Chamber of Commerce and Industry

Chamber Building
38 Grivas Dhigenis Ave
3 Deligiorgis Street
PO Box 1455
Nicosia
Tel. (2) 449500 462312
Fax (2) 458630

MALTA

Miller distributors Ltd

PO Box 25
Malta International Airport
LQA 05 Malta
Tel. 66 44 88
Fax 67 67 99

TÜRKIYE

Pres Gazete Kitap Dergi Pazarlama Dagitim Ticaret ve sanayi AŞ

Narlibaçhe Sokak N. 15
Istanbul-Cagaloğlu
Tel. (1) 520 92 96 - 528 55 66
Fax 520 64 57
Telex 23822 DSVO-TR

ISRAEL

ROY International

PO Box 13056
41 Mishmar Hayarden Street
Tel Aviv 61130
Tel. 3 496 108
Fax 3 648 60 39

EGYPT
MIDDLE EAST

Middle East Observer

41 Sherif St.
Cairo
Tel Fax 39 39 732

UNITED STATES OF AMERICA / CANADA

UNIPUB

4611-F Assembly Drive
Lanham, MD 20706-4391
Tel. Toll Free (800) 274 4888
Fax (301) 459 0056

CANADA

Subscriptions only
Uniquement abonnements

Renouf Publishing Co. Ltd

1294 Algoma Road
Ottawa, Ontario K1B 3W8
Tel. (613) 741 43 33
Fax (613) 741 54 39
Telex 0534783

AUSTRALIA

Hunter Publications

58A Gipps Street
Collingwood
Victoria 3066
Tel. (3) 417 5361
Fax (3) 419 7154

JAPAN

Kinokuniya Company Ltd

17-7 Shinjuku 3-Chome
Shinjuku-ku
Tokyo 160-91
Tel. (03) 3439-0121

Journal Department

PO Box 55 Chitose
Tokyo 156
Tel. (03) 3439-0124

SOUTH-EAST ASIA

Legal Library Services Ltd

STK Agency
Robinson Road
PO Box 1817
Singapore 9036

SOUTH AFRICA

Safto

5th Floor, Export House
Cnr Maude & West Streets
Sandton 2146
Tel. (011) 883-3737
Fax (011) 883-6569

AUTRES PAYS
OTHER COUNTRIES
ANDERE LÄNDER

Office des publications officielles des Communautés européennes

2, rue Mercier
L-2985 Luxembourg
Tél. 499 28-1
Télex PUBOF LU 1324 b
Fax 48 85 73/48 68 17

3/94

15 CG-NA-15741-EN-C

NOTICE TO THE READER

All scientific and technical reports published by the European Commission are announced in the monthly periodical **'euro abstracts'**. For subscription (1 year: ECU 60) please write to the address below.

ISBN 92-826-4367-0

OFFICE FOR OFFICIAL PUBLICATIONS
OF THE EUROPEAN COMMUNITIES

L-2985 Luxembourg

9 789282 643679